

Tom Proulx *Editor*

Civil Engineering Topics, Volume 4

Proceedings of the 29th IMAC,
A Conference on Structural Dynamics, 2011



 Springer

The Springer logo, which consists of a stylized chess knight piece facing left, followed by the word "Springer" in a serif font.

Conference Proceedings of the Society for Experimental Mechanics Series

For other titles published in this series, go to
www.springer.com/series/8922

Tom Proulx
Editor

Civil Engineering Topics, Volume 4

Proceedings of the 29th IMAC, A Conference on Structural
Dynamics, 2011

Editor

Tom Proulx
Society for Experimental Mechanics, Inc.
7 School Street
Bethel, CT 06801-1405
USA
tom@sem1.com

ISSN 2191-5644 e-ISSN 2191-5652
ISBN 978-1-4419-9315-1 e-ISBN 978-1-4419-9316-8
DOI 10.1007/978-1-4419-9316-8
Springer New York Dordrecht Heidelberg London

Library of Congress Control Number: 2011923969

© The Society for Experimental Mechanics, Inc. 2011

All rights reserved. This work may not be translated or copied in whole or in part without the written permission of the publisher (Springer Science+Business Media, LLC, 233 Spring Street, New York, NY 10013, USA), except for brief excerpts in connection with reviews or scholarly analysis. Use in connection with any form of information storage and retrieval, electronic adaptation, computer software, or by similar or dissimilar methodology now known or hereafter developed is forbidden.

The use in this publication of trade names, trademarks, service marks, and similar terms, even if they are not identified as such, is not to be taken as an expression of opinion as to whether or not they are subject to proprietary rights.

Printed on acid-free paper

Springer is part of Springer Science+Business Media (www.springer.com)

Preface

Civil Structures Topics represents one of six clusters of technical papers presented at the 29th IMAC, A Conference and Exposition on Structural Dynamics, 2011 organized by the Society for Experimental Mechanics, and held in Jacksonville, Florida, January 31 - February 3, 2011. The full proceedings also include volumes on Advanced Aerospace Applications; Modal Analysis, Linking Models and Experiments, Rotating Machinery, Structural Health Monitoring, Shock and Vibration; and Sensors, Instrumentation, and Special Topics.

Each collection presents early findings from experimental and computational investigations on an important area within Structural Dynamics. The current volume on *Civil Structures Topics* includes studies on Human Loading, Vibration Control, Bridges, Modal Parameter Identification, System Identification, Modal Testing, Experimental Techniques, and Processing Modal Data.

Understanding the dynamic response of large civil structures improves design and safety, extends life, and reduces maintenance. IMAC has become a principle technical venue for dissemination of the latest techniques devoted to field testing of civil structural systems and components, processing of response data and identification of dynamic structural properties, calibration and validation of numerical structural models, and assessment of structural condition based on dynamic properties.

The organizers would like to thank the authors, presenters, session organizers and session chairs for their participation in this track.

Bethel, Connecticut

Dr. Thomas Proulx
Society for Experimental Mechanics, Inc

Contents

1	Multi-dimensional Calibration of Impact Dynamic Models	1
	L.G. Horta, M.C. Reaves, M.S. Annett, K.E. Jackson, NASA Langley Research Center	
2	Dynamic Analysis of Railway Bridges by Means of the Spectral Method	21
	G. Catania, S. Sorrentino, University of Bologna	
3	Advanced Operational Modal Analysis Methods for Linear Time Periodic System Identification	31
	M.S. Allen, University of Wisconsin-Madison; S. Chauhan, Brüel & Kjær Sound & Vibration Measurement A/S; M.H. Hansen, Risø National Laboratory	
4	Normalization of Complex Modes from Mass Perturbations	45
	D.-W. Seo, F. Moghim, D. Bernal, Northeastern University	
5	Numerical Continuation of Periodic Orbits for Harmonically Forced Nonlinear Systems	51
	M.W. Sracic, M.S. Allen, University of Wisconsin-Madison	
6	Identification of the Tensile Force in Tie-rods of Historical Constructions	71
	H.T.M. Luong, L.F. Ramos, R. Aguilar, University of Minho	
7	Data Fusion for System Identification of the Humber Bridge	83
	M. Döhler, INRIA; B. Jaishi, The University of Sheffield; L. Mevel, INRIA; J.M.W. Brownjohn, The University of Sheffield	
8	Human-induced Vibration Propagation on a Composite Floor System	99
	O.F. Tigli, McNamara/Salvia Inc. Consulting Engineers	
9	Mitigation of Low-velocity, Wind-induced Vibration of an Architectural Spire	109
	O.F. Tigli, McNamara/Salvia Inc. Consulting Engineers; L. Caracoglia, Northeastern University	
10	Closed-loop System Identification of Alstom 3MW Wind Turbine	121
	C.E. Carcangiu, I.F. Balaguer, ALSTOM Wind; S. Kanev, ECN Wind Energy; M. Rossetti, ALSTOM Wind	
11	Reduced Order Modal-space Wireless Control of Civil Engineering Structures	129
	R.A. Swartz, Michigan Technological University	

12	Wind Turbine Structural Damping Control for Tower Load Reduction	141
	A. Rodríguez T., C.E. Carcangiu, I. Pineda, Alstom Wind; T. Fischer, B. Kuhnle, M. Scheu, Universität Stuttgart; M. Martin, Alstom Wind	
13	Identification of Dynamic Properties of Open-deck Viaducts Under Passing Train Loads	155
	K. Matusoka, K. Kaito, Osaka University; T. Watanabe, M. Sogabe, Railway Technical Research Institute	
14	Risk Assessment of Dolphin Protected Bridge Pier Considering Collision Point Analysis	163
	H.-J. Kim, J. Lim, W. Park, H.-M. Koh, Seoul National University	
15	OMAX Testing of a Steel Bowstring Footbridge	173
	E. Reynders, D. Degrauwe, M. Schevenels, G. De Roeck, Katholieke Universiteit Leuven; P. Van den Broeck, KaHo Sint-Lieven; K. Deckers, P. Guillaume, Vrije Universiteit Brussel	
16	Bridge Pier Scour Measurement by Means of Bragg Grating Arrays: Laboratory Tests and Field Applications	183
	F. Ballio, A. Cigada, G. Crotti, F. Inzoli, S. Manzoni, Politecnico di Milano	
17	Numerical Investigation on the Measurement Uncertainty in Operational Modal Analysis of a Civil Structure	191
	A. Cattaneo, S. Manzoni, M. Vanali, Politecnico di Milano	
18	Measurement and Application of Bouncing and Jumping Loads Using Motion Tracking Technology	201
	V. Racic, J.M.W. Brownjohn, A. Pavic, The University of Sheffield	
19	Operational Modal Analysis for Guangzhou New TV Tower	211
	Y. Niu, P. Kraemer, C.-P. Fritzen, University of Siegen	
20	On the use of Shape Memory Alloys Dampers to Reduce the Vibration Amplitudes of Civil Engineering Cables	221
	L. Dieng, LCPC; V. Torra, CIRG-DFA-ETSECCPB; P. Pilvin, Université de Bretagne	
21	Dynamic Behavior of ‘Palazzo Lombardia’ Helisurface, Comparison Between Operational and Experimental Modal Analysis	235
	G. Busca, A. Cigada, Politecnico di Milano; E. Mola, ECSD S.r.l.; F. Mola, M. Vanali, Politecnico di Milano	
22	Human-structure Interaction: Effects of Crowd Characteristics	247
	K.A. Salyards, R.J. Firman, III, Bucknell University	
23	Delamination Detection in Concrete Plates Using Output-only Vibration Measurements	255
	S. Xing, M.W. Halling, P.J. Barr, Utah State University	
24	Semi-active Control of Staircase Vibration Under Human Excitation	263
	R. Philp, P. Reynolds, D.S. Nyawako, The University of Sheffield	

- 25 A System Identification Based Approach for Estimating Modal Frequencies of Bridges Under Environmental Influence** 273
H. Nandan, Virginia Polytechnic Institute and State University; M.P. Singh, National Science Foundation Arlington
- 26 Feature Assimilation in Structural Health Monitoring Applications** 285
Saurabhu Prabhu, Jordan Supler, Sez Atamturktur, Clemson University
- 27 Decentralized Modal Analysis and System Identification Using Embedded Markov Parameter Extraction Within Distributed Wireless Sensor Networks** 297
J. Kim, J.P. Lynch, University of Michigan
- 28 Comparison Study of Output-only Subspace and Frequency-domain Methods for System Identification of Base Excited Civil Engineering Structures** 305
J. Kim, J.P. Lynch, University of Michigan
- 29 Footbridge Response Predictions and Their Sensitivity to Stochastic Load Assumptions** 313
L. Pedersen, C. Frier, Aalborg University
- 30 Modal Parameter Variations due to Earthquakes of Different Intensities** 321
R.P. Carreño, R.L. Boroschek, University of Chile
- 31 Operational Modal Analysis of a Historic Tower in Bari** 335
M. Diaferio, D. Foti, M. Mongelli, University of Bari; N.I. Giannoccaro, University of Salento; P. Andersen, Structural Vibration Solutions A/S
- 32 Monitoring of a Movable Bridge Mechanical Components for Damage Identification Using Artificial Neural Networks** 343
T. Dumlupinar, F.N. Catbas, University of Central Florida
- 33 Ambient Vibration Based Modal Identification of a Flexible Retaining Wall** 349
C. Rainieri, A. Dey, C. Laorenza, G. Fabbrocino, F. Santucci de Magistris, University of Molise
- 34 Structural Health Monitoring of a Bridge Model Using ARX Models** 357
T. Terrell, M. Gul, F.N. Catbas, University of Central Florida
- 35 Structural Health Monitoring and Evaluating Structural Performance of a Stadium** 365
H.O. Sazak, F.N. Catbas, M. Gul, University of Central Florida
- 36 Estimation of Damping for one of the New European Court Towers in Luxembourg** 373
R. Brincker, Aarhus University; A. Brandt, University of Southern Denmark; C.T. Georgakis, J.H. Roldsgaard, Technical University of Denmark; D. Schilz, INCA Ingenieurs Conseils Associes
- 37 Use of Wireless Smart Sensors for Detecting Human Falls Through Structural Vibrations** 383
B.T. Davis, J.M. Caicedo, S. Langevin, V. Hirth, University of South Carolina
- 38 Structural Health Indices for Steel Truss Bridges** 391
R.K. Giles, R. Kim, B.F. Spencer, Jr., L.A. Bergman, University of Illinois at Urbana-Champaign; C.K. Shield, University of Minnesota; S.C. Sweeney, U.S. Army ERDC-CERL

Multi-Dimensional Calibration of Impact Dynamic Models

Lucas G. Horta, Mercedes C. Reaves, Martin S. Annett, and Karen E. Jackson

NASA Langley Research Center

Hampton, VA 23681

ABSTRACT

NASA Langley, under the Subsonic Rotary Wing Program, recently completed two helicopter tests in support of an in-house effort to study crashworthiness. As part of this effort, work is on-going to investigate model calibration approaches and calibration metrics for impact dynamics models. Model calibration of impact dynamics problems has traditionally assessed model adequacy by comparing time histories from analytical predictions to test at only a few critical locations. Although this approach provides for a direct measure of the model predictive capability, overall system behavior is only qualitatively assessed using full vehicle animations. In order to understand the spatial and temporal relationships of impact loads as they migrate throughout the structure, a more quantitative approach is needed. In this work impact shapes derived from simulated time history data are used to recommend sensor placement and to assess model adequacy using time based metrics and orthogonality multi-dimensional metrics. An approach for model calibration is presented that includes metric definitions, uncertainty bounds, parameter sensitivity, and numerical optimization to estimate parameters to reconcile test with analysis. The process is illustrated using simulated experiment data.

NOMENCLATURE

$g_i(t)$	scalar function with time variation
i, k, l	integer indices
m	number of measured locations
n	number of impact shapes used in reconstruction
p	parameter vector
t	Time
v	response vector used for calibration
y	response vector
E	modulus of elasticity
E_t	tangent modulus
I	identity matrix
L	total number of time samples
M_1	calibration Metric 1
M_2	calibration Metric 2
N	number of solutions

Q	scalar with 2-norm of response vector for analysis
Q_e	scalar with 2-norm of response vector for experiment
δ_i	i^{th} impact shape contribution to response
ΔT	sample time
σ_i	i^{th} singular value
	i^{th} impact shape vector at measured locations
\mathbf{K}	shape matrix at un-measured locations
Φ	shape matrix at measured locations
$\bar{\Psi}, \bar{\Phi}$	normalized impact shape matrices
$Prob$	probability
max	maximum value
$\langle \cdot \rangle$	relational operators
$\left(\begin{array}{c} \cdot \\ \cdot \\ \cdot \end{array} \right)$	maximum of all maxima
$\left(\begin{array}{c} \cdot \\ \cdot \\ \cdot \end{array} \right)$	minimum of all minima
$(\cdot)^T$	matrix transpose

1 INTRODUCTION

As computational capabilities continues to improve and the cost associated with test programs continue to increase, certification of future rotorcraft will rely more on computational tools along with strategic testing of critical components. Today, MIL-STD 1290A (AV) [1] encourages designers of rotary wing vehicles to demonstrate compliance with the certification requirements for impact velocity and volume loss by analysis. Reliance on computational tools, however, will only come after rigorous demonstration of the predictive capabilities of existing computational tools. NASA, under the Subsonic Rotary Wing Program, is sponsoring the development and validation of such tools. *Jackson* in [2] discussed detailed requirements and challenges associated with certification by analysis. Fundamental to the certification effort is the demonstration of verification, validation, calibration, and algorithms for this class of problems. Work in this paper deals with the model calibration of systems undergoing impact loads.

The process of model calibration, which follows the verification and validation phases, involves reconciling differences between test and analysis. Most calibration efforts combine both heuristics and quantitative methods to assess model deficiencies, to consider uncertainty, to evaluate parameter importance, and to compute required model changes. Calibration of rotorcraft structure models presents particular challenges because the computational time, often measured in hours, limits the number of solutions obtainable in a timely manner. Oftentimes, efforts are focused on predicting responses at critical locations as opposed to assessing the overall adequacy of the model. For example *Kamat* in [3] conducted a survey, which at the time, studied the most popular finite element analysis codes and validation efforts by comparing impact responses from a UH-1H helicopter drop test. Similarly, *Wittlin* and *Gamon* in [4] used the KRASH analysis program for data correlation of the UH-1H helicopter. Another excellent example of a rotary wing calibration effort is that of *Cronkhite* and *Mazza* in [5] comparing results from a U.S. Army's Composite helicopter with simulation data from the KRASH analysis program. Recently, *Tabiei*, *Lawrence*, and *Fasanella* [6] reported on a validation effort using anthropomorphic test dummy data from crash tests to validate an LS-DYNA finite element model. Common to all these calibration efforts is the use of scalar deterministic metrics.

One complication with calibration efforts of nonlinear models is the lack of universally accepted metrics to judge model adequacy. Work by *Oberkampff et al.* [7] and later *Schwer et al.* [8] are two noteworthy efforts that provide users with metrics to evaluate nonlinear time histories. Unfortunately, seldom does one see them used to assess model adequacy. In addition, the metrics as stated in [7] and [8] do not consider the multi-dimensional aspect of the problem explicitly. A more suitable metric for multi-dimensional calibration exploits the concept of impact shapes as proposed by *Anderson et al.* in [9] and demonstrated by *Horta et al.* in [10]. Aside from the metrics themselves, the verification, validation, and calibration elements, as described by *Roach* [11], *Oberkampff* [12], *Thaker* [13], and *Atamturktur* [14], must be adapted to rotorcraft problems. Because most applications in this area use commercially available codes, it is assumed that code verification and validation have been addressed elsewhere. Thus, this work concentrates on calibration elements only.

Fundamental to the success of the model calibration effort is a clear understanding of the ability of a particular model to predict the observed behavior in the presence of modeling uncertainty. The approach proposed in this paper is focused primarily on model calibration using parameter uncertainty propagation and quantification, as opposed to a search for a reconciling solution. The process set forth follows a three-step approach. First, Analysis of Variance (ANOVA) as described in references [15-18] is used for parameter selection and sensitivity. To reduce the computational burden associated with variance based sensitivity estimates, response surface models are created and used to estimate time histories. In our application, the Extended Radial Basis Functions (ERBF) response surface method, as described by *Mullur* [19-20], has been implemented and used. Second, after ANOVA estimates are completed, uncertainty propagation is conducted to evaluate uncertainty bounds and to gage the ability of the model to explain the observed behavior by comparing the statistics of the 2-norm of the response vector between analysis and test. If the model is reconcilable according to the metric, the third step seeks to find a parameter set to reconcile test with analysis by minimizing the prediction error using the optimization scheme proposed *Regis and Shoemaker* [21]. To concentrate on the methodology development, simulated experiment data has been generated by perturbing an existing model. Data from the perturbed model is used as the target set for model calibration. To keep from biasing this study, changes to the perturbed model were not revealed until the study was completed.

In this paper, a general description of the helicopter model will first be presented, followed by a description of basic model calibration elements. These elements include time and spatial multi-dimensional metrics, parameter selection, sensitivity using analysis of variance, and optimization strategy for model reconciliation. Other supporting topics discussed are sensor placement to assure proper evaluation of multi-dimensional orthogonality metrics, prediction of unmeasured responses from measured data, and the use of surrogates for computationally efficiency. Finally, results for the helicopter calibrated model are presented and, at the end, the actual perturbations made to the original model are revealed for a quick assessment.

2 DESCRIPTION OF HELICOPTER TEST ARTICLE

A full-scale crash test of an MD-500 helicopter, as described by *Annett and Polanco* in [22], was conducted at the Landing and Impact Research (LandIR) Facility at NASA Langley Research Center (LaRC). [Figure 1a](#) shows a photograph of the test article while it was being prepared for test, including an experimental dynamic energy absorbing honeycomb structure underneath the fuselage designed by *Kellas* [23]. The airframe, provided by the US Army's Mission Enhanced Little Bird

(MELB) program, has been used for civilian and military applications for more than 40 years. NASA Langley is spearheading efforts to develop analytical models capable of predicting the impact response of such systems.

3 LS-DYNA MODEL DESCRIPTION

To predict the behavior of the MD-500 helicopter during a crash test, an LS-DYNA [24] finite element model (FEM) of the fuselage, as shown in [Figure 1b](#), was developed and reported in [22]. The element count for the fuselage was targeted to not exceed 500,000 elements, including seats and occupants; with 320,000 used to represent the energy absorbing honeycomb and skid gear. Shell elements were used to model the airframe skins, ribs and stiffeners. Similarly, the lifting and pullback fixtures, and the platform supporting the data acquisition system (mounted in the tail) were modeled using rigid shells. Concentrated masses like the rotor, tail, and fuel were modeled using ballast. For materials, the fuselage section is modeled using Aluminum 2024-T3 with elastic-plastic properties, whereas the nose is fiberglass and the engine fairing is Kevlar fabric. Instead of using the complete “as-tested” FEM model, this study uses a simplified model created by removing the energy absorbing honeycomb, skid gears, anthropomorphic dummies, data acquisition system, and lifting/pull-back fixtures. After these changes, the resulting simplified model is shown in [Figure 2](#). Even with all these components removed, the simplified model had 27,000 elements comprised primarily of shell elements to represent airframe skins, ribs and stiffeners. The analytical test case used for calibration, simulates a helicopter crash onto a hard surface with vertical and horizontal speeds of 26 ft/sec and 40 ft/sec, respectively. For illustration, [Figure 3](#) shows four frames from an LS-DYNA simulation as the helicopter impacts the hard surface.

4 PROBLEM FORMULATION

Calibration of models is a process that requires analysts to integrate different methodologies in order to achieve the desired end goal which is to reconcile prediction with observations. Starting with an analytical model that incorporates the physics of the test article, this model is initially judged based on some pre-established calibration metrics. Although there are no universally accepted metrics, the work in this paper uses two metrics; one that addresses the predictive capability of time responses and a second metric that addresses multi-dimensional spatial correlation of sensors for both test and analysis data. After calibration metrics are established, the next step in the calibration process involves parameter selection and uncertainty estimates using engineering judgment and available data. With parameters selected and uncertainty models prescribed, the effect of parameter variations on the response of interest must be established. If parameter variations are found to significantly affect the response of interest, then calibration of the model can proceed to determine a parameter set to reconcile the model. These steps are described in more detail, as follows.

4.1 Time Domain Calibration Metrics

Calibration metrics provide a mathematical construct to assess fitness of a model in a quantitative manner. Work by *Oberkampf* [7] and *Schwer* [8] set forth scalar statistical metrics ideally suited for use with time history data. Metrics in terms of mean, variance, and confidence intervals facilitate assessment of experimental data, particularly when probability statements are sought. For our problem, instead of using response predictions at a particular point, a vector 2-norm of the system response is used as a function of time. An important benefit of using this metric is that it provides for a direct measure

of multi-dimensional closeness of two models. In addition, when tracked as a function of time, closeness is quantified at each time step.

Because parameters are uncertain, statistical measures of the metric need to be used to conduct assessments. With limited information about parameter uncertainty a uniform distribution function, which is the least informative distribution function, is the most appropriate representation to model parameter uncertainty. This uncertainty model is used to create a family of N equally probable parameter vectors, where N is arbitrarily selected. From the perspective of a user, it is important to know the probability of being able to reconcile measured data with predictions, given a particular model for the structure and parameter uncertainty. To this end, let $Q(t, p) \triangleq \|v(t, p)\|_2$ be a scalar time varying function, in which the vector v is defined as the 2-norm of the response at time t , using parameter vector p . Furthermore, let $\underline{\sigma}(t) = \min_{v,p} Q(t, p)$ be the minimum value over all parameter variations, and let $\bar{\sigma}(t) = \max_{v,p} Q(t, p)$ be the maximum value. Using these definitions and N LS-DYNA solutions corresponding to equally probable parameter vectors, a calibration metric can be established to bound the probability of test values falling outside the analysis bounds as;

$$M_1 = \text{Prob}(\underline{\sigma}(t) < Q_e(t) \vee Q_e(t) > \bar{\sigma}(t)) \ll 1/N \quad (4.1)$$

where $Q_e(t)$ is the 2-norm of responses from the experiment. Note that N controls tightness of the bounds and also the number of LS-DYNA solutions required.

The use of norms, although convenient, tends to hide the spatial relationships that exist between responses at different locations in the model. In order to study this spatial multi-dimensional dependency explicitly, a different metric must be established.

4.2 Spatial Multi-Dimensional Calibration Metric

Spatial multi-dimensional dependency of models has been studied in classical linear dynamic problems in terms of mode shapes or eigenvectors resulting from a solution to an eigenvalue problem. Unfortunately, the nonlinear nature of impact problems precludes use of any simple eigenvalue solution scheme. Alternatively, an efficient and compact way to study the spatial relationship is by using a set of orthogonal impact shapes basis vectors. Impact shapes, proposed by *Anderson* [9] and later by *Horta* [10], are computed by decomposing the time histories using orthogonal decomposition. For example, time histories from analysis or experiments can be decomposed using singular value decomposition as

$$y(x, t) = \sum_{i=1}^n \sigma_i \phi_i(x) g_i(t) \quad (4.2)$$

In this form, the impact shape vector ϕ_i sized $m \times 1$ contains the spatial distribution information for m sensors, $g(t)$ contains the time modulation information, σ contains scalar values with shape participation factors, and n is the number of impact shapes to be included in the decomposition, often truncated based on allowable reconstruction error. Although Eq. (4.2) is written in continuous time form, for most applications, time is sampled at fixed intervals such that $t = k\Delta T$ where the integer $k=0, \dots, L$ and ΔT is the sample time. From Eq. (4.2), the fractional contribution of the i^{th} impact shape to the total response is proportional to δ_i , defined as;

$$\delta_i = \sigma_i / \sum_{l=1}^n \sigma_l \quad (4.3)$$

Mimicking the approach used in classical dynamic problems, impact shapes can now be used to compare models using the orthogonality. Orthogonality, computed as the dot product operation of vectors (or matrices), quantifies the projection of one vector onto another. If the projection is zero, vectors are orthogonal, i.e., uncorrelated. This same idea applies when comparing test and analysis impact shapes. Numerically, the orthogonality metric is computed as;

$$M_2 = \bar{\Phi}^T \bar{\Psi} \quad (4.4)$$

where $\bar{\Phi}$ is sized $m \times l$ with l measured impact shapes at m locations and $\bar{\Psi}$ sized $m \times l$ are shapes computed using simulation data. Note that both $\bar{\Phi}$ and $\bar{\Psi}$ are normalized matrices such that $\bar{\Phi}^T \bar{\Phi} = I$ and $\bar{\Psi}^T \bar{\Psi} = I$. Because individual impact shape vectors are stacked column-wise, metric M_2 is a matrix sized $l \times l$ with diagonal values corresponding to the vector projection numerical value. If vectors are identical then their projection equals 1. Consequently, when evaluating models, multi-dimensional closeness with experiment is judged based on similarity of impact shapes and shape contributions. Two direct benefits of using impact shapes are discussed in the next two sections.

4.2.1 Algorithm for Response Interpolation

Adopting impact shapes as a means to compare models has two advantages. First, it allows for interpolation of unmeasured response points, and second, it provides a metric to conduct optimal sensor placement. During most test programs, the number of sensors used is often limited by the availability of transducers and the data acquisition system. Although photogrammetry and videogrammetry measurements provide significantly more data, even these techniques are limited to only those regions in the field of view of the cameras. At times, the inability to view responses over the full structure can mislead analysts as to their proper behavior. For this purpose, a hybrid approach has been developed to combine measured data with physics-based models to provide more insight into the full system response. Although the idea is perhaps new in the impact dynamics area, this approach is used routinely in modal tests where a limited number of measurements is augmented with predictions using the analytical stiffness matrix. This takes advantage of the inherent stiffness that relates the motion at different locations on the structure. Because in impact dynamic problems, the stiffness matrix is likely to be time varying, implementation of a similar approach is difficult. An alternate approach is to use impact shapes as a means to combine information from physics-based models with experimental data. Specifically, responses at unmeasured locations are related to measured locations through impact shapes. To justify the approach, Eq. (4.2) is re-written as;

$$\begin{pmatrix} y(t) \\ y_e(t) \end{pmatrix} = \sum_{i=1}^n \begin{bmatrix} \phi_i \\ \kappa_i \end{bmatrix} \sigma_i g_i(t) = \begin{bmatrix} \Phi \\ \mathbf{K} \end{bmatrix} S G(t) \quad (4.5)$$

where the matrix partitions are defined as

$$\begin{bmatrix} \Phi \\ \mathbf{K} \end{bmatrix} \triangleq \begin{bmatrix} \phi_1 & \cdots & \phi_n \\ \kappa_1 & \cdots & \kappa_n \end{bmatrix}; S \triangleq \begin{bmatrix} \sigma_1 & 0 & 0 \\ 0 & \ddots & 0 \\ 0 & 0 & \sigma_n \end{bmatrix}; G(t) \triangleq \begin{bmatrix} g_1(t) \\ \\ g_n(t) \end{bmatrix} \quad (4.6)$$

In contrast to Eq. (4.2), Eq. (4.5) shows explicitly responses at an augmented set of locations named $y_e(t)$, constructed using impact shapes κ_i at q unmeasured locations.

Using Eq. (4.5) with experimental data, the time dependency of the response can be computed as

$$SG(t) = (\Phi^T \Phi)^{-1} \Phi^T y(t) \quad (4.7)$$

Consequently, predictions for unmeasured locations can now be computed as

$$y_e(t) = K(\Phi^T \Phi)^{-1} \Phi^T y(t) \quad (4.8)$$

Although Eq.(4.7) requires a matrix inversion, the rank of this matrix is controlled by sensor placement. Hence, judicious pretest sensor placement must be an integral part of this process. Fortunately, because the impact shapes are computed using singular value decomposition, they form an orthonormal set of basis vectors, i.e. $(\Phi^T \Phi)^{-1} \cong I$. It is important to note that measured data is used to compute the impact shapes (at sensor locations) and the time dependent part of the response, whereas data from the analytical model are used to compute impact shapes at all unmeasured locations.

4.2.2 Optimum Sensor Placement for Impact Problems

Optimal sensor placement must be driven by the ultimate goals of the test. If model calibration is the goal, sensor placement must focus on providing information to properly evaluate the established metrics. In multidimensional calibration efforts using the orthogonality metric, sensor placement is critical because if sensors are not strategically placed, it is impossible to distinguish between impact shapes. Fortunately, the use of impact shapes enables the application of well established sensor placement algorithms routinely used in modal tests. Placement for our example used the approach developed by *Kammer* [25]. Using this approach sensors are placed to ensure proper numerical conditioning of the orthogonality matrix.

4.3 Parameter Selection

The parameter selection (parameters being in this case material properties, structural dimensions, etc., process relies heavily on the analyst's knowledge and familiarity with the model and assumptions. After an initial parameter selection is made, parameter uncertainty must be quantified empirically if data are available or oftentimes engineering judgment is ultimately used. With an initial parameter set and an uncertainty model at hand, parameter importance is assessed here using uncertainty propagation. That is, the LS-DYNA model is exercised with parameter values created using the *Halton* [26] deterministic sampling technique. Time history results are processed to compute the metrics and to assess variability. A by-product of this step produces variance-based sensitivity results which are used to rank the parameters. In the end, adequacy of the parameter set is judged based on the probability of one being able to reconcile test with analysis. If the probability is zero, as will be shown later in the example, the parameter selection must be revisited.

4.4 Optimization strategy

With an adequate set of parameters selected, the next step is to use an optimization procedure to determine values that reconcile test with the analysis. A difficulty with using classical optimization tools in this step is in the computational time it takes to obtain LS-DYNA solutions. Although in this helicopter example the execution time was optimized to be less than five minutes, the full model execution time is measured in days. This is why optimization tools for this step ideally must take advantage of all LS-DYNA solutions at hand. To address this issue, optimization tools that use surrogate models in addition to new LS-DYNA solutions are ideal. For the present application the Constrained Optimization using Response Surface (CORS) algorithm, developed by *Regis and Shoemaker* [21], has been implemented in MATLAB for reconciliation.

Specifically, the algorithm starts by looking for parameter values away from the initial set of LS-DYNA solutions, then slowly steps closer to known solutions by solving a series of local constrained optimization problems. This optimization process will produce a global optimum if enough steps are taken. Of course, the user controls the number of steps and therefore the accuracy and computational expense in conducting the optimization. In cases where the predictive capability of the surrogate model is poor, CORS adds solutions in needed areas. Convergence is therefore not dependent on the quality of surrogates. Because parameter uncertainty is not used explicitly in the optimization, this approach is considered to be deterministic. If a probabilistic approach was used instead, in addition to a reconciling set, the user should also be able to determine the probability that the parameter set found is correct. Lack of credible parameter uncertainty data precludes the use of probabilistic optimization methods at this time, but future work could use the same computational framework.

4.5 Analysis of Variance

Parameter sensitivity in most engineering fields is often associated with derivative calculations at specific parameter values. However, for analysis of systems with uncertainties, sensitivity studies are often conducted using ANOVA. In classical ANOVA studies, data is collected from multiple experiments while varying all parameters (factors) and also while varying one parameter at a time. These results are then used to quantify the output response variance due to variations of a particular parameter, as compared to the total output variance when varying all the parameters simultaneously. The ratio of these two variance contributions is a direct measure of the parameter importance. *Sobol et al.* [15] and others [16-18] have studied the problem as a means to obtain global sensitivity estimates using variance based methods. To compute sensitivity using these variance based methods, one must be able to compute many response predictions as parameters are varied. In our implementation, after a suitable set of LS-DYNA solutions are obtained, response surface surrogates are used to estimate additional solutions.

4.6 Response Surface Methodology

A response surface (RS) model is simply a mathematical representation that relates input variables (parameters that the user controls) and output variables (response quantities of interest), often used in place of computationally expensive solutions. Many papers have been published on response surface techniques, see for example *Myers* [27]. The one adopted here is the Extended Radial Basis Functions (ERBF) method as described by *Mullur* [19-20]. In this adaptive response surface approach, the total number of RS parameters computed equals $N(3n_p+1)$, where n_p is the number of parameters and N is the number of LS-DYNA solutions. The user must also prescribe two additional parameters: 1) the order of a local polynomial (set to 4 in the present case), and 2) a smoothness parameter (set to 0.15 here). Finally, the radial basis function is chosen to be an exponentially decaying function $e^{-(p-p_i)^2/2r_c^2}$ with characteristic radius r_c set to 0.15. A distinction with this RS implementation is that ERBF is used to predict full time histories, as opposed to just extreme values. In addition, ERBF is able to match the responses used to create the surrogate with prediction errors better than 10^{-10} .

5 RESULTS

Results described here are derived from the simplified LS-DYNA model, as shown in [Figure 2](#). This simplified model reduced the computational time from days to less than seven minutes and allowed for timely debugging of the software and

demonstration of the methodology, which is the main focus of the paper. Nonetheless, the same approach can be applied to the complete “as-tested” FEM model without modifications.

For evaluation purposes, simulated data is used in lieu of experimental data. Because more often than not analytical model predictions do not agree with the measured data, the simplified model was arbitrarily perturbed. Knowledge of the perturbations and areas affected are not revealed until the entire calibration process is completed. Data from this model, referred to as the perturbed model, takes the place of experimental data. In this study, no test uncertainty is considered. Therefore, only 1 data set is used for test.

Figure 4(a) depicts a wireframe of the simplified model showing only 405 nodes. Superimposed is a second wiring frame with connections to 34 nodes identified by an optimal sensor placement algorithm. At each node there can be up to 3 translational measurements, however, here the placement algorithm was instructed to place only 41 sensors. Figure 4(b) shows the location for the 41 sensors. Results from the optimal sensor placement located 8 sensors along the x direction, 10 sensors along the y direction, and 23 sensors along the z direction.

5.1 Initial Parameter Selection

Calibration efforts begin by selecting model parameters thought to be uncertain. Selecting these parameters is perhaps the most difficult step. Not knowing what had been changed in the perturbed model, the initial study considered displacements, stress contours, and plastic strain results at different locations on the structure before selecting the modulus of elasticity and tangent modulus at various locations. The parameters and uncertainty ranges selected are shown in Table 1. Without additional information about parameter uncertainty, the upper and lower bounds were selected using engineering judgment with the understanding that values anywhere between the bounds were equally likely.

With the parameter uncertainty definition in Table 1, LS-DYNA models can be created and executed to study the calibration metrics as described earlier. As an example, 150 LS-DYNA runs with the simplified model have been completed while varying parameters over the ranges shown in Table 1. To construct the uncertainty bounds, for each of the 150 runs $Q(t, p)$ is computed from velocities at 41 sensors (see Figure 4) and metric M_1 , in terms of $\bar{\sigma}, \underline{\sigma}$, are plotted in Figure 5 as a function of time; analysis (dashed-blue) and the simulated test (solid-red). With this sample size, the probability of being able to reconcile test with analysis during times when test results are outside the analysis bounds is less than 1/150. Figure 5 shows that during the interval between 0.01 and 0.02 seconds, the analysis bounds are above the test. Therefore, it is unlikely that one would be able to find parameter values within the selected set to reconcile analysis with test. This finding prompted another look at parameter selection and uncertainty models to determine a more suitable set.

5.2 Updated Parameter Selection

A second search for a revised parameter set involved conversations with the model developer and additional runs while varying parameter bounds to see their effect on M_1 . The second set of parameters selected, after considering several intermediate sets, consisted of thicknesses at various locations in the structure. A concern with varying thickness is its effect

on structural mass. However, because 80% of the helicopter model is comprised of non-structural masses, thickness changes had little impact on the total mass. [Table 2](#) shows a revised parameter set and ranges selected for the second study.

5.2.1 Evaluation of Calibration Metrics with Updated Parameter Set

Results for metric M_1 using the revised parameter set are shown in [Figure 6](#); solid red is $Q_e(t)$ with the simulated test data and in dotted blue lines are analysis bounds using 50 LS-DYNA runs. With 50 runs, the probability that LS-DYNA would produce results outside these bounds is less than 1/50. Consequently, if the test results are outside these bounds, the probability of reconciling the model with test is also less than 1/50. Even though [Figure 6](#) shows that, in certain areas, test results are very close to the analysis bounds; this new parameter set provides enough freedom to proceed with the calibration process.

Thus far, in this study, metric M_1 has been used exclusively to evaluate parameter adequacy and uncertainty bounds. What is missing from this evaluation is how well the model predicts the response at all locations. Considering that impact shapes provide a spatial multi-dimensional relationship between different locations, two models with similar impact shapes, all else being equal, should exhibit similar responses at all sensor locations. With this in mind, orthogonality results for the simplified model versus “test”, i.e., the perturbed model, are shown in [Figure 7](#). Essentially, the matrix M_2 , as defined in Eq. (4.4), is plotted with analysis along the ordinate and test along the abscissa. Colors represent the numerical value of the vector projections, e.g. a value of 1 (black) indicates perfect matching between test and analysis. Listed on the labels are the corresponding shape contribution to the response for both analysis (ordinate) and simulated test (top axis). For example, the first impact shape for analysis (bottom left) contributes 0.4 of the total response as compared to 0.39 for test. It is apparent that initial impact shape matching is poor at best with the exception of the first two shapes. An example of an impact shape is provided in [Figure 8](#). Here, a sequence of 8 frames for the test impact shape number 2 (contribution $\delta_2 = 0.18$) expanded to 405 nodes, is shown. Motion of the tail and floor section of the helicopter dominates.

5.2.2 Sensitivity with Updated Parameter Set

Another important aspect of the calibration process is in understanding how parameter variations affect the norm metric $Q(t, p)$. This information is used as the basis to remove or retain parameters during the calibration process. As mentioned earlier, sensitivity results in this study look at the ratio of the single parameter variance to the total variance of $Q(t, p)$. This ratio is plotted in [Figure 9](#) for each of the six parameters considered (as defined in [Table 2](#)). Along the abscissa is time in seconds and the ordinate shows contribution to variance. Colors are used to denote individual parameter contribution, total sum equals 1. In addition, $Q(t, p)$ is shown across the top, for reference. Because only 50 LS-DYNA runs are executed, an ERBF surrogate model is used to estimate responses with 1000 parameter sets for variance estimates. From results in [Figure 9](#), note that parameter contributions vary significantly over time but for simulation times greater than 0.04 sec the upper tail thickness clearly dominates.

5.3 Optimization for Calibration Results

The optimization problem is instructed to find parameter values to minimize the natural log of the prediction error using CORS. Starting with only 50 LS-DYNA solutions, CORS is allowed to compute 60 additional LS-DYNA runs. After completing the additional runs, the calibrated parameter set in Table 2 produced an overall prediction error reduction of 8%. Because the number of LS-DYNA runs is set by the user, the calibrated parameter set in Table 2 is not a converged set but rather an intermediate set. Nonetheless, it is referred to as the calibrated parameter set. The optimization process is purposely set up this way to control the computational expense in computing new LS-DYNA solutions. To show the impact of the parameter changes on the vector norm $Q(t, p)$, Figure 10 shows a comparison of results with data from the simulated test (solid blue), the baseline model using nominal values (dotted red), and the calibrated model (dashed-dot black). When comparing vector norms an overall assessment of the model predictive capability is quantified. However, users may prefer to evaluate improvements at specific sensor locations. For example, Figure 11 shows the velocity for the simulated test, baseline model, and the calibrated models at location 34 (see fig 1) in the z-direction. Improvements like those shown in Figure 11 are common for most locations but not all. Furthermore, after calibration, significant improvements are also apparent in the orthogonality results, as shown in Figure 12. As in Figure 7, results from the calibrated model are along the ordinate and the abscissa contains simulated test impact shapes. When comparing results against the baseline model (see Figure 7), it is clear that impact shape predictions have improved significantly, i.e., responses from the calibrated model and test are closer.

5.4 Revealing the Correct Answer

After completing the calibration process it is instructive to examine the actual changes made to the simplified model that resulted in the perturbed model. Because data from the perturbed model served as our target test data set, revealing the changes effectively gives the reader the true answer to the problem. Figure 13a depicts all the sections altered in the perturbed model. Alterations consisted of $\pm 20\%$ change in thickness at these locations. In contrast, Figure 13b shows the sections updated during the calibration process. It is interesting to see that although exact changes were not identified, regions where changes needed to be made were identified.

6 CONCLUDING REMARKS

An approach to conduct model calibration of nonlinear models has been developed and demonstrated using data from a simulated crash test of a helicopter. Fundamental to the approach is the definition and application of two calibration metrics: 1) metric M_1 compares the statistical bounds of the 2-norm of the velocity response from analysis versus test, and 2) metric M_2 evaluates the orthogonality between test and analysis impact shapes. The ability to reconcile analysis with test, assessed using metric M_1 , is evaluated by sampling the response when parameters are varied to establish response bounds. Once the adequacy of the model is established, the process of reconciling model and test proceeds through a constrained optimization to minimize the natural log of the prediction error. The optimization approach takes advantage of surrogate models to reduce the computational time associated with executing hundreds LS-DYNA runs. Because the computational time is significant, users must trade the number of LS-DYNA solutions allowed against the predictive accuracy. However, for problems where time constraints are not prohibitive, the optimization algorithm should converge to a global optimum.

For the simulated helicopter example studied in the paper, a flawed parameter set was evaluated and found to be inadequate using metric M_1 . After determining a revised set of parameters, results from calibration show an overall prediction error reduction of 8%. Although this may appear to be a relatively small overall reduction, improvements at specific sensor locations can be significantly better. Furthermore, improvements in orthogonality values after calibration resulted in matching 7 impact shapes with orthogonality values greater than 0.9 as compared to the initial model that only matched 1 impact shape. Improvements in orthogonality produced multi-dimensional improvements in the overall model predictive capability. Finally, because the calibration process was demonstrated using simulated experiment data, it was shown that although exact changes were not identified, regions where changes needed to be made were identified.

7 REFERENCES

1. Military Standard, MIL-STD-1290A (AV), Light Fixed and Rotary-Wing Aircraft Crash Resistance, Department of Defense, Washington, DC, Sept. 1988.
2. Jackson, K.E., Fasanella, E.L., and Lyle, K.H.: "Crash Certification by Analysis-Are We There Yet?" Proceedings of the 62nd Annual Forum of American Helicopter Society, Phoenix AZ, May 2006.
3. Kamat M.P.: "Survey of Computer Programs for Prediction of Crash Response and of Its Experimental Validation." Measurement and Prediction of Structural and Biodynamic Crash-Impact Response. Proceedings of the Winter Annual Meeting of the ASME, Pg 33-48, Dec. 1976.
4. Wittlin, G. and Gamon, M.A.: "Experimentally Verified Analytical Techniques for Predicting Vehicle Crash Responses." Proceedings of the AIAA 11th Annual Meeting and Technical Display, AIAA Paper No. 75-273, Feb. 1975.
5. Cronkhite, J.D., and Mazza, L.T.: "KRASH Analysis Correlation with the Bell ACAP Full-Scale Aircraft Crash Test." Proceedings of the National Technical Specialists' Meeting on Advanced Rotorcraft Structures: Requirements Vs. Opportunities, a Look at the Future. VA, Oct. 1988.
6. Tabiei, AL, Lawrence, C., Fasanella, E.L.: "Validation of Finite Element Crash Test Dummy Models for Predicting Orion Crew Member Injuries During a Simulated Vehicle Landing." NASA TM-2009-215476, March 2009.
7. Oberkampf, W.L. and Barone, M.F.: "Measures of Agreement Between Computation and Experiment: Validation Metrics." Journal of Computational Physics, 217 (2001) 5-56, www.elsevier.com/locate/jcp
8. Schwer, L.E.: "Validation Metrics for Response Histories: Perspectives and Case Studies." Engineering with Computers (2007), 23:295-309.
9. Anderson, M.C., Gan, W., and Haselman, T.K.: "Statistical Analysis of Modeling Uncertainty and Predictive Accuracy for Nonlinear Finite Element Models." Proceedings of the 69th Shock and Vibration Symposium, Minneapolis/St. Paul, MN, 1998.
10. Horta, L.G., Lyle, K.H., Lessard, W.B.: "Evaluation of Singular Value Decomposition Approach for Impact Dynamic Data Correlation." NASA TM 2003-212657, Oct. 2003.
11. Roach, P.P.: Verification and Validation in Computational Science and Engineering, Hermosa Publishers, Albuquerque, NM, 1998.

12. Oberkampf, W.L., Trucano, T.G., and Hirsch, C.: "Verification, Validation, and Predictive Capability in Computational Engineering and Physics." SAND 2003-3769, Feb. 2003.
13. Thacker, B.H.: "The Role of Non-determinism in Computational Model Verification and Validation." Proceedings of the 46th AIAA/ASME/ASCE/AHS/ASC Structures, Structural Dynamics, & Materials Conference, Austin TX, AIAA 2005-1902, April 2005.
14. Atamturktur, S, Hemez, F, and Unal, C.: "Calibration Under Uncertainty for Finite Element Models of Masonry Monuments." Los Alamos National Laboratory (LANL) Technical Report, LA-14414, Feb. 2010.
15. Sobol, I.M., Tarantola, S., Gatelli, D., Kucherenko, S.S, and Mauntz, W.: "Estimating Approximation Error When Fixing Unessential Factors in Global Sensitivity Analysis." Reliability Engineering and System Safety 92 (2007) 957-960.
16. Mullershon, H., and Liebsher, M.: "Statistics and Non-Linear Sensitivity Analysis with LS-OPT and DSPEX." Presented at the 10th International LS-DYNA Users Conference, pp. 4-1,4-13., Dearborn, MI, June 8-10, 2008.
17. Homma, T, and Saltelli, A.: "Importance Measures in Global Sensitivity Analysis of Nonlinear Models." Reliability Engineering and System Safety 52 (1996) 1-17.
18. Sudret, B.: "Global Sensitivity Analysis Using Polynomial Chaos Expansion." Reliability Engineering and System Safety 93 (2008) 964-979.
19. Mullur, A. and Messac, A.: "Extended Radial Basis Functions: More Flexible and Effective Metamodeling." AIAA Journal, Vol., 43, No. 6, June 2005.
20. Mullur, A. and Messac, A.: "Metamodeling Using Extended Radial Basis Functions: A Comparative Approach." Engineering with Computers (2006) 21: 203-217 DOI 10.1007/s00366-0005-7.
21. Regis, R.G., and Shoemaker, C.A.: "Constrained Global Optimization of Expensive Black Box Functions Using Radial Basis Functions." Journal of Global Optimization (2005) 31: 153-171, Sept. 2005.
22. Annett, M.S, and Polanco, M.A.: "System-Integrated Finite Element Analysis of a Full-Scale Helicopter Crash Test with Deployable Energy Absorbers." Proceedings of the 66th American Helicopter Annual Forum, Phoenix, AZ, May 11-13, 2010.
23. Kellas, S. and Jackson, K. E.: "Deployable System for Crash-Load Attenuation," Proceedings of the 63rd American Helicopter Annual Forum, VA Beach, May 1-3, 2007
24. Anonymous: LS-DYNA Keyword User's Manual Version 940, Livermore Software Technology Corporation, Livermore, CA, 1997
25. Kammer, D.C.: "Sensor Placement for On-Orbit Modal Identification and Correlation of Large Space Structures." Journal of Guidance, Control, and Dynamics, Vol. 14, No. 2, pp. 251-259, 1991.
26. Halton, J.H.: "On the Efficiency of Certain Quasi-Random Sequences of Points in Evaluating Multi-Dimensional Integrals." Numerische Mathematik, Vol. 2, pp. 84-90, 1960.
27. Myers, R.H. and Montgomery, D.C: Response Surface Methodology, 2nd Edition, Copyright © 2002 John Wiley and Sons, Inc., 2nd Edition, Copyright © 2002 John Wiley and Sons, Inc.

Table 1 Initial parameter description

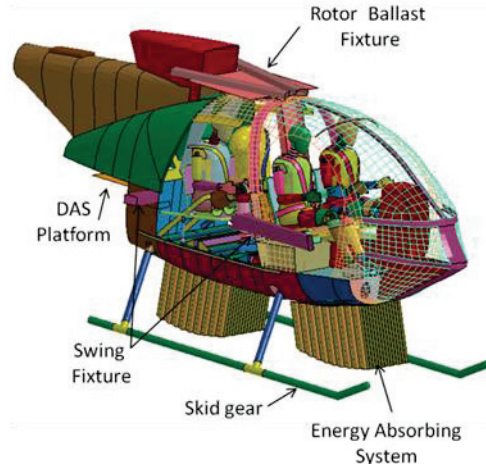
No.	Parameter Description	Nominal	Lower Bound	Upper Bound
1	E back panel (lbs/in ²)	10,000,000	8,000,000	12,000,000
2	E subfloor ribs (lbs/in ²)	10,000,000	8,000,000	12,000,000
3	E keel beam web (lbs/in ²)	9,880,000	7,904,000	11,856,000
4	E stinger upper tail (lbs/in ²)	10,000,000	8,000,000	12,000,000
5	E stinger lower tail (lbs/in ²)	10,000,000	8,000,000	12,000,000
6	E_t subfloor ribs (lbs/in ²)	134,200	107,360	161,040
7	E_t keel beam web (lbs/in ²)	134,200	107,360	161,040
8	E_t lower tail stinger (lbs/in ²)	134,200	107,360	161,040

Table 2 Revised parameter description

No.	Parameter Description	Nominal	Lower Bound	Upper Bound	Calibrated Value
1	Keel beam stiffener thickness (in)	0.020	0.015	0.025	0.0161
2	Belly panel thickness (in)	0.090	0.08	0.135	0.1008
3	Keel beam thickness (in)	0.040	0.035	0.045	0.0358
4	Lower tail thickness (in)	0.040	0.035	0.045	0.0414
5	Back panel thickness (in)	0.020	0.015	0.025	0.0166
6	Upper tail thickness (in)	0.020	0.015	0.025	0.0168



1a) during test preparations



1b) "as-tested" finite element model

Figure 1. MD-500 helicopter model.

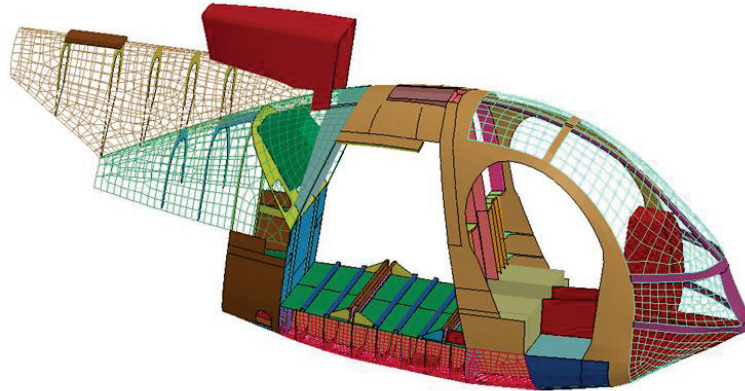


Figure 2. Simplified finite element model.

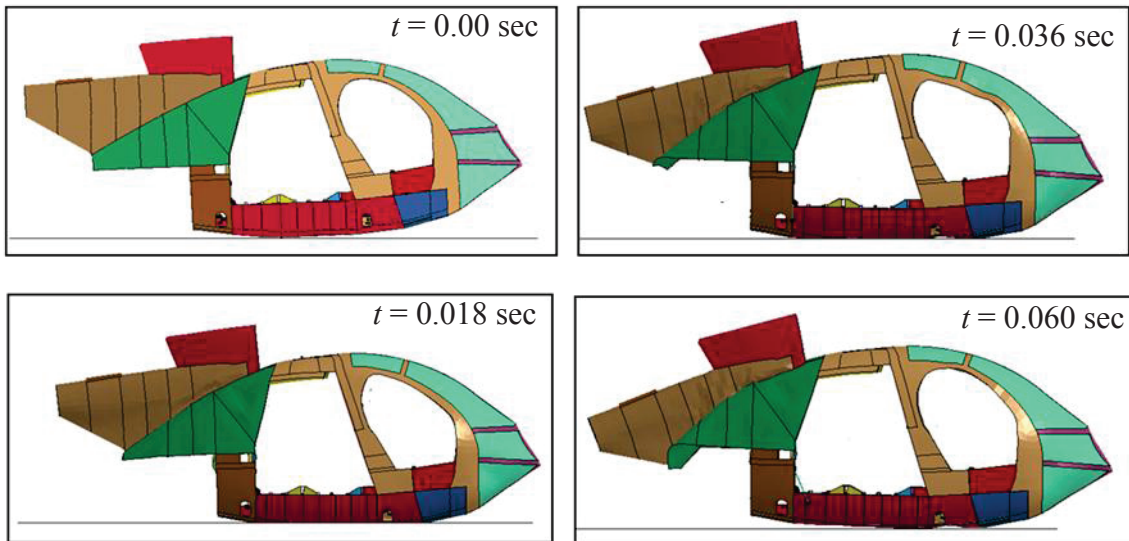


Figure 3. Four frames of the LS-DYNA simulation as the helicopter impacts the hard surface.

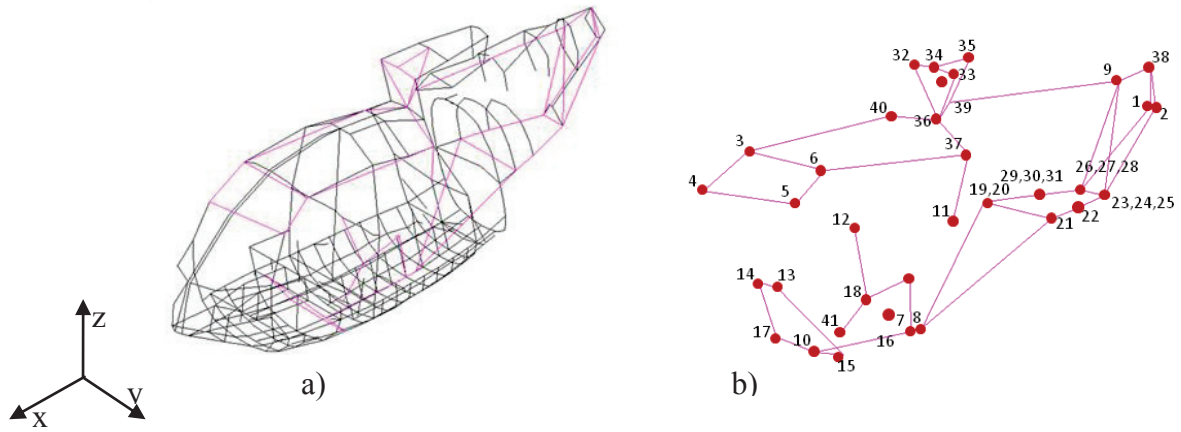


Figure 4. Helicopter wireframe for a) simplified model b) simulated test sensor placement and numbering.

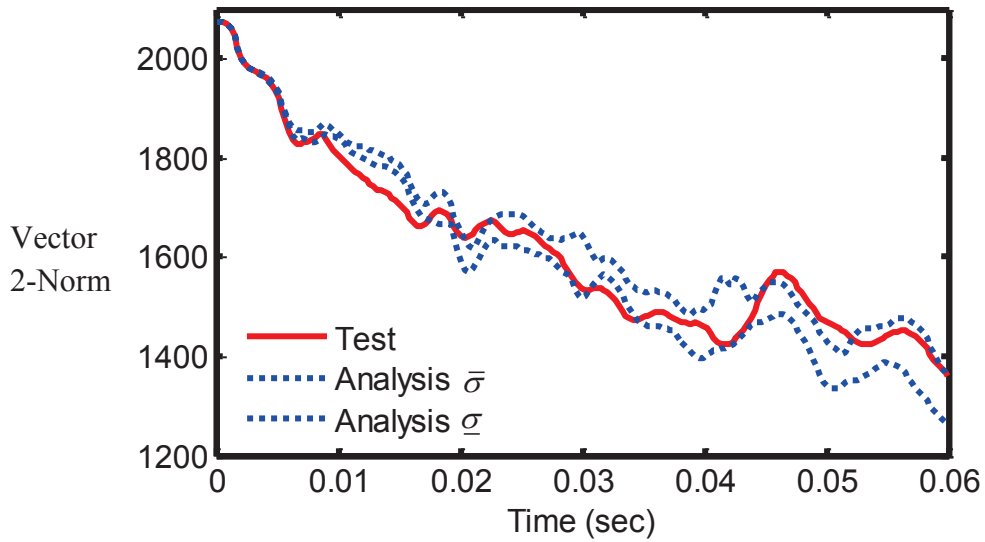


Figure 5. Velocity vector 2-norm for analysis (with 150 LS-DYNA runs) and for simulated test.

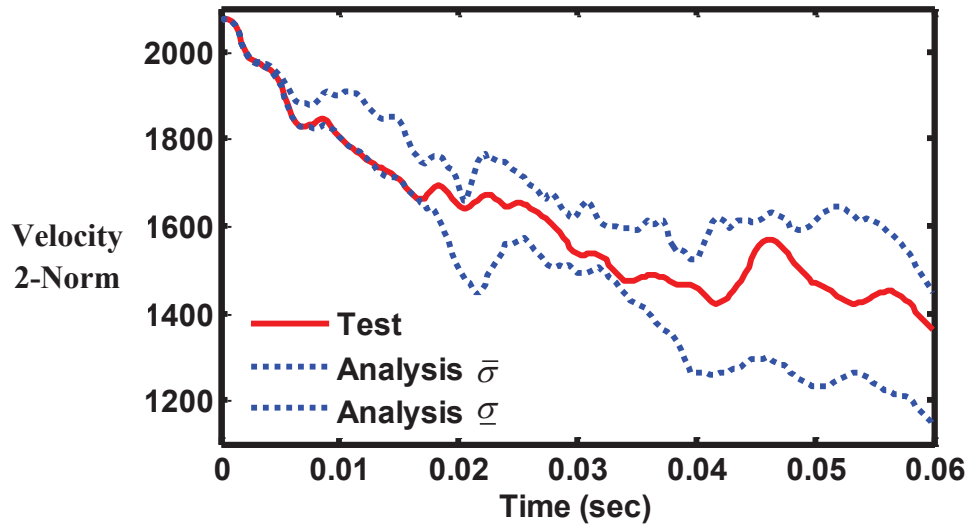


Figure 6. Velocity vector 2-norm for analysis (with 50 LS-DYNA runs) and for simulated test.

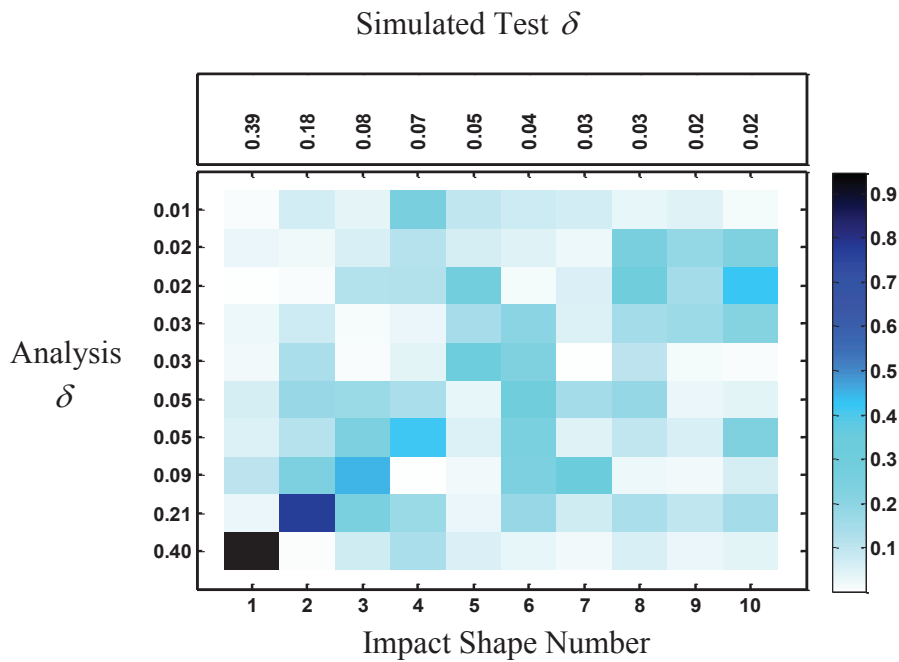


Figure 7. Orthogonality results using impact shapes from the simulated test and baseline model.

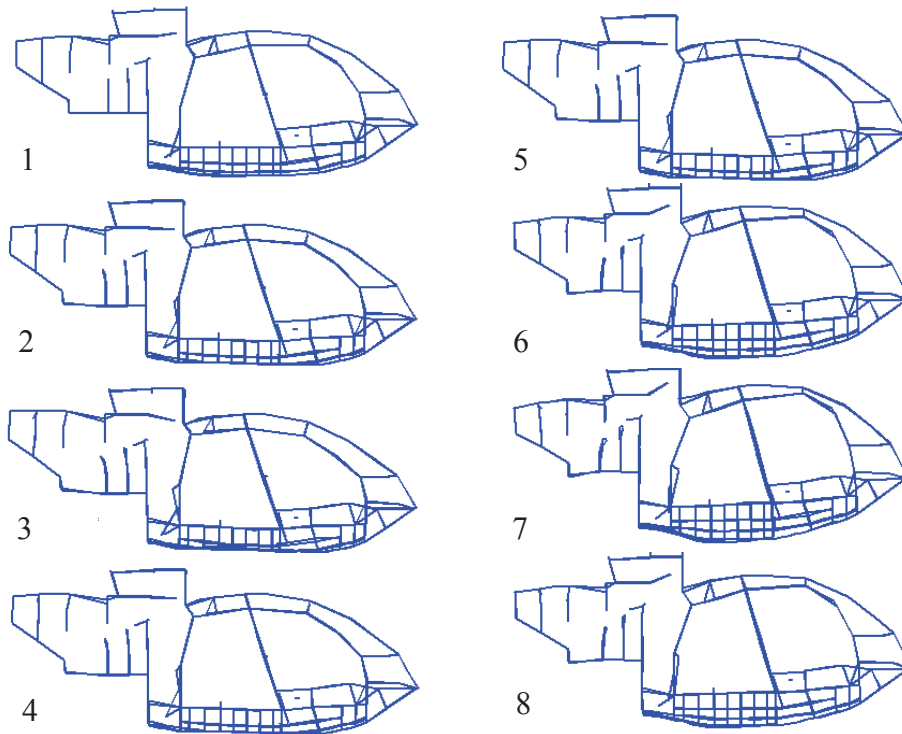


Figure 8. Test impact shape number 2 ($\delta_2 = 0.18$) animation sequence.

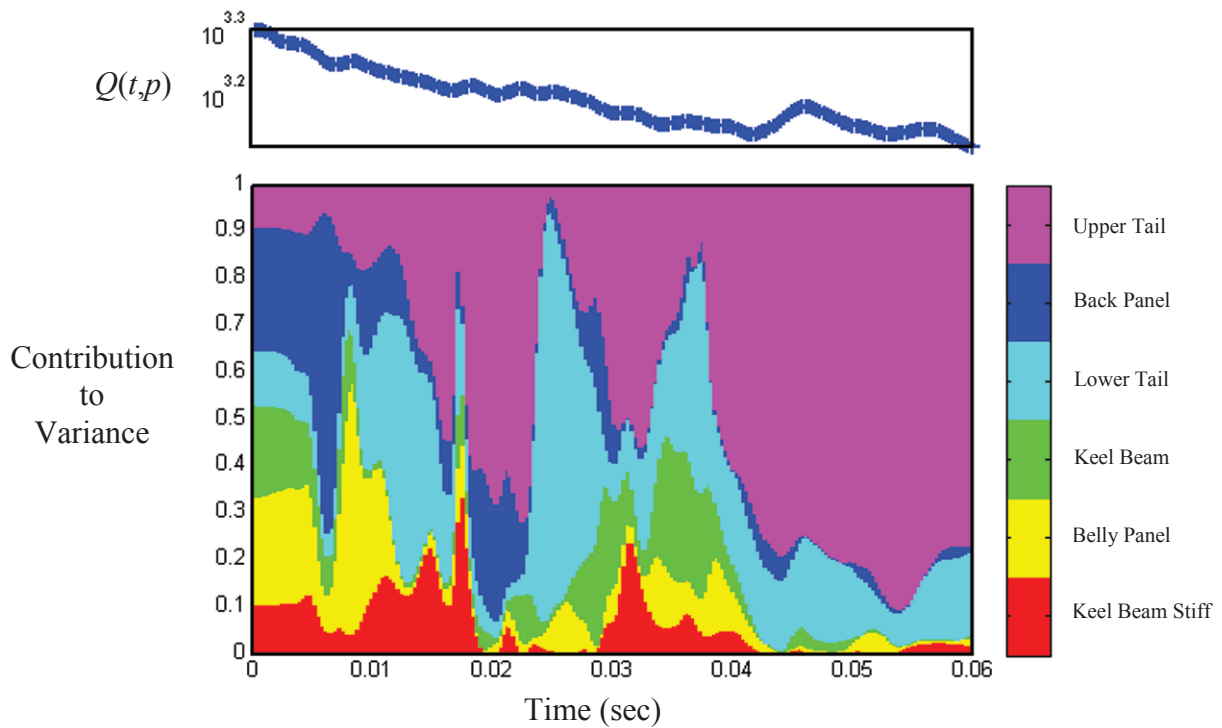


Figure 9. Norm metric $Q(t,p)$ and sensitivity for thickness parameters.

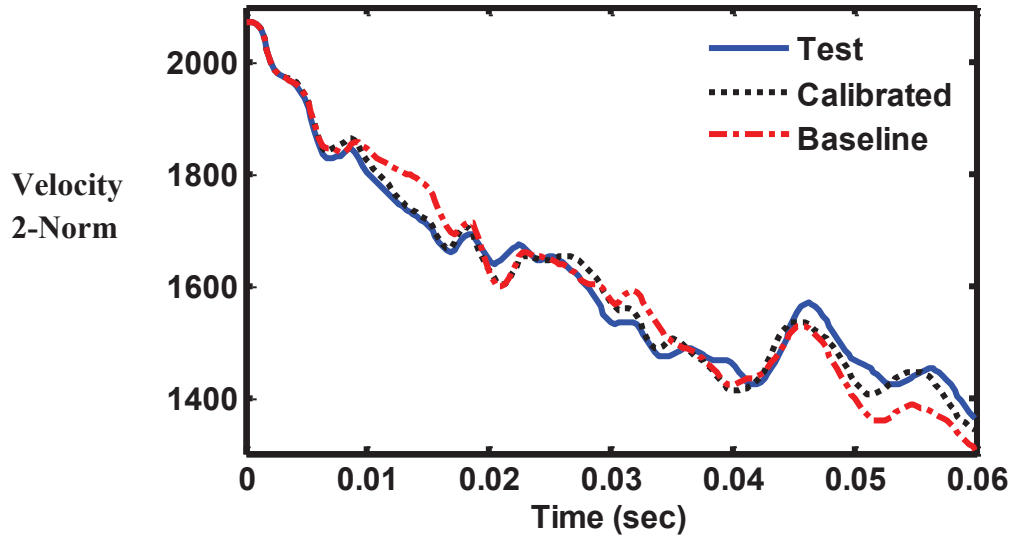


Figure 10. Comparison of the velocity 2-norm using simulated test, baseline, and calibrated model data.

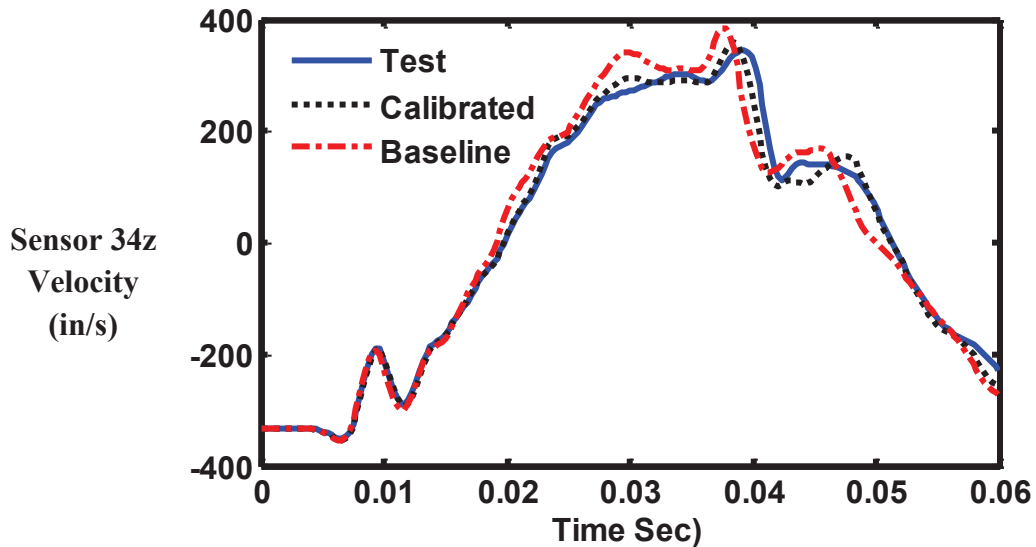


Figure 11. Comparison of velocity response for the simulated test, baseline, and calibrated model data.

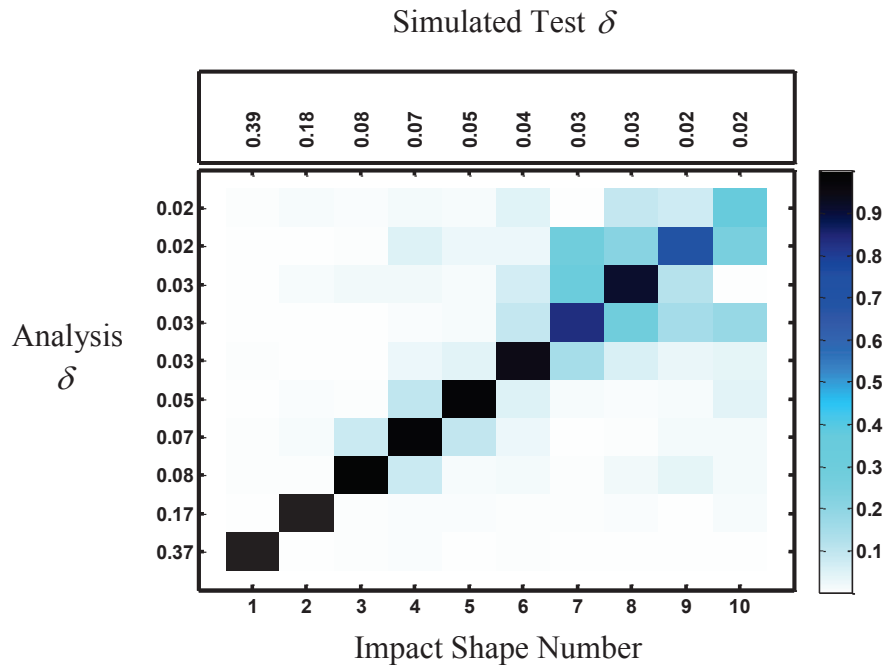


Figure 12. Orthogonality results using impact shapes from the simulated test and calibrated model.

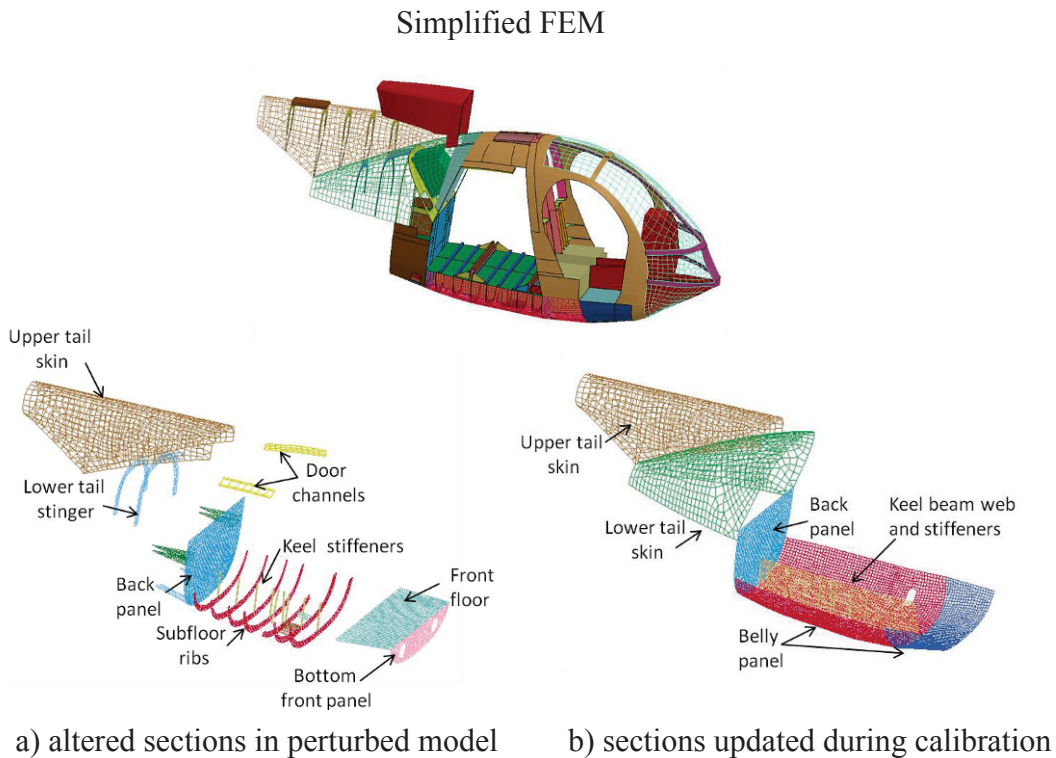


Figure 13. Sections altered to create the perturbed model and changes suggested during calibration.

Dynamic analysis of railway bridges by means of the spectral method

Giuseppe Catania, Silvio Sorrentino

DIEM, Department of Mechanical Engineering,
University of Bologna, Viale del Risorgimento 2, 40136 Bologna, Italy

ABSTRACT

This study investigates the dynamic behaviour of railway bridges crossed by travelling trains. A simplified formulation was adopted in order to perform a direct analysis of the effects of the parameters involved in the problem. The bridge is modelled as a rectangular plate, while the trains are modelled as travelling inertial distributed loads. The formulation is accomplished by the use of the Rayleigh-Ritz method, yielding a low order model with time-dependent coefficients. Several numerical examples are presented and discussed, aimed at investigating the effects of each of the model-governing parameters.

Keywords

Railway bridges, moving loads, Rayleigh-Ritz method.

Nomenclature

C	damping matrix	u	unit step distribution
D	stiffness of the plate	V	potential of applied loads
E	Young's modulus	v	velocity of the load
g	gravity acceleration	w	displacement
H	velocity response function	x	spatial coordinate
h	thickness of the plate	y	spatial coordinate
K	stiffness matrix	α	velocity ratio
L	length	β	frequency parameter
l	width	ε	relative error
M	mass matrix	Φ	modal matrix
n	modal index	μ	length ratio
p	load per unit area	ν	Poisson's ratio
r	mass ratio	ρ	mass per unit area
q	modal coordinate	ω_n	modal natural frequency
t	time	ξ	moving coordinate
U	potential of strain energy	ζ	damping factor

1 Introduction

In the analysis of dynamic effects of railway vehicles on bridges, simplified models are suggested and usually used, taking into account only some aspects, such as deterministic, vertical effects, and the influence of moving forces and masses [1-2]. Inertial effects of both bridge and vehicle can be influential, and not negligible, since the mass of the external load introduces a coupling effect between the load and the structure. Other important aspects, such as dynamic properties of travelling vehicles and track irregularities, are not considered in the present study.

The railway bridge model most commonly used is a continuous Euler Bernoulli beam [2], or a Timoshenko beam [3], traversed by either concentrated [4] or distributed moving loads [5]. Possible applications of lumped vibration absorbers have also been investigated [6]. However, in the present study a homogeneous Kirchhoff plate is considered, allowing the analysis of lateral vibrations due to trains travelling on double-track bridges. Structure damping is included in the model, as it may play an important role.

The train is simply modelled by means of a continuous load in the form of a moving strip, an idealization which can be adopted when the span of the bridge is large in comparison with the distance between axles [2]. A constant speed of motion of vehicles along the bridge is assumed.

The formulation is accomplished by the use of the Rayleigh-Ritz method [7], and the solution is expressed in terms of a linear combination of functions, which in the present study are selected as tensor products of eigenfunctions of prismatic pinned-pinned and free-free beams in flexural vibration. This approach yields a reduced order model with time-dependent coefficients, allowing a parametric analysis of plates loaded by travelling distributed masses.

Different example cases are presented and discussed in detail, analyzing the effects of velocity, mass and length of the train on the plate's dynamic response with respect to the mass, stiffness and damping of the plate itself.

2 Theoretical model

A homogeneous isotropic Kirchhoff plate is considered, simply supported on two opposite sides, free on the other two sides and crossed by a travelling distributed load. The load per unit area p over the plate may be expressed as:

$$p(x, y, t) = -\rho_t f(\xi, y) \left[g + \frac{d^2 w(x, y, t)}{dt^2} \right], \quad \xi = x - v_x t, \quad (1)$$

where w is the vertical displacement of a point of the plate or of the load (Fig.1), ρ_t is the equivalent mass per unit area of the load, g is the gravity acceleration, v_x is the travelling speed in the x direction, ξ is a moving coordinate in the same direction [1] and f models the translating strip representing the instantaneous position of the load:

$$f(\xi, y) = [u(\xi + L_t) - u(\xi)] [u(y - \delta) - u(y - \delta - l_t)]. \quad (2)$$

Note that within the present study ρ_t is assumed to be constant; however, piecewise-constant or other distributions $\rho_t(\xi)$ may be considered and adopted in the following developments.

Equation 2 contains the unit step distribution $u(\cdot)$, L_t and l_t are the length and the width of the strip modelling the train, and δ is the distance between the side of the strip and the edge $y = 0$ of the plate, as shown in Fig. 1. The second term on the right-hand side of Eq. 1 describes the inertial action of the load. The total acceleration may be expressed in the following general form:

$$\frac{d^2 w}{dt^2} = \frac{\partial^2 w}{\partial t^2} + v_x^2 \frac{\partial^2 w}{\partial x^2} + 2v_x v_y \frac{\partial^2 w}{\partial x \partial y} + v_y^2 \frac{\partial^2 w}{\partial y^2} + 2v_x \frac{\partial^2 w}{\partial x \partial t} + 2v_y \frac{\partial^2 w}{\partial y \partial t} + a_x \frac{\partial w}{\partial x} + a_y \frac{\partial w}{\partial y} \quad (3)$$

where v_x , v_y , a_x , a_y express the velocities and accelerations of the travelling load in the x and y directions respectively [1]. Considering a train travelling at constant speed v in the x direction, Eq. 3 reduces to:

$$\frac{d^2 w}{dt^2} = \frac{\partial^2 w}{\partial t^2} + 2v \frac{\partial^2 w}{\partial x \partial t} + v^2 \frac{\partial^2 w}{\partial x^2} \quad (4)$$

The first term of the right-hand side of Eq. 4 expresses the influence of vertical acceleration of the moving load, the second term the influence of Coriolis acceleration, and the third term the influence of track curvature [1].

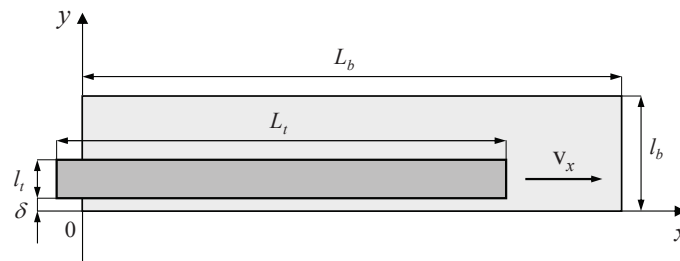


Fig. 1 Model scheme

The functional of the total potential energy of the coupled system can be written as the sum of a term U due to the strain energy plus a term V representing the potential of all applied loads (including the inertial forces):

$$\Pi = U + V \quad (5)$$

The potential of the strain energy can be written in terms of second order derivatives of the out-of-plane displacement w :

$$U = \frac{1}{2} \int_0^{l_b} \int_0^{L_b} D \left[w_{xx}^2 + w_{yy}^2 + 2\nu w_{xx} w_{yy} + 2(1-\nu) w_{xy}^2 \right] dx dy, \quad D = \frac{Eh^3}{12(1-\nu^2)} \quad (6)$$

where the subscripts denote differentiation with respect to the spatial variables and D is the flexural stiffness of the plate, expressed as a function of Young's modulus E , Poisson's ratio ν and thickness h [7]. In the adopted formulation the inertial forces are included in the potential of applied loads V as follows:

$$V = \int_0^{l_b} \int_0^{L_b} (\rho_b w \ddot{w} - wp) dx dy \quad (7)$$

where ρ_b is the mass per unit area of the plate and p is the load in Eq. 1. The out-of-plane displacement w is expressed by means of a linear combination of shape functions, selected as products of homogeneous uniform prismatic beam eigenfunctions ϕ :

$$w = \sum_{n=1}^N q_n \phi_n(\xi, \eta) \Rightarrow w = \boldsymbol{\phi}^T \mathbf{q} \quad (8)$$

where \mathbf{q} is the generalized coordinate vector. Introducing the displacement expansion in the quadratic functional Π , and imposing its stationarity, yields the following algebraic eigenproblem:

$$[\mathbf{M} + r\Delta\mathbf{M}]\ddot{\mathbf{q}} + 2r\alpha\beta[\Delta\mathbf{C}]\dot{\mathbf{q}} + \beta^2[\mathbf{K} + r\alpha^2\Delta\mathbf{K}]\mathbf{q} = -r\mathbf{g}\mathbf{f} \quad (9)$$

with:

$$r = \frac{\rho_t}{\rho_b}, \quad \alpha = \frac{v}{L_b\beta}, \quad \beta = \frac{1}{L_b^2} \sqrt{\frac{D}{\rho_b}} \quad (10)$$

where β is a frequency parameter and α is a dimensionless parameter depending on the speed v . The matrices in square brackets in Eq. 9 can be regarded as dimensionless quantities, and they can be computed according to the following integrals:

$$\begin{aligned} \mathbf{M} &= \int_0^{l_b} \int_0^{L_b} (\boldsymbol{\phi}\boldsymbol{\phi}^T) dx dy, \quad \Delta\mathbf{M} = \int_{\delta}^{\delta+l_t} \int_{x_0}^{x_1} (\boldsymbol{\phi}\boldsymbol{\phi}^T) dx dy, \quad \Delta\mathbf{C} = L_b \int_{\delta}^{\delta+l_t} \int_{x_0}^{x_1} (\boldsymbol{\phi}\boldsymbol{\phi}_x^T) dx dy \\ \mathbf{K} &= L_b^4 \int_0^{l_b} \int_0^{L_b} [\boldsymbol{\phi}_{xx}\boldsymbol{\phi}_{xx}^T + \boldsymbol{\phi}_{yy}\boldsymbol{\phi}_{yy}^T + \nu(\boldsymbol{\phi}_{xx}\boldsymbol{\phi}_{yy}^T + \boldsymbol{\phi}_{yy}\boldsymbol{\phi}_{xx}^T) + 2(1-\nu)(\boldsymbol{\phi}_{xy}\boldsymbol{\phi}_{xy}^T)] dx dy \\ \Delta\mathbf{K} &= 2L_b^2 \int_{\delta}^{\delta+l_t} \int_{x_0}^{x_1} (\boldsymbol{\phi}\boldsymbol{\phi}_{xx}^T) dx dy, \quad \mathbf{f} = \int_{\delta}^{\delta+l_t} \int_{x_0}^{x_1} \boldsymbol{\phi} dx dy \end{aligned} \quad (11)$$

In Eq. 11 the integration interval $[x_0, x_1]$ is time-dependent. Introducing the ratio between the lengths L_t and L_b :

$$\mu = \frac{L_t}{L_b} \quad (12)$$

then x_0 and x_1 vary according to Tab. 1.

Table 1 Time-dependent interval of integration

case $\mu < 1$	case $\mu = 1$	case $\mu > 1$
$0 \leq vt < L_t \Rightarrow \begin{cases} x_1 = vt \\ x_0 = 0 \end{cases}$	$0 \leq vt < L_b \Rightarrow \begin{cases} x_1 = vt \\ x_0 = 0 \end{cases}$	$0 \leq vt < L_b \Rightarrow \begin{cases} x_1 = vt \\ x_0 = 0 \end{cases}$
$L_t \leq vt < L_b \Rightarrow \begin{cases} x_1 = vt \\ x_0 = vt - L_t \end{cases}$	$L_b \leq vt < 2L_b \Rightarrow \begin{cases} x_1 = L_b \\ x_0 = vt - L_b \end{cases}$	$L_b \leq vt < L_t \Rightarrow \begin{cases} x_1 = L_b \\ x_0 = 0 \end{cases}$
$L_b \leq vt < L_b + L_t \Rightarrow \begin{cases} x_1 = L_b \\ x_0 = vt - L_t \end{cases}$		$L_t \leq vt < L_t + L_b \Rightarrow \begin{cases} x_1 = L_b \\ x_0 = vt - L_t \end{cases}$

To model energy dissipation within the structure, a dimensionless damping matrix \mathbf{C} may be defined by means of the plate modal matrix Φ (mass normalized) and eigenvalues ω_n (computed from the \mathbf{M} and \mathbf{K} matrices), and considering a modal damping ratio ζ equal for all modes:

$$2\zeta\mathbf{C} = 2\zeta\Phi^{-T} \text{diag}\left(\frac{\omega_n}{\beta}\right)\Phi^{-1} = \Phi^{-T} \text{diag}\left(2\zeta\frac{\omega_n}{\beta}\right)\Phi^{-1} \quad (13)$$

Introducing Eq. 13 in Eq. 9 yields:

$$[\mathbf{M} + r\Delta\mathbf{M}]\ddot{\mathbf{q}} + 2\beta[\zeta\mathbf{C} + r\alpha\Delta\mathbf{C}]\dot{\mathbf{q}} + \beta^2[\mathbf{K} + r\alpha^2\Delta\mathbf{K}]\mathbf{q} = -rg\mathbf{f} \quad (14)$$

Equation 14 is a reduced order discretized model with time-dependent coefficients, which can be solved numerically.

3 Numerical results

Some numerical examples are presented for studying the dynamic behaviour of the model described in section 2. The influence of parameters v , r , μ , β , ζ governing Eq. 14 is highlighted by studying time responses $w(t)$ and dynamic response functions H of the dimensionless frequency α (playing the role of ‘frequency response functions’) defined according to:

$$H(x, y; \alpha) = \frac{\max_t [w(t)]}{w_s} \Big|_{x, y; \alpha} \quad (15)$$

where w_s is the static deflection due to the load centered in $L_b/2$.

Numerical solutions of Eq. 14 are computed using the Runge-Kutta algorithm, expanding the solution w (Eq. 8) with 4×2 beam eigenfunctions (4 pinned – pinned eigenfunctions along x direction and 2 free – free eigenfunctions along y direction). Realistic values for parameter β are computed by means of the empirical expression:

$$\beta = \frac{2\pi a}{\lambda_1^2} L_b^{-\gamma} \quad (16)$$

based on large collections of experimental data [2], where a and γ are parameters depending on the kind of bridge considered, as reported in Tab. 2. The values (in Hz) of the first natural frequency and of parameter β for different kinds of bridges are reported as functions of the length L_b in Fig.2.

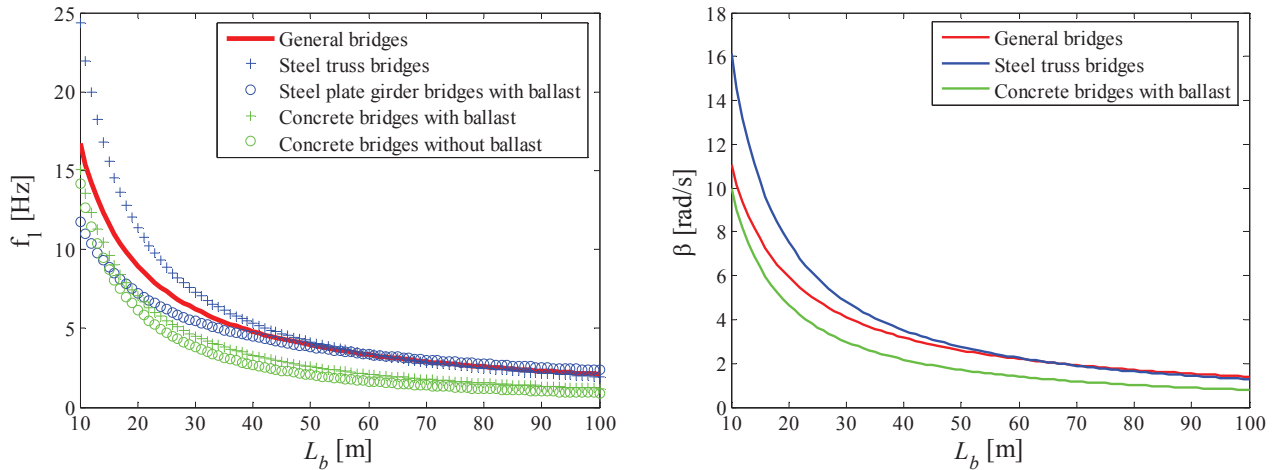


Fig. 2 First natural frequency f_1 [Hz] (left) and frequency parameter β [rad/s] (right) as functions of the length L_b for different kinds of bridges

Table 2 Parameters in Eq.16, as reported in [2]

Kind of bridge	a	γ
General bridges (average case)	133	0.9
Steel truss bridges	307	1.1
Steel plate girder bridges with ballast	59	0.7
Steel plate girder bridges without ballast	208	1
Concrete bridges with ballast	190	1.1
Concrete bridges without ballast	225	1.2

Effect of the speed of the load

As a reference case study, the following values for the parameters are assumed:

Plate: $L_b = 50$ m, $l_b = 10$ m, $\beta = \sqrt{5}$ rad/s, $\zeta = 0.05$.

Moving load: $\mu = 1.4$, $l_t = 2.5$ m, $\delta = 1.5$ m, $r = 0.5$.

Time responses $w(t)$ are computed at coordinate $x = L_b/2$, $y = l_b/2$ with speed v varying from 30 m/s to 50 m/s (108 Km/h to 180 Km/h), as shown in [figure 4](#).

Maximum deflection at different points

Parameter values are assumed as in the reference case. Response functions $H(\alpha)$ are computed at different points (x, y) along the structure, as reported in [Fig. 3](#). The frequency parameter varies from 0.1 up to 1, i.e. v varies from 40 Km/h up to 400 Km/h. Functions $H(x, y; \alpha)$ show a peculiar undulating trend, not significantly affected by the choice of coordinate x .

Effect of the mass of the load

Parameter values are assumed as in the reference case with $v = 40$ m/s = 144 Km/h, varying r from 0.1 to 1. Response functions $w(t)$ and $H(\alpha)$ are computed in $x = L_b/2$, $y = l_b/2$, as reported in [Fig. 4](#).

Effect of the length of the load

Parameter values are assumed as in the reference case with $v = 40$ m/s = 144 Km/h, varying μ from 0.1 to 2. Response functions $w(t)$ and $H(\alpha)$ are computed in $x = L_b/2$, $y = l_b/2$, as reported in [Fig. 5](#). Parameter μ (related to L_t) is able to significantly affect the behaviour of $H(\alpha)$. Note that the plots of $H(\alpha)$ in the case $\mu \geq 1$ are superimposed.

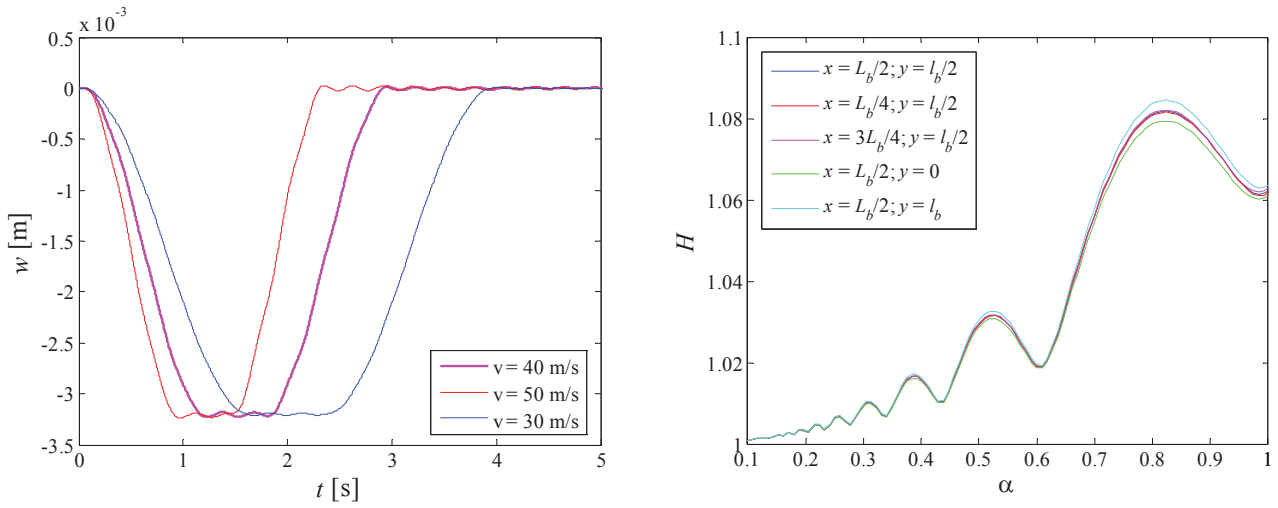


Fig. 3 Effect of parameter v on $w(t)$ (left); $H(\alpha)$ at different points (x, y) (right)

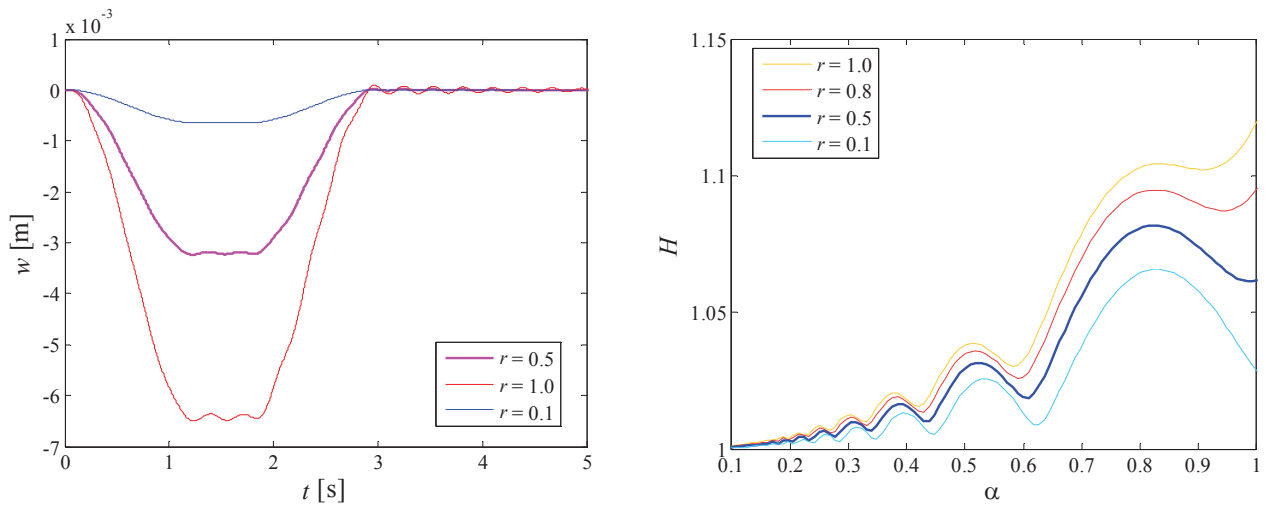


Fig. 4 Effect of parameter r on $w(t)$ (left); effect of parameter r on $H(\alpha)$ (right)

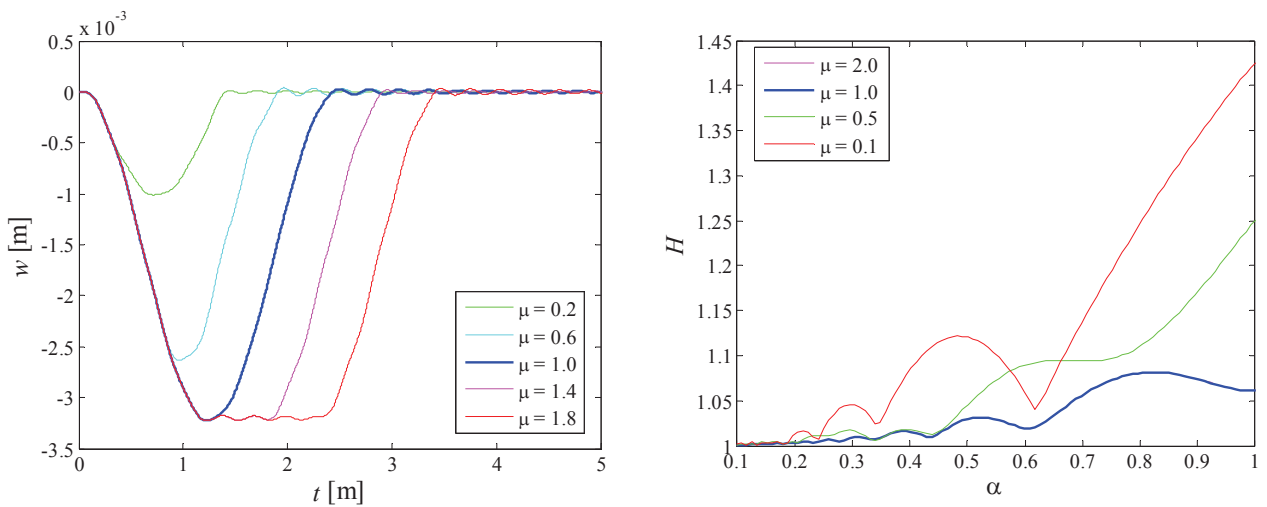


Fig. 5 Effect of parameter μ on $w(t)$ (left); effect of parameter μ on $H(\alpha)$ (right)

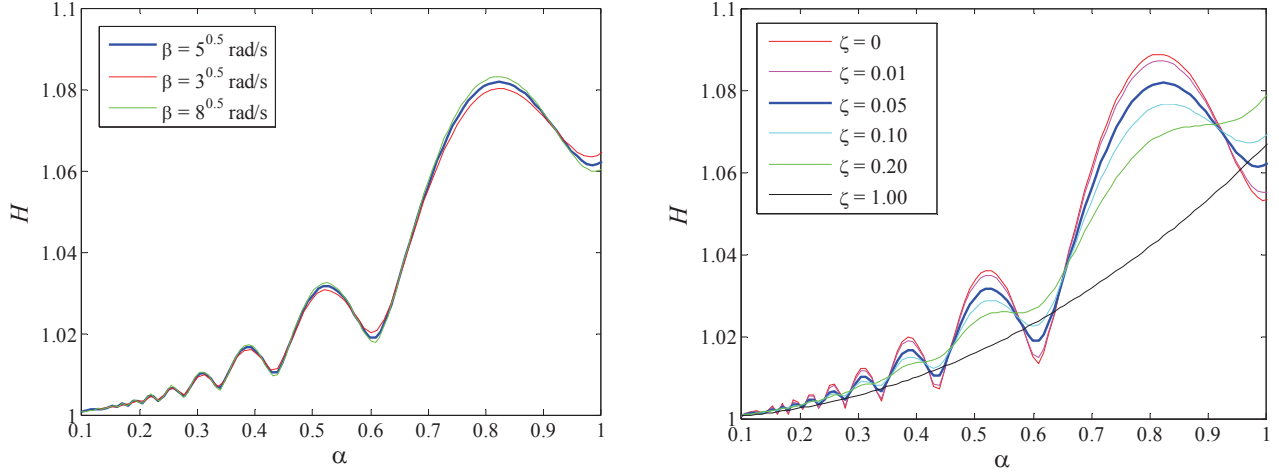


Fig. 6 Effect of parameter β on $H(\alpha)$ (left); effect of parameter ζ on $H(\alpha)$ (right)

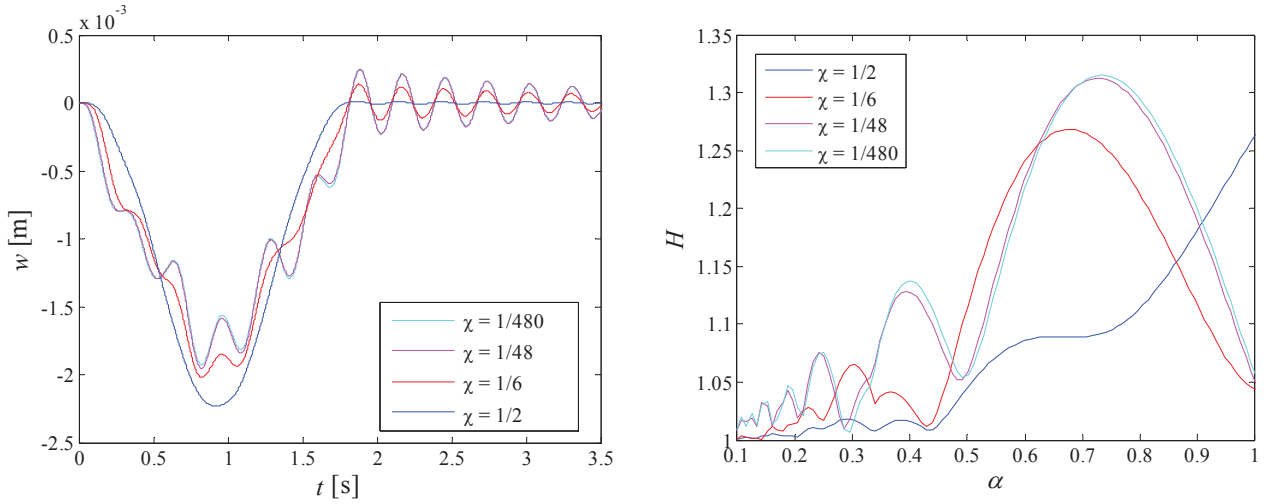


Fig. 7 Effect of partially distributed load on $w(t)$ (left); effect of partially distributed load on $H(\alpha)$ (right)

Effect of structural stiffness

Parameter values are assumed as in the reference case, varying β from $\sqrt{3}$ rad/s to $\sqrt{8}$ rad/s. Response functions $H(\alpha)$ are computed in $x = L_b/2, y = l_b/2$, as reported in Fig. 6. The plots are almost superimposed.

Effect of structure damping

Parameter values are assumed as in the reference case, varying ζ from 0 to 1. Response function $H(\alpha)$ is computed in $x = L_b/2, y = l_b/2$, as reported in Fig. 6. Raising ζ reduces the amplitude of oscillation of $H(\alpha)$, until its behaviour becomes monotonic (however this is not the case for real bridge structures).

Effect of partially distributed load

Parameter values are assumed as in the reference case, with $L_t = 24$ m and $v = 40$ m/s = 144 Km/h. Different loading distributions are compared: the continuous one (as represented in Fig. 1) and ‘partial’ distributions consisting of two shorter sections in which the load is distributed.

The assumed ‘partial’ distributions are given by:

$$0 \leq \xi \leq \frac{L_t}{\chi} \quad \text{and} \quad \left(L_t - \frac{L_t}{\chi} \right) \leq \xi \leq L_t \quad (17)$$

with $\chi < 0.5$ ($\chi = 0.5$ yields the ‘continuous’ distribution). Since for the continuously distributed load it is assumed $r_0 = 0.5$, for the ‘partially distributed’ load described by Eq. 17 r_0 increases to $r = 1/(2\chi) \times r_0$. Response functions $w(t)$ and $H(\alpha)$ are computed in $x = L_b/2$, $y = l_b/2$ for different values of χ (1/6, 1/48, 1/480) as reported in Fig. 7. Load distribution variations such as that described in Eq. 17 may dramatically affect the behaviour of the response function $H(\alpha)$.

Effect of time dependent matrices

Parameter values are assumed as in the reference case, with $v = 40$ m/s = 144 Km/h. The effect of neglecting the time dependent matrices $\Delta\mathbf{M}$, $\Delta\mathbf{C}$, $\Delta\mathbf{K}$ on the solution $w(t)$ is evaluated by introducing a relative error, according to:

$$\varepsilon_M = \frac{w(t) - [w(t)]_{\Delta\mathbf{M}=\mathbf{0}}}{\max_t |w(t)|} \quad (18)$$

where $[w(t)]_{\Delta\mathbf{M}=\mathbf{0}}$ refers to the solution computed assuming $\Delta\mathbf{M} = \mathbf{0}$ in Eq. 14.

Similarly, ε_C and ε_K can be defined, considering $\Delta\mathbf{C} = \mathbf{0}$ and $\Delta\mathbf{K} = \mathbf{0}$.

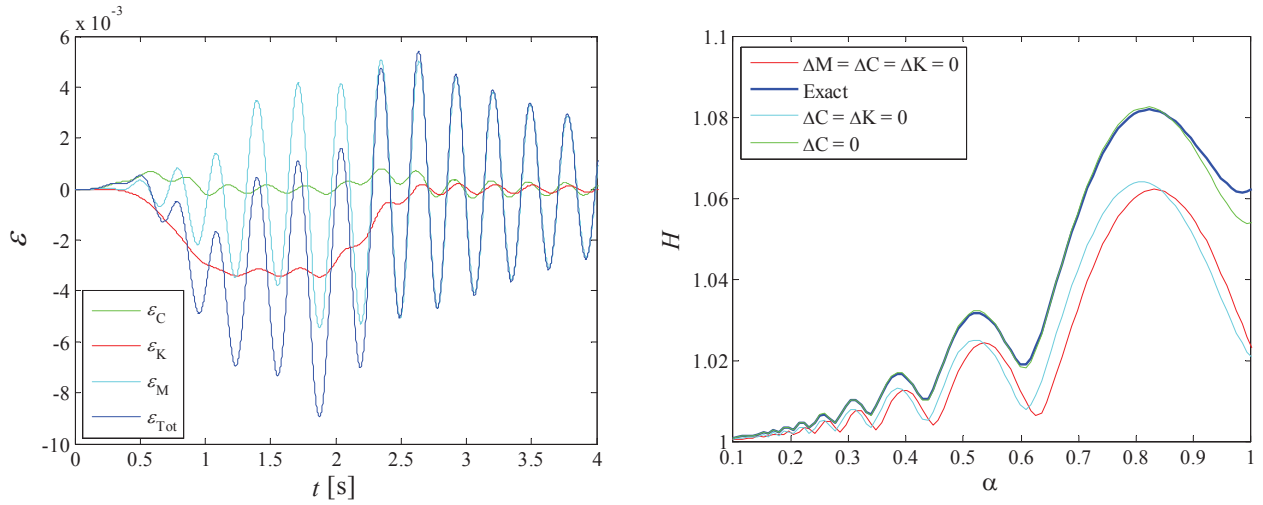


Fig. 8 Effect of neglecting time dependent matrices $\Delta\mathbf{M}$, $\Delta\mathbf{C}$, $\Delta\mathbf{K}$ on $w(t)$ (left) and on $H(\alpha)$ (right)

The error functions ε_M , ε_C and ε_K are plotted versus time in Fig. 8, where ε_{Tot} represents the total error, assuming $\Delta\mathbf{M}$, $\Delta\mathbf{C}$ and $\Delta\mathbf{K}$ equal to $\mathbf{0}$ at the same time. The smallest, and negligible contribution to the error ε_{Tot} appears to be ε_C , while the main contribution is due to ε_M . Fig. 8 also shows the effect on $H(\alpha)$ of neglecting the time dependent matrices $\Delta\mathbf{M}$, $\Delta\mathbf{C}$, $\Delta\mathbf{K}$. Again, the effect of neglecting $\Delta\mathbf{C}$ is very small. The total error, on the contrary, can be significant.

4 Discussion

Function $H(x, y; \alpha)$ appears to be an effective tool for studying the dynamic behaviour of a structure crossed by travelling loads with constant speed, in some way equivalent to a ‘frequency response function’ for time-varying coefficient systems. This function shows peculiar undulating trends (Fig. 3), influenced by the parameters governing Eq. 14. The response can be evaluated at any coordinate point (x, y) of the plate, making it possible to study the variation of structural deflection also along the y coordinate (Fig. 3). Mass parameter r can produce important shifts in magnitude, but not in shape (Fig. 4). On the contrary, length parameter μ controls both shape and magnitude of $H(\alpha)$ (Fig. 5), but only in the case $0 < \mu \leq 1$. The damping parameter ζ has the effect of progressively smoothing the oscillation of $H(\alpha)$, until it becomes monotonic (Fig. 6, though the latter limit case is not realistic for actual bridge structures): in general, the reduction in amplitude becomes particularly significant at high speed. Frequency parameter β , within the range of real bridges, scarcely affects the behaviour of $H(\alpha)$ (Fig. 6), so H may be considered independent from β . Changes in the spatial distribution of the load can produce dramatic variations in $H(\alpha)$ (Fig. 7): this result should highlight the importance of properly modelling the ballast, directly influencing the load distribution on the actual structure.

The contribution to the solution of the time dependent matrices $\Delta\mathbf{M}$, $\Delta\mathbf{C}$ and $\Delta\mathbf{K}$ is globally not negligible (Fig. 8), however the effect of $\Delta\mathbf{C}$ is usually very small in comparison with the contributions of $\Delta\mathbf{K}$, and especially of $\Delta\mathbf{M}$.

5 Conclusions and future work

In this study, the dynamical behaviour of railway bridges crossed by travelling trains was investigated by adopting a simplified model, i.e. a plate loaded by a travelling distributed mass, solved by means of the Rayleigh-Ritz method.

The effects of each of the model governing parameters was studied introducing a dynamic function of the travelling speed, equivalent to a ‘frequency response function’ for time-varying coefficient systems. This function can be an effective tool for studying the dynamic behaviour of a structure crossed by travelling loads, since the travelling speed is the most important parameter influencing the dynamic stresses in railway bridges, which in general increase with increasing speed.

In particular, it was shown how different spatial distributions of the load can deeply influence the dynamic response of the structure, highlighting the importance of properly modelling the ballast. Future work will thus concern this significant problem.

Acknowledgments

This study was developed within the INTERMECH laboratory with the contribution of the Regione Emilia Romagna - Assessorato Attività Produttive, Sviluppato Economico, Piano telematico, PRRIIT misura 3.4 azione A Obiettivo 2.

References

- [1] Fryba L., *Vibration of Solids and Structures under Moving Loads*, 3rd edition, Telford, 1999.
- [2] Fryba L., *Dynamics of Railway bridges*, Telford, 1996.
- [3] Lin Y.H., “Vibration analysis of Timoshenko beams traversed by moving loads”, *Journal of Marine Science and Technology* 2 (4), pp. 25-35, 1994.
- [4] Stancioiu D., Ouyang H., Mottershead J.E., “Vibration of a continuous beam excited by a moving mass and experimental validation”, *Journal of Physics*, Conference series 181, 1999.
- [5] Adetunde I.A., “Dynamical Behavior of Euler-Bernoulli Beam Traversed by Uniform Partially Distributed Moving Masses”, *Research Journal of Applied Sciences* 2 (4), pp. 476-483, 2007.
- [6] Lin Y.H., Cho C.H., “Vibration suppression of beam structures traversed by multiple moving loads using a damped absorber”, *Journal of Marine Science and Technology* 1 (1), pp. 39-48, 1993.
- [7] Timoshenko S., Young D.H., Weaver W., *Vibration problems in engineering*, 4th edition, Wiley, 1974.

Advanced Operational Modal Analysis Methods for Linear Time Periodic System Identification

Mathew S. Allen,

*Department of Engineering Physics
University of Wisconsin
Madison, WI 53706
msallen@engr.wisc.edu*

Shashank Chauhan

*Brüel & Kjær
Sound & Vibration Measurement A/S
Skodsborgvej 307
DK-2850 Nærum, Denmark
schauhan@bksv.com*

&

Morten Hartvig Hansen

*Wind Energy Department
Risø National Laboratory
P.O. Box 49, DK-4000 Roskilde
Denmark*

ABSTRACT

Often structural dynamic systems cannot be modeled with constant stiffness, mass and damping. For example, wind turbines, helicopters, turbomachinery, and a variety of nonlinear structures linearized about a periodic limit cycle all may contain time-periodic terms in their equations of motion even if the equations are still linear. Linear time periodic systems such as these may exhibit parametric resonance, where the damping in the system is negative at certain rotational frequencies, leading to catastrophic failure. The authors previously presented an extension of operational modal analysis to linear time periodic systems. The previous work introduced a new type of spectrum, dubbed the harmonic autospectrum, discussed how to interpret the spectra, and showed how the simple peak picking method could be used to extract an estimate for the linear time-periodic model of a system from measurements. This paper builds on that work, revealing how more advanced operational modal analysis methods can be extended to linear time-periodic systems. Curve fitting approaches for both the harmonic autospectra and the positive harmonic spectra are applied to simulated measurements from two time-periodic systems, and the OMA based Enhanced Mode Indicator Function (EMIF) method is used to extract the modal parameters from the enhanced positive power spectrum. These extensions are found to provide more accurate estimates of the damping of the modes of the time-periodic systems, and to provide good estimates of the mode shapes of the systems so long as the measurements stand out clearly above the noise. Application of the complex mode indicator function and the EMIF algorithm makes it possible to separate the forward and backward whirling modes of a wind turbine, which is difficult since each of these modes is manifest at several harmonics due to the anisotropy in the tower supporting the turbine.

1. INTRODUCTION

Many important structural systems require time-varying terms in their equations of motion. For example, the stiffness matrix of a two-bladed wind turbine [1] or any wind turbine with non-identical blades [2] depends on the angle of the rotor, and if the rotor speed is constant the equations of motion become linear time periodic (LTP). Linear time periodic equations of motion are commonly used to model other kinds of rotating machinery [3], for studying the stability of various classes of nonlinear systems linearized about a periodic limit cycle, and they have also been used to accelerate laser Doppler vibrometry measurements using the Continuous Scan (CSLDV) approach [4].

In a prior work, the authors presented a operational modal analysis (OMA) methodology for linear time periodic systems and validated it using simulated measurements from a Mathieu oscillator and a rotating wind turbine [5, 6]. Measurements from the latter were simulated using HAWC2 [7], a high fidelity simulation code that includes the random loading that the wind applies to the rotating turbine. The LTP-OMA methodology was subsequently applied to continuous scan laser vibrometry measurements from a few different structures [8], revealing that the methodology is capable of extracting detailed mode shapes from real experimental measurements.

The authors' original work [5, 6] presented the LTP-OMA methodology and focused on interpreting spectral measurements from the time-periodic systems. The simple peak-picking method was used to extract time-periodic models of the systems from the autospectrum of the output. Several more advanced techniques exist for interrogating and curve fitting operational modal analysis measurements from linear time invariant systems. This work shows how some of those methods can be applied to measurements from linear time periodic systems. Methods for curve fitting the spectra to a modal model, both the full harmonic power spectra as well as the positive harmonic spectra, and the two methods are compared. The OMA based Enhanced Mode Indicator Function (EMIF) method [9], an extension to the complex mode indicator function (CMIF) is also applied to the measurements and its performance is evaluated.

The following section reviews the LTP-OMA identification methodology and shows how the advanced OMA methods can be adapted to measurements from the time periodic system. In Section 3 the methods are applied to simulated measurements from two linear time periodic systems, a Mathieu oscillator and a 5MW wind turbine in operation. Section 4 presents the conclusions.

2. THEORY

The state space equations of motion of a linear time-periodic (LTP) system can be written as follows,

$$\begin{aligned}\dot{x} &= A(t)x + B(t)u \\ y &= C(t)x + D(t)u\end{aligned}\tag{1}$$

where $A(t+T_A) = A(t)$ and the other matrices are periodic as well with the same period. The fundamental frequency of the time-periodic system is denoted $\omega_A = 2\pi/T_A$. The state transition matrix (STM) [10] gives the free response of such a system at time t via the relationship,

$$x(t) = \Phi(t, t_0)x(t_0).\tag{2}$$

One can also write the forced response of the system in terms of the STM as follows.

$$y(t) = C(t)\Phi(t, t_0)x(t_0) + \int_{t_0}^t C(t)\Phi(t, \tau)B(\tau)u(\tau)d\tau\tag{3}$$

In the absence of degenerate roots, the state transition matrix of an LTP system can be represented as a modal sum [11, 12],

$$\Phi(t, t_0) = \sum_{r=1}^N \psi_r(t) L_r(t_0)^T e^{\lambda_r(t-t_0)} \quad (4)$$

where λ_r is the r th Floquet exponent of the state transition matrix, ψ_r is the r th time-periodic mode vector of the STM and L_r is the r th column of $\Psi(t) = [\psi_1(t) \ \psi_2(t) \ \dots]^T$. The Floquet exponents of an LTP system are analogous to the eigenvalues of a Linear Time Invariant (LTI) system, which can be written in terms of the damping ratio ζ_r and natural frequency ω_r as $\lambda_r = -\zeta_r \omega_r + i \omega_r \sqrt{1 - \zeta_r^2}$ for an underdamped mode.

In a prior work [5, 6], the authors used this equation to derive an expression for the output auto spectrum of a linear time periodic system in terms of the modal parameters of the state transition matrix. In order to achieve this, first an exponentially modulated version of the output signal is developed as follows,

$$\mathbf{Y}(\omega) = [\dots \ y_{-1}(\omega)^T \ y_0(\omega)^T \ y_1(\omega)^T \ \dots]^T \quad (5)$$

where

$$y_n(\omega) = \int_{-\infty}^{\infty} y(t) e^{(-i\omega - in\omega_A)t} dt \quad (6)$$

is simply the Fourier transform of $y(t)$, shifted in frequency by $n\omega_A$ where n is an integer. Then, the harmonic autospectrum $S_{yy}(\omega) = E(\mathbf{Y}(\omega)\mathbf{Y}(\omega)^H)$ is given by the following equation when $D(t) = 0$.

$$[S_{yy}(\omega)] = \sum_{r=1}^N \sum_{l=-\infty}^{\infty} \sum_{s=1}^N \sum_{k=-\infty}^{\infty} \frac{\bar{\mathbf{C}}_{r,l} \mathbf{W}(\omega)_{r,s,l,k} \bar{\mathbf{C}}_{s,k}^H}{[i\omega - (\lambda_r - il\omega_A)][i\omega - (\lambda_s - ik\omega_A)]^H} \quad (7)$$

The matrix $\mathbf{W}(\omega)$ is a function of the input spectrum and is assumed to be reasonably flat. The dominant terms in the summation above are those for which $i\omega - (\lambda_r - il\omega_A)$ and $i\omega - (\lambda_s - ik\omega_A)$ are both minimum at the same frequency. If the sidebands for mode r do not overlap with those for mode s , then the largest terms occur when $r=s$ and $l=k$ and the expression becomes the following.

$$[S_{yy}(\omega)] \approx \sum_{r=1}^N \sum_{l=-\infty}^{\infty} \frac{\bar{\mathbf{C}}_{r,l} \mathbf{W}(\omega)_{r,l} \bar{\mathbf{C}}_{r,l}^H}{[i\omega - (\lambda_r - il\omega_A)][i\omega - (\lambda_r - il\omega_A)]^H} \quad (8)$$

This is a summation of terms with $(i\omega - \lambda)(i\omega - \lambda)^H$ in the denominator, or squared modal contributions, so the harmonic autospectrum has the same mathematical form as the output autospectrum of a multi-output linear time invariant system. However, there are a few important differences. First, the expression contains a summation over both the modes, whose eigenvalues are λ_r , and also a summation over the harmonics of ω_A using the integer index l . As a result, the autospectrum of the LTP system will have peaks near each natural frequency, ω_r , and also at the frequencies $\omega_r \pm l\omega_A$ for any integer l . Second, the mode vectors $\bar{\mathbf{C}}_{r,l}$ are actually the Fourier coefficients of the time-varying mode shapes of the LTP system as discussed in [5, 6]. These vectors could have infinite dimension, but in practice some finite number of terms N_p is

sufficient to accurately describe the mode shape. Hence, if the system has N_o outputs, then the vectors $\bar{\mathbf{C}}_{r,l}$ have length $N_o \times N_p$, where N_p is the number of modulations used to form $\mathbf{Y}(\omega)$ in eq. (5). Many different vectors $\bar{\mathbf{C}}_{r,l}$ can be identified, but each contains the same Fourier coefficients of the observed mode vectors shifted by l . Specifically, if the time varying mode shape at the output is

$$C(t)\psi_r(t) = \sum_{n=-\infty}^{\infty} \bar{\mathbf{C}}_{r,n} e^{jn\omega_A t} \quad (9)$$

then $\bar{\mathbf{C}}_{r,l}$ is given by.

$$\bar{\mathbf{C}}_{r,l} = [\dots \bar{\mathbf{C}}_{r,-1-l}^T \quad \bar{\mathbf{C}}_{r,-l}^T \quad \bar{\mathbf{C}}_{r,-1-l}^T \quad \dots]^T \quad (10)$$

Additional details of this theory can be found in [5, 6].

In a previous work [5], the authors used the peak picking method together with the expressions developed above to estimate the natural frequencies and the mode vectors $\bar{\mathbf{C}}_{r,l}$ of the LTP system. This work explores other more advanced methods, including curve fitting and advanced spatial domain tools, such as CMIF, based methods for the purpose of modal parameter estimation of LTP systems.

2.1. Curve fitting autospectra

Since the harmonic autospectrum, (or equivalently harmonic power spectral density, here denoted HPSD) of an LTP system was shown in eq. (8) to have same mathematical form as an LTI system (i.e. it is a summation of modal contributions squared), it can be put into a convenient form for curve fitting. Assuming underdamped modes $\lambda_{r+(N/2)} = \lambda_r^*$, where $()^*$ denotes complex conjugate, and contribution due to each underdamped mode can be collected and written as follows after a partial fraction expansion.

$$[S_{yy}(\omega)] \approx \sum_{r=1}^{N/2} \sum_{l=-\infty}^{\infty} \frac{\mathbf{A}_{r,l}}{[i\omega - (\lambda_r - il\omega_A)]} + \frac{\mathbf{A}_{r,l}^*}{[i\omega - (\lambda_r - il\omega_A)^*]} + \frac{\mathbf{B}_{r,l}}{[-i\omega - (\lambda_r - il\omega_A)]} + \frac{\mathbf{B}_{r,l}^*}{[-i\omega - (\lambda_r - il\omega_A)^*]} \quad (11)$$

Alternatively, this could be written as a matrix polynomial model with complex coefficients in even powers of $(i\omega)$. Various algorithms can fit a model of this form to a set of measurements. For this work the Algorithm of Mode Isolation (AMI) [13] was modified to fit a model of the form described above and used to extract modes from the harmonic autospectrum.

2.2. Positive Power Spectra

The power spectrum of a signal possesses four quadrant symmetry, and hence it includes information of system poles twice. This can also be seen in eq. (11), which contains each of the poles, once having positive damping and other having negative damping (note that same is true for the complex conjugate pole as well). These extra negatively damped poles can lead to difficulty when estimating the modal parameters of the system.

This problem can be dealt with by considering positive power spectra instead of power spectra. The inverse FFT of the power spectrum is found, and then a rectangular window is used in the time domain to eliminate the negatively damped modes by retaining only the decaying part of the impulse response function. Thus PPS functions have the same form as a typical frequency response function (FRF) has, making them more suitable for modal parameter estimation. The process of estimating PPS functions from power spectra is described in detail in [9].

In this work, the same approach is used to convert a set of harmonic power spectra into positive harmonic power spectra. Once this has been done, the negatively damped poles are no

longer present and the positive harmonic power spectrum (pHPSD or $S_{yy}^+(\omega)$) can be written in the following mathematical form.

$$\left[S_{yy}^+(\omega) \right] \approx \sum_{r=1}^{N/2} \sum_{l=-\infty}^{\infty} \frac{\mathbf{A}_{r,l}}{[i\omega - (\lambda_r - il\omega_A)]} + \frac{\mathbf{A}_{r,l}^*}{[i\omega - (\lambda_r - il\omega_A)^*]} \quad (12)$$

The pHSPD has the usual magnitude and phase relationship as a frequency response function, so it can often be more accurately curve fit. In the following the AMI algorithm in [13, 14] was used to fit a model of the form above to the power spectra in order to construct the time periodic modes of the system. Since the pHSPD has the same mathematical form as a frequency response function, no modification to the AMI algorithm was necessary when doing this.

2.3. EMIF based Method

The enhanced mode indicator function (EMIF) method was proposed for operational modal analysis in [9]. Here that approach is adapted to parameter estimation on harmonic power spectral measurements (HPSD). OMA-EMIF method works on positive power spectra, which are defined in section 2.2. One begins by choosing a frequency range of interest and also the number of modes to be identified in the chosen frequency range. The number of modes to be identified is typically equal to the number of dominant peaks in the CMIF plot over the chosen frequency range. The positive power spectra in the chosen frequency range are then assembled in an augmented matrix form as shown below, where N_{tot} is the number of responses and N_f is number of frequency lines in chosen frequency range. For an LTP system there are N_p responses for each measurement point, so $N_{tot} = N_o N_p$.

$$[A_0]_{N_{tot} \times (N_{tot} N_f)} = \begin{bmatrix} S_{11}^+(\omega_i) & \dots & S_{11}^+(\omega_{i+N_f}) & \dots & S_{21}^+(\omega_i) & \dots & S_{21}^+(\omega_{i+N_f}) & \dots & S_{p1}^+(\omega_i) & \dots & S_{p1}^+(\omega_{i+N_f}) \\ \vdots & \vdots & \vdots & \vdots & \vdots & \vdots & \vdots & \vdots & \vdots & \vdots & \vdots \\ S_{pq}^+(\omega_i) & \dots & S_{pq}^+(\omega_{i+N_f}) & \dots & \dots & \dots & \dots & \dots & \dots & \dots & S_{pq}^+(\omega_{i+N_f}) \end{bmatrix} \quad (13)$$

This matrix now has all of the spatial information contained in the autospectrum, over all of the frequency lines that have been included in $[A_0]$. A singular value decomposition of this augmented matrix yields left and right singular vectors along with the singular values. Supposing that N_b modes are to be identified from the measurements, the first N_b dominant left singular vectors are chosen to create an enhanced positive power spectra in the chosen frequency range of interest. This is shown in below, where $[U]$ is a matrix of left singular vectors of the augmented matrix.

$$ePPS(\omega) = [\bar{S}(\omega)]_{N_b \times N_{tot}} = [U]_{N_b \times N_{tot}}^T [S^+(\omega)]_{N_{tot} \times N_{tot}} \quad (14)$$

The ePPS functions can now be used to identify the N_b modes by applying a single degree-of-freedom unified matrix polynomial [15] algorithm to each of the peaks in the ePPS. The modal vectors obtained from ePPS functions are in a condensed set of coordinates and can be converted back into physical domain by pre-multiplying the obtained modal vectors with $[U]_{N_b \times N_{tot}}$.

3. Simulated Application Examples

3.1. Mathieu Oscillator

This section applies the proposed methodologies to two different systems. The first is the simple Mathieu oscillator, a spring mass-damper system with time-periodic spring stiffness. The equation of motion for the oscillator is

$$\ddot{y} + 2\zeta\omega_0\dot{y} + (\omega_0^2 + \omega_1^2 \cos(\omega_A t))y = \frac{u(t)}{m} \quad (15)$$

with $2\zeta\omega_0 = c/m$, $\omega_0^2 = k_0/m$, $\omega_1^2 = k_1/m$, and input $u(t)$. The parameters used in this work are the following, $m=1$, $k_0=1$, $k_1=0.4$, and $\omega_A=0.8$ rad/s, which are the same as those used in [5, 6].

3.1.1. Curve Fitting HPSD

The response of the Mathieu oscillator to a broadband random input was simulated using time integration, and the harmonic autospectrum (HPSD) was then computed with $p=2$, so $n = -2 \dots 2$ in eq. (6) so $N_p=5$ and a 5×5 HPSD matrix was produced. The primary column of this matrix (i.e. the $(p+1)^{\text{th}}$ or 3^{rd} column in this case) contains all of the information needed to identify the parameters of the system, so only it will be considered in the curve fit. The composite [13], or average, of this 5×1 matrix is shown in Figure 1 with a black line. The composite of a curve fit is also shown as well as the difference between the two. The curve fit can be seen to follow the measurements closely near each of the peaks in the spectrum, but the baseline level of the curve fit is too high so the highest frequency peak is almost obscured by the tails of the dominant modes.

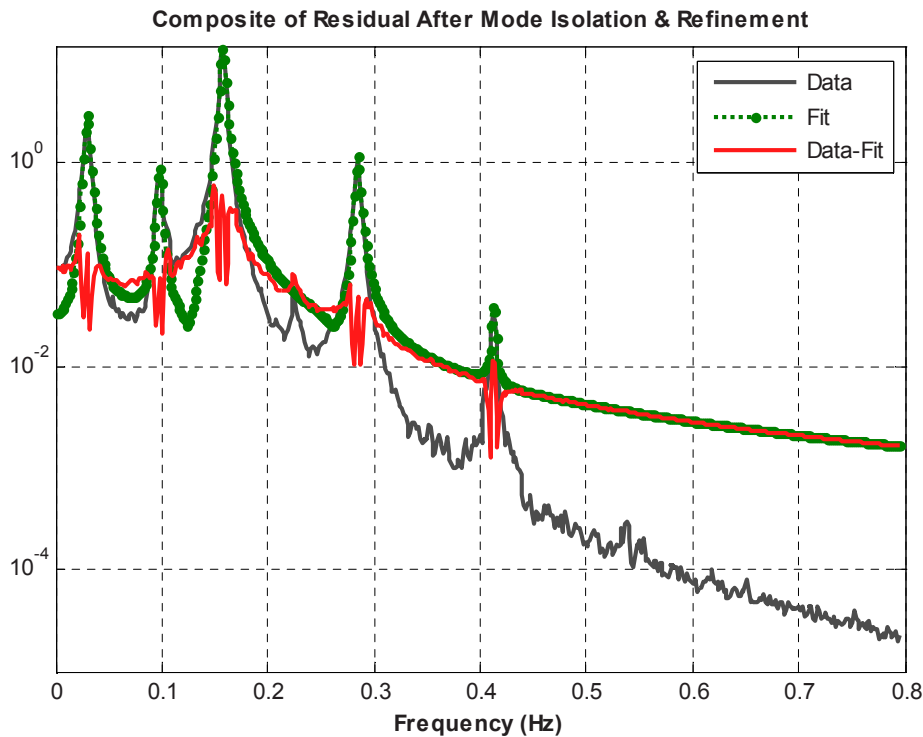


Figure 1: Harmonic Autospectrum of Mathieu Oscillator response with: (black line) composite of actual autospectrum, (green dotted) curve fit to the HPSD and (red) composite of the difference between the curve fit and the measurements.

The authors have seen this same phenomena occur when fitting conventional autospectra of structural systems. For those systems the curve fitting routine seems to ascribe more complexity to the modes than is warranted. Better results can sometimes be obtained if the curve fitting routine is forced to fit a real mode model to the measurements, but that is not possible for measurements from an LTP system since the HPSD must be fit to a complex mode model. The

authors also noted that the damping obtained for each of the modes seemed to be somewhat sensitive to the number of points around each peak that was used in the curve fit.

3.1.2. Curve Fit to Positive HPSD (S_{yy}^+)

The positive power spectra of the measurements were formed as discussed in Section 2.2. Figure 2 shows a composite of the 5x1 positive power spectrum in the same format used in the previous figure, as well as a curve fit. The positive power spectrum seems to be smoother than the full HSPD, and the fit agrees very well with the measurements. The residual (red line) is small and seems to contain only noise, suggesting that the curve fit has extracted all of the meaningful information from the measurement. The results of the curve fits shown in Figures 1 and 2 are summarized in Table 1, which will be discussed later.

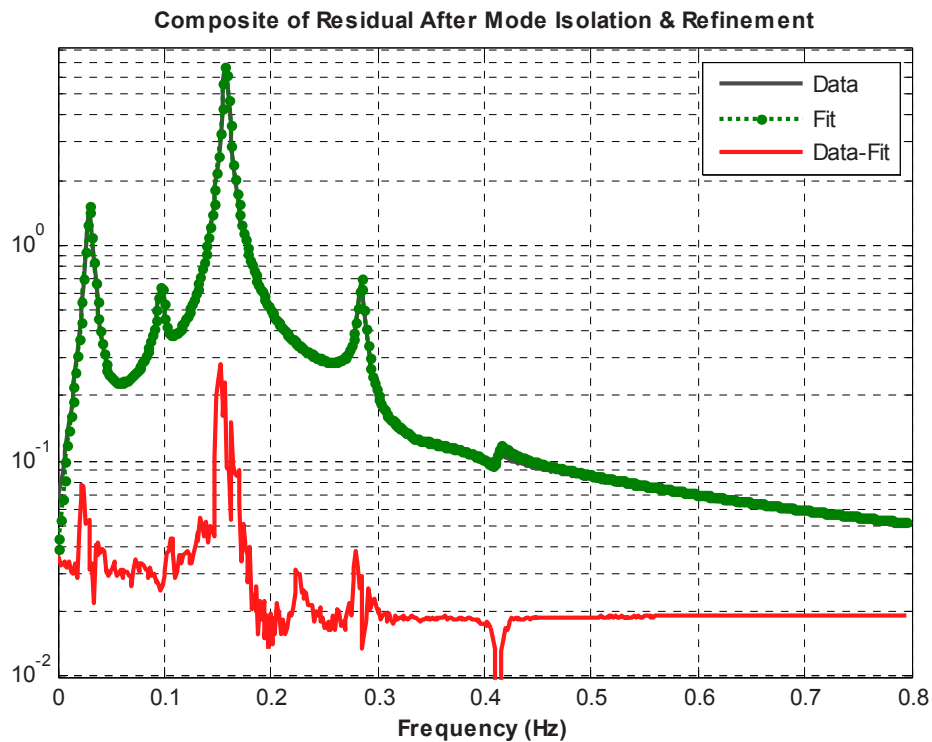


Figure 2: Positive Harmonic Autospectrum (S_{yy}^+) of Mathieu Oscillator response with: (black line) composite of actual autospectrum, (green dotted) curve fit to the HPSD and (red) composite of the difference between the curve fit and the measurements.

3.1.3. Application of OMA-EMIF Method to HPSD

The OMA-EMIF method was also applied to the simulated measurements from the Mathieu oscillator. In doing so, the full power spectrum matrix for $p=2$ was used (rather than the column used in the previous two subsections). A CMIF plot was first created from the HPSD matrix, which is shown in Figure 3. The CMIF plot is far more convenient to view than the individual elements of the harmonic power spectrum matrix, which were shown in [5, 6], yet it retains information regarding the mode shapes of the system that can be used to detect modes with close natural frequencies. In this plot, the peak at 0.982 Hz is the Floquet exponent of the system and other peaks of the same amplitude that appear in the plot are modulations of the Floquet exponent, $\lambda + in\omega_A$, for $n = -2, \dots, 2$, where $\omega_A = 0.8$ rad/s. Other weaker peaks are also visible in the CMIF for other values of n .

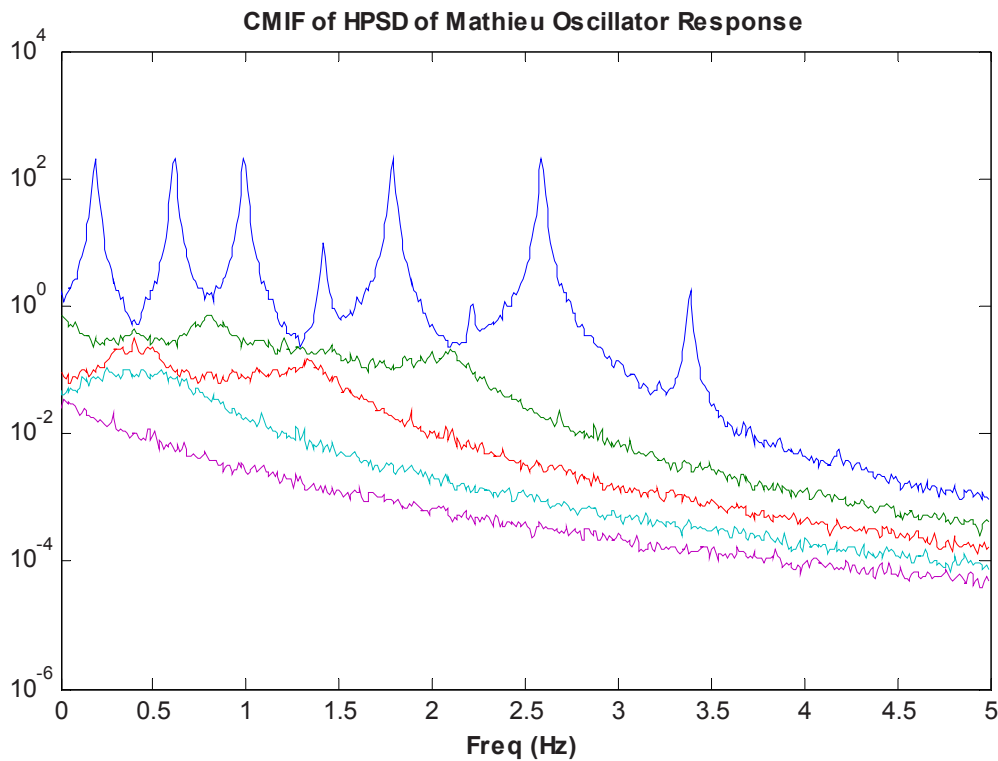


Figure 3: CMIF of the HPSD of the Mathieu oscillator response. The individual curves correspond to different singular values of the HPSD matrix at each frequency.

The EMIF methodology was then applied to the measurements, by creating the enhanced positive power spectrum and then fitting low-order modal models to them. The modal parameters of each of the peaks were identified, but for brevity only the mode identified at the 0.982 Hz peak will be considered.

3.1.4 Comparison of Numerical Results

Table 1 shows the result of parameter estimation using various methods. The column labeled “Peak Picking” shows the result obtained by peak picking, which was previously published in [6]. Each of the peaks in the HPSD, pHPSD and CMIF were fit by each method, and they all may contain useful information regarding the mode shapes and eigenvalues of the LTP system. However, for brevity only the result obtained from the primary peak near 0.98 rad/s is compared.

n	<i>Fourier Coefficients of the Mathieu Oscillator Mode Shape $\bar{C}_{1,n}$</i>				
	Analytical	Peak Picking	Fit to Harmonic PSD	Fit to Positive HPSD	OMA-EMIF
-2	0.067	0.0650 - 0.0090i	0.0667 + 0.00233i	0.0652 + 0.00095i	0.063 - 0.014i
-1	-0.220	-0.220 + 0.0061i	-0.217 - 0.00151i	-0.219 - 0.00113i	-0.219+0.009i
0	1	1	1	1	1
1	0.092	0.0906 + 0.0011i	0.0910 - 0.00126i	0.0902 - 0.00212i	0.094 + 0.001i
2	0.00320	0.0028 - 0.0001i	0.00340 + 0.00050i	0.00308 + 0.00029i	0.003 + 0.0004i
λ	-0.0200 + 0.987i	-0.0270 + 0.986i	-0.0169 + 0.987i	-0.0172 + 0.988i	-0.0124 + 0.988i
ω_n	0.987	0.986	0.987	0.988	0.988
ζ	0.0203	0.0274	0.0171	0.0174	0.0123

Table 1: Mode shape coefficients identified at the fundamental peak using various methods. The analytical vector $\bar{C}_{1,0}$ is shown in the first column.

The results obtained by each of these methods are quite similar. The only large discrepancy between the methods occurs for the damping ratio, which is poorly estimated using the peak picking method as expected. The results obtained using the HPSD and the positive HPSD seem to have similar quality, even though the curve fit on the positive power spectrum seemed to be far more satisfying. The OMA-EMIF agrees well with the other two curve-fitting methods.

The result is somewhat surprising if the fit to one of the weak peaks is compared. Table 2 compares the Fourier coefficients obtained at the 2.6 rad/s peak in Figures 1 and 2. This peak was very weakly represented in the measurements, and was seen to be almost buried in the residual in the HPSD curve fit in Figure 1. The estimates of the Fourier coefficients produced by the peak picking method are up to four times larger than the true coefficients, but the curve fitting methods give results with even greater errors. This anomaly is readily explained. The measurements from which the coefficients 2, 3 and 4 were obtained were plotted (not shown here) and it was observed that none of those measurements showed any visual evidence of a mode near 2.6 rad/s. The spurious values seen in the table seem to arise as the least squares procedure attempts to fit a mode to the shoulder of one of the more prominent peaks. On the other hand, a weak peak was visible in the measurement from which the $n=1$ coefficient was estimated, but even there the peak picking method seems to have achieved a better estimate of the Fourier coefficient.

n	<i>Fourier Coefficients of the Mathieu Oscillator Mode Shape $\bar{C}_{1,n}$</i>			
	Analytical	Peak Picking	Fit Harmonic PSD	Fit Positive HPSD
0	1	1	1	1
1	0.092	0.0918 + 0.00090i	0.0626 + 0.0246i	-0.0701 + 0.00662i
2	0.003197	0.0136 - 0.00054i	-0.32764 + 0.055243i	0.940 + 0.184i
3	0.000039	0.000824 - 0.000289i	-0.0137 - 0.0133i	-0.112 - 0.0409i
4	-0.000015	0.000053 - 0.00021i	-0.000688 + 0.00072i	-0.0152 - 0.00348i
λ	-0.0200 + 2.587i	-	-0.0185 + 2.592i	-0.0223 + 2.593i
ω_n	2.587	2.588	2.592	2.593

Table 2: Mode shape coefficients identified at the 2.6 rad/s peak in the HPSD and pHPSD using various methods.

3.2. Simulated Measurements from a Wind Turbine

This section applies the proposed LTP system identification methods to a much more challenging problem, a 5MW wind turbine rotating at constant speed due to aerodynamic forcing. Turbulence in the incoming wind provides a source of broadband random excitation. The system and conditions studied here are identical to those reported in the authors' prior work [5, 6], where peak picking was used to identify the edgewise modes of the turbine. In that work, some difficulty was reported in distinguishing the forward and backward whirling modes of the turbine since many of their harmonics overlap. Here the advanced LTP system identification algorithms will be applied to that system in an effort to enhance the results. The wind turbine is rotating at a constant rate of 0.201 Hz in these measurements, driven by a wind with logarithmic shear with 18 m/s velocity at hub height.

Measurement of the edgewise motion of each of the three blades was simulated, as well as lateral and fore-aft motion of the tip of the tower. The harmonic autospectrum matrix was computed for these five measurements with $n=-2\dots 2$. The total measurement set is quite difficult to visualize, so two separate CMIFs were created, shown in Figures 4 and 5. Figure 4 shows a CMIF including the two measurement points on the tower and all of their harmonics. As with the results in the previous section, only the primary column of the HPSD matrix was used, so the CMIF is based on a 10×2 matrix. The CMIF clearly shows the presence of the first two modes of the tower, both near 0.27 Hz. The forward whirling mode of the rotor is also visible at 1.16 Hz, and there is a very small peak near 0.76 Hz, where the corresponding backward whirling mode should be. A harmonic of the forward mode also seems to be visible near 1.36 Hz. Finally, there is a large triangular shaped peak in the spectrum near the blade-pass frequency of 0.6 Hz. This is due to the aerodynamic forcing function of the system and is not a mode of the structure, as discussed in [6, 16].

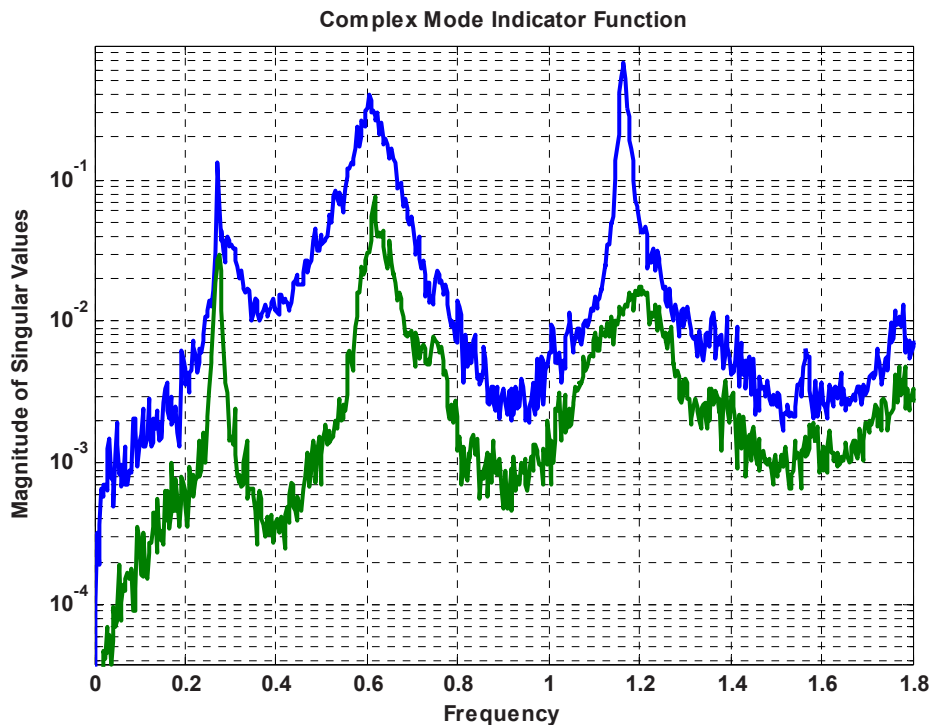


Figure 4: CMIF of the HPSD for tower motion of wind turbine.

Figure 5 shows the CMIF using the three edgewise blade measurements as references. In this spectrum, contamination is clearly visible at the rotor speed and its harmonics: 0.2 Hz, 0.4

Hz, 0.6 Hz and (diminished) at 0.8 Hz. The dominant peaks in the spectrum are the edgewise modes of the turbine near 0.96 Hz. These are the same forward and backward whirling modes that were seen in [Figure 4](#), but the blade measurements were taken in the rotating reference frame so those two modes appear at the same frequency in these measurements. The second singular value seems to show a coherent peak at 0.96 Hz, indicating that two modes are present at this peak. Each of these modes are expected to appear at modulations of this frequency: $0.96 + n0.201\text{Hz}$ as well. Any modulations below 0.96 Hz would be obscured by the harmonics of the rotor frequency, but two harmonics are visible at 1.16 and 1.36 Hz. However, only one singular vector is visible at each of those peaks, suggesting that one of the two modes is obscured by noise at those frequencies due to the non-ideal nature of the input spectrum.

In order to quantify these modes, the OMA-EMIF algorithm was applied to the peaks at 0.96 Hz and 1.36 Hz. Two modes were identified at the former frequency and one at the latter with natural frequencies 0.9623, 0.9636, and 1.366 Hz. The corresponding mode vectors are shown in [Table 6](#). The magnitude and phase (in degrees) of each Fourier coefficient is shown. The first mode (0.9323 Hz) shows significant harmonics at $n=0$ and $n=2$, the latter being about 6-7% of the former in magnitude. The other harmonics seem to be caused by noise in the measurements. In contrast, the second mode (0.9636 Hz) only has significant Fourier coefficients for $n=0$; all of its other Fourier coefficients seem to be at the level of the noise. The coefficients identified at 1.366 Hz are due to a modulation of one or both of the first two modes by twice the rotational frequency. Their Fourier coefficients have been shifted (e.g. to account for l in eq. (10)) so that they can be compared with the other two modes. The resulting harmonics agree very well with those for the first mode in both magnitude and phase. This suggests that the mode identified at 1.366 Hz is merely a replicate of the 0.9323 Hz mode due to the modulation in eq. (7).

These results agree very well with what would be expected for a turbine such as this. The phases of the $n=0$ harmonics of the first mode decrease from blade 1 to 2 to 3, revealing that this is a forward whirling mode. Its $n=2$ harmonics show phase angles that increase from blade 1 to 2 to 3, indicating that the $n=2$ harmonics are a backward whirling component of this forward whirling mode. This same behaviour was observed for a simulated turbine in [2] and arises due to the anisotropy of the tower. The phases of the $n=0$ harmonic of the second mode reveal that this mode is a backward whirling mode. None of the other harmonics for that mode show the expected phase relationship, so they are all most likely due to noise.

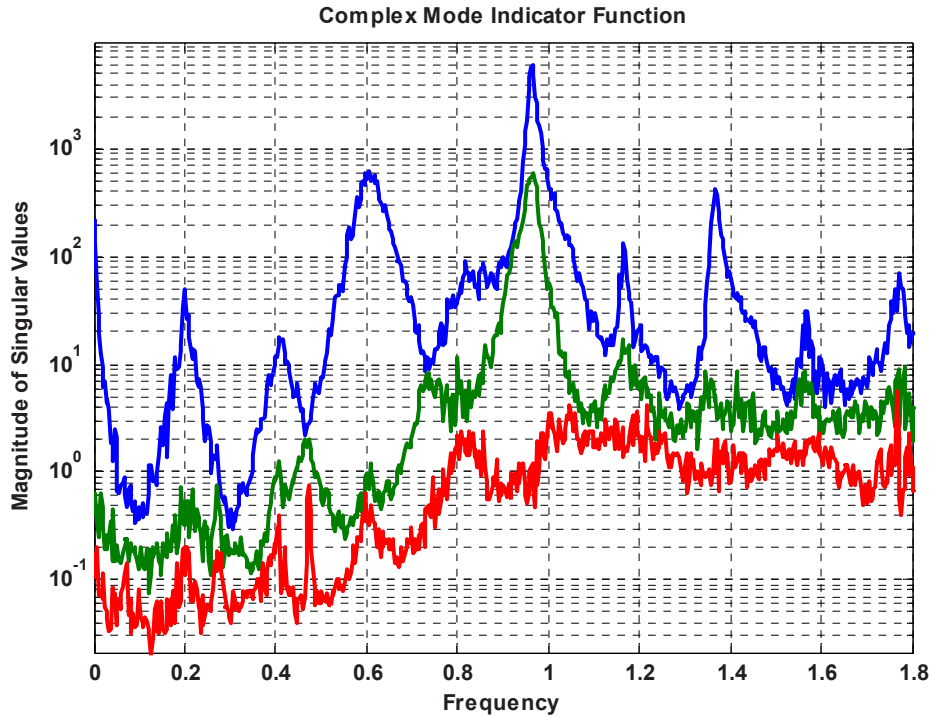


Figure 5: CMIF of the HPSD for edgewise motion of the three blades of the wind turbine.

n	Blade	0.9623 Hz, M1		0.9636 Hz, M2		1.366 Hz	
		Mag	Phs (°)	Mag	Phs (°)	Mag	Phs (°)
-2	B1	0.023	-174	0.123	-158	-	-
-2	B2	0.024	-179	0.142	-165	-	-
-2	B3	0.024	-175	0.116	-171	-	-
-1	B1	0.017	-4	0.040	19	-	-
-1	B2	0.006	139	0.036	110	-	-
-1	B3	0.018	-78	0.028	-88	-	-
0	B1	1	0	1	0	1	0
0	B2	0.957	-121	1.039	119	0.948	-122
0	B3	0.964	122	1.045	-117	0.946	122
1	B1	0.025	-117	0.015	-123	0.022	-117
1	B2	0.022	-114	0.032	54	0.020	-108
1	B3	0.015	-135	0.036	-29	0.016	-126
2	B1	0.068	-102	0.006	50	0.072	-102
2	B2	0.070	21	0.011	0	0.072	21
2	B3	0.067	138	0.009	15	0.069	138
3	B1	-	-	-	-	0.002	-73
3	B2	-	-	-	-	0.003	125
3	B3	-	-	-	-	0.008	64

Table 6: Fourier coefficients identified from the HPSD using the OMA-EMIF method.

4. CONCLUSIONS

This paper has extended several advanced methods for operational modal analysis to linear time periodic systems. Curve fitting methods were demonstrated both on the harmonic autospectrum and the positive harmonic autospectrum. The latter were found to be simpler to curve fit and to produce good agreement between the reconstructed and measured positive autospectra. Even then, both methods were found to identify natural frequencies, damping ratios

and mode shapes of similar quality. On the other hand, when the curve fitting methods were applied to very weak peaks in the harmonic autospectra, both methods gave overly large estimates for the Fourier coefficients that were buried in the noise. In this respect, the peak picking method was preferred for these very weak peaks. In any event, it seems advisable to question the accuracy of any Fourier coefficient that is not well represented in the spectrum.

The methods were also applied to simulated measurements from a 5MW wind turbine which was rotating at constant speed. Complex Mode Indicator Functions were formed from the measurements and shown to reveal many of the modes of the turbine, including the first edgewise modes of the turbine, which are of special interest since they tend to be lightly damped and hence can limit the life of the turbine. The OMA-EMIF method was also applied to the measurements and was successful in extracting the forward and backward whirling modes, both of which appeared at the same frequency in the blade measurements. This method proved to be a significant aide; in the authors previous work [5, 6] the shapes identified by peak picking were shown and with that method it was very difficult to separate those two modes.

5. ACKNOWLEDGEMENT

The first author was supported by the National Science Foundation under Grant CMMI-0969224 while completing this work.

6. REFERENCES

- [1] K. Stol, M. Balas, and G. Bir, "Floquet modal analysis of a teetered-rotor wind turbine," *Journal of Solar Energy Engineering-Transactions of the ASME*, vol. 124, pp. 364-371, Nov 2002.
- [2] P. F. Skjoldan and M. H. Hansen, "On the similarity of the Coleman and Lyapunov-Floquet transformations for modal analysis of bladed rotor structures," *Journal of Sound and Vibration*, vol. 327, pp. 424-439, 2009.
- [3] I. Bucher and O. Shomer, "Detecting asymmetry in rotating structures a combined acutation and signal processing approach," in *23rd International Modal Analysis Conference (IMAC XXIII)* Orlando, Florida, 2005.
- [4] M. S. Allen and M. W. Sracic, "A New Method for Processing Impact Excited Continuous-Scan Laser Doppler Vibrometer Measurements," *Mechanical Systems and Signal Processing*, vol. 24, pp. 721-735, 2010.
- [5] M. S. Allen, M. W. Sracic, S. Chauhan, and M. H. Hansen, "Output-Only Modal Analysis of Linear Time Periodic Systems with Application to Wind Turbine Simulation Data," in *28th International Modal Analysis Conference (IMAC XXVIII)* Jacksonville, Florida, 2010.
- [6] M. S. Allen, M. W. Sracic, S. Chauhan, and M. H. Hansen, "Output-Only Modal Analysis of Linear Time Periodic Systems with Application to Wind Turbine Simulation Data," *Mechanical Systems and Signal Processing*, vol. submitted Oct. 2010, 2010.
- [7] M. O. L. Hansen, J. N. Sørensen, S. Voutsinas, N. Sørensen, and H. A. Madsen, "State of the art in wind turbine aerodynamics and aeroelasticity," *Progress in Aerospace Sciences*, vol. 42, pp. 285-330, 2006.
- [8] S. Yang and M. S. Allen, "Output-Only Modal Analysis Using Continuous-Scan Laser Doppler Vibrometry and Application to a 20kW Wind Turbine," in *29th International Modal Analysis Conference (IMAC XXIX)* Jacksonville, Florida, 2011.
- [9] S. Chauhan, R. Martell, D. L. Brown, and R. J. Allemang, "Considerations in the Application of Spatial Domain Algorithms to Operational Modal Analysis," in *International Seminar on Modal Analysis* Leuven, Belgium, 2006.
- [10] J. S. Bay, *Fundamentals of Linear State Space Systems*. Boston: McGraw-Hill, 1999.

- [11] M. S. Allen, "Frequency-Domain Identification of Linear Time-Periodic Systems using LTI Techniques," *Journal of Computational and Nonlinear Dynamics* vol. 4, 24 Aug. 2009.
- [12] M. Allen and J. H. Ginsberg, "Floquet Modal Analysis to Detect Cracks in a Rotating Shaft on Anisotropic Supports," in *24th International Modal Analysis Conference (IMAC XXIV)* St. Louis, MO, 2006.
- [13] M. S. Allen and J. H. Ginsberg, "A Global, Single-Input-Multi-Output (SIMO) Implementation of The Algorithm of Mode Isolation and Applications to Analytical and Experimental Data," *Mechanical Systems and Signal Processing*, vol. 20, pp. 1090–1111, 2006.
- [14] M. S. Allen and J. H. Ginsberg, "Global, Hybrid, MIMO Implementation of the Algorithm of Mode Isolation," in *23rd International Modal Analysis Conference (IMAC XXIII)* Orlando, Florida, 2005.
- [15] R. J. Allemang and D. L. Brown, "A Unified Matrix Polynomial Approach to Modal Identification," *Journal of Sound and Vibration*, vol. 211, pp. 301-322, 1998.
- [16] D. Tcherniak, S. Chauhan, and M. H. Hansen, "Applicability limits of Operational Modal Analysis to Operational wind turbines," in *28th International Modal Analysis Conference (IMAC XXVIII)* Jacksonville, Florida, 2010.

Normalization of Complex Modes from Mass Perturbations

Dong-Woo Seo¹, Farid Moghim², Dionisio Bernal³

¹ Graduate students, Northeastern University, Civil and Environmental Engineering, Boston, MA 02115, USA

² Professor, Northeastern University, Civil and Environmental Engineering, Center for Digital Signal Processing, Boston, MA 02115, USA

ABSTRACT

Operational modal analysis has become an alternative for structures in which input data is difficult to measure. The sensitivity-based operational mode shape normalization technique was originally introduced by Parloo et al. in 2002. The technique has been widely used and is still receiving a considerable amount of attention by modal analysis researchers. Up to this point attention has been focused on real mode shapes. There are instances, however, where complex modes may have to be used because the modal density or the damping distribution is such that the use of a normal modes model is not warranted. The essential problem in normalizing complex modes using eigenvalue sensitivity is the variability of the real part of the poles. This paper examines two options: 1) neglecting modal complexity and using standard real mode fit and 2) using the complex mode. Results from an experiment using these two alternatives are presented.

1. Introduction

The sensitivity-based operational mode shape normalization technique for the scaling of operational mode shapes was introduced by Parloo et al. [1]. In recent years, some variations of this strategy have been proposed [1-4]. The motivation for these studies being to improve accuracy given the experimental limitation with which small changes in eigenvalues can be identified. All of the equations for estimating scale factor developed thus far have the assumption that the mode shapes of the system are real. It is understood, however, that this assumption may not be valid in many cases. The approach originally suggested by Parloo et al. [1] was not explicitly formulated for the case of complex modes but its extension to this case was conceptually outlined in the original reference and is used here to derive the explicit form of the equation for the scaling in the case of the complex eigensolution [5,6]. In this paper we begin by with an analytical examination of the issue of selecting between real or complex modes and subsequently present some results from an experiment.

2. Mass Change Method

2.1. Some theoretical relations

The mass change method consists of performing operational modal analysis on both the original and a modified structure. The modification is carried out by attaching masses to selected locations. The mass matrix of the modified structure can be written as

$$M = M_0 + \beta M_1 \quad (1)$$

where, M_0 is the mass matrix prior to the perturbation; M_1 is a matrix describing the spatial distribution of the mass modification and β is a scaling parameter with respect to which the rates of change are computed. The arbitrarily normalized mode ψ_j and the mass normalized one ϕ_j are related by a constant α_j , namely

$$\phi_j = \alpha_j \psi_j \quad (2)$$

The expression that normalizes the modes to unit modal mass based on eigenvalue sensitivity when the eigenvectors are complex is [5]

$$\alpha_j^2 = \frac{-\frac{d\lambda_j}{d\beta}}{(\bar{\psi}_j^T M_1 \bar{\psi}_j) \lambda_j^2} \quad (3)$$

where, λ_j is the complex eigenvalue. The expression that normalizes the modes to unit modal mass when the eigenvectors are real is [1]

$$\alpha_j^2 = \frac{-\frac{d\omega_j^2}{d\beta}}{(\phi_j^T M_1 \phi_j) \omega_j^2} \quad (4)$$

where, ω_j is the undamped natural frequency and ϕ_j is the real arbitrarily scaled mode shape. Eq.3 and Eq.4 are exact but cannot be evaluated without approximation because there is no way to get the exact value of the derivatives using finite difference (unless the mathematical function connecting the eigenvalue to β is known). To minimize the error coming from estimation of the derivatives by finite difference one strives to use as small as possible mass perturbation. Nevertheless, approximation in the identification needs to be considered when selecting the magnitude of the change. Note that variability in the identification may have a larger affect on Eq.3 than on Eq.4 because the real parts of the eigenvalues are known to have a much larger coefficient of variation than the imaginary parts.

To get some idea of the possible effect of considering modal complexity we begin by comparing Frequency Response Functions (FRFs) computed using Eq.3 and Eq.4 in the case of a system that is non-classically damped and where the real modes are approximated by normalizing the maximum amplitude of the complex mode to unity and then discarding the imaginary parts.

The structure considered is a 3-DOF lumped mass tower where a concentrated dashpot externally grounded is added on the first level. In Fig.1 shows the drive-point FRF for the third coordinate obtained using $\beta = 0.01$ and 0.1 . As expected, the accuracy of the complex mode solution deteriorates some due to the finite difference approximation of the derivative when $\beta = 0.1$ but the result is in all cases notably more accurate that the approximation obtained with the normal modes.

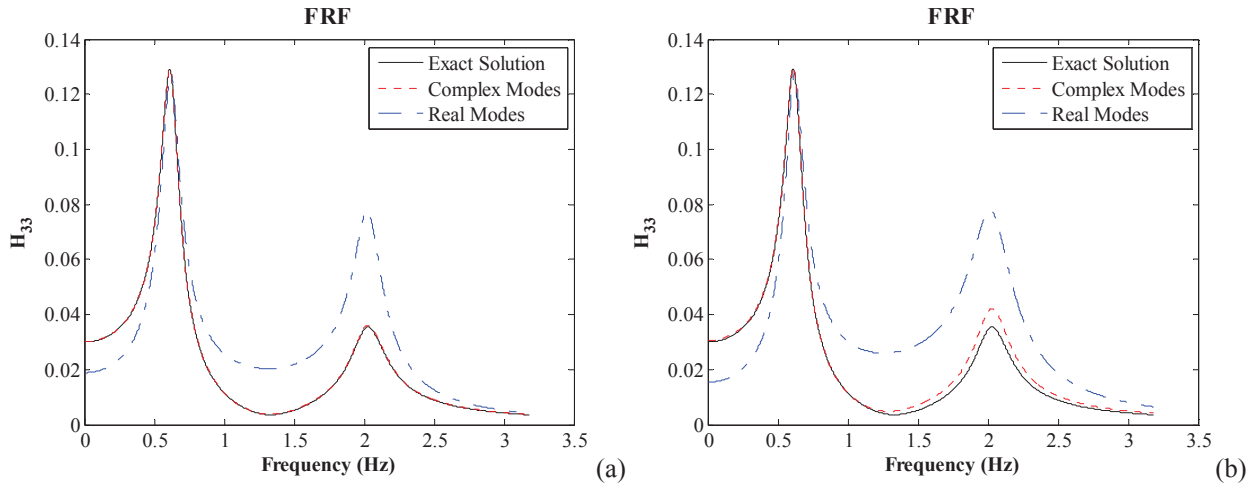


Figure 1: Comparisons of FRFs among three solutions: (a) is H_{33} with β equal to 0.01; (b) is H_{33} with β equal to 0.1

3. Experiment

3.1. Magnetic damper

In an attempt to introduce modal complexity we added a localized damping force to a 4 story tower structure. The localized damping was realized using magnets that were attached to a fixed structure and copper plates that were affixed to the structure. The principle used is the fact that the motion of the copper plate on the magnetic field induced electrical current. This current then creates its own magnetic field and based on the Lenz's law the secondary magnetic field opposes the initial field (the field of a moving magnet) and the interaction causes a force that resists the change in magnetic flux which opposite to the relative velocity and is thus dissipative in nature (see Fig. 2).

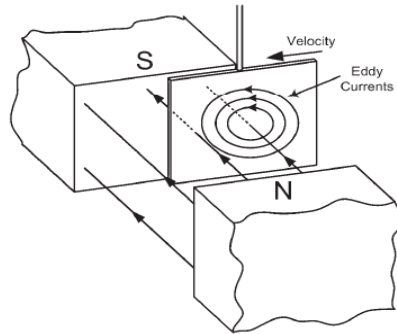


Figure 2: Time varying magnetic flux [7]

The magnitude of the dissipation increases with: 1) stronger magnetic fields, 2) faster changing fields and 3) using thicker conductive plate and lower resistivity materials, since the movement of the electrons is easier in this case.

4. Experimental Campaign

4.1. Experiment setup

The set up used to create the concentrated dissipation is shown in Fig.3. A copper plate with a thickness of

1/8" is used as a conductor sheet. For creating the magnetic field Neodymium magnets were used. These magnets are attached to the piece of the Plexiglas. The Plexiglas is attached to a stand and placed in front of the copper plate which is glued to the floor of the structure.

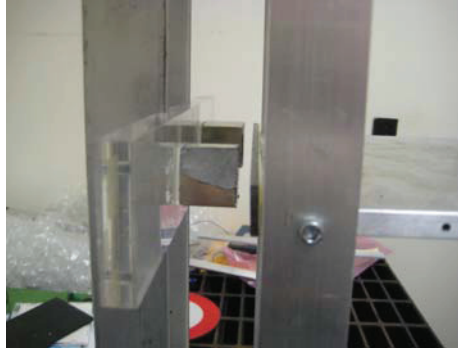


Figure 3: Close view between the magnets and the structure

The structure considered is the 5-story aluminum tower depicted in Fig.4. The structure is instrumented with 5 accelerometers, one attached one each level. The excitation used to drive the system is a burst random signal supplied by a shaker located on the first level (not shown in the figure).

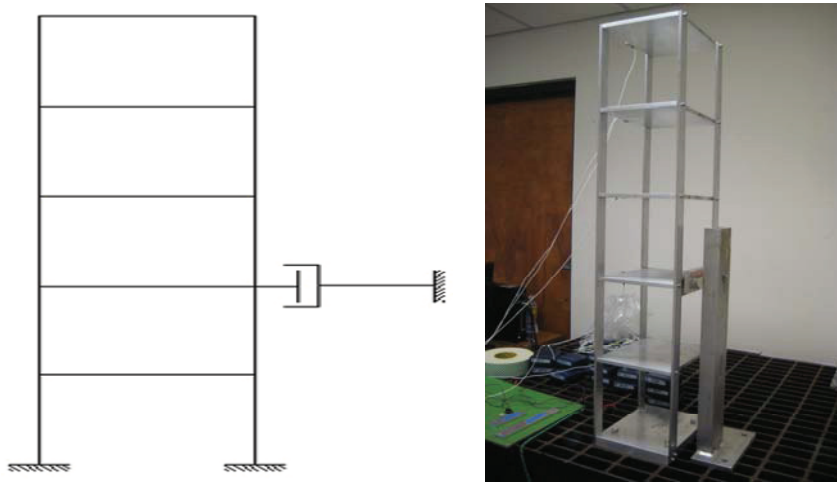


Figure 4: A 5-story aluminum tower with magnets on the second level

Results for a drive point FRF at coordinate #1 computed using the identified arbitrarily scaled modes normalized using Eqs. 3 and 4 are compared with result experimentally extracted by treating the input as known in Fig.5. As can be seen the results are reasonably good and the match of the complex model is somewhat better than that achieved by the normal modes. It's worth noting that the added mass used in this case was $\beta = 0.12$, which is quite large.

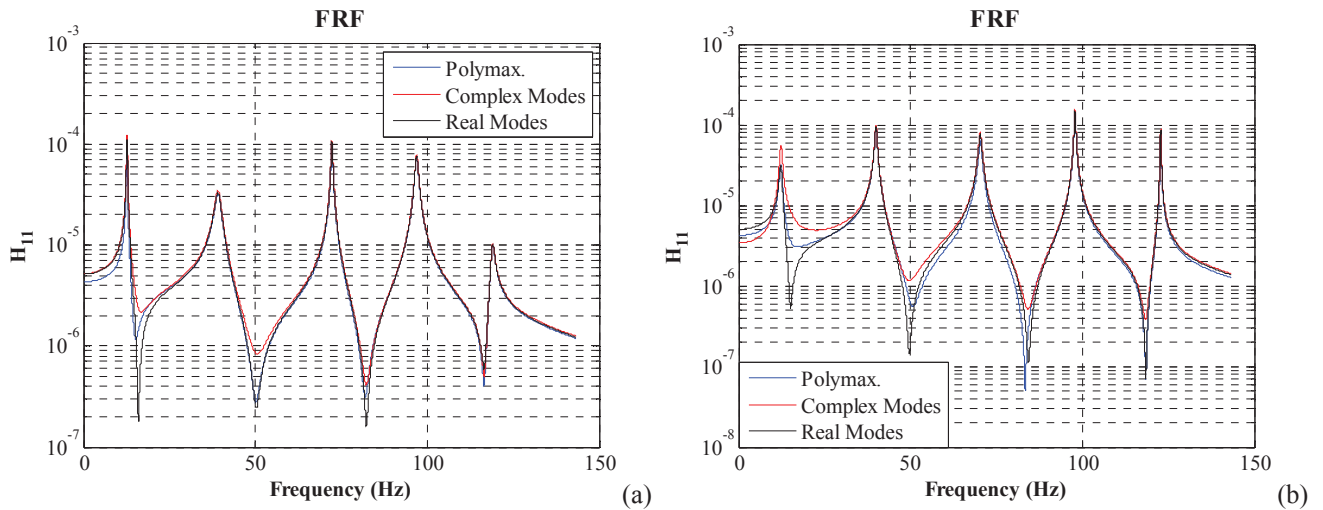


Figure 5: Comparisons of FRFs: (a) is with magnets on the second level; (b) is with magnets on the fifth level, both are H_{11} with β equal to 0.12

To gain some idea on the variability the test previously described was repeated a number of times. The statistics of the results obtained are summarized in [Table 1](#).

Table 1: Variability of the complex scaling factor.

Mode	Real Part		Imag. Part	
	SD	CoV	SD	CoV
1	0.0853	4.66%	0.0560	0.31%
2	0.0822	1.52%	0.0771	0.13%
3	0.2401	7.96%	0.1731	0.13%
4	0.0544	48.86%	0.1709	0.10%
5	0.0701	10.12%	0.1770	0.08%

5. Concluding Remarks

This study presents a pilot examination of work on the normalization of complex modes obtained from operational modal analysis using the mass change strategy. It was found that while the complex equation can provide improved results when complexity is significant a key issue is the question of identification variability. In particular, the fact that the real part of the complex eigenvalue typically has a large coefficient of variation and thus the estimation of the real part of the eigenvalue derivative is generally very uncertain.

Acknowledgements

This study was initiated as part of the course, CIVG 7343, taught by professor D. Bernal at Northeastern University. The help with the experimental setup provided by Mr. Michael Macneil, the Laboratory Technician of the Department of Civil and Environmental Engineering, is thankfully acknowledged.

References

- [1] Parloo, E., Verboven, P., Cuillame, P., Vsn Overmerire, M., "Sensitivity-based operational mode shape normalization", *Mechanical systems and signal processing*, Vol. 16, P: 757-767, 2002.
- [2] Brinker. R., Andersen. P. A., "Way of getting scaled mode shapes in output-only modal testing", In: 21st International modal anlaysis conference, Kissimmee, Florida, 2003.
- [3] Bernal, D., "Modal Scaling from Known Mass Perturbation", *Journal of engineering mechanics*, Vol. 130(9), P: 1083-1088, 2004.
- [4] Fernández-Canteli M., Brincker, R., Fernández-Canteli, A., "Some methods to determine scaled mode shapes in natural input modal analysis" In: 22nd International modal analysis conference, Feb. 2004.
- [5] Bernal, D., "Complex eigenvector scaling from mass Perturbation", Submitted to journal of engineering mechanics, 2010.
- [6] Cadwell, L. H., "Magnetic damping: analysis of an eddy current brake using an airtrack", *American journal of physics*, Vol. 64(7), P: 917-923, 1996.
- [7] Wiederick, H. H., Gauthier, N., Campbell, D. A., Rochon, P., "Magnetic braking: simple theory and experiment", *American journal of physics*, Vol. 55(6) P: 500-503, 1987.
- [8] Heald, M. A., "Magnetic braking: improved theory", *American journal of physics*, Vol. 56(6), P: 521-522, 1988.
- [9] Sodano, H. A., Inman, D. J., Belvin, W. K., "Development of a new passive-active magnetic damper for vibration suppression", *Journal of vibration and acoustics*, Vol. 128(3), P:318-328, 2006.

Numerical Continuation of Periodic Orbits for Harmonically Forced Nonlinear Systems

Michael W. Sracic
Graduate Research Assistant, Ph.D Candidate
mwsracic@wisc.edu

&

Matthew S. Allen
Assistant Professor
msallen@engr.wisc.edu
Department of Engineering Physics
University of Wisconsin-Madison
534 Engineering Research Building
1500 Engineering Drive
Madison, WI 53706

ABSTRACT

A nonlinear structure will often respond periodically when it is excited with a sinusoidal force. Several methods are available that can compute the periodic response for various drive frequencies, which is analogous to the frequency response function for a linear system. The simplest approach would be to compute a sequence of simulations where the equations of motion are integrated until damping drives the system to steady state, but that approach suffers from a number of drawbacks. Recently, numerical methods have been proposed that use a solution branch continuation technique to find the free response of unforced, undamped nonlinear systems for different values of a control parameter. These are attractive because they are built around broadly applicable time-integration routines, so they are applicable to a wide range of systems. However, the continuation approach is not typically used to calculate the periodic response of a structural dynamic system to a harmonic force. This work adapts the numerical continuation approach to find the periodic, forced steady-state response of a nonlinear system. The method uses an adaptive procedure with a prediction step and a mode switching correction step based on Newton-Raphson methods. Once a branch of solutions has been computed, it explains how a full spectrum of harmonic forcing conditions affect the dynamic response of the nonlinear system. The approach is developed and applied to calculate nonlinear frequency response curves for a Duffing oscillator and a low order nonlinear cantilever beam.

1. Introduction

Many engineering structures exhibit nonlinear behavior. Some common examples include: shock absorbers in automotive suspension systems, bolted joints in aerospace structures and nonlinear elastic tissues in biomechanical systems. Nonlinearities can be due to geometric effects such as buckling, nonlinear constitutive relationships in materials, or dissipative effects such as the damping due to mechanical joints. The nonlinearities greatly affect the dynamic response of a structure and can lead to resonance phenomena that are not predicted by linear theory. One needs to accurately characterize the nonlinear dynamic response to accurately predict the structure's response and avoid structural failure.

Many nonlinear systems are operated under the presence of harmonic forcing that induces a periodic response. Some common examples of harmonically forced nonlinear systems include rotor systems with bearing nonlinearities [1-3], turbomachinery [4, 5], wind turbines [6], and nonlinear electrical circuits [7-9]. The response of the human musculoskeletal system is also highly nonlinear [10-13], and researchers often study neural network control systems as a form of oscillatory control force [14-17]. Even if a system does not naturally operate periodically under harmonic forcing, it is typical to perform experimental vibration testing using harmonic forcing (i.e. sine sweep testing) to better understand its behavior. Whenever a nonlinear system is harmonically forced, the specific forcing configuration can greatly affect the response of the system. For example, a nonlinear system that is excited with a sinusoid may respond harmonically at a number of

frequencies, and the dominant frequency could be different from the forcing frequency. In another case, there may be several possible periodic solutions (stable or unstable) for a single forcing function. For certain forcing configurations, the response of a highly nonlinear system may be approximately linear, while a weakly nonlinear system may exhibit strong nonlinearity. In order to fully understand the dynamics of a nonlinear structure, especially one that will be harmonically forced, it is important to predict and characterize the periodic responses that are produced by each forcing configuration.

Many techniques have been developed to calculate the periodic solutions of nonlinear systems, and those techniques usually take one of two basic approaches. The first approach is to approximate the analytical solution to the differential equations. The *harmonic balance technique*, which is similar to what is done for linear forced oscillations, is a popular approach where one assumes a harmonic series for the solution and usually truncates the series after one harmonic term [18, 19]. This approximate method tends to exhibit large error when the response contains strong higher harmonics; so additional terms can be included in the series, but this makes the mathematical formulation more difficult. The *method of multiple scales* and the *method of averaging* are commonly used perturbation techniques where one attempts to find an asymptotic linearization of the nonlinear solution, again using an approximating functional form for an analytical solution. A number of applications of these methods can be found in the following works [18, 20, 21]. All of these methods can provide accurate solutions in certain situations, but they can be difficult to implement for higher order systems that are strongly coupled, they are not straightforward to automate for a large range of forcing configurations, and they involve approximations so considerable expertise may be needed to be sure that those approximations are warranted. The second approach to calculating periodic solutions for nonlinear systems employs numerical methods. Essentially, one deals with the exact nonlinear equations for a system and uses direct time integration to search for the solution. This direct approach is powerful because closed form equations of motion are not required. If a system is damped then one can always calculate the periodic orbit conditions by integrating the equations of motion from a given set of initial conditions for a long enough time that the system settles into a steady periodic orbit. Typically, an adaptive time step control, fourth-order Runge-Kutta method [22, 23] or Newmark method [24] is used for time integration of structural dynamics systems. Although this approach is straightforward, it can be computationally expensive, and methods have been developed over the years to streamline such calculations. In fact, methods that find the periodic solutions of general differential equations are somewhat mature [25]. Two typical approaches are to evaluate and update a cost function with optimization [26, 27] or to solve a boundary value problem using a Newton-Raphson correction method [25]. The latter approach is widely used because the Newton-Raphson method converges quadratically. These approaches are usually started with an initial guess, which is subsequently corrected to satisfy convergence criteria, and this overall procedure is generally termed a *shooting* method. A parameter of interest can then be varied and the shooting method applied multiple times to compute a branch of solutions, and this is termed a *continuation* method. A general overview of shooting and continuation techniques is provided in [28].

Generally speaking, the methods for forced continuation can be categorized as corrector techniques, predictor-corrector techniques, or adaptive predictor-corrector techniques. Correction techniques use the general shooting technique to calculate solutions. Continuation is commonly performed with these methods by incrementing the forcing frequency (perhaps sequentially), using the previous solution as the initial conditions for the shooting method calculation of the solution. This procedure is improved by using a predictor-corrector algorithm, where each solution is used to calculate a prediction for the next solution on the curve. A prediction can be made for both the new forcing frequency and the new periodic response values. Then, the prediction is used as the initial guess for some form of shooting method that calculates the actual solution, and the convergence is usually much faster than without a prediction. Predictions can be made with a number of different geometric calculations, for example by calculating the tangent to the branch of solutions. More advanced methods will use an adaptive predictor-corrector algorithm, where the number of convergence calculations are recorded and used to adapt the prediction increment size between successive solutions, which further improves the efficiency of the calculations. A few well developed packages exist that use various forms of adaptive predictor-corrector methods for nonlinear system calculations. AUTO [29] is a code that is available for download. It has many sophisticated computational methods for nonlinear systems, but it does not contain a straightforward algorithm for calculating the periodic solutions of harmonically forced nonlinear systems. MATCONT [30] is another well developed package. It can be run in MATLAB and has a graphical user interface, but it is more suited towards calculating periodic solutions of autonomous systems. These codes are freely available for use but are not suited for all problems, so many researchers are still developing their own algorithms. A few of these use a simple corrector approach. In [31], a shooting method was applied to find periodic solutions of autonomous nonlinear systems. A single initial guess was used to calculate an entire branch of solutions for one parameter of interest, as opposed to performing some form of continuation from one solution to the next. In [23], a continuation method was used to calculate the forced-response periodic displacements of the center of a low-order model of a beam with clamped ends. A secant predictor step was used to vary the forcing frequency, but no predictions were calculated for the response solutions. The method showed promising results, but the algorithm could not follow sharp turns of the periodic solution branch. In [32], the harmonic balance method was used to calculate the periodic solutions of a reduced order torsional subsystem. Then, an

adaptive predictor continuation algorithm was used to find additional solutions as the operating frequency was varied. This method produced very detailed periodic solution curves but still requires one to use the approximations required by the harmonic balance method. If too few terms are used in the expansion then the algorithm may not predict important nonlinear features, as noted in [32]. A form of predictor-corrector continuation was also used in [22, 33-35]. They incremented the forcing frequency sequentially and then calculated a prediction for only the state vector with a first order Euler expansion from the previous solution. The algorithm provides quite robust performance. For example, in regions where a periodic solution branch has a turning point (i.e. a multiple solutions region), the algorithm included a re-parameterization of the solution curve in order to follow the turning point. The algorithm was applied to a few low order systems and showed promising results. More recently, a similar form of predictor-corrector continuation was presented in [24]. This method employs a *pseudo-arc length* continuation procedure that has a tangent predictor step and orthogonal corrector steps. Furthermore, the algorithm automatically controls the step size and exploits symmetry in the response to increase computational efficiency. So far, the authors of this method have computed the periodic solutions of a number of unforced, undamped nonlinear systems of high complexity and high order [24, 36-42] with exceptional detail. However, they have not extended their methods to the calculations of periodic solution branches of harmonically forced nonlinear systems.

The goal of this work is to create a continuation method for efficiently calculating the periodic solutions of harmonically forced nonlinear systems. This work will utilize techniques primarily from [24] in order to do this. A Newton-Raphson correction technique will be used to calculate the first solution from an initial guess that the user must supply. In order to calculate the subsequent solutions, an adaptive predictor step is used with a mode-switching correction step that employs two additional Newton-Raphson correction methods. The forcing frequency is the parameter that is varied. The most important difference of this work from the previous methods is that the prediction calculation and the Newton-Raphson correction methods includes extra terms that quantify how the periodic orbit varies as the forcing frequency is varied. Additionally, the forced periodic orbit is uniquely determined by the phase of the forcing, so the periodic orbits are calculated with respect to zero phase on the force, and since the frequency of the forcing is varied, the equations of motion change with each periodic orbit calculation; this is accounted for by the proposed method. The procedure of the proposed continuation method will first be outlined. Then, the shooting method and the Newton-Raphson correction method will be reviewed, and the necessary changes of those procedures due to the harmonic forcing will be derived. The continuation procedure will then be explained in detail. In Sections 3 and 4, the algorithm will be applied to calculate the periodic solutions of one and two degree of freedom systems, respectively. The results will be used to better understand the nonlinear systems, and discussion will be provided regarding the performance of the algorithm. Conclusions will be provided in Section 5.

2. Theory

A nonlinear system with input $u(t)$ can be described by the following state space differential equation

$$\dot{z} = f(z(t), u(t)) \quad (1)$$

where $z \in \mathbb{R}^n$ is the time dependent state vector, $u \in \mathbb{R}^p$ is a time dependent input vector, and t is the time variable. For structural dynamic systems the state variable z is the vector valued function of time $z = [x^T \ \dot{x}^T]^T$ composed of the N displacement degrees of freedom (DOF) $x \in \mathbb{R}^N$ and the N time derivatives of the displacement DOF, \dot{x} , where $n=2*N$. The superscript 'T' denotes the matrix transpose operator. It is assumed that f is a C^1 (at least one-time continuously differentiable) nonlinear function defined on an open subset of \mathbb{R}^n that contains all the possible positions and velocities of the system of interest. For a specific input, the vector field f generates the flow $Z_t \in \mathbb{R}^n$ that contains families of solution curves of the differential equation [43]. A single solution curve is defined by its initial state vector z_0 and input vector u_0 and by tracing the flow $Z_t(z_0)$ for a finite time.

This work considers systems with harmonic forcing so $\bar{u}(t+T) = \bar{u}(t)$ and hence $\dot{z} = f(z, T)$, where the dependence of the system on the fundamental period T is explicitly shown. Under these conditions and when the system reaches steady state, it is assumed that the flow contains at least one periodic orbit γ with period T , and $\bar{z}(t+T) = \bar{z}(t)$ for any state $\bar{z} \in \gamma$. (From here forward, the overbar will be dropped from the state vectors when talking about states from a periodic orbit in order to simplify the notation.) Depending on the configuration of the system and its parameters, including the forcing frequency and amplitude, the flow may contain multiple periodic orbits [43, 44]. Tracking the periodic orbits in a nonlinear system can be difficult because a small change in the parameters of the system, such as the forcing frequency, may drastically change the dynamics of the flow. For example, a stiffening system has a frequency response peak that bends to higher frequencies, and

the response can jump from a high amplitude response to a very low amplitude response as the frequency is increased beyond the critical value. In order to characterize all of the periodic orbits that exist in the flow of the differential equation, one must calculate each pairing of initial state vector and period (z_0, T) of the orbits.

This work presents a continuation method that is used to calculate many of the periodic orbits of the differential equation, thereby producing a frequency response function. The general procedure is outlined below and shows the different steps of the algorithm.

1. Provide a starting guess: $(z_{0,(0)}, T_{(0)})$
 - The method begins after the user supplies $(z_{0,(0)}, T_{(0)})$ where the subscript zero in parentheses designates that these conditions are the starting initial conditions.
2. Calculate a starting solution: $(z_{0,(1)}, T_{(1)})$
 - The proposed continuation method must be started from an actual periodic orbit of the system. To calculate this first solution, a Newton-Raphson correction method (NRCM 1), which accounts for changes in both the state vector Δz_0 and the period ΔT , can be employed to calculate the first periodic orbit solution $(z_{0,(1)}, T_{(1)})$.
3. Initiate the predictor-corrector procedure to calculate a branch of solutions: $(z_{0,(j)}, T_{(j)})$, $j=1,2,3,4,\dots$
 - a. Prediction Step: $(z_{0,pr,(j+1)}, T_{pr(j+1)})$
 - The current solution is used to calculate a prediction $(z_{0,pr,(j+1)}, T_{pr(j+1)})$ for the initial conditions of the next periodic solution. The prediction is then corrected to find a true solution near the predicted one.
 - b. Correction Step: $(z_{0,(j+1)}^{(k)}, T_{(j+1)}^{(k)})$, $k=1,2,3,\dots$
 - The prediction step is used as the initial guess, $(z_{0,(j+1)}^{(0)}, T_{(j+1)}^{(0)})$, for the second Newton-Raphson procedure. The second Newton-Raphson correction method (NRCM 2) includes all the equations from NRCM 1, but it has an additional equation that constrains the corrections to be orthogonal to the prediction. NRCM 2 is used to calculate corrections to the initial conditions, $(z_{0,(j+1)}^{(k)}, T_{(j+1)}^{(k)})$, until the $(j+1)^{th}$ periodic solution is obtained.
 - If a solution is obtained: After each $(j+1)^{th}$ solution is calculated, Step 3 is repeated.
 - If a solution is not obtained: If the convergence criteria are not met within some pre-set number of iterations:
 1. The procedure calculates a new prediction, $(z_{0,pr,(j+1)}, T_{pr(j+1)})$, using a smaller step and the correction portion of Step 3 is restarted.
 2. The procedure switches to a third form of the Newton-Raphson correction method (NRCM 3). This form accounts for changes in the state vector Δz_0 only, so that the period is held fixed (i.e. $\Delta T=0$), and there are no geometric constraints placed on the corrections. The prediction initial condition is used for an initial guess, and the NRCM 3 is used to calculate the periodic solution. When the solution is calculated, Step 3 above is repeated.

The details of this procedure will be provided below, but first the general Newton-Raphson correction method is derived. Some parts follow the derivation from [24], but there are several differences that arise due to the forcing, which causes the function f in Eq. (1) to depend explicitly on time, t , and on the period, T , of the forcing frequency.

2.1 Shooting Function

The proposed method is an iterative process that seeks to find the periodic solutions of a system for different forcing frequencies. The *shooting function* is created to quantify whether a certain set of initial conditions, (z_0, T) produce a periodic response. First, the forcing frequency is set to $\Omega=2\pi/T$ and Eq. (1) is integrated over the interval $(0, T)$ from an initial state vector z_0 . Then, the shooting function $H \in \mathbb{R}^n$ is defined as

$$H(z_0, t, T) \equiv z_T(z_0, t, T) - z_0 \quad (2)$$

where $z_T = z(z_0, t=T, T)$ is the state vector found by integrating with initial condition z_0 until $t=T$. This equation represents a two-point boundary value problem for the periodic orbit of the system where the forcing has zero phase at $t=0$ and $t=T$. Eq. (2) will be satisfied when $H(z_0, T) = \{0\}$. In practical numerical computation, the shooting function will be satisfied when $H(z_0, T) \approx \{0\}$ for some chosen convergence criterion. In this work, the convergence criterion defined in [24] is used

$$\frac{\|H(z_0, T)\|}{\|z_0\|} = \frac{\|z_T - z_0\|}{\|z_0\|} < \varepsilon \quad (3)$$

where $\varepsilon=1e-6$ is the convergence value. Each time the equations of motion are integrated over the assumed period, the shooting function is subsequently calculated and the convergence is evaluated.

2.2 Newton-Raphson Correction Methods

When the given calculation of the shooting function does not satisfy the convergence criterion, a Newton-Raphson [25] method is used to calculate updates Δz_0 and ΔT to the initial conditions. Following the approach used in [24], the shooting function can be expanded in a Taylor series about $(z_0 + \Delta z_0, T + \Delta T)$,

$$H(z_0, t = T, T) + \frac{\partial H}{\partial z_0} \Big|_{(z_0, T)} \Delta z_0 + \frac{\partial H}{\partial T} \Big|_{(z_0, T)} \Delta T = \{0\}, \quad (4)$$

where only the linear terms have been retained. The partial derivatives in the Taylor expansion must be carefully calculated. The first partial derivative, $[\partial H / \partial z_0] \in \mathbb{R}^{n \times n}$, has the same form as in [24], and can be expanded as

$$\frac{\partial H}{\partial z_0} \Big|_{(z_0, T)} = \frac{\partial z(z_0, t, T)}{\partial z_0} \Big|_{t=T} - [I] \quad (5)$$

where $[I]$ is the $n \times n$ identity matrix. The time varying Jacobian matrix $[\partial z / \partial z_0] \in \mathbb{R}^{n \times n}$, which is the variation of the state vector at time t due to a small change in the initial conditions, can be calculated using one of two methods described in detail in [24]. The first method, which uses a finite differences approach, can be used even when the equations of motion are not available in closed form, but it is more computationally expensive so it is not used in this work. The second approach is to form the following system of time varying differential equations by differentiating Eq. (1) with respect to z_0 , switching the order of differentiation on the left hand side, and applying the chain rule on the right hand side.

$$\frac{d}{dt} \left(\frac{\partial z(z_0, t, T)}{\partial z_0} \right) = \left[\frac{\partial f(z, t, T)}{\partial z} \Big|_{z=z(t)} \right] \left[\frac{\partial z(z_0, t, T)}{\partial z_0} \right] \quad (6)$$

In this equation, the Jacobian matrix $[\partial f / \partial z] \in \mathbb{R}^{n \times n}$ is simply the linearization of f about the state $z(t)$ for each time instant t in the interval $(0, T)$. Since, the state response was calculated on the interval $(0, T)$ in order to evaluate the shooting function, it can be easily stored in order to integrate the system of Eq. (6) from initial conditions $[\partial z(z_0, t = 0, T) / \partial z_0] = [I]$. The solution matrix $[\partial z / \partial z_0]$ can then be evaluated at $t = T$ and used to calculate $[\partial H / \partial z_0]$.

The vector $\{\partial H / \partial T\} \in \mathbb{R}^n$ in Eq. (4) differs from the result presented in [24], since the function f depends explicitly on t and T . This partial derivative can be expanded using the chain rule as

$$\frac{\partial H}{\partial T} = \frac{\partial H}{\partial t} \Big|_{t=T} + \frac{\partial H}{\partial T} \Big|_{t=T} \quad (7)$$

where the first term represents the change in the shooting function due to a change in the instant that is taken to be the end of the period and can be calculated from Eq. (1) as in [24].

$$\frac{\partial H}{\partial t} \Big|_{t=T} = f(z_T, t = T, T) \quad (8)$$

The second term in Eq. (7) was not present in [24], but arises here due to the forcing since $f(z, t, T)$ has explicit dependence on the period of the forcing, T . The term represents the change in the shooting function due to a change in the period of the input.

$$\left. \frac{\partial H}{\partial T} \right|_{t=T} = \left. \frac{\partial z(z_0, t, T)}{\partial T} \right|_{t=T} \quad (9)$$

Note that the second term of the shooting function does not appear in either of these expressions because $\{\partial z_0 / \partial T\} = \{0\}$. Using the same approach that was used to derive Eq. (6), one can derive the following system of time varying differential equations that can be solved to calculate $\{\partial z / \partial T\}$.

$$\frac{d}{dt} \left(\frac{\partial z(z_0, t, T)}{\partial T} \right) = \left[\left. \frac{\partial f(z, t, T)}{\partial z} \right|_{z=z(t)} \right] \left\{ \frac{\partial z(z_0, t, T)}{\partial T} \right\} + \frac{\partial f}{\partial T} \quad (10)$$

The term $\{\partial f / \partial T\} \in \mathbb{R}^n$ has arisen because $f(z, t, T)$ and $z(z_0, t, T)$ both have explicit dependence on the period of the forcing, T . Hence, this second set of differential equations must be integrated from initial conditions $\{\partial z(z_0, t = T, T) / \partial T\} = f(z_T, t = T, T)$ over the interval $(0, T)$ in order to compute $\{\partial z(z_0, t, T) / \partial T\}$.

After calculating partial derivatives in Eq. (4), an algebraic system of equations can be formed to solve for an update $(\Delta z_0, \Delta T)$ to the initial conditions. These partial derivatives are used in slightly different ways at different steps in the continuation algorithm, as explained below.

2.3 Continuation Procedure

2.3.1 Provide a starting guess: $(z_{0,(0)}, T_{(0)})$

In order to start the continuation procedure, the user must supply a starting guess. A good starting point guess $(z_{0,(0)}, T_{(0)})$ consists of a low frequency (i.e. a long period) solution for the underlying linear system (i.e. for $T_{(0)}$ the underlying linear system can be solved for the periodic conditions $z_{0,(0)}$). This is often called a Homotopy approach [18, 25].

2.3.2 Calculate a starting solution: $(z_{0,(1)}, T_{(1)})$

The starting guess is used to calculate a set of initial conditions (z_0, T) that lead to a shooting function, $H(z_0, T)$, that satisfies convergence. To calculate the starting solution, the system is integrated from the starting guess, the shooting function is calculated, and the convergence is evaluated. If the initial guess does not satisfy convergence, then the partial derivatives are calculated and the following system is formed to calculate corrections to both the state vector Δz_0 and the period ΔT . This system is the NRCM 1 mentioned above.

$$\begin{bmatrix} \left. \frac{\partial H}{\partial z_0} \right|_{(z_0, T)} & \left. \frac{\partial H}{\partial T} \right|_{(z_0, T)} \end{bmatrix} \begin{Bmatrix} \Delta z_0 \\ \Delta T \end{Bmatrix} = \begin{Bmatrix} -H(z_0, t = T, T) \\ 0 \end{Bmatrix} \quad (11)$$

The right hand side vector contains the vector value of the shooting equation. The new initial conditions are $(z_{0,(1)} = z_{0,(0)} + \Delta z_0, T_{(1)} = T_{(0)} + \Delta T)$. Since the period has been updated the harmonic forcing frequency must also be updated in the equations of motion (i.e. $\Omega_{update} = 2\pi / (T_{(1)})$ such that $u = u(\Omega_{update} t)$). Then, these new conditions are used to integrate the equations of motion and check the shooting function for convergence. One then repeats this two stage process until the desired convergence is achieved at which point the first periodic orbit solution $(z_{0,(1)}, T_{(1)})$ has been calculated. The Newton-Raphson corrector method is a local technique, so the starting guess, $(z_{0,(0)}, T_{(0)})$, must be close to the actual solution or the correction scheme will diverge. The first periodic orbit solution and the Jacobian matrices that were used to produce it can be used to initiate the next step.

2.3.3 Initiate the predictor-corrector procedure to calculate a branch of solutions: $(z_{0,(j)}, T_{(j)})$, $j=1,2,3,4,\dots$

In order to calculate an entire branch of solutions, an adaptive *pseudo arc-length* continuation [28] method is employed that uses a prediction step which is followed by a correction step. Predictor-corrector methods can follow complex solution branches because the prediction step follows the direction in which the branch of solutions actually evolves. The prediction step, which is calculated using information from the current periodic solution, is used to calculate new initial conditions for the next periodic orbit. The prediction step can be further adapted to evaluate the convergence of the previous correction steps and adjust the step size accordingly. After the prediction step, the shooting method is employed, but now with a new Newton-Raphson correction method that varies the state vector and the forcing frequency in a constrained direction.

2.3.3.1 Prediction Step: $(z_{0,pr,(j+1)}, T_{pr,(j+1)})$

The basic process is to use the previous periodic orbit solution, which is denoted as the j^{th} solution, to calculate a tangent predictor step for the $(j+1)^{\text{th}}$ periodic orbit conditions, including a prediction for the initial state vector and the forcing period. The prediction $\{P\} \in \mathbb{R}^{n+1}$, which has components $\{P_z\} \in \mathbb{R}^n$ and $P_T \in \mathbb{R}$ corresponding to the states and period respectively, is the tangent vector to the solution branch and can be calculated with the following system of equations.

$$\begin{aligned} \left[\begin{array}{c} \frac{\partial H}{\partial z_0} \Big|_{(z_{0,(j)}, T_{(j)})} \quad \frac{\partial H}{\partial T} \Big|_{(z_{0,(j)}, T_{(j)})} \end{array} \right] \{P_{(j)}\} &= \begin{Bmatrix} \{0\} \\ 0 \end{Bmatrix} \\ \{P_{(j)}\} &= [P_{z,(j)}^T \quad P_{T,(j)}]^T \end{aligned} \quad (12)$$

The components of the left hand side matrix come from the Taylor series expansion of the shooting function, and were previously defined. They characterize the vector space that is normal to the periodic solution curve, and once they are found, the desired tangent vector $\{P\}$ in Eq. (12) is simply the vector that is in the null space of the matrix on the left in Eq. (12).

Once the tangent vector $\{P\}$ has been calculated it can be normalized to unit length, and the predictions for the next periodic solution can be calculated with

$$z_{0,pr,(j+1)} = z_{0,(j)} + s_{(j)} P_{z,(j)} \quad (13)$$

$$T_{pr,(j+1)} = T_{(j)} + s_{(j)} P_{T,(j)} \quad (14)$$

$$\Omega_{pr,(j+1)} = 2\pi/T_{pr,(j+1)} \quad (15)$$

where $z_{0,pr,(j+1)}$ and $T_{pr,(j+1)}$ are the prediction initial conditions for the $(j+1)^{\text{th}}$ solution and $s_{(j)}$ is the j^{th} step size. One must be sure to again update the differential equations so that the external forcing reflects the change in frequency (i.e. $u=u(\Omega_{pr,(j+1)}t)$).

The step size is critical to the success and efficiency of the computation. One can fix the step size to a very small value and ensure that very small increments are made between successive solutions, but this can be impractical because computation times may be long. A better approach is to provide an automated step size control algorithm. In this work, the step size control algorithm from [24] is employed. The first step size is provided by the user, while all subsequent step sizes are determined by the following equation

$$s(j) = \text{sign} \left(s_{(j-1)} \{P_{(j)}\}^T \{P_{(j-1)}\} \right) \left(\frac{K^*}{K_{(j-1)}} \right) |s_{(j-1)}| \quad (16)$$

where $K_{(j-1)}$ is the integer number of iterates that were required to update the previous shooting function solution and K^* is an optimal number of shooting iterates which is supplied by the user. The signum function $\text{sign}(\bullet)$, ensures that the step used to calculate the predictions follows the solution curve in the same direction. Furthermore, it is helpful to place maximum and minimum bounds on the step size. When the step size is increased beyond these bounds, it can be automatically reduced below the maximum or increased above the minimum.

2.3.3.2 Correction Step: $(z_{0,(j+1)}^{(k)}, T_{(j+1)}^{(k)})$, $k=1,2,3,\dots$

As discussed in [24], the Newton-Raphson updates to the shooting functions can be made more efficient by forcing the corrections to be orthogonal to the tangent predictor vector. Therefore, at this point in the algorithm the correction steps are calculated with the following algebraic system, which is the NRCM 2 mentioned previously,

$$\begin{bmatrix} \frac{\partial H}{\partial z_0} \Big|_{(z_{0,(j+1)}^{(k)}, T_{(j+1)}^{(k)})} & \frac{\partial H}{\partial T} \Big|_{(z_{0,(j+1)}^{(k)}, T_{(j+1)}^{(k)})} \\ \{P_{z,(j)}\}^T & P_{T,(j)} \end{bmatrix} \begin{Bmatrix} \Delta z_{0,(j+1)}^{(k)} \\ \Delta T_{(j+1)}^{(k)} \end{Bmatrix} = \begin{Bmatrix} -H(z_{0,(j+1)}^{(k)}, T_{(j+1)}^{(k)}) \\ 0 \\ 0 \end{Bmatrix} \quad (17)$$

where all the components have been previously defined. The solution to this equation provides the k^{th} corrections $\Delta z_{0,(j+1)}^{(k)}$ and $\Delta T_{(j+1)}^{(k)}$ to the guess for the $(j+1)^{\text{th}}$ solution. The algorithm then alternates between a shooting function calculation $H(z_{0,(j+1)}^{(k)}, T_{(j+1)}^{(k)}) \approx \{0\}$ and a correction step calculation $z_{0,(j+1)}^{(k+1)} = z_{0,(j+1)}^{(k)} + \Delta z_{0,(j+1)}^{(k)}$ and $T_{(j+1)}^{(k+1)} = T_{(j+1)}^{(k)} + \Delta T_{(j+1)}^{(k)}$, where $k=0, \dots, K_{(j+1)}$. The integer $K_{(j+1)}$ is the number of correction iterations required to converge on the solution and $k=0$ corresponds to the predictions $z_{0,(j+1)}^{(0)} = z_{0,pr,(j+1)}$, $T_{(j+1)}^{(0)} = T_{pr,(j+1)}$. When one of the correction steps leads to a shooting function that converges, then the periodic orbit solution is stored and a new prediction is calculated as the algorithm advances to the $(j+2)^{\text{th}}$ step.

In some cases the correction steps may diverge (i.e. the norm of consecutive shooting function values may increase instead of decreasing to zero), or they may converge very slowly. In order to account for these issues, the shooting function values can be tracked to ensure that the norm of consecutive shooting functions are decreasing and the number of correction steps can be bounded with K_{max} . In this work, when either of these constraints is not met, the following two procedures are initiated in order to try to find a solution. The default procedure is to calculate a new prediction using a smaller step size. In particular, the step size is divide by two, $s(j)=s(j)/2$, Eqs. (13-15) are recalculated, and the correction step procedure is followed again. Usually, for small enough step sizes, the predicted initial guess is close to the previous periodic solution, and the algorithm is likely to converge on the new solution. However, the authors have found cases where this does not always lead to convergence. Therefore, a minimum step size is defined that is on the order of the convergence value. When the minimum step size is surpassed, the algorithm tries a second alternate procedure that uses the current prediction step initial conditions, $(z_{0,pr,(j+1)}, T_{pr,(j+1)})$, which were just recalculated with the minimum step size. First, the predictions are used as the initial conditions for the next solution (i.e. $z_{0,(j+1)}^{(0)} = z_{0,pr,(j+1)}$, $T_{(j+1)}^{(0)} = T_{pr,(j+1)}$), but the period is fixed such that there will be no correction calculated (i.e. $\Delta T_{(j+1)}^{(k)} = 0$). Then, a solution is calculated with the following NRCM 3 system

$$\begin{bmatrix} \frac{\partial H}{\partial z_0} \Big|_{(z_{0,(j+1)}^{(k)}, T_{(j+1)})} \end{bmatrix} \Delta z_{0,(j+1)}^{(k)} = -H(z_{0,(j+1)}^{(k)}, T_{(j+1)}). \quad (18)$$

where corrections are calculated only for the state vector $\Delta z_{0,(j+1)}^{(k)}$. Once convergence is obtained the solution is stored and the predictor-corrector method returns to the prediction step above.

2.3.4 Discussion

The proposed algorithm is used to calculate an entire branch of solutions. The starting and stopping frequencies must be input by the user. Additionally, the step size must be very carefully monitored and controlled (by maximum and minimum step size bounds and by setting the appropriate values of K^*). The algorithm typically converges and produces good results, but sometimes the algorithm parameters do still need to be manually adjusted during the calculations to provide convergence or at least efficient computation.

2.4 Computational Efficiency

Nonlinear systems are inherently sensitive to changes in the harmonic forcing, so other manual control techniques may also be required to efficiently calculate frequency response functions. Harmonically forced nonlinear systems exhibit responses similar to linear systems with resonance peaks near linear natural frequencies and low response bands between away from resonance peaks. Therefore, the turning points are likely to be located near the linear natural frequencies. Away from those frequencies, where the response is low and in general very flat, it may be more efficient to apply *sequential continuation*, where the frequency band of interest is divided into a number of evenly spaced frequency values and a solution for each is sought sequentially. When this is done, NRCM 3 can be used as a method to calculate the periodic solutions at each frequency value in the interval. Because there are fewer calculations involved and hence less computation time required, the sequential method may be more efficient for the regions away from resonance, but it fails near resonance where the response amplitude can change dramatically with a small change in frequency. A very efficient algorithm is one that seamlessly switches between different types of continuation depending on which type is currently the most efficient. One can quantify the efficiency of the method being used by assessing the number of iterations it takes before a periodic solution is achieved (i.e. if $K_{(j)}$ is consistently larger than K^* , one might switch methods). These types of constraints were not included for this work because the solution branches for the systems considered were calculated efficiently with the proposed method, but such constraints can easily be added to the procedure.

2.5 Stability of Periodic Orbits

Using the proposed method, the stability of a periodic orbit can be calculated whenever convergence of a periodic solution is achieved (this was also discussed in [24]). The matrix $[\partial z(z_0, t = T, T) / \partial z_0]$ in Eq. (5) from the final Newton-Raphson calculation ($k=K_{(j+1)}$) is the Monodromy matrix [45] of the periodic orbit. (Recall that it was formed from a linearization of the system about its periodic orbit and was calculated at $t = T$.) The stability of this periodic orbit can be determined from the eigenvalues of this matrix. If the eigenvalues of the Monodromy matrix are inside (outside) the unit circle, then the orbit is stable (unstable). So the stability of periodic solution is conveniently found without additional calculations when using this method.

3. Application to a Duffing Oscillator

Figure 1 illustrates a single degree of freedom Duffing oscillator, which will be used to illustrate the proposed algorithms. The system has a discrete mass m with displacement degree of freedom x . The system mass is connected to a dashpot with damping coefficient c and to a linear spring with spring stiffness k and a nonlinear spring with spring constant k_3 . External forcing is applied with F_d .

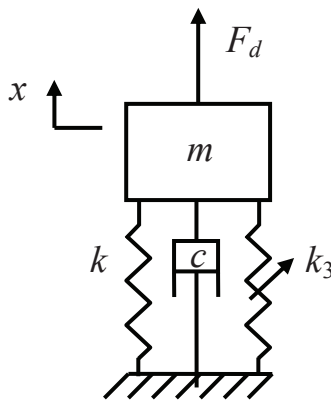


Fig. 1 Single degree of freedom oscillator with a nonlinear spring.

The nonlinear spring provides a quadratic nonlinear spring stiffness $k_3 x^2$, so the equation of motion for the Duffing oscillator is given by the following,

$$m\ddot{x} + c\dot{x} + kx + k_3 x^3 = F_d \quad (19)$$

which can be written as follows in the state space after first dividing through the entire equation by m and defining the nondimensional parameters $2\zeta\omega = c/m$, $\omega^2 = k/m$, $\omega_3^2 = k_3/m$, and $F = F_d/m$ where ζ is the coefficient of critical damping.

$$\begin{cases} \dot{x} \\ \dot{x} \end{cases} = \begin{cases} \dot{x} \\ -2\zeta\omega\dot{x} - \omega^2x - \omega_3^2x^3 + F \end{cases} \quad (20)$$

The parameters used in this study are: $\zeta=0.01$, $\omega=1$, and $\omega_3=0.5$. The system is driven with the following harmonic forcing function

$$F(t) = A \sin(\Omega t) \quad (21)$$

where A is the forcing amplitude and Ω is the circular driving frequency. The proposed continuation algorithm will be used to calculate an entire branch of state solutions for a range of forcing frequencies between $\Omega=0.1$ and 10 rad/s and for three different forcing amplitudes: $A=0.01$, 0.1, and 1. The starting guess for the algorithm was calculated from the underlying linear system that was forced at $\Omega=0.1$ rad/s. The algorithm was then allowed to run in an automated fashion until the solutions were found for a forcing frequency of at least of 10 rad/s. Since the linear natural frequency of this system is $\omega=1$ rad/s, the largest responses are expected to occur within this frequency band.

Figure 2 shows the periodic solution curves, which are plotted versus forcing frequency, for forcing amplitude $A=0.01$. The forcing frequencies in the all of the following plots are normalized by dividing by the linear natural frequency $\omega=1$ rad/s so that the abscissa values are reported as dimensionless values of Ω/ω . The state displacement initial condition is plotted in (a), and the state velocity initial condition is plotted in (b). When a displacement and velocity pair is chosen for a specific frequency, these initial conditions and forcing frequency can be integrated for time $T=2\pi/\Omega$ to provide the full trajectory of the corresponding periodic orbit. In the figure, the solutions to stable periodic orbits are shown with solid lines (FCont Stable) and the unstable periodic orbit solutions are shown with dashed lines (FCont Unstable). The stable periodic orbit solutions were verified by using extended time integration (Ext Int), shown with open circles. The first extended integration solution was also used as the initial guess for the continuation algorithm. For all of the subsequent solutions with extended integration, the solution at the previous forcing frequency was used as an initial condition and the system was integrated until it reached a steady state periodic orbit. The solution branch calculated with the continuation algorithm agrees very well with the solutions calculated with extended integration. The distinct resonance peak in the displacement curve is similar to that of a linear, single degree of freedom frequency response function, but it appears to bend slightly to the right. Moreover, the solutions on the lower frequency arm of the peak are stable while some of the solutions on the higher frequency arm of the peak are unstable. When the displacement peaks near $\Omega/\omega=1$, the velocity magnitude becomes large and negative, but as the frequency increases the velocity goes through a zero and then sharply becomes large and positive. The inset axes in (b) shows a detail view of the sharp peak in the velocity curve. It reveals the unstable solutions in the velocity curve, which form a loop turning point. For higher frequencies, the displacement and velocity decrease to very small positive values.

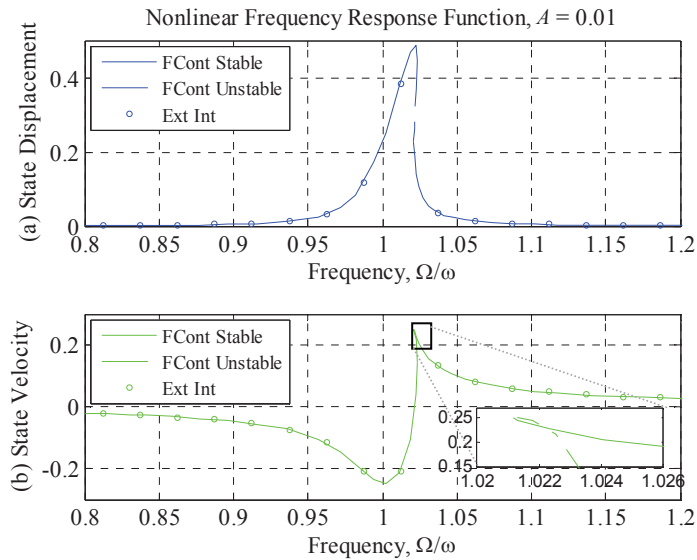


Fig. 2 Initial conditions that result in periodic responses for $A=0.01$ plotted versus dimensionless forcing frequency

When the forcing amplitude is $A=0.01$, the response of the system is nearly linear. The displacement values in the figure are very characteristic of a linear frequency response function, and the peak in the displacement bends only slightly towards higher frequencies due to hardening [18]. However, as evinced in the figure, there is a small portion of the displacement solution branch that is unstable and where multiple responses are possible for a single value of forcing frequency.

The same procedure was followed after increasing the forcing amplitude to $A=0.1$. The periodic solutions for displacement and velocity initial conditions, 3(a) and 3(b), respectively, are plotted in Figure 3. Several periodic solutions that were calculated with extended integration are also shown, marked by open circles, and similar to the first case the agreement is very good. There is a sharp peak in the displacement versus frequency curve, which starts to increase in amplitude near $\Omega/\omega=1$. The maximum amplitude of this peak occurs near $\Omega/\omega=1.65$. Unlike a linear response curve, this peak bends strongly to higher frequencies. The lower frequency arm of the peak contains stable solutions, while the higher frequency arm of the peak has unstable periodic solutions until the displacement amplitude reaches a low value again. The velocity curve 3(b) has a large loop in it. The lower half of the loop contains the stable solutions that correspond to the lower frequency arm of the displacement peak. When the displacement curve reaches its maximum value, the velocity goes through zero and then enters the upper half of the loop, which contains the unstable solutions. There is a significant band between $\Omega/\omega=1.1$ and 1.65 where multiple periodic solutions exist for single forcing frequencies, so the actual response observed depends on the initial conditions and the system's response might jump between those solutions if perturbed.

The inset in 3(a) provides a detailed view of the tip of the displacement versus frequency curve. In this expanded view the stable orbits that were found with continuation are marked with dots and the unstable ones with open squares. Near the tip the solutions that were found are very closely spaced, revealing that the continuation algorithm required small predictor steps in this region. The turning point in the displacement peak is very sharp, yet the continuation algorithm calculates the turn accurately by automatically reducing the step size between successive periodic solutions.

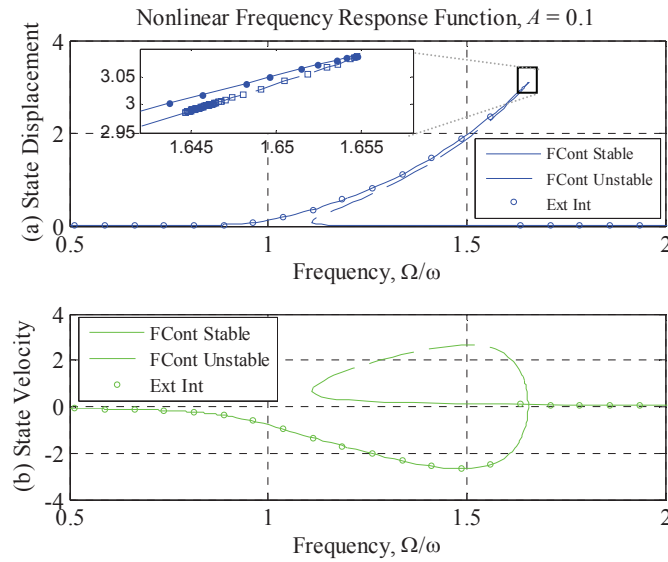


Fig. 3 Initial conditions that result in periodic responses for $A=0.1$ plotted versus dimensionless forcing frequency

In the final case, a forcing with amplitude of $A=1$ is applied to the system and the results are shown in [Figure 4](#), in the same format as the previous cases. Solutions were calculated with extended integration and are shown again with the open circles, although for frequencies above $\Omega/\omega=1.35$ only every tenth extended integration solution is plotted for clarity. The displacement solution branch in 4(a) has a large sharp peak that bends significantly to higher frequencies over the range of $\Omega/\omega=1.5$ to 4.7. Here, the displacement solutions are plotted with a logarithmic scale for the ordinate because the lower frequency and higher frequency arms of the large peak are very close to each other. The shape of the bent peak on a linear scale has a very similar form to that in [Figure 3\(a\)](#). The higher frequency arm of the bent peak is plotted with a dashed line. The velocity solution branch has a very similar shape to the velocity periodic solution curve of the previous forcing case. The main difference is that the large loop reaches larger negative and positive values for the lower solid line and upper dashed line, respectively. At low frequencies, the displacement shows several sharp peaks that have smaller magnitude than the dominant peak in the curve. [Figure 5](#) shows a detailed view of the displacement and velocity curves for a frequency band of $\Omega/\omega=0.1$ to 0.5. The displacement curve peaks near $\Omega/\omega = 0.1, 0.13, 0.16, 0.23,$ and 0.39 , and the peak near 0.39 appears to bend towards higher frequencies. As the displacement peaks near $\Omega/\omega=0.39$, the velocity condition curve changes from negative to positive and contains a small loop, which is very similar in shape the velocity initial condition curve of [Figure 2\(b\)](#). All of the periodic orbit solutions calculated with extended integration in [Figures 4](#) and [5](#) agree very well with the results produced with the continuation algorithm.

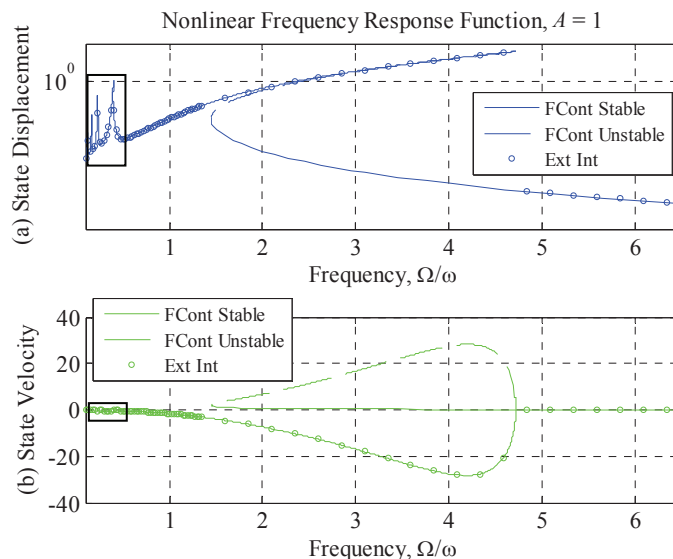


Fig. 4 Initial conditions that result in periodic responses for $A=1$ plotted versus dimensionless forcing frequency

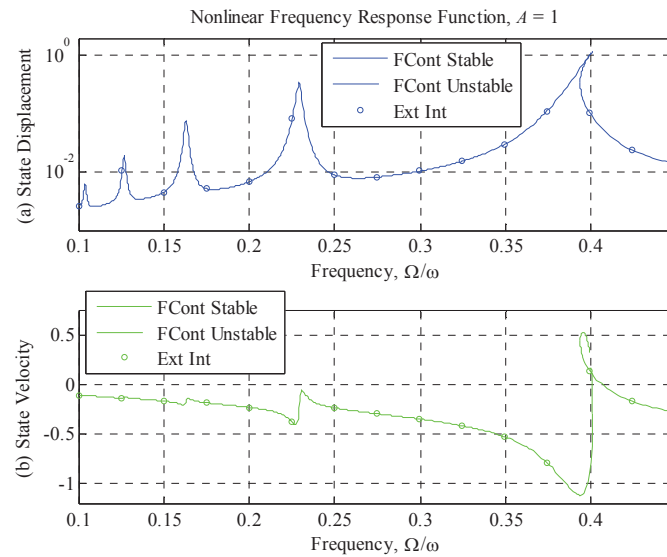


Fig. 5 Expanded view of the region indicated with a box in [Figure 4](#)

When the forcing amplitude is $A=1$, the system exhibits strong nonlinearity. The displacement curve shows a very strong spring hardening effect, so that multiple solutions exist for the frequencies from $\Omega/\omega=1.5$ to 4.7. There are three periodic orbits for most of this region. Two of these orbits are stable and correspond to low and high amplitude responses to the same forcing function. The third orbit is unstable and similar to the higher amplitude branch. Because the unstable orbit is close to the stable orbit, it is difficult to calculate either of the periodic orbits along these curves, especially with extended integration. A very small frequency increment had to be used when the extended integration procedure, otherwise the system would tend to settle to the very small amplitude branch. The continuation algorithm does not have this problem, and is able to calculate both the stable and unstable branches in this region with great detail. The numerous superharmonic resonance peaks [18, 19] are another consequence of the strong forcing amplitude. These tend to occur when the drive frequency is a fraction of the linear natural frequency. One can see from [Figure 5](#) that it is very easy to miss the detail of these phenomena when using extended integration unless a very small frequency increment is used. Furthermore, when using other techniques such as harmonic balance, a separate analytical derivation would have to be performed for each of the peaks. Using the forced continuation approach presented here, these peaks are automatically detected and are well resolved.

3.1 Discussion

The periodic solutions that were calculated with continuation were verified using extended integration, but these calculations took approximately an order of magnitude longer to compute. In frequency bands where multiple periodic orbits exist for single forcing frequencies, the extended integration method will seem to settle at random on different parts of the periodic solution curve. Extended integration has to be carefully used with the appropriate initial conditions to remain on a given curve. For example, in [Figure 3](#) extended integration solutions are calculated for many points at frequencies below the resonance, but no solutions were found on the low amplitude branch between $\Omega/\omega = 1.2$ and 1.65 because the initial conditions used for each extended integration calculation were from the previous periodic orbit solution, and the procedure was started at low frequency. This could have been remedied by starting at high frequency, but in any event the extended integration method could not be used to calculate the unstable periodic orbits, because the system will not naturally settle on an unstable orbit.

The accuracy of the forced continuation solutions can also be verified by calculating the maximum magnitude of each periodic orbit for the different forcing frequencies and amplitudes. When these values are plotted versus the forcing frequency, the result is the traditional frequency response curve in terms of the magnitude of the response. Furthermore, the method in [24] can be used to calculate the unforced periodic solutions of the system, which should provide the backbone curve of the nonlinear frequency response functions. [Figure 6](#) shows the results of these calculations. The nonlinear frequency response curves are plotted for $A= 0.01, 0.1$, and 1 with a blue, green, and red line, respectively. The unstable solutions are plotted with a dashed line. The periodic solutions of the conservative system (i.e. unforced and undamped) are plotted with the black line.

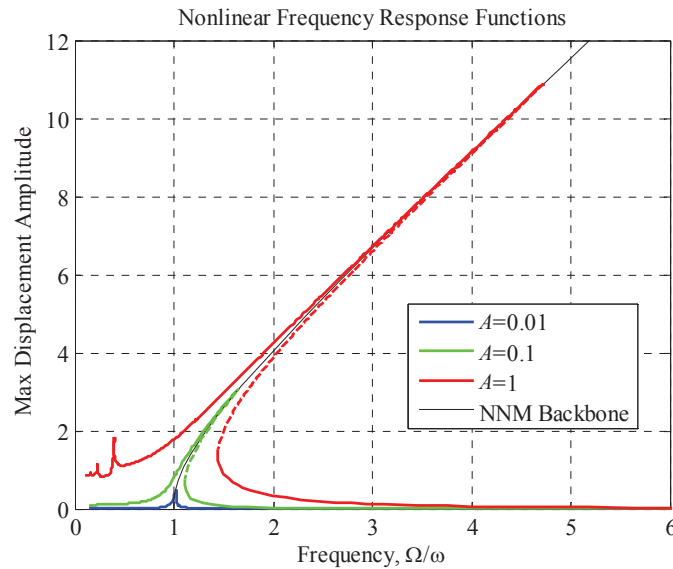


Fig. 6 Conservative System Backbone Curve and Nonlinear Frequency Response Functions for all the Forcing Amplitudes

The forced solutions in the figure track the backbone curve very accurately and the peak of each forced curve crosses the backbone curve. The figure also shows that the frequency response functions do not scale with the magnitude of the forcing, which increases by powers of ten; this is a distinct property of nonlinear systems.

Stability tracking is very convenient with the forced continuation algorithm. Since the Monodromy matrix is calculated as part of the shooting procedure, it can always be used to calculate and store the eigenvalues. These eigenvalues define the stability for each periodic orbit, so one can track the paths of the eigenvalues and quantify the amount of stability or instability each periodic orbit as it is forced at a given frequency. Figure 7 shows the turning point that occurs in the displacement curve near $\Omega/\omega=1.65$ for forcing at $A=0.1$. The top plot, 7(a), shows a magnified view of the displacement curve in the region of interest from Figure 3. For 7(b), the continuous time eigenvalues were calculated by taking the natural logarithm of the eigenvalues from the Monodromy matrix and dividing by the corresponding period. Then, the real part of the continuous time eigenvalue is plotted for the region of interest. In continuous time, stable eigenvalues have negative real parts, and the curve in 7(b) clearly shows that the eigenvalues on the stable curve have essentially constant damping until they quickly jump from stable to unstable as the turning point is crossed.

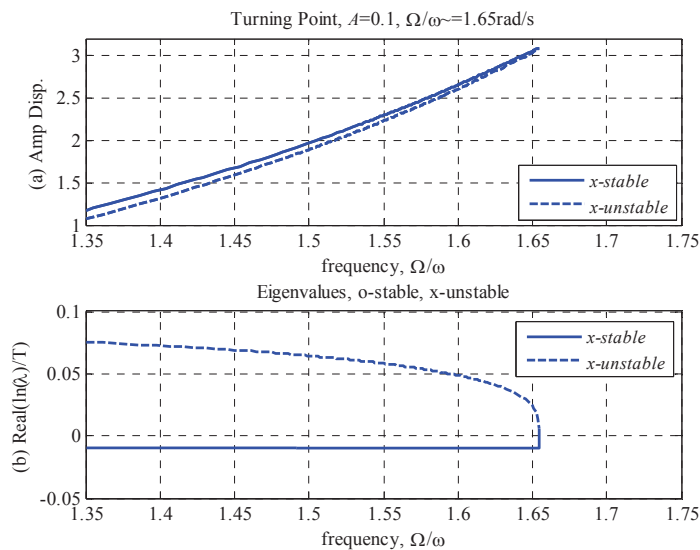


Fig. 7 Turning point near $\Omega/\omega=1.65$ for $A=0.1$ and eigenvalue stability

4. Application to a Nonlinear Beam

The proposed continuation technique is formulated so that it can be easily extended to higher order systems. The second system considered for this work is a cantilever beam with a cubic spring attached to the tip and is shown schematically in Figure 8. The coordinate, x , describes the location along the axis of the beam, y describes the transverse deflection at a given position x , and F_d describes the harmonic external forcing function applied to the beam. The beam is assumed to have uniform parameters: density ρ , elastic modulus E , cross sectional area A_b , transverse moment of inertia I , and length L .

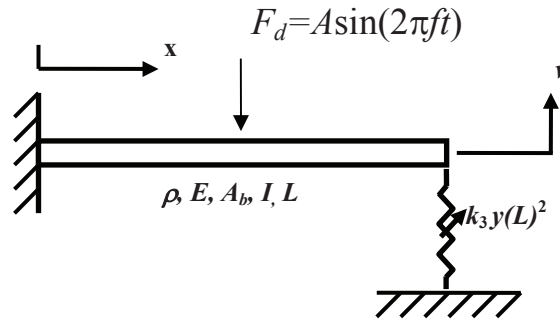


Fig. 8 Cantilever beam with a nonlinear spring attached to the tip.

This system can be achieved in experiment [46, 47], so a model of the beam can be useful to study the periodic responses of the experimental system under different harmonic forcing parameters. A Ritz-Galerkin approach was used to create a two degree of freedom model for the beam where the degrees of freedom are located at the beam's center and tip. In order to reproduce response properties on the order of the responses from the experimental system in Sracic, 2011 #192}, the following parameters were used in for the model: $\rho=2700 \text{ kg/m}^3$, $E=68\text{e}9 \text{ N/m}^2$, $A_b=3.23\text{e}-4 \text{ m}^2$, $I=4.34\text{e}-9 \text{ m}^4$, $L=1.016 \text{ m}$. The equations of motion for this model were derived for a uniform, prismatic beam with these parameters and assuming linear-elastic behavior of the beam so that all of the nonlinearity in the system is due to the nonlinear spring. Only the final result is shown here in state space format, but the full details are provided in [46].

$$\begin{aligned} \begin{Bmatrix} \{\dot{y}\} \\ \{y\} \end{Bmatrix} &= \begin{Bmatrix} \{y\} \\ [M]^{-1} \left(-[C] \{\dot{y}\} - [K] \{y\} - k_3 y(L)^3 \begin{Bmatrix} \psi_{1,2} \\ \psi_{2,2} \end{Bmatrix} + A \sin(\Omega t) \begin{Bmatrix} \psi_{1,1} \\ \psi_{2,1} \end{Bmatrix} \right) \end{Bmatrix} \\ [M] &= \begin{bmatrix} 0.3989 & 0.0746 \\ 0.0746 & 0.1246 \end{bmatrix} \text{Kg}, \quad [K] = 10^4 \begin{bmatrix} 3.1546 & -0.9886 \\ -0.9886 & 0.3945 \end{bmatrix} \text{N/m} \\ [C] &= \begin{bmatrix} 1.8166 & -0.3535 \\ -0.3535 & 0.3079 \end{bmatrix} \text{N/(m/s)}, \quad [\Psi] = \begin{bmatrix} 0.9250 & 1.4015 \\ 2.7244 & -1.9637 \end{bmatrix} \end{aligned} \quad (22)$$

The matrix $[\Psi]$ has the numerical values of the mode vectors for specific position coordinates on the beam (i.e. mode one is column one and degree of freedom one is in row one). Using these properties with the Ritz-Galerkin method, the two linear natural frequencies of the system were equal to $f_1=9.97 \text{ Hz}$ and $f_2=62.51 \text{ Hz}$. In the experiment, a thin strip of spring steel is mounted between the free end of the cantilever and a fixed support and is used to create the geometric nonlinearity [46]. The transverse stiffness contribution of this element is approximated in the model as $k_3=1.4764\text{e}9 \text{ N/m}^3$.

The continuation algorithm was used to calculate the periodic solutions of the beam in the forcing frequency range from 5-100 Hz and for a forcing amplitude of $A=1.0 \text{ N}$ and using a convergence criterion of $\varepsilon=1\text{e}-6$. The first periodic solution was calculated by using extended integration on the system, which was initially at rest. Figure 9 shows the periodic solution curves that were calculated with the continuation algorithm. Two dominant resonances are present in this bandwidth, and those are separated into the left ((a) and (b)) and right ((c) and (d)) columns of plots. The displacements in 9 (a) are plotted with a logarithmic scale on the ordinate. The format from the plots in the previous section is used, but here there is an additional degree of freedom, so the displacement for the second degree of freedom is plotted in red and the velocity in black in order to distinguish them. The stable and unstable solutions are designated as before with solid and dashed lines, respectively. Extended integration was used to calculate periodic solutions in the frequency range and those are plotted with

the open circles. The displacement solutions of both degrees of freedom form sharp peaks in (a) that bend strongly towards higher frequencies. The solutions for the second degree of freedom are larger in magnitude since it is located at the tip of the cantilever which is very active when the first mode is excited. As the frequency increases, the peaks of both degrees of freedom converge on near the same point. There is a small positive and negative peak in the low amplitude displacement curves near 21 Hz, and the negative peak in the red curve shows as a gap due to the logarithmic scale. The solutions for the velocity of degree of freedom one looks similar in shape to some of those for the Duffing oscillator, but the curve for the second degree of freedom is more complicated, changing sign three times before the turning point is reached.

The displacement solution curves for the second mode have opposite signs, as expected since the points are at the midpoint and tip and this is a second bending mode of a cantilever beam. Both curves in (c) have a peak that bends to higher frequencies. There is only a very small region in the curves of the second mode where the solutions are unstable. The frequencies between 23 and 59 Hz were not shown, because all of the solutions were very flat and at low magnitude in that region.

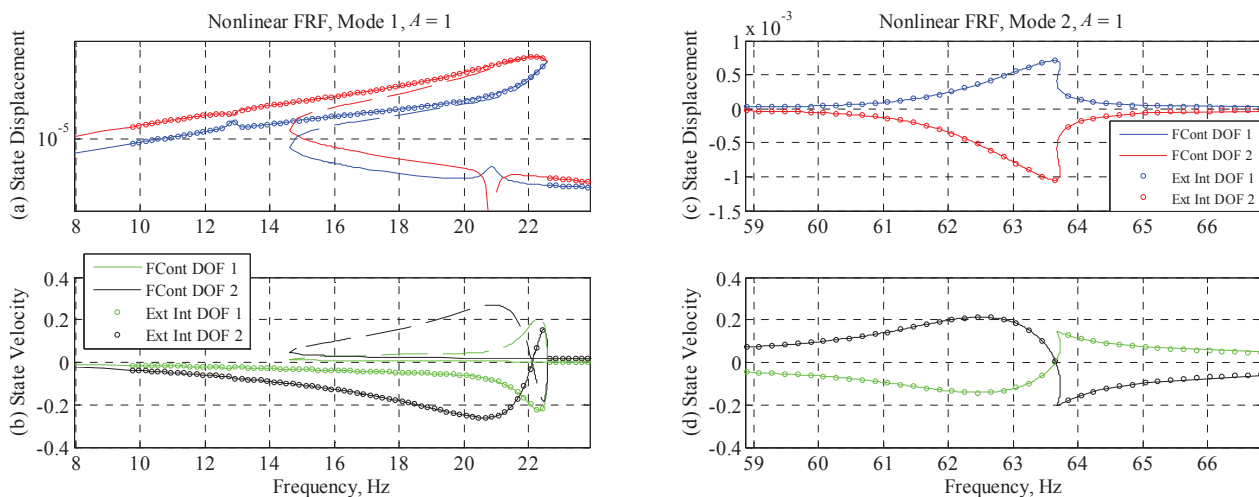


Fig. 9 Initial conditions that result in periodic responses for $A=1$ plotted versus forcing frequency

The addition of the second degree of freedom brings a lot of new dynamics to the frequency response curves, but many of the same features remain. The peak in the first mode bends across about 12 Hz, so the system response is highly nonlinear for this mode. The region that contains three periodic solutions span about 7 Hz, and in that region, the stable and unstable arms of the peaks are nearly identical in magnitude. The turning point in the peaks occurs near 22.5 Hz, and the curves of the two degrees of freedom seem to deflect towards each other the forcing frequency approaches the turning point. The small peak near 21 Hz in (a) is a superharmonic resonance for the second mode, as evidenced by the fact that this frequency is about a third of the frequency where Mode 2 peaks and the fact that the displacements have opposite signs as in Mode 2. The Mode 1 velocity solution curve for the tip degree of freedom has a second loop in it, and near 22 Hz the three solutions all have very similar values for the velocity of the tip (the location on the curve where the black line crosses three times). Since this curve changes sign three times in the band near 22 Hz, it would be very difficult to obtain an initial guess for extended integration in this region. The second mode is less nonlinear than the first. Except for the sign differences, the curves for modes 1 and 2 resemble the high and low amplitude curves for the Duffing oscillator. The first mode is expected to be more nonlinear than the second because since the effect of discrete springs generally decreases with increasing frequency. The solutions that were calculated with extended integration agree very well with those that were calculated with the continuation technique. As before, the extended integration performed in an upward frequency sweep so some of the solutions were missed with that method.

4.1 Discussion

The continuation algorithm worked well to calculate the periodic solution curves of this two degree of freedom system. The algorithm was generally written for n^{th} -order systems, so the code was the same as that used for the previous cases. The curves included richer dynamics than the single degree of freedom case, and the continuation captured a detailed description of these dynamics. For the higher order system, the calculations naturally took longer than the single degree of freedom case, but the continuation remained at least an order of magnitude faster than extended integration. The calculations can be made faster in regions of very low response (i.e. in the flat response regions between the modes) by allowing the algorithm to

switch into a sequential arc-length continuation, where only the initial conditions for the state vector need to be corrected after the prediction is made. This method switching was applied in this work.

The low frequency superharmonic resonances for the first mode of this beam were not calculated in this work. These phenomena become very complicated for multi-degree-of-freedom systems such as this, especially because the dominant frequency in the periodic orbit may be much higher than the frequency of the forcing. The gradient matrix calculations in the continuation algorithm will be biased towards the dominant terms in the period orbit, and the algorithm has a harder time converging on the periodic orbit solution since it will want to change the frequency to the dominant frequency. These difficulties will be addressed in future work.

5. Conclusions

A pseudo arc-length continuation technique was developed to calculate the periodic solutions for harmonically forced nonlinear systems. The algorithm relies on an initial guess, and then uses a Newton-Raphson updating technique to make corrections to the initial guess in order to converge on an actual periodic orbit solution. This can be done for a single forcing frequency, or over an entire band of forcing frequencies. In order to calculate a curve of solutions as the forcing frequency is varied, a tangent prediction step is calculated from the previous solution and then corrections are made to converge to the next solution. A number of successive solutions can be joined to construct a frequency response curve for the nonlinear system in terms of the steady state amplitudes. The algorithm is applicable to n^{th} order systems, and by construction can follow the path of the solutions around turning points to fully characterize the system's dynamics. Superharmonic, hardening, and softening resonances can all be calculated as long as those phenomena occur in the band over which the frequency is varied. Unstable periodic solutions can also be calculated, and the eigenvalues that determine stability are readily available for all solutions. In this work, the nonlinear frequency response functions were calculated for a single degree of freedom Duffing oscillator at three forcing amplitudes and a two degree of freedom Galerkin representation of a nonlinear beam at one forcing amplitude. The algorithm was able to calculate the detailed frequency response curves of both systems, and the results were verified by integrating the equations of motion for an extended time until they reached steady state. These numerical solutions agreed well with the results calculated with continuation, but the continuation algorithm was at least an order of magnitude faster per periodic orbit solution. Additionally, detailed results were calculated for the superharmonic resonances of the Duffing oscillator, and an eigenvalue migration plot was provided to show the convenience of stability calculations with the proposed method. The nonlinear beam had highly nonlinear frequency response functions since the geometric nonlinearity of the system was so strong, yet its frequency response curves were efficiently calculated over a range of frequencies.

6. References

- [1] L. Lin, *et al.*, "Application of AE Techniques for the Detection of Wind Turbine Using Hilbert-Huang Transform," presented at the Prognostics & System Health Management Conference (PHM2010), Macau, China, 2010.
- [2] C.-W. Chang-Jian, "Non-Linear Dynamic Analysis of Dual Flexible Rotors Supported by Long Journal Bearings," *Mechanism and Machine Theory*, vol. 45, pp. 844-866, 2010.
- [3] G. T. Flowers, *et al.*, "The Application of Floquet Methods in the Analyses of Rotordynamic Systems," *Journal of Sound and Vibration*, vol. 218, pp. 249-259, 1998.
- [4] P. Kumar and S. Narayanan, "Nonlinear Stochastic Dynamics, Chaos, and Reliability Analysis for a Single Degree of Freedom Model of a Rotor Blade," *Journal of Engineering for Gas Turbines and Power*, vol. 131, pp. 012506-1 - 012506-8, 2010.
- [5] C. Siewert, *et al.*, "Multiharmonic Forced Response Analysis of a Turbine Blading Coupled by Nonlinear Contact Forces," *Journal of Engineering for Gas Turbines and Power*, vol. 132, pp. 082501-1 -08501-9, 2010.
- [6] J. W. Larsen and S. R. K. Nielsen, "Nonlinear Parametric Instability of Wind Turbine Wings," *Journal of Sound and Vibration*, vol. 299, pp. 64-82, 2007.
- [7] I. Dobson, *et al.* (1992) Voltage Collapse in Power Systems, Circuit and System Techniques for Analyzing Voltage Collapse are Moving Toward Practical Application - and None too Soon. *IEEE Circuits and Devices Magazine*. 40-45.
- [8] Q. Mu, *et al.*, "Circuit Approaches to Nonlinear-ISI Mitigation in Noise-Shaped Bandpass D/A Conversion," *IEEE Transactions on Circuits and Systems*, vol. 57, pp. 1559-1572, 2010.
- [9] N. Garcia, "Periodic Steady-State Solutions of Nonlinear Circuits Based on a Differentiation Matrix," presented at the 2010 IEEE International Symposium on Circuits and Systems (ISCAS), 2010.
- [10] S. R. Anderson, *et al.*, "Nonlinear Dynamic Modeling of Isometric Force Production in Primate Eye Muscle," *IEEE Transactions on Biomedical Engineering*, vol. 57, pp. 1554-1567, 2010.

- [11] R. F. Ker, *et al.*, "The Spring in the Arch of the Human Foot," *Nature*, vol. 325, pp. 147-149, 1987.
- [12] J. B. Dingwell and J. P. Cusumano, "Nonlinear time series analysis of normal and pathological human walking," *Chaos*, vol. 10, pp. 848-63, 2000.
- [13] J. A. Nessler, *et al.*, "Nonlinear Time Series Analysis of Knee and Ankle Kinematics During Side by Side Treadmill Walking," *Chaos*, vol. 19, pp. 026104.1-026104.11, 2009.
- [14] J. Duysens and H. W. A. A. Van de Crommert, "Neural Control of Locomotion; Part 1: The Central Pattern Generator from Cats to Humans," *Gait and posture*, vol. 7, pp. 131-141, 1998.
- [15] A. D. Kuo, "The Relative Role of Feedforward and Feedback in the Control of Rhythmic Movements," *Motor Control*, vol. 6, pp. 129-145, 2002.
- [16] M. Schultze and D. G. Thelen, "Use of a Central Pattern Generator for Control of a Muscle-Actuated Simulation of Pedaling," in *ASME 2009 Summer Bioengineering Conference (SBC2009)*, Lake Tahoe, California, USA, 2009.
- [17] G. Taga, *et al.*, "Self-Organized Control of Bipedal Locomotion by Neural Oscillators in Unpredictable Environment," *Biological Cybernetics*, vol. 65, pp. 147-159, 1991.
- [18] A. H. Nayfeh and D. T. Mook, *Nonlinear Oscillations*. New York: John Wiley and Sons, 1979.
- [19] Z. K. Peng, *et al.*, "Comparison Between Harmonic Balance and Nonlinear Output Frequency Response Function in Nonlinear System Analysis," *Journal of Sound and Vibration*, vol. 311, pp. 56-73, 2008.
- [20] A. F. Vakakis and C. Cetinkaya, "Analytical Evaluation of Periodic Responses of a Forced Nonlinear Oscillator," *Nonlinear Dynamics*, vol. 7, pp. 37-51, 1995.
- [21] T. K. Caughey and A. F. Vakakis, "A Method for Examining Steady State Solutions of Forced Discrete Systems with Strong Non-Linearities," *International Journal of Non-Linear Mechanics*, vol. 26, pp. 89-103, 1991.
- [22] C. Padmanabhan and R. Singh, "Analysis of Periodically Excited Non-linear Systems by a Parametric Continuation Technique," *Journal of Sound and Vibration*, vol. 184, pp. 35-58, 1995.
- [23] P. Ribeiro, "Non-linear Forced Vibrations of Thin/Thick Beams and Plates by the Finite Element and Shooting Methods," *Computers and Structures*, vol. 82, pp. 1413-1423, 2004.
- [24] M. Peeters, *et al.*, "Nonlinear Normal Modes, Part II: Towards a Practical Computation Using Numerical Continuation Techniques," *Mechanical Systems and Signal Processing*, vol. 23, pp. 195-216, 2009.
- [25] S. M. Roberts and J. S. Shipman, *Two-Point Boundary Value Problems: Shooting Methods*. New York: American Elsevier Publishing Company, Inc., 1972.
- [26] J. C. Slater, "A Numerical Method for Determining Nonlinear Normal Modes," *Nonlinear Dynamics*, vol. 10, pp. 19-30, 1996.
- [27] J. C. Slater, "An Optimization Based Technique for Determining Nonlinear Normal Modes," presented at the ASME Design Engineering Division on Active Control of Vibration and Noise, Atlanta, Georgia, USA, 1996.
- [28] R. U. Seydel, *Practical Bifurcation and Stability Analysis: From Equilibrium to Chaos*, 2nd ed. New York: Springer-Verlag, 1994.
- [29] E. Doedel, "Auto, Software for Continuation and Bifurcation Problems in Ordinary Differential Equations," (<http://indy.cs.concordia.ca/auto/>).
- [30] W. Govaerts, *et al.*, "MATCONT : CL_MATCONTM: A Toolbox for Continuation and Bifurcation of Cycles of Maps," <http://sourceforge.net/projects/matcont/>, 2008.
- [31] J. Awrejcewicz and J. Someya, "Periodic, Quasi-Periodic and Chaotic Orbits and Their Bifurcations in a System of Coupled Oscillators," *Journal of Sound and Vibration*, vol. 146, pp. 527-532, 1991.
- [32] T. C. Kim, *et al.*, "Super- and Sub-Harmonic Response Calculations for a Torsional System with Clearance Nonlinearity Using the Harmonic Balance Method," *Journal of Sound and Vibration*, vol. 281, pp. 965-993, 2005.
- [33] C. Padmanabhan and R. Singh, "Dynamics of a Piecewise Non-Linear System Subject to Dual Harmonic Excitation Using Parametric Continuation," *Journal of Sound and Vibration*, vol. 184, pp. 767-799, 1995.
- [34] C. Padmanabhan and R. Singh, "Analysis of Periodically Forced Nonlinear Hill's Oscillator with Application to a Geared System," *Journal of Acoustical Society of America*, vol. 99, pp. 324-334, 1996.
- [35] C. Padmanabhan and R. Singh, "Influence of Mean Load on the Response of a Forced Non-Linear Hill's Oscillator," presented at the ASME Design Engineering Technical Conferences Boston, Massachusetts, 1995.
- [36] G. Kerschen, Kowtko, J., McFarland, D.M., Bergman, L., Vakakis, A., "Theoretical and Experimental Study of Multimodal Targeted Energy Transfer in a System of Coupled Oscillators," *Nonlinear Dynamics*, vol. 47, pp. 285-309, 2007.
- [37] G. Kerschen, Peeters, M., Golinval, J.C., Vakakis, A.F., "Nonlinear Normal Modes, Part I: A Useful Framework for the Structural Dynamicist," *Mechanical Systems and Signal Processing*, vol. 23, pp. 170-194, 2009.
- [38] G. Kerschen, *et al.*, "Theoretical and Experimental Study of Multimodal Targeted Energy Transfer in a System of Coupled Oscillators," *Nonlinear Dynamics*, vol. 47, pp. 285-309, 2007.

- [39] G. Kerschen, *et al.*, "Theoretical and Experimental Modal Analysis of Nonlinear Mechanical Systems, IMAC XXVIII Preconference Course," in *28th International Modal Analysis Conference (IMAC XXVIII)*, Jacksonville, Florida, USA, 2010.
- [40] S. L. Lee, *et al.*, "Complicated Dynamics of a Linear Oscillator with a Light, Essentially Nonlinear Attachment," *Physica D*, vol. 204, pp. 41-69, 2005.
- [41] R. Viguie, *et al.*, "Energy Transfer and Dissipation in a Duffing Oscillator Coupled to a Nonlinear Attachment," *Journal of Computational and Nonlinear Dynamics*, vol. 4, pp. 041012-1 - 041012-13, 2009.
- [42] F. Georgiades, *et al.*, "Modal Analysis of a Nonlinear Periodic Structure with Cyclic Symmetry," *AIAA Journal*, vol. 47, pp. 1014-1025, 2009.
- [43] J. Guckenheimer and P. Holmes, *Nonlinear Oscillations, Dynamical Systems, and Bifurcations of Vector Fields* vol. 42. New York: Springer-Verlag New York Inc., 1983.
- [44] A. H. Nayfeh and B. Balachandran, *Applied Nonlinear Dynamics: Analytical, Computational and Experimental Methods*. New York: John Wiley & Sons, Inc., 1995.
- [45] P. Montagnier, *et al.*, "The Control of Linear Time-Periodic Systems Using Floquet-Lyapunov Theory," *International Journal of Control*, vol. 77, pp. 472-490, 2004.
- [46] M. W. Sracic and M. S. Allen, "Identifying Parameters From Nonlinear Cantilever Beams using Linear Time-Periodic Approximations," presented at the 29th International Modal Analysis Conference (IMAC XXVI), Jacksonville, Florida, USA, 2011.
- [47] F. Thouverez, "Presentation of the ECL Benchmark," *Mechanical Systems and Signal Processing*, vol. 17, pp. 195-202, 2003.

Identification of the Tensile Force in Tie-rods of Historical Constructions

Hoa T. M. Luong ¹, Luís F. Ramos ², Rafael Aguilar ³

¹Master Student (SAHC), Department of Civil Engineering – ISISE, University of Minho, Campus de Azurém 4800 - 058 Guimarães, Portugal

²Assistant Professor, Department of Civil Engineering – ISISE, University of Minho, Campus de Azurém 4800 - 058 Guimarães, Portugal

³Ph.D. Student, Department of Civil Engineering – ISISE, University of Minho, Campus de Azurém 4800 - 058 Guimarães, Portugal

ABSTRACT

This paper addresses the problem of the bending curvature due to self-weight of tie-rods when using dynamical approach to identify the tensile force in tie-rods of historical constructions. Although several dynamic testing methods have been proposed in the literature, the effect of bending curvature due to self-weight of the rods on their frequency values has not been studied. In this work, the bending curvature due to self-weight of tie-rods with small cross-section-to-length ratios is proven to have significant effect on their frequency values of the first vibration mode at low tensile stresses. As a result, the accuracy of the identified tensile force in tie-rods will be affected if the effect is not accurately considered. Four tie-rod specimens of different characteristics were tested in laboratory by dynamic tests. A numerical model was developed for axially loaded tie-rod using a FE program, assuming Euler beam with uniform cross-section and rotational springs at both supports. By calibrating the experimental and numerical results, the most suitable dynamical analysis for tie-rod models to take into account the effect of bending curvature due to their self-weights is concluded. In particular, the analysis should be performed in two steps: (i) first, the static geometric non-linear analysis to obtain the deflected shape of the tie-rod due to its self-weight and an applied tensile force; (ii) then, the modal analysis is run on the deflected tie-rod to achieve the frequencies and mode shapes via free vibration at that applied tensile force. When the effect of bending curvature due to self-weight of tie-rods is neglected, the frequency of the first mode should be excluded. Based on these conclusions, two techniques to identify in-situ the tensile stress in tie-rods are discussed. They are frequency-based identification techniques that minimize the measurement errors. In addition, a methodology to estimate a range of tensile stress using a formula or two self-constructed standard charts is proposed.

1. INTRODUCTION

Metallic tie-rods were often used in ancient masonry buildings to eliminate the lateral load exercised by the vaults and arches and contribute fundamentally to the structural equilibrium [1]. In the field of preservation of these historical structures, it is critical to identify the tensile forces acting in tie-rods. To date, several static and dynamical methods have been proposed to estimate the tensile forces in metallic tie-rods of masonry arches and vaults. Bati and Toniatti [2] introduced a method and experimental procedure based on a single static test. Another technique proposed by [3] combined static and dynamic identification. The tie-rod was modeled as a simply supported Euler beam with two identical rotational springs at the edges. To identify the tensile force and the stiffness of the rotational springs, two equations were used: (i) a static equation giving the central deflection of the rod under a given load, and (ii) a dynamic equation giving the fundamental natural frequency of the rod. Both methods were tested in laboratory providing good results.

However, fully dynamical methods have been received more attention because they are non-destructive (ND) and generally require less experimental effort. Lagomarsino and Calderini [4] presented an algorithm as an approximate numerical solution to identify the axial tensile force in ancient tie-rods using the first three natural frequencies. The method was tested on a

number of ideal tie-rods, modeled as an Euler beam of uniform cross-section, simply supported at the ends with additional rotational springs, and on real tie-rods. The dynamical identification of cable tension force has been proposed by [5] using a sensitivity-based methodology. It determines the tension force, flexural rigidity and axial rigidity of the cable from measured natural frequencies. Recently, Amabili et al. [1] developed a ND technique to identify the in-situ tensile force in tie-rods. They measured the first four to six natural frequencies of tie-rods by dynamic test. Then, a numerical model, based on the Rayleigh–Ritz method, was developed for the axially loaded tie-rod using the Timoshenko beam theory. The unknowns, i.e. (i) the tensile force, (ii) the stiffness of the foundation and in some cases, (iii) the length of the rod inside the wall, were identified by minimizing a weighted difference between the calculated and identified natural frequencies. The technique was tested on five real tie-rods giving reasonable results.

Although several methods have been presented in the literature for the estimation of the tensile force in tie-rods, for what concerns to strictly dynamical approach, none of the methods took into account the deflected shape of the tie-rod due to its self-weight. The work by the Authors gives proof of the significant effect of bending curvature due to self-weight of tie-rods with small cross-section-to-length ratios on the values of their natural frequencies. As a result, it affects the accuracy of the identified tensile force in tie-rods. Therefore, this paper addresses the problem of identifying experimentally the tensile force in metallic tie-rods of historical constructions by dynamic tests considering the effect of bending curvature due to self-weight of tie-rods. The dynamic tests were performed for four tie-rod specimens in laboratory. The experimental results were compared with that of numerical models using a FE program, taking into account the effect of bending curvature due to the self-weights of the rods. After that, the effect of bending curvature due to self-weight will be concluded. The most suitable dynamical analysis method for tie-rods will be recommended. Based on that, two techniques to identify in-situ the tensile stress in tie-rods will be discussed. The techniques are similar to the recently proposed technique [1]. A development is made for the technique to accurately consider the effect of bending curvature due to self-weight of tie-rods. Finally, a methodology to estimate a range of tensile stress in tie-rods using a theoretical formula or two proposed standard charts will be presented.

2. LABORATORY TESTS

2.1 Test Set-up and Performance

Four tie-rods of different characteristics were tested in laboratory. Their characteristics are presented in Table 1. The material properties of all specimens are the mass density of 7850 kg/m^3 , the elastic modulus of 210 GPa and the Poisson's ratio of 0.30. Using modal analysis tests, the frequencies and the first five to eight modes of vibration were determined at different applied tensile forces. For each tie-rod, the tests were performed with two types of boundary conditions to simulate the boundary conditions of real tie-rods. The first type of boundary conditions is pinned-pinned (PP) and the second type is fixed-fixed (FF). Figure 1 shows the set-up of the two boundary conditions and Figure 2 gives an example of the test overview.

Table 1: Tie-rod specimens for laboratory tests

Specimen	Length, L (m)	Cross-section	
		Shape	Size: height (h) \times width (b) or diameter (d) (m)
Tie-rod "S1"	2.7	Square	0.04×0.04
Tie-rod "S2"	5.4	Square	0.04×0.04
Tie-rod "C3"	2.7	Circular	0.02
Tie-rod "C4"	5.4	Circular	0.02

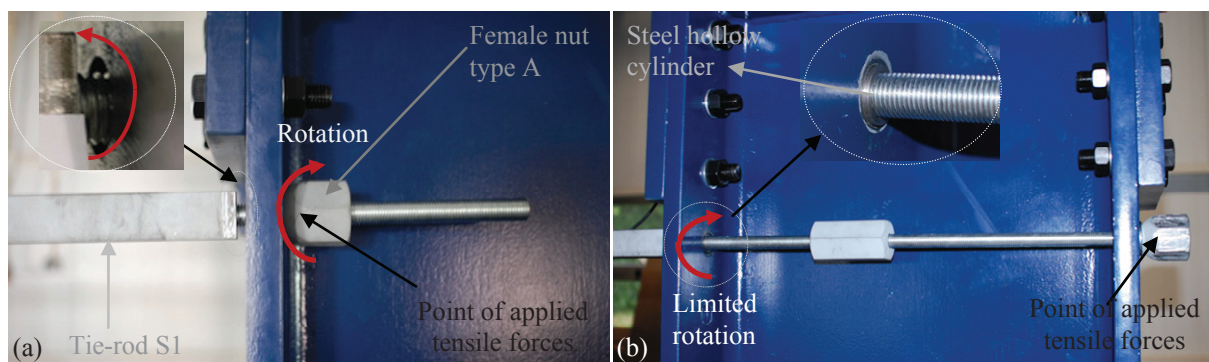


Figure 1 – Experimental boundary conditions: (a) type PP, (b) type FF

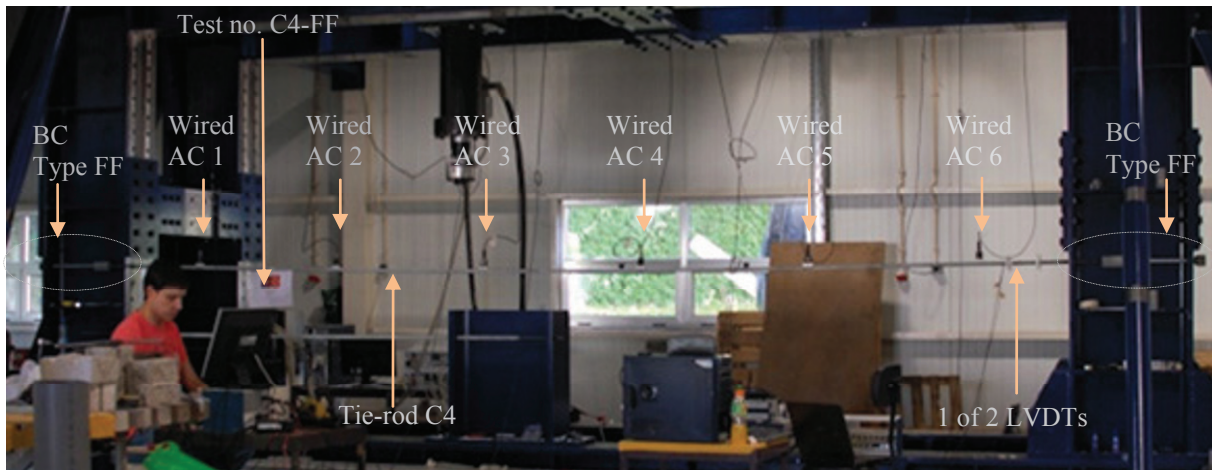


Figure 2 – Tests of tie-rod C4 with boundary conditions type FF (“AC”: accelerometer)

The tests were repeated for each specimen with four or five values of measured tensile stresses in tie-rods. The tensile forces were applied manually using a wrench to tighten the specimens at one end. To control the values of the applied tensile force, the tests were carried out by displacement-control using two Linear Variable Differential Transformers (LVDTs). From the measured displacements of the LVDTs, the strains and the actual tensile stresses in the tie-rods were calculated. The LVDTs were placed on both sides of a tie-rod at the same location to take the average value of the two measurements. They were glued parallel to and at the same level as the centre line of the tie-rod’s cross-section.

To illustrate the effect of tensile force on the frequency, Figure 3 presents the overlaying of the two Frequency Response Spectrums (FRSs) at two measured tensile stresses in tie-rod S2. The FRS at higher tensile stress is shifted to the right.

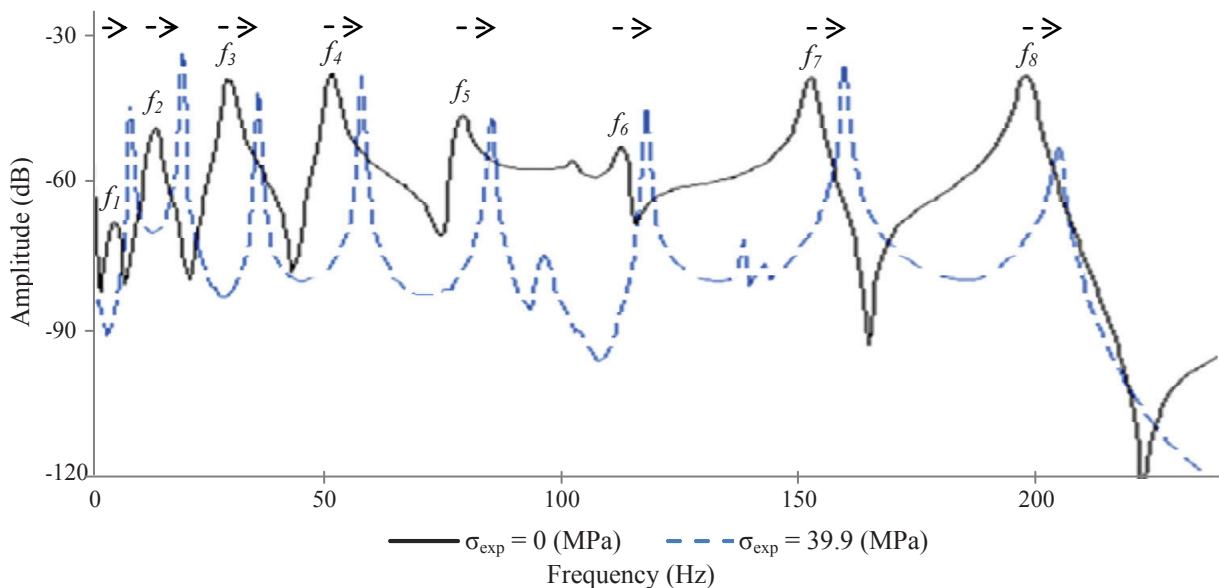


Figure 3 – FRSs of tie-rod S2 at two values of tensile stresses - Effect of tensile stress on the frequency f

2.2 Measured Deflected Shapes of Tie-rod Specimens

The deflections of the tie-rod at initial tensile stress and for each increment of the tensile stress were measured using a laser meter. Figure 4 shows the measured deflected shapes of tie-rod C4 at different tensile stresses in the tests with the boundary conditions type FF. The maximum deflection at initial zero tensile stress is 35 mm. The deflection of the tie-rod was highly sensitive to the changes in the tensile stress.

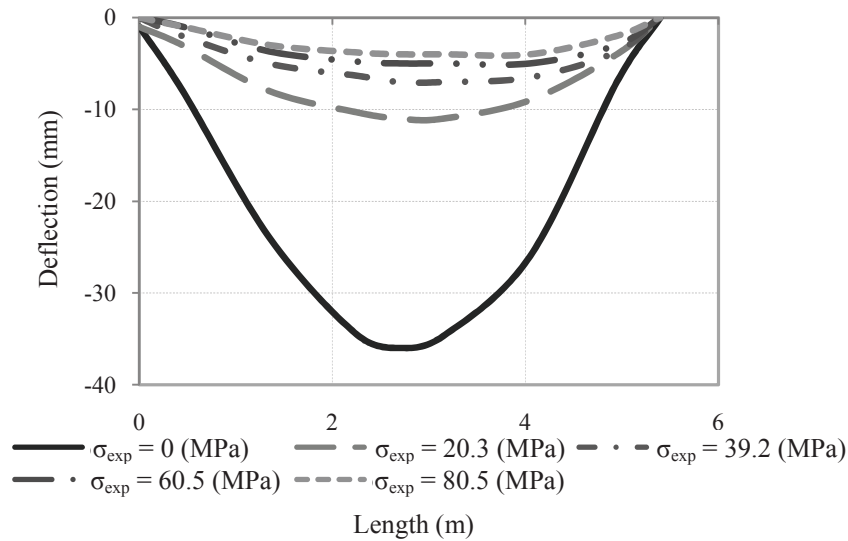


Figure 4 – The measured deflected shapes of tie-rod C4 in tests with boundary conditions type FF

Table 2 gives a summary of the maximum and minimum deflections in all the tests together with the tensile stress values. For short tie-rods with the length equal or less than 2.7 m, the bending curvature due to self-weight of the rods is insignificant; for long tie-rods with the length of 5.4 m or more, the effect should be assessed.

Table 2: The measured maximum and minimum deflections and tensile stresses in the tie-rod specimens

Test no.	Specimen	Max. deflection, $W_{exp,max}$ (mm)	Initial tensile stress, $\sigma_{exp,0}$ (MPa)	Min. deflection, $W_{exp,min}$ (mm)	Max. tensile stress, $\sigma_{exp,max}$ (MPa)
S1-PP	S1	2.0	0.0	0.0	60.2
S1-FF	-	2.0	0.0	0.0	59.5
S2-PP	S2	27.0	0.0	11.5	59.5
S2-FF	-	29.0	0.0	7.0	60.9
C3-PP	C3	7.0	0.0	2.5	79.1
C3-FF	-	3.0	0.0	1.0	80.5
C4-PP	C4	22.5	0.0	7.5	80.5
C4-FF	-	36.0	0.0	4.0	80.5

The results of the experiments will be first compared with the numerical results without, and then with, the effect of bending curvature due to self-weight of tie-rods. After that, a conclusion regarding the effect of bending curvature due to self-weight on the frequency values of tie-rods will be made.

3. NUMERICAL MODEL

To make a comparison between the experimental and numerical results, the four tie-rods in the laboratory tests were modeled using DIANA [6]. The geometrical characteristics, material properties and tensile stresses are the same as the tie-rods in the laboratory tests. The reference structural system consisted of a beam with uniform cross-section and supported by rotational springs at both ends while subjected to a constant tensile force. Two-node Euler - Bernoulli beam elements were used. The model has 20 elements and 21 nodes. The numerical models include the mass of the accelerometers plus the cable applied at their corresponding locations, which is approximately 0.3 kg each. The modal frequency and the first eight modes of vibration were determined via free vibration. The model is illustrated in Figure 5.

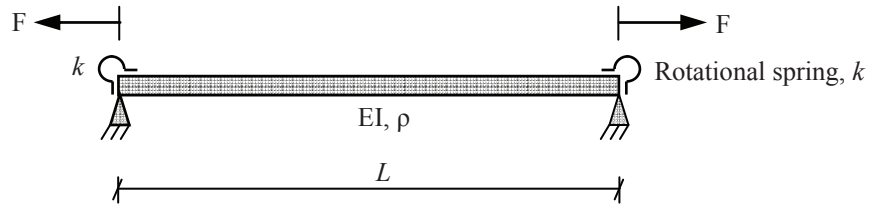


Figure 5 – The numerical model with rotational spring at the supports

4. COMPARISON BETWEEN THE EXPERIMENTAL AND NUMERICAL RESULTS

Figure 6 compares the frequency values obtained from the experiments of tie-rod C4 with boundary conditions type FF with that of the numerical models with both pinned-pinned and fixed-fixed end conditions. The results are consistent except for that of the first mode at initial tensile stresses. The reason is highly related to the effect of bending curvature due to self-weight of the tie-rod. It can be seen that this effect is significant on the first mode only at low tensile stresses.

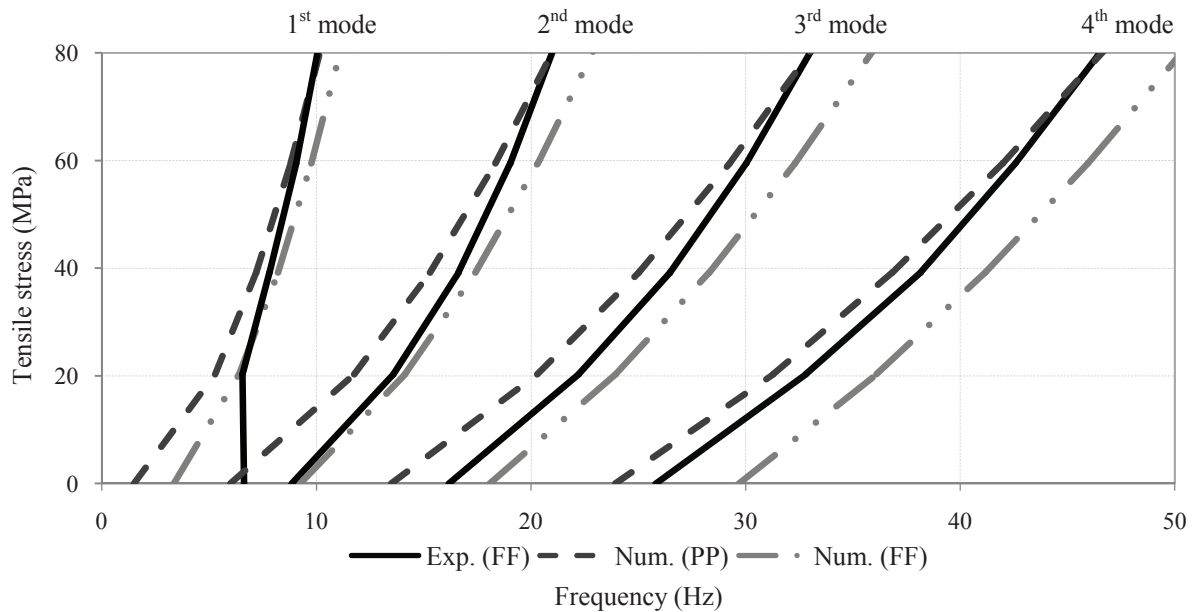


Figure 6 – The experimental and numerical results for the first four modes of tie-rod C4 (“Exp. (FF)” - experimental result with boundary conditions type FF; “Num. (PP or FF)” - numerical result with pinned-pinned or fixed-fixed end conditions)

Among the four tie-rods, tie-rod C4 is the most affected by the effect of bending curvature due to its self-weight, followed by tie-rods S2, C3 and S1. The effect is more significant for circular tie-rods due to higher slenderness.

4.1 Effect of Bending Curvature due to Self-weights of Tie-rods

To assess the effect of the bending curvature due to self-weight, the geometry of the models were updated with the measured deflected shapes. After that, the model was re-run by the modal analysis to obtain the frequencies and modes of vibration. Only the frequencies of the first mode are affected. The numerical results of the first mode of tie-rod C4 before and after updating the geometry of the model are compared with the experiment results of the tie-rod in the tests with boundary conditions type FF in Figure 7.

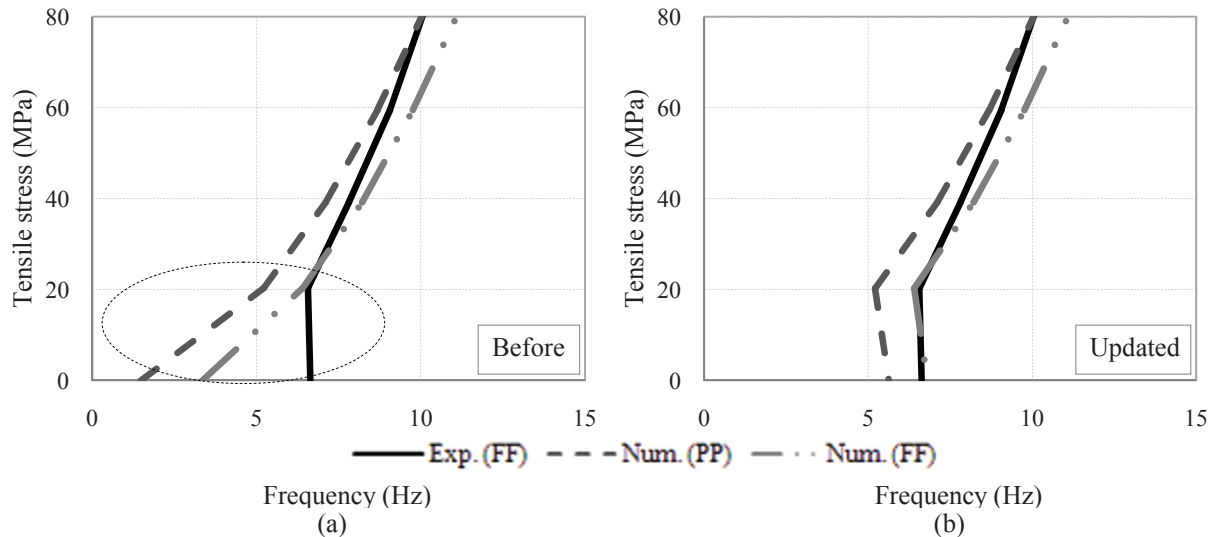


Figure 7 – Comparison of the experimental and numerical results for the first mode of tie-rod C4: The numerical results: (a) neglect the bending curvature due to self-weight of the rod; (b) consider the bending curvature due to self-weight of the rod

To conclude, the effect of bending curvature due to self-weight should be taken into account when performing the dynamic tests and numerical analyses of metallic tie-rods. Depending on the length and cross-section of the tie-rod, the effect is small and might be neglected for tie-rods S1 and C3 with the length of 2.7 m. However, for tie-rods S2 and C4 with the length of 5.4 m, the effect is highly significant on the frequency of the first mode at low tensile stresses. Based on the experiments, low values of tensile stress could be in a range from 0 to 20 MPa. The effect will become negligible when the tie-rod is sufficiently stressed.

4.2 Discussion about the Experimental Uncertainty

Several types of uncertainty are discussed hereafter to validate the accuracy of the experimental results. The first type of uncertainty was associated with the magnitude of applied tensile forces creating tensile stresses in the tie-rod specimens. The tensile forces were applied manually and controlled based on the average measured displacements of two LVDTs. The values of the changes in the displacements were small, for example 0.0143 mm corresponding to an increase of 20 MPa in tensile stress. In addition, they might be affected by other sources of vibrations and noise. The second type was associated with the non-uniform distribution of the applied tensile force on the tie-rod's cross-section. As a result, the strains measured on both sides of the tie-rod at the same location were not equal like in ideal cases. The third type was related to the possible deviation of the LVDTs from the desired positions parallel to and at the same level as the centre line of the tie-rod's cross-section. This could result in the effect of a bending moment due to self-weight of tie-rods on the accuracy of the measured strains. In conclusion, the experimental uncertainties involved the measurement of small strains and thus affected the values of the corresponding tensile stresses. The adopted approach was to combine the experimental and numerical results to assess the estimation of tensile stress in tie-rods.

5. CALIBRATION OF THE NUMERICAL MODELS

5.1 Introduction

To evaluate the experimental uncertainties, the system identification analysis using the Finite Element Model Updating method (FEMU) [7] was carried out. The difference between the experimentally measured and numerically identified frequencies of tie-rods was minimized to find the best-suited values of several parameters including the tensile stress in tie-rods. Following the recommendations of [8], the selected parameters to be updated were the tensile stress, rotational stiffness of the supports and elastic modulus of the tie-rods. In addition, the most suitable numerical analysis method to describe accurately the dynamic behavior of tie-rods taking into account the bending curvature due to their self-weights was studied.

The optimization process was done in Matlab [9] and DIANA [6]. The experimental and numerical results were calibrated in two cases which first neglected, and then considered, the effect of bending curvature due to self-weight. In the later case, two types of analyses were performed. They were static linear and geometric non-linear analyses. In particular, in the linear analysis case, the loadings included the self-weight of the tie-rod, the weight of the accelerometers and an applied tensile

force. The deformed shape of the tie-rod was obtained by static linear analysis which corresponded to that tensile force. The geometry of the model was updated with the deformed shape. After that, the calibration process began with a value set of the updating parameters. The model was run by the modal analysis to obtain the frequencies and modes of vibration. Each time when the tensile stress was updated, the model was re-run by static linear analysis to obtain a new deflected shape. The geometry of the model was updated with this new deflected shape and the calibration process continued. In the geometric non-linear analysis, the calibration process was similar to that using the linear analysis, except that the deflected shapes were obtained by the geometric non-linear analysis; and every time when one of the two parameters, i.e. tensile stress or the elastic modulus, was updated, the geometric non-linear analysis was re-run.

5.2 Comparison of the Calibration Results using Different Analysis Methods

Table 3 gives a summary of the updated results of all different numerical analysis methods for tie-rod C4 model, together with the experimental results. The six different analyses are:

- Analysis I: neglecting the bending curvature due to self-weight, including the frequency of the first mode;
- Analysis II: neglecting the bending curvature due to self-weight, excluding the frequency of the first mode;
- Analysis III: considering the bending curvature due to self-weight, linear analysis for deflection, including the frequency of the first mode;
- Analysis IV: considering the bending curvature due to self-weight, linear analysis for deflection, excluding the frequency of the first mode;
- Analysis V: considering the bending curvature due to self-weight, geometric non-linear analysis for deflection, including the frequency of the first mode;
- Analysis VI: considering the bending curvature due to self-weight, geometric non-linear analysis for deflection, excluding the frequency of the first mode.

Table 3: The experimental and updated numerical results using different analysis methods for tie-rod C4

Analysis method	Tensile stress, σ (MPa)		Rotational stiffness, k (N/m)		Elastic modulus, E (GPa)		Average freq. error, $\text{error}_{\text{ave}}$ (%)	Max. freq. error, $\text{error}_{\text{max}}$ (%)	Freq. error of the 1 st mode, $\text{error}_{\text{mode.1}}$ (%)
	Exp.	Num.	Exp.	Num.	Exp.	Num.			
Analysis I	0.0	17.1	FF	85	210	200	7.6	-35.6	-35.6
Analysis II	0.0	13.8	FF	83	210	206	1.6	-2.80	-
Analysis III	0.0	0.01	FF	71	210	200	4.5	-9.80	5.20
Analysis IV	0.0	21.9	FF	113	210	200	2.4	-4.60	-
Analysis V	0.0	9.50	FF	63	210	200	6.2	-16.7	-16.7
Analysis VI	0.0	12.4	FF	51	210	200	1.3	3.00	-

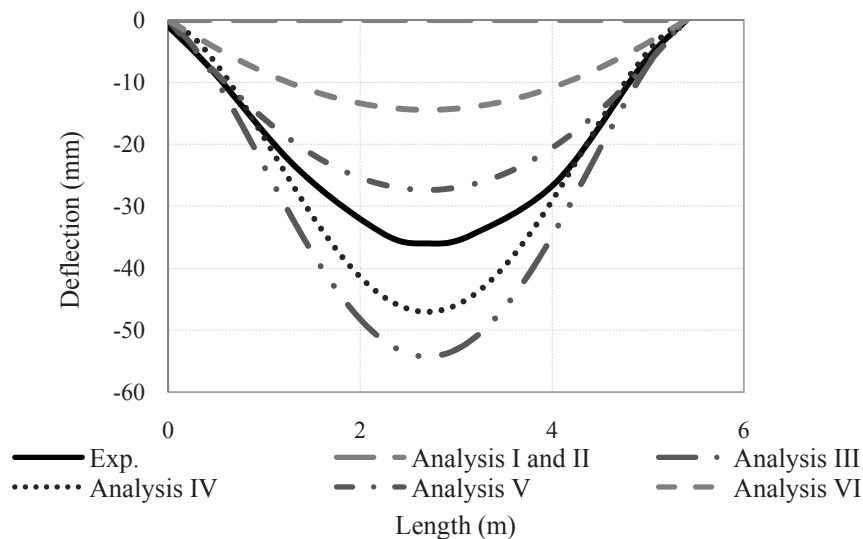


Figure 8 – Comparison between measured experimental and updated numerical deflections using different analysis methods

In terms of the deflection, the analysis method V provides the closest result to the measured value. The obtained deflection using the geometric non-linear analysis is smaller than the measured one. This could be due to the several factors related to the numerical model such as the type of elements used, the number of elements, etc. In terms of the tensile stress, the analysis method III gives the closest result followed by the analysis method V. In terms of the maximum frequency error, it is certain that the analysis methods II, IV and VI give smaller values than the other methods because they exclude the frequency of the first mode but on the other hand, the analysis method IV provides unreasonable result of the tensile stress. Overall, only three analyses II, III and V should be used. Further study was made for these analyses at higher tensile stress as shown in Figure 9.

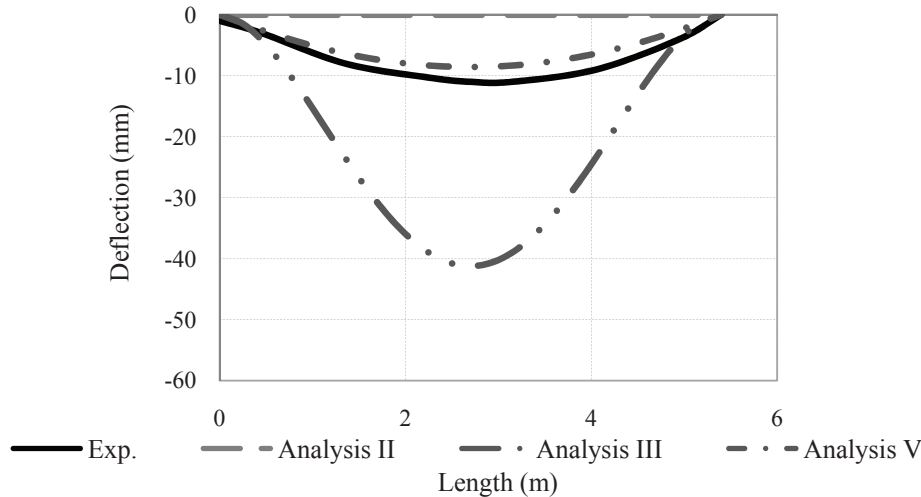


Figure 9 – Comparison between the experimental and three numerical deflected shapes of tie-rod C4 at $\sigma_{exp} = 20.3$ MPa

The linear analysis for deflection, i.e. analysis III, is not suitable to obtain the deflections of tie-rods at higher tensile stresses, because the effect resulting from an increase in the tensile stress is not sufficiently reflected. The tie-rods subject to relatively large deformations due to the effect of tensile stress and therefore, the geometric non-linear analysis which accounts for large deformations, i.e. analysis V, should be used. In conclusion, in all cases, the analysis methods II and V can be used. The difference between the two methods is method II will provide more conservative results in terms of tensile stress in tie-rods. Moreover, the method II does not give the deflections of tie-rods.

6. DISCUSSION ABOUT THE TECHNIQUE TO IDENTIFY IN-SITU THE TENSILE STRESS IN TIE-RODS

Figure 10 presents the two techniques using dynamical approach to identify the tensile stress in tie-rods noting the effect of bending curvature due to self-weight of tie-rods.

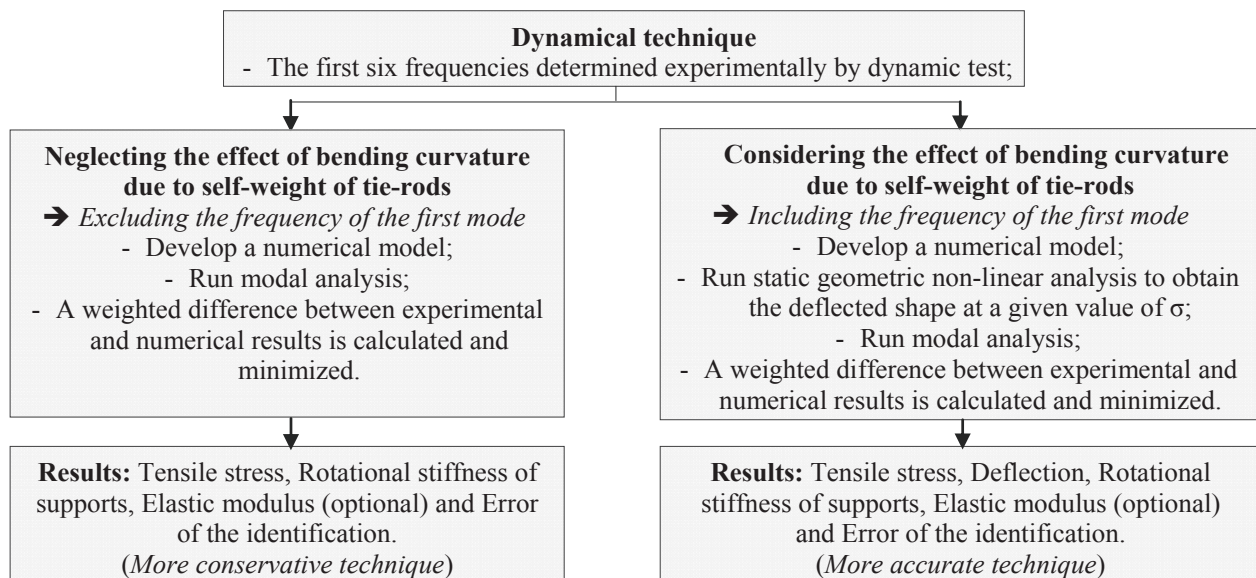


Figure 10 – Summary of the dynamical techniques to identify the tensile stress, σ , in tie-rods

7. PROPOSED STANDARD CHARTS

The development of some practical and reliable charts that can be used to rapidly assess a range of the tensile force in tie-rods is of great interest. Based on the conclusions in Figure 10 to utilize the method which neglects the bending curvature due to self-weight of tie-rods for simplification, a numerical parametric study was carried out using DIANA [6]. The numerical model was the same as that described in Section 3. In total, there were 432 models of different lengths and cross-sections, considering different tensile stresses and boundary conditions.

7.1 Comparison of the FE Results with Theoretical Equation

The complete theoretical equation for the frequency of a tie-rod with pinned-pinned end condition derived by [4] is as below:

$$f_n = \frac{n}{2} \sqrt{\frac{\pi^2 \cdot n^2 \cdot EI}{\bar{m} \cdot L^4} + \frac{T}{\bar{m} \cdot L^2}} \quad (1)$$

where f_n is the frequency of mode n^{th} (Hz); n is the mode number; L is the length of the tie-rod (m); EI is the bending stiffness (Nm^2), T is the tensile force (N) and \bar{m} is mass per unit length of the tie-rod (kg/m).

The numerical results with pinned-pinned condition match perfectly with the theoretical Eq. (1). The experimental results lie between the numerical results of tie-rods with pinned-pinned and fixed-fixed supports. Therefore, a range of tensile stress can be estimated when knowing the relationship between the frequency of fixed-fixed and pinned-pinned system. The frequencies of the fixed-fixed system are divided by those of pinned-pinned end condition for 432 case studies. The ratios are highly consistent. Maximum ratio is 2.267 for the first mode and 1.563 for the second mode.

Table 4 summarizes the effect of all the factors that affect the frequency of tie-rods. There are six factors in total, in which x_σ denotes the ratio between the new and original tensile stresses. Similarly, x_h , x_{mode} and x_L are the ratios between the new and original heights of the cross-section, mode numbers and lengths respectively. And shape of cross-section refers to the effect when the cross-section is changed from rectangular to circular assuming the height h is equal to the diameter d .

Table 4: Factors affecting the frequency of tie-rods based on 432 numerical case studies

No.	Factor	Effect*	Estimated max. effect on freq.	Level of influence*	Level of dependence*
1	Tensile stress	(+)	$\sqrt{x_\sigma}$	Medium	High
2	Boundary condition	(+)	2.267	Medium	Low
3	Size of cross-section	(+)	x_h	Medium	High
4	Mode number	(+)	x_{mode}^2	High	Medium
5	Length	(-)	$1/x_L^2$	High	Medium
6	Shape of cross-section (when $h = d$)	(-)	0.867	Medium	High

*Remarks in Table 4: “Effect (+)” means positive effect such that when the factor is increased, the frequency is also increased and vice versa. This is opposite to “(-)” or negative effect; “Level of influence”: the effect on the frequency in comparison with other factors’ effects; “Level of dependence”: the change of the effect of a factor on the frequency in combination with other factors’ effects.

7.2 Estimation of a Range of Tensile Force in Tie-rods using a Formula

Based on the theoretical Eq. (1) of a tie-rod with pinned-pinned condition combined with the results of the numerical parametric study and calibration process, a range of tensile force in any tie-rods can be estimated by the following Eq., noting that the frequency of the first mode must be excluded:

$$\begin{cases} T = \frac{4\bar{m}L^2 \cdot f_n^2}{n^2} - \frac{\pi^2 n^2 \cdot EI}{L^2} \\ \frac{1}{1.563} \cdot f_n \leq f_n \leq \frac{1}{0.8} \cdot f_n \end{cases} \quad (2)$$

7.3 Estimation of a Range of Tensile Stress in Tie-rods using Two Proposed Standard Charts

The construction of the standard charts is based on the combined effect of different factors. It is necessary to find the correction factors (CFs) to relate the tie-rods of different characteristics, i.e. different cross-sections, lengths or mode numbers, to the ones already known in the charts. The CFs and proposed standard charts are presented in details in [10].

Tie-rod C4 in the test with boundary conditions type PP was chosen to verify the proposed standard charts. Figure 11 shows the values of the tensile stress determined in the Chart I (maximum tensile stress corresponding to pinned-pinned end condition) and Chart II (minimum tensile stress corresponding to fixed-fixed end condition). The range of tensile stress is from 15 MPa to 50 MPa. The obtained maximum value of 50 MPa by the proposed standard charts is close to the value in the experiment, i.e. 47.6 MPa and value after the calibration process using the analysis method II, i.e. 49.4 MPa.

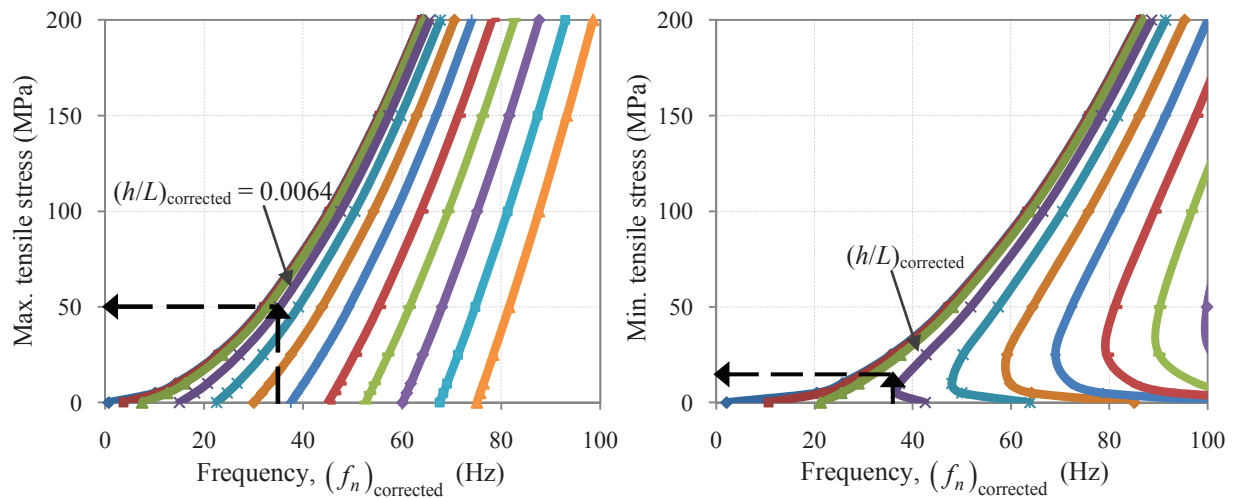


Figure 11 – Verification of the proposed standard charts I and II

8. CONCLUSIONS

The effect of bending curvature due to self-weight of tie-rods should be taken into account in the numerical simulation and dynamical analysis of tie-rods. For long tie-rods like those with the length of 5.4 m, this effect cannot be neglected. The effect is highly significant on the first mode of vibration at low values of tensile stress.

At low tensile stresses, the tie-rod experiences certain behavior that is similar to a catenary cable. However, it cannot be analyzed as a cable because it is necessary to account for bending stiffness. When it is subjected to increasing tensile stresses, large displacements occur. Therefore, the analysis to obtain the deflected shapes of tie-rods should be geometric non-linear. After that, the geometry of the numerical model should be updated with the deflected shape and modal analysis can be performed to obtain the frequencies and modes of vibration.

When the deflections are not interested, the analysis which neglects the effect of bending curvature due to self-weight of tie-rods can be used, however, the frequency of the first mode should be excluded. This analysis provides more conservative results because of higher tensile stress.

In addition, the preliminary estimation of a range of tensile force or tensile stress in tie-rods can be done using a formula or two proposed standard charts which provide convenience to the target users.

9. REFERENCES

- [1] Amabili, M., Carra, S., Collini, L., Garziera, R., Panno, A., Estimation of tensile force in tie-rods using a frequency-based identification method, *Journal of Sound and Vibration* 329(11): 2057-2067 (2010).
- [2] Bati, B. and Toniatti, S., Experimental methods for estimating in situ tensile force in tie-rods, Reston, VA, ETATS-UNIS, American Society of Civil Engineers (2001).
- [3] Blasi, C. and Sorace, S., Determining the axial force in metallic rods, *Structural Engineering International (IABSE)* 4, 241-246 (1994).
- [4] Lagomarsino, S. and Calderini, C., The dynamical identification of the tensile force in ancient tie-rods, *Engineering Structures* 27: 846–856 (2005).
- [5] Park, S., Choi, S., Oh, S.-T., Stubbs, N. and Song, H.-C., Identification of the tensile force in high-tension bars using modal sensitivities, *International Journal of Solids and Structures* 43(10): 3185-3196 (2006).
- [6] DIANA, Finite Element Analysis, User's Manual and CD-ROM, Release 9.3, Netherlands (2008).
- [7] Douglas, B. M. and Reid, W. H., Dynamic Tests and System Identification of Bridges, *ASCE Journal of the Structural Division* 108(10): 2295-2312 (1982).
- [8] Ramos, L. F., Damage Identification on Masonry Structures Based on Vibration Signatures, Ph.D. thesis, University of Minho, Portugal (www.civil.uminho.pt/masonry) (2007).
- [9] Matlab, Matlab User Manual, Release 7.2, The MathWorks, USA (2006).
- [10] Luong, T.M.H., Identification of The Tensile Force in Tie-rod Using Modal Analysis Tests, M.Sc. Thesis, University of Minho, Portugal (2010).

Data Fusion for System Identification of the Humber Bridge

Michael Döhler, Bijaya Jaishi, Laurent Mevel, and James M.W. Brownjohn

Abstract In Operational Modal Analysis (OMA) of large structures, ambient vibration data from multiple non-simultaneously recorded measurement setups is often needed to be processed. These setups share some sensors in common, while the others are moved from one setup to the next. Like this detailed mode shapes of the structure can be obtained, mimicking lots of sensors, while in fact only a few sensors are used for the measurements. Recently, the “Pre Global Estimation Re-Scaling” (PreGER) for the Stochastic Subspace Identification (SSI) was proposed to obtain global modal parameters of the structure. It is a fully automated method that takes differences in the unmeasured background excitation levels between the setups into account, merges the data and does the global system identification. Like this, the different measurement setups can be processed in one step and do not have to be analyzed separately. In this paper, system identification results of the Humber bridge are presented, which is a challenging example as a big number of setups is available and special measures need to be taken to avoid numerical explosion of the computation. The results are compared to the PoSER approach (Post Separate Estimation Re-Scaling) with data-driven SSI.

1 Introduction

Subspace-based linear system identification methods have been proven efficient for the identification of the eigenstructure of a linear multivariable system in many applications. In this paper, the main motivation is output-only structural identification

Michael Döhler, Laurent Mevel
INRIA, Centre Rennes - Bretagne Atlantique, Campus de Beaulieu, F-35042 Rennes, France, e-mail: michael.doehler@inria.fr, laurent.mevel@inria.fr

Bijaya Jaishi, James M.W. Brownjohn
Department of Civil & Structural Engineering, University of Sheffield, Sir Frederick Mappin Building, Sheffield S1 3JD, UK, e-mail: b.jaishi@sheffield.ac.uk, j.brownjohn@sheffield.ac.uk

in vibration mechanics, of a structure subject to ambient unmeasured vibrations, by using accelerometer measurements or strain gauges, when several successive data sets are recorded, with sensors at different locations in the structure. For doing this, some of the sensors, called the *reference sensors*, are kept fixed, while the others are moved. Like this, we mimic a situation in which lots of sensors are available, while in fact only a few are at hand.

However, there is one unpleasant feature of structural identification of structures subject to ambient excitation, namely that excitation is typically turbulent in nature and nonstationary. Like this, the excitation level can change from setup to setup, which has to be taken into account when merging the sensor data for structural identification.

Two merging strategies are considered that differ in the order of the normalization, identification and merging step: the classical PoSER approach and the previously presented PreGER approach in [6, 8]. Special care is taken of the PreGER approach, which is improved to be able to handle a large number of measurement setups without running into memory problems. The PoSER and the now modular PreGER approach are tested and compared on data measured on the Humber bridge in England using 26 different measurement setups with the data-driven SSI algorithm UPC [12, 11].

2 Stochastic Subspace Identification (SSI)

2.1 Single Setup

2.1.1 State Space Model

We consider a linear multi-variable output-only system described by a discrete-time state space model

$$\begin{cases} X_{k+1} = F X_k + V_{k+1} \\ Y_k^{(\text{ref})} = H^{(\text{ref})} X_k \\ Y_k^{(\text{mov})} = H^{(\text{mov})} X_k \end{cases} \quad (1)$$

with

- X_k the state vector at time instant k ,
- $Y_k^{(\text{ref})}$ the observed output vector of the reference sensors (which are a subset of all sensors),
- $Y_k^{(\text{mov})}$ the observed output vector of all the sensors minus the reference sensors (the remaining sensors),
- $H^{(\text{ref})}$ the observation matrix with respect to the reference sensors,
- $H^{(\text{mov})}$ the observation matrix with respect to the remaining sensors,
- F the state transition matrix,
- V_k the unmeasured stationary Gaussian white noise.

Let furthermore

- $Y_k = \begin{pmatrix} Y_k^{(\text{ref})} \\ Y_k^{(\text{mov})} \end{pmatrix}$ all the observed output at time instant k ,
- $H = \begin{pmatrix} H^{(\text{ref})} \\ H^{(\text{mov})} \end{pmatrix}$ the full observation matrix,
- N the number of measurements ($k = 1, \dots, N$),
- r the total number of sensors and $r^{(\text{ref})}$ the number of reference sensors.

2.1.2 SSI with Unweighted Principal Component (UPC) Algorithm

The classical reference-based data-driven subspace identification of the eigenstructure (λ, ϕ_λ) of the system (1) consists of the following steps for the Unweighted Principal Component algorithm [11, 12]: The parameters p and q are chosen, normally as $p+1 = q$ as recommended in [1]. Then, the data matrices

$$\mathcal{Y}_{p+1}^+ \stackrel{\text{def}}{=} \begin{pmatrix} Y_{q+1} & Y_{q+2} & \vdots & Y_{N-p} \\ Y_{q+2} & Y_{q+3} & \vdots & Y_{N-p+1} \\ \vdots & \vdots & \vdots & \vdots \\ Y_{q+p+1} & Y_{q+p+2} & \vdots & Y_N \end{pmatrix}, \quad \text{and} \quad \mathcal{Y}_q^- \stackrel{\text{def}}{=} \begin{pmatrix} Y_q^{(\text{ref})} & Y_{q+1}^{(\text{ref})} & \vdots & Y_{N-p-1}^{(\text{ref})} \\ Y_{q-1}^{(\text{ref})} & Y_q^{(\text{ref})} & \vdots & Y_{N-p-2}^{(\text{ref})} \\ \vdots & \vdots & \vdots & \vdots \\ Y_1^{(\text{ref})} & Y_2^{(\text{ref})} & \vdots & Y_{N-p-q}^{(\text{ref})} \end{pmatrix} \quad (2)$$

are built and the “subspace matrix”¹

$$\mathcal{H}_{p+1,q} = \mathcal{Y}_{p+1}^+ \mathcal{Y}_q^{-T} \left(\mathcal{Y}_q^- \mathcal{Y}_q^{-T} \right)^{-1} \mathcal{Y}_q^- \quad (3)$$

is computed. With the factorization $\mathcal{H}_{p+1,q} = \mathcal{O}_{p+1} \mathcal{X}_q$ into matrix of observability and Kalman filter state sequence with

$$\mathcal{O}_{p+1} \stackrel{\text{def}}{=} \begin{pmatrix} H \\ HF \\ HF^2 \\ \vdots \\ HF^p \end{pmatrix} \quad (4)$$

the matrices H as the first block row of \mathcal{O}_{p+1} and F from the least squares solution of

¹ As $\mathcal{H}_{p+1,q}$ is usually a very big matrix and difficult to handle, we continue the calculation in practice with the R part from an RQ-decomposition of the data matrices, see [11] for details. This will lead to the same results as only the left part of the decomposition of $\mathcal{H}_{p+1,q}$ is needed.

$$\begin{pmatrix} H \\ HF \\ \vdots \\ HF^{p-1} \end{pmatrix} F = \begin{pmatrix} HF \\ HF^2 \\ \vdots \\ HF^p \end{pmatrix}$$

are retrieved. Finally, the eigenstructure (λ, ϕ_λ) of the system (1) is obtained from

$$\det(F - \lambda I) = 0, \quad F \phi_\lambda = \lambda \phi_\lambda, \quad \phi_\lambda = H \phi_\lambda.$$

In the following, the subscripts of the matrices $\mathcal{H}_{p+1,q}$, \mathcal{Y}_{p+1}^+ , \mathcal{Y}_q^- and \mathcal{O}_{p+1} are skipped for simplicity.

2.2 Multiple Setups

Instead of a single record for the output (Y_k) of the system (1), N_s records

$$\underbrace{\begin{pmatrix} Y_k^{(1,\text{ref})} \\ Y_k^{(1,\text{mov})} \end{pmatrix}}_{\text{Record 1}} \quad \underbrace{\begin{pmatrix} Y_k^{(2,\text{ref})} \\ Y_k^{(2,\text{mov})} \end{pmatrix}}_{\text{Record 2}} \quad \cdots \quad \underbrace{\begin{pmatrix} Y_k^{(N_s,\text{ref})} \\ Y_k^{(N_s,\text{mov})} \end{pmatrix}}_{\text{Record } N_s} \quad (5)$$

are now available collected successively. Each record j contains data $Y_k^{(j,\text{ref})}$ from a fixed *reference* sensor pool, and data $Y_k^{(j,\text{mov})}$ from a *moving* sensor pool. To each record $j = 1, \dots, N_s$ corresponds a state-space realization in the form

$$\begin{cases} X_{k+1}^{(j)} = F X_k^{(j)} + V_{k+1}^{(j)} \\ Y_k^{(j,\text{ref})} = H^{(\text{ref})} X_k^{(j)} & (\text{reference pool}) \\ Y_k^{(j,\text{mov})} = H^{(j,\text{mov})} X_k^{(j)} & (\text{sensor pool } n^o j) \end{cases} \quad (6)$$

with a single state transition matrix F .

Note that the unmeasured excitation $V^{(j)}$ can be different for each setup j as the environmental conditions can slightly change between the measurements. However, during each setup j the noise $V^{(j)}$ is assumed to be stationary. Note also that the observation matrix $H^{(\text{ref})}$ is independent of the specific measurement setup if the reference sensors are the same throughout all measurements $j = 1, \dots, N_s$.

For each setup j we obtain a “local” subspace matrix

$$\mathcal{H}^{(j)} = \mathcal{Y}_{(j)}^+ \mathcal{Y}_{(j)}^{-T} \left(\mathcal{Y}_{(j)}^- \mathcal{Y}_{(j)}^{-T} \right)^{-1} \mathcal{Y}_{(j)}^- \quad (7)$$

according to equations (2)-(3), where $\mathcal{Y}_{(j)}^+$ is filled with data from all the sensors and $\mathcal{Y}_{(j)}^-$ with data from the reference sensors of this setup (see Equation (2)). The question is now how to adapt the subspace identification from Section 2.1 to

- merge the data from the multiple setups $j = 1, \dots, N_s$ to obtain global modal parameters (natural frequencies, damping ratios, mode shapes), and to
- normalize or re-scale the data from the multiple setups as the background excitation may differ from setup to setup.

In the following section we present two approaches for this problem: the common practice approach PoSER that processes all the setups separately and merges them at the end, and the recently generalized approach PreGER, that processes all the setups together.

3 Merging Strategies

3.1 Post Separate Estimation Re-Scaling (PoSER)

In this work, reference based SSI-DATA algorithm [12] is used for system identification as PoSER approach. It involves two main steps; processing and modal parameter identification of each setup separately and then merging the modal data. The first step consists of (i) assembly of and QR factorization of data block Hankel matrix (ii) SVD of projection matrix (iii) calculation of system matrices (iv) computation of modal parameters. In the second step, the modal data from each setup are merged to get the global values of system. The values of all setups are averaged to get the natural frequencies and damping ratios of whole structure.

Every setup of simultaneously measured channels yields after identification a part of the global mode shape. These parts are glued together with the aid of the reference sensors, common to all setups. Least squares approximation is used to determine the scaling factor of a certain mode between two setups. The scaling factor is different from one if the (unknown) excitation changes from one setup to another, which is generally the case. The whole procedure is summarized in [Figure 1](#). For large structures having a huge number of test setups, this approach is time consuming as many stabilization diagrams have to be analyzed. In most of the cases,



Fig. 1 Merging partial mode shape estimates $\phi^{(j)}$, $j = 1, \dots, N_s$ into a global mode shape estimate $\phi^{(all)}$ in the PoSER approach.

all modes are not well excited in all setups and mode pairing between different setups is difficult.

3.2 Pre Global Estimation Re-Scaling (PreGER)

3.2.1 General PreGER Merging Strategy

The PreGER merging approach was introduced in [9, 10] and recently generalized [6, 8]. It makes use of a factorization of the subspace matrix of each setup into observability and some other matrix on the right side, and normalizes them with a common right factor to introduce the same excitation factor to all the setups. In this work, it is simplified and adapted to a large number of setups.

For each setup $j = 1, \dots, N_s$ the subspace matrix (7) is built that has the factorization property $\mathcal{H}^{(j)} = \mathcal{O}^{(j)} \mathcal{X}^{(j)}$. In order to merge the data, first the different excitation factors of each setup are taken into account, which are present in the Kalman filter state sequence $\mathcal{X}^{(j)}$ since the matrix of observability is only dependent of the observation matrix $H^{(j)}$ and state matrix F that are not affected. In the first step, all the subspace matrices $\mathcal{H}^{(j)}$ are re-scaled with a common Kalman filter state sequence $\mathcal{X}^{(j^*)}$ of one fixed setup j^* , then the resulting matrices are merged and a global modal parameter estimation is finally done on the merged matrix.

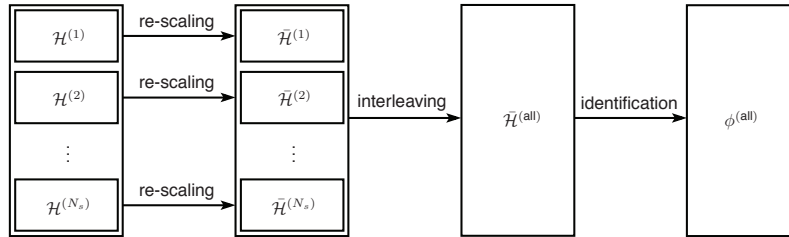


Fig. 2 Merging subspace matrices of each setup to obtain a global subspace matrix and global mode shape estimate $\phi^{(\text{all})}$ in the PreGER approach from [6, 8].

In detail (see also [6]), the subspace matrices $\mathcal{H}^{(j)}$ are separated into matrices $\mathcal{H}^{(j,\text{ref})}$ and $\mathcal{H}^{(j,\text{mov})}$ by taking the appropriate rows of $\mathcal{H}^{(j)}$ that correspond to the reference resp. moving sensor data from $\mathcal{Y}_{(j,\text{ref})}^+$ resp. $\mathcal{Y}_{(j,\text{mov})}^+$. Then, the matrices $\mathcal{H}^{(j,\text{ref})}$, $j = 1, \dots, N_s$ are juxtaposed to

$$\mathcal{H}^{(\text{all},\text{ref})} = (\mathcal{H}^{(1,\text{ref})} \mathcal{H}^{(2,\text{ref})} \dots \mathcal{H}^{(N_s,\text{ref})})$$

and with the help of an SVD this matrix is decomposed to

$$\mathcal{H}^{(\text{all},\text{ref})} = \mathcal{O}^{(\text{ref})} (\mathcal{X}^{(1)} \mathcal{X}^{(2)} \dots \mathcal{X}^{(N_s)}), \quad (8)$$

from where the matrices $\mathcal{X}^{(j)}$ and the observability matrix with respect to the reference sensors $\mathcal{O}^{(\text{ref})}$ are obtained. One of the setups $j^* \in \{1, \dots, N_s\}$ is chosen and the matrices $\mathcal{H}^{(j, \text{mov})}$ are rescaled to

$$\tilde{\mathcal{H}}^{(j, \text{mov})} = \mathcal{H}^{(j, \text{mov})} \mathcal{X}^{(j)\dagger} \mathcal{X}^{(j^*)},$$

where \dagger denotes the pseudoinverse. In the last step the block rows of the matrices $\tilde{\mathcal{H}}^{(j, \text{mov})}$, $j = 1, \dots, N_s$, and the matrix $\mathcal{H}^{(j^*, \text{ref})}$ are interleaved, to obtain the merged matrix $\tilde{\mathcal{H}}^{(\text{all})}$ with the factorization property

$$\tilde{\mathcal{H}}^{(\text{all})} = \mathcal{O}^{(\text{all})} \mathcal{X}^{(j^*)} \quad \text{with} \quad \mathcal{O}^{(\text{all})} = \begin{pmatrix} H^{(\text{all})} \\ H^{(\text{all})}F \\ H^{(\text{all})}F^2 \\ \vdots \\ H^{(\text{all})}F^p \end{pmatrix} \quad \text{and} \quad H^{(\text{all})} = \begin{pmatrix} H^{(\text{ref})} \\ H^{(1, \text{mov})} \\ H^{(2, \text{mov})} \\ \vdots \\ H^{(N_s, \text{mov})} \end{pmatrix}. \quad (9)$$

On this global subspace matrix the subspace system identification can be performed to obtain the global modal parameters.

3.2.2 Modular PreGER Merging Strategy

The PreGER approach is now modified to handle a large number of setups, as in such a case the global subspace matrix $\tilde{\mathcal{H}}^{(\text{all})}$ can get very big, which can pose memory problems. Also, an SVD of $\tilde{\mathcal{H}}^{(\text{all})}$ has to be done to obtain the observability matrix $\mathcal{O}^{(\text{all})}$, and from this matrix the state transition matrix F is obtained from a least squares solution. These are operations involving large matrices in the case of many setups and memory problems can arise again.

In order to circumvent these problems, the matrix $\mathcal{O}^{(\text{all})}$ is built directly instead of $\tilde{\mathcal{H}}^{(\text{all})}$, similar to the modular merging approach in [7], so that no further SVD has to be done. With $\mathcal{O}^{(j, \text{mov})} \stackrel{\text{def}}{=} \mathcal{H}^{(j, \text{mov})} \mathcal{X}^{(j)\dagger}$ and Equation (9), $\mathcal{O}^{(\text{all})}$ can also be built directly by interleaving the block rows of the matrices $\mathcal{O}^{(j, \text{mov})}$, $j = 1, \dots, N_s$, and the matrix $\mathcal{O}^{(\text{ref})}$. From $\mathcal{H}^{(j, \text{ref})} = \mathcal{O}^{(\text{ref})} \mathcal{X}^{(j)}$ the relation

$$\mathcal{O}^{(j, \text{mov})} = \mathcal{H}^{(j, \text{mov})} \mathcal{X}^{(j)\dagger} = \mathcal{H}^{(j, \text{mov})} \mathcal{H}^{(j, \text{ref})\dagger} \mathcal{O}^{(\text{ref})}$$

follows and hence in Equation (8) only the matrix $\mathcal{O}^{(\text{ref})}$ is needed. Then, the SSI using the modular PreGER merging – only involving small matrices coming from single setups if necessary – consists of the following steps:

- Get the matrix $\mathcal{O}^{(\text{ref})}$ from the SVD of $(\mathcal{H}^{(1, \text{ref})} \mathcal{H}^{(2, \text{ref})} \dots \mathcal{H}^{(N_s, \text{ref})})$. If the latter matrix is too big, an iterative thin RQ decomposition can be done prior to the SVD, that involves only one matrix $\mathcal{H}^{(j, \text{ref})}$ in one step. See also [7] for details.
- Build the matrices $\mathcal{O}^{(j, \text{mov})} = \mathcal{H}^{(j, \text{mov})} \mathcal{H}^{(j, \text{ref})\dagger} \mathcal{O}^{(\text{ref})}$, $j = 1, \dots, N_s$

- Solve the least squares problem for the state transition matrix F either from $\mathcal{O}^{(\text{all})}$ (which results from interleaving $\mathcal{O}^{(j,\text{mov})}$, $j = 1, \dots, N_s$, and $\mathcal{O}^{(\text{ref})}$) or iteratively by directly using the matrices $\mathcal{O}^{(j,\text{mov})}$, $j = 1, \dots, N_s$, and $\mathcal{O}^{(\text{ref})}$ one after each other, see also [7] for details. Get the global observation matrix $H^{(\text{all})}$ from the first block row of $\mathcal{O}^{(j,\text{mov})}$, $j = 1, \dots, N_s$, and $\mathcal{O}^{(\text{ref})}$.
- Get the natural frequencies, damping ratios and mode shapes from F and $H^{(\text{all})}$.

This modular PreGER approach is summarized in [Figure 3](#).

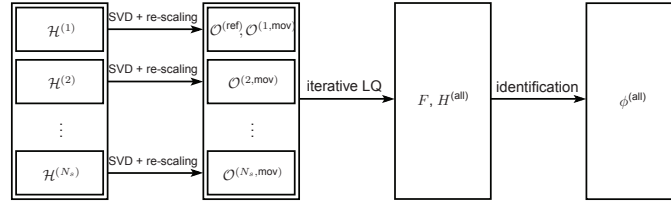


Fig. 3 Merging subspace matrices of each setup to obtain a global subspace matrix and global mode shape estimate $\phi^{(\text{all})}$ in the modular PreGER approach.

4 Analysis of Humber Bridge

4.1 Bridge Description and Ambient Vibration Test

The Humber Bridge ([Figure 4](#)), which was opened in July 1981, has a main span of 1410 m with side spans of 280 m and 530 m. The spans comprise 124 units of 18.1 m long 4.5 m deep 140 prefabricated sections 28.5 m wide including two 3 m walkways. The top of the box section constitutes an orthotropic plate on which



Fig. 4 Views of Humber Bridge from North and South.

mastic asphalt surfacing is laid, and the sections have four internal bulkheads. At the end of each span there is a pair of A-frame rocker bearings that provide restraint in three degrees of freedom. The slip-formed reinforced concrete towers rise 155.5 above the caisson foundations and carry the two main cables which have a sag of 115.5 m. These cables each have sectional area of 0.29 m^2 and consist of almost 15,000 5 mm 1.54 kN/mm^2 UTS wires grouped in strands.

The bridge was previously tested in July 1985 [2]. The testing was motivated by a requirement to validate FE procedures for suspensions bridges. The 1985 testing used only three accelerometers, several km of cables, an analog tape recorder and a two-channel spectrum analyzer and it was possible to identify over 100 vibration modes of the main span, side spans and towers up to a frequency of 2 Hz. After 23 years, the original signals and resulting digital mode shapes were no longer available, just the values in published papers and reports. Because of the quality uncertainties and lack of digital data for the EPSRC project, a retest of the bridge was necessary.

The current test was conducted during the week 14th-18th in July 2008 as part of EPSRC funded research project. To avoid lengthy post-processing of data a different strategy was required for the system identification, making use of autonomous recorders with precise timing of GPS-synchronized clocks. The system for using autonomous recorders pioneered by researchers at FEUP in Portugal [4, 5] was adopted and a team from FEUP brought their recorders and assisted in the testing and post-processing. Between FEUP and University of Sheffield ten GEOSIG recorders were available. These recorders used either internal force balance accelerometers, external Guralp CMG5 accelerometers of a triaxial arrangement of QA750 accelerometers.

With up to five days of measurement available with a maximum of 10 hours per day due to recorder batteries, an optimal plan was formulated that involved separate setups to cover 76 positions. Sensor locations for one of the setup is shown in [Figure 5](#), in each of these two pairs of triaxial recorders would be maintained at two permanent reference locations, leaving the remaining three pairs to rove either deck or in East/West tower pylons. Each measurement generated one hour of 30-channel (10 in each direction) acceleration records, in four 15-minute segments. The entire day of measurements was pre-programmed into each recorder, leaving 10-minute periods between measurements to move the six rovers. Several cross-calibration measurements were made to test the synchronization and relative calibrations of the recorders by positioning them together. For side-span measurements an extra pair of recorders was kept as a side-span reference and on the final day, a single pair of recorders was kept in the main span with a pair of recorder left on the top of each



Fig. 5 Sensor locations for setup 24: sidespan measurement.

tower (one on each pylon) and the remaining pairs roved in the tower. The details of test procedure can be found in [3].

4.2 Preprocessing of the Data

In this work, only vertical direction data from 26 different setups are processed. The analysis of the experimental data involved initial preprocessing operations of trend removal, low-pass filtering and resampling, considering that the range of frequencies of interest is rather low, of the order of 1 Hz, compared to the original sampling rate of 100 Hz.

4.3 PoSER Approach

Several values for SSI parameters are tried and the following parameters are selected:

- Expected system order: 45
- Model order range: 2, 4, 6, 8, . . . , 100
- References: 4 reference channels

The set of 18 modes that had been extracted from the data in the frequency range of interest [0-1 Hz] is shown in [Figure 6](#). These modes can be characterized as:

- Vertical bending modes 1, 3 and 4 possesses symmetry in all three spans.
- Vertical modes 5, 8 and 11 and torsional mode 10 possesses anti-symmetry in main span and symmetry in long side span.
- Vertical modes 6, 9, 12, 15, 18 and torsional mode 13 have symmetry in main span.
- Vertical mode 2 possesses symmetry with respect to sides spans and anti-symmetry in main span.
- Vertical mode 7 possesses symmetry with respect to main span and long side span.
- Vertical modes 14 and 17 and torsional mode 16 possesses anti-symmetry in main span.

The shapes of the 6th vertical mode is not found perfect due to difficulty in analyzing the very closely spaced mode in the stabilization diagram. The extracted modal parameters are in good agreement with other methods that are reported in [3] except the values of the damping ratios.

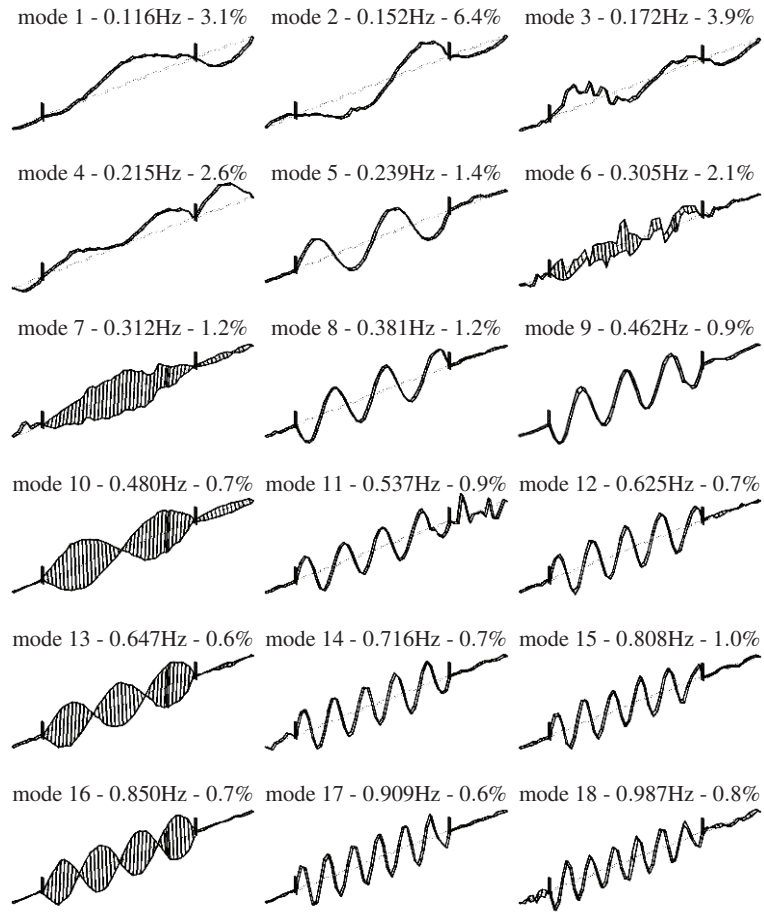


Fig. 6 Modes identified with data-driven SSI from the PoSER approach.

4.4 PreGER Approach

For the PreGER merging approach, all 26 setups were processed together and special care was taken of the presence of the data from the different setups and the resulting partial subspace matrices in memory only when they were needed for the merging procedure described in Section 3.2.2. For the analysis $p + 1 = q = 50$ was selected to build the subspace matrices, and having 4 reference sensors available the maximal model order was 200. The stabilization diagram obtained from the global merged subspace matrix is presented in [Figure 8](#), from where the modes were chosen.

All the identified mode shapes can be seen in [Figure 7](#). They correspond very well to the results of the PoSER approach, as well as the frequencies and damping ratios. However, the very closely spaced modes 6 and 7 are well separated now.

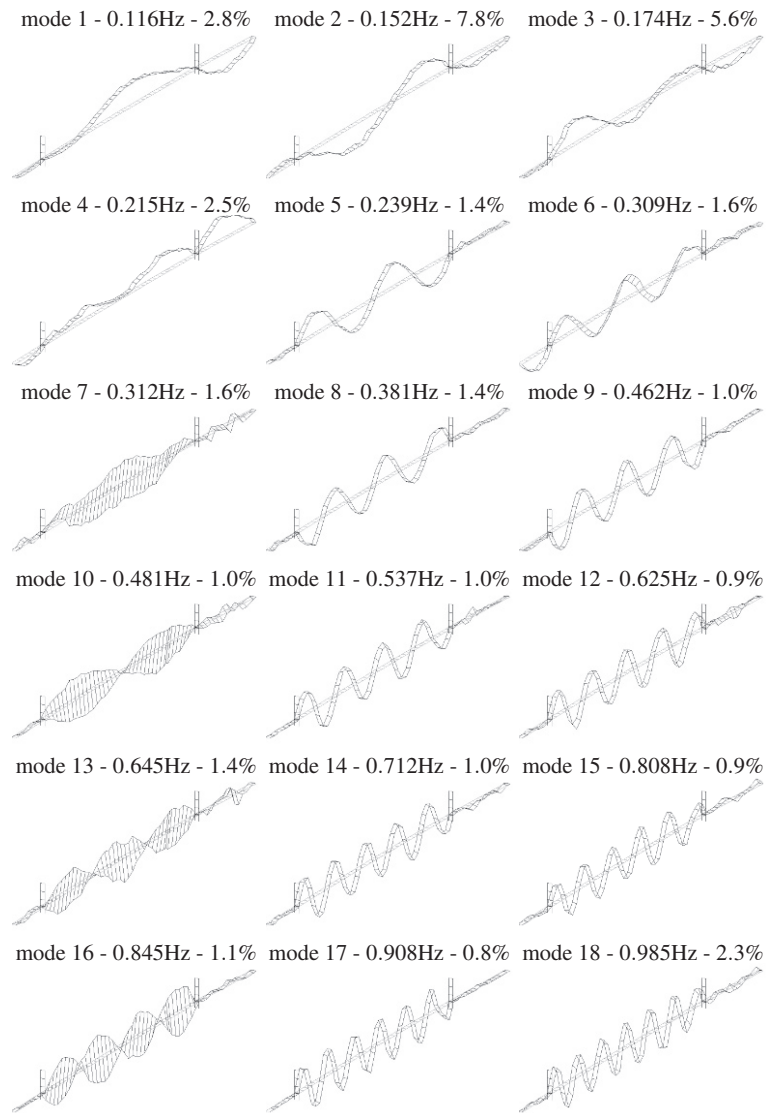


Fig. 7 Modes identified with data-driven SSI from the modular PreGER approach.

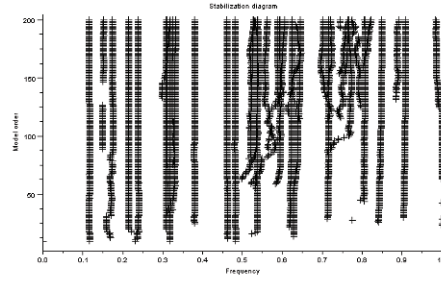


Fig. 8 Stabilization diagram containing the natural frequencies of Humber bridge from the PreGER approach.

5 Summary of Results and Comparison

[Table 1](#) provides a comparative overview of the natural frequencies and damping ratios estimated with the PoSER and PreGER merging approach using the data-driven SSI-cov/ref method. For a comparison of the mode shapes the Modal Assurance Criterion (MAC) of the real parts of the mode shapes between PoSER and PreGER approach is shown in [Figure 9](#). The following observations can be made:

#	PoSER		PreGER	
	f (in Hz)	d (in %)	f (in Hz)	d (in %)
1	0.116	3.1	0.116	2.8
2	0.152	6.4	0.152	7.8
3	0.172	3.9	0.174	5.6
4	0.215	2.6	0.215	2.5
5	0.239	1.4	0.239	1.4
6	0.305	2.1	0.309	1.6
7	0.312	1.2	0.312	1.6
8	0.381	1.2	0.381	1.4
9	0.462	0.9	0.462	1.0
10	0.480	0.7	0.481	1.0
11	0.537	0.9	0.537	1.0
12	0.625	0.7	0.625	0.9
13	0.647	0.6	0.645	1.4
14	0.716	0.7	0.712	1.0
15	0.808	1.0	0.808	0.9
16	0.850	0.7	0.845	1.1
17	0.909	0.6	0.908	0.8
18	0.987	0.8	0.985	2.3

Table 1 An overview of the estimated natural frequencies f and damping ratios d obtained from the different merging strategies using data-driven SSI.

- The differences in natural frequencies for the PoSER and the PreGER approach are less than 1 %.
- For the damping ratios, the differences between PoSER and PreGER estimates are larger but still not significant considering the large standard deviations on the estimates. In general, the PreGER estimates are slightly larger than the PoSER estimate, which might be due to the fact, that the natural frequencies in each setup are slightly different. Then, the resulting frequency for each mode obtained by the PreGER approach is associated to a higher damping ratio, consequence from the merging of overlapping frequencies.
- The MAC values between most of the mode shapes of the different merging approaches are very close to one, meaning that the identified mode shapes are very similar. Only mode shape 6, that could not be identified clearly in the PoSER approach, shows a big difference. Also mode shape 11 shows some difference, due to some noise in the mode shape estimate of the PoSER approach in the side span of the bridge, that is not present in the PreGER approach.

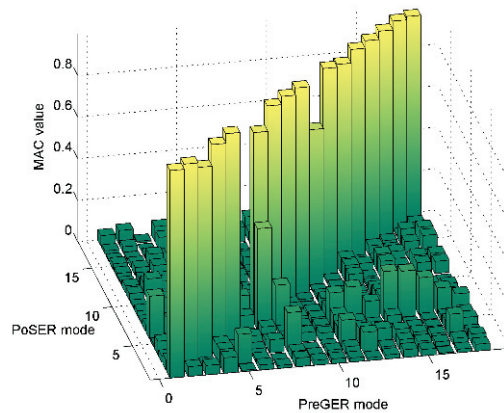


Fig. 9 MAC values between the real parts of the mode shapes obtained by PoSER and PreGER approach.

6 Conclusion

In this work, the PreGER merging approach for Stochastic Subspace Identification was further modified to handle a large number of measurement setups containing moving sensors and a set of fixed reference sensors. It is adapted to be completely modular and hence it has the same memory requirements as the PoSER merging approach.

Both PoSER and PreGER approaches offer comparable qualitative modal identification results on the Humber bridge, whereas the PreGER approach has the advantage of also separating closely spaced modes properly. The modal identification results compare well with previously published results from different identification algorithms in [3], showing also the feasibility of the new PreGER merging approach. In addition, the PreGER merging approach may have the following preferences:

- theoretically sound, taking the difference in the excitation already in the modeling into account;
- just one stabilization diagram has to be analyzed without the need of matching of modes between measurement setups.

Acknowledgments

This work was partially supported by the European project FP7-NMP CP-IP 213968-2 IRIS.

References

1. Basseville, M., Benveniste, A., Goursat, M., Hermans, L., Mevel, L., van der Auweraer, H.: Output-only subspace-based structural identification: from theory to industrial testing practice. *Journal of Dynamic Systems, Measurement, and Control* **123**(4), 668–676 (2001)
2. Brownjohn, J., Dumanoglu, A., Severn, R., Taylor, C.: Ambient vibration measurements of the humber suspension bridge and comparison with calculated characteristics. In: *Proc. of the Institution of Civil Engineers (London)*, vol. 83, pp. 561–600 (1987)
3. Brownjohn, J., Magalhães, F., Caetano, E., Cunha, A.: Ambient vibration re-testing and operational modal analysis of the Humber Bridge. *Engineering Structures* **32**(8), 2003–2018 (2010)
4. Cunha, A., Caetano, E., Delgado, R.: Dynamic tests on large cable-stayed bridge. *Journal of Bridge Engineering* **6**(1), 54–62 (2001)
5. Cunha, A., Caetano, E., Magalhães, F.: Output-only dynamic testing of bridges and special structures. *Structural Concrete* **8**(2), 67–86 (2007)
6. Döhler, M., Andersen, P., Mevel, L.: Data merging for multi-setup operational modal analysis with data-driven SSI. In: *Proceedings of the 28th International Modal Analysis Conference (IMAC-XXVIII)*. Jacksonville, FL, USA (2010)
7. Döhler, M., Mevel, L.: Modular subspace-based system identification and damage detection on large structures. In: *Proceedings of the 34th IABSE Symposium*. Venice, Italy (2010)
8. Döhler, M., Reynders, E., Magalhães, F., Mevel, L., Roeck, G.D., Cunha, A.: Pre- and post-identification merging for multi-setup OMA with covariance-driven SSI. In: *Proceedings of the 28th International Modal Analysis Conference (IMAC-XXVIII)*. Jacksonville, FL, USA (2010)
9. Mevel, L., Basseville, M., Benveniste, A., Goursat, M.: Merging sensor data from multiple measurement setups for nonstationary subspace-based modal analysis. *Journal of Sound and Vibration* **249**(4), 719–741 (2002)
10. Mevel, L., Benveniste, A., Basseville, M., Goursat, M.: Blind subspace-based eigenstructure identification under nonstationary excitation using moving sensors. *IEEE Transactions on Signal Processing* **SP-50**(1), 41–48 (2002)

11. van Overschee, P., De Moor, B.: Subspace Identification for Linear Systems: Theory, Implementation, Applications. Kluwer (1996)
12. Peeters, B., De Roeck, G.: Reference-based stochastic subspace identification for output-only modal analysis. *Mechanical Systems and Signal Processing* **13**(6), 855–878 (1999)

Human-induced Vibration Propagation on a Composite Floor System

*Omer F. Tigli, Research Engineer, McNamara/Salvia Inc. Consulting Engineers,
160 Federal Street, 5th Floor, Boston, MA, 02110, USA*

ABSTRACT

Floor vibration serviceability has recently become one of the main building design criteria especially for structures with long spans of light-weight construction. This paper presents the analytical modeling, in situ vibration tests, modal parameter estimation and response prediction of an office floor where excessive vibrations have been reported on a particular bay. Preliminary analytical studies of the floor system, a steel-light-weight-concrete composite floor system occupied by office cubicles, showed that the problem area was susceptible to foot-fall induced vibrations. Moreover, one of the calculated mode shapes indicated that the source of the annoying vibrations could have been located not only on the bay where they are mostly felt but also on other parts of the floor. In order to investigate the vibration propagation issue and to verify calculated modal parameters and response predictions, a series of vibration tests have been conducted. Walking tests conducted on the problematic bay produced acceleration levels that were above the vibration criterion proposed for office environments. The walking tests conducted on other bays produced non-negligible acceleration levels on the problematic bay, indicating the existence of vibration propagation. However, the magnitude of the propagating vibrations measured on the problem area was found to be at allowable levels. Finally, the floor vibration serviceability has been assessed and compared against measurements following the guidelines given in AISC – Design guide 11 and Arup’s method.

1. Introduction:

Increased strength of new building materials gave rise to the construction of light-weight, long-span, slender structures, which although satisfy ultimate limit state and allowable deflection criteria, are found to be very susceptible to excessive vibrations. As a result, vibration serviceability has become a governing design criterion for many structures with a variety of uses including shopping malls, offices, healthcare facilities, high-tech labs etc.

Assessment of vibration serviceability of a given structure requires clear understanding of three essential components: (1) *Receiver* (Most of the time, humans or sometimes sensitive equipment): What are the tolerable vibration limits? (2) *Source*: (Mostly human activities such as walking, dancing, jumping and in some cases operating mechanical equipments, nearby traffic etc.): What is an accurate representation of the dynamic forces exerted on the structure? (3) *Path* (Physical medium relating the source to the receiver): How does the structure respond to the excitation? [1]

Human perception of vibrations has been researched extensively on a wide variety of applications. The interested reader is referred to the literature for a detailed review [2, 3]. The description and modeling of vibration sources, especially the ones related with human activities drew significant attention from many researchers. The reader is referred to Racic *et al.*, [4] for a recent comprehensive review of the available forcing function models regarding human walking forces, to Racic and Pavic, Ellis and Ji [5, 6] regarding human jumping forces, to Ji and Ellis [7] for dancing type loads. Once a vibration criterion specific to the receiver and a forcing function associated with the vibration source are defined, the last step is to model the path, the structure, and calculate the response at the receiver location.

Historically, most of the vibration problems are reported to be on open-plan composite steel-concrete floor systems with long spans [2, 8, 9]. In fact, this explains why most of the available design guidelines [10, 11] dealing with vibration serviceability are exclusively for this type of floor construction. In most instances, the source of the vibration problem is human walking. Humans tend to walk at a step frequency in the range of 1.6 Hz – 2.2 Hz [10] (1.5 Hz – 2.5 Hz [12]) and they apply a nearly harmonic load at the step frequency and at its multiples (harmonics). The magnitude of the load reduces with the harmonic number and it is usually considered that after the fourth harmonic there is not sufficient energy to excite the floor at a significant level.

The type of floor response to human walking depends on the relationship between the walking frequency and the floor frequencies. For instance, if the step frequency or any of its significant harmonics coincides with one of the floor frequencies,

a resonance type response will be obtained and the associated floor will be classified as a low-frequency floor. On the other hand, if the smallest frequency of the floor system is larger than the fourth harmonic of the step frequency, a transient type response will likely be realized and the corresponding floor is classified as a high-frequency floor [11, 13]. Therefore, there are two different types of analysis that could be performed depending on the relationship between the step frequency and the floor frequencies. For instance, a floor system with a lowest frequency of 5 Hz will be considered a low-frequency floor for step frequencies of 1.25 Hz and larger and a resonance-type analysis is required, while the same floor system will be a high-frequency floor for step frequencies less than 1.25 Hz, hence a transient type analysis will be more appropriate. Even though a step frequency of 1.25 Hz (75 steps per minute) may seem too slow for regular walk along a corridor, it can be considered a reasonable pace for walking within a small room or between branches in a laboratory. In fact, AISC design guide calls walking with 75 steps per minute “moderate walking” for vibration analysis of floors involving sensitive equipment [10].

The primary focus of this paper is a four-story office building where annoying floor vibrations are reported on a particular bay at the third floor (Figure 1). Each floor is framed with composite steel beams, metal deck and light-weight concrete. Preliminary inspection of the building suggested that the source of the vibrations was the human walking at or near the problematic bay.

First, a finite element model (FEM) of the third floor has been constructed using the structural analysis and design software ETABS [14]. The lowest natural frequencies of the problematic bay were calculated as 4.39 Hz and 4.44 Hz which indicated that the floor was a low-frequency floor and a resonance type analysis was required. The mode shapes associated with these frequencies had significant components not only at the problematic bay but also at distant bays of the floor. This suggested that there could be vibration propagation between different parts of the floor.

The floor accelerations at the problematic bay due to walking at the same bay and at adjacent bays were predicted based on two approaches: (1) Design guide - 11 published by American Institute of Steel Construction (AISC) [10], (2) The technique developed by Arup [12], referred to Arup’s method in the paper. Analytical predictions confirmed the excessive vibrations at the problematic bay.

Next, a series of dynamic tests (heel-drop and walking tests) were conducted at and nearby the problematic bay. The modal parameters of the floor were extracted from acceleration measurements taken during heel-drop tests. Since the forcing function was not measured, subspace-identification method for output-only systems was employed for modal parameter estimation [15].

Measurements taken during walking tests indicated that acceleration levels on the problematic bay were above the allowable limits suggested for office environments. The issue of vibration propagation has been investigated by conducting walking tests at locations which were found to be coupled with the problematic bay based on the mode shapes calculated. Measurements taken on the problematic area during these tests verified the existence of vibration propagation. The magnitude of these propagating vibrations was, however, found to be less than allowable limits, which was also in good agreement with the predictions obtained from Arup’s method.

The rest of the paper is as follows: Section 2 gives the description of the floor, explains how the initial finite element model is constructed and presents the response predictions calculated based on the AISC design guide and Arup’s method. Section 3 presents the acceleration data measured and compare to the FEM results. Section 5 concludes the paper with a critical review.

2. Building the Finite Element Model of the Floor

Excessive vibrations were reported within the bay located between the structural grid lines E2-E5 and EA-EC (see Figure 1) on the third level of a four-story office building. Floor framing consists of a composite slab with 6.67 cm (2-5/8”) thick light weight concrete on 7.62 cm (3”) metal deck with beams (W21x44) spanning approximately 13.6 m (44.73 ft), while girders along grid line EA (W21x50) are spanning 6 m (20 ft) and those along grid line EC (W24x76) are spanning 8.1 m (26.7 ft).

The finite element model (FEM) of the floor was constructed using the structural analysis and design software ETABS [14]. The composite floor system was modeled by shell elements with an equivalent thickness and an orthotropic material model incorporating the contribution of the steel deck and light-weight concrete following the procedure proposed by El-Dardiry and Ji [16]. Steel beams and girders were modeled by frame elements which are eccentrically placed with respect to the shell elements [17]. The columns of the floors above and below were also modeled by frame elements and pinned at their far ends [13]. The beam-beam and beam-column connections were assumed to transfer moments regardless of their design intent as suggested by previous researchers [13]. This is due to the fact that even the connections that are designed to transfer only

shear forces provide sufficient capacity to transfer small amount of moments that are generated during floor vibrations. A second consequence of the small magnitude of vibrations is that the dynamic Young’s modulus of concrete is higher than that used for static analysis. In this paper, it is increased by 35% following the recommendations given by AISC design guide [10]. The floor was restrained from moving in the horizontal direction so as to limit the calculated modes to the vertical floor modes only. All the shell and frame members were consistently meshed into smaller size elements in order to capture a more realistic distribution of mass and stiffness of the floor. Since the floor is currently occupied by cubicles and file cabinets, additional masses of 191 N/m² (4 psf) for miscellaneous mechanical and electrical items and 527 N/m² (11 psf) for the furniture were considered following the recommendations of AISC guide [10]. A critical damping ratio of 2 % has been assumed for all of the modes.

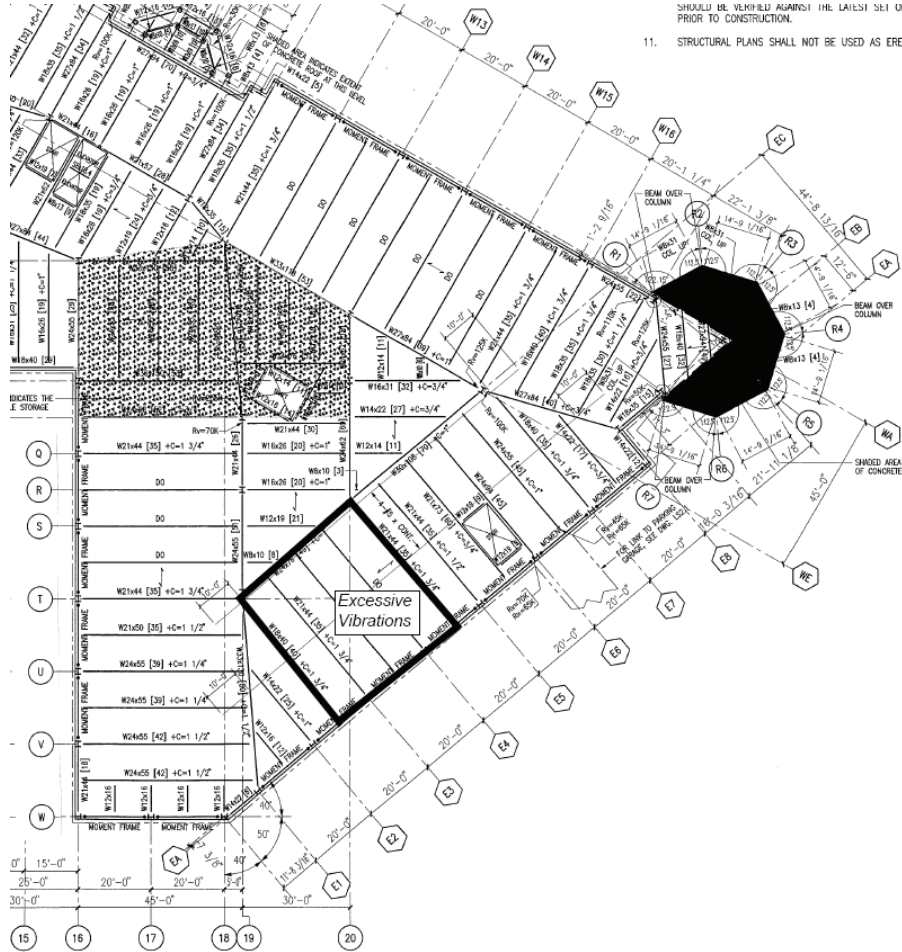


Fig. 1 Plan view of the problematic bay

2.1 Modal Analysis and Results

First eighty modes of the floor, corresponding to a frequency range of 4.14 Hz to 13.14 Hz, were calculated. The natural frequencies of the first four modes and associated mode shapes are presented in Figure 2. The second mode with a frequency of 4.39 Hz is the lowest frequency of the problematic bay and can easily be excited by humans walking at a frequency of 2.2 Hz, which could potentially produce a resonance response since the second harmonic coincides with the floor frequency. In other words, the problematic bay is a “low-frequency” floor and a resonance-type analysis will be required to predict the response of the bay.

It is interesting to note that the second and third modes (4.39 Hz and 4.44 Hz) are closely spaced modes and both will actually be excited by a walking excitation at 2.2 Hz. Even though the mode shapes associated with these modes have their largest modal amplitudes over the problematic bay, there are non-negligible modal amplitudes at other locations of the floor such as between grid lines WE-WA and W13-W16 and less profoundly between grid lines 16 - 19 and O and T (Figures 1

and 2). This suggests that the problematic bay could potentially be excited by humans walking within these two distant bays indicating a probable vibration propagation issue.

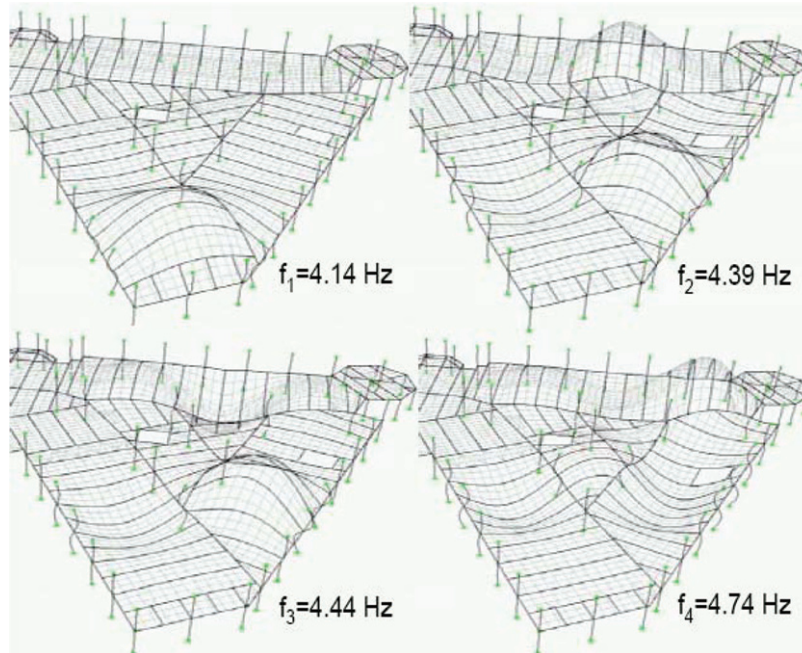


Fig. 2 The first four natural frequencies and corresponding mode shapes

2.2 Prediction of Floor Response to Human Walking Excitation

Assuming an individual generates identical and exactly repeatable footfalls at a constant step frequency, human walking excitation can be modeled as a vertical forcing function, $F(t)$, in the form of a sum of Fourier components [5];

$$F(t) = G + \sum_{m=1}^l G\alpha_m \sin(2\pi m f_s t + \phi_m) \quad (1)$$

where, G is the static weight of the walking person, α_m is the Fourier coefficient for the m^{th} harmonic, l is the number of harmonics contributing to the forcing function, f_s is the step frequency, and ϕ_m is the phase shift of the m^{th} harmonic in radians. The response of the problematic floor was calculated following two methods: (1) AISC Design guide – 11 [10], (2) Arup's method [12]. The Fourier coefficients proposed by these methods are given in Table 1.

Table 1 Fourier coefficients for human walking vertical force models

Reference	Walking Frequency Range (Hz)	Fourier Coefficients			
		α_1	α_2	α_3	α_4
AISC Guide	1.6 - 2.2	0.5	0.2	0.1	0.05
Arup's Method	1.0 - 2.8	$0.41(f_s - 0.95) \leq 0.56$	$0.069 + 0.0112f_s$	$0.033 + 0.0192f_s$	$0.013 + 0.026f_s$

2.2.1 AISC Design guide – 11:

AISC design guide is currently the most widely used vibration analysis reference in United States. The method assumes that the largest accelerations are obtained when the walking frequency or any of its first four harmonics matches one of the floor frequencies, usually the lowest one. The floor is idealized as a single degree of freedom system and the peak acceleration at steady-state is calculated from

$$a_{peak} = \frac{R\alpha_m G}{\zeta M} \quad (2)$$

where, a_{peak} is the peak floor acceleration as a fraction of gravitational acceleration, R is a reduction factor taken as 0.5 for floors and 0.7 for footbridges, G is taken as 0.7 kN (157 lb), ζ is the modal damping ratio and M is the modal mass. The reduction factor in Equation 2 is devised to take into account the fact that the theoretical full resonance response is not achieved. This is because the number of cycles needed to reach to full resonance response is usually more than the number of footfalls that an individual generates when crossing a structure. Moreover, walking excitation is a moving load; hence each footfall will not be applied to the most critical location on the mode shape.

According to AISC guide, the acceptable floor vibration for an office environment is limited to a peak value of 0.5% of g . Moreover, AISC guide provides procedures involving hand calculations to determine the floor frequency and the modal mass. These parameters are directly taken from the FEM of the floor in this study. Table 2 presents all the input parameters and the resulting floor acceleration predicted. A peak acceleration of 2.2 % of g was predicted, which clearly indicates that the structural bay considered does not satisfy the vibration criterion.

Table 2 Calculation of peak response per AISC design guide

G (N) (lbs)	M (kg) (slugs)	ζ (%)	m	α_m	R	a_{peak} (m/s ²) (ft/s ²)	a_{peak} (% of g)
700	16208.0	2	2	0.2	0.5	0.2159	2.20
157	1110.6					0.7068	

2.2.2 Arup's Method:

The method employs a forcing function similar to the one defined in Equation 1. Recommended Fourier coefficients for design, which are associated with a 25% of exceedance, are presented in Table 1. While AISC method is based on a single mode analysis, Arup's method requires the computation of all the modes having frequencies up to 1.5 times the fourth harmonic of the step frequency.

The method first calculates the steady-state acceleration response (a_{mn}) of each mode (n) to each harmonic (m) of the walking forcing function taking into account the location of the excitation and response coordinates;

$$a_{mn} = \mu_{in}\mu_{on} \left(\frac{mf_s}{f_n} \right)^2 \frac{P_m}{M_n} r \left(\frac{1}{1 - \left(\frac{mf_s}{f_n} \right)^2 + 2\zeta \frac{mf_s}{f_n} j} \right) \quad (3)$$

where, μ_{in} and μ_{on} are the modal amplitudes at the excitation and response coordinates of the n^{th} mode, f_n is the natural frequency of the n^{th} mode, $P_m (= \alpha_m G)$ is the m^{th} harmonic force component, M_n is the modal mass of the n^{th} mode, j is equal to $\sqrt{-1}$ and r is a reduction factor incorporated for the same reasons stated previously for the reduction factor of the AISC guide and given by;

$$r = 1 - e^{-2\pi\zeta N} \quad (4)$$

where, N is equal to $0.55mL/l$ and L is the span length of a structural bay an individual crossing and l is the step length of the individual.

The total floor response caused by each harmonic is obtained by summing the contribution of each mode in the complex plane and then taking the absolute value (square root of the sum of squares – SRSS – of the real and imaginary parts) of the resulting complex number. The total floor response caused by all harmonics is calculated by taking SRSS of the responses calculated for each harmonic [12].

Arup's method was used to calculate the response at the center of the problematic bay assuming an individual ($G=0.7\text{ kN}$) is walking at a frequency of 2.2 Hz following the path $W1$ shown in Figure 3. Both response and excitation points are assumed to be located in the center of the bay. A total of 80 modes, each having a damping ratio of 2% of the critical, have been considered in the computations. Taking the span length as 13.72 m (45 ft) and stride length 0.91 m (3 ft), the method yielded an acceleration level of 0.74 % of g which is almost one third of what AISC guide estimated, yet larger than allowable maximum acceleration of 0.5% of g recommended for office environments.

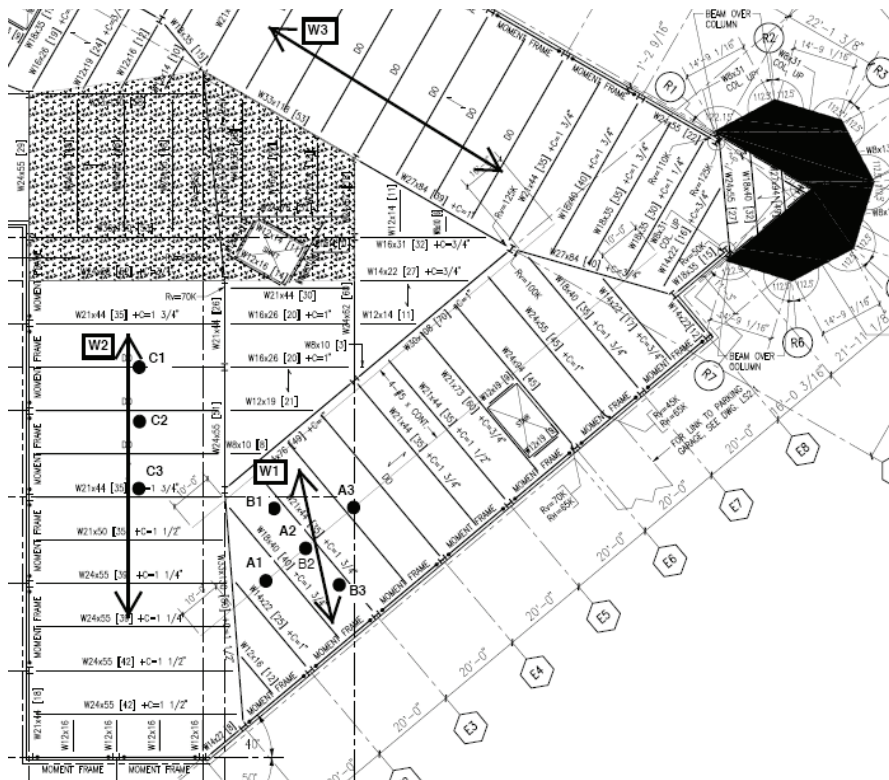


Fig. 3 Locations of walking paths and accelerometers

Then, the issue of vibration propagation between different parts of the floor was investigated using the Arup's method. The same computations carried out previously were repeated except the location of the excitation was moved first to the center of the walking path $W2$ and then to the center of the path $W3$ (Figure 3). Taking $L=13.72\text{ m}$ (45 ft) and $l=0.91\text{ m}$ (3 ft), peak accelerations of 0.27 % of g and 0.18 % of g were calculated respectively at the center of the problematic bay. Even though the calculated accelerations are less than the allowable limits, they are not at a trivial level, which indicate the presence of a vibration propagation phenomenon.

It is interesting to note that the modal amplitudes of the two closely spaced modes along the walking path $W3$ reverse their sign with respect to the modal amplitudes at the problematic bay (see Figure 2); hence the contribution of each mode to the response at the problematic bay cancel each other to a certain extent. Along the path $W2$, however, both mode shapes carry the same sign. This is why the response at the problematic bay is larger when a walking excitation is applied along $W2$ than it is applied along $W3$, even though the modal amplitudes are larger in magnitude over the path $W3$.

3. Vibration Measurements

Dynamic tests in the form of heel-drop tests and walking tests were conducted in order to verify the modal parameters and the floor responses calculated in the previously. The vertical floor response was measured with three PCB Piezotronics

Model 393B05 accelerometers with 10 V/g sensitivity. Digital data acquisition was performed using a National Instrument USB-9234 DAQ card, which has four 24-bit input channels.

The three accelerometers were set up at three different configurations, two of which being located in the problematic bay (A and B in Figure 3) while the last configuration (C in Figure 3) in an adjacent bay which is found to be coupled with the problematic bay through the second and third mode shapes calculated from FEM.

3.1 Impact Tests

A series of heel-drop tests were performed by a 185-lb male at the center of the problematic bay for configurations A and B and near the accelerometer labeled C2 (Figure 3) for configuration C. The response of the floor at each measurement location was simultaneously recorded at a sampling frequency of 1652 Hz. Since the floor frequencies of interest, those that can be excited by human walking, are relatively at low frequencies, the measured data was first low-pass filtered with a cut off frequency of 103.25 Hz and then down-sampled to a sampling frequency of 206.5 Hz.

Given that the forcing function associated with heel-drops was not measured, the modal parameters were estimated using output-only subspace identification technique [15]. Identified natural frequencies, damping ratios and the mode shapes normalized with respect to largest amplitude are shown in Table 3. It should be noted that these values represent average values of multiple modal identification results performed on each heel-drop test measurements.

Note that the first natural frequency of the problematic bay was identified as 4.33 Hz which is in good agreement with the calculated frequency of 4.39 Hz. Besides, the calculated and measured mode shapes look very similar (Figure 2 and Table 3). The second mode identified in the problematic area is at 5.15 Hz from configuration A and at 6 Hz from configuration B. The reason why the modes at 5.15 Hz and 6 Hz could not be identified from configurations B and A respectively could be attributed to an observability problem. For instance, the mode shape associated with the 5.15 Hz mode has its smallest amplitude at the accelerometer labeled A2, which is on the same line of accelerometers employed in configuration B. Similarly, the mode shape corresponding to 6.0 Hz mode has its smallest amplitude at the accelerometer labeled B2 which is located on the same line of accelerometers employed in configuration A.

As opposed to the FEM, no other modes were identified in the vicinity of 4.33 Hz. The question of whether the two closely spaced modes exist in the problematic area or not is still unanswered. Further experimental work involving forced vibration tests is needed to clarify the issue.

It appears that the damping ratios identified are higher than what is usually recommended for open floor plans (2 – 3 % [10]) or measured values published in the literature [2]. Therefore, the heel-drop test measurements taken at accelerometers labeled A2 and B2 were band-pass filtered between 4.0 Hz to 4.5 Hz and the logarithmic decrement method [18] was used to estimate the damping. It was found that the damping ratio of the first mode identified in the problem area was only about 2% – 2.5%, as opposed to 6% identified from subspace-identification method [15].

Table 3 Measured modal parameters at configurations A, B and C

CONFIG. A	Mode Number	f_n (Hz)	ζ (%)	Mode Shape			
				A1	A2	A3	
	1	4.33	6.0	0.55	1.00	0.80	
	2	5.15	3.5	1.00	0.64	-0.64	
CONFIG. B	Mode Number	f_n (Hz)	ζ (%)	Mode Shape			
				B1	B2	B3	
	1	4.33	6.0	0.80	1.00	0.68	
	2	6.00	6.0	1.00	0.57	0.57	
CONFIG. C	Mode Number	f_n (Hz)	ζ (%)	Mode Shape			
				C1	C2	C3	
		1	3.90	6.5	0.35	1.00	0.70
		2	4.50	4.0	0.90	1.00	-0.45
	3	5.85	5.0	1.00	-0.70	0.60	

3.2 Walking Tests

A 185-lb male was asked to walk along the paths W1 and W2 for configuration A, along the path W1 for configuration B and along the path W2 for configuration C (see [Figure 3](#)) at a predetermined frequency which is controlled by a hand-held metronome. Walking frequencies were selected such that their second harmonic coincided with the floor frequencies measured during impact tests. Specifically, along the path W1 walking frequencies of 2.1 Hz, 2.2 Hz and 2.3 Hz and along the path W2 walking frequencies of 1.87 Hz, 1.93 Hz, 2.0 Hz and 2.3 Hz were chosen.

Measurements taken during each walking test were band-pass filtered from 1 Hz to 20 Hz. Peak accelerations recorded at each measurement location are presented in [Tables 4](#) and [5](#) together with the associated walking paths and frequencies. It can be concluded that the acceleration limit (0.5% of g) was exceeded in the center of the problem area at all the walking frequencies considered. The largest acceleration (0.76% of g) was measured at the center of the bay at a walking frequency of 2.3 Hz.

When the acceleration measurements are compared against the analytical predictions, it becomes clear that AISC design guide overestimated the response by almost three times. On the other hand, the estimates obtained from Arup's method (0.74% of g) are in perfect agreement with the measurements. Moreover, Arup's method successfully predicts the acceleration levels that are propagated to the problematic area from the walking path W2: a calculated value of 0.27% of g versus the measured value of 0.26% of g .

[Table 5](#) present the peak acceleration measured along the path W2 when a series of walking tests are conducted along the path W2. The acceleration levels are found to be barely above the limits, explaining why there were no reported complaints about the floor vibrations at that part of the floor.

Table 4 Peak accelerations in % of g measured on the problem area during walking tests

Walking Path	Measurement Loc.	Walking Frequencies		
		2.1 Hz	2.2 Hz	2.3 Hz
W1	A1	0.42	0.50	0.71
	A2	0.56	0.63	0.76
	A3	0.44	0.44	0.51
W1	B1	0.35	0.60	0.43
	B2	0.46	0.58	0.46
	B3	0.34	0.64	0.48
W2	A1	0.17	0.26	0.19
	A2	0.18	0.20	0.16
	A3	0.19	0.15	0.16

Table 5 Peak accelerations in % of g measured during walking tests

Walking Path	Measurement Loc.	Walking Frequencies		
		1.93 Hz	2.0 Hz	2.3 Hz
W2	C1	0.40	0.37	0.51
	C2	0.45	0.35	0.51
	C3	0.35	0.33	0.46

The response of the problematic bay measured by accelerometer A2 due to walking at 2.2 Hz along the path W1 is presented in [Figure 4a](#) while the magnitude spectrum of the same data is shown in [Figure 4b](#). It is clear that the second harmonic of the walking frequency is very close to the floor frequency which is the main reason why the response increases at every other peak in the time history. Similarly, the frequency domain data shows significant components around the second harmonic (4.4 Hz) of the walking frequency.

4. Conclusions

Analytical and experimental studies were carried out to assess the vibration serviceability of an open plan office floor located on the third level of a four-story building. First, a finite element model of the floor was constructed and the modal parameters

were calculated. Then, the floor response to human walking excitation was predicted following the procedures given by AISC design guide and Arup's method. Analytical predictions showed that the acceleration levels at the problematic bay were above the vibration criterion suggested for office environments. Moreover, calculated mode shapes associated with floor frequencies in the range of the second harmonic of walking frequency indicated that the problem area was coupled with other parts of the floor. In other words, human walking at these distant locations could excite the floor and generate waves that could potentially excite the problem area. Analytical predictions indicated the presence of vibration propagation but estimated acceleration levels were found to be less than the office vibration criteria.

In order to verify calculated modal parameters and predictions mentioned above, a series of in-situ dynamic tests were conducted. Measurements verified that the acceleration level at the problem area was above the criterion suggested for office environments. In this regard, the procedure given by AISC design guide overestimated the response by almost three times, while the predictions based on Arup's method were found to be very close to measurements. In-situ walking tests verified the existence of vibration propagation issue; however, the measured response levels were within the criterion. Even though two closely spaced modes were calculated from finite element model, this could not be verified by the measurements taken. Further tests involving forced vibrations need to be conducted to conclude whether closely spaced modes exist or not. The damping estimates obtained from subspace identification technique using the measured data taken during hell-drop tests were found to be overestimated. Instead, a more basic approach such as peak picking yielded more realistic damping estimates.

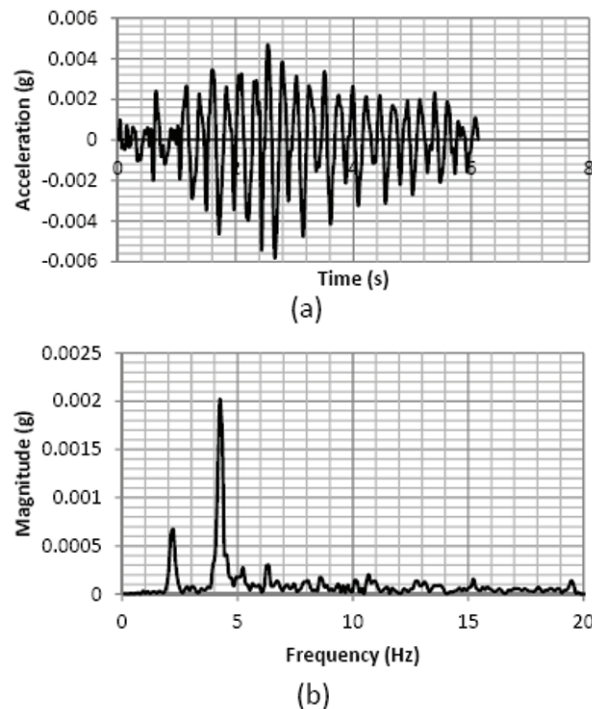


Fig. 4 Measured response by the accelerometer A2 due to walking along W1 at 2.2 Hz

ACKNOWLEDGMENTS

Mr. Mark Aho, principal at McNamara/Salvia Inc, and Mr. Jeremiah O'Neill, project engineer at McNamara/Salvia Inc, are gratefully acknowledged for their assistance during the dynamic tests conducted. Special thanks go to Mrs. Gulhan Tigli for her continuous support throughout the preparation of the paper.

REFERENCES

- [1] ISO, Bases for Design of Structures—Serviceability of Buildings Against Vibrations, ISO 10137, International Standardization Organization, Geneva, Switzerland, 1992.
- [2] Hicks, S., Vibration characteristics of steel-concrete composite floor systems, *Progress in Structural Engineering and Materials, Composite Construction*, Vol.6, Issue 1, pp. 21-38, 2004
- [3] Parsons K.C., Griffin M.J., Whole-body vibration perception thresholds, *Journal of Sound and Vibration*, 121(2), pp. 237-258, 1988

- [4] Racic V., Pavic A., Brownjohn J.M.W., Experimental identification and analytical modeling of human walking forces: Literature review, *Journal of Sound and Vibration*, Vol. 326, Issues 1-2, pp. 1-49, 2009
- [5] Racic V., Pavic A., Mathematical model to generate asymmetric pulses due to human jumping, *Journal of Engineering Mechanics*, Vol. 135, No. 10, pp.1206-1211, 2009
- [6] Ellis B.R., Ji T., Loads generated by jumping crowds: numerical modeling, *The Structural Engineer*, pp. 35-40, September 7th, 2004
- [7] Ji T., Ellis B. R., Floor vibration induced by dance type loads: theory, *The Structural Engineer*, Vol. 72, No. 3, pp.37–44, 1994
- [8] Pavic A., Miskovic Z., Reynolds P., Modal testing and finite element model updating of a lively open-plan composite building floor, *ASCE Journal of Structural Engineering*, Vol. 133, No.4, pp.550-558, 2007
- [9] Hanagan L.M., Walking-induced floor vibration case studies, *Journal of Architectural Engineering*, Vol. 11, Issue 1, pp.14-18, 2005
- [10] Murray M.M, Allen D.E., Ungar E.E., *Floor Vibrations due to Human Activity AISC-Steel Design Guide Series – 11*, AISC, Second Printing, October 2003 (First Printing, 1997)
- [11] Wyatt T.A., *Design guide on the vibration of floors*, SCI Publication 076 : Ascot: Steel Construction Institute, 1989.
- [12] Willford M., Young P. and Field C., *Improved methodologies for the prediction of footfall induced vibration*. Omaha, Nebraska, 2006,
- [13] Middleton C.J., Brownjohn J.M.W, Response of high frequency floors: A literature review, *Engineering Structures*, 32, pp. 337-352, 2010
- [14] ETABS, *Extended three dimensional analysis of building systems*, Nonlinear version 9.7.1, Computers and Structures, Inc. Berkeley, CA
- [15] Van Overschee P, De Moor B. Subspace algorithm for the stochastic identification problem, *Automatica*, 29(3), pp. 649–60, 1993.
- [16] El-Dardiry E., Ji T., Modeling of the dynamic behavior of profiled composite floors, *Engineering Structures*, 28, pp. 567-579, 2006
- [17] El-Dardiry E., Ji T., The effect of eccentricity on the free vibration of composite floors, *Computers and Structures*, 85, Issue 21-22, pp. 1647-1660, 2007
- [18] Chopra A.K., *Dynamics of Structures: theory and applications to earthquake engineering*, Prentice Hall, 2nd Edition, 2001

Mitigation of Low-velocity, Wind-induced Vibration of an Architectural Spire

*Omer F. Tigli, Research Engineer, McNamara/Salvia Inc. Consulting Engineers,
160 Federal Street, 5th Floor, Boston, MA, 02110, USA*

*Luca Caracoglia, Assistant Professor, Department of Civil and Environmental Engineering,
Northeastern University, 360 Huntington Avenue, Boston, MA 02115, USA*

ABSTRACT

This paper presents the results of analytical and experimental studies conducted on an architectural spire, which experienced wind-induced vibrations shortly after its construction. The circular spire is attached to the corner of a 30-story building along the upper ten stories then cantilevers up for 21.44 m (70.33 ft) with a pipe cross-section of 0.508 m (20 in)-diameter for the first 3.86 m (12.67 ft) and 0.406 m (16 in)-diameter for the last 17.58 m (57.67 ft). Experimental studies showed that the spire's first natural frequency was 0.88Hz with a damping ratio of 0.1 – 0.2 % of the critical value. Average wind speed during vibrations, recorded on ground within 8 km (5 miles) of the site was 1.79 m/s (4.0 mph). Vortex-shedding was indicated as the preliminary cause, since the projected wind velocity at the spire elevation was low and compatible with the Strouhal relationship based on the 0.406 m (16 in)-diameter region of the spire, which yielded a vortex-shedding frequency of 0.88Hz ($=0.2 \cdot 1.79 / 0.406$). Due to time limitations, only two mitigation techniques were considered. First, a chain damper was installed inside the pipe, which increased the damping ratio to at least 2.0%. Finally, the mass of the spire was increased by sand-infilling, which reduced the first-mode frequency to 0.69Hz and the wind speed to 1.39 m/s (3.1 mph) for possible "lock-in"; most importantly, an increment in the Scruton number was calculated. Hence, the susceptibility to vortex-shedding decreased.

1. Introduction

Estimation of wind-induced dynamic response of structures has become an essential step in structural analysis and design over the last few decades. Given the complexity of the problem, the analyses usually involve a joint application of theoretical formulations, mathematical modeling, wind tunnel tests and code provisions.

From a structural engineering perspective, the complexity of the problem is also directly related to the type of structures. For instance, while the wind-resistant design of a conventional building structure can be easily achieved by following the guidelines provided by codes, the design of very tall buildings, bridges or very slender structures usually require a wind-tunnel test combined with advanced numerical modeling and dynamic simulations.

Vortex shedding is one of the complex wind-induced phenomena, which often controls the design of very slender structures such as light poles, chimneys, stacks, telecommunication antennas, spires and very tall buildings [1-4]. Vortex shedding can be experienced by slender structures characterized by a cylindrical cross section, similar to the spire under investigation. Alternating low pressure zones are generated on the downwind side of the cross section. As a result of the alternating pressure distribution on the external surface, a periodic excitation is induced in the direction orthogonal to the flow. The frequency of the generation of vortices, responsible for the across-wind loading, is the vortex-shedding frequency (f_v) and it can be calculated by $f_v = (SV)/D$ where S is the Strouhal number (a constant parameter usually independent of wind velocity but a function of the shape of the body), V is the wind velocity and D is the structure diameter in consistent units [5].

When the frequency of the vortex shedding gets closer to one of the frequencies of the structure, the structure will "lock-in", and the frequency of the shedding will tune to the natural frequency of the structure. Lock-in is an aeroelastic phenomenon, in which the vortex shedding forces "tune" to the motion of the structure and is accompanied by a drastic increment in the span-wise correlation of the loading (measured along the longitudinal axis of the structure), usually extremely limited when f_v does not coincide with the natural frequency of the structure. This correlated loading may lead to non-negligible vibration amplitudes, which can be exacerbated by low structural damping of the structure. If the structural damping level is too low,

the aeroelastic response controls and the associated stress levels could potentially lead to fatigue-related failure after a large number of stress cycles.

Although vortex shedding can lock-in and continue as the velocity increases or decreases slightly, it is generally accepted that if the wind velocity is non-stationary with relative variations more than 20 percent with respect to the value causing lock-in, the vibration will likely stop. Vortex-shedding-induced vibration tends to occur with low-turbulence steady winds conditions. If the wind velocity is greater than 15 to 20 m/s (above 35 mph), turbulence usually interferes with the flow by promoting a more irregular detachment of vortices with a reduction in the span-wise correlation of the loading, even during at lock-in; this usually reduces the susceptibility to large-amplitude vibration [5].

This paper presents the analytical and experimental analyses conducted to mitigate an existing architectural spire experienced large-amplitude wind-induced vibrations. The circular spire is attached to the corner of a 30-story building along the upper ten stories then cantilevers up for 21.44 m (70.33 ft) with a pipe cross-section of 0.508 m (20 in)-diameter for the first 3.86 m (12.67 ft) and 0.406 m (16 in)-diameter for the last 17.58 m (57.67 ft). (see [Figure 1](#)) Shortly after its construction, it was reported on a wind-wise quiet day that the spire started to oscillate apparently in its first sway mode with a top horizontal deflection of around 30.5 cm (12 in) in the plane parallel to the axis of the connection of the spire to the building. By counting the number of cycles, it was determined that the spire was oscillating with a frequency of approximately 0.9 Hz. Due to concerns about a possible fatigue failure, the spire was tied back from its mid height down to the roof of the main structure through a rope, which effectively stopped the oscillations.

The vibrations occurred at a time when the construction of the base building was near completion, which put a challenging time constraint for the mitigation of the spire, because the only access to the spire was through the tower crane which was scheduled to be taken down within few weeks.

Considering the fact that vortex-induced vibrations are actually the resonance response of the spire, the most effective mitigation could be achieved by increasing the available damping which is estimated to be around 0.1 – 0.2%. Therefore, first a chain damper was designed and installed [6,7]. Based on free decay acceleration measurements taken at the top of the spire, it was determined that the damping of the spire had been increased to at least 2%. However, the chain damper option was rejected due to the noise generated when the chain hit inside the steel pipe.

As an alternative to the chain damper, increasing the mass of the spire was preferred for three reasons: (1) Increasing the mass is known to increase the Scruton number [5]. (2) When the mass is increased, the natural frequency goes down, which reduces the critical wind velocity at which lock-in may occur. The smaller the wind velocity, the smaller the magnitude of the aeroelastic force at lock-in. For vertical masts, critical velocities less than 1 to 2 m/s are usually too low to induce large-amplitude vibrations [4]. (3) Statistically, the possibility of having a wind velocity lower than 1.79 m/s (4 mph) at the given site was very rare based on available historical wind data. Therefore, three quarters of the 16" diameter portion of the spire was filled with sand. Experimental observations as well as analytical predictions showed that the natural frequency of the spire decreased to 0.69 Hz. The critical wind velocity associated with lock-in for that frequency is about 1.39 m/s (3.1 mph).

The rest of the paper is organized as follows: Section 2 describes the experimental and analytical studies conducted to determine the dynamical characteristics of the spire. Section 3 presents mitigation techniques considered and associated experimental and analytical test results. Section 4 provides the conclusions.

2. Dynamical Properties of the Spire:

2.1 Analytical Work

A three-dimensional finite element model (FEM) of the spire including its connection to the main building was constructed in SAP2000 [8]. Calculated natural frequencies and mode shapes of the first four modes are given in [Figure 2](#). A cursory comparison of the calculated mode shapes and the deflected shape of the oscillating spire during the low-velocity wind-induced vibration revealed that it was the second natural frequency (0.93 Hz) of the finite element model that coincided with the vortex-shedding frequency (0.88 Hz), which resulted in large-amplitude vibrations.

The discrepancy between the calculated and measured frequencies can be attributed to the assumptions made during the process of building the finite element model. Some of these include but not limited to the fact that only a small portion of the base building has been modeled, each floor of the base building is restrained laterally in the horizontal plane, members with welded connections are modeled as rigid, while bolted beam-to-beam connections are modeled as pinned, material properties

of steel and concrete used in the model are approximate. Although the finite element model could have been updated by adjusting sensitive modeling parameters with the objective of bringing calculated frequency closer to the measured frequency, the current model was considered sufficiently accurate for the purposes of this study.

2.2 Experimental Studies

The natural frequency of the spire was estimated to be around 0.90 Hz during the vibrations; however the damping ratio was not determined. In order to verify the natural frequency and to estimate the inherent damping, free-decay tests were conducted. A target with marks ranging from -30.5 cm (-12 in) to +30.5 cm (+12 in) was installed at the top of the spire such that zero reading coincided with the centroid of the spire. The top deflection of the spire was monitored by surveyors using a total station located on the ground. A video camera was also set up next to the total station to record the motion of the spire.

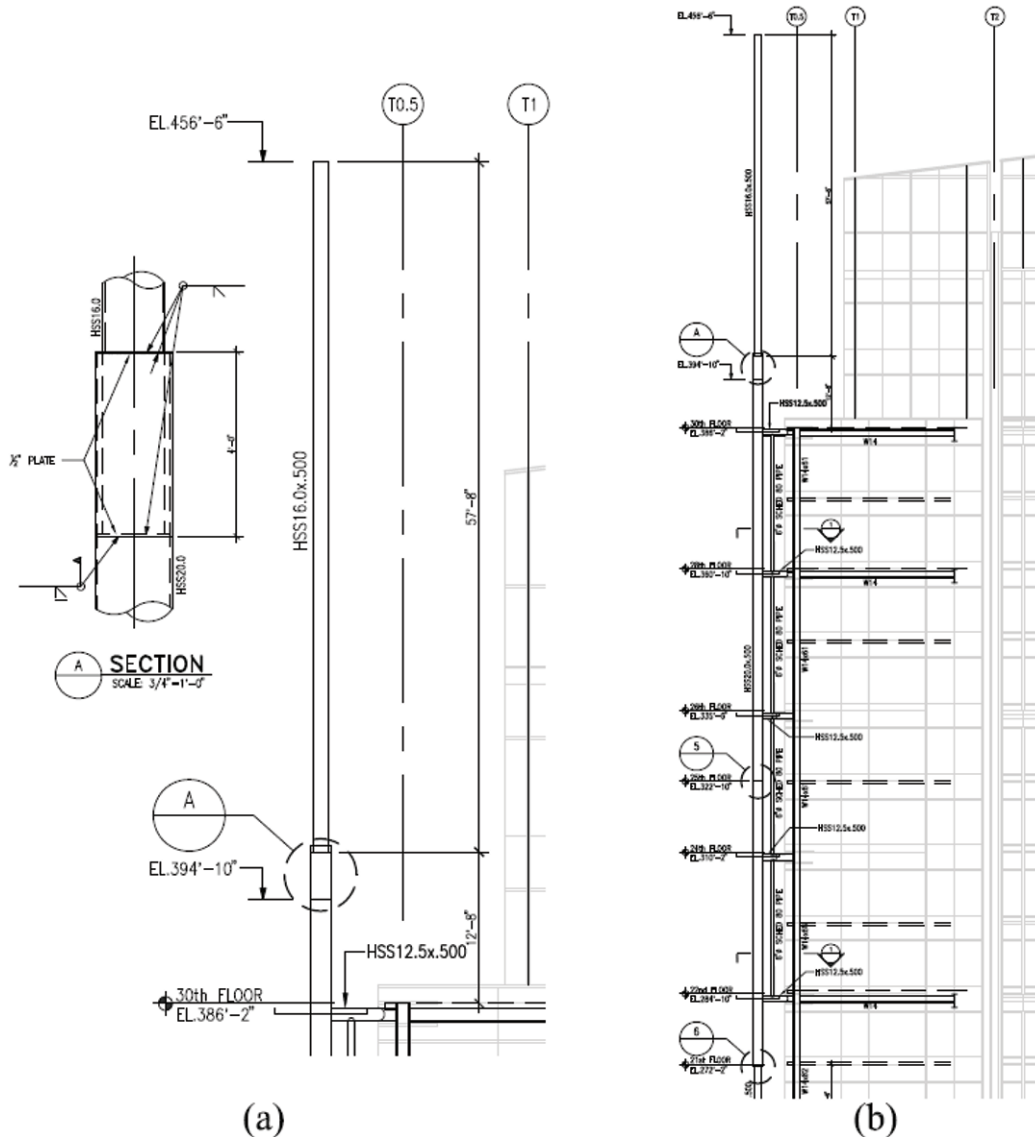


Fig. 1 (a) Elevation view of the top 21.44 m (70.33 ft) of the spire with the transition section detail from 0.508 m (20 in)-diameter to the 0.406 m (16 in)-diameter pipe, (b) Elevation view of the spire at full length

The top of the spire was pulled and released at a frequency of 0.9 Hz manually by pulling the spire at an elevation corresponding to the penthouse level of the base building in the direction parallel to the connection of the spire to the building. The spire was released as soon as the top deflection reached to 30.5 cm (12 in) and then left to oscillate freely until the movements practically stopped. This procedure was repeated two times. Analysis of the recorded motion of the spire

revealed that the natural frequency of the spire was 0.88 Hz. Following the logarithmic decrement method, the inherent damping of the spire is calculated from [9];

$$\zeta = \frac{1}{2\pi j} \ln \left(\frac{u_i}{u_{i+j}} \right) \quad (1)$$

where ζ is the critical damping ratio, u_i is the displacement at the i^{th} peak of the free decay data and j is the number of cycles between the i^{th} and $(i+j)^{\text{th}}$ peaks. The top displacement and the corresponding time elapsed during the free decay of the spire, are presented in Table 1 together with the damping estimates based on Equation 1. Given the approximate nature of the data collection, it can be concluded that the inherent damping of the spire is in the range of 0.1 % to 0.2 %. Moreover, it appears that the damping of the spire is directly related to the amplitude of vibrations.

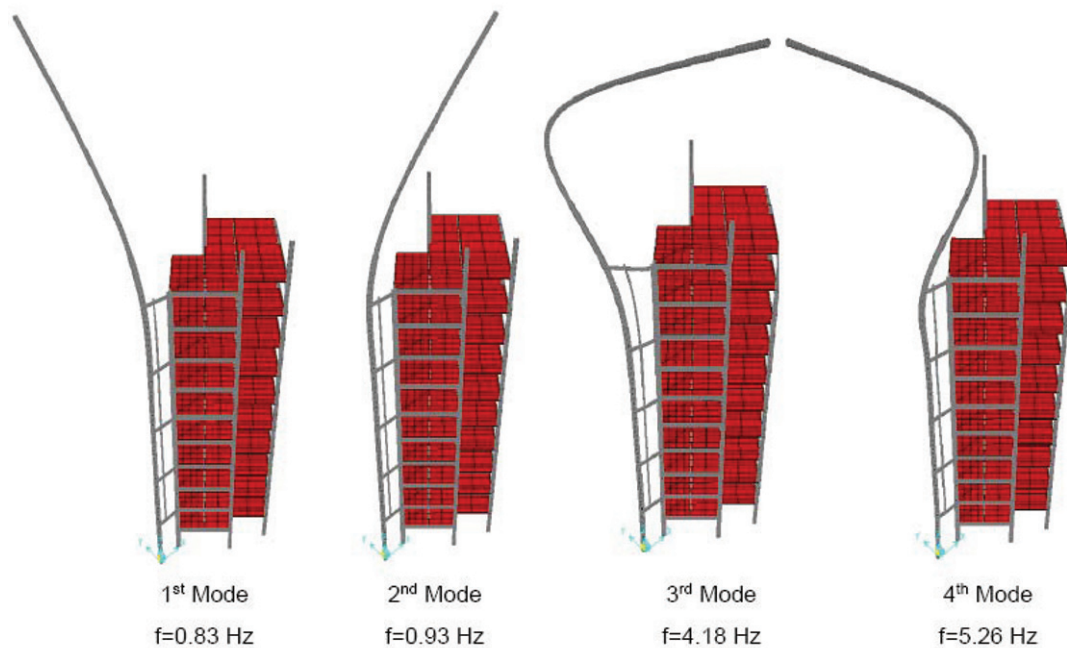


Fig. 2 Calculated first four modes of the spire

Table 1 Free decay data of the spire and estimated damping ratios

Test # 1			Test # 2		
Time Elapsed sec	Top Deflection cm (in)	Estimated Damping Ratio (%)	Time Elapsed sec	Top Deflection cm (in)	Estimated Damping Ratio (%)
0.0	30.48 (12)	-	0.0	30.48 (12)	-
56.0	15.24 (6)	0.22	65.7	15.24 (6)	0.19
119.0	10.16 (4)	0.12	123.4	10.16 (4)	0.13
181.3	7.62 (3)	0.08	181.1	7.62 (3)	0.09

3. Mitigation of Wind-Induced Vibrations

Several measures can be taken to suppress excessive vortex shedding induced vibrations. These include

- Strengthening and/or increasing the stiffness
- Increasing the mass
- Increasing the structural damping

- Changing the aerodynamic characteristics of the cross section (helical strakes, aerodynamic appendages, etc..)

Among these alternatives, the most effective solution is to increase the damping given the fact that resonance response is governed by the available damping in the system. One way to achieve this is to add supplemental damping elements such as tuned mass dampers, impact dampers etc [1,6,7].

Given the time constraints a hanging-chain impact damper was initially selected as a supplemental damping element. Design of the damper, installation and the measured response of the spire with the damper are discussed in detail in Section 3.1. Even though the chain damper worked satisfactorily, the noise it generates rendered this option prohibitive.

As an alternative to the chain damper, increasing the mass of the spire was considered. The configuration of the spire allowed in-filling the 16-inch-diameter portion of the spire with sand from the top. This is due to the fact that the transition section from 20" diameter pipe to 16" diameter pipe involves a 0.5 in thick cap plate at the end of the 20" diameter pipe (see [Figure 1a](#)). The details of this strategy are given in section 3.2.

3.1 Hanging-Chain Damper

A hanging-chain damper as a supplemental damping element is most suitable for tall flexible structures. Reed provided the theory as well as the experimental verification of the use of chain dampers to suppress the vibration of very slender tower-like structures [10]. Koss and Melbourne elaborated the operational design of chain dampers and provided the four case histories [7]. As the name implies, a hanging-chain damper is a chain hung from top of a tower like structure. When the structure to which the chain damper is attached starts to move, the chain begins its motion in the opposite direction. If the tip deflection of the chain gets sufficiently large, the first impact occurs. While the number of impacts per cycle is an important parameter to determine the level of damping added, the optimum performance is attained when two impacts per cycle is realized. Most of the energy dissipation occurs during the impacts while a negligible contribution is usually offered by friction between the chain links. It is worth noting that chain dampers work only if the structural vibration is dominated by motion in one (vertical) plane (e.g., across wind). In contrast, a "whirling" motion of the chain is experienced for three-dimensional vibration and no impact is realized [7]. Finally, chain dampers are not effective at very low amplitude of vibrations [11].

3.1.1 Design of the Chain Damper

Essential parameters used in the design of a hanging-chain damper are (see [Figure 3](#)): the effective damping coefficient (c_e), the length of the chain (l), the mass per unit length of the chain (m), the frequency of forced vibration (ω), clearance between the chain and the structure/enclosing container (d), the steady state amplitude of forced vibration (x_0), the natural frequency of the chain ($\omega_1=1.2(g/l)^{0.5}$) where g is the gravitational acceleration in consistent units.

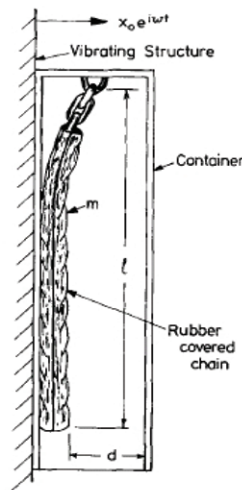


Fig. 3 Hanging-chain damper configuration [10, 7]

These variables are converted into three non-dimensional parameters: the damping ratio ($c_e/lm\omega$), the frequency ratio (ω/ω_1) and the gap ratio (d/x_0). The frequency ratio determines the impact mechanism and regime: no impact, partial impact or full impact. While low values of the frequency ratio results in no impact, with increasing frequency ratio, one enters into the

partial impact region first, then the full impact region. Beyond a critical frequency ratio, another no impact region starts. The gap ratio determines the boundaries of these three distinct behaviors. Optimum damping for a given gap ratio is given by

$$\left(\frac{c_e}{lm\omega}\right)_{opt} = 4\pi^{-2} \frac{d}{x_0} \tag{2}$$

which occurs near the critical frequency ratio. Figure 4 presents experimentally obtained critical gap ratio versus the critical frequency ratio as well as the distinct regions of impact and no impact cases. Impact regions are further divided into subgroups as two and more than two impacts per cycle. The design objective is to have two impacts per cycle and optimum damping ratio [7]. Design parameters for the spire are given in Table 2. The natural frequency of the spire is obtained from observations as explained previously, while the effective mass is taken from the finite element model.

The chain design partly depends on the available chain sizes on the market as well as the size of the container. Since the inner diameter of the spire was only 38.1 cm (15 in), the spire, itself, has been considered to be the container for the chain damper. Following Figure 4, a chain with 9.17 cm (3.61 in) width was selected; this gave a gap ratio of 6 as shown in Table 2. Then, the length of the chain was designed to be 3.35 m (11 ft) which has a natural frequency of 0.33 Hz and a mass per unit length of 13.4 kg/m (0.00028 k-s²/ft). Next, a target damping ratio of 3% was selected. The maximum displacement at the optimum damping was calculated by Equation 2 as 4.83 cm (1.9 in). In the theoretical development, the maximum displacement is defined as the displacement of the mount structure which is considered to be rigid throughout the length of the chain, which is not exactly true for the spire. In fact, based on the calculated mode shape of the spire, the ratio of the modal amplitudes at the location 3.05 m (10 ft) below the top of the spire to that at the top of the spire is 0.8, pointing out the fact that the top deflection of the spire at optimum damping could be around 6 cm (2-3/8 in).

Table 2 Chain damper design parameters for the spire and the chain

Spire	Height	Diameter	Natural Frequency	Modal mass	Max. Displ.	Target Damping Ratio (%)	c_e	ω/ω_1	$c_e/(l^*m^*\omega)$
	m (ft)	m (in)	(Hz)	kg (k-s ² /ft)	cm (in)				
	21.44 (70.33)	0.406 (16)	0.88	1852.23 (0.12484)	4.83 (1.9)	0.03	0.0424	2.75	2.43
Chain	Length	Container Inside Diameter	Chain Frequency	Mass	Chain width	Chain Clearance	$l^*m^*\omega$	d/x_0	$(4/\pi^2)^*d/x_0$
	m (ft)	m (in)	(Hz)	kg/m (k-s ² /ft /ft)	cm (in)	cm (in)			
	3.35 (11)	0.38 (15)	0.33	13.4 (0.00028)	9.17 (3.61)	28.83 (11.39)	0.0174	5.99	2.43

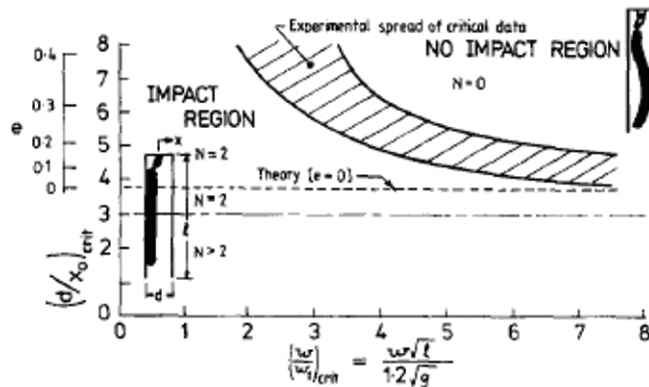


Fig. 4 Critical gap ratio vs critical frequency ratio (N=number of chain-container impact per cycle) [10, 7]

3.1.2 Experimental Verification

The chain damper designed in Section 3.1.1 was installed at the top of the spire and preliminary acoustical tests were conducted. It was concluded that the noise generated at each impact was incompatible with the standards for office buildings.

In order to reduce the noise, a fire hose sleeve was installed. Then, a series of experimental measurements were taken while the spire was excited as described in Section 2.2. The measurement system was composed of a triaxial accelerometer (CXL10GP3 by crossbow technology), a 30.5 m (100 ft) long shielded cable and the data acquisition card (USB6009 by National Instruments).

Free decay acceleration data in three axes were recorded at a sampling frequency of 200 Hz. Out of the three axes, only the measurements along the axis parallel to the connection of the spire to the base building were at significant levels, indicating that the excitation was successful to produce response in the desired direction, which corresponds to the plane of vibration for the mode shape requiring mitigation.

Figure 5a shows the raw data contaminated by the measurement noise. This data was taken when the top of the spire was forced to move 0.3 m (12 in) in each direction and then left to oscillate freely till the movements stopped. Given the response was dominant in the first sway mode, the data was band-pass filtered with cut off frequencies of 0.4 Hz and 4 Hz, which reduced the noise significantly as shown in Figure 5b. The natural frequency of the spire is estimated to be 0.85 Hz from the measured data.

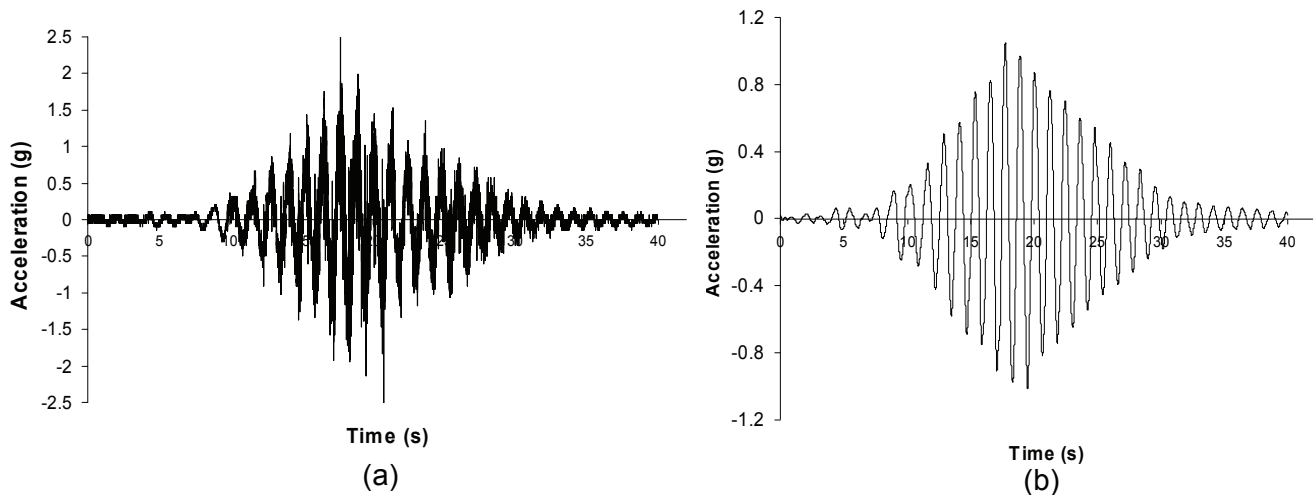


Fig. 5 (a) Measured raw acceleration data (test #1), (b) Band-pass filtered acceleration data (test #1)

The acceleration data presented in Figure 5b was numerically integrated twice to estimate the displacement recorded at the top of the spire, as shown in Figure 6a. The maximum instantaneous deflection was around 0.36 m (14 in), which is compatible with a 0.3 m (12 in) top deflection simultaneously inferred by the surveyors through long-distance optical measurement.

Figure 7 shows the variation of the damping ratio with respect to the top deflection of the spire. Damping estimates are calculated based on Equation 1 from the free decay time-history data given in Figure 6. Damping ratios are calculated at every cycle from both the decay of the positive (test #1, test #2) and negative (test #1 neg, test #2 neg) peaks.

It can be concluded that the addition of the chain damper increased the inherent damping of the spire from 0.1 – 0.2 % to at least an average of 2 % and to around 8 % at maximum. It is worth noting that the level of damping associated with the impacts depends on the vibration amplitude and it appears that the maximum damping ratio is attained when the top deflection of the spire is between 3.8 cm to 6.4 cm (1.5” to 2.5”), which confirms well with the design parameters of the chain damper (see Section 3.1.1). It must be noted that the day of the tests was windy and some influence on the damping estimation cannot be excluded.

3.2 Increment of Mass

Mitigation of the spire with a hanging-chain damper was rejected even after the fire hose installation due to excessive noise generated due to each impact. As an alternative, increasing the mass of the spire which improves the performance in the following three ways was considered.

- (1) The vibration of the spire during lock-in is controlled by a dimensionless mass/damping ratio, which is a measure of the ratio between the dissipation forces of the structure (i.e., associated with inherent mechanical damping) and the aeroelastic loading (i.e., the aerodynamic forces responsible for the vibration). This ratio is known as the Scruton number [5, 12]

$$K_s = \frac{m\zeta}{\rho D^2} \quad (3)$$

where m is the modal mass of the spire per unit length associated with a specific mode of vibration, ζ is the inherent structural damping ratio, ρ is the air density and D is the diameter of the spire. This relationship shows that increasing the mass or the damping ratio increases the Scruton number, hence reduces the response of the spire during vortex shedding. For circular cross-section slender structures, it is recommended a K_s value larger than 1.5 to eliminate the risk of “lock-in” large-amplitude vibrations [12].

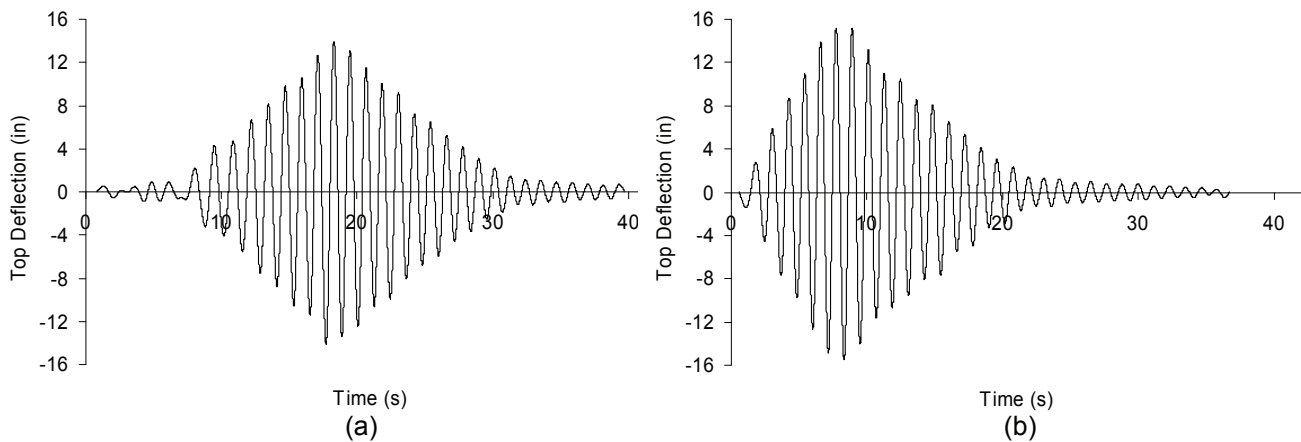


Fig. 6 (a) Spire top displacement data (test #1), (b) Spire top displacement data (test #2)

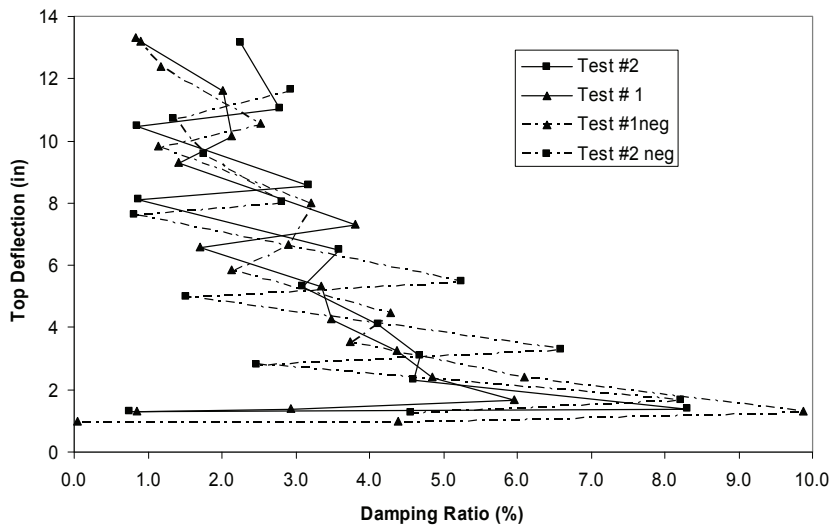


Fig. 7 Damping estimates as a function of the top deflection of the spire

- (2) By adding mass, the natural frequency of the problematic mode, hence the vortex-shedding frequency goes down. Because the diameter of the spire does not change, the wind speed that may trigger vortex-shedding goes down following the Strouhal relationship. If the wind velocity is very low (1 - 2 m/s), the flow will be highly irregular and poorly stratified (i.e., atmospheric flow is unstable), therefore reducing the aeroelastic effects, which usually require a stationary and regular wind to engage the structure in an unstable motion.
- (3) Based on the last five year wind history data of the site, there is a smaller chance to have a wind with a lower speed than the wind speed that caused vortex-shedding.

Given the expected improvements, it was decided to infill the three quarters of the 0.406 m (16 in)-diameter pipe section of the spire with sand. In total, 78 bags of 31.8 kg (70-lb) dry sand were used to infill the pipe through a length of 14.2 m (46.67 ft).

3.2.1 Analytical Work

The finite element model of the spire developed previously was updated to reflect the changes in the mass after the sand infill. The natural frequencies of the first four modes went down as expected: $f_1=0.66$ Hz, $f_2=0.75$ Hz, $f_3=3.11$ Hz and $f_4=3.84$ Hz. Although the corresponding mode shapes are not presented due to space limitations, they looked very similar to those shown in Figure 2 with little changes. The Scruton numbers before and after the mass increase are presented in Table 3. An increment K_s from 0.6 to 1.3 can be observed, with the latter value being very close to the $K_s=1.5$ threshold recommended in [12] as the criterion for likely elimination of large-amplitude across-wind vibration.

Table 3 Estimation of Scruton number before and after the sand infill

	Modal Mass (kg)	Modal Mass per unit length (kg/m)	Damping Ratio (%)	Air Density (kg/m ³)	Spire Diameter (m)	Scruton Number, K_s
Before	1852.23	86.39	0.15	1.25	0.4064	0.628
After	3864.24	180.24	0.15	1.25	0.4064	1.310

3.2.2 Experimental Studies

The performance of the spire after sand infilling has been tested through free-decay experiments. The same test set-up and procedure, as described in Section 2.2, were followed. Analysis of the recorded motion of the spire revealed that the natural frequency of the spire was 0.69 Hz. This was considered to confirm well with the analytical prediction of 0.75 Hz.

The free decay data of the spire including the top displacement and the corresponding time elapsed is presented in Table 4 together with the damping estimates based on Equation 1. Given the approximate nature of the data collection, it can be concluded that the inherent damping of the spire after the sand infill is in the range of 0.1 % to 0.2 %, similar to the damping estimates obtained before the sand infill. It is interesting to note that at smaller amplitude of vibrations, the damping ratio estimates after the sand in-fill tends to be larger than the damping ratio before the sand in-fill (compare damping estimates from Table 1 and 4 at a top deflection of 6.3 cm to 7.6 cm (2.5 in to 3 in). Assuming that the estimated damping is the sum of the structural damping of the spire and the damping of the sand in-filled, it appears that additional damping associated with the sand is more noticeable at low amplitude of vibrations than large amplitude of vibrations.

Table 4 Free decay data of the spire after sand infilling

Test # 1			Test # 2			Test # 3		
Time Elapsed (s)	Top Deflection cm (in)	Estimated Damping Ratio (%)	Time Elapsed (s)	Top Deflection cm (in)	Estimated Damping Ratio (%)	Time Elapsed (s)	Top Deflection cm (in)	Estimated Damping Ratio (%)
0.0	30.48 (12)	-	-	-	-	-	-	-
92.9	16.51 (6.5)	0.15	0.0	15.24 (6)	-	0.0	20.32 (8)	-
182.9	9.53 (3.75)	0.14	120.0	7.62 (3)	0.13	120.0	10.16 (4)	0.13
239.8	6.35 (2.5)	0.16	150.0	6.35 (2.5)	0.14	180.0	6.35 (2.5)	0.18

4. Discussion and Conclusions

Analytical and experimental studies conducted on an architectural spire, which experienced cross-wind high-amplitude vibrations during a low wind-speed event have been presented. Vortex-shedding was indicated to be the primary cause of the

extreme event. The shape of the spire oscillations during the event pointed out that it was the first sway mode of the spire in the direction parallel to the connection of the spire to the base building at a frequency of 0.88Hz, which corresponded to the second mode calculated from the finite element model.

First, a chain damper was designed and installed. Both analytical and experimental studies showed that the damping of the spire was increased at least 10 times and at its optimum value up to 40 times the damping of the spire without the chain damper. It is determined that the level of damping after the installation of the chain damper is related to the top deflection of the spire. The maximum damping ratio was attained when the top deflection of the spire was between 3.8 cm to 6.4 cm (1.5 in to 2.5 in), which was found to be in good agreement with the design parameters of the chain damper. Even though the chain damper performed very well, it has been rejected due to the annoying noise generated at each impact.

Instead, the mass of the spire was increased by filling the lower three quarters of the 0.406 m (16 in)-diameter portion of the spire. The structural damping of the spire did not change noticeably after the sand infill, except at relatively low-amplitude of vibrations. The natural frequency of the problematic mode decreased, leading to a smaller critical wind speed which is associated with a much less probability of occurrence for the specific site. In any case, the significant increment in the mass-damping parameter (Scruton number) is expected to eliminate the likelihood of large-amplitude vibration at lock-in for this mode.

An interesting question one might ask is “What is the chance of vortex shedding occurring at other natural frequencies of the spire and how does the current mitigation influence the performance?” Note that the spire at its original configuration had two sway modes in two orthogonal directions and the paper focused on the second sway mode (0.88 Hz) since it was the mode excited by vortex-shedding. In theory, the first mode (~0.8 Hz) could also be excited by vortex-shedding provided that a steady continuous wind blows in the correct direction with a critical wind speed of 1.6 m/s (3.6 mph). The mass increment helps mitigate the possible vortex-induced vibrations in the first mode in the same way as it does for the second mode. In fact, in the current configuration, the critical wind speed for the first mode is even lower (<3 mph) than it is for the second mode (~3.1 mph).

The calculated frequencies for the third and fourth modes of the spire in its original configuration were 4.18Hz and 5.26Hz respectively. After the addition of the mass, they went down to 3.11Hz and 3.84Hz, which are associated with critical wind speeds of 6.3 m/s (14.1 mph) and 7.8 m/s (17.4 mph). The potential for vortex-shedding induced vibrations of these higher modes and possible mitigation measures are currently under investigation.

ACKNOWLEDGMENTS

Ms. Sara Coyle and Mr. Farid Moghim, undergraduate and graduate students in the Department of Civil and Environmental Engineering of Northeastern University, are gratefully acknowledged for their assistance during the free-decay acceleration tests.

REFERENCES

- [1] Deavy C.P., Allsop A., Jones K., The Spire of Dublin, *The Structural Engineer*, Vol. 83, No. 16, pp.20-25, 2005
- [2] Baker W.F., Korista D.S., Novak L.C., Engineering the World's Tallest – Burj Dubai, CTBUH 8th World Congress, pp. 43-52, March 3-5 2008
- [3] Repetto, M. P., and Solari, G. Dynamic crosswind fatigue of slender vertical structures, *Wind and Structures*, 5(6), pp. 527-542, 2002
- [4] Robertson, A. P., Holmes, J. D., and Smith, B. W. Verification of closed-form solutions of fatigue life under along-wind loading, *Engineering Structures*, 26(10), pp. 1381-1387, 2004
- [5] Simiu, E., Scanlan, R. H., *Wind effects on structures*, 3rd edition Ed., John Wiley and Sons, New York, NY, USA, 1996
- [6] Caracoglia, L., and Jones, N. P. Numerical and experimental study of vibration mitigation for highway light poles, *Engineering Structures*, 29(5), pp. 821-831, 2007.
- [7] Koss L.L., Melbourne W.H., Chain Dampers for Control of Wind-induced vibration of tower and mast structures, *Engineering Structures*, Vol. 17, No. 9, pp. 622-625, 1995
- [8] Sap2000, Static and Dynamic Finite Element Analysis of Structures, Advanced 14.2.0, Computers and Structures, Inc. Berkeley, CA
- [9] Chopra A.K., *Dynamics of Structures: theory and applications to earthquake engineering*, Prentice Hall, 2nd Edition, 2001
- [10] Reed W.H. III, Hanging-chain impact dampers: a simple method for damping tall flexible structures, *Int. Research Seminar – Wind Effects on Buildings and Structures*, Ottawa, Canada, pp. 283-321, 11-15 September, 1967

- [11] Masri, S. F., and Caughey, T. K., On the stability of the impact damper, *Journal of Applied Mechanics, Transactions ASME*, 33, pp. 586-592, 1966
- [12] Melbourne, W.H. Predicting the cross-wind response of masts and structural members. *Journal of Wind Engineering and Industrial Aerodynamics* 69-71, pp. 91-103, 1997.

Closed-Loop System Identification of Alstom 3MW Wind Turbine

Carlo Enrico Carcangiu^{1*}, Iciar Font Balaguer¹, Stoyan Kanev², Michele Rossetti¹

¹ALSTOM Wind, 78, Roc Boronat, 08005 Barcelona (Spain)

²ECN Wind Energy, P.O. Box 1, 1175LE Petten (Netherlands)

* e-mail: carlo-enrico.carcangiu@power.alstom.com

ABSTRACT

Control algorithms for wind turbines are traditionally designed on the basis of (linearized) dynamic models. On the accuracy of such models depends hence the performance of the control, and validating the dynamic models is an essential requirement for achieving the optimum design. The aim of this work is to identify, at different wind speeds, the dynamic model of a wind turbine in operation. Experimental modal analysis (EMA) is the selected technique for system identification, and band-limited pseudo-random binary excitation signals (PRBS) are summed to the controlled inputs of the wind turbine system. The method is applied to the Alstom Eco100 3MW wind turbine.

Fairly good match is found in frequency and damping ratio for a frequency range up to 1 Hz. The time domain validation indicates in all cases reasonable model quality. The frequency domain comparison carried out for selected wind speeds shows close overlap around the first tower fore-aft and side-to-side frequencies, even though some discrepancies are found at first drive train frequencies.

Keywords: Closed-Loop System Identification, Experimental Modal Analysis, PRBS, Wind Turbine Control.

INTRODUCTION

Control algorithms for wind turbines are traditionally designed on the basis of (linearized) dynamic models. On the accuracy of such models depends hence the performance of the control, and validating the dynamic models is an essential requirement for achieving the optimum design. Experimental modal analysis (EMA) is a promising approach to perform closed loop system identification on modern wind turbines.

However, only limited attention in the literature of EMA has been directed so far at wind energy applications. The application of “exciter methods”, where rather unrealistic direct and measurable excitation on several points on the blades is assumed, was first investigated by Bialasiewicz [1]. Recently, research on modal analysis was performed within the framework of the European research project “STABCON” - Stability and control of large wind turbines”, where both simulation studies and experimental results were included [2][3]. The simulation studies are based on blade excitations that are difficult to perform in practice. More realistic excitation signals were investigated at Risø National Laboratory, by using the blade pitch and generator to excite with harmonic signals the first two tower bending modes, even though the measurement of the decaying response was proved to be unsuitable for an accurate estimation of the damping [3]. The identification of open-loop drive train dynamics from closed-loop experimental measurements on a fixed-pitch variable-speed wind turbine is presented in [4], for control algorithm design purposes.

Because the experimental modeling is based on data collected from a wind turbine during operation, i.e. with the controller operating, closed-loop system identification must be applied. Prior to the current work, a detailed review has been hence carried out of the available closed-loop identification (CLID) approaches to wind turbine model identification, listed below:

- Direct method [5],
- Indirect method [5],
- Joint Input/output method [5],
- Closed-loop instrumental variable method [6],
- Tailor made instrumental variable method [7],
- Closed-loop N4SID subspace identification [8],
- Parsimonious subspace identification method (PARSIM) [9],
- Subspace identification based on output predictions (SSARX) [10].

Initial studies using simulation data from both linear and nonlinear aeroelastic simulations have indicated the methods Direct, SSARX and PARSIM as most promising for wind turbine applications, with the Direct method often outperforming the other methods.

The EMA system identification has been applied on the Alstom Eco100 wind turbine in order to extract modal information at different operational conditions. Proper band-limited pseudo-random binary excitation signals (PRBS) have been carefully arranged to avoid the induction of undesired significant loads on the tower and rotor, taking also into account the constraints of the actuators. How this can be achieved without introducing unacceptable additional loads will be hereafter discussed. Moreover, special attention has also been paid on data-driven model validation, for which purpose several techniques have been developed.

METHODS

In order to identify accurate (i.e. unbiased) input-output models using the above-mentioned system identification methods, it is necessary that the inputs are additionally excited by signals that are uncorrelated with the wind.

Excitation signal design

A schematic system identification setup is depicted in Fig. 1. Typical inputs are the (collective) blade pitch angle θ and generator setpoint T_g , and outputs are generator speed Ω and tower fore-aft v_{nod} and sideways v_{nay} velocities (or accelerations). The blocks K_g and K_θ in the feedback loops represent the generator and the pitch controllers, respectively, which are not required in the Direct identification methods. Time series of these typical inputs and outputs allow the identification of the transfer functions from θ to v_{nod} , from T_g to Ω , and from T_g to v_{nay} , from which the tower fore-aft, tower side-to-side and drive train dynamics can be analyzed.

The frequency range where the models can be accurately identified depends on the bandwidth of the excitation signals: r_θ (on the blade pitch) and/or r_g (on the generator). When the frequency and damping of the first tower mode need to be identified, the bandwidth should at least include the expected first tower frequency. When the first drive-train mode is needed, the excitation bandwidth must at least include the first drive-train frequency. Hence, the proper choice of excitation signals is key-important for achieving informative experiment under reasonable amount of excitation.

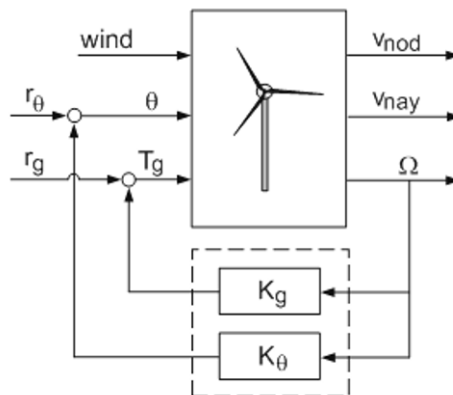


Fig. 1 System identification setup

Two opposite objectives exist indeed, and a trade-off should be made. On the one hand, a good excitation for system identification can be achieved by choosing a high energy excitation signal with wide flat spectrum. On the other hand, the system limitations (such as hardware limits, loads, etc.) impose the use of low-energy, narrow bandwidth excitation. The design of excitation signals should therefore prescribe that (a) the signals remain within the hardware limits, (b) the additional loads are as small as possible, and (c) the dynamic models are still accurately identified.

For the considered wind turbine specifically, the excitation signals r_θ and r_g have been designed in such a way, that no unacceptable loads are induced, the excited pitch demand has acceptable speed and acceleration, and the electric power remains within acceptable limits. To this end,

- the pitch excitation signal r_θ is designed as a pseudo-random binary signal (PRBS) with amplitude of 0.5 degrees, filtered with a low-pass FIR filter with cutoff frequency of 1 Hz, and an elliptic bandstop filter with 20 dB reduction, 1 dB ripple, and stop-band of 30% around the expected first tower frequency (0.32 Hz). In this way, the pitch excitation does not excite the region around the expected first tower frequency, as well as frequencies above 1 Hz.

- the generator excitation signal r_g is also designed as PRBS signal, but uncorrelated with the one used for pitch excitation, and with an amplitude of 3% of the rated signal, filtered with a lowpass FIR filter with cutoff frequency of 2 Hz, so that the excitation is concentrated in the frequency region up to 2 Hz.

Simulations made with an aeroelastic code have demonstrated that these excitations do not introduce significant increment in loads.

Modal parameters estimation

Once a model of the wind turbine is identified, there are different ways to extract modal parameters, such as the first tower and drive-train frequencies and damping. One way to do that is by performing model reduction on the identified mode, to reduce the model order, such as there is only one mode in a specified interval of interest where the frequency is expected to lie. For the considered wind turbine, the selected interval is [0.25, 0.40] Hz for the tower, and [0.7, 1] Hz for the drive train. The retained mode is the mode with the largest participation factor. The frequency and damping of this mode are then selected from the reduced system.

Model validation methods

Model validation is the process of deciding whether an identified model is reliable and suitable for the purposes for which it has been created.

The following model validation methods have been used to check the accuracy of the identified model:

- *Variance-accounted-for* (VAF): this is a model validation index often used with subspace identification methods. It is expressed in percentage. A VAF above the 95% is usually considered to represent a very accurate model.
- *Prediction error cost* (PEC): this is the value of the prediction error cost function, defined above. The smaller the value, the better the model accuracy.
- *Auto-correlation index* (R_{ix}^e): when a consistent model estimate is made, the prediction error ε should be a white process, so that its auto-correlation function $R_\varepsilon(\tau)$ should be small for non-zero τ , where τ denotes the discrete time step. For a given confidence level α (e.g. $\alpha = 99\%$), a bound $R_{\varepsilon}^{bound}(\alpha)$ can be derived such that for an accurate model the inequality $|R_\varepsilon(\tau)| \leq R_{\varepsilon}^{bound}(\alpha)$ should hold for all $\tau \geq 1$. The index R_{ix}^e is then computed as the square sum of the distance between each value of the correlation function $R_\varepsilon(\tau)$ and the bound $R_{\varepsilon}^{bound}(\alpha)$, where only the values outside the bound are used.
- *Cross-correlation index* (R_{ix}^{cu}): in the closed-loop situation the prediction error will be correlated with future values of the input, but should be uncorrelated with past inputs when the model is consistent. The cross-correlation function $R_{cu}(\tau)$ should then be limited in absolute value for $\tau \geq 1$.

It is important to point out that the data set used for validating the models should be different from the data used for obtaining the model, as otherwise wrong conclusions could be drawn.

RESULTS

Preliminary simulations

Time domain closed-loop system identification methods (CLID) are applied to both simulations, used to verify loads and to check identification methodologies, as well as to measurement data from an Alstom ECO100 wind turbine using PRBS signals as defined in the previous section.

Fig. 2 and **Fig. 3** show the PRBS excitation signals added to the collective pitch and generator demand following the scheme presented in **Fig. 1**.

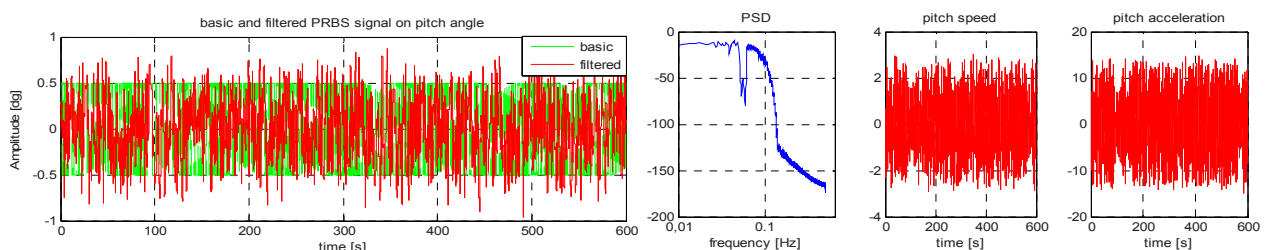


Fig. 2 PRBS excitation signal on collective pitch

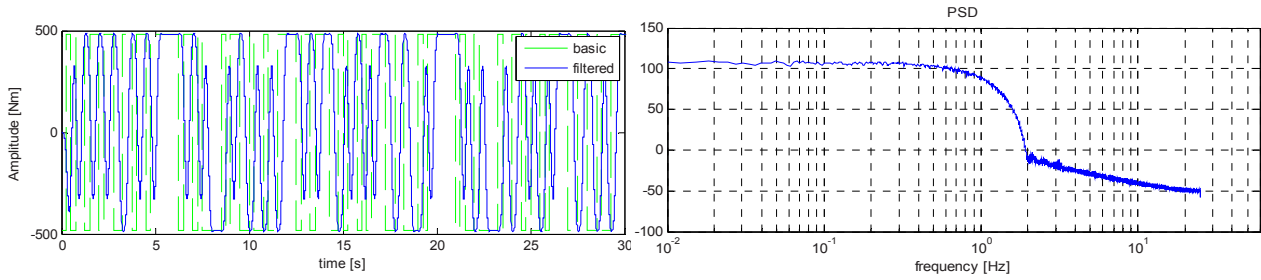


Fig. 3 PRBS excitation signal on generator

Closed-loop identification techniques are used to identify open loop models. Given the identified models, the corresponding frequency and damping of the first tower fore-aft and side-to-side mode and the first drive train mode of the open-loop wind turbine can be computed at different wind speeds. Time and frequency validation methods are used to evaluate each method.

As first step, closed-loop identification techniques are applied to (excited) input/output data from aeroelastic simulations. Simulations show that no significant loads were induced on the turbine, the excited pitch demand had acceptable speed and acceleration, and the electric power remained within acceptable limits.

As second step, studies on the closed-loop identification methods are carried out using simulation data. Since no information about the controller and the exact excitation signals used (r_o and r_g) is provided, the Direct, SSARX and PARSIM appear to be the most promising methods for wind turbine applications.

Table 1 Signals stored from the real wind turbine

Ω	Generator speed	rpm
v_{fa}	Tower top fore-aft acceleration	m/s^2
v_{sd}	Tower top fore-aft acceleration	m/s^2
θ	Excited blade pitch angle demand	deg
T_g	Excited generator torque	Nm
V_{nac}	Wind speed at nacelle	m/s

The measurement campaign

The same closed-loop identification techniques are applied using real (excited) input/output data collected from measurements on Alstom ECO100 3MW wind turbine. The measurement campaign was performed at below rated wind speeds, varying between 4 and 8 m/s. The control inputs, collective pitch demand and generator demand, have been simultaneously excited with the PRBS signals in order to obtain the transfer functions from these inputs to the outputs generator speed and tower top fore-aft and sideward velocities. The input/output measurement data collected are summarized in [Table 1](#).

Experience shows that working with tower top velocities improves the quality of the identified models around the first tower modes. Hence, for the estimation of the tower modes, the outputs v_{fa} and v_{sd} are integrated to velocities v_{nod} and v_{nay} . Four measurement time series are selected, each taken during partial load operation. Due to the fact that each of these four measurements cases contains some irrelevant information from the identification point of view, they have been concatenated. As indicated in the [Table 2](#), Test 1 and 2 have the same mean wind speed. Hence, Test 1 data can be used for model identification, while Test 2 can be used as validation data at 4.5 m/s. The same holds for Test 3 and 4, where the mean wind speed is 6.3 m/s.

Table 2 Measurement time series from the real wind turbine

<i>Test case</i>	<i>Data length</i>	<i>Mean (V_{nac})</i>	<i>Purpose</i>
Test 1	1459 s	4.5 m/s	Ident.4.5 m/s
Test 2	1130 s	4.8 m/s	Valid.4.5 m/s
Test 3	1651 s	6.2 m/s	Ident.6.3 m/s
Test 4	983 s	6.5 m/s	Valid.6.3 m/s

Tower first fore-aft mode identification

In order to estimate the tower first fore aft modal frequency and damping, the transfer function from pitch angle demand to the tower top fore-aft velocity v_{nod} is identified. For identification the test set Test 1 and test 3 are used.

In **Fig. 4** the Bode plots are compared of the identified models at 4.5 m/s with the linearized model obtained from the aeroelastic code (indicated as “Lin. mod.”) at 5 m/s. From **Fig. 4**, it can be also observed that the identified models are reasonably close to the models around the first tower frequency. Given the identified models, the corresponding frequency and damping are computed as explained in the **Methods** section. The modal frequencies and logarithmic decrements, computed from the identified modes are compared to those obtained from the linearized models at 5 and 7 m/s (**Table 3**).

The validation results, based on sets Test 2 and Test 4, are summarized in the **Table 4**, indicating that all models have comparable high accuracy.

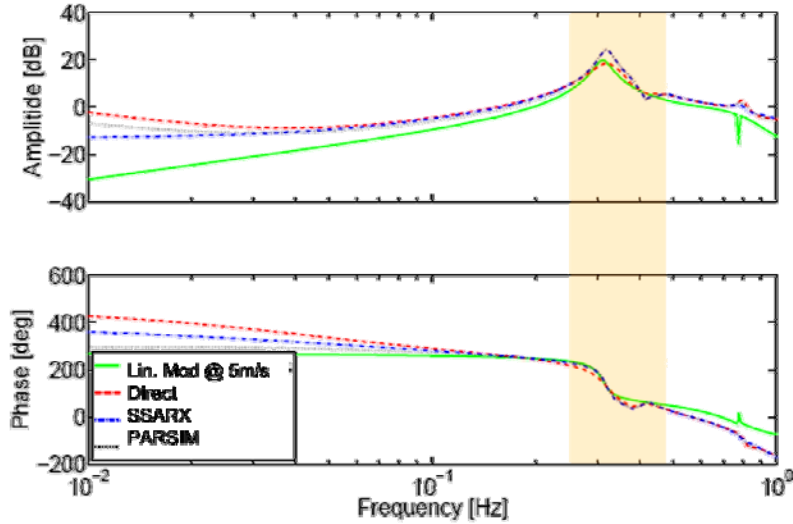


Fig. 4 Bode plot of the identified tower fore-aft models at mean wind speed of 4.5 m/s and linearized model at 5 m/s. (Transfer: Collective pitch angle demand \rightarrow Nacelle x-velocity)

Table 3 Frequency and logarithmic decrement of the tower first fore-aft mode

Wind [m/s]	Method	Freq [Hz]	Log.decr [%]
5.0	Lin. Mod.	0.3133	27.45
4.5	Direct	0.3195	36.80
4.5	SSARX	0.3202	27.41
4.5	PARSIM	0.3204	21.38
7.0	Lin. mod.	0.3161	33.49
6.3	Direct	0.3228	35.05
6.3	SSARX	0.3222	36.85
6.3	PARSIM	0.3278	29.55

Table 4 Validation results for identified models of the tower first fore-aft

Wind (m/s)	Method	VAF	PEC ($\times 10^{-5}$)	R_{ix}^e	R_{ix}^{ex} ($\times 10^{-2}$)
4.5	Direct	97.43	3.592	0.7129	1.200
4.5	SSARX	97.26	3.706	2.744	1.344
4.5	PARSIM	95.99	4.487	2.517	6.346
6.3	Direct	97.36	4.684	0.7638	3.590
6.3	SSARX	97.36	4.680	0.6674	3.843
6.3	PARSIM	97.18	4.841	0.8528	4.164

Tower first side to side mode identification

Similarly, to estimate the tower first side to side modal frequency and damping, the transfer function from generator demand T_g to the tower top side to side velocity v_{nay} is identified. In **Fig. 5** the bode plots of the identified models at 6.3 m/s with linearized model at 7 m/s are shown.

A close overlap is observed between the identified models and the linearized model. Those similarities are quantified in terms of frequency and logarithmic decrement in the [Table 5](#). The time domain validation results are shown in [Table 6](#).

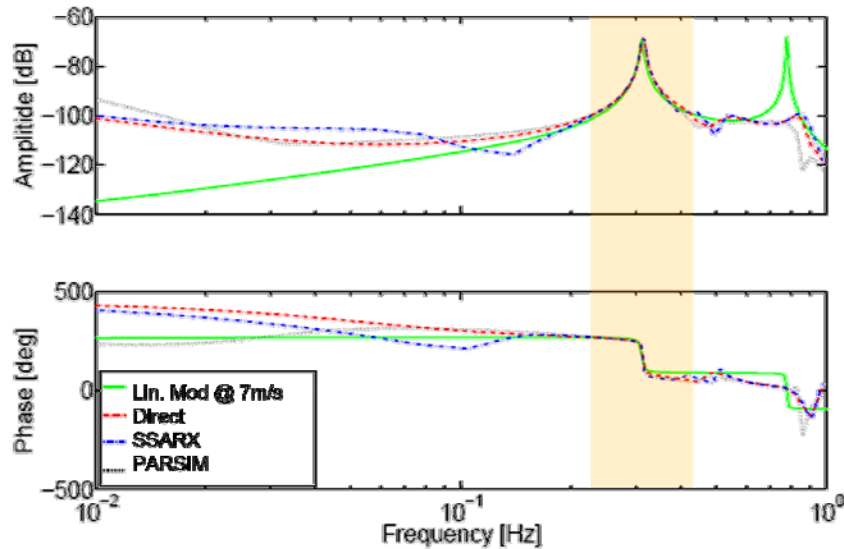


Fig. 5 Bode plot of the identified tower side to side models at mean wind speed of 6.3 m/s and linearized model at 7 m/s. (Transfer: Generator torque \rightarrow Nacelle y-velocity)

Table 5 Frequency and logarithmic decrement of the tower first sideward mode

<i>Wind [m/s]</i>	<i>Method</i>	<i>Freq [Hz]</i>	<i>Log.decr [%]</i>
5.0	Lin. mod.	0.3115	5.426
4.5	Direct	0.3151	3.037
4.5	SSARX	0.3156	2.549
4.5	PARSIM	0.3147	4.763
7.0	Lin. mod.	0.3115	5.556
6.3	Direct	0.3148	5.883
6.3	SSARX	0.3143	2.170
6.3	PARSIM	0.3153	3.861

Table 6 Validation results for identified models of the tower first sideward mode

<i>Wind [m/s]</i>	<i>Method</i>	<i>VAF</i>	<i>PEC ($\times 10^{-5}$)</i>	R_{ix}^e	R_{ix}^{ei}
4.5	Direct	99.99	4.487	1.118	0.009
4.5	SSARX	99.99	4.506	1.174	0.000
4.5	PARSIM	99.99	4.030	1.467	0.136
6.3	Direct	99.99	5.514	0.899	0.000
6.3	SSARX	99.99	5.399	0.808	0.000
6.3	PARSIM	99.99	6.557	0.967	0.116

First drive train mode

Finally, the first drive train frequency and damping are estimated from the identified transfer function from the generator demand T_g to the generator speed Ω .

In [Fig. 6](#) the Bode plots of the transfer functions identified with the Direct, SSARX and PARSIM method are shown, compared to the linear model obtained from the aeroelastic code.

As reported in [Table 7](#), the identified drive-train frequency is about 10% higher than the linearized model. Comparing the linearized model obtained with the aeroelastic code to the identified model using PARSIM method, a better estimation is obtained. In any case, the drive train frequency is not clearly evident in the input-output data.

In contrast with the frequency domain results showed in [Table 7](#), the Time domain validation methods shows excellent results ([Table 8](#)).

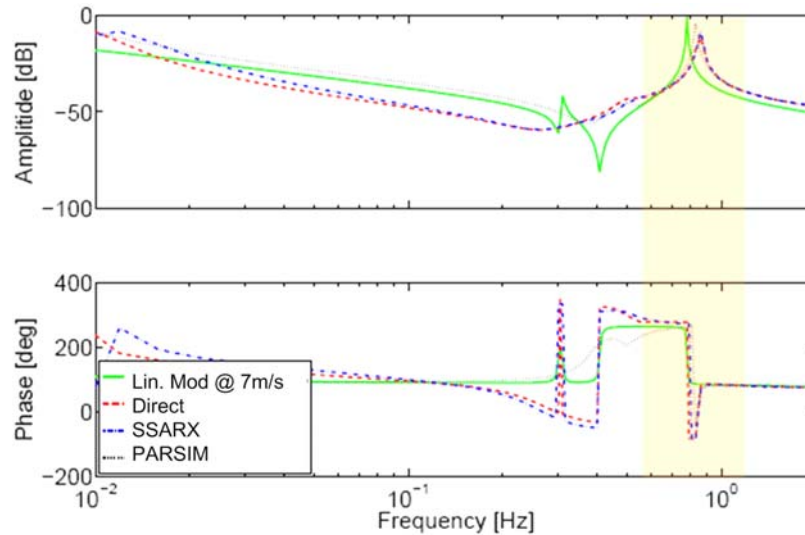


Fig. 6 Bode plot of identified first drive train models at mean wind speed of 6.3 m/s and linearized model at 7 m/s. (Transfer: Generator torque \rightarrow Generator speed)

Table 7 Frequency and logarithmic decrement of the first drive train mode

<i>Wind [m/s]</i>	<i>Method</i>	<i>Freq [Hz]</i>	<i>Log.decr [%]</i>
5.0	Lin. mod.	0.7777	1.304
4.5	Direct	0.8773	14.120
4.5	SSARX	0.8780	16.610
4.5	PARSIM	0.8261	6.877
7.0	Lin. mod.	0.7780	1.642
6.3	Direct	0.8496	1.499
6.3	SSARX	0.8534	1.822
6.3	PARSIM	0.8305	3.857

Table 8 Validation results for identified models of the first drive train mode

<i>Wind [m/s]</i>	<i>Method</i>	<i>VAF</i>	<i>PEC ($\times 10^{-3}$)</i>	R_{ix}^e	R_{ix}^{eu}
4.5	Direct	99.98	6.797	0.070	0.732
4.5	SSARX	99.98	6.731	0.051	0.670
4.5	PARSIM	99.96	10.040	0.847	0.856
6.3	Direct	100	5.970	0.240	0.100
6.3	SSARX	100	5.962	0.181	0.256
6.3	PARSIM	100	6.908	0.130	0.421

An explanation for those differences could be either that the drive-train frequency is not well represented in the data due to the presence of a drive-train damping filter existing in the control or that in reality, the drive train is less flexible than in the linearized model obtained from the aeroelastic code. Further experiments need to be performed to clarify the reasons of such discrepancies.

CONCLUSIONS

Theory and results of an innovative experimental system identification method for estimating modal parameters of a wind turbine in operation is presented.

In the mentioned method, additional excitation signals on the controllable inputs of the turbine (pitch and/or generator) are needed. These signals are designed in such a way that accurate models are identified, but preventing the occurrence of extra loads on the wind turbine. In order to validate the identified open-loop models, both time-domain validation methods and frequency-domain comparisons to linearized aeroelastic models are made. After preliminary simulations with aeroelastic models, an experimental campaign has been carried out on the ECO100 3 MW wind turbine for different below-rated operational conditions.

Fairly good match is found in frequency and damping ratio for a frequency range up to 1 Hz. The time domain validation indicates in all cases reasonable model quality. The frequency domain comparison carried out for selected wind speeds shows close overlap around the first tower fore-aft and side-to-side frequencies, even though some discrepancies are found at first drive train frequencies. Further experiments need to be performed to clarify the exact reason of this divergence by either increasing the generator excitation amplitude or by de-activating the drive-train filter in the controller.

The estimated modal parameters can be used for either improving the existing control loops, for achieving additional functionality by designing new control strategies for fatigue reduction or for updating the existing FEM and multi-body models.

ACKNOWLEDGEMENTS

This work has been partially performed by ECN Wind Energy within the SenternNovem long-term research project “SusCon: a new approach to control wind turbines” (EOSLT02013), and partially within the InVent project-ACC1Ó (CIDEM | COPCA).

REFERENCES

- [1] Bialasiewicz, J., *Advanced System Identification Techniques for Wind Turbine Structures*. Report NREL/TP-442-6930, NREL. Prepared for the 1995 SEM Spring Conference, Grand Rapids, Michigan, USA (1995)
- [2] Marrant, B. and van Holten T., *System Identification for the analysis of aeroelastic stability of wind turbine blades*, Proceedings of the European Wind Conference & Exhibition, pp. 101-105 (2004)
- [3] Hansen, M.H., Thomsen K., Fuglsang P. and Knudsen T., *Two methods for estimating aeroelastic damping of operational wind turbine modes from experiments*, Wind Energy, 9(1-2):179-191 (2006)
- [4] Novak, P., Ekelund, T., Jovik, I. and Schmidbauer, B., *Modeling and control of variable-speed wind-turbine drive-system dynamics*. IEEE Control Systems, 15(4):28-38 (1995)
- [5] Ljung, L., *System Identification. Theory for the User*. Prentice Hall (1999)
- [6] Van den Hof, P. and Bombois, X., *System Identification for Control*. Delft Center for Systems and Control, TU-Delft. Lecture notes, DISC: Dutch Institute for Systems and Control (2004)
- [7] Van den Hof, P. and Gilson M., *Closed-loop system identification via a tailor-made IV method*. Proceedings of the 40th Conference on Decision and Control. Orlando, Florida, pp. 4314-4319 (2001)
- [8] Van Overschee, P. and De Moor, B., *Closed-loop Subspace System Identification*. Proceedings of the 36th Conference on Decision and Control. San Diego, California, USA (1997)
- [9] Qin, S. and Ljung, L., *Closed-Loop Subspace Identification with Innovation Estimation*. Proceedings of the 13th IFAC Symposium on System Identification, pp. 887-892 (2003)
- [10] Ljung, L. and McKelvey, T., *Subspace identification from closed loop data*. Signal Processing, 52:209-215 (1996)

Reduced Order Modal-Space Wireless Control of Civil Engineering Structures

R. Andrew Swartz, Assistant Professor, Department of Civil and Environmental Engineering, Michigan Technological University, 1400 Townsend Dr., Houghton, MI 49931

Abstract Semi-active actuators are capable of providing control forces to reject unwanted vibrations due to wind or seismic effects in civil structural systems by affecting strategic modifications to structural properties (*e.g.* stiffness or damping). Such devices enjoy the advantage of being low-cost and low-power (compared to active devices), and are inherently stable, however limitations on the magnitudes of their achievable output forces necessitate the use of numerous (distributed) semi-active devices in order to be effective. Coordination of large, decentralized networks is a natural task for wireless networks given their adaptability and low-cost to install. Low-power wireless sensor nodes are capable of sensing, communication, computation of control forces (using for example, state feedback and state estimation), and issuing commands due to their inherent collocated computing power. However, their relatively low computational speed adds undesirable latency to the control system as models grow large. In this study, a low-order model based on modal condensation is used within a wireless control network to reduce seismically induced vibrations within a six-story steel structure. Tradeoffs between model size and control latency are explored. Both simulation and experimental results are presented.

Introduction

For tall civil structures, it is often prohibitively expensive to resist large seismically induced lateral loads through strength alone. Modern seismic design practices address this limitation by exploiting the ductility of a well designed structure to dissipate unwanted seismically induced kinetic and strain energies in the structure through hysteresis. When occupant life safety is the only goal, this approach has proven to be highly successful. However, the inelastic behavior exhibited by the structure during extreme seismic events is a direct result of damage to the structure that may make the structure uninhabitable until repairs may be affected; or the damage may be so severe that the structure must be demolished. In addition, large relative displacements of components within the structural system are strongly correlated with damage to both structural and non-structural systems. In critical emergency response structures (*e.g.*, hospitals, emergency shelters, or fire stations) or structures housing economically critical activities, damage that results any interruption in occupancy is oftentimes considered to be unacceptable. In such cases, the protection afforded to the structure can be enhanced by the addition of a structural control system that can remove unwanted seismically induced energy from the structure through non-hysteretic means [1-3].

Most structural control technologies can be classified as either passive, active, or semi-active in their approach [4]. Passive control strategies (*e.g.*, tuned mass dampers, tuned liquid dampers, viscoelastic dampers) rely on devices that are carefully tuned to the structure's dynamic properties, as well as the anticipated seismic excitations, to remove energy from the system during earthquakes or large wind storms. These devices are quite reliable and usually require no energy input. Active control technologies (*e.g.*, active mass dampers) represent a much more aggressive approach, strategically adding energy to the system in order to achieve a desired control result (*e.g.*, minimization of acceleration or interstory drift). In contrast to passive control strategies, the design of active structural control systems can be more aggressive and may be targeted to minimize specific responses, however such systems are expensive to install and maintain. In addition, active controllers introduce reliability concerns given the large amount of energy required for their operation and the likelihood of power outages during the extreme seismic events that these systems are intended to protect against. More recently, semi-active controllers have gained popularity as a balance between these two approaches. Semi-active control devices (*e.g.*, variable stiffness dampers, magneto- or electro-rheological dampers, or variable-orifice dampers) do not impart energy directly into the system, but instead affect real-time changes in dynamic properties of the structure. As such, these devices are relatively inexpensive, require little energy (making them appropriate for short-term battery powered operation), and these devices are often inherently stable [4]. Because the forces generated by semi-active devices are often considerably smaller in magnitude than those produced by active damper systems, considerably larger numbers are required to produce equivalent results.

Due to the large size and distributed nature of civil structures, connecting actuation signal cables between these devices and a centralized control computer can be prohibitively expensive [5]. Similar to sensor systems, signal cables can incur installation costs of up to a few thousand dollars per channel in large structures [6]. These additional costs can erode the apparent attractiveness of this technology and present a barrier to their widespread adoption. One approach to alleviate these costs is to install these devices without centralized coordination. The Kajima Corporation's HiDax system (for example) makes use of semi-active dampers that use locally measured sensor data to compute their control actions and that operate independently of the other actuators in the structure [7]. However, despite their lack of coordination, the control efforts of these actuators are inescapably coupled. Therefore, a low-cost method to coordinate their actions and achieve improved performance is desirable.

In structural sensing and monitoring applications significant cost savings have been realized by replacing traditional cable-based sensor networks with wireless smart sensors that can collect data without the need for expensive signal cables [5, 8]. However, wireless sensors are subject to significantly more restrictive digital data transmission limits than are cable-based sensors. In addition, in battery powered applications, data transmission represents the largest consumer of the battery energy available to the node. For these reasons, embedded data processing has been advanced as an important tool to preserve communication bandwidth and battery power [9]. Wireless sensors have inherent memory and computational resources that can be leveraged to execute engineering algorithms, interrogate raw data, and reduce the communication burden within the network [9]. Building on the idea of embedded and autonomous data processing, wireless smart sensors can provide the platform to achieve the low-cost coordination of actions between semi-active control devices.

Wireless smart sensors with embedded actuation interfaces can be enabled to collect response data and command collocated actuators [10]. Wireless sensors can be used solely as data collection and actuation devices in wireless control applications [11], however this practice does not take advantage of the computational resources available within the wireless sensor node and is especially susceptible to delays in the system due to dropped data packets. Emulating the centralized control computer within the wireless network helps to alleviate the effects of dropped packets if the sensors are equipped with estimation algorithms that can provide usable estimates of the response of the structure when measured data is lost [12, 13]. Yang, *et al.* deployed and validated a wireless control network capable of commanding semi-active controllers for seismic disturbance rejection in a 3 degree of freedom (DOF) system in which wireless control units were made responsible for sensing feedback from the structure, computing estimates of the structural state, computing control forces, communicating data to other control units, and commanding collocated actuators [12]. However, Yang, *et al.* demonstrated that further reduction of the dependency of the wireless control network on the communication channel yielded additional gains in control performance [14]. Reducing the level of data sharing between the network nodes allowed for reduced latency in the control algorithm, in many cases improving performance for both the 3 DOF structure and a 6 DOF structure [14]. Using faster wireless radio, Swartz and Lynch [15] traded bandwidth for control performance in a 6 DOF structure, communicating only the most necessary response data between units and improving the quality of service of the wireless channel. In these studies, a common theme emerges of a tradeoff between the reduction of latency and improved coordination (through sharing of data) to improve control performance. The common thread in the approaches cited is to limit latency due to wireless communication through the use of state estimators and additional sensor level computing. However, this practice is also not without its drawbacks.

To achieve low power operation, wireless controller design relies on low power components that have considerably less computational power and memory than their wired counterparts. Lower computational power results in increased latency in computationally intensive operations. As additional computational demands are placed on the wireless sensor (through more complicated control algorithms or increasing structure size) the latency introduced by large numbers of embedded floating point arithmetic operations begins to negatively affect control performance to a significant extent. This study seeks to explore the use of modal condensation to produce reduced order models for the control law that can reduce the computational latency in the system. In this study, the model of the plant (the structure to be controlled) is transformed into modal coordinates, the higher order modes removed from the model, and feedback control gains and estimators derived for the reduced order system. By sacrificing model fidelity, computation time can be reduced, decreasing the overall latency in the control system. The tradeoff between control time step and model size is explored in both simulation and experimentally for a 6 DOF structure controlled by magneto-rheological dampers over a wireless control network.

The following section of the paper presents the theory informing the algorithm used in this study. The section that follows describes the wireless control platform that serves as the basis for the time step limitations (versus model size) defined for the simulation study and that is used in the experimental portion of the study. The simulation and experimental studies are described in the next section with results, discussion, and conclusions follow.

Theory

A state-space representation of the model is chosen to handle the multiple-input multiple-output (MIMO) nature of the control problem (a six-story structure with a sensor and actuator located at each floor). The state-space formulation is derived from the matrix form of the equation of motion for a six-story lumped-mass shear structure:

$$\mathbf{M}\ddot{\mathbf{x}}(t) + \mathbf{C}_d\dot{\mathbf{x}}(t) + \mathbf{K}\mathbf{x}(t) = -\mathbf{M}\ell\ddot{x}_g(t) + \mathbf{T}\mathbf{u}(t) \quad (1)$$

where \mathbf{x} is the vector of lateral story displacements, \mathbf{M} , \mathbf{C}_d , and \mathbf{K} are mass, damping, and stiffness matrices respectively, \mathbf{u} is the vector of control forces, \mathbf{T} is a matrix that describes the connections between the actuators and the floors, and ℓ is a column vector consisting of all ones. In state-space, Equation (1) becomes:

$$\begin{aligned} \dot{\mathbf{z}}(t) &= \mathbf{A}\mathbf{z}(t) + \mathbf{B}\mathbf{u}(t) + \mathbf{E}\ddot{x}_g(t) \\ \mathbf{y}(t) &= \mathbf{C}\mathbf{z}(t) + \mathbf{D}\mathbf{u}(t) + \mathbf{F}\ddot{x}_g(t) \end{aligned} \quad (2)$$

$$\mathbf{A} = \begin{bmatrix} \mathbf{0} & \mathbf{I} \\ -\mathbf{M}^{-1}\mathbf{K} & -\mathbf{M}^{-1}\mathbf{C}_d \end{bmatrix} \quad \mathbf{B} = \begin{bmatrix} \mathbf{0} \\ \mathbf{M}^{-1}\mathbf{L} \end{bmatrix} \quad \mathbf{E} = \begin{bmatrix} \mathbf{0} \\ -\ell \end{bmatrix} \quad (3)$$

The output matrices \mathbf{C} , \mathbf{D} , and \mathbf{F} , are dependent on the mechanism of the sensor output. If displacement measurements are available for feedback (*i.e.*, displacement relative to ground measured indirectly, using linear variable differential transducers to find the interstory drift and subtracting the displacement measure from the floor below):

$$\mathbf{C} = \begin{bmatrix} [\mathbf{0}] & \begin{bmatrix} 1 & & 0 \\ & \ddots & \\ 0 & & 1 \end{bmatrix} \end{bmatrix} \quad \mathbf{D} = [\mathbf{0}] \quad \mathbf{F} = [\mathbf{0}] \quad (4)$$

If acceleration feedback is available:

$$\mathbf{C} = [-\mathbf{M}^{-1}\mathbf{K} \quad -\mathbf{M}^{-1}\mathbf{C}_d] \quad \mathbf{D} = [-\mathbf{M}^{-1}\mathbf{L}] \quad \mathbf{E} = [-\ell] \quad (5)$$

The LQR control law produces an optimal control feedback gain that minimizes the cost function, J :

$$J(\mathbf{u}) = \sum_{k=1}^{\infty} (\mathbf{z}^T(k)\mathbf{Q}_1\mathbf{z}(k) + \mathbf{u}^T(k)\mathbf{Q}_2\mathbf{u}(k)) \quad (6)$$

where \mathbf{Q}_1 and \mathbf{Q}_2 are positive semi-definite and positive definite matrices, respectively, selected by the designer that weight control effort expended against control performance [16]. By choosing the magnitude of \mathbf{Q}_1 to be relatively large compared to \mathbf{Q}_2 a control solution that produce large control forces to minimize response is favored. As the magnitude of \mathbf{Q}_2 increases relative to \mathbf{Q}_1 , larger control forces are penalized. The optimal control force is described by:

$$\mathbf{u}(t) = -\mathbf{G}\mathbf{z}(t) = -[[\mathbf{Q}_2 + \mathbf{B}^T\mathbf{P}\mathbf{B}]^{-1}\mathbf{B}^T\mathbf{P}\mathbf{A}]\mathbf{z}(t) \quad (7)$$

where \mathbf{P} is the solution to the algebraic Riccati equation [17]. It is necessary to convert the model to a digital (discrete-time) representation to implement the controller on a digital computer. A zero-order hold approximation produces the state-space representation:

$$\mathbf{z}(k+1) = \mathbf{\Phi}\mathbf{z}(k) + \mathbf{\Gamma}\mathbf{u}(k) + \mathbf{\Lambda}\ddot{x}_g(k) \quad (8)$$

$$\Phi = e^{AT_s} \quad \Gamma = \left(\int_0^{T_s} e^{A\tau} d\tau \right) \mathbf{B} \quad \Lambda = \left(\int_0^{T_s} e^{A\tau} d\tau \right) \mathbf{E} \quad (9)$$

where T_s is the time required by the controller to sense, compute, communicate, and send command signals to the actuator [17]. For many applications, direct measurement of the entire state vector is impossible (or at least highly impractical), therefore a state estimator is often employed. The Kalman based estimator utilized in this study seeks to minimize the covariance:

$$\mathbf{P}_e = \lim_{t \rightarrow \infty} [(\mathbf{z} - \hat{\mathbf{z}})(\mathbf{z} - \hat{\mathbf{z}})^T] \quad (10)$$

where $\hat{\mathbf{z}}$ is the state estimate [17]. Here the estimation error is treated as a disturbance to be rejected and an optimal control gain, \mathbf{L} , is derived. The estimate of the full state vector is then:

$$\hat{\mathbf{z}}(k+1) = \bar{\mathbf{z}}(k+1) + \mathbf{L}(\mathbf{y}(k) - \mathbf{C}\hat{\mathbf{z}}(k)) \quad (11)$$

where:

$$\bar{\mathbf{z}}(k+1) = \Phi \hat{\mathbf{z}}(k) + \Gamma \mathbf{u}(k) \quad (12)$$

In this wireless application where computational efficiency is of prime importance, the matrices multiplying the old state estimate can be combined a priori to save computations during the estimator step:

$$\hat{\mathbf{z}}(k+1) = \mathbf{A}_{est} \hat{\mathbf{z}}(k) + \mathbf{B}_{est} \mathbf{y}(k) \quad (13)$$

$$\mathbf{A}_{est} = \Phi - \Gamma \mathbf{G} - \mathbf{L} \mathbf{C} \quad \mathbf{B}_{est} = \mathbf{L} \quad (14)$$

Because the LQR controller is dependent on knowledge of the state of the system in order to be optimal, the effectiveness of the system is dependent upon the error produced by the estimator.

Because the size of the control gain matrix and the estimator gain matrices grow with model size at a rate of \mathcal{O}^2 , computation of estimates and control gains does not scale well in the wireless microcontroller for high DOF systems. In order to reduce the latency of the controller a simple reduced-order model is utilized based on modal condensation. To derive the reduced-order model, the system must first be converted into modal coordinates. The i^{th} column of the conversion matrix, Ψ , used for this conversion is the i^{th} mode shape, ψ_i (norm 1), derived from the eigenvectors of:

$$\Psi = [\psi_1 \quad \dots \quad \psi_n] \quad (15)$$

$$\psi_i = \text{eigenvectors}(\mathbf{M}^{-1}\mathbf{K}) \quad (16)$$

where n the number of floors in the structure. A change of basis matrix, \mathbf{T}_0 , is:

$$\mathbf{T}_0 = \begin{bmatrix} \Psi & \mathbf{0} \\ \mathbf{0} & \Psi \end{bmatrix} \quad (17)$$

and the system representation in the modal-domain is:

$$\begin{aligned} \mathbf{A}_0 &= \mathbf{T}_0^{-1} \mathbf{A} \mathbf{T}_0 & \mathbf{B}_0 &= \mathbf{T}_0^{-1} \mathbf{B} & \mathbf{E}_0 &= \mathbf{T}_0^{-1} \mathbf{E} \\ \mathbf{C}_0 &= \mathbf{C} \mathbf{T}_0 & \mathbf{D}_0 &= \mathbf{D} & \mathbf{F}_0 &= \mathbf{F} \end{aligned} \quad (18)$$

A reduced representation of the system is derived by simply eliminating the rows and columns of the state-space matrices associated with the higher order modes that may contribute to the overall response of the system under seismic load.

Naturally, reduced order control law that directly accounts for the neglected higher-order modes (*e.g.*, H-infinity), but are not utilized in this study to help to better underline the benefits derived from increased controller speed in the wireless network.

The reduced system model is derived in continuous-time, an optimal LQR control law is derived, the closed-loop system is then transformed into the discrete-time domain, and a Kalman estimator for the reduced discrete time system derived. The size of the control and estimation matrices (\mathbf{G}_r , \mathbf{A}_{est_r} , and \mathbf{B}_{est_r}) will then be dependent on the number of sensors, p , the number of controllers, q , and the number of states retained, m :

$$\mathbf{G}_r \in \mathbb{R}^{q \times m} \quad \mathbf{A}_{est_r} \in \mathbb{R}^{m \times m} \quad \mathbf{B}_{est_r} \in \mathbb{R}^{m \times p} \quad (19)$$

The time step achievable for a given model size, m , is directly dependent on the wireless computing platform available. The platform used in this study is described in the next section.

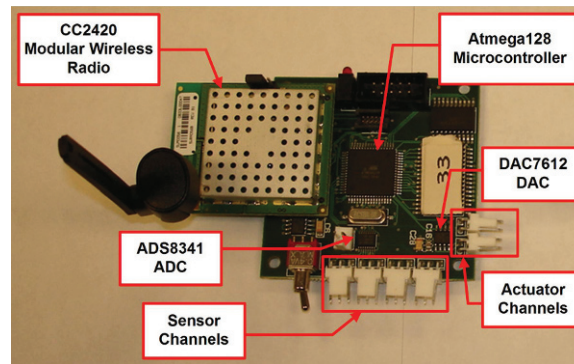


Fig. 1 *Narada* wireless sensing and actuation node

Narada Wireless Sensing and Control Platform

The tradeoff examined in this study is predicated upon the capabilities of the hardware platform that is used in as the wireless controller in the installed system. This study relies upon the *Narada* wireless sensing and control platform (Figure 1). Developed at the University of Michigan for use in civil engineering applications, the *Narada* wireless system is intended for low cost sensing and actuation applications where dense sensor/actuator deployments are desired [10]. The system is designed to be low powered. The computational core of the unit consists of an Atmel Atmega128 microcontroller that is responsible for managing physical operations of the platform (*e.g.*, sensing, actuation, communication, data management) as well as execution of the embedded engineering algorithms. The Atmega128 has 128 kB of programmable Flash memory, to store programming instructions, and 4 kB of static random access memory (SRAM), to store data and variables, and has been augmented with an additional external 128 kB of SRAM for data storage. The unit's link to both the user (via a network enabled laptop computer), and to other units, is its communication interface composed of a CC2420 IEEE802.15.4 compliant, 2.4 GHz spread-spectrum radio transceiver (manufactured by Texas Instruments). The CC2420 is designed for low-power, *ad hoc* network applications and supports outdoor communication distances up to 100 m using standard output power levels and a 1.0 dBm gain omni-directional antenna, and communication distances of up to 500 m with a power boosted output and a 6 dBm gain directional antenna. The sensing interface consists of a Texas Instruments ADS8341 16-bit, 4-channel analog to digital converter (ADC) intended to make the unit suitable for civil engineering sensing applications under ambient loading conditions (where signal levels are small and high resolution is key). Finally, to command actuators, the *Narada* wireless sensors incorporate an actuation interface consisting of a Texas Instruments DAC7612 12-bit, 2-channel digital to analog converter (DAC).

The AVR core microcontroller is capable of executing one instruction for every clock cycle (the *Narada* unit clock operates at 8 MHz). Unfortunately, floating point arithmetic operations require multiple assembly-level instructions to complete. The computational time required for control force calculations and state estimation becomes increasingly significant as a portion of the total time step as the model size grows larger. In addition, fixed computational overhead exists for data sampling, data communication, computation of command voltage from desired control force, and actuation. The time required for these operations for models of various sizes are derived experimentally (rounded up to the nearest ms) and used to as parameters in the computational portion of this study described in the next section.

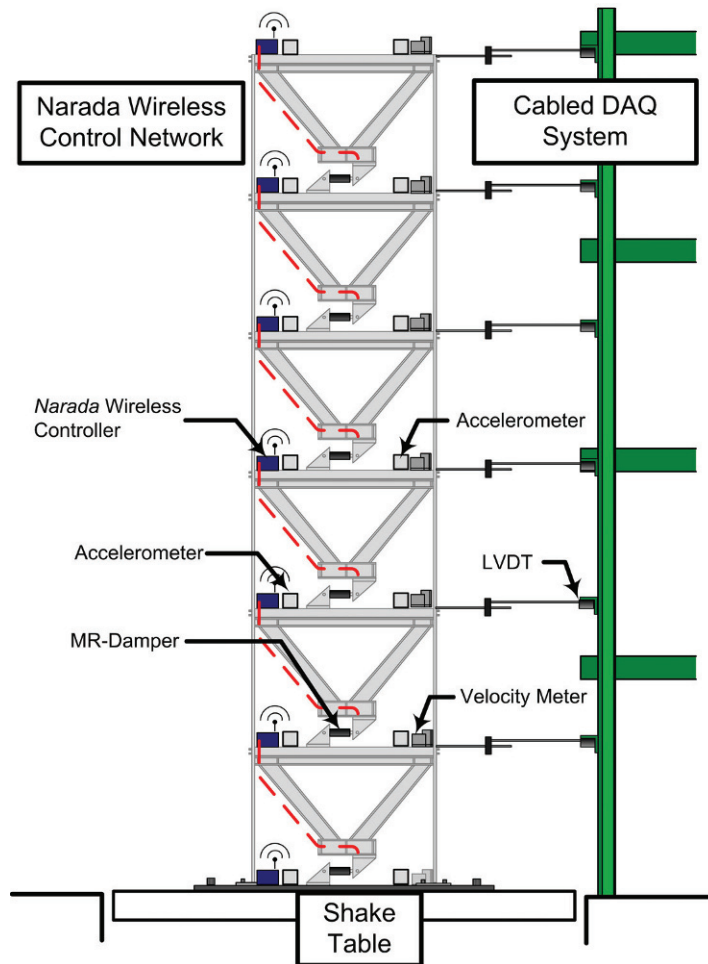


Fig. 2 Six-story scale steel structure with sensors and magneto-rheological dampers

Computational Simulation Study

Validation of the proposed approach is accomplished in both the simulation environment and experimentally. For consistency, the structural model used in the simulation portion of the study is based on the properties of the experimental structure (Figure 2). The structure is a scale, six-story steel building that measures 1.0 m from floor to floor. The floors measure 1.5 m wide by 1.0 m deep and consist of an angle iron perimeter that supports a steel plate. Rectangular bar stock columns support the floors (the lateral excitation applied to the structure is oriented in their weak-axis direction). The mass of each floor is taken to be 640 kg, story stiffness between floors is approximately 2.4×10^6 N/m (experimentally derived), and the structure is lightly damped, exhibiting approximately 1.25% Rayleigh damping. Simulated magneto-rheological dampers are located between floors and their behavior is modeled using a bi-linear, bi-viscous Bouc-Wen model [18]. The simulated dampers have a saturation force level of 2.0 kN. Actuation voltage levels are selected from a dynamic lookup table of achievable control forces given a finite range of voltage levels, the desired control force (from the LQR control law), and a sensor's estimate of the interstory velocity that the damper experiences. The simulation considers lateral base excitation of the structure based on the El Centro 1940 NS (USGS Station 117) earthquake acceleration record. The record is normalized to a peak acceleration level of 1.0 m/s^2 (100 gals).

To be used in the reduced order, modal-domain controller, the model of the system is converted into modal coordinates. These coordinates are dependent upon the mass and stiffness properties of the structure; both the standard and modal coordinate basis vectors for the scale six-story structure are depicted in Figure 3. The LQR control law is formulated to penalize interstory drift in the structure; interstory drift is linked to damage in both structural support systems as well as non-structural building systems. The LQR formulation is the same for both the simulation and experimental portions of the study

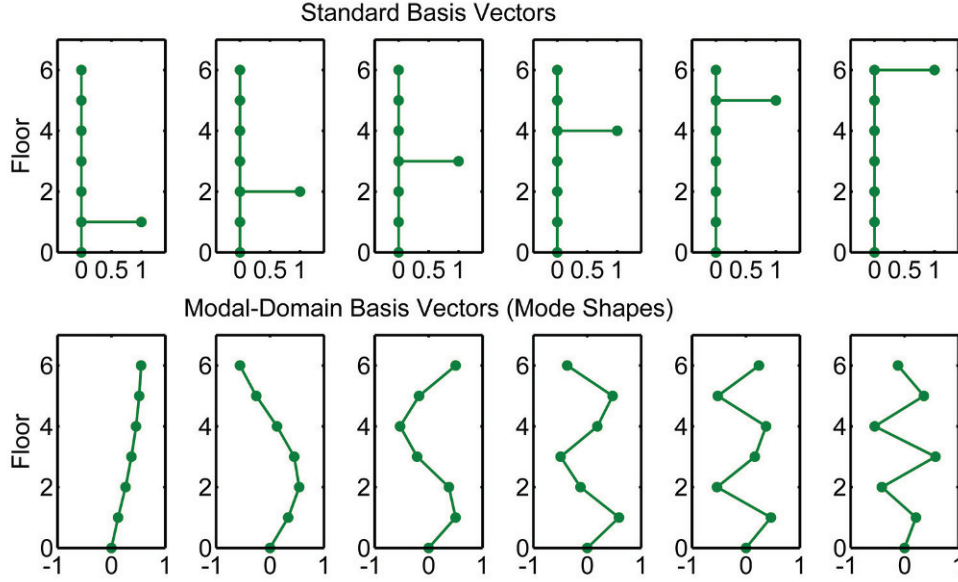


Fig. 3 Standard basis vectors versus modal-domain basis vectors for six-story structure

and is derived in the modal coordinate system. The weighting matrices, \mathbf{Q}_1 and \mathbf{Q}_2 , of Equation (6) selected for this study are:

$$\mathbf{Q}_1 = \hat{\mathbf{Q}}^T \hat{\mathbf{Q}} \quad \mathbf{Q}_2 = 2.0^{-9} \mathbf{I} \quad (20)$$

$$\hat{\mathbf{Q}} = \begin{bmatrix} \mathbf{c}\Psi & \mathbf{0} \\ \mathbf{0} & \mathbf{I}\Psi \end{bmatrix}$$

$$\mathbf{c} = \begin{bmatrix} 9 & 0 & 0 & 0 & 0 & 0 \\ -9 & 4 & 0 & 0 & 0 & 0 \\ 0 & -4 & 1 & 0 & 0 & 0 \\ 0 & 0 & -1 & 1 & 0 & 0 \\ 0 & 0 & 0 & -1 & 1 & 0 \\ 0 & 0 & 0 & 0 & -1 & 1 \end{bmatrix} \quad (21)$$

Higher penalties are given to drifts near the base of the structure as those drifts tend to be the largest and most critical to control. The conversion to modal coordinates is taken care of using the mode shape matrix, Ψ , in the $\hat{\mathbf{Q}}$ term in Equation (21).

Simulated wireless sensors collect response data from each floor. Both acceleration and displacement feedback scenarios are simulated and artificially created Gaussian white noise is added to the acceleration and displacement response signals. The response of the structure to the combined effect of the seismically induced base acceleration and the actions of the control network is simulated using Newmark integration (average acceleration method) [19]. The time necessary to complete a control step is derived experimentally from the *Narada* wireless actuation units and is programmed into the simulation. The model size is varied from high (all six lateral modes considered) to low (only one mode considered) and the time required to complete the control step established. Those step sizes are given in Table 1.

Table 1. Sampling time derivation.

Modes Retained	Fixed Time (ms)	LQR Time (ms)	Estimator Time (ms)	Total Time (T_s) (ms)
6	16	1	24	41
5	16	0.7	18.3	35
4	16	0.5	13.5	30
3	16	0.3	9.7	26
2	16	0.2	6.8	23
1	16	0.1	3.9	20

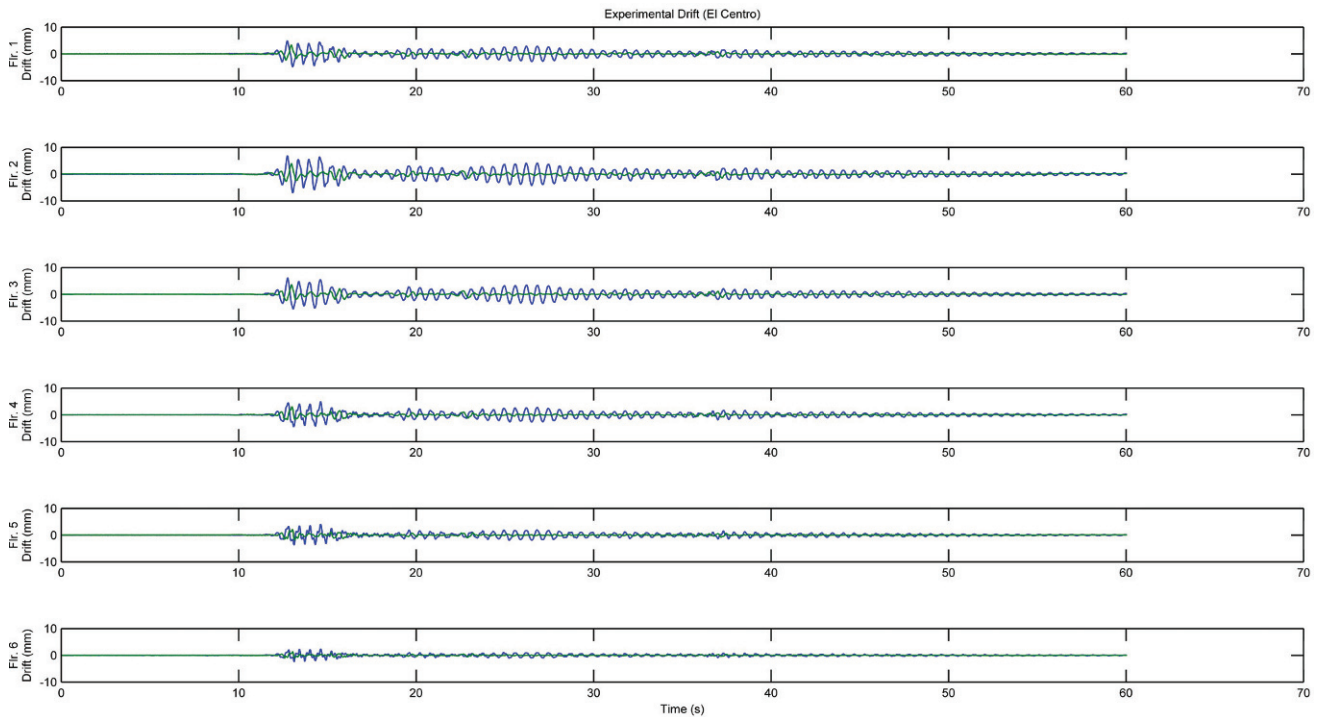


Fig. 4 Sample time-history results: interstory drift from experimental data run, 2 modal DOF model

From [Table 1](#), it is evident that the step size increases in an approximately affine manner in this range of model sizes considered and the slope is approximately 4 ms/DOF. In order to fully take advantage of the simulation environment, not only are the achievable ranges of time steps considered in this portion of the study, but the unachievable model-size/time step combinations are also considered to better visualize the effect of both latency and model size.

Experimental Study

The simulation study is designed to closely match the design and physical realities of the experimental study. The laboratory structure ([Figure 2](#)) is installed upon a 5 m x 5 m, 6 DOF shaking table. Ground excitations based on the scaled El Centro data record are applied to the structure in its lateral weak direction. Lateral braces are connected below each floor that support Lord Corp. RD-1005-3 magneto-rheological dampers. The braces are designed to be significantly stiffer than the columns to minimize any changes to interstory stiffness not associated directly with the dampers (and thus, not accounted for by the Bouc-Wen model). *Narada* wireless control units are placed on each floor with an extra unit at the floor to measure base response. For the experimental portion of the study, only acceleration tests are performed due to the impracticality of making direct measurements of displacement with respect to ground. For the acceleration tests, *Narada* units are supplied with accelerometers and compute acceleration relative to ground using data communicated from the base unit. The wireless sensors compute their state estimates and control forces based on the six available model sizes. Once control forces are computed, command voltages are computed from the lookup table and a voltage output on the actuation interface. A voltage to current converter translates the command voltage to a linearly scaled current level and applies it to the damper. After each test completes, the wireless sensors communicate their collected data, state estimates, and control forces to a laptop for later analysis.

Results

The wireless control network is designed to reject unwanted seismically induced energy in the structure and minimize damaging interstory drifts in the structure during earthquakes. An example time history plots showing the reduction in drift over the length of a time record (from the experimental portion of the study: acceleration feedback, model size of 2) is provided in [Figure 4](#). The figure depicts the baseline (uncontrolled) drift record and the controlled drift record with reduction in drift over the entire span of the earthquake. Three cost functions are adopted from Ohtori, *et al.* to better quantify the control performance [20]. The first cost function, J_1 , concerns the peak drift experienced during the earthquake at any floor

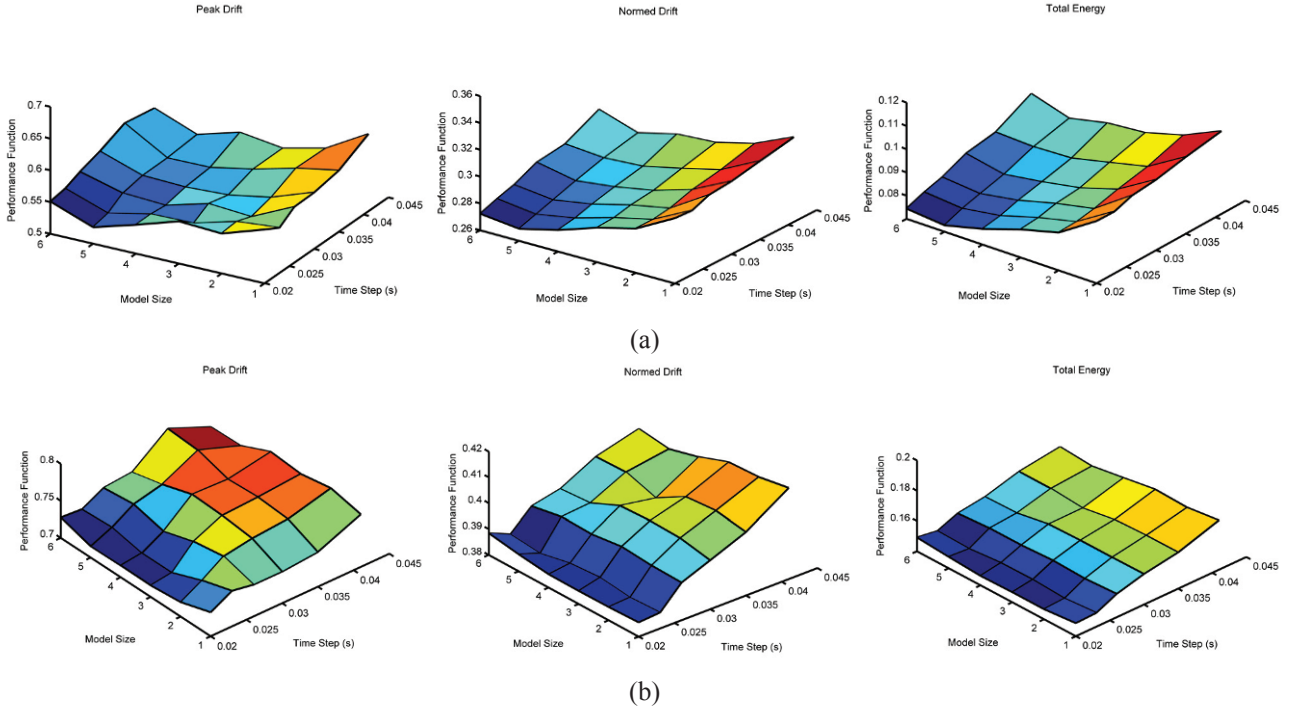


Fig. 5 3D simulation cost function profiles: (a) Acceleration feedback results; (b) Displacement feedback results

normalized by the same response found during the uncontrolled case:

$$J1 = \frac{\max_{Floor,t}(|drift_{controlled}|)}{\max_{Floor,t}(|drift_{uncontrolled}|)} \quad (22)$$

The second cost function, $J2$, is based on the norm of the drift time-series record and gives a picture of the performance of the controller in a more average sense:

$$J2 = \frac{\text{norm}(|drift_{controlled}|)}{\text{norm}(|drift_{uncontrolled}|)} \quad (23)$$

The final cost function, $J3$, relates to the energy in the system (a combination of kinetic and strain energy) and is also computed and averaged over the length of the record:

$$J3 = \frac{\left[\frac{1}{N} \sum_{i=1}^N \mathbf{z}_i^T \begin{bmatrix} \mathbf{K} & \mathbf{0} \\ \mathbf{0} & \mathbf{M} \end{bmatrix} \mathbf{z}_i \right]_{controlled}}{\left[\frac{1}{N} \sum_{i=1}^N \mathbf{z}_i^T \begin{bmatrix} \mathbf{K} & \mathbf{0} \\ \mathbf{0} & \mathbf{M} \end{bmatrix} \mathbf{z}_i \right]_{uncontrolled}} \quad (24)$$

These performance metrics are computed for each feedback type and for each model size. In the computational portion of the study, it is also possible to compute the cost functions for combinations of model size and time step length that are not achievable in reality. In the experimental portion of the study, only peak achievable time step lengths are tested for each model size. Three dimensional plots of the cost functions versus model size calculated during the computer simulation study are presented in Figure 5. In Figure 5(a), results from the acceleration study are presented; in Figure 5(b), the displacement results are presented. The acceleration feedback results show a strong tradeoff between model size and time step length as faster control action and larger model sizes both lead to improved performance. The displacement results are dominated by

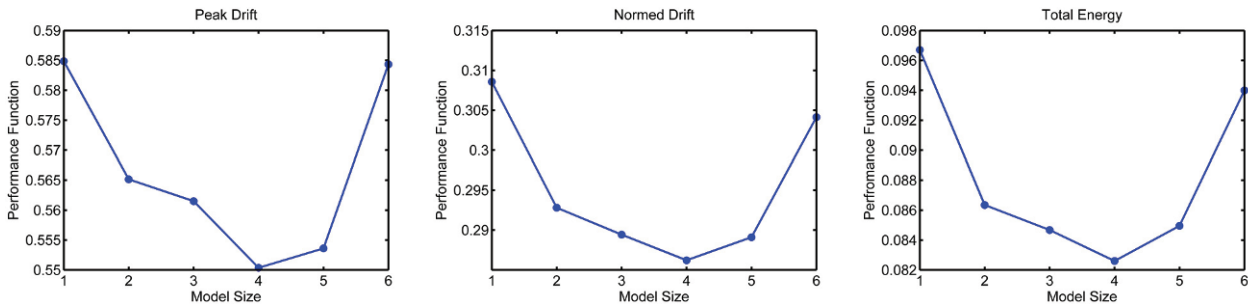


Fig. 6 Simulation cost function profiles of best-case achievable time step lengths: acceleration feedback

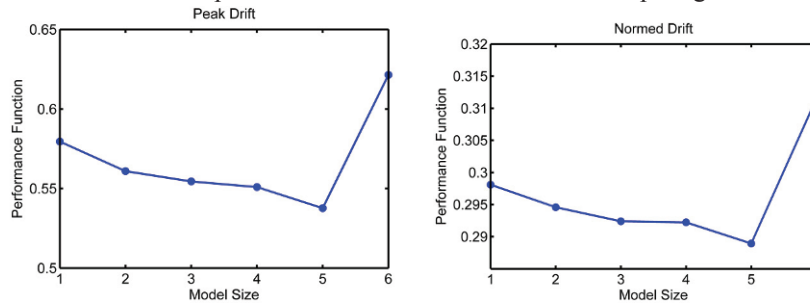


Fig. 7 Experimental peak drift cost function: acceleration feedback

the time step size, with little gain coming from increasing the model size. The simulation results for the best-case achievable combinations of model size and time step size for acceleration feedback are presented in Figure 6 and show the same trend. Similar results are evident from the experimental study, shown in Figure 7. Figure 7 shows a strong tradeoff between model size and time step length under acceleration feedback. Cost functions derived during the experimental portion of the study correlate generally well to those derived in the simulation study. For acceleration feedback, increasing the model size results in improved performance until either 4 or 5 modes are considered. As the model size grows past that, the time step begins to grow too large, and the controllers higher order models do not perform as well.

Discussion and Conclusions

This study was intended to explore the tradeoffs inherent in resource constrained wireless control networks with regard to model size and control time step length. As model size increases, the performance of the controller improves for a while. As the time step length grows larger, the control performance begins to suffer. This result is not particularly surprising given the magnitude of the control time step for the higher model sizes. The 6 DOF model requires a time step of 41 ms (equivalent to a sampling time of 24.4 Hz). Since the highest frequency mode of the structure has a natural frequency of 19.1 Hz, the ability of the slow 6 DOF controller to properly control this mode is rather limited at best. More interesting, is the simulation showing that, under displacement feedback (impractical to implement experimentally) the time step length dominates the effectiveness of the controller with little improvement gained by larger model sizes. This result suggests that, in this application, the major effect that ignored higher-order modes have on the control system is on the estimation side. In both cases, the effect that the ignored high-order modes have on the LQR controller is essentially the same (they are independent of feedback type). However, the acceleration feedback controller is much more dependent on the estimator than is the displacement feedback controller that has a direct measurement of a full half of the state vector.

Additional work should be performed beyond this tradeoff investigation to characterize the optimum model size for arbitrary structures and control laws. In addition, to show as directly as possible the effect of the modal truncation, more sophisticated model order reduction methods (*e.g.*, H-infinity control) were not used for this study in lieu of simple modal condensation. While good control performance was achieved using the simple modal condensation method, more advanced methods are available and their implementation should be investigated as a next step in this line of inquiry. In addition, it is expected the new wireless control devices capable of significantly faster floating point matrix multiplication operations will be available soon. These devices will change the balance between model size versus time step length and will allow for effective real-time control using significantly larger models. At the same time, model reduction will help to leverage those potential new devices for physical systems that are larger still. It is expected that a similar tradeoff will exist at higher model size, but that tradeoff will have to be investigated and characterized as well.

Acknowledgements

The author would like to express his gratitude to Prof. Jerome P. Lynch of the University of Michigan, Ann Arbor, MI, and Prof. C.-H. Loh of National Taiwan University, Taipei, R.O.C. as well as the students and staff of the National Center for Research in Earthquake Engineering (NCREE), Taipei, R.O.C. for their invaluable support.

References

- [1] Yao, J.T.P., *Concept of structural control*. Journal of the Structural Division, **98**(7): p. 1567-1574. 1972.
- [2] Housner, G.W., et al., *Structural control: past, present, and future*. Journal of Engineering Mechanics, **123**(9): p. 897-971. 1997.
- [3] Spencer, B.F. and S. Nagarajaiah, *State of the art of structural control*. Journal of Structural Engineering, **129**(7): p. 845-856. 2003.
- [4] Chu, S.Y., T.T. Soong, and A.M. Reinhorn, *Active, Hybrid, and Semi-Active Structural Control: a Design and Implementation Handbook*, New York, NY: Wiley. 2005.
- [5] Lynch, J.P. and K.J. Loh, *A summary review of wireless sensors and sensor networks for structural health monitoring*. The Shock and Vibration Digest, **38**(2): p. 91-128. 2006.
- [6] Celebi, M., *Seismic Instrumentation of Buildings (with Emphasis on Federal Buildings)*. United States Geologic Survey (USGS): Menlo Park, CA. 2002.
- [7] Kajima Corporation, *Advanced Structural Control Technologies, HiDAX: High Damping System in the Next Generation*, in *Technical Pamphlet 06-134E*. Kajima Corporation: Tokyo, Japan. 2006.
- [8] Nagayama, T., *Structural Health Monitoring Using Smart Sensors*, in *Department of Civil and Environmental Engineering*. University of Illinois at Urbana-Champaign: Urbana, IL. 2007.
- [9] Straser, E. and A.S. Kiremidjian, *Modular, Wireless Damage Monitoring System for Structures*. John A. Blume Earthquake Engineering Center: Stanford, CA. 1998.
- [10] Swartz, R.A., et al. *Design of a wireless sensor for scalable distributed in-network computation in a structural health monitoring system*. in *5th International Workshop on Structural Health Monitoring*. Stanford, CA. 2005.
- [11] Kawka, P.A. and A.G. Alleyne. *Stability and feedback control of wireless networked systems*. in *2005 American Control Conference*. Portland, OR. 2004.
- [12] Wang, Y., et al. *Wireless feedback structural control with embedded computing*. in *Proceedings of SPIE--11th International Symposium on Nondestructive Evaluation for Health Monitoring and Diagnostics*. San Diego, CA. 2006.
- [13] Loh, C.-H., et al., *Experimental verification of a wireless sensing and control system for structural control using MR dampers*. Earthquake Engineering and Structural Dynamics, **36**(10): p. 1303-1328. 2007.
- [14] Wang, Y., et al., *Decentralized civil structural control using real-time wireless sensing and embedded computing*. Smart Structures and Systems, **3**(3): p. 321-340. 2007.
- [15] Swartz, R.A. and J.P. Lynch, *Strategic utilization of limited bandwidth in a wireless control system for seismically excited civil structures*. Journal of Structural Engineering, **135**(5): p. 597-608. 2009.
- [16] Stengle, R.F., *Optimal Control and Estimation*, Mineola, NY: Dover Publications Inc. 1994.
- [17] Franklin, G.F., J.D. Powell, and A. Emami-Naeini, *Feedback Control of Dynamic Systems*. 4th ed, Upper Saddle River, NJ: Prentice Hall. 2002.
- [18] Lin, P.-Y., P.N. Roschke, and C.-H. Loh. *System identification and real application of a smart magneto-rheological damper*. in *2005 International Symposium on Intelligent Control*. Limassol, Cyprus. 2005.
- [19] Chopra, A.K., *Dynamics of Structures: Theory and Applications to Earthquake Engineering*, Upper Saddle River, NJ: Prentice Hall. 2001.
- [20] Ohtori, Y., R.E. Christenson, and B.F. Spencer, Jr., *Benchmark control problems for seismically excited nonlinear buildings*. Journal of Engineering Mechanics, **130**(4): p. 366-385. 2004.

Wind Turbine Structural Damping Control for Tower Load Reduction

A. Rodríguez T.^{1*}, C.E. Carcangiu¹, I. Pineda¹, T. Fischer², B. Kuhnle², M. Scheu² and M. Martin¹

¹Alstom Wind, Roc Boronat 78, 08005 Barcelona (Spain)

²Endowed Chair of Wind Energy, Universität Stuttgart, Allmandring 5B, D-70569 Stuttgart (Germany)

* e-mail: arturo.rodriquez-tsouroukdissian@power.alstom.com

ABSTRACT

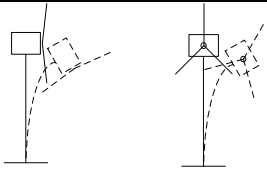
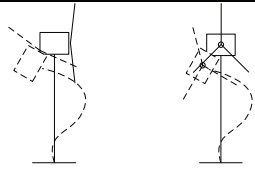
Being wind a random excitation, wind turbines experience complex dynamic load conditions. This is becoming a growing challenge for designing larger, tall wind turbine towers and substructures in both onshore and offshore wind farms. In order to keep the structural integrity of multi-megawatt wind turbine, different structural damping strategies have been implemented in the past years like tuned mass dampers. Other techniques rely on the available control actions, as the generator torque control to reduce the side-to-side excitation and the blade pitch control to limit fore-aft movements. All those strategies aim at limiting fatigue and buckling loads, as well as the dynamic interaction with the rotor harmonics without a parallel increase of material (i.e. of costs). It was proven that the achievable load reduction in significant design cases can be as high as 20% and the tower mass can consequently be reduced by up to 10%.

Keywords: Extreme & Fatigue Loads, Wind Turbine Structural Control, Passive and semi-active dampers.

INTRODUCTION

Being wind a random excitation, wind turbines experience complex dynamic load conditions. This is becoming a growing challenge for designing larger, tall wind turbine towers and substructures in both onshore and offshore wind farms. In order to keep the structural integrity of multi-megawatt wind turbine, different structural damping strategies have been implemented in the past years like tuned mass dampers. Other techniques rely on the available control actions, as the generator torque control to reduce the side-to-side excitation and the blade pitch control to limit fore-aft movements. All those strategies aim at limiting fatigue and buckling loads, as well as the dynamic interaction with the rotor harmonics without a parallel increase of material (i.e. of costs). It was proven that the achievable load reduction in significant design cases can be as high as 20% and the tower mass can consequently be reduced by up to 10%.

As wind turbines grow taller, the larger the rated power of the generators is; therefore, the larger is the impact of the turbulent wind and the thrust on the tower. Moreover, as wind turbines get taller, the Eigen frequencies go down, making the wind turbine modes proximate to resonant induced vibrations, due to rotor harmonic closeness. It is essential to avoid this closeness, in order to avoid severe damages, which may grow to a total destruction of the turbine. For a wind turbine tower, the movements in the direction orthogonal to the rotor blade plane, called Fore-Aft-Movement and parallel to the rotor blade plane, called Side-to-Side-Movement have to be distinguished as seen in the next table. The most critical Eigen modes for the tower are the first and the second Eigen mode as they have energetically the highest potential. The degrees-of-freedom and loads, which the wind turbine is subjected is shown in [Figure 1](#).

MODE NAME	1 st mode	2 nd mode
	Mode	Mode
Fore aft (FA) & Side to Side (S2S)		

Structural excitation of an onshore wind turbine is generally based only on wind loads. Several investigations have been done in the past to dissipate dynamic energy consisting in vibrations. Materials and construction details influence this behavior in a way that a high level of damping guarantees a more efficient dissipation of energy. The seismic reaction of the turbine, which increases with a taller and heavier tower, can be investigated with a module in GL Bladed®, multi body software for the calculation of wind turbines [1]. It is one of the most widely used software for

the certification process and will be employed for all the investigations about the integration of damping systems in wind turbines. The most important factor during a wind turbine's lifetime is the wind impact on the structure. The influence of the wind on the turbine is defined by different parameters. First of all, every turbine has a specified wind class, which characterizes a specific maximum certification wind speed for the wind turbine and therefore an application area. Every wind class has in addition a specific turbulence which is classified by a difference of the wind from the actual mean wind speed and is 3-dimensional. Rotor diameter, hub height, cut-in and cut-out wind speed influence how strong the impact of the wind on the turbine is.

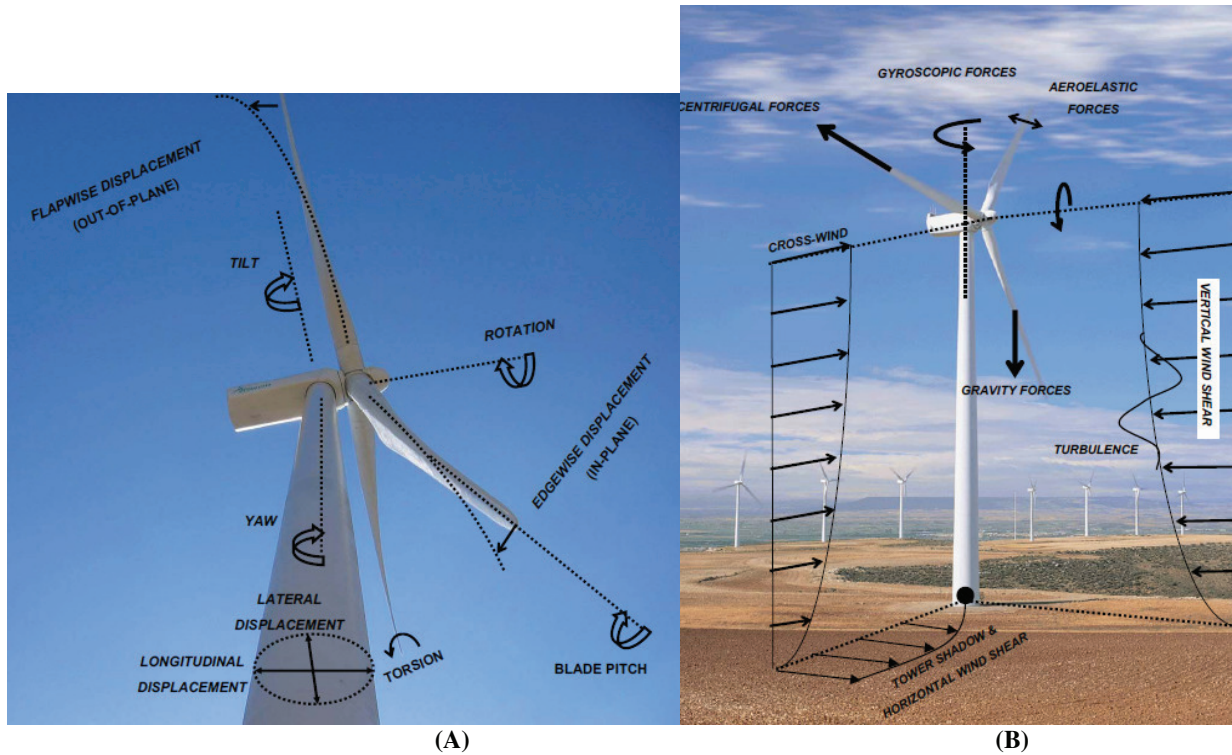


Figure 1 - (A) represents the degrees-of-freedom of the wind turbine and (B) represents the loads acting on the wind turbine.

Up to now, passive, semi-active, active, and hybrid damping devices have been mainly used in buildings and bridges to solve wind excitation or seismic protection problems [1]. So far only passive devices like tuned mass dampers have been integrated in wind turbines (Figure 2). Compared to stiff buildings, wind turbine structures are slender and tall. However different analysis's already proved that the potential for load reduction in the tower is big. As the normal damping ratio is relatively small, a small increase already strongly affects the tower loads and highly decreases them [13]. The technological transfer is a big challenge due to the small space availabilities, the strong demand in reliability and the amount of excitation energy to be dissipated. On the other hand, big benefits are expected and it could lead to completely new configurations for towers concerning height, diameter and wall thickness, which had not been considered so far.

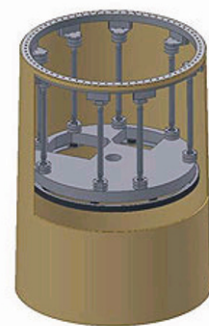


Figure 2 - Passive Tuned Mass Damper (Wind Turbine) by ESM GmbH

Control and regulation can be distinguished into: (i) Rotor speed control using pitch actuators, (ii) Rotor speed control using generator torque control. Up to now mostly single-input-single-output (SISO) loops have been used, and the input signals are: (i) generator speed and (ii) generator power. These two signals are used in the SISO, or more advanced in a combination of multiple SISO's, to regulate as well pitch as torque demand. Upcoming multiple-input-multiple-output (MIMO) control loops use several inputs as there are accelerations of nacelle, blades or tower, combining all the measured signals to command. These advanced controls are not only designed to optimize the power production but also to mitigate loads on the blades and tower [8].

TOGGLE-BRACE SYSTEM DESCRIPTION

The integration of a damping system into a wind turbine tower is a challenging task. The correct position for the damper has to be found in both height and horizontal distribution. Also, a supporting structure, which increases the dampers effectiveness, is advised (i.e. bracing). Compared to already known and used configurations in stiff buildings, the integration in a slender structure like a wind turbine seems to be easier, because of the higher deflections. As damping systems in general need deflection for the dissipation of energy, a higher movement of the tower is in the first approach helpful for an effective application.

Depending on the configuration, a magnification of the damper force in plane and therefore of the dissipated energy can be achieved. It has to be kept in mind, that the magnification factor is only valid for a stiff system. Bending levels cause in reality a decreased magnification factor [13]. First, mathematical basics are shown roughly, which shall help to get the idea of the sense from certain damper configurations [12]. In summary, there are two main ideas for toggle brace systems:

- The amount of magnification of the damping force depends on the geometry
- The device displacements can be greater than the structural drift

Device displacement:

$$u_D = f \cdot u \quad \text{Eq. 1}$$

u_D	Device displacement
u	Structural drift
f	Magnification factor

Transfused damping force:

$$F = f \cdot F_D \quad \text{Eq. 2}$$

F	Force on the structure
F_D	Force along damper axis
f	Magnification factor

Damping force:

$$F_D = C_o \cdot |\dot{u}(t)|^\alpha \text{sgn}(\dot{u}(t)) \quad \text{Eq. 3}$$

F_D	Force along damper axis
C_o	Damping coefficient
$\dot{u}(t)$	Relative velocity between the ends of the damper along its axis
$\text{sgn}(\dot{u}(t))$	Signum function of the velocity
α	Damper Exponent, values between 0.3 and 1.0 → Providing a velocity limit. For velocities above the limit, damping force is constant

Damping ratio:

$$\xi_D = \frac{T_k \sum_j C_j \phi_{rj}^2 f_j^2}{4\pi \sum_i m_i \phi_i^2} \quad \text{Eq. 4}$$

T	Period of vibration of k^{th} mode of the structure
C_j	Damping coefficient of the damper j
ϕ_{rj}	Reactive modal displacement of the damper j of the k^{th} vibration mode
f_j	Magnification factor of damper j
m_i	Reactive weight on top of the damping system or at level i
ϕ_i	Modal displacement on top of the damping system or at level i

The magnification factor has an important influence on the damper force (consequently damping ratio). The magnification factor is realized by a certain alignment of so-called damper braces. Several configurations for bracing systems have been studied. All of them use different geometrical alignments to reach high magnification factors. Typical values for magnification factors are between 2.5 and 3.5 for the configurations presented in this assignment. Theoretically, magnification factors can reach values up to infinity [3]. These are not taken into account, as they do not fit to geometrical restrictions like tower diameter, maximal installation height, minimum installation angles, etc. All magnification factors mentioned in the following consider a fixed installation height (the installation height constitutes the distance between the upper and the lower connection of the damper assembly). The damping device configurations studied are shown as follows:

1. Scissor-jack bracing

The scissor-jack, originally developed by [3] for buildings and adjusted for wind turbines in [10], can reach values of magnification factor up to 2.2 to 2.8. The variation of the angles ψ and θ will increase the magnification factor as seen in Figure 3. A big advantage of the scissor-jack [3] system is the ability to be installed even in tight space. Even then, the amplification factor can reach relatively high values, making it an interesting solution. Another important point is the connection between Beam and Column. In case of a “Rigid-Simple” connection, a higher damping ratio than in case of a “Simple-Rigid” connection can be achieved. The geometry of a Scissor-jack brace system is comparatively to other bracing systems relatively complicated. In order to achieve a high magnification factor and a reliable product, this device is not playing a role for further investigations. The magnification factor of The Scissor-jack geometry is defined as:

$$f = \frac{\tan \theta}{\cos \psi} \quad \text{Eq. 5}$$

Figure 3 - Scissor-jack bracing geometric alignment (left) and deformed (right)

2. Lower-toggle bracing

The lower toggle bracing configuration, originally developed by [3] for buildings and adjusted for wind turbines in [10], depends on many different values and the limits, which are not only given by the stroke of the damper, some general constraints have to be listed. First of all, the angle θ_1 has to be smaller than the diagonal connection between the lower left boundary and the upper right boundary to ensure maneuverability. For every specific possible angle θ_1 , it has to be ensured, that the brace is simply not longer than D . The last constraint is given by the maximal possible deflection in the horizontal plane. It has to be prohibited, that the braces snap through. The magnification factor of the lower-toggle bracing system is defined as:

$$f = \frac{\sin \theta_2 \sin(\theta_1 + \theta_3)}{\cos(\theta_1 + \theta_2)} \quad \text{Eq. 6}$$

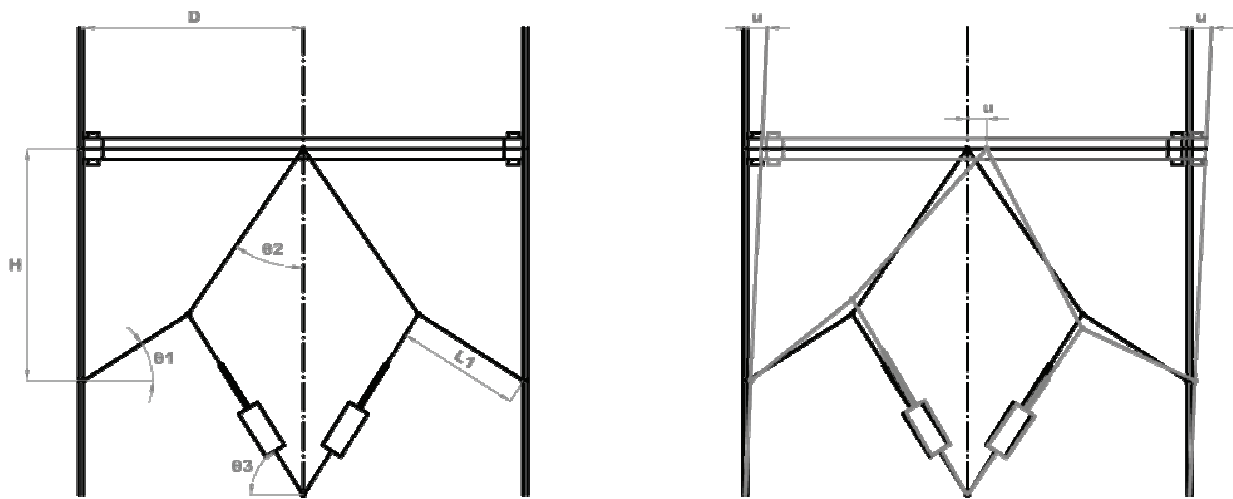


Figure 4 - Lower-toggle bracing geometry alignment (left) and deformed (right) [2]

Further details may be found in “Wind turbine structural damping ratio augmentation hybrid device” by A. Rodriguez-Tsouroukdissian [2]. The lower-toggle configuration can achieve magnification factors up to 2.2 with the restrictions fixed for this example [3]. Compared to other systems, the Lower-toggle assembly has big space requirements. Additionally, the magnification factor does not reach the highest values. Therefore, this geometrical alignment is not taken into account for further project steps.

3. Upper-toggle bracing

The upper toggle bracing, , originally developed by [3] for buildings and adjusted for wind turbines in [10], follows the same constraints as for the lower toggle bracing. Up to now, the upper-toggle bracing provides the highest possible magnification factor. Values are getting up to 3.191 [3]. As it can be seen in Figure 5, the magnification factor depends on the brace-length, the installation height “H” and the three angles.

$$f = \frac{\sin \theta_2}{\cos(\theta_1 + \theta_2)} + \cos(\theta_2) \quad \text{Eq. 7}$$

Further information can be found in [10]. The upper-toggle-bracing needs less space compared to the lower-toggle. Additionally, the magnification factor is very high. For this project, the upper-toggle assembly seems to be the most suitable one.

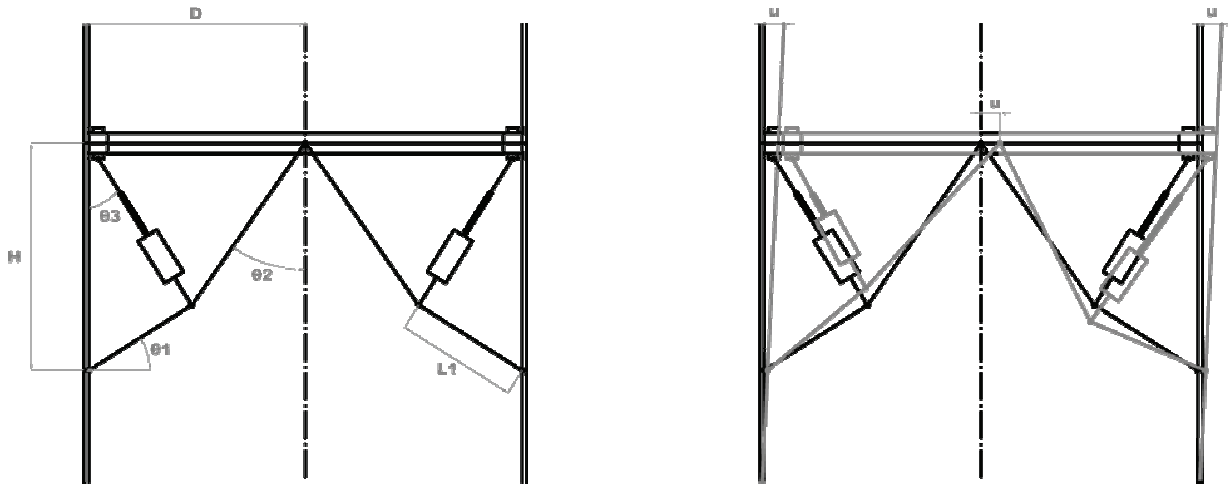


Figure 5 - Upper-toggle bracing geometry alignment (left) and deformed (right) [2]

4. Reverse-toggle and other bracing systems

The difference between the reverse-toggle and the upper-toggle is the rigid 90° connection between damper brace and beam. A disadvantage of this alignment would be the need to strengthen the connection between damper and brace regarding cyclic loadings. Because of that, the reverse-upper-toggle is not taken into account for further research, as the upper-toggle system seems to be the optimal configuration for this project.

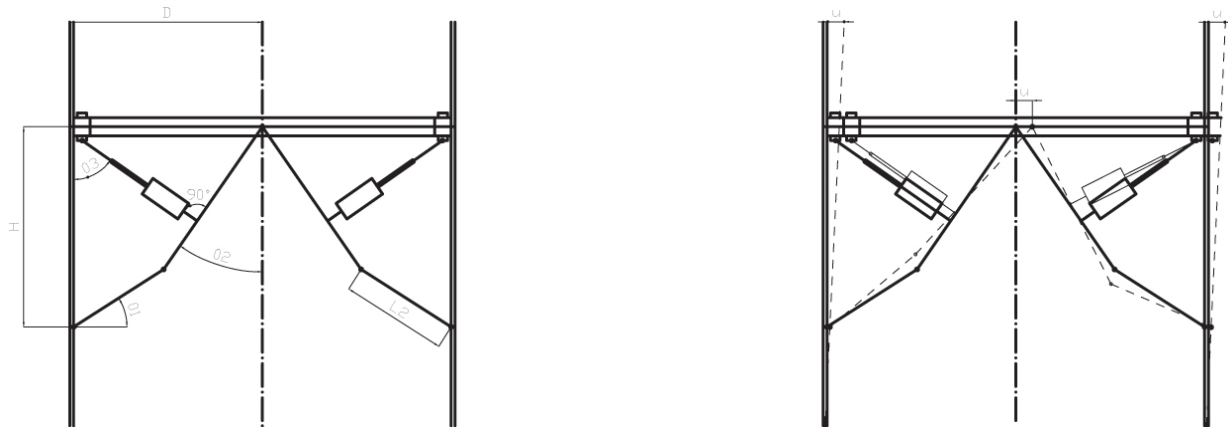
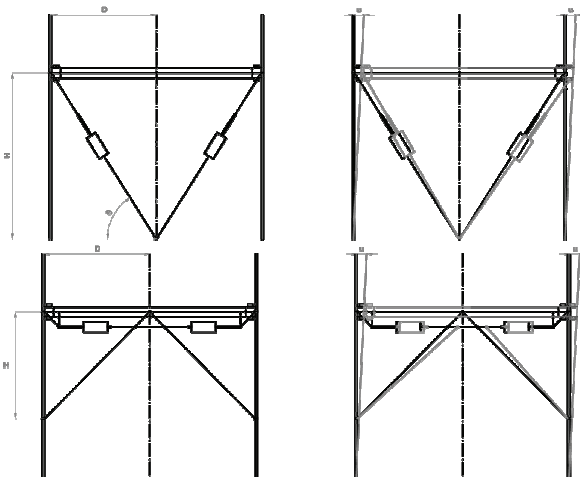


Figure 6 - Reverse-toggle bracing geometry alignment (left) and deformed (right) [2]

Other bracing systems like a simple diagonal bracing (

Figure 7, top), which has a magnification factor below one ($f = \cos(\theta)$), or a chevron bracing (

Figure 7, bottom) with a magnification factor of one ($f = 1$), all toggle brace configurations can provide a higher damper force with a damper of the same size and technical characteristics. This magnification allows achieving a demanded damping with a comparatively small damper. As the bracing geometry can be manufactured in a simple way (most components are standard parts), and the damper itself is the most important cost driver, this geometrical assembly will have a positive effect of the all in all damping device costs definitely.



**Figure 7 - Diagonal bracing (top);
chevron bracing (bottom) [2]**

Optimal toggle configuration

A specific toggle configuration has to be chosen due to the present geometry. It has to be kept in mind that the magnification factor found for the upper toggle is in most of the cases larger than for the other ones. Thus the upper toggle is more efficient in the energy dissipation than the other configurations. On the other hand, integration and simulation of the upper bar toggle is more difficult than of the other configurations. The scissor jack can be assembled outside the tower and added afterwards, the lower toggle's damper does not need to be lifted. But for dissipation reasons, the decision is made to use the upper configuration as it is the most cost effective if it is assumed that the damper itself, is the most expensive part of the assembly. With the same amount of demanded damper force, a higher reduction can be observed with the toggle bracing configurations compared to the diagonal braces. It has additionally to be mentioned that the damping ratio itself as well is affected by the choice of the configuration. The same damper, which offers for example an increase of the damping ratio up to 5% of critical in a chevron brace, increases the damping ratio installed in a toggle brace up to 30-50% of critical [10]. Even though, an optimal solution is to insert these toggle-damping systems at each flange, is not economical feasible and more costly than just using more steel for the tower. Therefore, after multiple coupled structural and aerolastic analysis (control included), the most optimal solution is at the base of the tower from the structural and mechatronic point of view, as well as economical and O&M point of view.

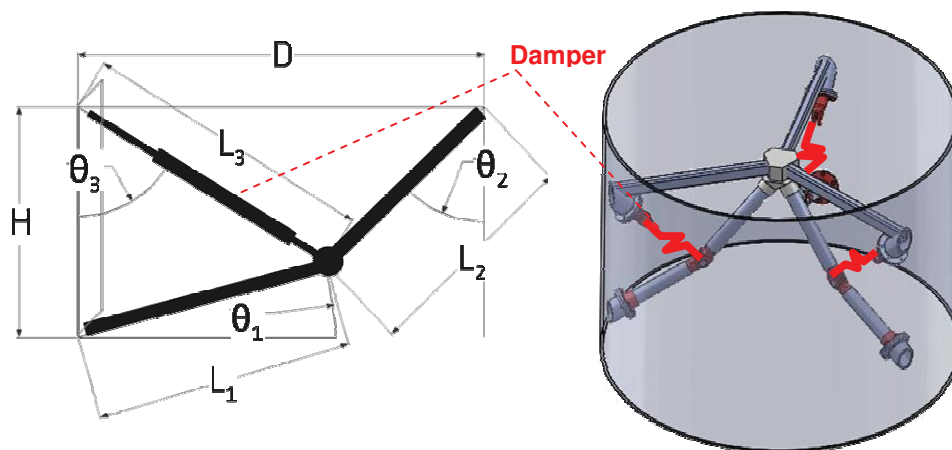


Figure 8 - Upper toggle brace sketch and tower implementation [2]

WIND TURBINE SPECIFICATION

The ECO100 platform is a modern 3MW wind turbine, certified for IEC IIA sites. As the design of the turbine is provided as an input for this project, the machine properties are only listed. The turbine characteristics are set as fixed in this project to perform a sensibility analysis between the baseline wind turbine and the ones with damper. The performance of the dampers to reduce the aerodynamics loads was tested in a full steel ECO100 90m tower and a hybrid (1st 10m of reinforced concrete and the remaining 80m of full steel). The ECO100 transfers the aerodynamic loads through a the ALSTOM PURE TORQUE™, which is a cast iron main frame that transfers all the aerodynamic induced loads and moments from the rotor to the tower. The low speed shaft of the drive train only perceives torque, making more robust and reliable the gearbox component. Thinking in a robust and reliable product is crucial and part of the ALSTOM design methodology; therefore, the same methodology was applied for the inclusion of damping devices in the tower. Not only the structural point of view was studied, by in parallel, the overall control of the wind turbine, the operation and maintenance, among many more. The geometrical integration is manly driven by the optimization of the geometry like restrictions in the tower diameter, geometry of the elevator and the cable system.

An optimization tool where all geometrical constraints, like the diameter and the installation height (total height of the damper assembly in the tower) was used as a design basis, planned to install the dampers at 3 station heights in the tower. These stations should be close to the flanges, because there are already platforms installed, where the maintenance would be possible. Additionally, these tower sections are very stiff and can therefore provide an efficient transmission of the damping forces into the tower. Figure 9 shows a possible assembly of the toggle brace damping system in the ECO100 T90 hybrid tower. It is planned to install the dampers above and beneath a flange or in only one plate close to a flange. The dampers themselves are planned to be installed in a 120° shift relative to each other as

seen in Figure 8. This assembly should provide a wide range of frequencies which can be damped. Furthermore, it is assumed, that the 120° shift provides a symmetrical behavior regarding stiffness added to the structure and directional changes of the excitation. Table 1 shows the specification of the chosen wind turbine.

Table 1: ECO100 T90 data overview

Wind turbine Class	IEC/EN-61400-1 IIA
Ideal mean annual wind speed	8.5m/s
Reference wind speed	42.5m/s
Extreme gust speed	59.5 m/s
Cut-in wind speed	3m/s
Cut-out wind speed	25m/s
Instant cut out wind speed	34m/s – 40m/s
Vertical wind inclination	8°
Rated power	3MW
Power density	2.66m ² /kW
Rotor diameter	100.8m
Swept area	7980m ²
Rotor yaw	Up wind
Number of blades	3
Speed range	7.94-14.3 r.p.m.
Gearbox cooling system	Active, forced ventilation
Gearbox lubrication	Forced oil lubrication
Control	Variable speed, individual pitch control
Ambient operational temperature	-10 to +40 degrees
Standstill temperature	t<-20 or t>+50 degrees
Lightning protection	IEC-61024 Level 1

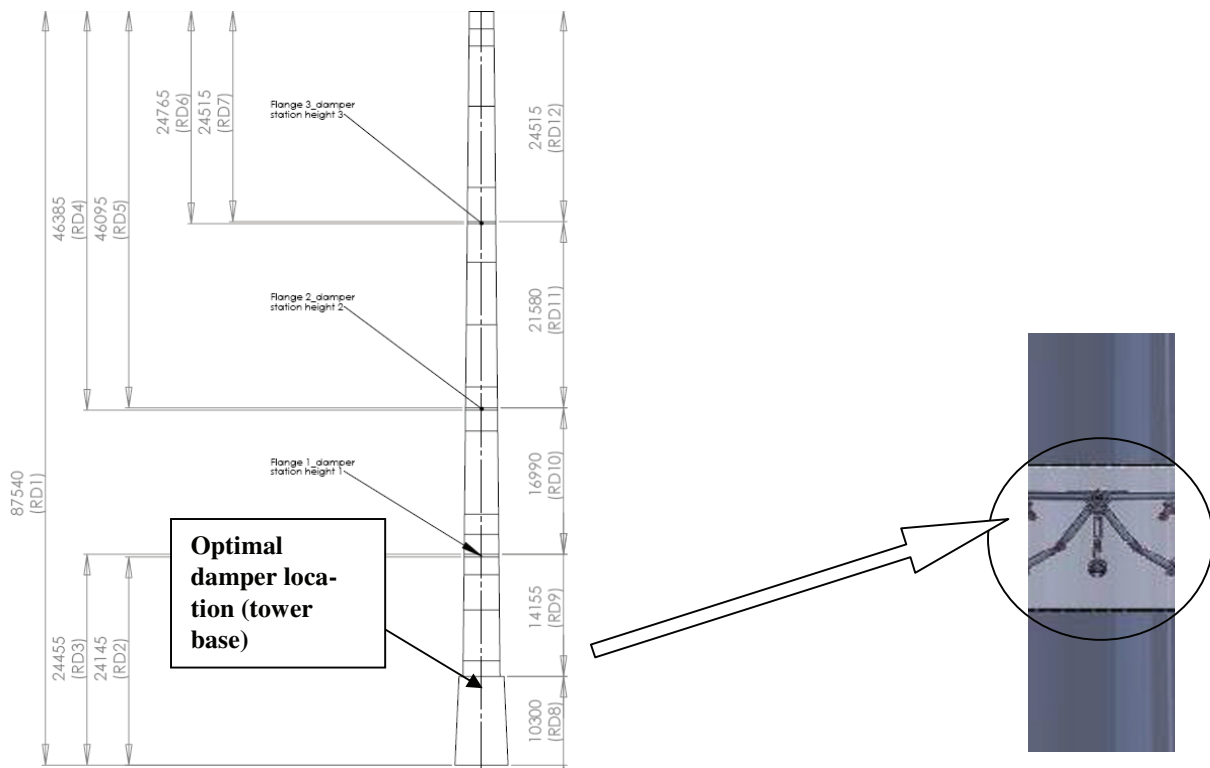


Figure 9 - Geometrical integration of 3 damping stations in the tower – global (left) and detailed view (right)

STRUCTURAL INFLUENCE OF THE DAMPING SYSTEMS

The dampers as seen in [Figure 8](#), have been studied in detailed in order to perceive hot spots in the tower and or the connecting points. The change in the eigenfrequency of wind turbines is tuned very sensitively due to the excitation frequency as a rotational system and the eigenfrequency of the tower system in combination with integrated damper systems is very hard to estimate, problems based on resonance events can occur [13]. Hysteretic dampers for example, especially with high stiffness and strength tend to form an alternate structural system and change the structures behavior more than just simply adding damping. However, an investigation [9] proved that the change in period is negligible for typical levels of structural damping up to 20% damping of critical. An increase of maximal 2% can be expected. It has also to be taken into account that the devices tend to have a larger effect on displacements, but only little effect on accelerations at very long periods. As energy dissipation is related to the stiffness of the system, an increase is desired. Also the damping ratio increases with an increase of the relation between the stiffness of the damper and the one of the structure. With a ratio of 1 concerning the stiffness, damping values in an order of 10-15% are a realistic target. A possibility would be to use a viscous damper and a friction damper in series to limit the maximum load for the viscous damper as friction dampers offer a rapid initial reduction in displacements with the vibrations continuing without further damping. In further cycles, there is no noticeable reduction of the loads due to the friction damper. The added damping by a viscous damper increases with the increase of the damping coefficient of the damper, but more slowly. This effect is observed, as an increased value of the damper coefficient reduces displacements, but the dissipated energy is proportional to the velocity, which is again proportional to the displacement. Thus, an increased damper coefficient leads to an increased reduction of the displacements and therefore to a smaller amount of dissipated energy. Thus, in theory, it can be proven, that for a fatigue driven tower, viscous damping is advantageous in contrast to extreme case driven towers, where friction dampers are more advantageous.

The magnification depends mainly on the flexibility of the assembly. It has also to be taken into account that gaps in the joints, due to manufacturing reasons, exist and lower the factor even more. As results of the elastic deformation of the configuration, the system not only behaves viscous. This may lead to an increased stiffness of the system and therefore a slippage in the eigenfrequencies. Nevertheless, high reductions in both the maximum relative displacement responses and the maximum absolute acceleration responses can be expected.

Due to the tolerance in manufacturing and slippage and distortion in the assembly, it has to be taken into account that changes from 0.3° to 0.5° may occur [3]. Considering the connections to the tower, stiff flanges are proposed to profit from the elastic behavior of the beams as an additional energy dissipating feature. The connection to the damper has to be realized by a spherical bearing to eliminate angular discrepancy and to provide all degrees of freedom to move. A spherical bearing also pretends moments to be transferred to the damper, which is, especially in terms of a long lifetime, very important. In reality, the approximation of small movements for the geometrical relations do not fit, which leads to a slightly higher magnification factor if the displacement is positive and a slightly lower factor if the displacement is negative [3]. Another important structural component is the connection to the tower. Investigation shows, that a rigid connection to the tower increases the real magnification factor [13]. Overall, it has to be said, that the decrement in displacement is due to a combination of an increased stiffness and an increased damping, while the decrease of acceleration is mainly due to the increased damping. The increase of the damping force due to an increased damping coefficient is not linear. The most important aspect concerning the efficiency of the damper system is in the stiffness of the supporting bracing system. As an effect on the structure, a reduction response takes always place hand in hand with a reduction of the shear response of the building. The energy dissipation of the damping device is released by form of heat, so steel fins surrounding the damper chamber have been considered. Moreover, temperature variation inside the tower has been considered to be small, due to the contained temperature gradient inside the tower and mechanical properties of the damping material used.

STRUCTURAL CONTROL METHOD

The tower of the wind turbine with its slender structure and structural components in the nacelle are very vulnerable to accelerations. Another important value is the deflection which causes high forces and moments in the tower base and therefore high stresses. Thus many different contributions affect the loads on a wind turbine and many different strategies in semi-active control and regulation can be applied as follows:

- relative displacements of the structures

- minimize displacements between the flanges
- minimize absolute accelerations
- minimize the structural response in the fundamental mode by weighting the measured absolute accelerations

It has to be kept in mind, that all the regulation approaches are based on acceleration. Therefore, a stable mathematical model is necessary for a good modeling of the system behavior. Also, an integrated signal out of the acceleration without initial velocity can cause an offset and even leads to a velocity run-away signal. The dampers are connected from the top part of a lower tower section to the bottom part of the subsequent tower section. This geometrical configuration magnifies the damping force by a factor of 2.5 to 3.5. The dampers can be passive viscous fluid dampers, semi-active magnetorheological (MR) dampers, or active hydraulic viscous fluid dampers. The dampers not only damp 1st fore-aft and 1st side-to-side tower modes, but as being semi-active, and/or active devices, the damping ratio can be tuned for a broader range of frequencies conforming multiple tower modes like the 2nd tower bending and/or 3rd rotational tower modes. The tower dampers were simulated using GH Bladed, with a specific add-on for this scope. The local tower acceleration signals are used to feed the new control loop, as depicted in Figure 10, providing a damper force demand as an output.

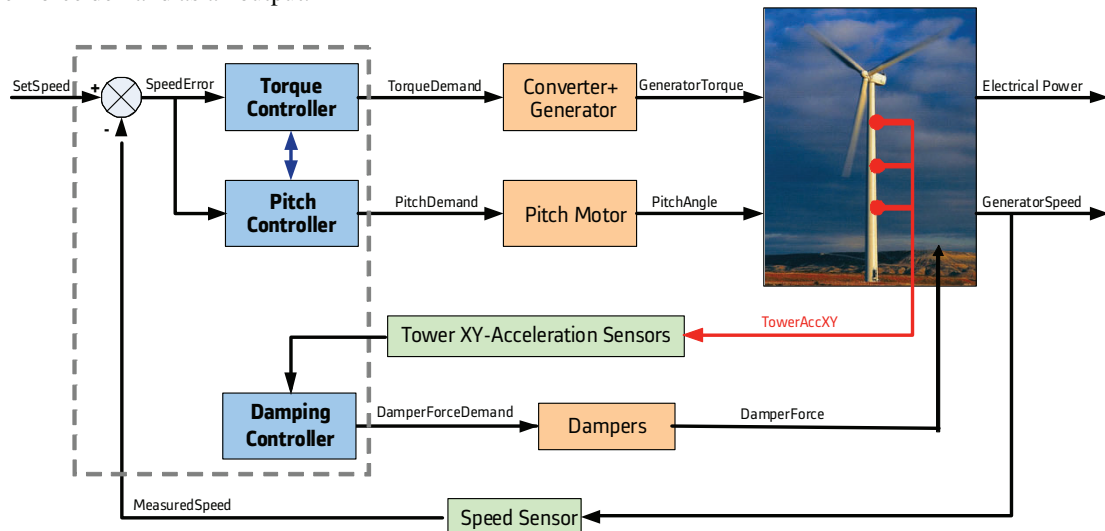


Figure 10 - Wind turbine control System with tower damping loop.

Neglecting active dampers due to their complexity and cost, passive and semi-active damper types were selected to be integrated into the wind turbine aero servo-elastic model of the ALSTOM ECO100 3MW (D = 100 m, H = 90 m) wind turbine provided with two tower configurations (steel and hybrid steel-concrete). A specific release of the code GL-Bladed [5] was used for the simulations, tailored for the scope. The tower acceleration signals were used to feed a new control loop (fictitious for the passive case, being not necessary in the real wind turbine), as depicted in Figure 1, giving the damper force demand as an output.

Figure 11 shows the principal of the control system. It consists of an acceleration sensor, which is marked as “Sensor 1”, damper force sensors called “Sensor 2 & 3” and, a data acquisition card “D.A.C.” where all signals are passing through, a Computer “PC” where the control algorithm is integrated and in the end a “Command signal”, what would be a current e.g. in case of a magnetorheological damper [2]. The input signal for the control proposes stated within this project is the tower acceleration. This acceleration is integrated over time to get the tower velocity. The velocity is used to generate the damper forces. As mentioned in the beginning, the damper forces are proportional to the velocity in case of a viscoelastic damper. To identify which damper has to be used, the excitation is split up in 3 components, which constitute the dampers in the 120° shift. Detailed information about the control used for the integration of the damper in the Bladed® model can be found in [8].

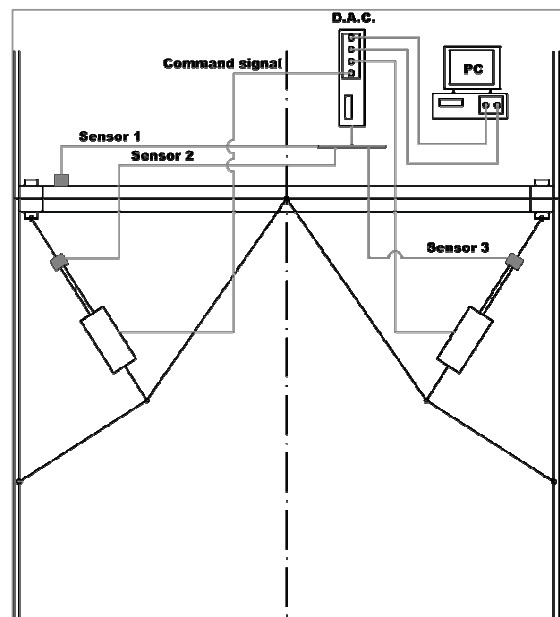


Figure 11 – Control scheme of damping device [2]

RESULTS

Several issues have been clarified first regarding the dimensioning and integration of dampers into a wind turbine. Generally, it has been found that the higher the dampers resultant force is the higher reductions are to be expected. The upper limit was hence set based on the local maximum of the ratio between required force and corresponding load reduction. The advantage of using 3-dampers 120-degrees out-of-phase system was proven with respect to 2 orthogonal dampers, being also less sensible to wind direction changes. The required resultant force resultant is more uniformly distributed among the dampers, (which can be smaller) and to the tower. The second design feature addressed was the installation height. The maximum effect will be obtained, where the highest deflections occurs. The design indication was to install the damping system as high as possible, but tower integration constraints arise. The optimum installation height obtained from simulations accounted for those limitation and results in positioning the dampers at nearly 87% of the whole tower height (large relative displacement between top and bottom tower cans). The use of several damping systems placed at different heights along the tower was preliminary investigated, which is common in civil application. Since the effect resulted minor, the choice of only 1 system in the upper part was finally preferred. Being the semi-active dampers attractive for the highest controllability and their potential for extreme events, such as wind gusts, a dedicated study was carried out on them. In Figure 12, the fore-aft tower base moment computed for a DLC-1.6 [6] is shown as one application example for both semi-active and passive damping. A clear reduction in the maximum is achieved when the semi-active is triggered; the generator speed derivative is enabled. It should be also noted how the oscillations after an extreme event are suppressed by both systems, and the total damping ratio increased. Nevertheless, the effectiveness of the semi-active system is highly dependent on the used trigger and on turbulent conditions, so that the passive system was thought to be preferable. Further load details see [12].

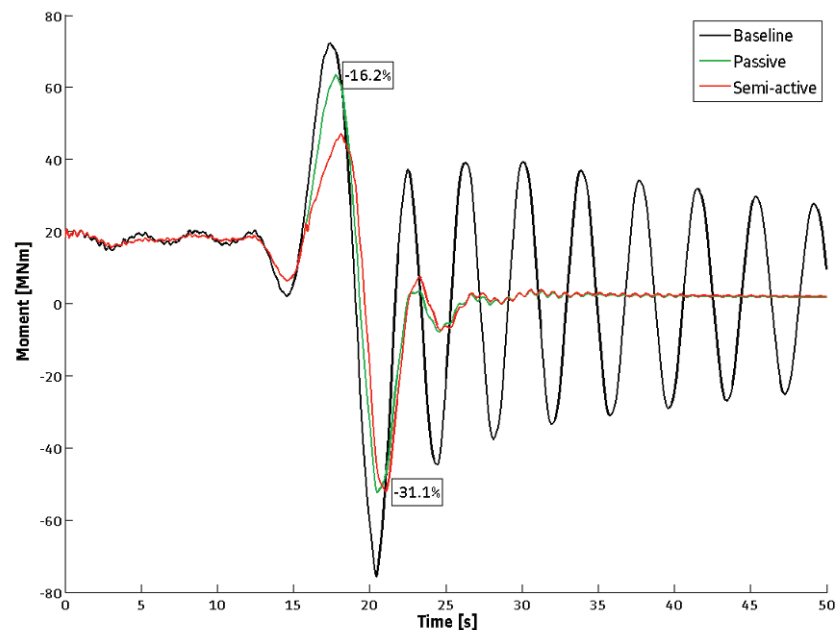


Figure 12 - Tower base fore-aft moment: semi-active vs. passive damping system

The loads reduction obtained for both the hybrid and the steel tower are finally presented. It is clearly appreciable the higher potential when adopting the steel configuration, as shown in Table 2 for the extreme and fatigue loads.

Table 2 Extreme and Fatigue Load reductions

EXTREME	Mx	My	Mxy	Mz
Hybrid tower	-15%	-7%	-13%	0%
Steel tower	-20%	-12%	-21%	-1%
FATIGUE (SN = 5)	Mx	My	-	-

Hybrid tower	-6.4%	-10.5%	-	-
Steel tower	-7.6%	-13.0%	-	-

CONCLUSIONS

Promising indications have been obtained regarding the effectiveness of viscous damper systems integrated into the tower of a wind turbine for structural load mitigation. The main tower base bending moments can be reduced up to 20% in the extreme cases and around 10% in fatigue. Several aspects were considered and clarified regarding the design and implementation of such devices, including practical implementation issues such as:

- Maximum damper force
- Number of dampers in-plane (i.e. per damping system)
- Installation height and number of damping systems
- Passive vs. Semi-active system
- Economics

In particular, a comprehensive economical analysis has been finally performed. The cost for the damping system has been estimated including manufacturing and transportation costs. Even though, special dampers are required for the application (able to bear the high number of cycles imposed by the wind turbine operation) a valuable decrease in the tower material still prevailed over the benefits. Furthermore, no overloading of other system quantities is found, as it is the case when active systems are used, such as generator-torque or tower-feedback controller. As future work, the effects of applying these devices on offshore wind turbines will be investigated. Here due to the presence of waves and especially for cases of non-availability, the implementation of semi-active damper systems will be very effective and will enable large optimization potentials and/or installations of economical monopile support structures in deeper waters. Preliminary results show promising load reduction along the tower. Moreover, big emphasis has been placed on the importance of applying these devices on offshore wind turbines. As waves are always acting, when the wind turbine is non-available, these devices will damp these extreme and normal state hydrodynamic loads without comprising the structural integrity of the whole wind turbine. The system is expected to be an excellent solution for tall wind turbine towers and substructures in both onshore and offshore (near-shore & floating) wind farms.

REFERENCES

- [1] Bossanyi E. A., *GH Bladed Users' manual*, 2010
- [2] Chu, S. Y., Soong, T. T., and Reinhorn, A. M., *Active, Hybrid and Semi-Active Structural Control*; New York / Buffalo, USA (2005)
- [3] Constantinou, M. C., Tsopelas, P., Hammel, W., and Sigaher, A. N. *Toggle-brace-damper seismic energy dissipation systems*. Journal of Structural Engineering. 127(2): 105–112. (2001)
- [4] Dyke S. J., Spencer, B.F. Jr, Quast, P., Sain, M.K., Kaspari, D.C. Jr., Soong, T.T. *Acceleration feedback control of MDOF structures*, Journal of Engineering Mechanics, Vol. 122, No. 9, September 1996.
- [5] IEC 61400-1, *Wind Turbines – Part 1: Design requirements*, third edition, 2005-08
- [6] Hwang, J.-S, Huang, Y.-N., and Hung, Y.-H. *Analytical and Experimental Study of Toggle-Brace-Damper Systems*, Journal of Structural Engineering, Vol. 131, No. 7, July 2005.
- [7] Bernd Kuhnle, *Design Optimization of the Alstom ECO100 3 MW wind turbine by using Structural Control Devices*, Internship Report ALSTOM – University of Stuttgart, August 2010
- [8] Laks, J. H., Pao, L. Y., Wright, A. D., *Control of Wind Turbines: Past, Present, and Future*, American Control Conference, ACC '09. St. Louis, MI, July 2009.
- [9] Marko, J., Thambiratnam, D. P., and Perera N. J., *Study of viscoelastic and friction damper configurations in the seismic mitigation of medium-rise structures*, Journal of Mechanics of Materials and Structures, 1(6), May 2006.
- [10] Rodriguez Tsouroukdissian, A., *Wind turbine structural damping ratio augmentation hybrid device*; Barcelona, 2009. Patent - EP 09167385.5
- [11] Rodriguez Tsouroukdissian, A., *Modeling and Identification of Magnetorheological (MR) Dampers for Civil Engineering Structures*; PhD Thesis in Structural Dynamics and Earthquake Engineering, Polytechnic University of Barcelona, Barcelona, 2009
- [12] Rodríguez T., A., Carcangiu, C.E., Pineda, I., Fischer, T., Kuhnle, B., Scheu, M. and Martin, M. *Enhancement of Wind Turbine Structural Damping by Using Passive, Active and Semi-Active Structural Control Devices for Tower Load Reduction*. DEWEK, Bremen, Germany, 2010.
- [13] Singh, M. P. and Moreschi L. M., *Optimal placement of dampers for passive response control*, Earthquake Engineering & Structural Dynamics, Vol. 31, Issue 4, pages 955–976, April 2002.

[14] Matti Scheu, *Structural damping devices for tower load reduction* , Internship Report ALSTOM – University of Stuttgart, August 2010

IDENTIFICATION OF DYNAMIC PROPERTIES OF OPEN-DECK VIADUCTS UNDER PASSING TRAIN LOADS

Kodai MATSUOKA, Student, Department of Civil Engineering, Osaka University,
k-matsuoka@civil.eng.osaka-u.ac.jp
Kiyoyuki KAITO, Associate Professor, Frontier Research Center, Osaka University,
kaito@ga.eng.osaka-u.ac.jp
Tsutomu WATANABE, Researcher, Railway Technical Research Institute
masamichis@rtri.or.jp
Masamichi SOGABE, Senior Researcher, Railway Technical Research Institute
tsutomuw@rtri.or.jp

ABSTRACT

When planning the introduction of high-speed trains on existing viaducts, it is important to grasp the resonance phenomenon by measuring the vibration of actual bridges and understand this phenomenon from the engineering perspective. In this study, the author focused on the open-deck viaducts in snowy cold regions, where high-speed trains will be introduced, carried out vibration monitoring of actual bridges utilizing the passing train loads and identified their dynamic properties with ERA (Eigensystem Realization Algorithm). When identifying dynamic properties, the first bending mode and the first torsional mode were studied, and it was found that the first torsional mode is dominant after a train has passed, while the first bending mode is dominant during the passing of a train. The damping ratio of the first bending mode was 1.5-1.9%, which is slightly lower than the commonly used value 2%. In addition, with the simplified model using the identified dynamic properties, the resonance phenomenon induced by high-speed trains was investigated empirically.

1. INTRODUCTION

As Japanese society is getting matured, the railroad infrastructure is indispensable for supporting economic activities and daily lives. High-speed trains take important roles for improving convenience while securing the safety and reliability of railroads, as the effect of shortening transportation and distribution time energizes economic activities further^[1]. From this viewpoint, the increase in train speed has been discussed continuously. On the other hand, civil infrastructures on which trains run are difficult to newly establish according to the improvement in train performance in many cases, and so it is necessary to discuss the applicability of existing structures to high-speed trains.

When a train with many railroad cars runs on a bridge, a viaduct, or the like, resonance phenomena, such as excessive response, noise, and ground vibration, are anticipated^[2]. The primary parameters of resonance are the oscillation cycle of the train, which is the oscillation source, the natural frequency and damping coefficient of a structure to be vibrated. As for the input into a structure by a train, “the speed effect of train load” has been researched continuously since the 1970s, though theoretical studies, model experiments, and bridge measurements^[3], and it has been summarized from the viewpoints of axle interval, railroad car length, and running speed, etc.^[4]. As trains become faster and low-rigidity girders are installed, it is necessary to cope with the resonance phenomena. Actually, natural frequency and damping coefficient were identified, and the numerical simulation of vibration was conducted many times, and then a dynamic design method using a nomogram has been proposed^[2].

As for open-deck viaducts discussed in this study, natural frequency has been identified through vibration measurement and numerical analysis and simulation have been carried out since 2008, the application into the increase in train speed is being discussed^[5]. However, natural vibration could not be excited by impact vibration at large amplitude, and so modal damping ratio, which determines dynamic response, has not been discussed enough.

In this study, the authors identify vibration characteristics, including natural frequency, vibration mode shape, and mode damping ratio by using the load of a running train as the vibration source and the Eigensystem Realization Algorithm (ERA)^[6]. Through the simplified analysis based on the identified vibration characteristics, the authors discuss resonance speed and

Table 1 Outline of target bridges

Bridge code	Span length [m]	Structure type	Crossbeam	Specified Young's modulus [kN/mm ²]	Second moment of area[m ⁴]	
					With roadbeds	Without roadbeds
B1	25	RC T-type girder	2	8	2.839	3.423
B2	25	RC T-type girder	2	8	2.839	3.423

Table 2 Specification of measurement devices

Device	Model	Specification
Piezoelectric accelerometer	PV85	Charge output, insulated, sensitivity : 6.42pC/(m/s ²), response frequency : 1Hz~7kHz

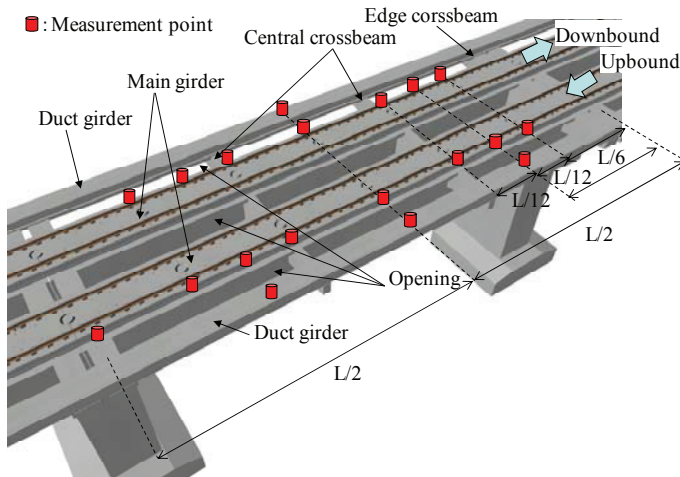


Figure 1 Open-deck viaduct and measurement point layout

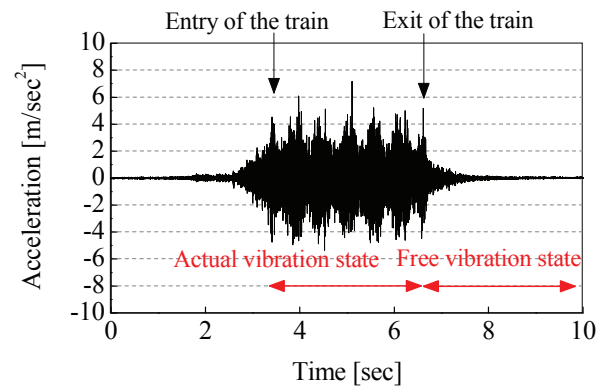


Figure 2 Acceleration response during the passing of a train (B1, measurement point 7)

the effects of railroad cars for the increase in train speed.

2. METHOD OF IDENTIFYING VIBRATION CHARACTERISTICS

In this study, the load of a running train is considered as the vibration source for identifying the vibration characteristics of a bridge. The vibrations excited by the load of a running train include (1) the transient vibration just after the entry of a train, (2) the actual vibration during the passing of a train, and (3) the free vibration after the passing of a train. ERA adopted for this study is an identification method based on free vibration response. Accordingly, it is difficult to discuss the transient vibration, in which amplitude increases, as free vibration. This study is targeted at the actual and free vibrations, and their vibration characteristics are identified with ERA. In ERA, it is assumed that a structure is a linear time-invariant system, and the vibration characteristics of a structure as a non-proportional damping system are identified based on the free vibration response⁵⁾. As the methods for producing the free vibration response, the RD method and the correlation function method are proposed, targeting especially stationary response. Both methods have been applied to actual structures, and the same results have been obtained under certain conditions. The RD method requires an enormous amount of time-series samples, and so it is difficult to adopt in this study. On the other hand, the correlation function method allows the use of fast Fourier transformation, and so even if only one vibration measurement is available, it is possible to produce free vibration response. Accordingly, the latter method is adopted in this study.

As for ERA, the literature [6], etc. discuss it theoretically, and so this paper just briefly explains it. ERA is the method for estimating characteristic matrix based on the minimum realization in the linear time-invariant system. Through the principal component analysis based on singular value decomposition and the eigenvalue analysis of state matrix, vibration characteristics are extracted from the time-series waveform measured at several points. Some indicators have been proposed for evaluating the accuracy of extracted vibration characteristics. In this study, model amplitude coherence (MAC)^[7] is adopted. In this study, the load of a running train is used, and so the inclusion of regular input components is expected. By considering the correlation with the theoretical mode shape for a target structure, the vibration components unique to a structure are extracted as vibration characteristics.

Table 3 Results of the identification in the free vibration state

	First-order displacement		First-order torsion		RMS [m/sec ²]	Train type	Train speed [km/h]
	Natural frequency	Damping	Natural frequency	Damping			
	[Hz]		[Hz]				
B1							
t1	5.53	0.018	8.93	0.016	0.017	Freight	71
t2	-	-	8.84	0.022	0.011	Freight	84
t3	-	-	8.95	0.027	0.010	Freight	85
t4	-	-	8.97	0.021	0.012	Freight	84
t5	-	-	8.90	0.028	0.015	Freight	80
t6	5.51	0.014	-	-	0.025	Express	135
t7	5.55	0.019	9.01	0.016	0.057	Express	138
t8	5.55	0.017	9.01	0.020	0.026	Express	135
Average	5.53	0.017	8.94	0.021			
Variation coefficient	0.003	0.110	0.007	0.213			
B2							
t9	-	-	9.21	0.017	0.022	Freight	77
t10	-	-	9.28	0.022	0.033	Freight	81
t11	-	-	9.16	0.017	0.043	Freight	89
t12	-	-	9.05	0.007	0.016	Freight	69
t13	-	-	9.01	0.007	0.018	Freight	90
t14	5.44	0.018	9.16	0.015	0.026	Express	138
t15	5.47	0.017	9.18	0.015	0.033	Express	133
t16	5.47	0.010	9.19	0.015	0.038	Express	139
t17	-	-	9.16	0.012	0.036	Express	112
t18	5.47	0.010	-	-	0.029	Express	123
t19	5.42	0.019	9.08	0.015	0.028	Express	137
Average	5.45	0.015	9.08	0.015			
Variation coefficient	0.005	0.253	0.009	0.311			

3. CASE OF APPLICATION INTO ACTURAL BRIDGES

(1) Outline of Target Bridges

This study is targeted at open-deck viaducts as mentioned in Section 1. A open-deck viaduct has a structure that does not have overhanging slab, central slab, or bridge railing, which prevents the accumulation of snow to secure safety and reduce snow load. This structure also reduces construction costs. This structure has been adopted in snowy cold regions since the 1980s, as part of countermeasures against snow disaster. It has been pointed out that open-deck viaducts have different vibration characteristics from ordinary structures that have slabs⁵⁾.

In this background, displacement and natural frequency have been already measured, targeting over 10 bridges whose span ranges from 5 m to 35 m. As a result, it was found that an open-deck viaduct with a span length of 25 m has relatively small bending rigidity ratio (measurement/specified value). In the above measurements, damping coefficient was not identified. This study is targeted at 2 open-deck viaducts with a span length of 25 m (Bridges B1 and B2). Table 1 shows the outline of the target bridges.

(2) Running Train Test

Fig. 1 shows the measurement points for B1. Its layout is aimed at grasping especially the dynamic behavior of main girders. For all of the 19 sensors, piezoelectric accelerometers were adopted, because large amplitude was expected during the passing of a train. Table 2 shows the specifications of the adopted piezoelectric accelerometer. The acceleration response measured by these accelerometers is recorded via an AD convertor in a laptop PC at a sampling frequency of 2 kHz. The frequency components of over 1 kHz are removed with an anti-aliasing filter. For the 2 target bridges, the same measurement system and accelerator are used. The bridges are on the same line, and freight and express trains run on them. Running speed was about 80 km/h for freight trains, and 130 km/h for express trains. As an example of the acceleration response during the passing of a train, Fig. 2 shows the variation in acceleration at measurement point 7 when t7 (express train) passed on B1. The status at the time of the coming, passing, and leaving of the train can be seen. In this study, the state between the entry and the exit of a train is defined as actual vibration, and the state after the exit is defined as free vibration, as shown in Fig. 2.

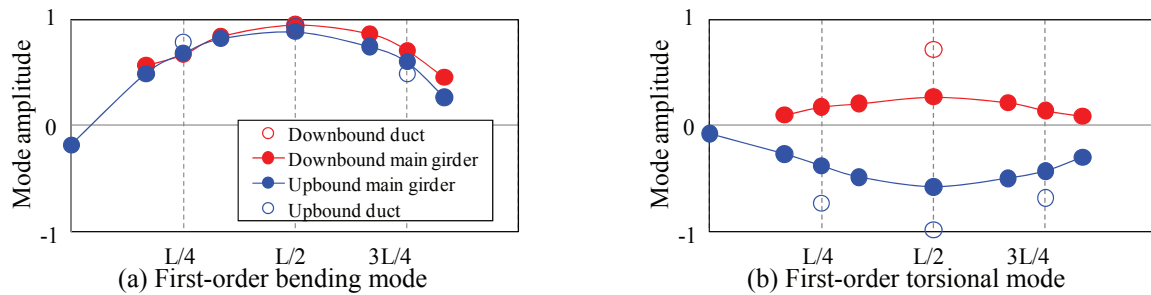


Figure 3 Examples of vibration mode shapes (the free vibration state after the passing of t-7)

Using the variation in acceleration, the authors discuss the vibration characteristics during the passing of a train, no matter whether resonance occurs.

(3) Identification of Vibration Characteristics in The Free Vibration State

Using the method described in Section 2 with the measurement results, vibration characteristics, including natural frequency, modal damping ratio, and vibration mode shape, are identified. Vibration characteristics are identified with the acceleration response in the free vibration state, before using the actual vibration. Here, a correlation function was not used for confirming the free vibration. The authors focused on the first-order bending mode and the first-order torsional mode, which are closely related to resonance. The measured acceleration response was filtered with a 40Hz low-pass filter, a 950×50 Hankel matrix was derived from the acceleration response at 19 measurement points, and vibration characteristics were identified with ERA. Table 3 shows the vibration characteristics of the free vibration state after the passing of a train, and Fig. 3 shows the vibration mode shape after the passing of t7 on B1. The vibration mode shape was normalized so that the maximum mode amplitude becomes 1.

The results shown in Fig. 3 represent the first-order bending mode, in which main girders and duct girders oscillate in the same phase, and the first-order torsional mode, in which they oscillate in the opposite phases.

The natural frequency of each bridge shown in Table 3 is summarized as follows. The average natural frequency is almost the same in the two modes for the two bridges. The variation coefficient of natural frequency of the two bridges is 1% or less, and so measurements are nearly constant in the free vibration state, regardless of the types of trains.

The first-order bending mode could not be identified in many cases, especially after the passing of a freight train. Meanwhile, the first-order torsional mode could be identified in most of the free vibration states. This is considered due to the fact that the contribution ratio of the torsional mode to all vibration components in the free vibration state is larger than that in the actual vibration state. Such a phenomenon is unique to open-deck viaducts.

As for modal damping ratio, variation coefficient is 10% to 30% for each mode. It can be understood that modal damping ratio varies more broadly than natural frequency. The average of the first-order bending mode was slightly lower than 2%, which is generally used for viaducts that have slabs.

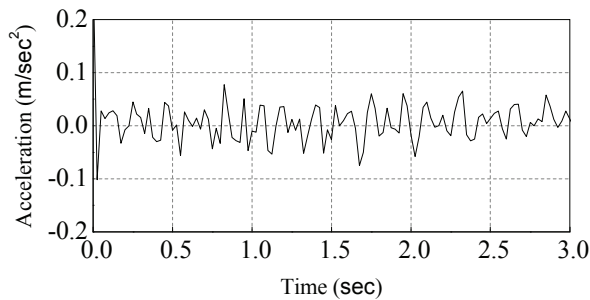
(4) Identification of Vibration Characteristics in The Actual Vibration State

By utilizing the acceleration response in the actual vibration state, the authors attempt to identify the vibration characteristics in the actual vibration state, including train weight and one-sided running. Fig. 4 shows the free vibration response produced by using a correlation function based on the acceleration response in the actual vibration state of B1 for a freight train (t5) and an express train (t6). Measurement point 5 was selected as the reference point of a cross-correlation function, because this measurement point does not become a node of the vibration mode. Measurement point 7 is shown in the figure. It is difficult to say that the free vibration response was sufficiently produced from the acceleration response during the passing of a freight train shown in (a), because of the effect of the regular input by the running train. In the case of an express train shown in (b), periodic vibration components can be seen regardless of the actual vibration state. In the same way, ERA was adopted for the free vibration response produced from the acceleration response in the actual vibration state for all trains, and vibration characteristics, including natural frequency, modal damping ratio, and vibration mode shape, were identified. The analysis conditions are the same as the free vibration state after the passing of a train.

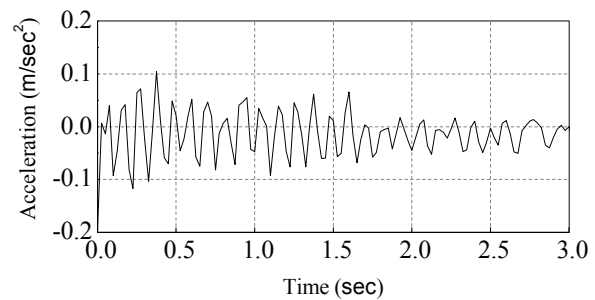
Table 4 shows the vibration characteristics in the actual vibration state. “*” in the table represents the strong effect of periodic components. This will be described later. Table 4 indicates that the first-order bending mode could be identified in most cases of the actual vibration state compared with the free vibration state. Meanwhile, the first-order torsional mode could not be identified in over half of cases. The first-order torsional mode is more remarkable in the free vibration state. During the passing of an express train, this mode was identified in only two cases. On the other hand, the first-order bending mode was identified in the actual vibration state during the passing of an express train like the free vibration state. As for B1,

Table 3 Results of the identification in the actual vibration state

	First-order displacement		First-order torsion		RMS [m/sec ²]	Train type	Train speed [km/h]
	Natural frequency		Natural frequency				
	[Hz]	Damping	[Hz]	Damping			
B1							
t1	5.42*	0.006	-	-	0.210	Freight	71
t2	5.86*	0.009	-	-	0.220	Freight	84
t3	5.31	0.025	8.67	0.012	0.219	Freight	85
t4	-	-	8.33	0.012	0.227	Freight	84
t5	5.66	0.094	8.92	0.015	0.208	Freight	80
t6	5.44*	0.004	-	-	0.232	Express	135
t7	5.55	0.015	8.98*	0.004	0.233	Express	138
t8	5.47	0.015	-	-	0.229	Express	135
Average	5.53	0.024	8.64	0.011			
Variation coefficient	0.033	1.311	0.035	0.442			
B2							
t9	-	-	-	-	0.251	Freight	77
t10	-	-	-	-	0.392	Freight	81
t11	-	-	9.21	0.014	0.234	Freight	89
t12	-	-	8.98	0.013	0.230	Freight	69
t13	-	-	9.23	0.061	0.237	Freight	90
t14	5.30*	0.002	-	-	0.241	Express	138
t15	5.52	0.011	-	-	0.245	Express	133
t16	5.35*	0.001	-	-	0.236	Express	139
t17	5.31	0.030	9.14*	0.004	0.287	Express	112
t18	5.34	0.012	-	-	0.251	Express	123
t19	5.36*	0.003	-	-	0.259	Express	137
Average	5.36	0.010	9.08	0.022			
Variation coefficient	0.015	1.156	0.011	1.046			



(a) Freight train



(b) Express train

Figure 4 Free vibration response produced using the acceleration response in actual vibration state (measurement point 7)

this mode was identified during the passing of a freight train. The average natural frequency of B2 in the first-order bending mode is slightly lower than that for the free vibration state. On the other hand, the average natural frequency of B1 in the first-order torsional mode is slightly lower than that for the free vibration state. For the two bridges, variation coefficient increased in each mode. However, its value is 1% to 3% in the actual vibration, which does not degrade the reliability of data. Modal damping ratio shows a variation of over 40%, and the maximum variation is about 130%. Accordingly, it is difficult to say that reliability is high. Especially, it indicates extremely small values (1% or less) in the case of “*.” In these cases, it is considered that the periodic input by a running train induces steady vibration. In addition, there was no significant relation between the characteristics of modal damping ratio and RMS. In the case of “*,” the effect of the periodic input by a running train can be seen in the vibration mode shape. For example, Fig. 5 shows the vibration mode shape of the first-order bending mode in the case where the train t14 runs on the bridge B2. The downbound train t14 runs on the downbound main girder represented by the red symbol in the figure. At the upbound main girder and the downbound main girders other than the

measurement points 6 and 10, the shape of the first-order bending mode can be seen, while the measurement points 6 and 10 have excessively large mode amplitude for the first-order bending mode. The interval of these measurement points is 12.5 m. Since the axle length of the express train is 12.3 m, it can be considered that the load input due to the axle length of the express train is mixed in the vibration mode shape of the first-order bending mode. In the case of “*” in Table 5, the above-mentioned effect of the load of a running train can be seen only for the girders where a train runs. In the first-order bending mode, the third-order resonance speed of an express train is about 127 km/h, and so the effect of the periodic input by a running train can be expected.

4. DAMPING RATIO AND RESONANCE IN VIADUCTS THAT HAVE NO SLABS

(1) Simplified Analysis Method

This section discusses the relation between the remarkable components in the first-order bending mode and the running speed of a train, with the spectral analysis using the simplified model.

The same method was adopted by Miyashita et al. for studying high-order local vibrations⁷⁾. They formulated the equation of motion, by using the load sequence inputted in a structure with the train load sequence model and a structure taking into account arbitrary mode order; and indicated that the forced solution of a simple beam can be expressed by the quasi-static displacement of the entire body and the impulse response excited by each load sequence. As for the quasi-static displacement, impact load increases as train speed becomes higher, and so the output of a bridge shows the same tendency. As for the impulse response excited by the load sequence of a train, the output of a bridge increases at a certain speed, because of the relation between the periodic input, which varies with train speed, and the vibration characteristics of a structure. This study is focused on the relation between periodically inputted load components and viaducts that have slabs while considering the variation in quasi-static displacement, because the variation in speed of the express train is small and resonance speed is discussed. When the equation of motion that takes into account only the impulse response excited by the load sequence of a running train undergoes the Fourier transform, the observation response of a structure $G(\omega)$ can be expressed by the following equation as the product of the spectrum based on the natural frequency of a structure H_s and the load sequence spectrum H_p . This equation is a function of angular frequency.

$$|G(\omega)| = |H_s(\omega)| \times |H_p(\omega)| \quad (1)$$

where the load sequence spectrum H_p can express the variation in input response due to resonance order by considering not only car length L_b but also wheel length L_c and axle interval L_d .

$$|H_p(\omega)| = |H_b| \times |H_c| \times |H_d| \quad (2)$$

where, H_b , H_c , and H_d can be expressed by the following equations, respectively, by using car length L_b [m], axle interval L_c [m], wheel length L_d [m], and train speed V [m/s]:

$$|H_d(\omega)| = 2|\cos(L_d\omega / 2V)| \quad (3a)$$

$$|H_c(\omega)| = 2|\cos(L_c\omega / 2V)| \quad (3b)$$

$$|H_b(\omega)| = |\sin(NL_b\omega / 2V) / \sin(L_b\omega / 2V)| \quad (3c)$$

where N is the number of train cars. By substituting the calculated load sequence spectrum and the amplitude spectrum $H_s(\omega)$ for the n -th mode (n is arbitrary) unique to a structure, it is possible to easily obtain the output response of a structure.

$$|H_s(\omega)| = \left| \frac{1}{m_n} \frac{1}{(i\omega + a_n)^2 + b_n^2} \right| \quad (4)$$

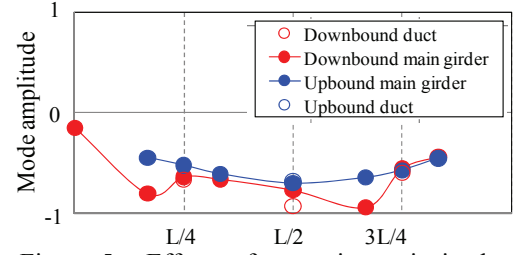


Figure 5 Effects of a running train in the vibration mode shape

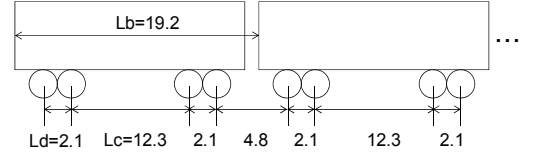


Figure 6 Vehicle model

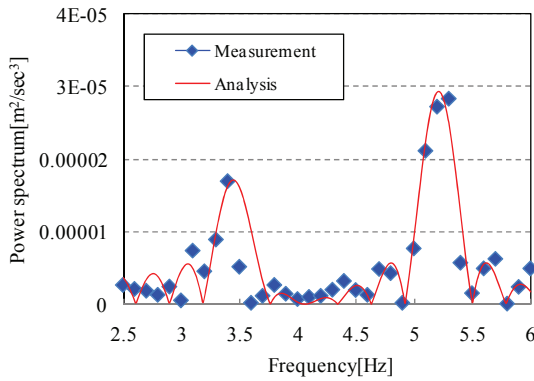


Figure 7 Analysis results (train speed: 123 km/h)

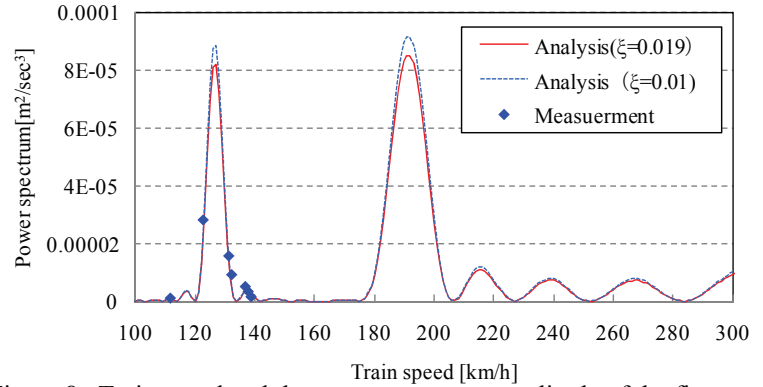


Figure 8 Train speed and the power spectrum amplitude of the first order bending mode

where m_n represents the mass including the effect of input load, and a_n and b_n can be expressed by the following equations (5a) and (5b) with natural angular frequency ω_n and modal damping ratio ξ_n :

$$a_n = \xi_n \omega_n \quad (5a)$$

$$b_n = \omega_n \sqrt{1 - \xi_n^2} \quad (5b)$$

For the natural frequency and modal damping ratio of a structure, the results of the identification of the first-order bending mode of the bridge B2 shown in Table 3 were used for reference. For the input load sequence, the specifications of the express train shown in Fig. 6 were used. As for m_n , including the effect of input load, the authors focused on the 6 first-order modes of the express train mentioned in Section 3.3, and specified it so as to minimize the deviation from the peak of the Fourier amplitude spectrum around the natural frequency of the span center of the girder where a train passed (measurement points 5 or 13).

By changing train speed with the above analytical model, the resonance between the periodic input load and the first-order bending mode is reproduced.

(2) Case of The Analysis of a Open Deck Viaduct

Fig. 7 shows the results of the analysis based on the simplified model described in Section 4.1 and the measurement results for the train t18. Around 5.45 Hz, around the natural frequency of the first-order bending mode, the outstanding components due to the resonance between the first-order bending mode and periodic excitation components could be reproduced. Fig. 8 shows the relation between the train speed calculated with this model and the power spectral amplitude for the first-order bending mode (5.45 Hz). Train speed is changed by 1 km/h's. In the figure, the analysis results are represented by the red lines, and the measurement results are denoted by the blue symbols. The number of samples is small, but the measurement results are well consistent with the analysis results. Fig. 8 shows the two outstanding speeds. Their local maximum values are 126.9 km/h and 188.3 km/h, which represent third-order and second-order resonance speeds, respectively. As a characteristic, the second-order resonance centered around 188.3 km/h has a broader range than the third-order one, and its effect is anticipated in the range from 180 km/h to 200 km/h. In the analytical model used in this study, the quasi-static flexural components due to the increase in train speed are not considered. When train speed is high, excitation force enlarges, and so the power spectrum amplitude in the first-order bending mode during the second-order resonance increases further. In the figure, the blue dotted line represents the case in which modal damping ratio ξ is 1%. The mass including the effect of input load m_n was defined in the same way. The results are consistent with the measurement results, like the case in which modal damping ratio is 1.9%. As modal damping ratio decreases, the power spectrum amplitude during resonance increases by about 7%. Considering that the minimum modal damping ratio is 1%, it can be said that the effect of modal damping ratio on the resonance phenomena is not significant.

4. CONCLUSION

In this study, the vibration characteristics of the two kinds of vibration states (free vibration and actual vibration states) were identified, with the purpose of identifying the vibration characteristics of a open-deck viaduct during the passing of a train and discussing the resonance phenomena as high-speed trains are introduced. Focusing on the variations in vibration characteristics, the authors clarified the averages, variances, and variation ranges of natural frequency and modal damping ratio; and found that there are no relations with amplitude in the case of the free vibration state. In addition, the relation

between the vibration characteristics of a open-deck viaduct and the periodic input components by a running train was clarified with the simplified analysis, and it was concluded that it is necessary to be careful about the second-order resonance when a high-speed train is introduced.

For resonance prediction, it is considered necessary to formulate impact coefficient, which is a more practical indicator, while considering the load that depends on speed, with FEM, etc. As a bullet train will supersede the current express train, it is considered necessary to discuss the variation in resonance speed and amplitude under different conditions.

ACKNOWLEDGMENT

Part of this study was carried out at Frontier Research Base for Global Young Researchers, Graduate School of Engineering, Osaka University based on the project of the Ministry of Education, Culture, Sports, Science and Technology titled “Promotion of Suitable Research Environment for Young Scientists’ Independent Research.”

REFERENCES

- [1] Council for Transport Policy: The Report of Council for Transport Policy, No.19, 2000. (in Japanese)
- [2] SOGABE Masamichi, et al: Dynamic Response and Design of Continuous Concrete Railway Bridge in Resonance Area, *Journal of Structure Mechanics and Earthquake Engineering*, Vol.724, I-62, pp.83-102, 2003. (in Japanese)
- [3] Fryba, L., *Vibration of Solids and Structures under Moving Load*, Noordhoff International, 1972.
- [4] HARA Tsuneo, et al, Development of a New Method to Reduce SHINKANSEN-Induced Wayside Vibrations Applicable to Rigid Frame Bridges, *Journal of Structure Mechanics and Earthquake Engineering*, Vol.766, I-68, pp.325-338, 2004. (in Japanese)
- [5] MATSUMOTO Teruya, SOGABE Masamichi, et al: Dynamic Characteristics of Open Floor Railway Viaduct and Its Applicability to High-Speed Railway, *Journal of railway mechanics*, pp.70-76, 2009.
- [6] Juang, J. N. and Pappa, R. S. : An Eigensystem Realization Algorithm For Modal Parameter Identification And Modal Reduction, *Journal of Guidance, Control, and Dynamics*, Vol.8, No.5, pp. 620-627, 1985.
- [7] MIYASHITA Takeshi, et al. : Understanding of High-Speed-Train-Induces Local Vibration of a Railway Steel Bridge Using Laser Measurement and Its Effect by Train Speed, *Journal of Structure Mechanics and Earthquake Engineering A*, Vol.63, No.2, pp.277-296, 2007. (in Japanese)

Risk assessment of dolphin protected bridge pier considering collision point analysis

Hyun-Joong Kim¹, Jeonghyun Lim², Wonsuk Park³, Hyun-Moo Koh⁴

¹ Doctor Course Student, Dept. of Civil and Environmental Engineering, Seoul National University, San 56-1, Shinlim-dong, Gwanak-gu, Seoul 151-742, Korea

² Unified Master's and Doctor's Course Student, Dept. of Civil and Environmental Engineering, Seoul National University, San 56-1, Shinlim-dong, Gwanak-gu, Seoul 151-742, Korea

³ Chief Researcher, Korea Bridge Design & Engineering Research Center, Seoul National University, San 56-1, Shinlim-dong, Gwanak-gu, Seoul 151-742, Korea

⁴ Professor, Dept. of Civil and Environmental Engineering, Seoul National University San 56-1, Shinlim-dong, Gwanak-gu, Seoul 151-742, Korea

Abstract: The collision of ship embraces some uncertainties, such as a direction, velocity, and location of the aberrant vessel. These uncertainties may affect on the risk from the collision and the final design of bridge and protective structures against the collision of ship. The importance of accurate consideration for uncertainties is more obvious on the protected bridges by the dolphin, since it alters the motions during the collision. This paper considers the effect of collision point along the height of the pier that usually is ignored as using a simple two-dimensional outline. In addition, it also analyzes the influence of the angle from the collision between vessel and pier. With the numerical example, it is possible to conclude that it is necessary to consider various vertical impact locations for safe design. Besides, it is sure to reduce the risk from the collision of ship, considering impact angle.

1 Introduction

As the number of ship-bridge collision accidents has been increased, many attempts have been made to protect the bridge against ship collision. Bridge safety is assured with risk assessment throughout the statistical approach, since the collision of ship is classified as an extreme event including uncertainties intrinsically. It is required to modify bridge design or emplace protective structure in various ways as introduced in [8], when estimated risk exceeds the standard criteria. It is important to accurately reflect consideration of uncertainties for reasonable and reliable design against the collision of ship, for example, direction, velocity, and location of aberrant vessel, although it is difficult to estimate them.

It is more increasing to reflect more accurate consideration of uncertainties in the case of the protected bridge by dolphin, since it alters the direction of vessels. The collided ship with dolphin is stopped, slowed down, or redirected; and it results in altering of impact and velocity. It is required to validate the effect on the ship collision risk with these changes in angle and velocity.

Hence, it is also necessary to analyze the collision of ship point between risk assessment procedure and bridge pier. This paper considers two parameters about collision point. First one is vertical impact location on pier, and second one is collision angle between ship and pier surface. It is presented to analyze the effect of these variables on the risk from the collision of ship throughout the procedure of AASHTO LRFD.

2 Effects on the risk from vertical collision location of ship at pier

2.1 Pier capacity considering water level variation

Pier capacities against ship collision are important factor in ship collision risk assessment. This capacity is affected by various uncertainties, such as types of vessels, drafts, water levels, ship's burdens, and so on. It requires much time and complicated process to consider exactly all of them, so it introduces and uses simplification and assumption. AASHTO LRFD suggests to assess resistance of bridge, when ship collided at MHWL. However, it may not guarantee conservative design against ship collision. For example, impact load on pile supported pier structure at lower water level may cause more severe damage compared to the impact at higher water level due to the local failure caused by direct collision on pile. Hence consideration of the water level variation may suggest more reliable results.

2.2 Analysis target

It is hard to consider every possible variance of water level in designing process, although it gives more reliable and accurate result, because it requires excessive time or lacks of enough information. Therefore, selecting representative water levels can be alternative method. In the case of Incheon Bridge [2], pier impact capacities against the collision of ship were determined considering two water levels; Mean high water level (MHWL) and Mean low water level (MLWL). Then, the numerical mean value which is determined by using all capacities at mean high level and at mean low water level were selected as final pier impact capacities. This approach somewhat may reflect the effect of the water level variation.

However, it has limitation since actual pier impact capacity does not vary linearly depends on water level.

Therefore, 4 ship collision risks of different situation will be analyzed and compared. Firstly, ship collision risk using pier capacity at mean high water level and at mean low water level will be compared. Secondly, ship collision risk using mean capacities and average value of two risks at MHWL and MLWL will also be compared.

3 Effect of collision angle between ship and pier on risk

Ship enables to collide with bridge pier at various angles. Most of initial kinetic energy is transformed to another energy form by the ship and the pier, when the impacted angle is large. On the other hand, it dissipates relatively small amount of energy with small impacted angle. However, most of the equivalent ship impact force equations assume right-angle impact against pier that every kinetic energy is transformed to collision energy. These approaches may overestimate the ship collision risk as the portion of oblique collision increases in total collisions. Therefore, it analyzes the influence on the ship collision risk with two approaches: Saul & Svensson's method and Pedersen & Zhang's method.

3.1 Estimation of collision energy

3.1.1 Using Saul and Svensson's approach

Saul and Svensson [7] proposed a method to calculate the impact forces occurring during the collision of a ship with bridge pier that was a basis for the impact force of AASHTO LRFD standard as commented in [1]. They also proposed collision energy equation in impact on a pier as a function of impact angle and friction coefficient. That equation is derived based on the law of momentum conservation and energy conservation. It is assumed that the colliding ship has only longitudinal velocity. The effects of transverse and the rotational velocity were reflected simply by introducing a reduced impact mass. Then, the collision energy is calculated with the coefficient η as follows that:

$$E_{col} = \eta E_k \quad (1)$$

where E_{col} is collision energy, E_k is initial kinetic energy of ship. And η is ratio of collision energy to initial kinetic energy as a function of impact angle α and friction coefficient μ (Fig. 1).

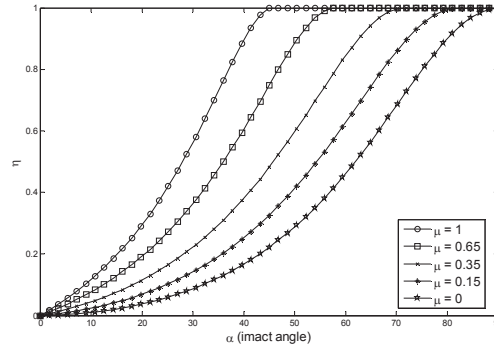


Fig. 1 Collision energy ratio η in relation to α and μ using Saul & Svensson’s method.

3.1.2 Using Pedersen and Zhang’s approach

Pedersen and Zhang [3] present analytical, closed-form expressions for the energy released for crushing and the impact impulse during ship-ship collisions. This method is also applied to the estimate ship-pier collision energy. The expressions for the collision energy are derived by solving the equation of motion for impact mechanics of ship collision and integrating accelerations for the direction of normal and perpendicular to the impact surface. Similar to Saul & Svensson’s method, impact angle and friction coefficient are main factors for the collision energy. With this method, it is possible to reflect the influence of transverse and rotational motion from ship and various ship characteristics such as mass and length.

Fig. 2 shows the energy ratio defined as the ratio of the collision energy by the total kinetic energy from the ship before the collision in relation to impact angle α and friction coefficient μ .

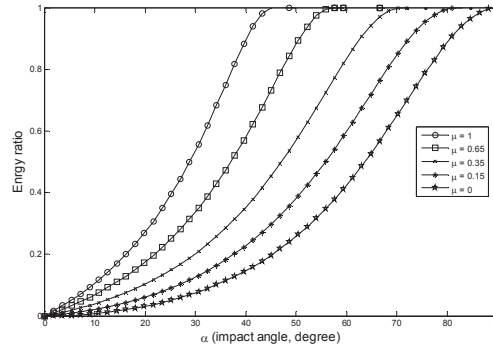


Fig. 2 Ratio of collision energy to initial kinetic energy in relation to α and μ using Pedersen & Zhang’s method.

Energy ratio curves of two approaches shows similar tendency according to impact angle and friction coefficient. For same friction coefficient, as impact angle increases (close to head-on collision), energy ratio converges to 1 that means most part of the initial energy is dissipated by crushing and/or impulse. On the other hand, as impact angle decreases (more glancing collision), the energy ratio approaches to zero that implies the impact dissipate less energy and ship brings more residuals. And impact with higher friction coefficient show larger collision energy for the impacts with same angle. Due to these effects, the collision of ship risk would be reduced as considering the impact angle between ship and bridge pier.

Fig. 3 shows the ratio of the energy using Saul & Svensson's method to the energy using Pedersen & Zhang's method without transverse velocity. Most range of impact angle expresses larger collision energy with former method. For these characteristics, ship collision risk using Pedersen & Zhang's method is expected to express smaller value.

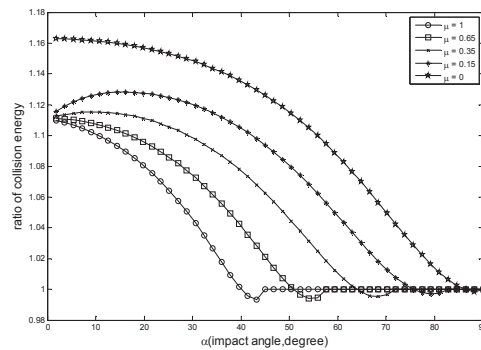


Fig. 3 Ratio of collision energy from Saul & Svensson's method to collision energy from Pedersen & Zhang's method.

3.2 Ship impact force of AASHTO LRFD standard

AASHTO LRFD [1] presents empirical equation of equivalent impact force for the risk assessment. Dead weight tonnage (DWT) and impact speed determine the impact force as equation (2)

$$P_s = 1.2 \times 10^5 V \sqrt{DWT} \quad (2)$$

That force can be modified with the estimated collision energy. Square root of energy ratio acquired using two different methods is multiplied to the impact force to represent the effect of reduced collision energy. It is assumed that impact force

is proportioned to the square root of the energy because of the numerical relation as equation (3).

$$\begin{aligned}\sqrt{E_k} &= \sqrt{\frac{1}{2}MV^2} \propto V \times \sqrt{M} \rightarrow V \times \sqrt{DWT} \\ \sqrt{\eta E_k} &= \sqrt{\frac{1}{2}\eta MV^2} \propto \sqrt{\eta} \times V \times \sqrt{M} \rightarrow \sqrt{\eta} \times V \times \sqrt{DWT}\end{aligned}\quad (3)$$

4 Ship-dolphin collision simulation program

To identify these effects of various water level and impact angle, ship collision risk assessment is performed. Annual Frequency of bridge collapse (AF) concept of AASHTO LRFD Standard is a representative method of the risk assessment of the ship collision event. However it is only applicable to the collision event for the bridge tower without any protection system because the speed and location of the ships are preliminarily determined once and their variations due to collision are not considered. If there are dolphin type protections, initially defined velocity and direction of ship may be changed by the collision with dolphins. It means that those post-collision variations in the velocity and direction of the ship must be analyzed to estimate AF of dolphin protected bridges.

In order to deal with the variations, therefore, 2D ship collision simulation program to estimate the post-behavior of the ship was developed and used. This program can account for local indentation force between ship and dolphin due to non-linear deformation of dolphin as well as ground force on dolphin. Indentation and ground forces on dolphin are calculated using simplified collision model with equivalent nonlinear springs of which properties are calibrated based on the energy dissipation result acquired by 3D FEM analysis. Finally, post-behavior of the ship was acquired by solving the equations of motions in [4] and [5] with the calculated external forces.

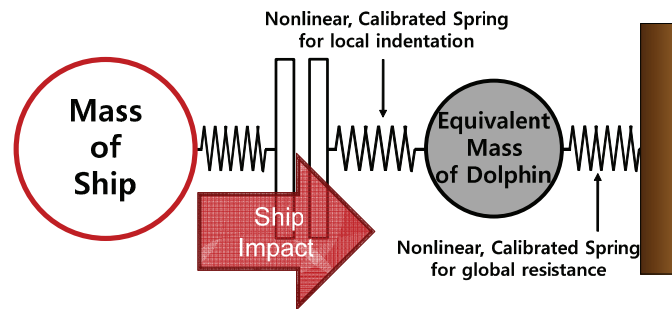


Fig. 4 Simplified collision model using nonlinear calibrated springs.

5 Numerical examples

Proposed methods and procedures are verified with the numerical example of Incheon Bridge using parameters of [2]. This bridge is located near ‘the port of Incheon’ where ship traffic is very congested. The difference between the rise and fall of the tide of this area is very large that the effect of vertical impact location can be more obvious.

A [table 5.1](#) shows the capacity at MHWL and MLWL and the mean value of two levels. And [figure 5](#) presents ship collision risks with each pier capacities and average values of risks at MHWL and MLWL.

In the case without protected structures, the collision of ship at MLWL is revealed as the most risky situation compared the event at MHWL. This tendency also discovered the same situation with dolphin, while it enables to reduce the risk. With these observations, it is perceived that risk assessment with consideration of the collision only at MHWL is not able to guarantee conservative design but may underestimate the risk.

The risk with the mean capacities and the mean value of risks from two locations are obtained to consider two risks at two vertical locations simultaneously. These two values are almost similar for each case while average risk is slightly higher. However, it is more appropriate to obtain a representative risk throughout the mean value of each risk at various vertical collision locations.

Table 5.1 Pier capacities at different water levels (MN).

	at Mean High Water Level (MHWL)	at Mean Low Water Level (MLWL)	average capacity of the two capacities
Pylon	35.00	26.00	30.50
Supplementary Pier	13.50	13.00	13.25
End Pier	14.50	14.50	14.50
Approach Pier	13.00	13.50	13.25

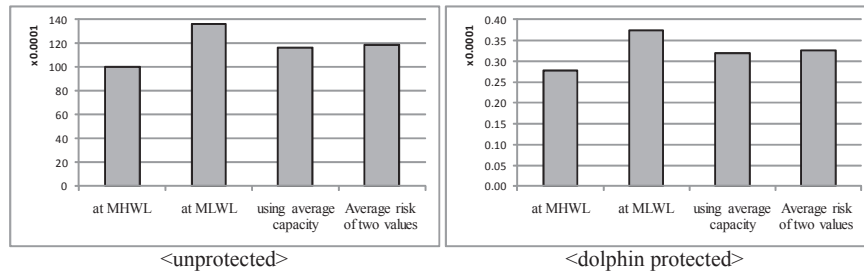


Fig. 5 Ship collision risks in relation to vertical impact location for unprotected & dolphin protected case.

Next ship collision risks are assessed to consider various vertical heights and angles; and shown in [fig. 6](#). It is perceived that the risks are decreased with the

consideration of impact angles for every situation (vertical location, with/without dolphins) because of the fact that collision energy is decreased. On the other hand, it is not significant when dolphin is set, because the effect of slowdown or redirection by dolphin itself overwhelms the total risk.

The risk of Saul & Svensson’s method is slightly higher than the risk of Pedersen & Zhang’s method, and a decreasing rate is slightly smaller as shown in fig 7. These results are agreed with the prediction in chapter 3.1.2. So it can be concluded that Saul & Svensson’s method has an advantage over the other method in convenience to use with almost same conservative result. On the other hand, Pedersen & Zhang’s method would be appropriate for the risk assessment with more accuracy since various factors such as transverse and rotational motions of the ship can be included reasonably.

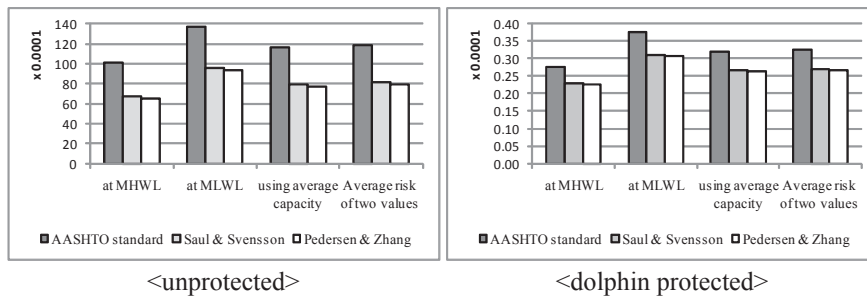


Fig. 6 Risks with considering impact angles by two different methods.

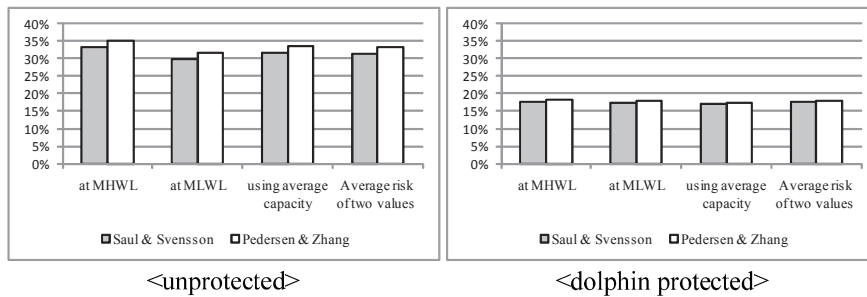


Fig. 7 Decreasing rates of risk with considering impact angles by two different methods.

6 Conclusions

In this paper, the effect of vertical collision point and the collision angle between vessel and pier is analyzed. To identify these effects, ship collision risk assessment

is performed with the developed 2D ship collision simulation program to estimate the post-behavior of the ship.

Vertical collision location of ship at pier determines pier capacities against ship collision. Therefore it is necessary to consider various vertical impact locations according to sea levels for safe design. However it is hard to consider every possible variance of water level in designing process. Therefore, selecting representative water levels can be alternative method. Numerical example shows that risk assessment with consideration of the collision on pier only at mean high water level is not able to guarantee conservative design but may underestimate the risk. The risk with the mean capacities and the mean value of risks from two locations are can be used to consider the effect of vertical collision location. However, it is assumed that the risk obtained throughout the mean value of each risk at various vertical collision locations is more appropriate as a representative risk since pier impact capacities do not vary linearly depends on water levels. To verify the assumption, risk assessment at more diverse sea levels need to be performed.

Effect of collision angle between ship and pier on risk is analyzed with two approaches: Saul & Svensson's method and Pedersen & Zhang's method. These two methods suggest the expressions to assess ship collision energy according to collision angle and friction coefficient. Then, modified ship impact forces based on that of AASHTO LRFD are calculated using the estimated collision energies. It is shown in the example that the risks are decreased with the consideration of impact angles for every situation while it is not significant when bridge is protected by dolphins. In addition to this, it is shown that Saul & Svensson's method has an advantage over the other method in convenience with almost same conservative result. On the other hand, Pedersen & Zhang's method would be appropriate for the risk assessment with more accuracy since various factors such as transverse and rotational motions of the ship can be included reasonably. Effects of those parameters of Pedersen & Zhang's method on ship collision risk will be analyzed compared with the value of Saul & Svensson's method in detailed for further research.

Acknowledgments This research was supported by the grant (10CCTI-A052531-03-000000) from the Ministry of Land, Transport and Maritime of Korean government through the Core Research Institute at Seoul National University for Core Engineering Technology Development of Super Long Span Bridge R&D Center.

Reference

- [1] AASHTO (1991) Guide Specification and Commentary for Vessel Collision Design of Highway Bridges. American Association of State Highway and Transportation Officials. Washington D.C.
- [2] Incheon Bridge Corporation (2004). Concessionaire Supplementary Requirements – Internal report.

- [3] Pedersen PT, Valsgaard S, Olsen D, Spangenberg S (1993) Ship Impacts: Bow Collisions. *International Journal of Impact Engineering* 13(2):163-197.
- [4] Pedersen PT, Zhang S (1998) On impact mechanics in ship collisions. *Marine Structures* 11:429-449.
- [5] Petersen MJ (1982) Dynamics of ship collisions. *Ocean Engng.* 9(4):295-329.
- [6] Petersen MJ, Pedersen PT (1981) Collisions between ships and offshore platforms. 13th Annual Offshore Technology Conference. 163-171.
- [7] Saul R, Svensson H (1982) On the theory of ship collision against bridge piers. *IABSE Proceedings P-51*: 29-38.
- [8] Svensson H (2009) Protection of bridge piers against ship collision. *Steel Construction* 1:21-32. doi: 10.1002/stco.200910004

OMAX testing of a steel bowstring footbridge

E. Reynders¹, D. Degrauwe¹, M. Schevenels¹, G. De Roeck¹, P. Van den Broeck², K. Deckers³ and P. Guillaume³

¹*K.U.Leuven, Dept. of Civil Engineering, Kasteelpark Arenberg 40, B-3001 Leuven, Belgium*

²*KaHo Sint-Lieven, Industrial Engineering Dept., Gebroeders Desmetstraat 1, B-9000 Gent, Belgium*

³*Vrije Universiteit Brussel, Dept. of Mechanical Engineering, Pleinlaan 2, B-1050 Brussel, Belgium*

Abstract A recent development in operational modal analysis (OMA) is the possibility of using measured, artificial loads in addition to the unmeasured, ambient excitation, while the ratio between forced and ambient excitation can be low compared to classical experimental modal analysis (EMA). Most of these so-called OMAX algorithms lack the intuitiveness of their EMA and OMA counterparts, since they fit a system model that takes both the measured and the operational excitation into account directly to the measured signals. A more physically intuitive subspace algorithm for OMAX, that starts with an accurate decomposition of the measured joint response in a forced and an ambient part, was recently introduced. In this paper, the performance of this algorithm, which is called CSI-ic/ref, is assessed by means of a case study, where a two-span steel arch footbridge is tested in operational conditions, with and without using additional actuators. From a comparison of the modal parameters with results from a finite element model, an OMA algorithm, and an alternative OMAX algorithm, it can be concluded that CSI-ic/ref yields accurate modal parameter estimates.

1 Introduction

Due to important improvements in structural design and manufacturing methods, and a related increasingly efficient use of structural materials, the slenderness and span length of bridges in general and footbridges in particular have increased significantly during the last decades. Lightweight, slender structures are, however, more sensitive to dynamic loads, and therefore the susceptibility of footbridges to vibrations has become an important design issue [1, 4]. The experimental verification of the design values, in particular the modal parameters, is essential for design validation, so for guaranteeing the safety and serviceability of the structure. Operational modal analysis (OMA) allows modal parameters to be determined in normal operating conditions, which is an important advantage over experimental modal analysis (EMA) since damping and boundary conditions may depend on vibration amplitude.

However, in OMA, the mode shapes can not be scaled in an absolute sense, e.g., to unit modal mass, unless a second measurement is performed after adding or removing a significant amount of mass to or from the structure [9], which is rather cumbersome for heavy structures such as (foot)bridges. Another disadvantage is that the frequency content of the ambient excitation is usually narrow banded, and as a result only a limited number of modes can be extracted from the ambient data with high quality. Therefore, there is an increasing interest towards operational modal analysis with exogenous inputs (OMAX) [6, 14], where an artificial force is used in operational conditions and a system model is identified that takes both the artificial and the operational forces into account. The main difference between OMAX and EMA is that the operational forces are not considered as unwanted noise but as useful excitation, and they are included in the identified system model. As a consequence, the amplitude of the artificial forces can be equal to, or even lower, than the amplitude of the operational forces. The feasibility of using small and practical actuators for modal testing of footbridges in an OMAX framework has been demonstrated recently in two case studies [16].

To date, two OMAX algorithms have been proposed and validated on real-life measurement data. The first one is a *Combined non-linear Least Squares Frequency method on Input Output spectra* (CLSF-IO) [3], for which recently the alternative name *OMAX Maximum Likelihood Estimation* (MLE-OMAX) was proposed [6]. This approach results in a non-linear minimization problem, which is solved iteratively. Local minima may occur, so good starting values are required for the system description. The second is a *Combined deterministic-stochastic Subspace Identification* (CSI) approach, both in a data-driven frequency-domain variant [2] and in a reference-based data-driven time-domain (CSI-data/ref) variant [14]. This approach is non-iterative and numerically robust, hence it requires a much smaller computational effort, while the obtained modal parameters are also highly accurate. It can be applied on its own, or for generating accurate starting values for the CLSF-IO method.

However, both algorithms lack the physical intuitiveness that is present in most algorithms for EMA and OMA: they fit a combined deterministic-stochastic system model directly to the measured input-output data. This can be attributed to the difficulty of decomposing the measured time response in a forced part and an ambient part in a statistically consistent way, i.e.,

in such a way that the separation becomes exact when the number of data samples goes to infinity. Recently, this decomposition problem was solved with a subspace approach, i.e., using data matrix projections, and a physically intuitive subspace algorithm for OMAX, called *Reference-based Impulse-Covariance driven Combined deterministic-stochastic Subspace Identification* or CSI-ic/ref, was developed [15]. CSI-ic/ref identifies a combined deterministic-stochastic state-space model directly from the impulse response sequence of the deterministic subsystem, and the output correlation sequence of the stochastic subsystem. It is a physically intuitive alternative for the CSI-data/ref algorithm for OMAX testing [14], just as the SSI-cov/ref algorithm is a physically intuitive alternative for the SSI-data/ref algorithm [10].

In this paper, the performance of the CSI-ic/ref algorithm is investigated in a real-life case study, where a steel bowstring footbridge is tested in operational conditions. The footbridge, which is located at Wetteren, Belgium, has two spans: a large span of about 75 m and a small span of about 30 m. The bridge was subjected to different OMA and OMAX tests, and the resulting data have been treated previously using the SSI-data/ref algorithm and the CSI-data/ref algorithm, respectively [16]. In order to assess the performance of the CSI-ic/ref algorithm, the modal parameters obtained with CSI-ic/ref are compared with these results.

The text is organized as follows. First, the Wetteren footbridge is presented and the ambient and combined modal tests are discussed. Then, the different steps of the CSI-ic/ref algorithm are presented and illustrated. Next, its application on the Wetteren OMAX data is discussed and the results are compared with the values obtained from alternative algorithms and tests and from a finite element model. The paper ends with the conclusions drawn from this comparison.

2 Operational modal testing of the Wetteren footbridge

2.1 The structure

The construction of a new roundabout at the N42 national road on top of the E40 highway at Wetteren, Belgium, created a potentially dangerous situation for cyclists and pedestrians due to the numerous approaches to and exits from the highway. In order to separate the bicycle track and the footpath completely from the road traffic, a new footbridge was built to the west of the roundabout in 2003 (Fig. 1a). This steel bridge has two spans, a short one of 30.33 m and a large one of 75.23 m. At the largest span, the bridge is of the bowstring type, with an inclination of 13.78° of the arches.

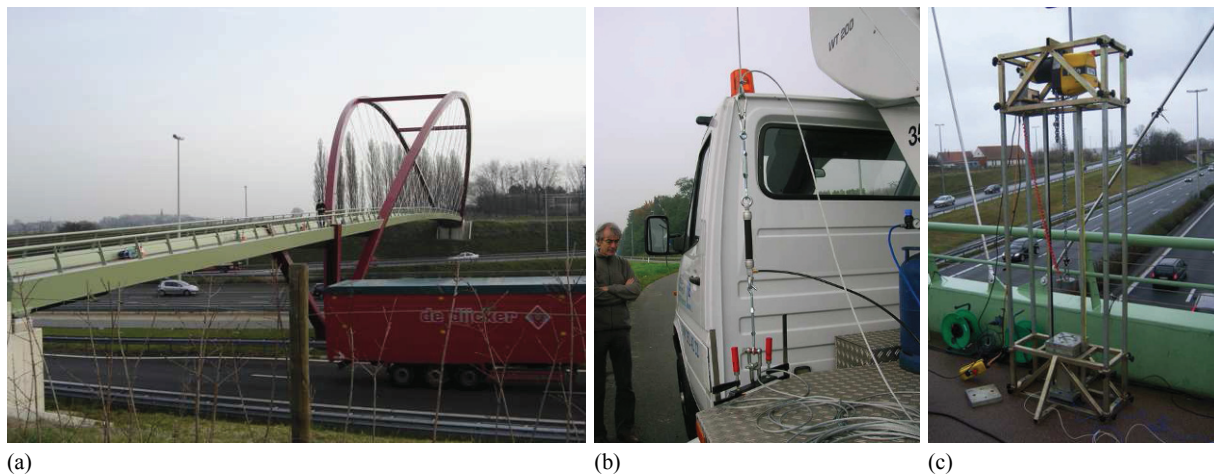


Fig. 1 Footbridge in Wetteren, Belgium: (a) view from the south side, (b) pneumatic artificial muscle, used as actuator, and (c) drop weight actuator.

Before the modal tests were performed, a detailed finite element model of the bridge was made [16]. The beams and arches were modeled with Timoshenko beam elements, the plain stainless steel bars connecting the arches and the bridge deck with truss elements, and the bridge deck with shell elements. The model shows that for most mode shapes, there is a strong interaction between the arches and the bridge deck; however, the first two modes consist mainly of lateral deformation of the arches while the bridge deck remains relatively undeformed.

2.2 Test description

An OMA test was performed on October 10, 2007, followed by an OMAX test one day later. For the OMAX test, a commercially available pneumatic artificial muscle (DMSP-20 from Festo) was used as actuator (Fig. 1b). The PAM produced a vertical force at node 192 (Fig. 2). A swept logarithmic sine between 0.1 and 10 Hz was chosen as force signal. The idea of using pneumatic artificial muscles (PAMs), which have originally been designed for application in robotics, for bridge testing, as well as the development, originated recently from the Acoustics and Vibration Research Group of Vrije Universiteit Brussel [5]. An additional OMAX test was performed on January 18, 2008, using a drop weight system as actuator (Fig. 1c).

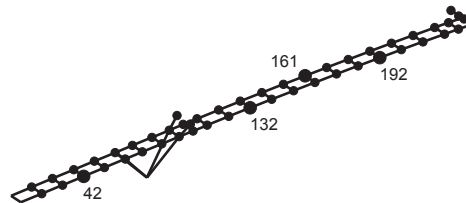


Fig. 2 Footbridge in Wetteren, Belgium: measurement grid. The numbered points appear in the text.

In both tests, 72 output degrees of freedom (DOFs) were measured in 5 setups: the vertical and horizontal acceleration of the bridge deck at 44 and 23 locations, respectively, and the out of plane acceleration of the arches at 5 locations (Fig. 2). Because of the large amount of traffic on the highway under the bridge, it was not possible to instrument the inclined arches in a safe way. Therefore, only the out of plane accelerations at the four lower ends of the arch and at one higher point on an arch were measured. More information on the structure and the different vibration tests can be found in [16].

3 Impulse-covariance-driven combined subspace identification (CSI-ic)

This section highlights the physically intuitive CSI-ic and CSI-ic/ref algorithms for OMAX testing [15], where CSI-ic/ref denotes the more general, reference-based version of CSI-ic. The algorithms identify a discrete-time state-space model for the structure in the considered frequency bandwidth, that accounts for both the forced excitation and the ambient, unmeasured excitation:

$$\mathbf{x}_{k+1} = \mathbf{A}\mathbf{x}_k + \mathbf{B}\mathbf{u}_k + \mathbf{w}_k \quad (1)$$

$$\mathbf{y}_k = \mathbf{C}\mathbf{x}_k + \mathbf{D}\mathbf{u}_k + \mathbf{v}_k, \quad (2)$$

where $\mathbf{y}_k \in \mathbb{R}^{n_y}$ is the measured response vector at time k , $\mathbf{u}_k \in \mathbb{R}^{n_u}$ the vector with the measured forces, $\mathbf{x}_k \in \mathbb{R}^n$ the state vector, and \mathbf{A} , \mathbf{B} , \mathbf{C} and \mathbf{D} state-space matrices that are to be identified. $\mathbf{w}_k \in \mathbb{R}^n$ accounts for the influence of the unmeasured, operational excitation on the state vector, and \mathbf{v}_k models both the direct transmission of the operational excitation to the measured response, as well as response measurement errors. (\mathbf{w}_k) and (\mathbf{v}_k) are assumed to be discrete-time white noise sequences:

$$\mathcal{E} \left(\begin{bmatrix} \mathbf{w}_{k+l} \\ \mathbf{v}_{k+l} \end{bmatrix} \begin{bmatrix} \mathbf{w}_k \\ \mathbf{v}_k \end{bmatrix}^T \right) = \begin{bmatrix} \mathbf{Q} & \mathbf{S} \\ \mathbf{S}^T & \mathbf{R} \end{bmatrix} \delta_1(l), \quad (3)$$

where \mathcal{E} denotes the expectation operator and $\delta_1(\square)$ is the unit impulse function, i.e., $\delta_1(0) = 1$ and $\delta_1(\square) = 0$ if $\square \neq 0$. The state-space model (1-3) may be derived from a linear time-invariant structural model such as a continuous-time finite element model, by applying zero-order hold time discretization to the measured and ambient forces, and assuming that both the ambient forces and the response measurement errors make up discrete white noise sequences, see, e.g., [14, 15]. Although the white noise model for the ambient forces is often a rough approximation, it turns out to be accurate enough in many operational modal analysis applications, and therefore it is very often used in OMA(X), see, e.g., the surveys [11, 13].

The CSI-ic(ref) algorithm identifies the state-space model (1-3) from the measured sequences (\mathbf{u}_k) and (\mathbf{y}_k) . First, the response sequence (\mathbf{y}_k) is decomposed in a deterministic, forced part (\mathbf{y}_k^d) , and a stochastic, ambient part (\mathbf{y}_k^s) . Then, the deterministic impulse response and the stochastic output correlation sequences are computed, and the system matrices are

determined from these sequences. The different stages are discussed in more detail in the following sections. Once the system matrices are identified, the eigenfrequencies, damping ratios, mode shapes and modal scaling factors can be computed as in [14].

3.1 Decomposition of the measured response in a forced and ambient part

Let the measured inputs and outputs be gathered in block Hankel matrices denoted as $\mathbf{U}_{k_1|k_2}$ and $\mathbf{Y}_{k_1|k_2}$, respectively, where

$$\mathbf{Y}_{k_1|k_2} \triangleq \begin{bmatrix} \mathbf{y}_{k_1} & \mathbf{y}_{k_1+1} & \mathbf{y}_{k_1+2} & \cdots & \mathbf{y}_{k_1+j-1} \\ \mathbf{y}_{k_1+1} & \mathbf{y}_{k_1+2} & \mathbf{y}_{k_1+3} & \cdots & \mathbf{y}_{k_1+j} \\ \vdots & \vdots & \vdots & \cdots & \vdots \\ \mathbf{y}_{k_2} & \mathbf{y}_{k_2+1} & \mathbf{y}_{k_2+2} & \cdots & \mathbf{y}_{k_2+j-1} \end{bmatrix} \quad \text{and} \quad \mathbf{U}_{k_1|k_2} \triangleq \begin{bmatrix} \mathbf{u}_{k_1} & \mathbf{u}_{k_1+1} & \mathbf{u}_{k_1+2} & \cdots & \mathbf{u}_{k_1+j-1} \\ \mathbf{u}_{k_1+1} & \mathbf{u}_{k_1+2} & \mathbf{u}_{k_1+3} & \cdots & \mathbf{u}_{k_1+j} \\ \vdots & \vdots & \vdots & \cdots & \vdots \\ \mathbf{u}_{k_2} & \mathbf{u}_{k_2+1} & \mathbf{u}_{k_2+2} & \cdots & \mathbf{u}_{k_2+j-1} \end{bmatrix}, \quad (4)$$

with k_1 and k_2 suitable integers that will be fixed later, and j an integer that is large enough so that these matrices have more columns than rows. Let $\mathbf{Y}_{k_1|k_2}^d$ and $\mathbf{Y}_{k_1|k_2}^s$ denote the forced (deterministic) and ambient (stochastic) parts of $\mathbf{Y}_{k_1|k_2}$, respectively. When the ambient response is not correlated with the forced loading, the following estimates for $\mathbf{Y}_{k+1|k+l}^d$ and $\mathbf{Y}_{k+1|k+l}^s$ are strongly consistent¹, assuming the structure under test is stable, for $k, j \rightarrow \infty$ [15]:

$$\hat{\mathbf{Y}}_{k+1|k+l}^d \triangleq \mathbf{Y}_{k+1|k+l} / \mathcal{U}_{1|k+l} \quad (5)$$

$$\hat{\mathbf{Y}}_{k+1|k+l}^s \triangleq \mathbf{Y}_{k+1|k+l} / \mathcal{U}_{1|k+l}^\perp, \quad (6)$$

where $\mathcal{U}_{1|k+l}$ denotes the row space spanned by the rows of $\mathbf{U}_{1|k+l}$, and $\mathcal{U}_{1|k+l}^\perp$ denotes the orthogonal complement of $\mathcal{U}_{1|k+l}$. Equations (5-6) imply that, contrary to most subspace algorithms, not only the number of block columns of the input and output Hankel matrices need to grow in order to converge to the exact values, but also the number of block rows of the input Hankel matrix. However, since in modal testing, the number of inputs is usually much smaller than the number of outputs, i.e., $n_u \ll n_y$, the corresponding increase in computational cost is fairly limited. $\hat{\mathbf{Y}}_{k+1|k+l}^d$ and $\hat{\mathbf{Y}}_{k+1|k+l}^s$ can be efficiently computed using LQ factorization, as explained in [15].

As an example, Fig. 3 shows a PAM force applied at point 192 of the Wetteren footbridge (Fig. 2), and the decomposed acceleration signals at points 42 and 192, all in the vertical direction. The decomposition was directly computed from (5-6), by setting $k = 120$ and $l = 1$. It can be noted that the forced and the ambient response signals are of similar amplitude, which illustrates the combined experimental-operational character of the performed OMAX test.

3.2 Estimation of the deterministic impulse response sequence

Suppose the first $2l$ samples of the impulse response sequence of the deterministic subsystem are of interest. Let ℓ denote any integer that is larger than the system order n . Let $\mathcal{H}_{0|2l-1}$ denote the matrix consisting of the impulse response matrices that we want to estimate, i.e.,

$$\mathcal{H}_{0|2l-1} \triangleq [\mathbf{H}_0^T \ \mathbf{H}_1^T \ \mathbf{H}_2^T \ \cdots \ \mathbf{H}_{2l-1}^T]^T. \quad (7)$$

As discussed in [15], when $\mathbf{Y}_{k+1|k+2l+\ell}^d$ is known, the impulse response can be exactly computed as

$$\mathcal{H}_{0|2l-1} = \mathbf{Y}_{k+1|k+2l+\ell}^d \begin{bmatrix} \mathbf{U}_{k+1|k+2l+\ell} \\ \mathbf{Y}_{k+1|k+\ell}^d \end{bmatrix}^\dagger \begin{bmatrix} \mathbf{0}_{n_u \ell \times n_u} \\ \mathbf{I}_{n_u} \\ \mathbf{0}_{(2l-1)n_u + \ell n_y \times n_u} \end{bmatrix}, \quad (8)$$

¹ A stochastic sequence $(\hat{\boldsymbol{\theta}}_N)$ is said to converge to $\tilde{\boldsymbol{\theta}}$ *almost surely* (a.s.) or, equivalently, *with probability 1* (w.p. 1) for almost all realizations of $(\hat{\boldsymbol{\theta}}_N)$, except for those with probability zero, when [12, p. 446]

$$\text{a.s.} \lim_{N \rightarrow \infty} \hat{\boldsymbol{\theta}}_N = \tilde{\boldsymbol{\theta}} \Leftrightarrow \forall \varepsilon > 0 : \lim_{N \rightarrow \infty} \mathcal{P}(\|\hat{\boldsymbol{\theta}}_N - \tilde{\boldsymbol{\theta}}\| \leq \varepsilon) = 1,$$

where $\mathcal{P}(\square)$ denotes the probability of \square . When an estimate converges almost surely to its exact value, the estimate is called *strongly consistent*.

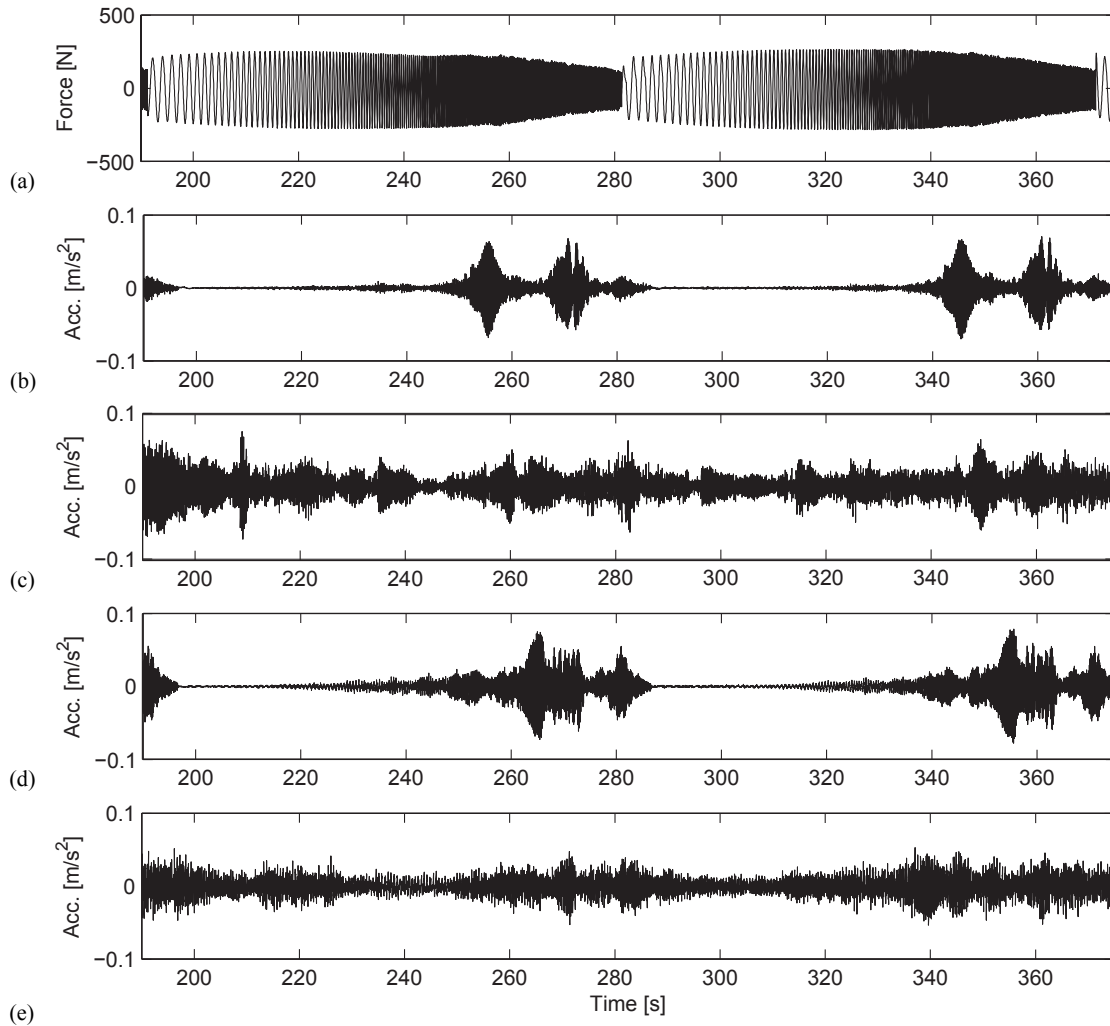


Fig. 3 Wetteren footbridge, PAM loading, first setup: (a) Applied logarithmic swept sine force at point 192, (b) forced response at point 42, (c) ambient response at point 42, (d) forced response at point 192, (e) ambient response at point 192. All of these signals are in the vertical direction.

where \square^\dagger denotes the Moore-Penrose pseudo-inverse. When the exact deterministic output matrix $\mathbf{Y}_{k+1|k+2l+\ell}^d$ is replaced by the estimate $\hat{\mathbf{Y}}_{k+1|k+2l+\ell}^d$, computed as in (5), the resulting impulse response estimate $\hat{\mathcal{H}}_{0|2l-1}$ is strongly consistent for $j \rightarrow \infty$.

3.3 Estimation of the stochastic output correlation sequence

In modal testing, typically many outputs are measured in order to achieve a good spatial resolution of the mode shapes. Instead of computing correlation matrices between all measured outputs for different time lags, it is more efficient to compute the correlation matrices between all outputs and a subset of outputs, called reference outputs [10, 14]. These correlation matrices are denoted as

$$\mathbf{\Lambda}_k^{ref} \triangleq \mathcal{E} \left(\mathbf{y}_{l+k} \mathbf{y}_l^{refT} \right) \quad \text{where} \quad \mathbf{y}_l^{ref} \triangleq \mathbf{S}^r \mathbf{y}_l, \quad (9)$$

with $\mathbf{S}^r \in \mathbb{R}^{n_y \times n_r}$ a selection matrix and n_r the number of reference outputs. In order not to lose information, it is important that any mode of interest is clearly present in at least one reference output. Good reference output candidates are usually driving point outputs, or, in case of measurements performed in different setups, the output channels common to all setups.

Let $\mathcal{L}_{0|2l-1}^{ref}$ denote the matrix consisting of the stochastic output correlation matrices that we want to estimate, i.e.,

$$\mathcal{L}_{0|2l-1}^{ref} \triangleq \left[\mathbf{\Lambda}_0^{refT} \quad \mathbf{\Lambda}_1^{refT} \quad \dots \quad \mathbf{\Lambda}_{2l-1}^{refT} \right]^T. \quad (10)$$

Since (6) delivers a strongly consistent estimate $\hat{\mathbf{Y}}_{k+1|k+2l}^s$ for $\mathbf{Y}_{k+1|k+2l}^s$, it follows immediately that

$$\hat{\mathcal{L}}_{0|2l-1}^{ref} \triangleq \frac{1}{j} \hat{\mathbf{Y}}_{k+1|k+2l}^s \hat{\mathbf{Y}}_{k+1|k+1}^{s,refT} \quad (11)$$

is a strongly consistent estimate of $\mathcal{L}_{0|2l-1}^{ref}$.

3.4 Determination of the system matrices

From the state-space model (1-2), it is clear that the deterministic impulse response can be parameterized as

$$\mathbf{H}_0 = \mathbf{D} \quad (12)$$

$$\mathbf{H}_k = \mathbf{C}\mathbf{A}^{k-1}\mathbf{B}, \quad k \geq 1. \quad (13)$$

When the impulse response matrices for $k \geq 1$ are gathered in the following block Hankel matrix, it can be decomposed as

$$\mathbf{H}_{1|l} \triangleq \begin{bmatrix} \mathbf{H}_1 & \mathbf{H}_2 & \dots & \mathbf{H}_l \\ \mathbf{H}_2 & \mathbf{H}_3 & \dots & \mathbf{H}_{l+1} \\ \vdots & \vdots & \dots & \vdots \\ \mathbf{H}_l & \mathbf{H}_{l+1} & \dots & \mathbf{H}_{2l-1} \end{bmatrix} = \underbrace{\begin{bmatrix} \mathbf{C} \\ \mathbf{C}\mathbf{A} \\ \vdots \\ \mathbf{C}\mathbf{A}^{l-1} \end{bmatrix}}_{:=\mathcal{O}_l} \underbrace{\begin{bmatrix} \mathbf{B} & \mathbf{A}\mathbf{B} & \dots & \mathbf{A}^{l-1}\mathbf{B} \end{bmatrix}}_{:=\mathcal{C}_l^d}. \quad (14)$$

The rank of $\mathbf{H}_{1|l}$ equals the system order n when $n_{y,l} \geq n$ and $n_{u,l} \geq n$. From the state-space model (1-2), it also follows that the stochastic output correlations can be parameterized as

$$\mathbf{\Lambda}_k = \mathbf{C}\mathbf{A}^{k-1}\mathbf{G}^{ref}, \quad k \geq 1,$$

where $\mathbf{G}^{ref} \triangleq \mathcal{E}(\mathbf{x}_{k+1}^s \mathbf{y}_k^{ref,sT})$. Consequently, when the stochastic output correlations are gathered in a block Hankel matrix $\mathbf{\Lambda}_{1|l}^{ref}$, which is defined as $\mathbf{H}_{1|l}$ but with the impulse response matrices replaced by output correlation matrices, one has

$$\mathbf{\Lambda}_{1|l}^{ref} = \mathcal{O}_l \underbrace{\begin{bmatrix} \mathbf{G}^{ref} & \mathbf{A}\mathbf{G}^{ref} & \dots & \mathbf{A}^{l-1}\mathbf{G}^{ref} \end{bmatrix}}_{:=\mathcal{C}_l^s}. \quad (15)$$

From the above decomposition, it follows that the rank of $\mathbf{\Lambda}_{1|l}^{ref}$ equals the system order n when $n_{r,l} \geq n$. From the combination of (14) and (15), one has

$$\begin{bmatrix} \mathbf{H}_{1|l} & \mathbf{\Lambda}_{1|l}^{ref} \end{bmatrix} = \mathcal{O}_l \begin{bmatrix} \mathcal{C}_l^d & \mathcal{C}_l^s \end{bmatrix}.$$

Depending on the input and output units chosen, $\mathbf{H}_{1|l}$ and $\mathbf{\Lambda}_{1|l}^{ref}$ may be of completely different orders of magnitude. Therefore, and in order to agree with the common practice in data-driven subspace identification [14], weighting matrices are introduced:

$$\mathbf{G}_{1|l} := \mathbf{W}_1 \begin{bmatrix} \mathbf{H}_{1|l} \mathbf{W}_2^d & \mathbf{\Lambda}_{1|l}^{ref} \mathbf{W}_2^s \end{bmatrix} = \mathbf{W}_1 \mathcal{O}_l \begin{bmatrix} \mathcal{C}_l^d \mathbf{W}_2^d & \mathcal{C}_l^s \mathbf{W}_2^s \end{bmatrix}.$$

The matrices \mathcal{O}_l , \mathcal{C}_l^d and \mathcal{C}_l^s can be obtained from $\mathbf{G}_{1|l}$, up to a similarity transformation of the \mathbf{A} matrix, using reduced singular value decomposition:

$$\mathbf{G}_{1|l} = \mathbf{USV}^T = \mathbf{US} \begin{bmatrix} \mathbf{V}^d & \mathbf{V}^s \end{bmatrix} \quad (16)$$

$$\mathcal{O}_l = \mathbf{W}_1^{-1} \mathbf{US}^{1/2} \quad \mathcal{C}_l^d = \mathbf{S}^{1/2} \mathbf{V}_D^T (\mathbf{W}_2^d)^{-1} \quad \mathcal{C}_l^s = \mathbf{S}^{1/2} \mathbf{V}_S^T (\mathbf{W}_2^s)^{-1}, \quad (17)$$

where $\mathbf{S} \in \mathbb{R}^{n \times n}$ contains the nonzero singular values and $\mathbf{U} \in \mathbb{R}^{m_y \times n}$ and $\mathbf{V} \in \mathbb{R}^{(n_u+n_r^{ref}) \times n}$ contain the corresponding singular vectors. Replacing $\mathbf{H}_{1|i}$ and $\mathbf{L}_{1|i}^{ref}$ by their estimates $\hat{\mathbf{H}}_{1|i}$ and $\hat{\mathbf{L}}_{1|i}^{ref}$, respectively, has the effect that \mathbf{S} contains more than n nonzero singular values. The system order n can then be estimated as the number of significant singular values of $\hat{\mathbf{G}}_{1|i}$, $\hat{\mathbf{H}}_{1|i}$ or $\hat{\mathbf{L}}_{1|i}^{ref}$.

The system matrices are easily obtained from \mathcal{O}_i , \mathcal{C}_i^d and \mathcal{C}_i^s . The \mathbf{C} matrix can be determined as the first n_y rows of \mathcal{O}_i , the \mathbf{B} matrix as the first n_u columns of \mathcal{C}_i^d , and the \mathbf{G}^{ref} matrix as the first n_r columns of \mathcal{C}_i^s . The matrix \mathbf{D} follows immediately from (12). For the determination of \mathbf{A} , we follow Kung's approach, which makes use of the shift structure of the matrix \mathcal{O}_i [8]:

$$\mathbf{A} = \underline{\mathcal{O}}_i^\dagger \overline{\mathcal{O}}_i, \quad (18)$$

where $\underline{\mathcal{O}}_i$ is equal to \mathcal{O}_i without the last n_y rows and $\overline{\mathcal{O}}_i$ is equal to \mathcal{O}_i without the first n_y rows.

3.5 Reference-based implementation

When reference outputs are introduced in (8), the computational effort needed for estimating the system matrices can be drastically reduced, especially when $n_y \gg n_r$. The resulting algorithm is termed the *reference-based* CSI-ic algorithm or CSI-ic/ref. It can also be noted that the data projections can be efficiently implemented by making use of the LQ-factorization technique, where the explicit computation of the Q-factor can be avoided, as in other subspace algorithms.

4 OMAX analysis of Wetteren footbridge using the CSI-ic/ref algorithm

Here, the CSI-ic/ref algorithm that was presented in the previous section is applied to the OMAX-PAM test at Wetteren footbridge as described in section 2.2.

The measured signals were digitally low-pass filtered with an eight-order Chebychev Type I filter with a cutoff frequency of 20 Hz, in both the forward and reverse directions to remove all phase distortion, and then re-sampled at 50 Hz. Subsequently, the data were high-pass filtered with a fourth-order Butterworth filter with a cutoff frequency of 0.2 Hz, again in both the forward and reverse directions. From these data, the modal parameters were estimated using the CSI-ic/ref algorithm, where the channels that are common to all setups were used as reference channels. The algorithm parameters were chosen as: $k = 280$, $\ell = 100$ and $\iota = 50$. A model order range from 2 to 200 in steps of 2 was chosen for the construction of the stabilization diagrams.

Fig. 4 shows some identified eigenfrequencies and mode shapes. The corresponding damping ratios can be found in table 1. Since there are no double modes and no localized dampers, real normal modes are expected, i.e., the phase difference between the coefficients of the mode shapes is expected to be 0° or 180° . The *modal phase collinearity* (MPC) is therefore a good quantity for assessing the quality of the mode shapes: an MPC value of 1 indicates a perfect normal mode, an MPC value near 0 denotes a highly complex mode [7]. For all identified modes, the corresponding MPC values are listed in table 1. The table also shows the eigenfrequencies, computed with the finite element model, when the *modal assurance criterion* (MAC) value between the identified and the corresponding computed mode shape is larger than 0.6. In that case, also the *modal scale factor* (MSF) between the identified and the computed mass-normalized mode shapes are plotted as well. The MSF gives a least-squares estimate of the ratio between both mass-normalized mode shapes [7]. When the MSF is real and close to 1, both mass-normalized mode shapes have nearly the same amplitude and phase. Since it only makes sense to calculate a MSF value when both modes are well correlated, the table only shows MSF values when the corresponding MAC exceeds 0.6.

5 Comparison with other results

In a previous study, the modal parameters have been extracted from the ambient data using the SSI-data/ref algorithm, and from the OMAX data using the CSI-data/ref algorithm [16]. The block Hankel matrices were constructed with $\iota = 30$ and $\iota = 40$ for both algorithms, respectively. All other parameters were the same as in the CSI-ic/ref analysis presented above. The results are also summarized in table 1. Modes 7 and 10 are not detected in the ambient test. The MPC values of modes 1, 4, 20, 25, 27 and 31 are significantly lower for the ambient data than for the OMAX data, which indicates less accurate mode shape estimates.

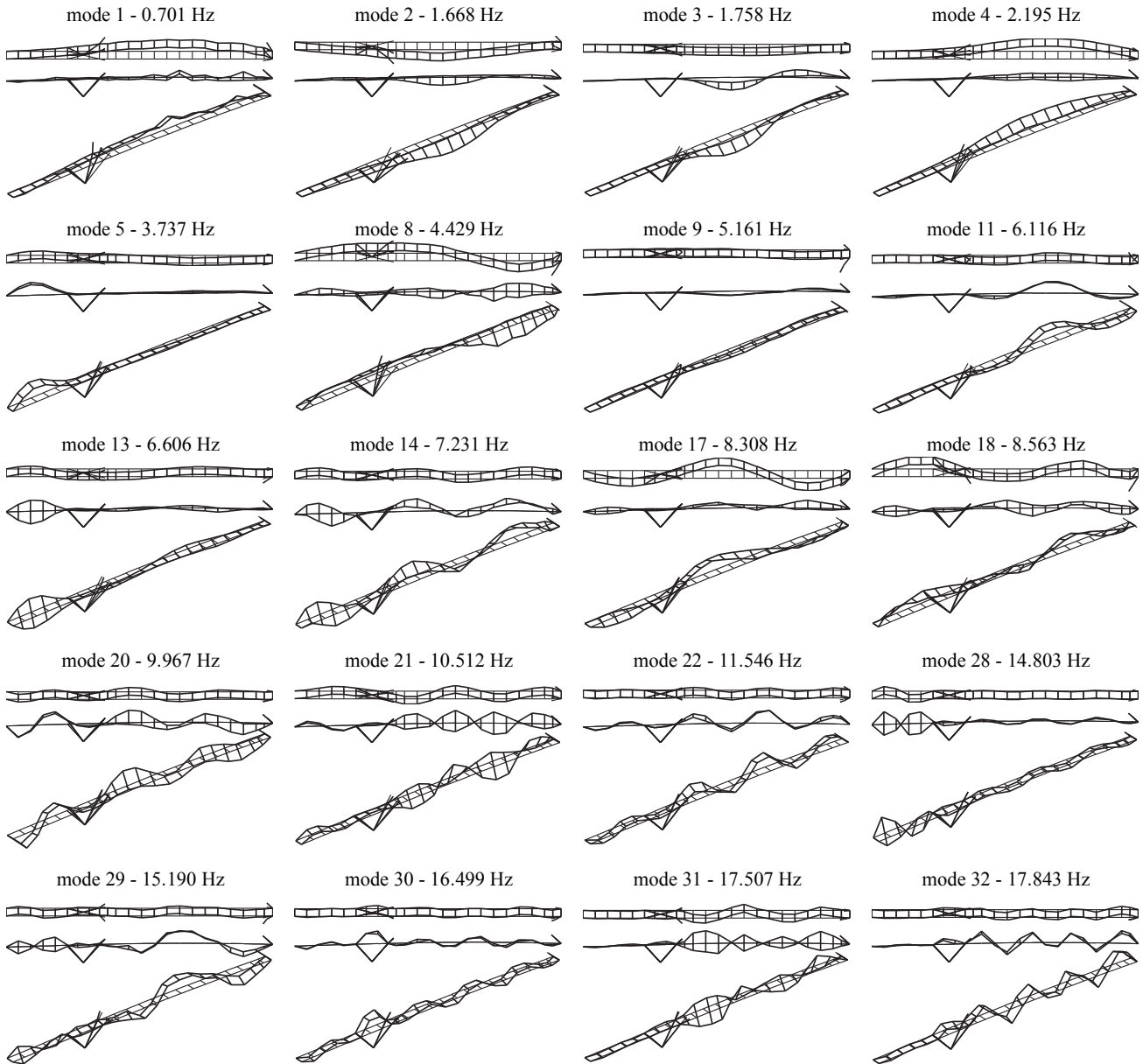


Fig. 4 OMAX testing of Wetteren footbridge: Some mode shapes, obtained with CSI-ic/ref (top: top view, middle: side view from the southeast side, bottom: three-dimensional view from the south side).

The estimates obtained with CSI-ic/ref and CSI-data/ref are very similar, except for some of the MSF values. This is probably due to the fact that many modes involve only small deformations at the excitation DOF, and the sometimes rather small ratio between forced and ambient response, as observed in Fig. 3. However, since it concerns an OMAX test, apart from the modal scaling factors, the other modal parameters of these modes are accurately determined, thanks to the fact that the operational excitation is fully taken into account.

nr.	FEM				Ambient - SSI-data/ref					OMAX - CSI-ic/ref					OMAX - CSI-data/ref				
	f_{udi} [Hz]	f_{udi} [Hz]	ξ_i [%]	MPC [-]	f_{udi} [Hz]	ξ_i [%]	MPC [-]	MAC [-]	MSF [-]	f_{udi} [Hz]	ξ_i [%]	MPC [-]	MAC [-]	MSF [-]	f_{udi} [Hz]	ξ_i [%]	MPC [-]	MAC [-]	MSF [-]
1	0.739	0.711	2.12	0.80	0.701	1.74	0.90	0.87	-0.16+0.01i	0.693	1.05	0.98	0.91	-0.47+0.21i					
2	1.739	1.671	0.21	1.00	1.668	0.15	0.98	0.88	-0.83+0.04i	1.669	0.23	0.99	0.86	1.79-0.37i					
3		1.769	0.59	0.97	1.758	0.57	0.98			1.758	0.76	0.98							
4	2.363	2.138	1.90	0.80	2.195	0.54	0.99	0.97	-0.91-0.01i	2.195	0.50	0.99	0.97	-1.01-0.02i					
5	3.250	3.743	0.76	0.98	3.737	0.68	0.98	0.70	-0.68-0.06i	3.731	0.55	0.98	0.70	1.01+0.14i					
6	3.833	3.836	0.67	0.95	3.840	0.54	0.98	0.78	1.31+0.00i	3.838	0.49	0.98	0.80	1.19-0.19i					
7					3.963	0.76	0.95			3.950	0.69	0.97							
8	3.891	4.442	0.56	0.99	4.429	1.78	0.89	0.82	0.01-1.22i	4.480	0.76	0.96	0.83	0.28-1.36i					
9	3.939	5.143	1.15	0.80	5.161	0.36	0.84	0.76	-0.94+0.03i	5.154	0.44	0.97	0.84	1.20-0.14i					
10					5.813	0.66	0.96			5.802	0.45	0.99							
11	6.377	6.111	0.52	0.89	6.116	0.25	0.93	0.85	-0.71-0.05i	6.117	0.27	0.99	0.87	0.87-0.01i					
12	6.662	6.321	0.73	0.98	6.320	0.50	0.95	0.91	-0.65-0.04i	6.321	0.50	0.99	0.92	1.76-0.14i					
13	6.991	6.621	0.62	0.98	6.606	0.53	0.98	0.88	1.26+0.05i	6.605	0.58	0.98	0.88	-0.69+0.04i					
14		7.209	2.15	0.84	7.231	2.65	0.85			7.238	2.34	0.79							
15	8.028	7.509	0.70	0.84	7.500	0.75	0.88	0.70	-0.73-0.01i	7.488	0.70	0.88	0.77	1.21+0.04i					
16		7.582	1.36	0.88	7.561	1.22	0.92			7.577	1.29	0.93							
17	8.599	8.322	1.18	0.97	8.308	1.45	0.94	0.76	1.26-0.03i	8.307	1.18	0.97	0.78	-0.35-0.02i					
18		8.556	0.58	0.93	8.563	0.68	0.96			8.565	0.68	0.95							
19		9.570	0.88	0.91	9.565	0.79	0.95			9.565	0.74	0.96							
20	10.395	9.962	1.28	0.87	9.967	1.04	0.95	0.62	-0.34-1.43i	9.967	1.10	0.94	0.63	-1.14+0.10i					
21	11.397	10.503	0.50	0.96	10.512	0.77	0.96	0.74	0.89+0.04i	10.475	0.64	0.97	0.75	1.12+0.04i					
22	11.864	11.245	0.66	0.97	11.246	0.72	0.96	0.84	1.58+0.15i	11.214	0.78	0.92	0.82	0.32+1.23i					
23	11.624	11.804	1.71	0.95	11.828	1.77	0.96	0.77	0.97+0.13i	11.821	1.68	0.97	0.78	0.99+0.08i					
24	13.146	12.739	0.28	0.87	12.727	0.30	0.87	0.65	0.32+0.08i	12.728	0.35	0.85	0.65	0.40-1.28i					
25	13.254	12.896	0.65	0.47	12.868	0.88	0.76	0.72	-0.04-0.86i	12.863	0.72	0.65	0.72	0.08+0.45i					
26	14.479	13.522	0.51	0.86	13.519	0.83	0.80			13.530	0.72	0.76							
27		13.648	0.60	0.77	13.602	0.38	0.88			13.606	0.39	0.92							
28	15.620	14.809	0.50	0.92	14.803	0.41	0.97	0.81	0.03-0.36i	14.810	0.41	0.95	0.78	0.48+0.77i					
29		15.225	0.69	0.86	15.190	0.36	0.86			15.213	0.46	0.87							
30	16.648	16.514	0.68	0.97	16.499	0.45	0.90	0.76	1.19+0.03i	16.502	0.53	0.96	0.80	-0.13-0.27i					
31		17.531	0.92	0.72	17.507	0.22	0.85			17.508	0.31	0.90							
32	18.537	17.839	0.26	0.87	17.843	0.31	0.87	0.83	-0.57-0.01i	17.833	0.28	0.88	0.83	0.03-0.42i					

Table 1 OMAX testing of Wetteren footbridge: comparison of undamped eigenfrequencies f_{udi} and damping ratios ξ_i , obtained from the ambient data, using SSI-data/ref, and from the OMAX data, using CSI-ic/ref and CSI-data/ref. The MAC and MPC values as well as the MSF between the measured mass-normalized mode shapes and the ones obtained from the finite element model, are shown as well.

6 Conclusions

In this paper, the performance of the CSI-ic/ref algorithm for OMAX testing was assessed in a real-life case study: modal testing of a two-span steel bowstring footbridge. From this study, as well as from simulations and case studies reported earlier, it can be concluded that:

- The modal parameters obtained from OMAX are more accurate than the modal parameters obtained from the classical EMA and OMA approaches, which can both be considered as limiting cases within the OMAX framework.
- In an OMAX framework, accurate eigenfrequency, damping ratio, and (unscaled) mode shape estimates can be obtained for modes that are well excited by *either* measured or unmeasured forces.
- In order to obtain good estimates for the modal scaling factors, the modes need to be well excited by the measured forces, also in an OMAX framework.
- Although their computational and statistical performance is similar, the CSI-ic/ref algorithm is slightly suboptimal w.r.t. the CSI-data/ref algorithm. However, CSI-ic/ref is physically more intuitive and therefore a valuable alternative to CSI-data/ref.

Acknowledgements

This research was partially supported by the Research Foundation - Flanders, Belgium (Research Project G.0343.04 and Postdoctoral Fellowship provided to the first author) and the Fund for Special Research of K.U.Leuven, Belgium (Postdoctoral Fellowship provided to the first author). The authors gratefully acknowledge the financial support from these institutes.

References

1. E. Caetano, Á. Cunha, and C. Moutinho. Implementation of passive devices for vibration control at Coimbra footbridge. In *Proceedings of the convergence on experimental vibration analysis for civil engineering structures - EVACES07*, pages 43–54, Porto, Portugal, October 2007.
2. B. Cauberghe. *Applied frequency-domain system identification in the field of experimental and operational modal analysis*. PhD thesis, Vrije Universiteit Brussel, 2004.
3. B. Cauberghe, P. Guillaume, P. Verboven, and E. Parloo. Identification of modal parameters including unmeasured forces and transient effects. *Journal of Sound and Vibration*, 265(3):609–625, 2003.
4. P. Dallard, A.J. Fitzpatrick, A. Flint, S. Le Bourva, A. Low, R.M. Ridsdill Smith, and M. Willford. The London Millennium Footbridge. *The Structural Engineer*, 79(22):17–33, 2001.
5. K. Deckers, P. Guillaume, D. Lefeber, G. De Roeck, and E. Reynders. Modal testing of bridges using low-weight pneumatic artificial muscle actuators. In *Proceedings of IMAC 26, the International Modal Analysis Conference*, Orlando, FL, February 2008. CD-ROM.
6. P. Guillaume, T. De Troyer, C. Devriendt, and G. De Sitter. OMAX - a combined experimental-operational modal analysis approach. In P. Sas and M. De Munck, editors, *Proceedings of ISMA2006 International Conference on Noise and Vibration Engineering*, pages 2985–2996, Leuven, Belgium, September 2006.
7. W. Heylen, S. Lammens, and P. Sas. *Modal analysis theory and testing*. Department of Mechanical Engineering, Katholieke Universiteit Leuven, Leuven, Belgium, 1997.
8. S.Y. Kung. A new identification and model reduction algorithm via singular value decomposition. In *Proceedings of the 12th Asilomar conference on circuits, systems and computers*, pages 705–714, Pacific Grove, CA, 1978.
9. E. Parloo, P. Verboven, P. Guillaume, and M. Van Overmeire. Sensitivity-based operational mode shape normalization. *Mechanical Systems and Signal Processing*, 16(5):757–767, 2002.
10. B. Peeters and G. De Roeck. Reference-based stochastic subspace identification for output-only modal analysis. *Mechanical Systems and Signal Processing*, 13(6):855–878, 1999.
11. B. Peeters and G. De Roeck. Stochastic system identification for operational modal analysis: A review. *ASME Journal of Dynamic Systems, Measurement, and Control*, 123(4):659–667, 2001.
12. R. Pintelon and J. Schoukens. *System Identification*. IEEE Press, New York, NY, 2001.
13. E. Reynders. *System identification and modal analysis in structural mechanics*. PhD thesis, Department of Civil Engineering, K.U.Leuven, 2009.
14. E. Reynders and G. De Roeck. Reference-based combined deterministic-stochastic subspace identification for experimental and operational modal analysis. *Mechanical Systems and Signal Processing*, 22(3):617–637, 2008.
15. E. Reynders and G. De Roeck. On the separation of a measured structural response in a forced and an ambient part for OMAX testing. In *Proceedings of ISMA2010 International Conference on Noise and Vibration Engineering*, pages 3287–3302, Leuven, Belgium, September 2010.
16. E. Reynders, D. Degrauwe, G. De Roeck, F. Magalhães, and E. Caetano. Combined experimental-operational modal testing of footbridges. *ASCE Journal of Engineering Mechanics*, 136(6):687–696, 2010.

Bridge Pier Scour Measurement by Means of Bragg Grating Arrays: Laboratory Tests and Field Applications

F. Ballio¹, A. Cigada², G. Crotti¹, F. Inzoli³, S. Manzoni²

1. Politecnico di Milano, D.I.I.A.R. – Piazza Leonardo da Vinci 32, 20133 Milan (Italy)
2. Politecnico di Milano, Department of Mechanics – Via La Masa 1, 20156 Milan (Italy)
e-mail: stefano.manzoni@polimi.it
3. Politecnico di Milano, Department of Energy – Via Lambruschini 4, 20156 Milan (Italy)

ABSTRACT

This paper deals with a new method to measure scour level at bridge piers. The proposed technique is based on an array of Bragg grating temperature sensors, heated by an electrical circuit. The Bragg gratings in water sense a lower temperature than those buried in the river bed, because of the different heat scattering principles in the two situations. Furthermore the response of each sensor is slower if it is buried in the bed, with respect to the case it is in water. The paper presents laboratory tests, showing the method effectiveness and reliability, and it explains the advantages with respect to other more traditional methodologies to measure scour level. Finally, the first field application is presented.

1 Introduction

Bridge collapses during floods are not so uncommon [1]. Scouring is one of the main reasons. Actually erosion at bridge piers is a continuous phenomenon, balanced by solid deposit; this balance is wiped off by floods, in which accelerated scouring takes place (Fig. 1). Scouring might dig holes in the order of several meters in a few hours. Many elements make any modelling forecast a hard task, as any eventual collapse is related to a long preceding history, then the fluid dynamics of scouring is quite complicated, involving a mix of vortex shedding and high speed streams from the top to the bottom. This phenomenon can be further complicated by the presence of debris stopped at the bridge piers and therefore causing a sort of Venturi's effect at the same time making the resisting section wider.

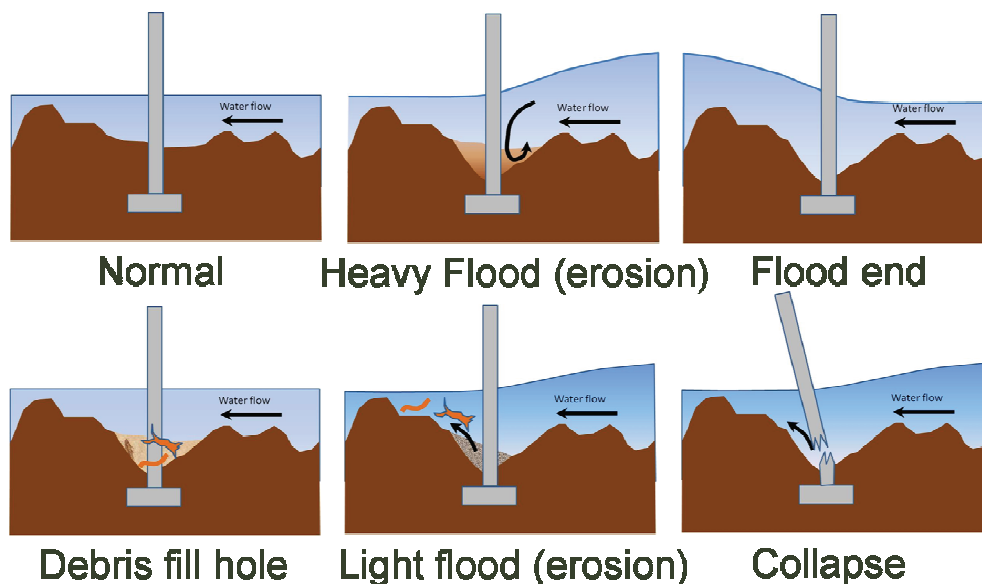


Fig. 1 Bridge pier collapse due to scour

As models have a wide uncertainty, making them unable to reliably predict the scour development, several methods have been developed allowing for in situ scour measurements. Many solutions have been tempted through the years, and they are described and revised in [2-6], pointing out both strengths and weaknesses. The most commonly adopted solutions are echo sounders, sounding rods and buried rods. Often echo sounders do not guarantee satisfactory measurement accuracy during floods, which are the most critical events for pier scour. Furthermore they have to be immersed in the flowing water, rich in debris making the measurement environment a very harsh one. Reliability cannot be guaranteed and therefore also safety for people crossing the bridge. Looking for new solutions the ideal condition would be having very small and robust sensors; in addition a further requirement should be avoiding to stay in the flowing water, for both mechanical resistance issues and also to prevent from electrical problems like short circuits or current leakage: the overall requirement is a reliable measurement, under both standard and flood conditions, finding the best compromise with the expected costs and installation complexity.

A new solution has been designed [7], based on optical fibres equipped with Bragg sensors to measure temperature. The paper will go through a preliminary evaluation of the strengths and weaknesses for the proposed approach, then a laboratory testing for a preliminary validation will be considered, together with all the possible signal processing techniques. Finally, the first field demonstration activities will be presented.

2 Measurement method

The basic idea is to adopt an array of temperature sensors based on Bragg gratings [8,9]. The array is laid down in the vertical direction, just fixed to the pier along its depth. Fig. 2 presents the system layout where many different sensors are shown.

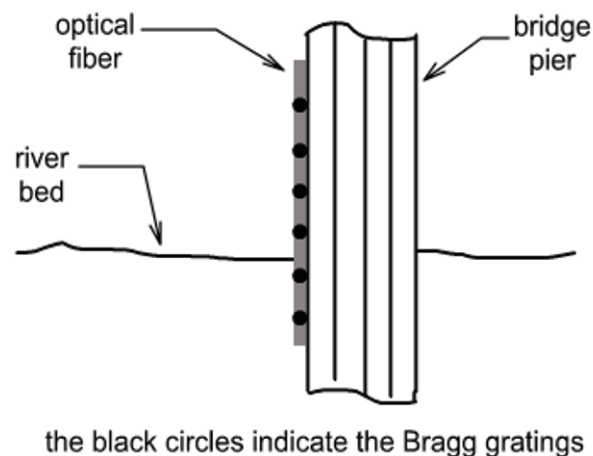


Fig. 2 Measurement system layout

Bragg gratings (FBG in the following) act as light wavelength filters: each sensor is obtained through a process by which a series of changes in the refraction index in the fiber is obtained. The spacing of these changes (grating pitch) is constant. In case white light is sent through the fiber (but a swept sine wavelength is good as well), interference phenomena are such that all wavelengths pass through the fiber except one, the so called Bragg wavelength, which is sent back to an optical analyzer, measuring its wavelength or frequency. As the fiber is subject to any kind of strain, related to both mechanical or thermal effects, the reflected frequency varies accordingly: any change in frequency means strain, which is a change in the grating pitch.

It is remembered that, while mechanical strain has a direct effect on the grating pitch, by changing its length, thermal strain has a twin effect, as it causes a direct thermal strain, but it also changes the refraction index.

Although the sensitivity to temperature is roughly ten times higher than the sensitivity to strain, all the same, for the case of bridge scouring, sensors should sense just temperature and nothing else; mechanical strain is considered an interfering variable which must be deleted from measurements. One possible solution, adopted for the present research, has consisted in inserting the fiber into a stainless steel (Fig. 3) tube filled with thermal paste, so to grant heat transfer, at the same time preventing from mechanical strain.

Referring to an array of temperature sensors one might ask why not using common thermocouples or Resistance Temperature Detectors. There are several reasons for this choice: first of all it has already been noted that light flows inside the sensors instead of electricity, so no short circuits can occur, the device has total immunity to electro-magnetic or radio frequency interference; in addition, being the fiber mainly made up of glass, it is a dielectric capable to suppress any unwanted electrical path. Furthermore the fiber is very thin, so it is possible to “hide” it somewhere in the structure; the same fiber hosting the

sensor can be used to transmit signals over very long distances, with a signal loss which can be in the order of 0.2 dB/km. In the end, one of the winning aspect of optical fibers is their multiplexing capability: a single fiber can host many sensors, provided that each grating has a different pitch and that no wavelength overlapping between adjacent gratings occurs even for the highest strain: if a certain wavelength is detected by the analyzer, this can be linked to one grating only. This is also a good fact for synchronization as the whole spectrum is detected at once without the delays typical of time of flight devices. This means that different FBGs with well separated Bragg wavelengths can be inserted into the same optical fibre: a fiber can host up to around 100 sensors.

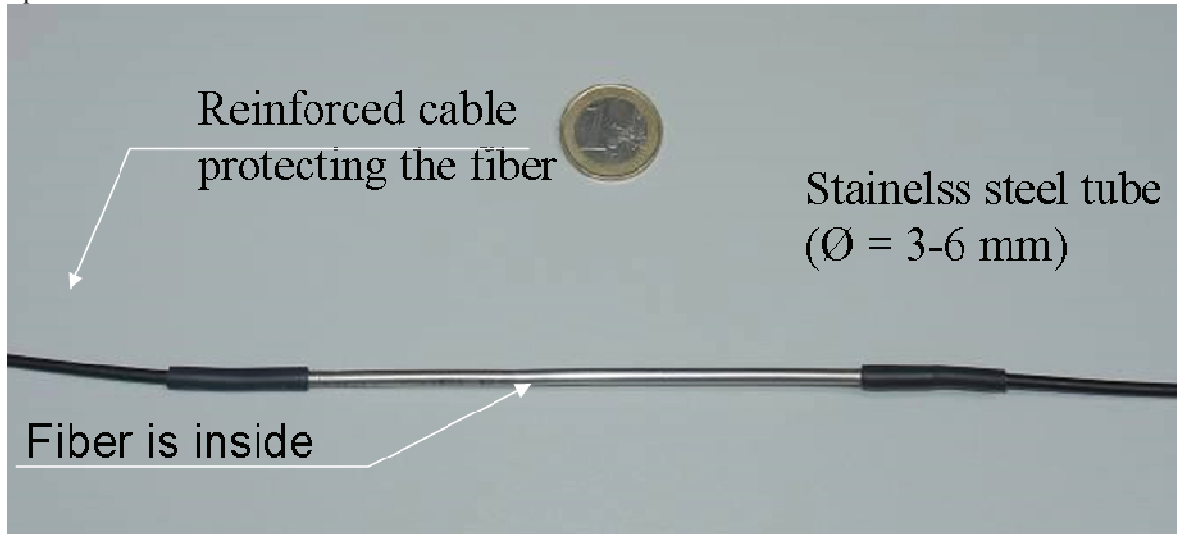


Fig. 3 Stainless steel tube protecting the fiber

Concerning the system description, the fiber, with the array of sensors, is fixed by some means to the bridge pier: each sensor has a different heat exchange mechanism when exposed to the river flow and when buried in the river bed. This could work, but there is some unbearable uncertainty as the day/night temperature inversion leads the river and its bed to have exactly the same temperature twice a day; it has therefore been decided to work on a principle similar to that of hot wire probes powered with constant current [10], by heating the fiber and therefore increasing the system sensitivity. Consequently, FBGs in water sense a lower temperature than those immersed in the bed as the dominating heat scattering principles are different in the two environments. When the river bed is encountered, a jump in temperature is observed: the river bed is therefore located between the two sensors showing the jump. Of course resolution of the device is related to the spatial spacing of the Bragg gratings: a 0.5 m value is considered a good value, as the river bed position is really a not well defined quantity (transition is not so clear, due to sand, mud, and to a turbulent boundary layer, so it is worthless to try increasing the chosen value). The fiber length should be able to cover the whole pier height (well below the seabed level).

A further remark is really important: very often a possible weakness of field instrumentation is the need to recalibrate it on site: in the present case in reality a correct temperature measurement is not the point: it is enough a meaningful jump is observed to get the result, so calibration is not strictly needed.

In the end it is noted that, although cheaper solutions exist, the same approach used to detect the position of the river bed can be applied to measure the water air interface with exactly the same approach, without the need of changing anything but the number of gratings which should be extended to reach the river surface.

A proper design must consider technological issues: heating should be such to grant the desired sensitivity, at the same time sparing electrical power, which can be a burdensome aspect for open air applications, when the overall power budget is usually limited, for instance by the need to use solar panels.

3 Preliminary tests and data management

A preliminary testing has been carried out in the experimental facilities of the Hydraulics Department at Politecnico di Milano to fix all the critical aspects and to test the different possibilities for data management and processing. Tests have been carried out in a water channel with a section of 100 cm (width) x 70 cm (height) (Fig. 4a).

The pier has been reproduced by means of a plastic cylinder placed inside the channel. The model had an outer diameter of 16 cm and a height of 80 cm (the water level was 60 cm). The fibre was attached to the pier (Fig. 4a), provided with three FBG temperature sensors and their spacing was 200 mm. The sensitivity was nearly 0.01 nm/K for all the sensors. To complete the experimental set-up both air and water temperatures were monitored by means of thermocouples.

As it was also needed to simulate situations in which temperature sensors were buried in the river bed, another structure has been built to this purpose (Fig. 4b). It is a cylinder with an outer diameter of 30 cm, thus greater than the external diameter of

the pier model. This second additional cylinder could be placed around the pier model and the space between them could be filled up with debris, of the same kind as those usually present in river beds. These debris were maintained wet by means of a water jet.

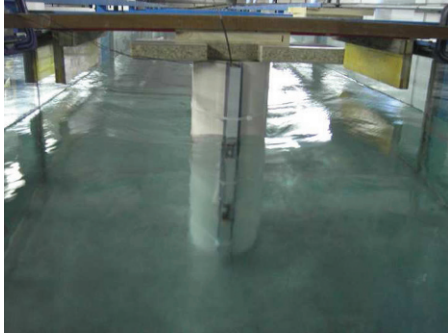


Fig. 4a Bridge model with the fiber in the water channel



Fig. 4b Bridge model and the additional external cylinder with debris

Concerning the heating system, three wires have been fixed along the stainless tube (Fig. 5) mentioned in Section 2. The total resistance of each wire of the electric circuit was about 50Ω and the voltage source they were linked to could be switched among six values (5, 10, 15, 20, 25 and 29 V). The total length of each wire was about 2 m (1 m from the power supply down to the fiber bottom and 1 m from the fiber bottom up to the power supply as explained in Fig. 5).

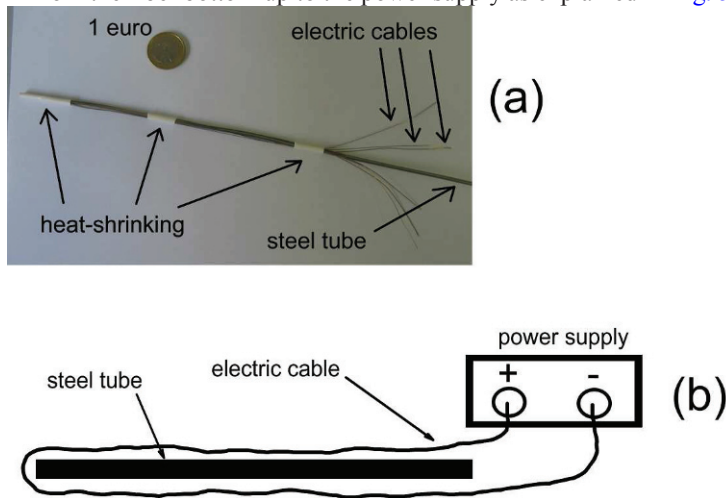


Fig. 5 Electrical wire layout

Due to the heating process and to the fact that energy budget cannot afford to keep all the sensors continuously powered, also the transient, after power has been switched on or off can be used to extract useful pieces of information about the river bed position: different strategies can be adopted in order to have a reciprocal check and improve the estimation reliability.

So the actual temperature measurements before switching power on or under steady state conditions, after the transient is over, can be cross checked with the time constants of the raising temperature of each Bragg sensor, considered to the extent of a common temperature transducer modelled by means of a first order model [10].

Fig. 6 shows the response of the same sensor in water (flow speed = 0.4 m/s) and in the debris, when the electric circuit is switched on (the dissipated power when the circuit was switched on was 50.5 W/m for the analysed case).

Two aspects are clearly observed from this figure: the different time constant and the different Δ temperature (steady state temperature – starting temperature): both can be used to recognize the river bed position.

Concerning the time constant it is remembered that this is the time requested by a first order instrument to reach 63% of step applied to the measurand or, alternatively, that a time lag equal to three time constants is needed to get into a 5% difference with respect to the steady state value [10]. For the considered tests, it appears that the time constant in flowing water is about 5 s while in the debris it raises up to about 11 s.

A check on dispersion means that tests in the two conditions must not be compatible, in the sense expressed by metrology: this means that the uncertainties related to the two time constant estimations for the two different conditions must not overlap. Data given in table 1 show that this is not happening.

Calculated parameter	Sensor in flowing water	Sensor in wet debris
τ mean value [s]	4.95	10.71
τ standard deviation value [s]	0.69	1.74

Table 1 Mean and standard deviation values of the time constant τ

Concerning steady state measurements, these of course depend upon the dissipated power. Some discussion about this point is given in the following.

Fig. 7 shows the temperature step after the electrical power is switched on: the Δ temperature is the difference between the temperature measured without heating and with heating (of course after a steady state condition is reached). The Δ temperature parameter is then plotted against the dissipated power in Watt per meter of fibre for one of the three sensors (the same already considered for the time constant approach) and for the two considered situations, free stream and still water with debris. A compromise must be sought, as increasing power of course tends to give a better separation of the two curves, but it requires more power.

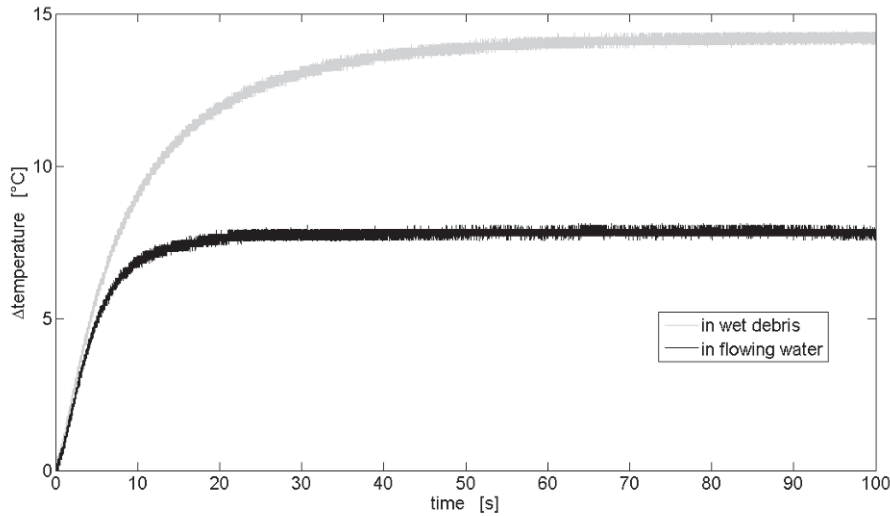


Fig. 6 Δ temperature (steady state temperature – starting temperature) time-histories for the same sensor in water and in debris when the electric circuit is switched on (sampling frequency = 1 kHz). The dissipated power per meter of fibre was 50.5 W/m.

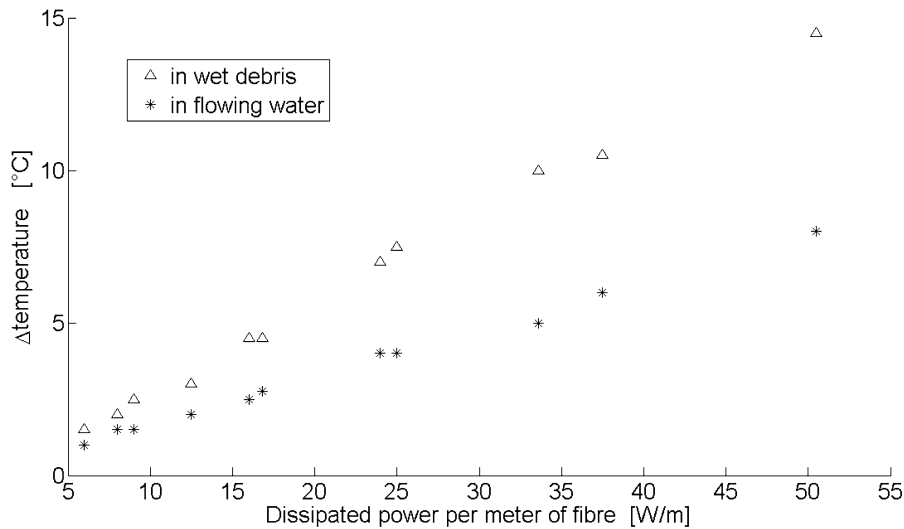


Fig. 7 Δ temperature (steady state temperature – starting temperature) as a function of the dissipated power in Watt per meter of fibre. The sensor is that already considered in Fig. 6.

4 Field testing

After preliminary testing, the public administration of Mantova offered the chance to test the new device on a real bridge over the river Po. This is considered a critical bridge, as the river is for sure the biggest in Italy, it is towards its end, with its biggest flow rates and, during the past years, floods have caused serious troubles; the bridge is the only way to join two rather big cities, Mantova and Modena. The bridge is not new, so, to test the method, it has been necessary to dig the river bottom and thrust a steel tube close to a bridge pier, with a fibre fixed to it, having 34 temperature sensors. A hard work has been carried out to properly shelter the sensors, at the same time giving the needed heating. Fig. 8 gives details of the mounting operation.

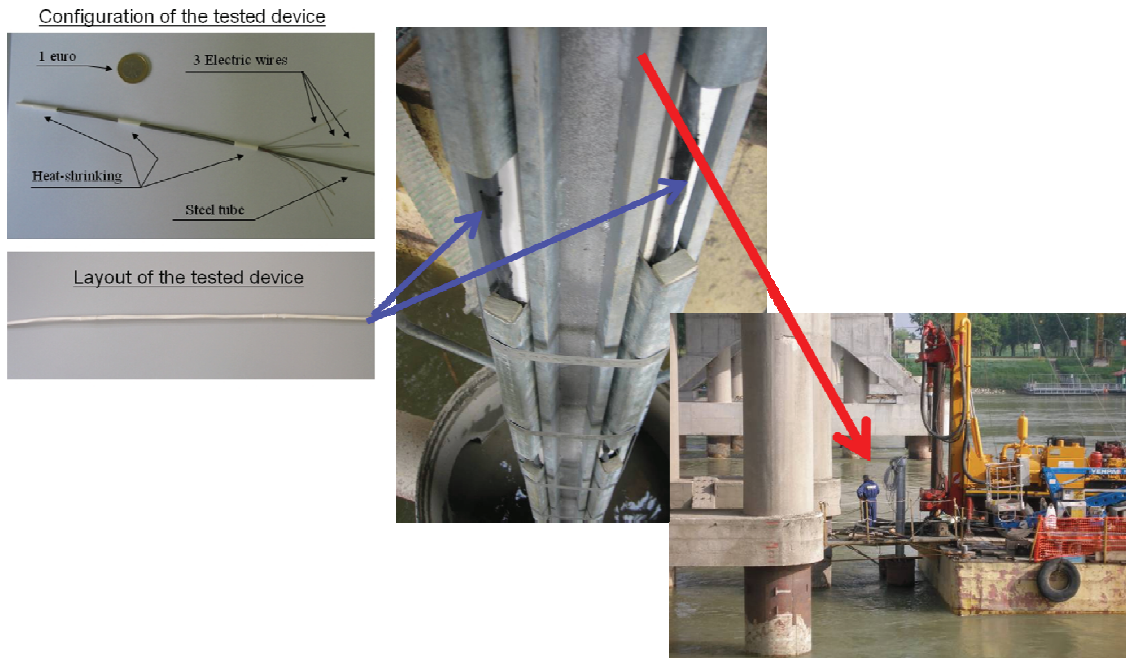


Fig. 8 Mounting operations at the Po river

Fig. 9 gives a sample of a possible measurement: in the case being analyzed the left picture shows the situation of the last sensor immersed in flowing water, in a series of subsequent transients in which heating is switched on (the decaying transient when power is switched off have been deleted from the figure as adding no further significant information). The right plot represents the first sensor immersed in the river bed: a reference for this has been made possible by the use of a graduated pole immersed in the river, until the bottom has been reached.

First of all a high repeatability with negligible dispersion is shown, as the series of events repeats similarly (the different tests shown in Fig. 9 have been carried out within few hours). Then some possible identification procedures are shown: one can point at the temperature under normal conditions (with no heating, but this has proven to be misleading), another one can consider the steady state absolute temperature after heating, a the third one is the temperature variation due to heating (the value comprised between the two red horizontal lines); a further possibility is, as previously pointed out, to work on the time constant during each transient. It appears it is not so hard to point out the differences which appear evident in the shape of the two plots.

The system just started working and the data presented are among the first sent by the monitoring system.

Another way to observe data, perhaps more effective, is to show the temperature variation after heating, for each sensor, as a function of position along the pier. Fig.10 gives this value recorded for a single test, in which the true river bed position is given by the two horizontal lines: the black one is the value from a pole with a ruler glued to it, while the red one is the value from an echo sounder. The green points are the FBG sensors and the number close to them are the level in meters above the sea; it is observed a sharp jump in passing from flowing water to still water when the river bed is reached: in this condition most sensors are buried in the river bed, but the intention is to go as deep as the bridge pile foundations, to provide information even under risky conditions, when scouring is at extreme levels.

5 Conclusion

The paper has presented an innovative method to measure scour level at bridge piers. This is based on FBG temperature sensor arrays heated through an external heating power supply. The main advantage is that this procedure is able to accurately give the scour level also during flood conditions, which are the most critical, where many traditional techniques fail. The new approach relies on two possible strategies as temperature sensors in water and debris are characterised by different outputs and by different time responses when the electric circuit is switched on. This double working principle, tested by means of laboratory experimental tests, increases the approach reliability. The first field tests are running at a first site, where this system is part of a monitoring system in which a lot of different data are fused together to get high reliability also under extreme conditions: in fact the system provides also images of what is happening, echo sounders data, river level measurements, and it is not excluded to add accelerations, as stated by the commonly adopted structural health monitoring strategies. All those data are part of a local network which can be remotely governed. It is thought that the first months of measurements will provide useful data to fix tolerable limits, warning and alarm levels.

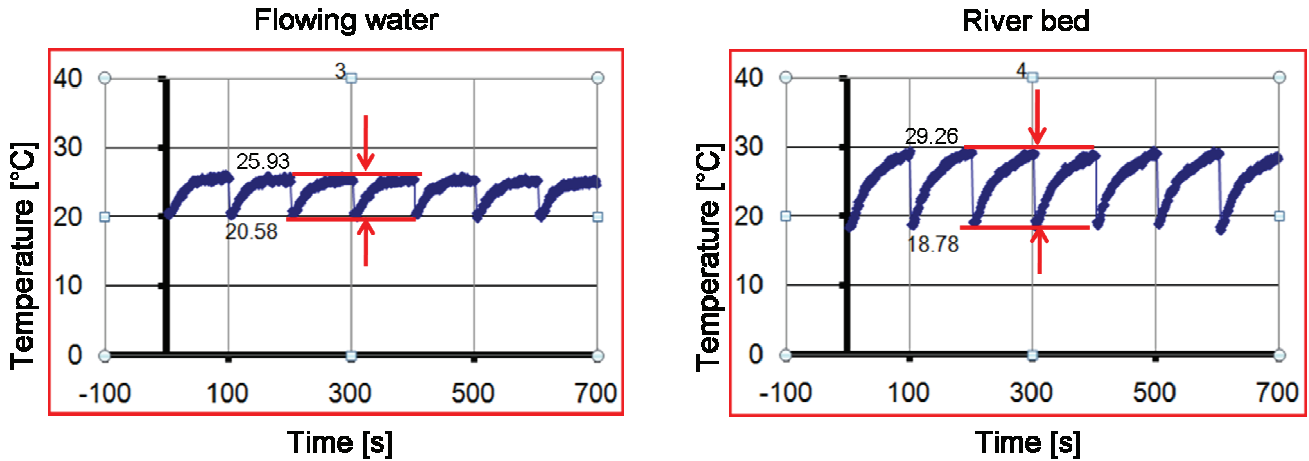


Fig. 9 Temperature trends when the heating system is switched on for the last sensor in water (left) and for the first buried in the river bed (right)

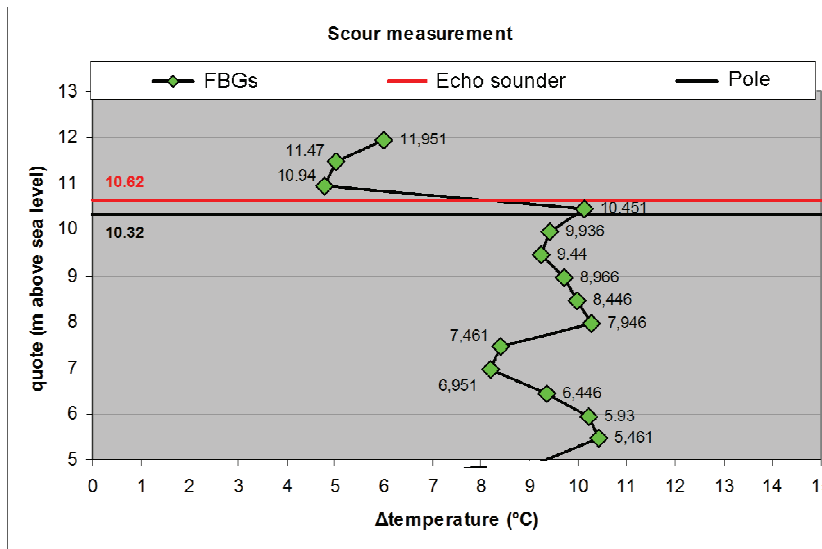


Fig. 10 Scour depth found out by different measuring methods (the numbers beside the FBG green points indicate the corresponding quote in meter above the sea level)

References

1. Ballio F, Orsi E, Time evolution of scour around bridge abutments, Water Engineering Research 2 4, 243-259, 2001.
2. National Cooperative Highway Research Program (NCHRP), Report 396 – Instrumentation for measuring scour at bridge piers and abutments, Transportation Board and National Research Council, 1997.

3. De Falco F, Mele R, The monitoring of bridges for scour by sonar and sediment, *Independent Nondestructive Testing and Evaluation International* 35 2, 117-123, 2002.
4. Radice S, Ballio F, A non-touch sensor for local scour measurements, *Journal of hydraulic research* 41 1, 105-108, 2003.
5. Lin Y-B, Chen J-C, Chang K-C, Chern J-C, Lai J-S, Real-time monitoring of local scour by using fiber Bragg grating sensors, *Smart Materials and Structures* 14, 664-670, 2005.
6. Lo K-F, Ni S-H, Huang Y-H, Zhou X-M, Measurement of unknown bridge foundation depth by parallel seismic method, *Experimental Techniques* 33 1, 23-27, 2009.
7. Cigada A, Ballio F, Inzoli F, Hydraulic Monitoring Unit, application for international patent n. PCT/EP2008/059075, publication n. WO/2009/013151 (2009).
8. Hill KO, Meltz G, Fiber Bragg grating technology fundamentals and overview. *Journal of Lightwave Technology* 15 8, 1263-1276, 1997.
9. James SW, Dockney ML, Tatam RP, Simultaneous independent temperature and strain measurement using in-fibre Bragg grating sensors. *Electronics Letters* 32 12, 1133-1134, 1996.
10. Doebelin EO, *Measurement systems: application and design*, Fifth Edition (The McGraw-Hill Companies, 2004).

Numerical Investigation on the Measurement Uncertainty in Operational Modal Analysis of a Civil Structure

A. Cattaneo, S. Manzoni, M. Vanali

Politecnico di Milano, Dipartimento di Meccanica – Via La Masa 1, 20156 Milan (Italy)
e-mail: stefano.manzoni@polimi.it

ABSTRACT

This paper deals with the study of the uncertainty associated to operational modal analysis parameter estimation. The main aim is to analyse how different key factors such as frequency resolution and average number can affect the accuracy of the estimated eigenfrequencies, non-dimensional damping ratios and mode shapes of a structure. This is considered a starting point towards any attempt to exploit structural health monitoring methods based on modal parameter changes. Knowing the parameter value and the associated spread is needed in order to assess those changes that are unusual and possibly caused by damages. Modal parameters of a civil structure are naturally evolving due to the environmental and operational conditions, this natural spread is added to the one given by the identification method leading to the final uncertainty value. Knowing the spread associated to the applied identification technique is therefore fundamental to identify and possibly compensate the changes given by the environment and thus achieve a complete knowledge of the actual structural condition. It has been decided to apply the uncertainty estimation to a real case in order to have the possibility to compare the numerical results to a set of experimental data.

The modal model of one of the G. Meazza stadium grandstands in Milan has been developed thanks to the great amount of data collected by the authors in the past. The Monte Carlo method has been applied to data coming from numerical simulations of the structural response to random excitation. The number and location of the simulated measurement point are the same as the ones actually existing on the structure. Starting from this simulated measurement set-up different conditions have been considered, changing the frequency resolution used in the identification and varying the base time record length and so the number of averages to obtain an estimation of structural free response. The different estimated uncertainties associated to the analysed conditions have been produced and compared to the results obtained with real operational data coming from the structure. The obtained results are useful to identify the spread given by the proposed identification method, and thus quantify the environmental parameter effects on the structure.

1 Introduction

Structural Health Monitoring (SHM) techniques are becoming a valuable tools in civil engineering to guarantee people and structures safety. Among the various available strategies, this paper is focused on those relying on modal parameter identification. This is one of the most widespread methods and the basic idea is to monitor possible modal parameter changes as they can be a sign of a structural change. The modal parameter which are investigated in this paper are eigenfrequencies, non-dimensional damping ratios and modal residues (i.e. mode shapes).

The main drawback of such an approach is that modal parameter changes are very little, especially considering eigenfrequencies and damping ratios, once the structure has changed. This means that it is of primary importance to understand which is the dispersion associated to the modal analysis results in order to comprehend if a certain modal value change can be recognised or not. It is of particular importance to understand what is the modal analysis result dispersion just due to the identification algorithm as this is a threshold under which it is not possible to find out any modal parameter change and therefore any structural evolution.

This study is inserted within a wider activity concerning the monitoring of the Giuseppe Meazza Stadium in Milano [1]. In such a case the modal parameter estimation is carried out by means of an Operational Modal Analysis (OMA) algorithm [2], which allows to exploit natural excitation sources (i.e. traffic, wind, etc.). Particularly, the adopted algorithm is the

Polyreference Least Square Frequency Domain (PolyMax) [3] which gives very stable results, especially with highly damped structures, which is the case of the Meazza stadium. The authors' aim is to estimate the OMA result dispersion to establish the mentioned lower threshold under which nothing can be stated about the structure.

Some results have already been obtained [4] by developing a modal model of a stadium grandstand. This is easier than considering the whole structure, allowing to focus on the final target and avoiding possible difficulties associated to developing a full stadium model. Such a model has been validated by means of experimental data collected on the grandstand during field measurement activities [9]. The reason why a model has been considered will be evident, once the whole procedure adopted to estimate OMA result dispersion will be described in Section 2. Such a procedure is based on Monte Carlo simulations. Then Section 3 gives an overview of the already obtained results.

Section 4 is devoted to explain the new results presented in this paper. The main difference between the older and the newer outcomes relies on the different time-base used to carry out OMA operations. It will be shown that such a parameter has significant consequences on the OMA result dispersion and the future research developments will be drawn down.

2 Estimation of operational modal analysis result dispersion

It has been mentioned in Section 1 that the identified modal parameter result dispersion has been computed thanks to Monte Carlo simulations. The application of such an algorithm has required the numerical generation of data, simulating the real acceleration signals acquired at the Meazza stadium. It has been assumed that the structure is excited by white random noise on the interesting frequency range, as recommended when applying the Natural Excitation Technique (NEXT) [2]. The considered structure is the grandstand shown in Fig. 1.

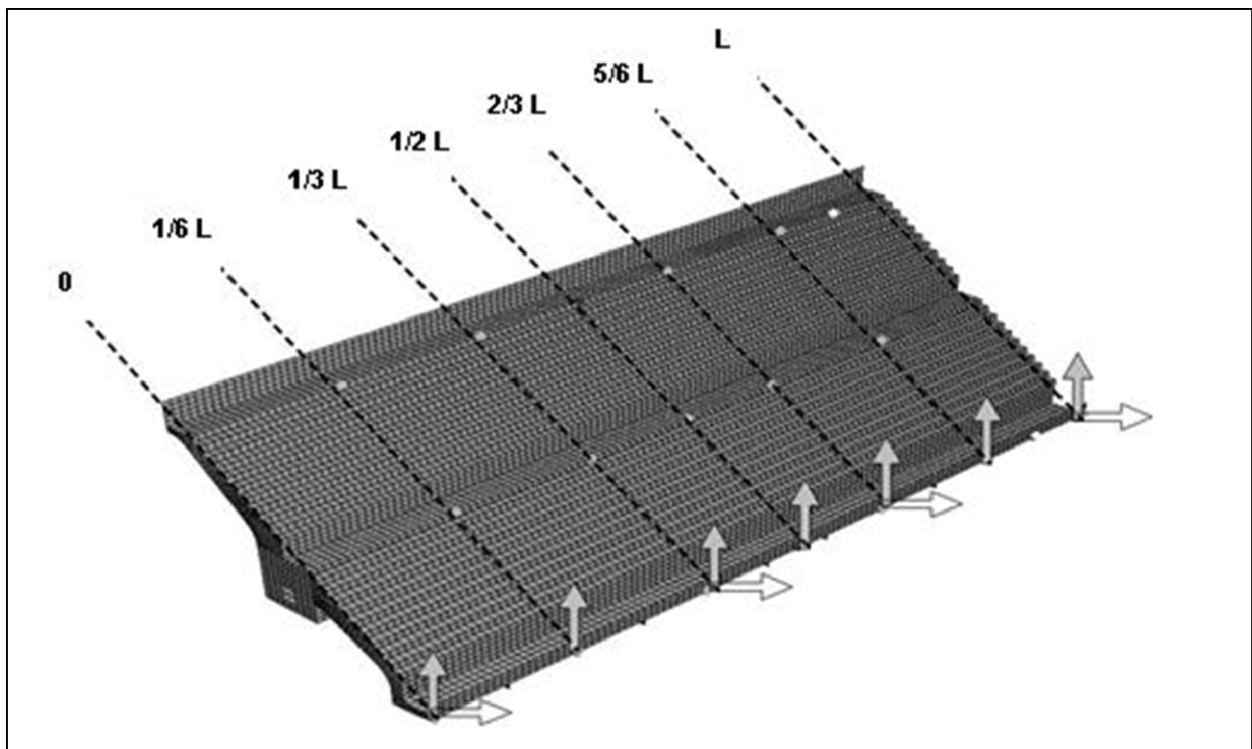


Fig. 1 A finite element model of the grandstand under analysis. The arrows indicate the accelerometer positions at the stadium and the measurement directions, in this paper only the vertical accelerations have been considered.

The whole considered procedure is described below, point by point:

- white random noise records have been generated numerically in the 0 – 100 Hz frequency range. These records have been adopted as the structure excitation; they have been built by analyzing the accelerometer signals acquired at the stadium while it was empty, and thus excited just by wind and traffic (low vibration levels). Each record is 3600 s

long as this is the time-base actually adopted in the signal processing and analysis of the data collected at the stadium;

- the acceleration vertical responses in seven grandstand points (those evidenced in Fig. 1) have been reconstructed by applying the generated excitations and exploiting the validated modal model mentioned in Section 1. This has been made possible by convolving [5] the excitation signals with the structure unit impulse responses obtained thanks to the modal model and inverse Fourier Transform operations. Each response in the seven points where accelerometers have been simulated has been obtained by the following relation (Equation 1):

$$y_j(t) = \sum_{i=1}^{Ne} \left(x_i(t) \otimes h_{ij}(t) \right) \quad (1)$$

where $y_j(t)$ is the time response in the j^{th} point, $x_i(t)$ is the input at the i^{th} point and $h_{ij}(t)$ is the response at the j^{th} point to a unit impulse applied at the i^{th} point. Finally Ne is the number of points where excitations have been applied;

- each data set has been analysed. A single set is composed by the seven acceleration responses, each with a length of 3600 s. The OMA algorithm is applied to the data set and the grandstand modal parameters are estimated;
- the same procedure is then applied to all other data sets generated repeating the points above, thus generating a statistical population for each modal parameter. The data set number depends on the Monte Carlo method convergence (an adaptive Monte Carlo simulation has been considered in order to lower the number the required iterations [6,7]). The obtained statistical populations allow to estimate the dispersion associated to each modal parameter estimation, only due to the OMA algorithm.

More details on the proposed algorithm can be found in [4] but a fact has to be pointed out. The OMA only requires the measurement of acceleration responses, as already mentioned. While the traditional modal analysis techniques where inputs and outputs are measured rely on system transfer functions, OMAs are based on response power spectral functions and on the assumption of a white random noise excitation on the frequency band of interest [2]. These power spectral functions are obtained by cutting the whole random time-histories into a number of sub-records and then averaging the results. [8]. What authors are interested in is the effect of the sub-record time length used to estimate the response power spectral functions, which are the starting data for the OMA.

The modal parameters used to build up the modal model are presented in Table 1. The reason why the first seven modes have been accounted for relies on the fact that they are enough to describe all the situations authors are interested in: isolated and well-defined modes, modes close in frequency and with high damping ratios. Furthermore these seven modes are those effectively excited by environment sources (e.g. wind and traffic) and by people moving over the structure during events [9].

Mode number	1	2	3	4	5	6	7
Eigenfrequency [Hz]	1.01	2.79	3.05	3.18	3.75	4.36	5.22
Non-dimensional damping ratio [%]	1.5	2.5	2.5	2.1	1.9	2.6	1.8
Eigenvector component at point 0	1.00	0.20	0.00	0.00	0.00	0.20	0.10
Eigenvector component at point $1/6 L$	1.00	0.70	0.70	0.70	0.60	0.50	0.65
Eigenvector component at point $1/3 L$	1	1	1	1	1	1	1
Eigenvector component at point $1/2 L$	1.00	1.50	1.30	1.30	0.00	1.20	0.00
Eigenvector component at point $2/3 L$	1.00	1.00	1.00	1.00	-1.00	1.00	-1.00
Eigenvector component at point $5/6 L$	1.00	0.70	0.70	0.70	-0.60	0.50	-0.65
Eigenvector component at point L	1.00	0.20	0.00	0.00	0.00	0.20	-0.10

Table 1 Modal parameter values used to build up the grandstand modal model; the eigenvector components are referred to [Fig. 1](#); eigenvectors are normalized at point $1/3 L$ of [Fig. 1](#)

3 Overview of the former results

The firstly performed Monte Carlo simulations relied on time-history sub-records (see Section 2) with a length of 50 s [0.02 Hz spectral resolution] [4]. The main results are summarised in [Table 2](#) where the obtained modal parameter mean values and standard deviations are presented. A further parameter worth being considered is the number of iterations required to have stable results ([Table 2](#)). Almost all the modal parameters have reached convergence, apart few of them. All these cases are discussed in [4] and the reason of such a behaviour is given. Nevertheless, these few variables not reaching convergence do not compromise the proposed analysis.

MODE 1 - 2499 identifications on 11950 iterations									
Parameter	frequency [Hz]	Non-dimensional damping ratio [%]	0	1/6 L	1/3 L	1/2 L	2/3 L	5/6 L	L
Population mean value on 2000 identifications	1.00E00	2.9E00	5.8E-01	8.3E-01	█	9.2E-01	6.6E-01	6.3E-01	5.6E-01
Population standard deviation on 2000 identifications	4E-03	5E-01	2E-02	7E-03	█	3E-03	2E-02	2E-02	2E-02
Convergence obtained for mean and standard deviation	YES YES	YES YES	YES YES	YES YES		YES YES	YES YES	YES YES	YES YES
MODE 2 - 413 identifications on 11950 iterations: Monte Carlo method not applicable [6]									
MODE 3 - 9617 identifications on 11950 iterations									
Parameter	frequency [Hz]	Non-dimensional damping ratio [%]	0	1/6 L	1/3 L	1/2 L	2/3 L	5/6 L	L
Population mean value on 9500 identifications	3.03E00	2.6E00	1.9E-03	6.9E-01	█	1.2E00	8.8E-01	6.2E-01	-5.9E-03
Population standard deviation on 9500 identifications	2E-02	5E-01	1E-03	1E-03	█	2E-02	2E-02	2E-02	3E-03
Convergence obtained for mean and standard deviation	YES YES	YES YES	NO YES	YES YES		YES YES	YES YES	YES YES	NO YES
MODE 4 - 10546 identifications on 11950 iterations									
Parameter	frequency [Hz]	Non-dimensional damping ratio [%]	0	1/6 L	1/3 L	1/2 L	2/3 L	5/6 L	L
Population mean value on 10500 identifications	3.19E00	2.5E00	2.2E-03	7.0E-01	█	1.3E00	1.0E00	7.3E-01	5.2E-03
Population standard deviation on 10500 identifications	1 E-02	4E-01	7E-04	2E-03	█	2E-02	3E-02	2E-02	1E-03
Convergence obtained for mean and standard deviation	YES YES	YES YES	NO NO	YES YES		YES YES	YES YES	YES YES	NO YES
MODE 5 - 9492 identifications on 11950 iterations									
Parameter	frequency [Hz]	Non-dimensional damping ratio [%]	0	1/6 L	1/3 L	1/2 L	2/3 L	5/6 L	L
Population mean value on 9000 identifications	3.75E00	2.2E00	2.1E-03	6.1E-01	█	1.6E-01	-7.8E-01	-4.6E-01	5.1E-03
Population standard deviation on 9000 identifications	6E-03	1E-01	3E-03	3E-03	█	4E-02	5E-02	4E-02	1E-03
Convergence obtained for mean and standard deviation	YES YES	YES YES	NO YES	YES YES		YES YES	NO YES	YES YES	NO YES
MODE 6 - 4072 identifications on 11950 iterations									
Parameter	frequency [Hz]	Non-dimensional damping ratio [%]	0	1/6 L	1/3 L	1/2 L	2/3 L	5/6 L	L
Population mean value on 4000 identifications	4.36E00	3.2E00	1.9E-01	5.2E-01	█	1.0E00	7.4E-01	3.4E-01	1.6E-01
Population standard deviation on 4000 identifications	8 E-03	2E-01	2E-03	9E-04	█	3E-02	4E-02	3E-02	4E-03
Convergence obtained for mean and standard deviation	YES YES	YES YES	YES YES	YES YES		YES YES	YES YES	YES YES	YES YES
MODE 7 - 9888 identifications on 11950 iterations									
Parameter	frequency [Hz]	Non-dimensional damping ratio [%]	0	1/6 L	1/3 L	1/2 L	2/3 L	5/6 L	L
Population mean value on 9500 identifications	5.22E00	2.1 E00	1.0 E-01	6.5 E-01	█	1.1 E-02	-9.8 E-01	-6.4 E-01	-9.8 E-02
Population standard deviation on 9500 identifications	5 E-03	1 E-01	1 E-04	7 E-05	█	3 E-03	5 E-03	3 E-03	5 E-04
Convergence obtained for mean and standard deviation	YES YES	YES YES	YES YES	YES YES		YES YES	YES YES	YES YES	YES YES

Table 2 Identified modal parameters for modes 1 to 7 (time length of sub-records is 50 s); the eigenvector components are referred to Fig. 1; eigenvectors are normalized at point 1/3 L of Fig. 1

Starting from these results the investigation on the influence of sub-record length on the OMA result dispersion and bias errors is faced within the next section.

4 Influence of time length on modal analysis results

The time base used for the former analyses was 50 s (see the previous section). Two further tests have been carried out with 25 and 100 s [0.04 and 0.01 Hz resolution respectively]. As the global length of each time-history is 3600 s, using a longer time base for the OMA means to improve frequency resolution but to lower the number of averages to estimate the accelerometer power spectra. Otherwise, if the time base is decreased, the frequency resolution gets worse but the number of averages of the power spectra increases with a benefit for the robustness of their estimation.

The first main evident outcome of changing the analysis time base is that the estimated bias error for the non-dimensional damping ratios decreases, once time length is increased (Fig. 2). Usually the estimated damping ratio is higher than the real value, when a bias error exists. As an increase of time length has both positive and negative effects (see previous section), a more detailed analysis is required to fully comprehend the effects of the number of averages and frequency resolution.

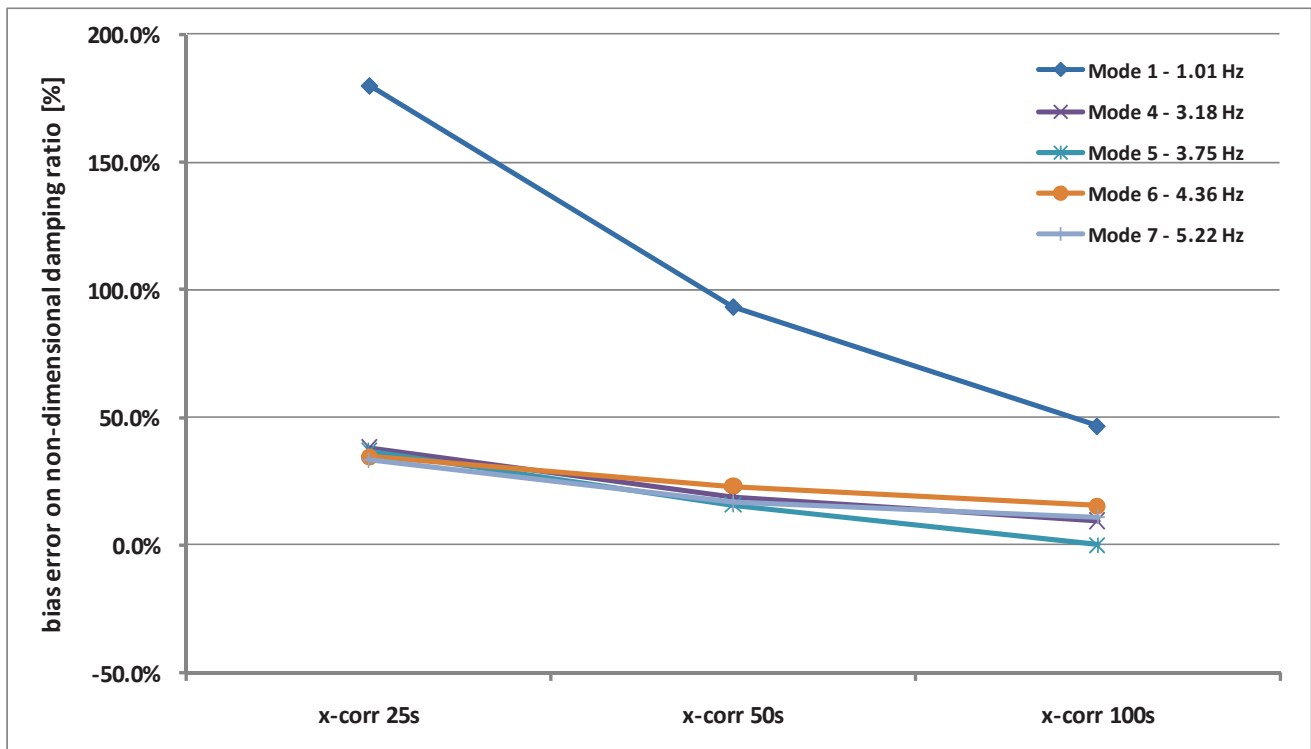


Fig. 2 Trend of the bias error of the non-dimensional damping ratio as a function of the time base (length of the correlation time window) for five modes of Table 1

Results analysis is still being performed but looking at all the data some outcomes can be evidenced. Once a peak is not well defined in the response power spectra, the bias errors on the modal residues estimations increases, even if frequency and damping ratio are well estimated (Table 3, the numbers evidenced in yellow for mode 5).

Looking at the autospectra of the simulated acceleration in Fig. 3 (arrow points at the fifth mode, formerly 3.75 Hz, at point 2/3L of Fig. 1) it can be seen that the mode is not clearly present in the autospectra as it is partly masked by the adjacent modes. The same thing does not happen for mode 7 as it is clearly visible as a peak in the PSD (Fig. 3 and the numbers evidenced in yellow in Table 3 for mode 7).

Mode 5 (Table 1)	f [Hz]	r [-]	0	1/6 L	1/2 L	2/3 L	5/6 L	L
Reference value	3.75	1.9	0.00	0.60	0.00	-1.00	-0.60	0.00
Mean on 9000 identifications (T 50 s)	3.75E+00	2.2E+00	2.1E-03	6.1E-01	1.6E-01	-7.8E-01	-4.6E-01	5.1E-03
Std Dev on 9000 identifications (T 50 s)	6E-03	1E-01	3E-03	3E-03	4E-02	5E-02	4E-02	1E-03
Mean on 8500 identifications (T 100 s)	3.75E+00	1.9E+00	2.8E-03	6.1E-01	1.5E-01	-7.9E-01	-4.6E-01	4.7E-03
Std Dev on 8500 identifications (T 100 s)	7E-03	1E-01	3E-03	3E-03	4E-02	5E-02	4E-02	1E-03
Mean on 10500 identifications (T 25 s)	3.75E+00	2.6E+00	-1.9E-03	6.1E-01	2.1E-01	-7.5E-01	-4.3E-01	6.7E-03
Std Dev on 10500 identifications (T 25 s)	5E-03	1E-01	1E-03	1E-03	1E-02	4E-02	3E-02	5E-04
Mode 7 (Table 1)	f [Hz]	r [-]	0	1/6 L	1/2 L	2/3 L	5/6 L	L
Reference value	5.22	1.8	0.10	0.65	0.00	-1.00	-0.65	-0.10
Mean on 9500 identifications (T 50 s)	5.22E+00	2.1E+00	1.0E-01	6.5E-01	1.1E-02	-9.8E-01	-6.4E-01	-9.8E-02
Std Dev on 9500 identifications (T 50 s)	5E-03	1E-01	1E-04	7E-05	3E-03	5E-03	3E-03	5E-04
Mean on 12000 identifications (T 100 s)	5.22E+00	2.0E+00	1.0E-01	6.5E-01	1.2E-02	-9.8E-01	-6.4E-01	-9.8E-02
Std Dev on 12000 identifications (T 100 s)	5E-03	9E-02	1E-04	8E-05	4E-03	6E-03	4E-03	6E-04
Mean on 11500 identifications (T 25 s)	5.22E+00	2.4E+00	1.0E-01	6.5E-01	1.5E-02	-9.8E-01	-6.4E-01	-9.8E-02
Std Dev on 11500 identifications (T 25 s)	6E-03	1E-01	2E-04	1E-04	9E-03	1E-02	6E-03	1E-03

Table 3 Results for mode 5 and 7 as a function of the time base

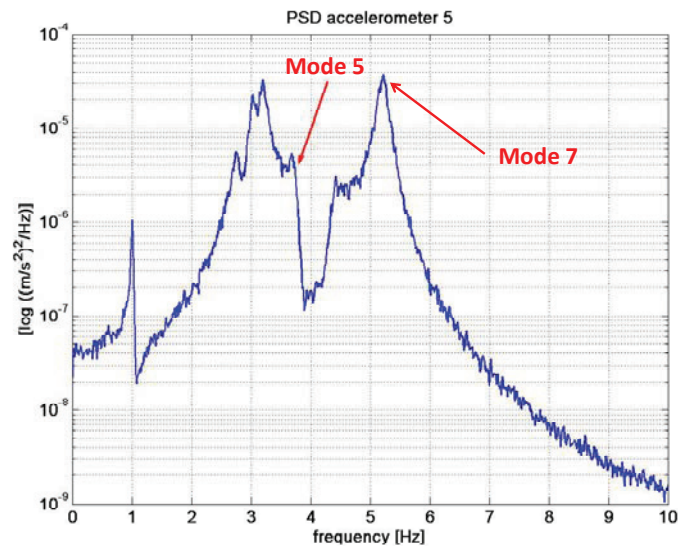


Fig. 3 Power spectral density of an acceleration response (point 2/3L in Fig. 1) where the red arrows indicate where the 5th and 7th mode are.

A further aspect has to be highlighted. Once frequency resolution is increased (worsened), sometimes eigenfrequencies are wrongly identified and doubled result occurrence distributions can be found as can be seen for the 1st mode in Figs. 4 to 6. Decreasing the resolution, seems to be a valid solution for this problem.

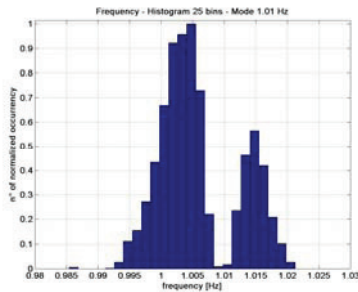


Fig 4 Occurrence histogram for the eigenfrequency of mode 1 (Table 1); time base = 25 s; the histogram has been normalised in order to have an height of 1 for the class with more occurrences

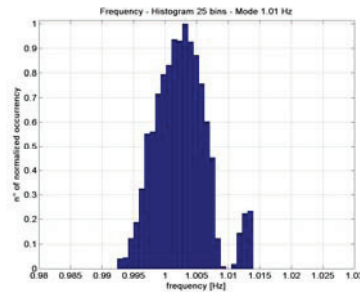


Fig 5 Occurrence histogram for the eigenfrequency of mode 1 (Table 1); time base = 50 s; the histogram has been normalised in order to have an height of 1 for the class with more occurrences

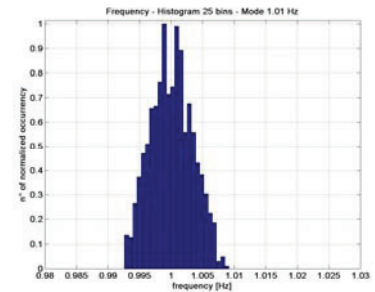


Fig 6 Occurrence histogram for the eigenfrequency of mode 1 (Table 1); time base = 100 s; the histogram has been normalised in order to have an height of 1 for the class with more occurrences

Things are more difficult to be understood for modal residues as there are different factors to be accounted for. Particularly, errors in the first part of identification (i.e. where eigenfrequencies and non-dimensional damping ratios are estimated) and their propagation in the steps where modal residues are identified can be error sources in modal residue estimation. An example is given in Figs. 7 to 9, where bias errors on damping ratio estimation has significant effects on the estimated modal residue value.

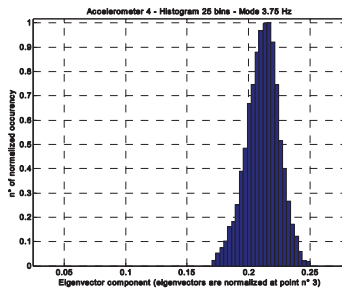


Fig 7 Occurrence histogram for the modal residue of mode 5 and position $1/2L$ (Table 1); time base = 25 s; the histogram has been normalised in order to have an height of 1 for the class with more occurrences

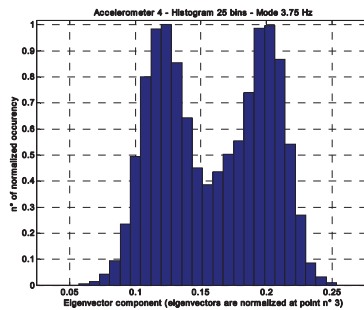


Fig 8 Occurrence histogram for the modal residue of mode 5 and position $1/2L$ (Table 1); time base = 50 s; the histogram has been normalised in order to have an height of 1 for the class with more occurrences

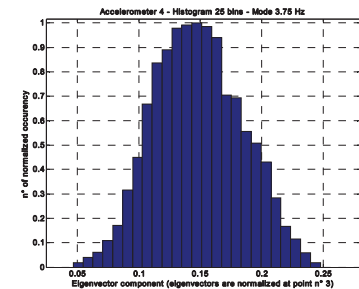


Fig 9 Occurrence histogram for the modal residue of mode 5 and position $1/2L$ (Table 1); time base = 100 s; the histogram has been normalised in order to have an height of 1 for the class with more occurrences

Table 3 shows that decreasing the frequency resolution for mode 5 leads to a decrease of the identified damping ratio (with a lower bias error). This causes a corresponding decrease of the estimated modal residue, once again with a lower bias error. A more detailed analysis will be performed, splitting the effects of frequency resolution and number of averages in the spectral response function estimation.

5 Conclusion

This paper has dealt with the result dispersion of operational modal analysis only due to the mathematical identification algorithm applied to a real case. A modal model of one of the G. Meazza stadium stands in Milan has been considered to generate simulated vibration responses. Monte Carlo simulation have been carried out in order to estimate the spread in the identification results.

The analysis has been focused on the effect of the time window length used to calculate the response power spectral functions which are the identification algorithm inputs. Although a bias error decrease for non-dimensional damping ratios has been found out when increasing the windows length and so reducing the frequency resolution in the spectral functions a more detailed analysis has still to be carried out.

When increasing the time window length the frequency resolution decreases but the number of averages in the estimation of the spectral response functions decreases too. Further simulations are carried out at the moment to investigate the effects of frequency resolution changes while keeping a constant number of averages.

References

1. Cigada A, Caprioli A, Redaelli M, Vanali M, Vibration testing at Meazza stadium: Reliability of operational modal analysis to health monitoring purposes, *Journal of Performance of Constructed Facilities*, v 22, n 4, p 228-237, 2008.
2. Peeters B, Van der Auweraer H, Vanhollenbeke F, Guillaume P, Operational modal analysis for estimating the dynamic properties of a stadium structure during a football game, *Shock and Vibration*, v. 14, n. 4, p. 283-303, 2007.
3. Peeters B, Van der Auweraer H, Guillaume P, Leuridan J, The PolyMAX frequency-domain method: a new standard for modal parameter estimation?, *Shock and Vibration*, v. 11, n. 3-4, p. 395-409, 2004.
4. Cattaneo A, Manzoni S, Vanali M, Measurement uncertainty in operational modal analysis of a civil structure, in *Proceedings of the International Conference on Uncertainty in Structural Dynamics – USD 2010*, p. ,5103-5116, Leuven (Blegium), 20-22 September 2010.
5. D'Antona G, Ferrero A, *Digital signal processing for measurement systems: theory and applications (information technology: transmission, processing and storage)*, Springer (2006).
6. ISO/IEC Guide 98-3:2008, *Uncertainty of measurement – Part 3: Guide to the expression of uncertainty in measurement (GUM:1995)*.
7. ISO/IEC GUIDE 98-3/Suppl.1:2008(E), *Uncertainty of measurement, Part 3: Guide to the expression of uncertainty in measurement (GUM:1995), Supplement 1: Propagation of distributions using a Monte Carlo method*.
8. Bendat JS, Piersol AG, *Random Data: Analysis and Measurement Procedures*, 3rd edition, Wiley-Blackwell (2000).
9. Cigada A, Moschioni G, Vanali M, Caprioli A, *The Measurement Network Of The San Siro Meazza Stadium In Milan: Origin And Implementation Of A New Data Acquisition Strategy For Structural Health Monitoring*, *Experimental Techniques*, January/February 2010

Measurement and Application of Bouncing and Jumping Loads Using Motion Tracking Technology

Vitomir Racic
James M. W. Brownjohn
Aleksandar Pavic
The University of Sheffield
Department of Civil and Structural Engineering,
Sir Frederick Mappin Building, Mappin Street
Sheffield S1 3JD, UK

ABSTRACT

State-of-the-art facilities for measuring bouncing and jumping ground reaction forces (GRFs) comprise typically equipment for direct force measurement, i.e. single or multiple floor-mounted force plates. Artificial laboratory conditions and constraints imposed by the direct measurement systems, such as small measuring area of a force plate, can have a strong influence on human ability to bounce and jump, naturally yielding unrepresentative force data. However, when dealing with issues like vibration serviceability assessment of real full-scale structures, such as floors, footbridges, staircases and grandstands, there is a growing need to estimate realistic GRFs under a wide range of natural conditions. This paper presents a novel method in the civil engineering context utilising ‘free-field’ measurement of human bouncing and jumping forces recorded continuously in time using motion capturing technology transferred and adapted from biomechanical research. Results showed that this kind of data can be used successfully in studies of human-structure dynamic interaction, specifically negative cue effect of a perceptibly vibrating structure on GRFs and energy flow and power in the human-structure system, as well as synchronisation between individuals when bouncing/jumping in groups on more or less perceptibly moving structures.

NOMENCLATURE

F_{GR}	ground reaction force	g	gravity
m_i	mass of i-th body segment	s	number of body segments
a_i	acceleration of i-th body segment		

1 INTRODUCTION

In the last decade, there have been rapidly growing numbers of grandstands and entertainment venues that have failed to perform satisfactorily when occupied and dynamically excited by multiple persons and large crowds bouncing and/or jumping in unison [1-3]. These mostly vibration serviceability problems have indicated high levels of uncertainty with which civil structural engineers are faced nowadays when designing any of the above mentioned structures which require vibration performance assessment.

There have been numerous attempts to provide reliable and practical descriptions of human bouncing and jumping loads by measuring the contact forces between the ground and test subjects, hence generally known as ground reaction forces (GRFs). For this purpose Ebrahimpour et al. [4] and Pernica [5] designed a ‘force platform’, whereas Rainer et al. [6] used the continuously measured reaction of a floor strip having known dynamic properties. Much research into GRFs has been done in the biomechanics community, as GRF patterns provide useful diagnostics in medical and sports applications [7, 8]. Therefore, it is not surprising that the present state-of-the-art equipment for the force measurements, i.e. the ‘force plate’, emerged from the field of biomechanics of human gait. However, there are a few disadvantages of force plates that make them less suitable in vibration serviceability assessment of civil engineering structures. Firstly, standard dimensions of force plates (typically 0.6x0.4 m) are not large enough to accommodate jumping for some individuals who must control and target their jumps to the relatively small force plate area so as to allow adequate recordings. As a result, this targeting effort can

affect ability to jump naturally and therefore alter GRF patterns [8]. Secondly, force plates cannot provide accurate measurements when mounted on a flexible structure due to self-inertia. This is because they behave like ‘accelerometers’ and produce outputs including inertia forces of the moving support surface [9]. Therefore a typical experimental setup includes force plates mounted on a rigid laboratory floor, thus limiting the measurements to laboratory conditions. However, when investigating issues related to vibration serviceability there is a growing need for monitoring many subjects during daily life activities in their natural environment, such as office, sport facility, or a footbridge.

Bearing all this in mind, one way forward is an alternative experimental approach to account for all drawbacks of force plates. Several biomechanical studies designed to estimate the contribution of motion of various body segments to vertical GRFs [10-12] offer a step in this direction. Using these biomechanical studies as a solid foundation, this paper aims to present a reader, conversant with vibration serviceability problems of civil engineering structures, with a novel method, in the context of a civil engineering application, to utilise ‘free-field’ measurement to obtain bouncing and jumping GRFs in a wide range of conditions. The free-field measurement applies the method to estimate the forces in the real world (i.e. naturally-occurring environments) rather than in a constrained laboratory setting. The method will also enable study of areas of significant interest and lack of knowledge, specifically human-structure dynamic interaction and coordination of movements between a number of people bouncing/jumping on more or less perceptibly moving structures.

In the context of this paper, human-structure dynamic interaction aims to address two related key issues. Firstly, how perceptible structural vibrations can influence forces induced by active human occupants, and secondly, how active human occupants influence the dynamic properties (e.g. damping) of a civil engineering structure they occupy and dynamically excite.

2 THEORETICAL BACKGROUND

According to Newton [13], the origin of dynamic forces is in momentum changes, which, for constant mass, means that the force is product of mass and acceleration. As applied to the human body, the vertical force acting upon the body (i.e. vertical ground reaction force F_{GR}) can be defined as [3]:

$$F_{GR} = \sum_{i=1}^s m_i (a_i - g) \quad (1)$$

where g is the static acceleration due to gravity (noting that upward accelerations are defined as positive, hence $g = -9.81 \text{ m/s}^2$ in the UK), m_i and a_i are mass and acceleration of the centre of the mass of the i -th body segment and s is the total number of body segments. This relation implies that the force a person generates against the surface must react against inertia of their body, so the sum of products of masses and accelerations for all body parts must equal the GRF at all times. Similar to earthquake engineering, the only source of external excitation is the inertial force, which then generates other forces through the human body, being transmitted ultimately to the support of the body and resulting in the GRF. This is the key principle behind the idea of estimating GRFs via measuring motion of the body segments.

In this study, physical parameters associated with each rigid segment, such as mass and position of its centre, are estimated using regression equations proposed by de Leva [14], while measurement of body motion was considered using Coda [15] optical motion capture technology. More detailed explanation of different methods for estimating anthropometry of human bodies and technology for body motion tracking can be found in a comprehensive literature review article published recently by the authors [16].

The strategy for verification of the method described by Equation (1) is as follows:

- 1) Measure simultaneously motion of test subjects jumping/bouncing and vertical response of a simple structure whose modal properties (of the empty structure) have previously been obtained from modal testing.
- 2) Perform forward response analysis by utilising the reproduced human induced loading in conjunction with the known modal properties of vertical modes of the empty test structure.
- 3) Compare these responses with their measured counterparts.

3 DATA COLLECTION

All preparatory steps necessary for the launch of the experiments are explained in Section 3.1. Results of the modal testing of a simple test structure are presented in Section 3.2, while synchronous monitoring of the body motion and structural response due to jumping/bouncing on the structure is elaborated in Section 3.3.

3.1 PREPARATORY PHASE

Two male volunteers (age 27 and 30 years, body mass 70 and 67 kg) participated in the experiment. Using a modelling strategy proposed by de Leva [14], 15 body segments and corresponding segmental masses and positions of segmental mass centres of each participant were defined. The segmentation comprised the pairs of the feet, the shanks, the thighs, the hands, the forearms, the upper-arms, as well as the pelvis, the trunk, and the head. The segmental ends were defined via nine motion tracking markers (also called ‘target’ markers) stuck to the head and major body joints such as ankle, wrist, knee or elbow, as illustrated in Figure 1b. Because the number of available markers is limited, as well as to reduce the subject’s preparatory time and to enable simple and time-efficient experiments, symmetry of motion in the vertical plane between the left and right body segments was assumed.

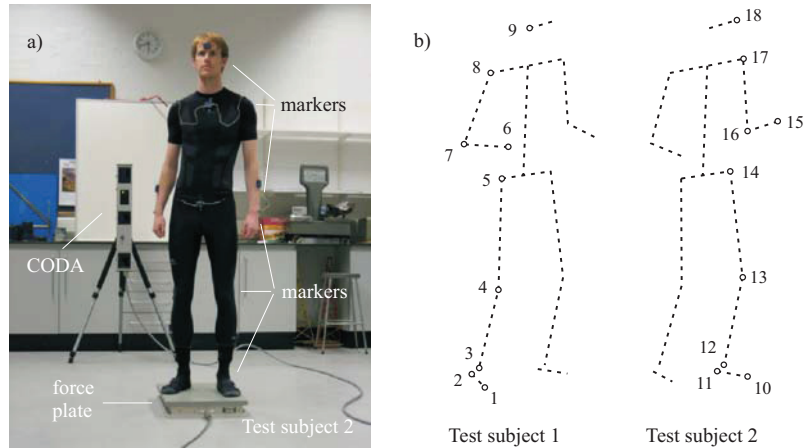


Figure 1: (a) Experimental setup. (b) Human body model and arrangement of markers.

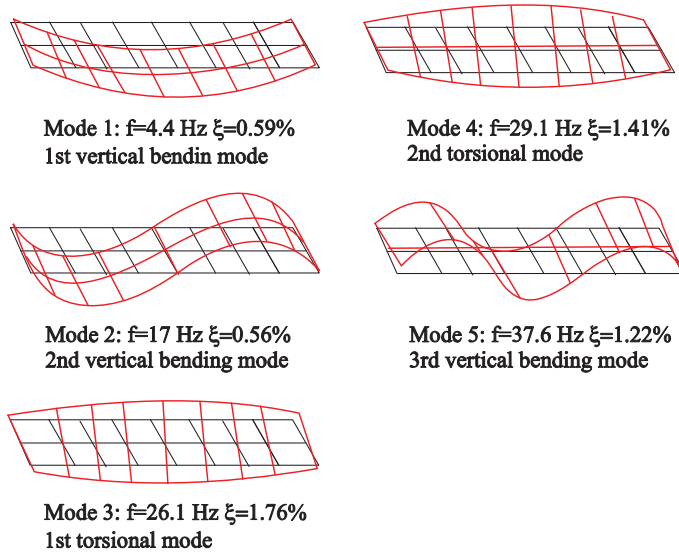


Figure 2: Experimentally estimated modal properties on the test structure (first three vertical bending modes, first two torsional modes).

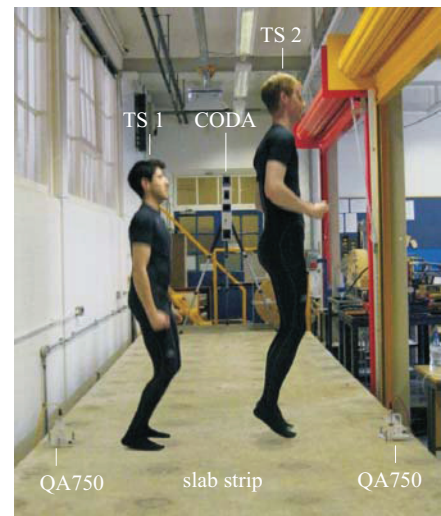


Figure 3: Two test subjects jumping together on the slab strip.

3.2 TEST STRUCTURE AND EXPERIMENTAL MODAL ANALYSIS

The test structure is a 15-tonne pre-stressed concrete slab strip situated in the Light Structure Laboratory of the University of Sheffield, UK. The slab strip is 11 m long and 2 m wide and, structurally, it presents a simply supported beam (Figures 2 and 3).

The natural frequencies, modal masses, modal damping ratios and mode shapes of the structure were determined by shaker modal testing. The modal testing is described in [3] and results are presented in Figure 2.

3.3 BODY MOTION DATA COUPLED WITH RESPONSE MEASUREMENTS OF THE STRUCTURE

Each test subject, fully instrumented with the Coda markers, was asked to either jump or bounce alone in the mid-span of the structure in response to regular metronome beats at three different tempos: 2, 2.2 and 2.5 Hz. Note that jumping and bouncing at 2.2 Hz excited the structure as near to resonance as possible by the second harmonic of the corresponding forces. On the other hand, closely spaced tempos at 2 and 2.5 Hz excited the structure out of resonance. Nominally identical tests were repeated when the two test subjects were jumping/bouncing together (Figure 3).

The Codamotion host computer enabled simultaneous acquisition of vertical movement of the body markers and response of the structure measured in the middle of the span by both a QA750 [17] accelerometer and a tracking marker. Both body motion data and vibration response were sampled at 200 Hz.

The aim was to calculate response of the structure by using the forces reproduced from the body motion data and the modal properties of the first vertical mode determined in Section 3.2. A good match between the calculated and directly measured accelerations should provide a proof that the forces can be reproduced successfully. This is the key aspect outlined in the next section, together with the possibility to use the reproduced forces in a study of human-structure dynamic interaction and synchronisation of people when jumping/bouncing in groups.

4 FORCES INDUCED ON TEST STRUCTURE

Movement of the skin relative to the underlying bone is one of the major sources of error when reconstructing human-induced forces from body motion data [16]. This is known as “soft tissue artefact” and is dominant during highly accelerated movements, e.g. when the feet abruptly hit the ground. Skin markers then oscillate considerably in an unsteady way with respect to the underlying bone, inducing high-frequency noise in the marker data. To filter out the noise, a fourth order low-pass digital Butterworth filter (LPF) having cut-off frequency 15 Hz was applied to accelerations of all markers. Figure 4 illustrates accelerations of the hip marker obtained with and without filtering out the noise above 15 Hz from the displacement data. It can be seen that the main visible features of the markers’ accelerations representing the whole body segment motion remain intact after the filtering.

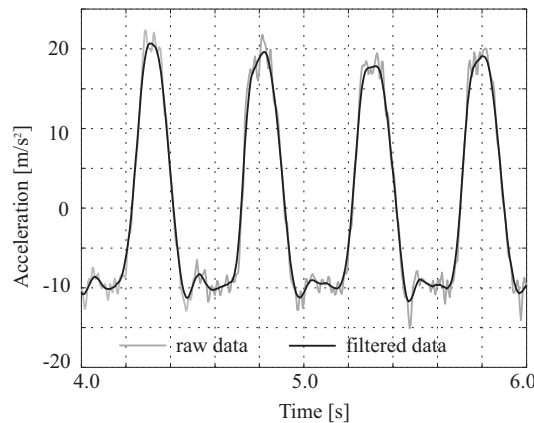


Figure 4: Raw and filtered accelerations (CF=15Hz) of a hip marker due to jumping at 2 Hz.

In the next two sections, filtered acceleration time histories of a kind given in Figure 4 will be used in conjunction with information about the values and locations of the segmental masses (see Section 3.1) to calculate the GRF time histories according to Equation (1).

4.1 SINGLE TEST SUBJECT

The force time histories generated in the mid-span of the structure when test subjects were bouncing or jumping alone in response to the regular metronome beats (at 2, 2.2 and 2.5 Hz) were reproduced from body motion data collected in Section 3.3. As an illustration, the reproduced force signals for Test Subject (TS) 1 bouncing are given in Figure 5a-c. The corresponding Fourier amplitude spectra in the vicinity of the second dominant harmonic are given in Figure 5d-f.

The best way to check if the reproduced forces are correct is to compare responses of the structure measured directly by the accelerometers (Section 3.3) and those calculated from the corresponding SDOF model of the structure. The latter can be obtained using the reproduced forces as the forcing function together with the nonlinear modal properties of the first vertical mode (Section 3.2).

A good match between the calculated and directly measured accelerations in the mid-span of the structure (Figures 5g-i) strongly suggest that the forces have been reproduced successfully. Strong Fourier amplitudes at 4 and 5 Hz and slight ‘spread’ of energy to adjacent spectral lines in Figures 5d and 5f indicate that TS 1 could follow metronome beats well when jumping and bouncing at 2 and 2.5 Hz, respectively. However, for jumping and bouncing at 2.2 Hz, the spread of energy is more prominent around 4.4 Hz (Figure 5e). The same effect was observed for TS 2 as well. This indicated that it was more difficult for them to follow the metronome beat when the structure was dynamically excited in resonance, i.e. they varied more their jumping/bouncing rate when structural responses were greater. As noted elsewhere [18], the most likely explanation for this happening is the influence of large levels of the resonant structural response on the ability of the test subjects to keep jumping/bouncing regularly. This is because the human body is a very sensitive vibration receiver characterized by the innate ability to adapt quickly to almost any type and level of vibration which normally occurs in nature [19].

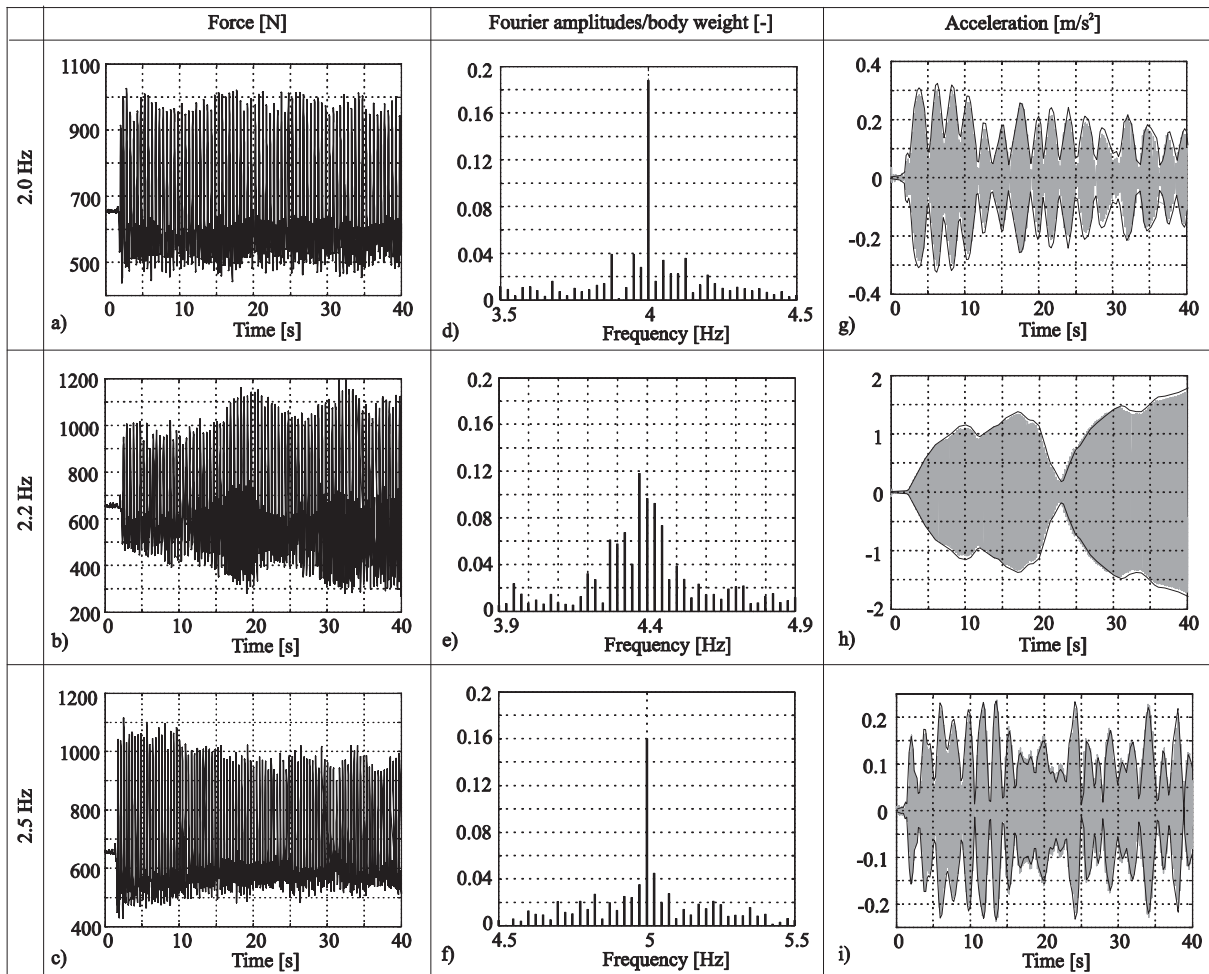


Figure 5: (a-c) Reproduced force time histories, (d-f) the corresponding Fourier amplitudes in the vicinity of the second dominant harmonic, and (g-i) measured (grey) and envelope of simulated (black) accelerations of the structure generated by TS 1 when bouncing on the test structure in response to regular metronome beats at 2, 2.2 and 2.5 Hz.

4.2 TWO TEST SUBJECTS

Following the same logic from the previous section, nominally identical analysis was carried out based on the motion data recorded for both test subjects bouncing and jumping together in the mid-span of the structure in response to regular metronome beats at 2, 2.2 and 2.5 Hz (Section 3.2). As in the case of single test subject, a proof of successful force reproduction for all jumping/bouncing rates is a good matching between the measured vibration responses (Section 3.2) and those calculated from the corresponding SDOF model using the reproduced forces and the modal properties. The results are elaborated in [3].

Although the test subjects were following the same metronome beats when jumping and bouncing together, there was a sporadic lack of coordination between their movements, which is reflected in a lack of synchronisation of the corresponding peak force amplitudes on a cycle-by-cycle basis. Here, one jumping or bouncing cycle corresponds to a period needed to complete one jump or bounce.

In Figure 6, there are cycles for which time instants of individual peak amplitudes match well, indicating a high synchronisation level. Also, this resulted in large peak amplitudes of the total sum force for these cycles. However, because humans are not machines, despite the metronome beat they could not keep moving in synchronisation for a long time, causing peaks to diverge and their sum to decrease. After a while, the process starts to reverse, i.e. the peaks start moving towards each other and finally meet, being synchronised again. Therefore, the lack of synchronisation can be quantified through relative changes of time lags Δt_i between peaks of individual force signals on a cycle-by-cycle basis (Figures 6b and 6d). A summary of mean values and standard deviations of Δt_i values extracted from 30 s duration of all group force signals is given in Table 1.

The largest values of the mean and standard deviation are for the excitation causing near-resonant response for both bouncing and jumping indicating that the synchronisation was most affected by the large structural vibrations. Also, for both resonant and non-resonant rates, synchronisation during jumping was better compared with the bouncing counterparts.

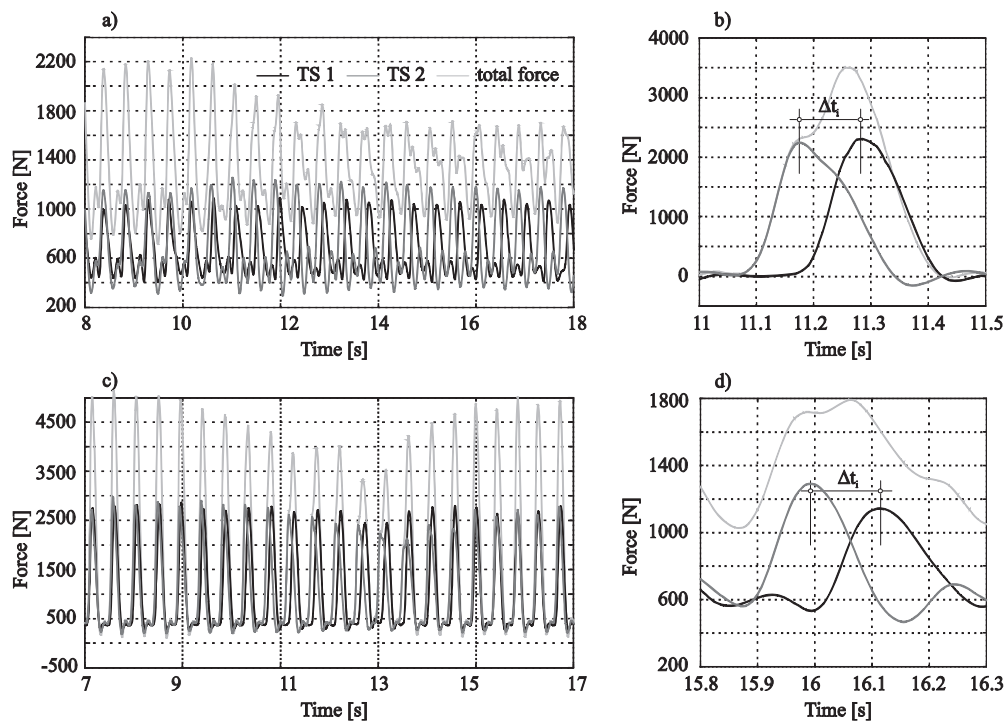


Figure 6: Synchronisation of (a-b) bouncing and (c-d) jumping forces. **Error! Reference source not found.** and 17 illustrate the same data.

Table 1: Summary of statistics (mean \pm standard deviation) of Δt_i :

Frequency [Hz]	bouncing [s]	jumping [s]
2.0	0.052 \pm 0.036	0.039 \pm 0.020
2.2	0.076 \pm 0.076	0.073 \pm 0.036
2.5	0.049 \pm 0.024	0.022 \pm 0.012

5 ENERGY FLOW AND POWER

A useful technique for studying human-structure dynamic interaction involves analysis of the power developed by human occupants moving on a structure and the power represented by the rate of internal energy dissipation in a structure conceptualised via damping forces [20]. Energy, with the units of Joules [J] or [Nm], is the time integral of power and is a more familiar quantity whose flow is easy to visualise. However graphical representation using power, with units of Watts [W] or [Nm/s], is simpler to study for comparative purposes.

For the slab strip, supply of energy to the structure at the point of contact is the instantaneous product of velocity $\dot{x}(t)$ and contact force $f(t)$. The contact force $f(t)$ could be obtained either directly by a load cell or reproduction from the marker motion, while velocity could be obtained by integrating accelerometer signals or differentiating contact point marker displacements. Here, the contact force is measured indirectly using Equation (1) and the velocity is obtained from displacements of a marker attached to the middle of the span where the activity was happening.

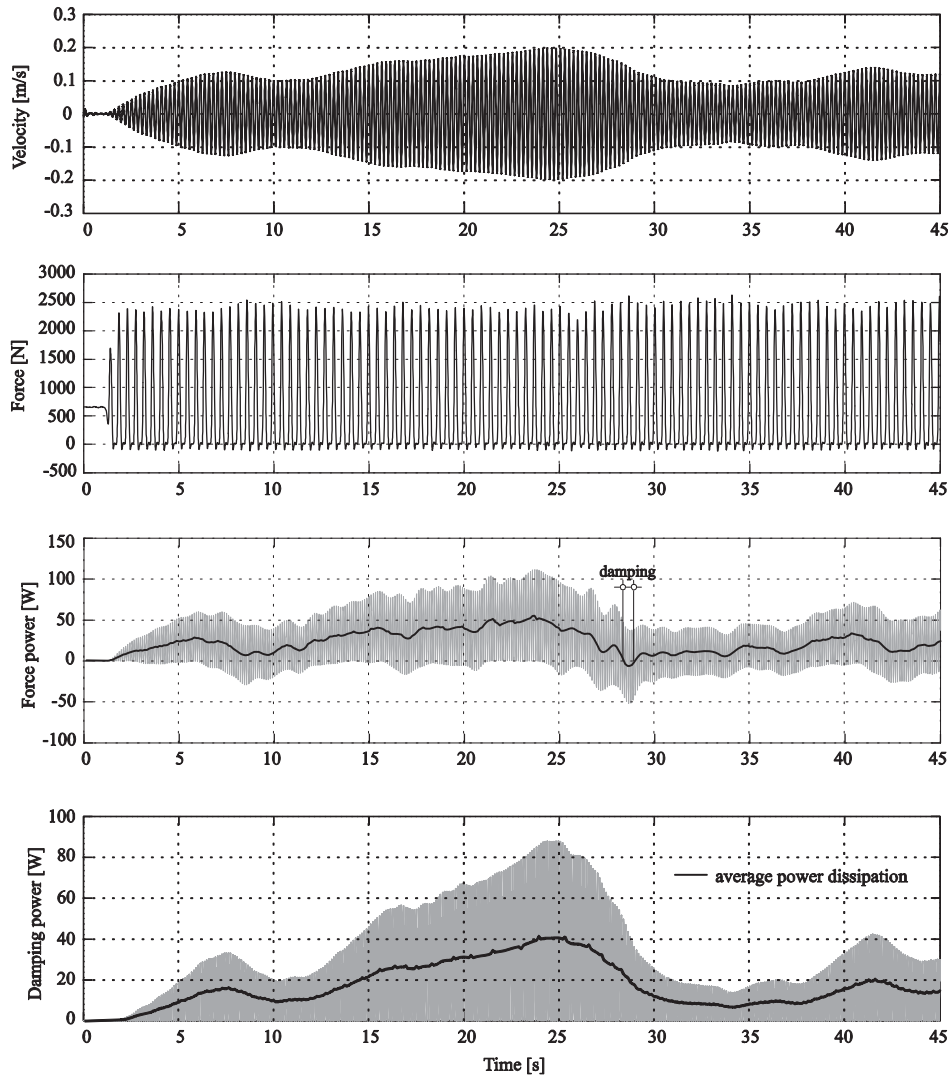


Figure 7: Energy flow and power due to TS 1 jumping in the middle of the span at resonant rate of 2.2 Hz.

Consider an equation of motion of a SDOF system, e.g. the first mode of vibration of the slab strip excited by a jumping force at the midpoint (antinode). If the mode shape is unity scaled at the midpoint then modal and physical displacements at the mid-point are identical and can both be represented by $x(t)$ which is a solution of the following well known differential equation [21]:

$$m\ddot{x}(t) + c\dot{x}(t) + kx(t) = f(t) \quad (2)$$

Here, m , c and k are the modal mass, damping and stiffness, respectively. Multiplying by the modal/physical velocity $\dot{x}(t)$, the equation of motion can be used to calculate instantaneous power $f(t)\dot{x}(t)$:

$$m\ddot{x}(t)\dot{x}(t) + c\dot{x}(t)\dot{x}(t) + kx(t)\dot{x}(t) = f(t)\dot{x}(t) \quad (3)$$

Here, $m\ddot{x}(t)\dot{x}(t)$ is kinetic power, $c\dot{x}(t)\dot{x}(t)$ is damping power and $kx(t)\dot{x}(t)$ is potential power.

In resonance it is well known that the inertia and stiffness forces are perfectly balanced with the interchange of kinetic and potential energy resulting in a constant value of energy and no net supply to either of them. Simultaneously, the external force simply provides positive power to compensate for the energy dissipated internally via damping (damping power):

$$\begin{aligned}
 m\ddot{x}(t)\dot{x}(t) &= kx(t)\dot{x}(t) \\
 c\dot{x}^2(t) &= f(t)\dot{x}(t) > 0
 \end{aligned}
 \tag{4}$$

Away from resonance in steady state the damping power is always positive (due to the square term in $c\dot{x}^2(t)$) but the external power has a zero-mean oscillating component which supplies and withdraws power during a cycle due to the imbalance of inertia and stiffness forces. During build up of response towards resonance the external force only supplies and never withdraws power to build up the constant level of total (i.e. kinetic plus potential) energy.

In the case of a single TS jumping, [Figure 7](#) shows positive power as response levels build up, with corresponding increasing damping power. The jumping human power cycles below zero, sometimes because the response is off-resonance, but also sometimes because the TS is actually out of synchronisation with the motion, resulting in net removal of energy. The cycle-by-cycle average power, represented by the heavy line, shows whether the human is active (driving) or passive (damping) overall. In [3], the same effect is illustrated for bouncing.

For the two TSs bouncing/jumping together ([Figure 8](#)), the individual cycle-by-cycle average power plots show that TS 1 was supplying energy to the system most of the time during the tests, while TS 2 was often acting as the strong damping element. This clearly explains why the resonance was very difficult to maintain for both activities. These tests also confirmed findings elsewhere [22] that the humans are characterised by huge inter-subject differences between their abilities to induce dynamic loads, to change the dynamic properties and to respond to nominally the same vibrations of the structure they occupy and dynamically excite.

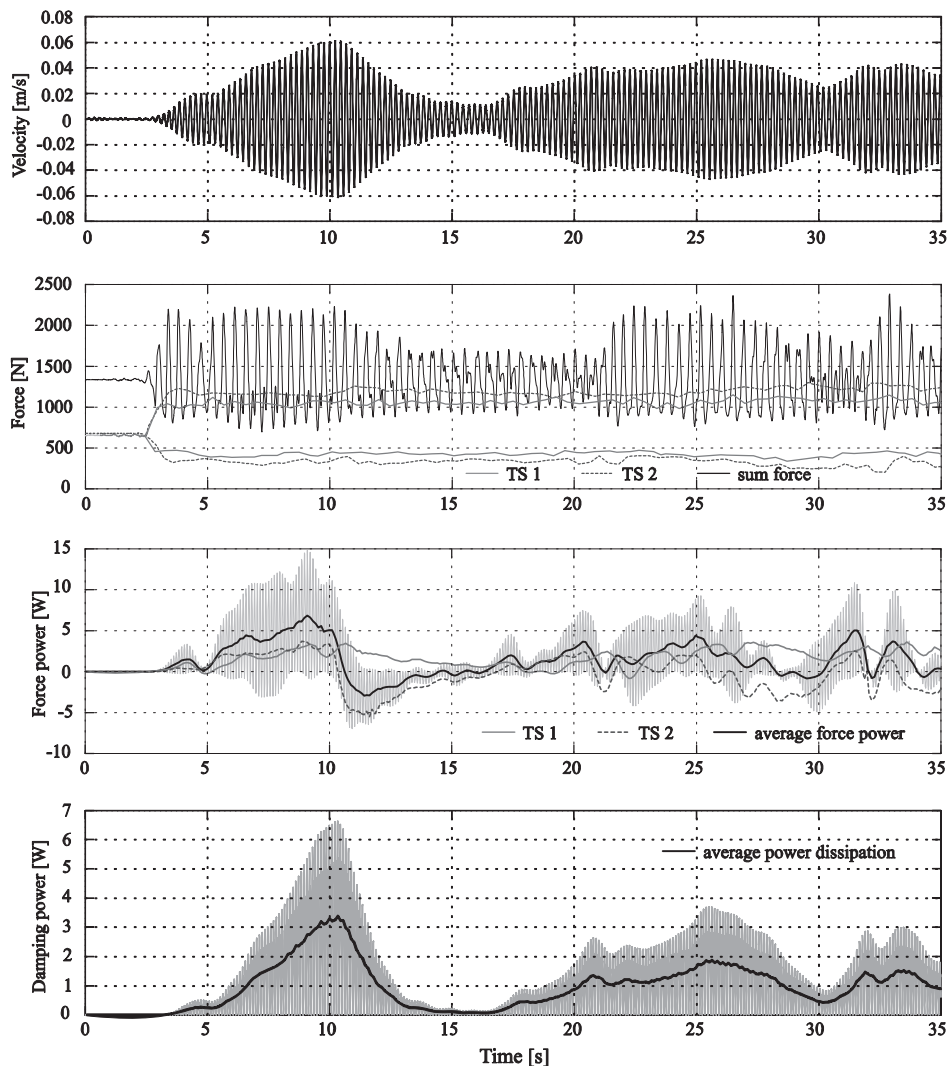


Figure 8: Energy flow and power due to both TSs bouncing together in the middle of the span at resonant rate of 2.2 Hz.

6 CONCLUSIONS

This paper presents a novel method in the civil engineering context to measure indirectly bouncing and jumping GRFs by combining human body motion tracking data and known/assumed body mass distribution. When compared with the traditional direct force measurements on floor-mounted force plates, a key advantage of the method proposed is utilisation of ‘free-field’ measurement of continuous bouncing and jumping GRFs. As demonstrated, indirect force measurements enable monitoring of people performing rhythmic activities in their natural environments, such as footbridges, grandstands, staircases and open-plan floors. Moreover, the method enables study areas of significant interest and uncertainty, specifically human-structure dynamic interaction and synchronisation between occupants when bouncing and jumping on flexible structures. Measurements have been able to show the negative cue effect of perceptible vibrations on the GRFs. Also, they indicated that in the joint human-structure dynamic system an active human can not only be the source of energy but they can also act as the strongest damping element. This happens either because the response is off-resonance or because they are out of phase with the structural motion resulting in net removal of energy. The effect is even stronger for multiple occupants due to the lack of synchronisation of their movements.

The method piloted in this paper has been validated using two male participants, who were jumping or bouncing either individually or as a pair on a realistic test structure. This means that there remains a requirement to carry out similar tests for single individuals and multiple occupants moving on a number of different, more or less vibrating real-life structures. Measurements can be used to develop and calibrate a new generation of badly needed models of rhythmic crowd loads. Therefore, this approach presents a timely opportunity to advance the whole field of vibration serviceability assessment of structures predominantly occupied and dynamically excited by bouncing/jumping humans, such as grandstands and entertainment venues.

REFERENCES

- [1] Racic V., Pavic A. Mathematical model to generate near-periodic human jumping force signals. *Mechanical Systems and Signal Processing* 24, pp. 138-152, 2010.
- [2] Racic V., Pavic A. Stochastic approach to modelling near-periodic jumping force signals. *Mechanical Systems and Signal Processing* 24, pp. 3037-3059, 2010.
- [3] Racic V., Brownjohn J.M.W., Pavic A. Reproduction and application of human bouncing and jumping forces from visual marker data. *Journal of Sound and Vibration* 329, 3397-3416, 2010.
- [4] Ebrahimpour A., Sack R.L., Saul W.E., Thinness G.L. Measuring dynamic occupant loads by microcomputer. In: K.M. Will, ed, *Proceedings of the Ninth ASCE Conference on Electronic Computation*, New York, USA, pp. 328-338, 1986.
- [5] Pernica G. Dynamic load factors for pedestrian movements and rhythmic exercises. *Canadian Acoustics* 18 (2), 3-18, 1990.
- [6] Rainer J.H., Pernica G., Allen D.E. Dynamic loading and response of footbridges. *Canadian Journal of Civil Engineering* 15 (1), pp. 66-71, 1988.
- [7] Winter D.A., *Biomechanics and motor control of human movement*, second edition. John Wiley & Sons, Toronto, Canada, 1990.
- [8] Perry J. *Gait analysis: Normal and pathological function*. Thorofare, New Yourk, USA, 1992.
- [9] *AMTI User manuals*, Advanced Mechanical Technology, Inc., Watertown, MA, USA, 2008.
- [10] Thorton-Trump A.B., Daher R. The prediction of reaction forces from gait data. *Journal of biomechanics* 8, pp. 173-178, 1975.
- [11] Miller D.I., Nissinen M.A. Critical examination of ground reaction force in the running forward somersault. *International Journal of Sport Biomechanics* 3, pp. 189-206, 1987.
- [12] Bobbert M.M., Schamhardt H.C., Nigg B.M. Calculation of vertical ground reaction force estimates during running from positional data. *Journal of Biomechanics* 24, pp. 1095-1105, 1991.
- [13] Sir I. Newton, *Philosophiae Naturalis Principia Mathematica (Mathematical principles of natural philosophy)*. Edmund Halley, ed., London, UK, 1687.
- [14] de Leva P. Adjustments to Zatsiorsky-Seluyanov's segment inertia parameters. *Journal of Biomechanics*, 29 (9), pp. 1223-1230, 1996.
- [15] *Codamotion user manuals*, Charnwood Dynamics Ltd., Leicestershire, UK, 2010.

- [16] Racic V., Pavic A., Brownjohn J.M.W. Experimental identification and analytical modelling of human walking forces: Literature review. *Journal of Sound and Vibration* 326, pp. 1-49, 2009.
- [17] *QA750 user manual*. Washington, USA, Honeywell International, Inc, 2010.
- [18] Yao S., Wright J.R., Pavic A., Reynolds P. Experimental study of human-induced dynamic forces due to jumping on a perceptibly moving structure. *Journal of Sound and Vibration* 296, pp. 150-165, 2006.
- [19] Griffin M.J. *Handbook of Human Vibration*. Academic Press, London, UK, 1996.
- [20] Brownjohn J.M.W. Energy dissipation from vibrating floor slabs due to human-structure interaction. *Shock and Vibration* 8, pp. 315-323, 2001.
- [21] Clough R.W., Penzien J. *Dynamics of structures*. Mcgraw-Hill, Inc, Singapore, 1993.
- [22] Bachmann H., Pretlove A.J., Rainer H. Dynamic forces from rhythmical human body motions, Appendix G. In: *Vibration problems in structures: practical guidelines*, Birkhäuser Verlag, Basel, Switzerland, 1995.

Operational Modal Analysis for the Guangzhou New TV Tower

Yan Niu, Peter Kraemer and Claus-Peter Fritzen
Center for Sensor Systems (ZESS), University of Siegen
Institute of Mechanics and Control Engineering-Mechatronics, University of Siegen
Paul-Bonatz-Strasse 9-11, 57076 Siegen, Germany
niu@imr.mb.uni-siegen.de, kraemer@imr.mb.uni-siegen.de, fritzen@imr.mb.uni-siegen.de

ABSTRACT

The 610 m high Guangzhou New TV Tower (GNTVT) is currently considered as a benchmark problem for structural health monitoring research. In the benchmark study task I, a set of 24-hour ambient vibration measurement data is available for output-only system identification and FE model updating. In this contribution, an Operational Modal Analysis (OMA) for GNTVT is performed using the Vector Autoregressive models (ARV) method. The extracted eigenfrequencies, damping ratios and mode shapes are presented and compared with the result obtained using the Stochastic Subspace Identification (SSI) method. Furthermore, results from some other benchmark testing groups are used for comparison. This study shows that the ARV-based method works successfully for this OMA purpose.

INTRODUCTION

Modal analysis has been widely used in many engineering fields, like aerospace, mechanical and civil engineering, where the obtained modal data serves as the basis for model updating, and afterwards model-based Structural Health Monitoring (SHM). Compared to traditional Experimental Modal Analysis (EMA), Operational Modal Analysis (OMA) has drawn more and more attention in the last two decades. Zhang et al. contributed a good overview of different OMA techniques [1]. In this paper, a Vector Autoregressive Models (ARV) method is adopted in the operational modal analysis for the Guangzhou New TV Tower (GNTVT), China. This method is based on the estimation of eigenmodes of arbitrary order autoregressive (AR) models [2], and has demonstrated its functionality in monitoring high towers of wind energy plants [3].

VECTOR AUTOREGRESSIVE MODELS (ARV) METHOD

The measurements obtained at equally spaced instants k can be modeled in an arbitrary order AR model as in Eq. 1.

$$y_k = b + \sum_{l=1}^p A_l \cdot y_{k-l} + \varepsilon_k \quad (1)$$

where y_k is the measurements from m sensors at time instant k , p is the number of this AR model, and $A_1, \dots, A_p \in R^{m \times m}$ are coefficient matrices. b is an intercept vector, and ε_k is an uncorrelated zero mean random vector, representing the residual between real measurements and the model at time instant k . Assuming b is a zero vector, the AR model of p -th order (AR(p) model) can be transformed to a state space form as in Eq. 2.

$$\begin{aligned} x_{k+1} &= A_d \cdot x_k + w_k \\ y_k &= C \cdot x_k \end{aligned} \quad (2)$$

where,

$$x_k = \begin{bmatrix} y_k^T & y_{k-1}^T & \cdots & y_{k-p+1}^T \end{bmatrix}^T \in R^{(m \cdot p) \times 1} \quad (3)$$

$$w_k = \begin{bmatrix} \varepsilon_{k+1}^T & 0 & \cdots & 0 \end{bmatrix}^T \in R^{(m \cdot p) \times 1} \quad (4)$$

$$A_d = \begin{bmatrix} A_1 & A_2 & \cdots & A_{p-1} & A_p \\ I & 0 & \cdots & 0 & 0 \\ 0 & I & \cdots & 0 & 0 \\ 0 & 0 & \ddots & 0 & 0 \\ 0 & 0 & \cdots & I & 0 \end{bmatrix} \in R^{(m \cdot p) \times (m \cdot p)} \quad (5)$$

$$C = [I \ 0 \ \cdots \ 0] \in R^{m \times (m \cdot p)} \quad (6)$$

Then the dynamical characteristics of the investigated structure can be extracted by solving the eigenvalue problem of the state matrix A_d .

$$A_d = \Psi \cdot \Lambda \cdot \Psi^{-1} \quad (7)$$

where Λ is a diagonal matrix of associated discrete time eigenvalues λ_i^d ($i=1, \dots, m \cdot p$), and Ψ contains corresponding eigenvectors. The continuous time eigenvalues λ_i^c can be calculated using Eq. 8.

$$\lambda_i^c = (\ln \lambda_i^d) / \Delta t \quad (8)$$

where Δt is the sampling time. Then for the q -th mode of this structure,

$$\lambda_q^c, \lambda_q^{c*} = -\xi_q \cdot \omega_q \pm j \cdot \omega_q \cdot \sqrt{1 - \xi_q^2} \quad (9)$$

Damped natural frequency: $f_q = \text{Im}(\lambda_q^c) / (2 \cdot \pi)$

Damping ratio: $\xi_q = -\text{Re}(\lambda_q^c) / |\lambda_q^c|$

Complex mode shapes: $\Phi = C \cdot \Psi$

In order to separate the physical modes from spurious ones caused by measurement noise, a stabilization diagram can be constructed, and the eigenvalues of AR($l-1$) model are compared with those of AR(l) model. The criteria adopted in this comparison procedure are as follows,

1. Criterion (stable frequencies): $f_{tol} = \frac{f_{l-1} - f_l}{f_{l-1}} \times 100\%$
2. Criterion (stable damping ratios): $\xi_{tol} = \frac{\xi_{l-1} - \xi_l}{\xi_{l-1}} \times 100\%$
3. Criterion (stable mode shapes): $MAC_{tol} = \frac{(\Phi_{l-1}^T \cdot \Phi_l)^2}{\|\Phi_{l-1}^T\|^2 \cdot \|\Phi_l\|^2}$

Depending on the quality of measurements, suitable tolerance values can be selected for each criterion.

FIELD MEASUREMENTS FROM GNTVT

The GNTVT is a 610 m high tube-in-tube structure completed in 2010 in Guangzhou, China. On this TV tower, a long-term SHM system consisting of more than 700 sensors has been designed and implemented for both in-construction and in-service real time monitoring, and the instrumented GNTVT is currently considered as a benchmark problem on SHM for high-rise slender structures [4]. In the benchmark study task I, the acceleration, wind direction, wind speed and ambient temperature were recorded from Jan. 19th, 2010, 18:00 h to Jan. 20th, 2010, 18:00 h (in total 24 one-hour periods). In this contribution, these are considered as field measurements for OMA. The temperature was measured every minute (1/60 Hz), and the acceleration and wind data were sampled with 50Hz. The accelerometer positions and measurement directions are shown in Fig. 1.

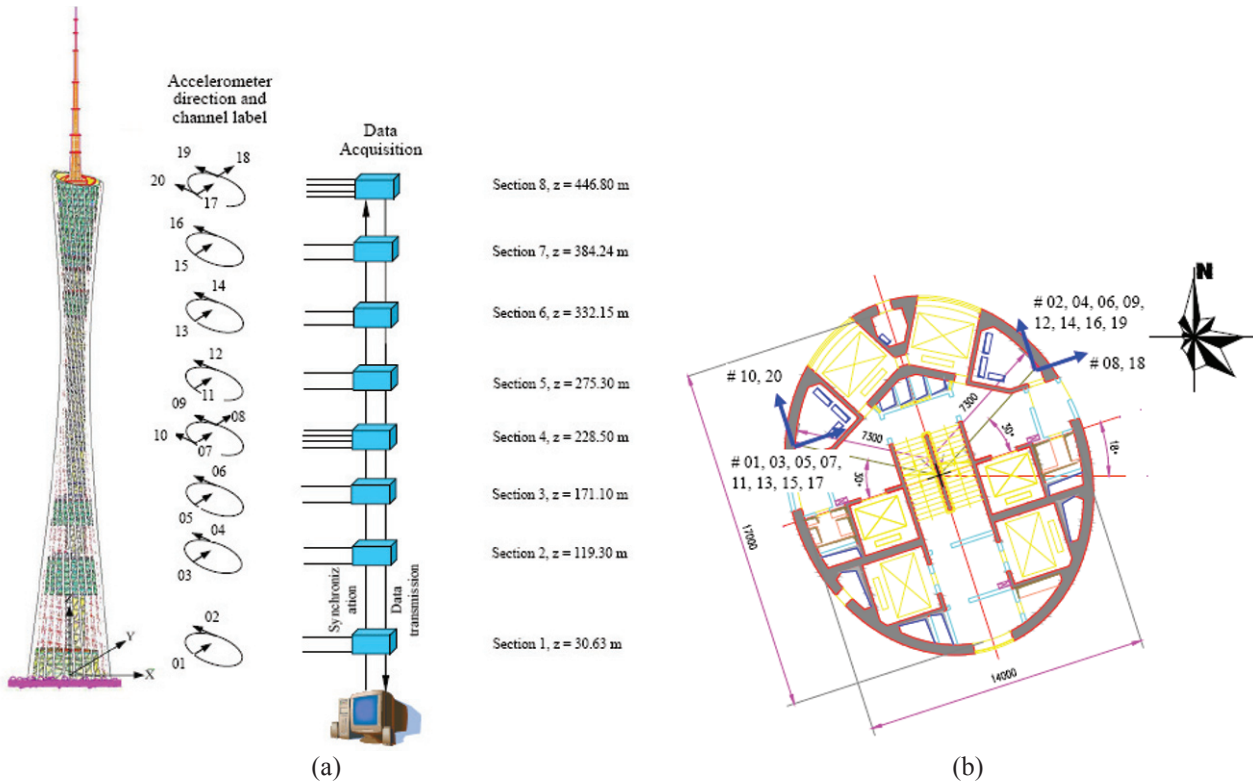


Fig. 1 (a) Positions of the accelerometers and data acquisition system (b) Measurement directions of acceleration and channel labels (Courtesy of Hong Kong Polytechnic University)

OPERATIONAL MODAL ANALYSIS (OMA) RESULT

In this study, the first 12 modes of GNTVT are investigated. The field acceleration measurements are first downsampled by a factor of 14 to decrease the computational load. Then the ARV method stated in Section 2 is applied to extract the natural frequencies, damping ratios and mode shapes of GNTVT based on each one-hour acceleration measurements. The criteria used for selecting stable poles from each stabilization diagram are all set as $f_{tol} = 0.1\%$, $\xi_{tol} = 10\%$, and $MAC_{tol} = 0.99$. One of the stabilization diagrams is shown in Fig 2, which shows a very clear picture of stable poles.

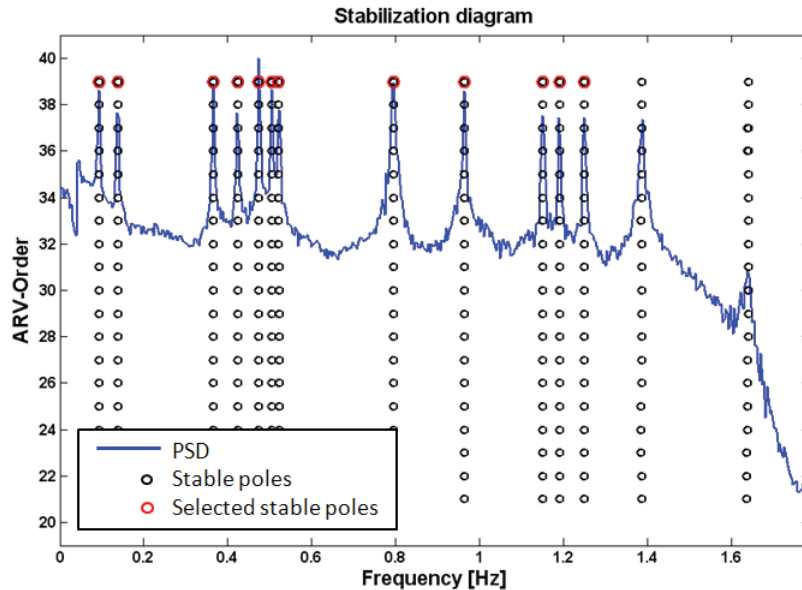


Fig. 2 Stabilization diagram for measurements between 14:00 h and 15:00 h on Jan. 20th, 2010

In total, 24 sets of eigenvalues and eigenvectors are obtained, and the calculated mean values and coefficients of variation (CV, CV = standard deviation / mean) of the identified natural frequencies and damping ratios are listed in [Table 1](#).

Table 1 OMA results from ARV

<i>Identified natural frequencies using ARV [Hz]</i>												
Nr.	f_1	f_2	f_3	f_4	f_5	f_6	f_7	f_8	f_9	f_{10}	f_{11}	f_{12}
Mean	0.0935	0.1386	0.3659	0.4237	0.4747	0.5055	0.5223	0.7952	0.9650	1.1506	1.1909	1.2504
CV	0.0034	0.0021	0.0017	0.0008	0.0006	0.0011	0.0007	0.0012	0.0012	0.0006	0.0004	0.0008
<i>Identified damping ratios using ARV [-]</i>												
Nr.	ξ_1	ξ_2	ξ_3	ξ_4	ξ_5	ξ_6	ξ_7	ξ_8	ξ_9	ξ_{10}	ξ_{11}	ξ_{12}
Mean	0.0098	0.0047	0.0029	0.0023	0.0011	0.0018	0.0017	0.0022	0.0024	0.0017	0.0011	0.0016
CV	0.8830	0.5447	0.2995	0.3833	0.4431	0.2987	0.3310	0.2381	0.2030	0.7511	0.1859	0.2903

For the purpose of comparison and verification, the Stochastic Subspace Identification (SSI) method is also adopted to extract the modal information, based on the same field acceleration measurements. In this procedure, a MATLAB toolbox MACEC is used [5][6]. The measurements are decimated by a factor of 10, which is the maximum decimation factor in this toolbox, and the half number of block rows i is chosen as 30. The calculated mean values and CV of identified results are listed in [Table 2](#).

Table 2 OMA results from SSI

<i>Identified natural frequencies using SSI [Hz]</i>												
Nr.	f_1	f_2	f_3	f_4	f_5	f_6	f_7	f_8	f_9	f_{10}	f_{11}	f_{12}
Mean	0.0935	0.1386	0.3659	0.4238	0.4747	0.5054	0.5224	0.7951	0.9650	1.1506	1.1909	1.2506
CV	0.0042	0.0027	0.0017	0.0008	0.0006	0.0010	0.0007	0.0012	0.0012	0.0005	0.0004	0.0008
<i>Identified damping ratios using SSI [-]</i>												
Nr.	ξ_1	ξ_2	ξ_3	ξ_4	ξ_5	ξ_6	ξ_7	ξ_8	ξ_9	ξ_{10}	ξ_{11}	ξ_{12}
Mean	0.0092	0.0045	0.0027	0.0021	0.0010	0.0016	0.0017	0.0023	0.0024	0.0012	0.0011	0.0015
CV	0.8765	0.4828	0.3271	0.3709	0.4333	0.3103	0.3563	0.3231	0.1957	0.3099	0.2153	0.2999

From [Table 1](#) and [Table 2](#), it can be seen that the result from ARV has a good accordance with that from SSI. Furthermore, the natural frequencies obtained from ARV are compared with those from the Finite Element (FE) model of GNTVT, as listed in [Table 3](#) [7]. The frequency difference values mean that the FE model still needs to be updated.

Table 3 Natural frequency comparison between FEM and OMA

<i>Natural frequencies [Hz]</i>												
Nr.	f_1	f_2	f_3	f_4	f_5	f_6	f_7	f_8	f_9	f_{10}	f_{11}	f_{12}
FEM	0.1104	0.1587	0.3463	0.3688	0.3994	0.4605	0.4850	0.7381	0.9026	0.9972	1.0373	1.1218
OMA	0.0935	0.1386	0.3659	0.4237	0.4747	0.5055	0.5223	0.7952	0.9650	1.1506	1.1909	1.2504
Diff.(%)	18.06	14.54	5.35	12.95	15.87	8.91	7.15	7.18	6.46	13.33	12.90	10.29

A set of the identified mode shapes using the ARV method is shown in [Fig. 3](#).

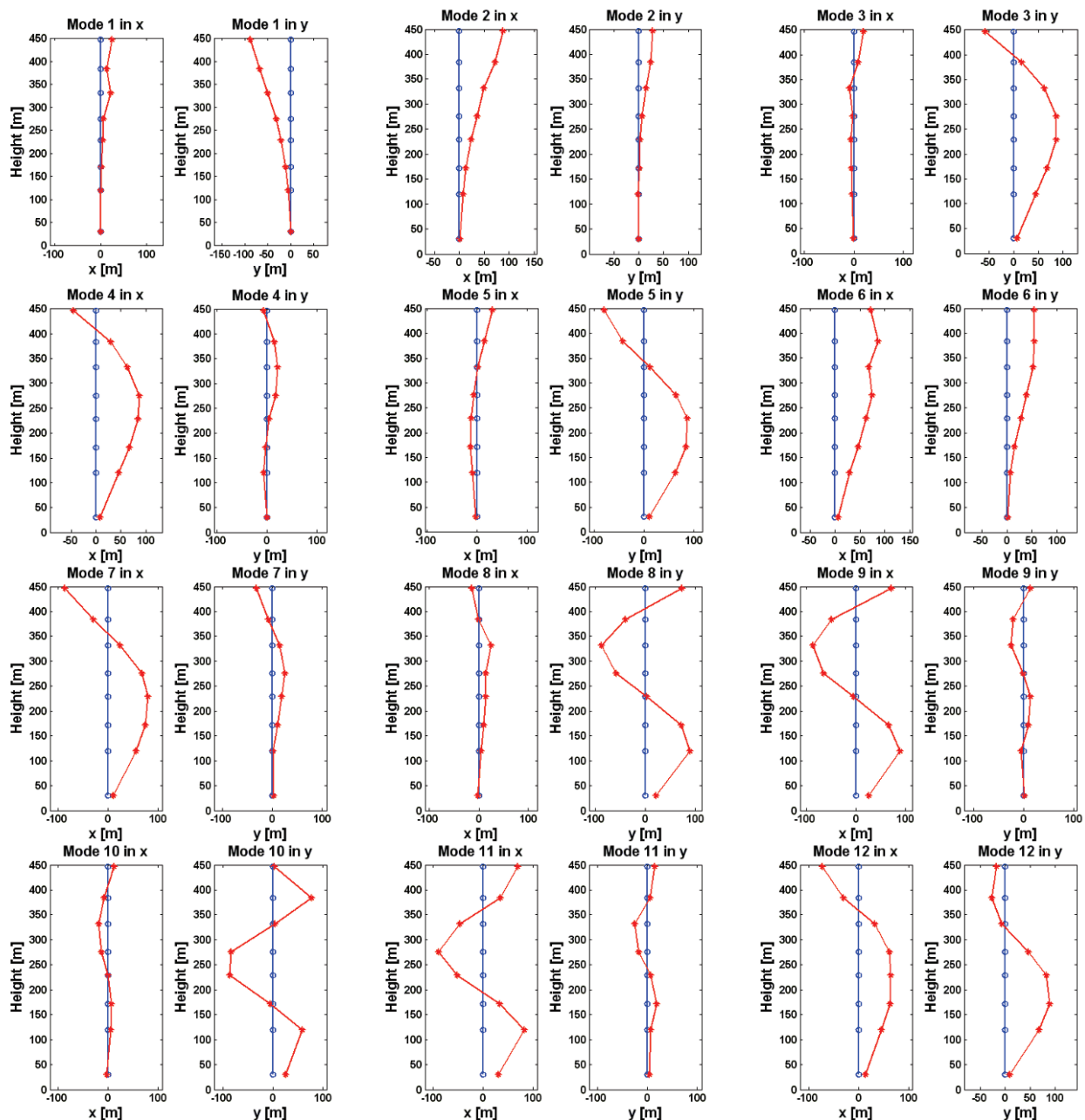


Fig. 3 Identified mode shapes based on measurements on Jan. 20th, 2010, between 14:00 h and 15:00 h
 (○ — : reference; ★ — : mode shape)

In Fig. 3, a sudden change is found in the mode shapes, especially in modes 1, 3, 6 and 8, in the x direction at the height of 332.15 m. According to the authors' study, MACEC shows the same results. This behavior could result from complicated tower design or measurement problems, and has to be investigated in the future.

EFFECT OF ENVIRONMENTAL CONDITIONS

In the field measurements, ambient temperature, wind direction and wind speed are provided, too, so it is also interesting to investigate the effect of these environmental conditions on the dynamical characteristics of this TV tower.

In Fig. 4, the changes of natural frequencies with respect to the ambient temperature are shown. The black stars are natural frequencies of each mode extracted at different temperatures, and the corresponding trends are shown using red lines

obtained based on robust regression analysis [8]. From these plots, it is obvious that natural frequencies decrease as temperature increases. This result also agrees with those presented in [3] and [9].

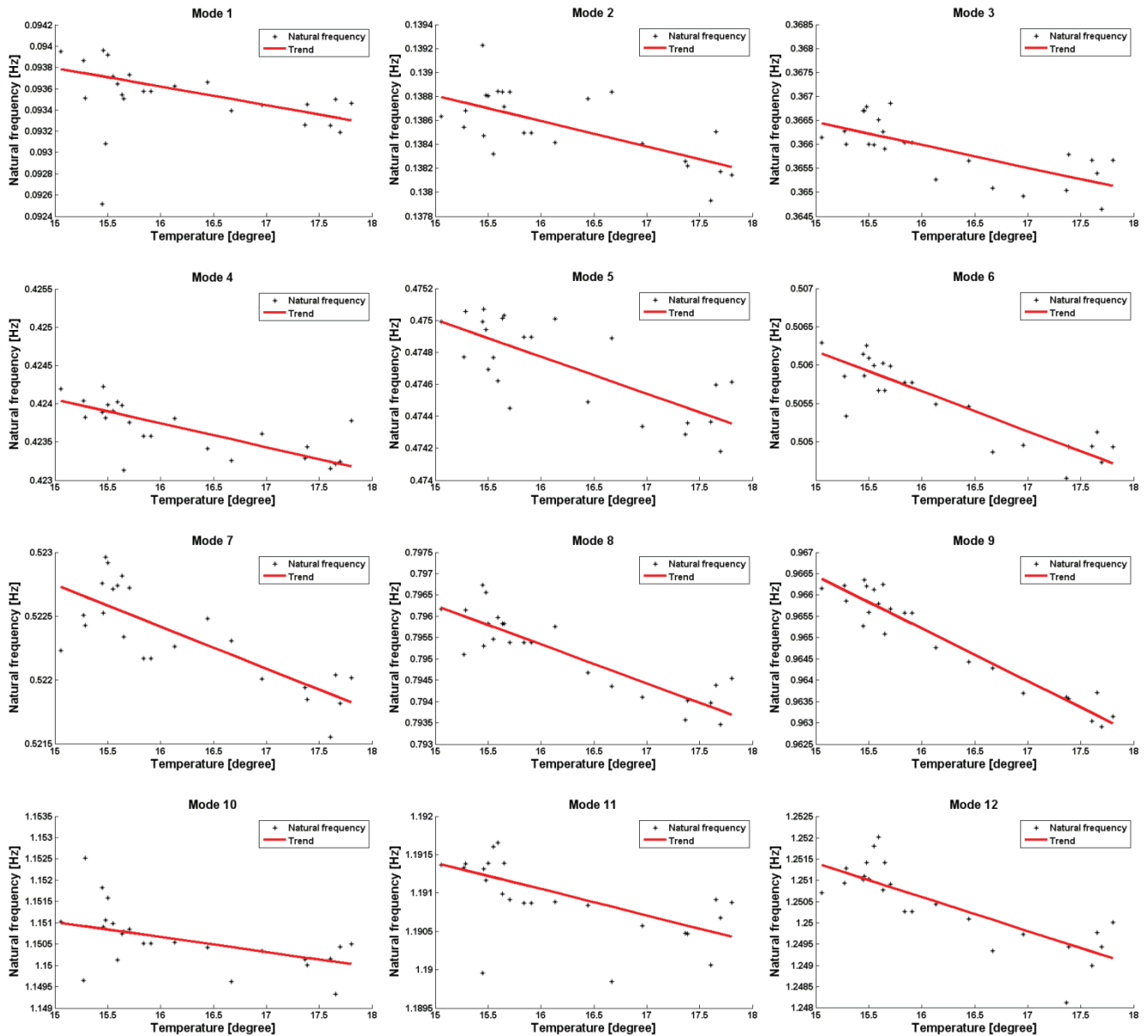


Fig. 4 Changes of natural frequencies with respect to the ambient temperature

In Fig. 5a and Fig. 5b, the changes of damping ratios with respect to the ambient temperature are shown. Different from the case for natural frequencies, no uniform trend is reflected.

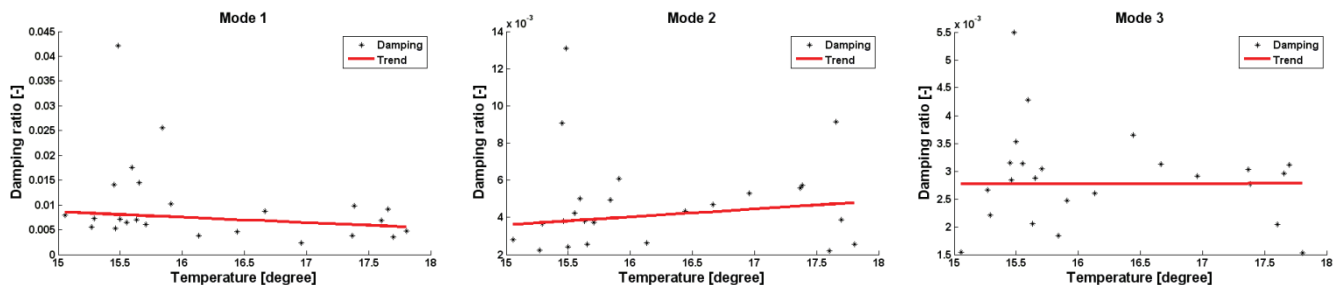


Fig. 5a Changes of damping ratios with respect to the ambient temperature

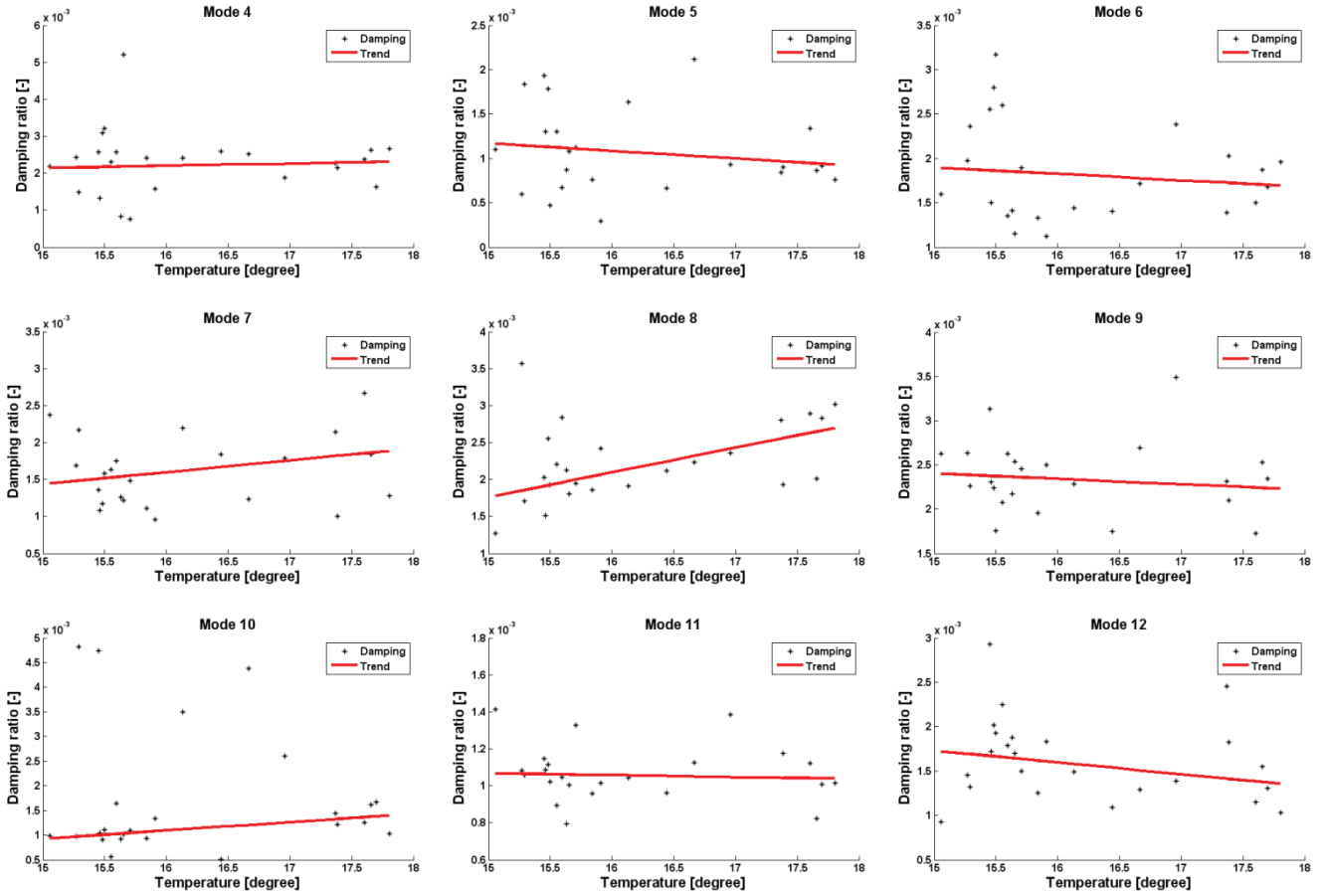


Fig. 5b Changes of damping ratios with respect to the ambient temperature

In Fig. 6, 24-hour wind direction and wind speed measurements are plot with respect to time. It can be seen that, after 2 o'clock, the wind direction is almost constant. So it is reasonable to study the effect of wind speed on the natural frequencies and damping ratios based on the measurements after 02:00 h. The changes of natural frequencies with respect to the wind speed are shown in Fig. 7. It can be seen that no uniform trend is reflected in this case.

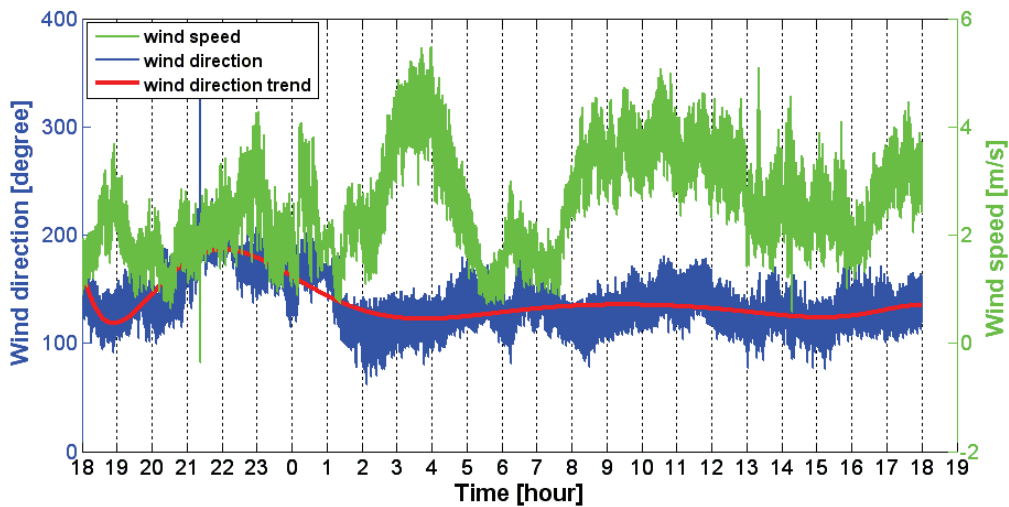


Fig. 6 24-hour Wind direction and wind speed measurements

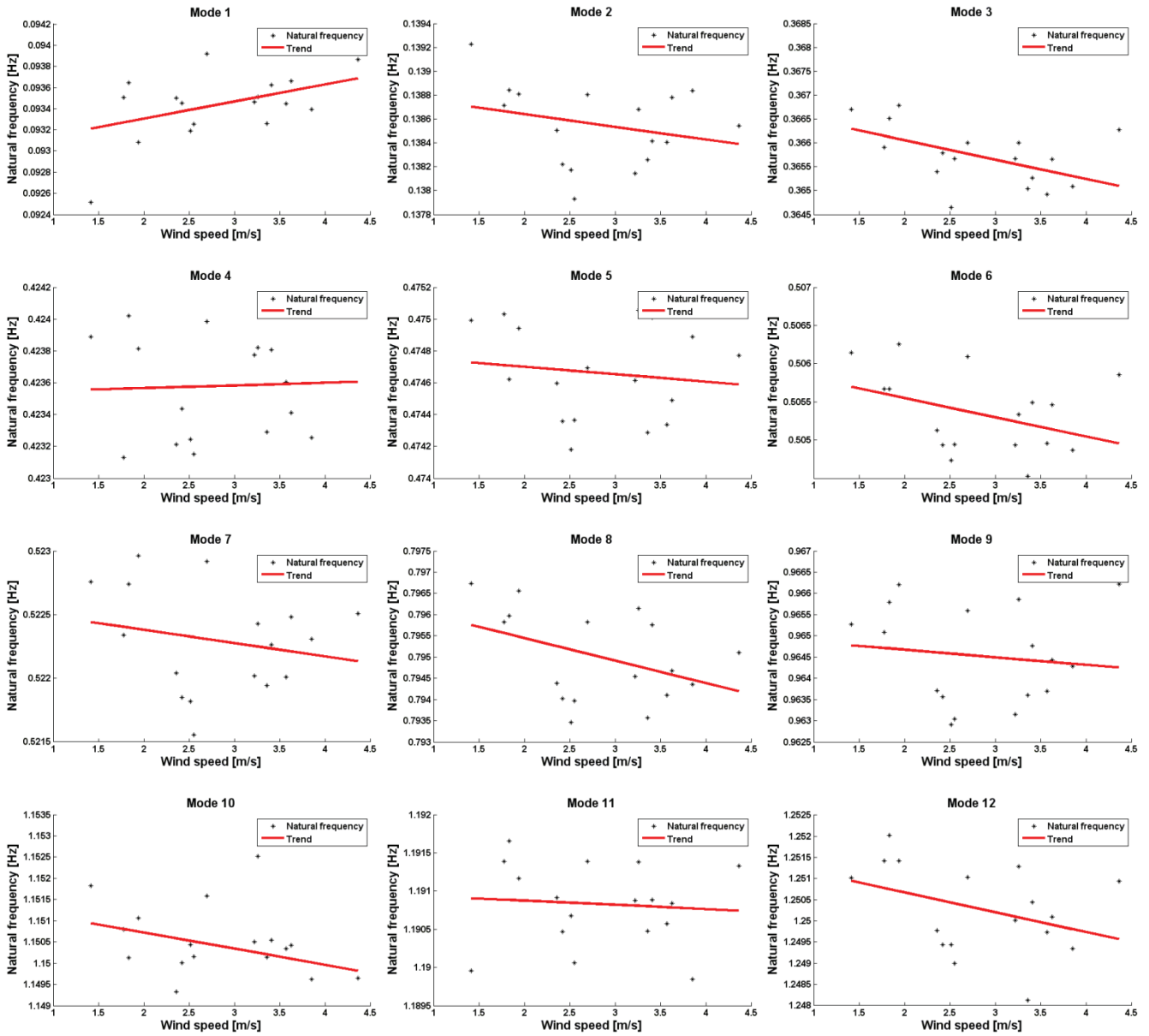


Fig. 7 Changes of natural frequencies with respect to the wind speed

In Fig. 8a and Fig. 8b, the changes of damping ratios with respect to the wind speed are shown.

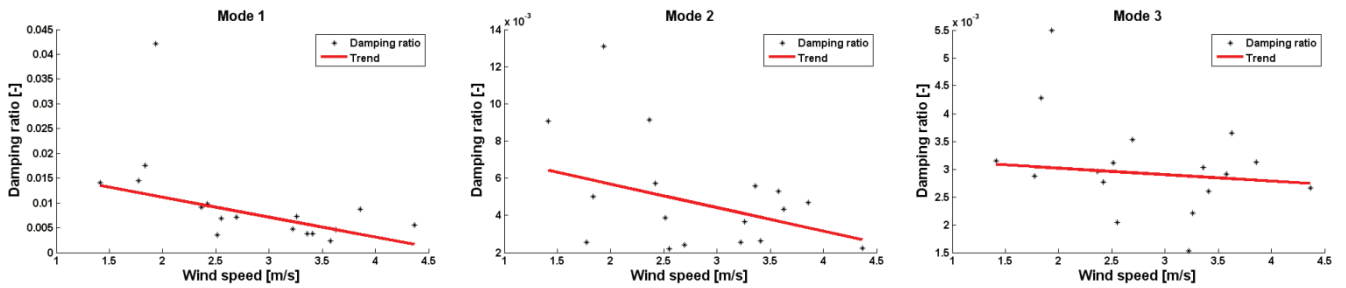


Fig. 8a Changes of damping ratios with respect to the wind speed

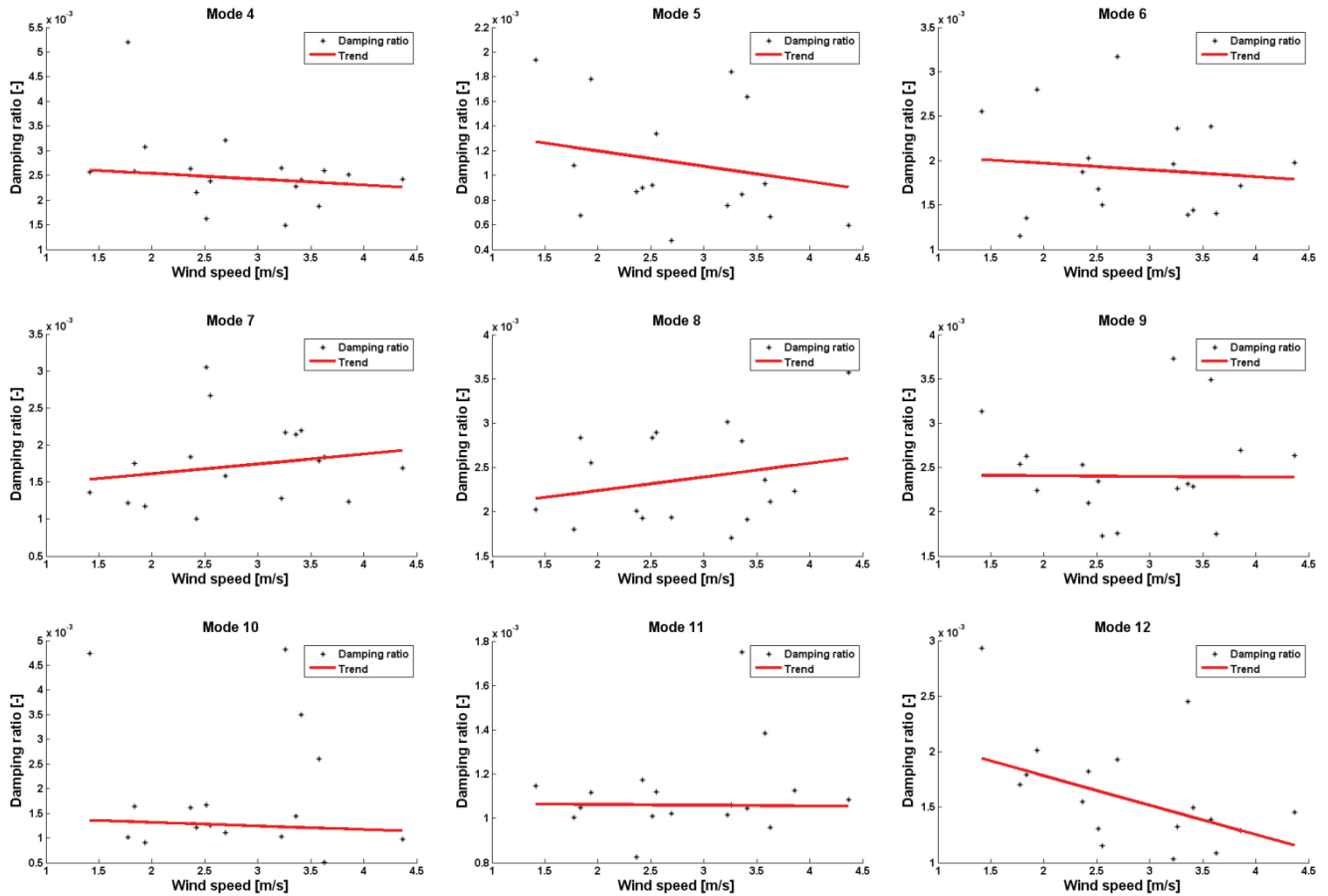


Fig. 8b Changes of damping ratios with respect to the wind speed

From Fig.8a and Fig.8b, it can be seen that no uniform trend is reflected in this case, too. This result is in common with that presented in [9], and it might be due to the low wind speed during the measurement. So it is interesting to do more analysis about this in the future based on measurements obtained under higher wind speed.

CONCLUSION

In this contribution, the Vector Autoregressive Models (ARV) method is adopted for the operational modal analysis of Guangzhou New TV Tower. The obtained results are compared with those extracted using the Stochastic Subspace Identification (SSI) method, and both results show a good accordance with each other. Furthermore, the effect of environmental conditions on the dynamical characteristics of this TV tower is discussed. It is shown that, the natural frequencies of this TV tower decrease as the ambient temperature increases, while the changes of natural frequencies with respect to the wind speed do not show uniform trend. The changes of damping ratios with respect to both the ambient temperature and wind speed do not show uniform trend. Further investigation will be performed in the future based on measurements under larger temperature change span and higher wind speed.

ACKNOWLEDGEMENT

Special thanks are given to Prof. Ni from Hong Kong Polytechnic University for the provided field measurement data. The authors are also grateful to the Research School on Multi-Modal Sensor Systems for Environmental Exploration (MOSES) and Center for Sensor Systems (ZESS) for their support to this research work.

REFERENCES

- [1] Zhang, L., Brincker, R., Andersen, P., “An Overview of Operational Modal Analysis: Major Development and Issues”, Proceedings of 1st International Operational Modal Analysis Conference: 179-190, April 26 – 27, 2005, Copenhagen, Denmark.
- [2] Neumaier, A., Schneider, T., “Estimation of Parameters and Eigenmodes of Multivariate Autoregressive Models”, ACM Transactions on Mathematical Software, Vol. 27, No. 1: 27-57, March, 2001.
- [3] Kraemer, P., Fritzen, C.-P., “Aspects of Operational Modal Analysis for Structures of Offshore Wind Energy Plants”, Proceedings of IMAC-XXVIII : 277-284, Jacksonville, Florida, USA, February 1-4, 2010,.
- [4] Ni, Y.Q., Xia, Y., Liao, W.Y., Ko, J.M., “Technology Innovation in Developing the Structural Health Monitoring System for Guangzhou New TV Tower”, Structural Control and Health Monitoring, 16: 73-98, 2009.
- [5] Peeters, B., De Roeck, G., “Reference Based Stochastic Subspace Identification in Civil Engineering”, Inverse Problems in Science and Engineering, Vol. 8 : 47-74, 2000.
- [6] De Roeck, G., Peeters, B., Ren, W., “Benchmark Study on System Identification Through Ambient Vibration Measurements”, Proceedings of IMAC 18 : 1106-1112, San Antonio, Texas, USA, February, 2000
- [7] Ni, Y.Q. et al., “A Benchmark Problem on Structural Health Monitoring of High-Rise Slender Structures, Phase I: Field Vibration Measurement and Model Updating, Description of the FE model and Model Reduction”, <http://www.cse.polyu.edu.hk/benchmark/index.htm> .
- [8] Montgomery, D.C., Peck, E.A., “Introduction to Linear Regression Analysis”, John Wiley & Sons, 4ed., 2006.
- [9] Faravelli, L., Ubertini, F., Fuggini, C., “Subspace Identification of the Guangzhou New TV Tower”, Proceedings of 5th World Conference on Structural Control and Monitoring, 5WCSCM-068, 2010.

On the use of Shape Memory Alloys dampers to reduce the vibration amplitudes of civil engineering cables

L.Dieng¹, V. Torra², and P. Pilvin³

Abstract Cables used in civil engineering bridge has very low intrinsic damping rate which makes them particularly susceptible to vibration related to weather (wind, rain) and traffic. The associated displacement amplitudes are relatively small near the anchor (about 5 mm), as well as vibration frequencies (1-10 Hz). This may cause damage and affect the sustainability of structures and the safety of people. To avoid these phenomena, several stay cable bridges are equipped with dampers to reduce the amplitude of displacement. Deep studies on SMA for damping applications (i.e., fatigue / fracture analysis, SMA creep effects, aging actions) was the basis for the SMA application to morphing. In fact, from damping to morphing the requirements for SMA are more demanding and particular studies are necessary. This paper focuses on the assessment of the effectiveness of the use of shape memory alloys (SMA) dampers to reduce the vibration amplitudes of civil engineering cables. Mechanical behavior under cyclic loading of SMA wires is studied and super-elastic polycrystalline SMA model parameters are identified. Experimental tests were performed in a LCPC laboratory on a 50 meters long cable equipped or not with a two NiTi wires dampers (diameter: 2.46 mm). The experimental results shown, evidence of a dramatic decrease in the amplitude of displacement which reached about four times the experimental value determined for cable without SMA dampers.

Key words: Civil engineering cable, Shape Memory Alloys, Dampers, Vibration

¹ LCPC

Centre de Nantes - Route de Bouaye - BP: 4129, 44341 Bouguenais, France
Tel. +332-40-33-40-82, Fax. +332-28-00-13-45
e-mail: lamine.dieng@lcpc.fr

² CIRG-DFA-ETSECCPB, UPC,

CAMPUS NORD B4-B5, E-08034 Barcelona, Catalonia, Spain
e-mail: vtorra@fa.upc.edu

³ LIMB - Université de Bretagne SUD -

Rue de Saint-Maudé, BP 92116 - 56321 Lorient Cedex, France
e-mail: philippe.pilvin@univ-ubs.fr

1 Introduction

1.1 Background

Many civil engineering structures include cables. These structures represent significant investments for managers who are concerned in particular about the sustainability of these structures and user safety. However, they are subject to severe dynamic loading that are causing their degradation over time. Broken wires due to fretting fatigue phenomena are the main constituent causes of cables deterioration. Recently, many researches have focused on the development of damping device to reduce the vibration amplitude and the number of cycles [2], [3]. Cable damping is caused by internal friction between the components of the cable or of its anchorages. They have a low intrinsic damping capacity. The most conventional way of limiting or eliminating cable vibration involves increasing their structural damping capacity by fitting special devices. This is effective for almost all kinds of vibration except parametric instability. According to information in the literature [5], rain and wind instability, for example, is avoided when the logarithmic decrement of the cable is greater than 3.0%. There are several kinds of dampers:

- External dampers : these are generally hydraulic devices exerting a transverse damping force on the cable, near the anchorages. they can be installed in pairs, directly on the cable (Fig. 1).
- Internals dampers : these are ring-shaped, and they are placed between the cable and a steel tube attached rigidly to the structure, near either of the anchorages. Internal dampers use the distortion of a dissipating material (specially formulated neoprene) or viscous friction or dry friction between two solids
- Stabilizing cables are also use to prevent some kinds of cable vibration. It consists in installing interconnecting metallic wires which stiffen the array of cables. They can provide additional damping, if appropriately designed, but they have proven to be less effective than dampers in preventing rain and wind instability.

However, these damper systems are less effective or no longer work when the vibration amplitudes or frequencies are very high and could be broken see [figure 2](#).

To overcome this problem the SMAs were proposed as useful passive devices for dampers in Civil Engineering see [4]. Shape memory alloys (SMAs) are a unique group of alloys with the ability to remember a shape even after quite severe deformations. At low temperatures they can be seemingly plastically deformed like other metal alloys, but this deformation can be recovered by a relatively modest increase in temperature (shape memory effect). The mechanism of this recovery is the transformation from a martensite phase to the parent austenite phase. Alloys like NiTi, CuZnAl, CuAlNi, AuCd and others have erasable strains of 3 - 8%. Other important characteristics of some of these materials are significant internal damping, rather large nonlinear elastic ranges (pseudoelasticity) and high yield stresses. Although the first SMAs were developed more than 50 years ago, it is fair to say that rigorous and reliable continuum-level constitutive models required for these engineering



Fig. 1 Dampers device of Iroise Bridge (FR)



Fig. 2 Broken Dampers device of Iroise Bridge (FR)

applications of the materials do not yet exist. During this time, the understanding of the micromechanical aspects of martensitic transformations has reached a comfortable level [1]. Nevertheless, the connection between microscopic and macroscopic behavior is very complex and has not yet been developed to the degree required by such models. This is partly due to the rather broad variation in the mechanical response with temperature, loading rate, strain range, specimen geometry, thermomechanical history, nature of the ambient environment, and to the interaction between several of these parameters. For examples of the state of modeling see [6], [7], [8] and [9]. Despite over 50 years of study, the amount of high quality experimental data of the macroscopic behavior of NiTi remains limited. Notable examples of experimental work on the mechanical behavior of NiTi include in [10], [11], [12] and [13]. An excellent experimental study of NiTi, in which the effects of temperature, strain range and mechanical cycling were investigated, in [14]

1.2 Motivations

Cables oscillate under the action of wind/rain/traffic. The oscillations induce crashing of steel wires or progressive experimental damage and, obviously, some relevant reduction of the cable's life. This type of problems is observed in St Nazaire Bridge (France) and, also, in other bridges submitted to higher winds as, for instance, in the Viaducts of Boulonnais: Herquelingue (260 m) Quehen (474 m) Echinghen (1309 m). The study is focused on the assessment of the effectiveness of the use of shape memory alloys (SMA) dampers to reduce the vibration amplitudes of civil engineering cables. In particular, the NiTi wires are used for the higher number of working cycles only in traction (no compression or bending)[17]. The present paper is organized in two main sections. In the first section, tests and experimental results are presented concerning the mechanical behavior of Ni-Ti alloys specimen under tensile loading-unloading. Numerical simulation are conducted in order to determine Ni-Ti hyper-elastic model parameters used to fit the experimental results. In the second section, a series of measurements of cable vibration without and with

SMA damper is presented. It permits to establish the effective possibilities of SMA wires to reduce the galloping actions in stayed cables for bridges.

2 Experimental test under uni-axial loadings characterizing the mechanical behavior of NiTi wires

2.1 Material and experimental equipment

The material used for all test is Ni-Ti SMA provided by SAES group (USA). The material is available as 2.46 mm diameter. Tests are performed at LIMB - Université de Bretagne SUD (France) with an Instron 5567 equipped with a strain sensor (Figure 3). A series of 10 tensile loading cycles was performed on samples of wire length 19 cm. The maximum strain is up to 4% and correspond to a maximum displacement of the cross of 8 mm. Results shows that the transformation from an austenite phase to the parent martensite phase is not uniformly throughout the area of the specimen. The transformation begins in a localized zone, in general one of the two ends, progressively propagate within the specimen, while maintaining a well defined interface between the martensite and the austenite. In fact, with only 10 cycles, the presence on Luders band is commonly noticed. This explains why we do not show the phenomenon on the load-strain curve as the transformation has not arrived in the area measured by the extensometer. Figure 4 shows the corresponding strain-stress curve with an extensometer placed in the middle of the specimen.

2.2 Model SMAs super-elastic behavior

The Model use to reproduce the experimental results is well detailed in [15]. In this macroscopic model, built with the assumption of small strain, the classical decomposition of the total strain, ε , is considered:

$$\begin{cases} \varepsilon = \frac{\sigma}{E} + \varepsilon^T; \\ \sigma = E (\varepsilon - \varepsilon^T); \end{cases}$$

where ε^T is the transformation strain, E the elastic modulus and σ the stress. According to [15], super elastic SMAs have a typical hysteretic mechanical behavior in which two thresholds can be defined: the first one for forward and the second for reverse phase-transformation. In their developed model two phase-transformation surfaces representing the two thresholds, have been introduced:

$$f_1 = \sigma_{eq} - (R(Z) + \sigma_0^t) \leq 0 (Z < 1)$$



Fig. 3 Material and experimental equipment

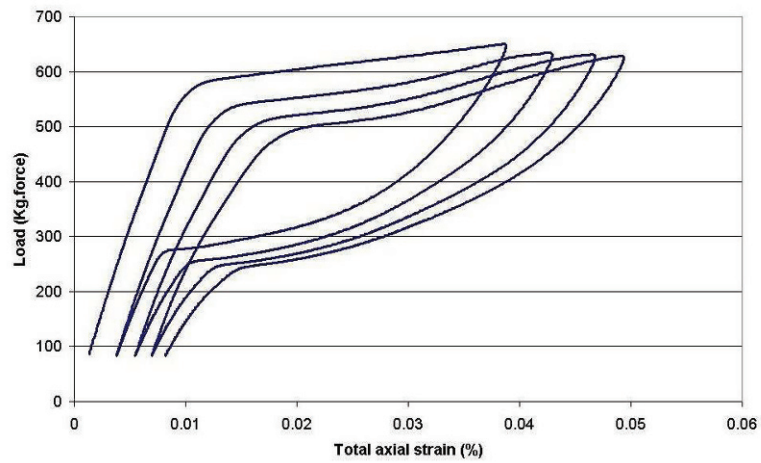


Fig. 4 Experimental stress - strain curve tensile loading-unloading at room temperature

$$f_2 = \overline{(\sigma - X)}g(y_{\sigma-x}) - (R(Z) + \sigma_0^t) \leq 0 (Z > 1)$$

Where R characterizes the size of the transformation surface, σ'_0 is the yield stress of forward phase transformation, σ_{eq} is a fraction of the Von Mises equivalent stress (see [16] and [15] for more details).

$y_\sigma = \frac{27\det(\underline{S})}{2\sigma_3}$ is the third invariant of the stress tensor, $g_{(y)}$ is a function making possible the modification of the shape of the transformation surface describing the characteristic asymmetry between tension and compression observed in SMAs. The tensor X locates the center of the reverse phase transformation surface f_2 . The martensite volume fraction is noted Z . $Z = 0$ defined the purely austenitic phases and $Z = 1$ designed the matensitic phases of shape memory alloy. Z is related to the equivalent transformation strain defined by Bouvet et al (2004) [16] and γ , a material parameter corresponding to the maximum transformation strain. γ is determined experimentally by:

$$Z = \frac{\varepsilon_{eq}^T}{\gamma}$$

The transformation strain evolution for forward and reverse phase are given by the following expression :

$$\dot{\underline{\varepsilon}}^T = \lambda_1 \frac{\partial f_1}{\partial \underline{\sigma}} \quad \text{forward transformation}$$

$$\dot{\underline{\varepsilon}}^T = -\lambda_2 \frac{\underline{\varepsilon}^T}{\sqrt{\frac{2}{3}\underline{\varepsilon}:\underline{\varepsilon}}}; \quad \text{reverse transformation}$$

where λ_1 and λ_2 are the transformation multipliers given by the consistency conditions. To simplify this model we assume that the function $g_{(y)}$ is equal to y and then :

$$\lambda_1 = \gamma \frac{\langle \dot{\underline{\sigma}} \rangle}{\max R g^t}$$

and

$$\lambda_2 = \frac{E \dot{\varepsilon} \text{sign}(\underline{\sigma} - X)}{\text{sign}(\underline{\varepsilon}^T) \left[\text{sign}(\underline{\sigma} - X) \left\{ E + 2 \frac{\max(R) g^t}{\gamma} \right\} + \frac{\max(R) g^t}{\gamma} \right]}$$

SiDoLo [18] was used to identify the parameters of this simplified model and to simulate the tensile behavior of specimens. Comparisons between numerical results and experimental points are shown on figures 5 and 6. For the forward transformation, the numerical model fits well the experimental values. However, for reverse transformation, gap values is more important. The function $g_{(y)}$ assumed to be equal to y in our simplified model does not allow us to accurately represented experimental points. To obtain a more representative model of the behavior of SMA, it is necessary to find an equation governing this function.

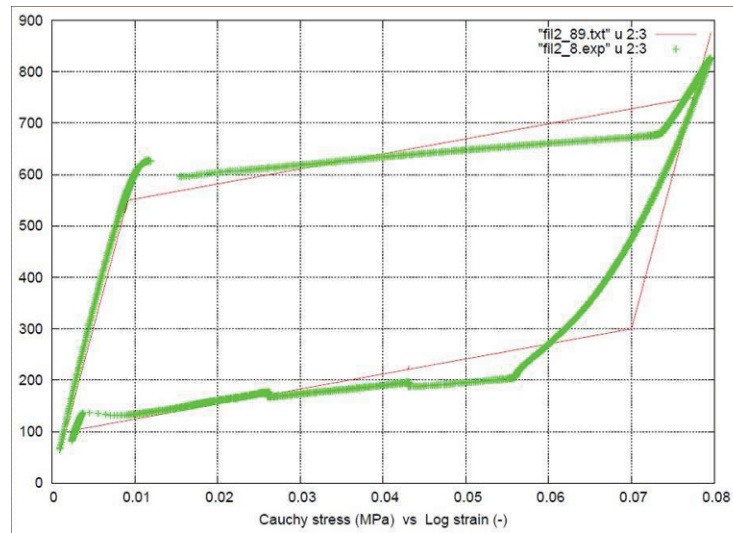


Fig. 5 Stress-strain comparison between Model and Exp. : first cycle.

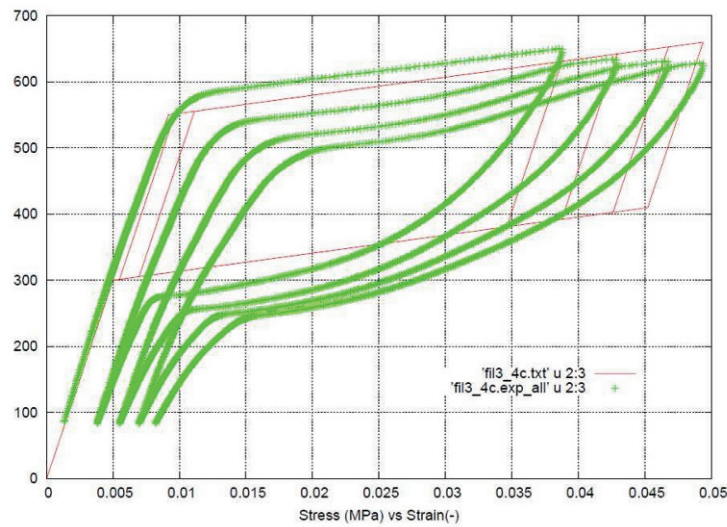


Fig. 6 Stress-strain comparison between Model and Exp. : 4 first cycles.

3 Experimental analysis of the cable equipped or not with SMA dampers

3.1 Testing conditions

The modal tests were carried out at the LCPC Centre de Nantes with a cable of 50 m length between the two fixed ends. The main characteristic values of the set-up

are reported in [Table 1](#). The cable was a locked coil strand made of 159 steel wires. The cross section of the strand is shown in [Figure 7](#). The helical wires in the outer layers of a locked coil strand are shaped and designed to contact one another when the strand is axially loaded with a tension force. The shaped wires were 4.5 mm high with a cross-section area of 16.3 mm². The bending stiffness value of the strand is not accurately defined from the geometrical and elastic characteristics of the wires because it depends in a complex manner on the inter-wire contact conditions. However, an approximate upper bound estimate is given by considering that the strand behaves in flexion like a steel beam of the same diameter. The theoretical estimate of the bending stiffness of the strand is then 90 kNm².

Table 1 Cable characteristics

Diameter (D) (mm)	Length (L) (m)	Mass μ (kg/m)	Position (P) (m)
55	50.57	16.1	25

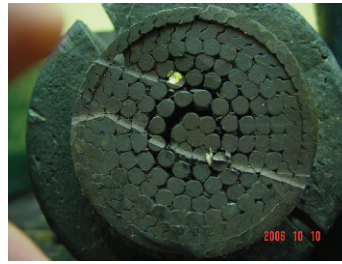


Fig. 7 Cross section of a locked coil strand.

The axial tensile force was applied to the strand with a hydraulic jack. When the tensile force reached the test value of 955 kN, the system was held in position with nuts. The axial force was measured with a load cell of limited accuracy due to the thermal drift of the electronic conditioning system, leading to variations within a range of 5% in a day. The extremities of the cable were held by a specific system of jaws shown in [Figure 8](#). The outline of the damper is situated in [figure 9](#), their structure permits different numbers of SMA wires (eventually with different diameters) and also SMA lengths. The shortened devices are used to induce a minor initial stress to the SMA wires. In the tests realized in LCPC only two trained wire is used with and without pre-stressing. The wire induces forces on the cable between zero and, for instance, 4000 N according to with the imposed deformation. Clamps permit their fixation on the bottom and on the cable. The device permits global slip associate to compression by sliding of the steel axis. Furthermore, each wire can, independently, avoid compression sliding in the cylindrical brass disc. The dampers



Fig. 8 Anchorage system of the strand.

device used to investigate the effect of Shape Memory alloys dampers during the cable vibrations was located one a half length. The experimental setup is shown in [Figure 10](#).

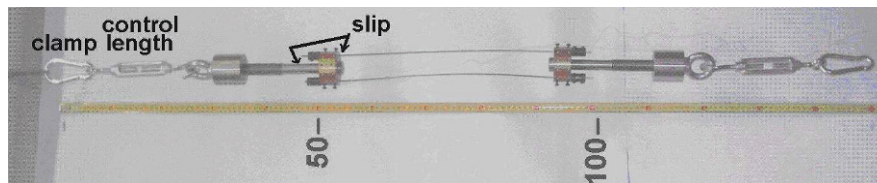


Fig. 9 Outline of the damper. The SMA wires and the steel axis can slip avoiding compressive part of cycles. The damper ends with clamps and includes two shortened devices, permitting appropriate tuning the SMA length

A series of force (0.5, 1, 2, 3 and 4 kN) perpendicular to the axis of the cable (angular deflection) is applied at the half length of the cable and instantaneously released, the cable freely oscillates, during 60 s of the free oscillation was measured. For each type of test we measure the loading force using a load cell "Z Dembo Technic" type. The applied force to SMA wires is also measured with another load cell fitted on the damper. The displacement of the cable are measured with a laser sensor, and the transient response accelerations by a tri-axial accelerometer. Temporal signals are analyzed to determine the vibration amplitude and damping coefficients. Such experimental setup allows to study the influence of certain parameters such as the position of the excitation point (for preferred modes of vibration even or odd) and the amplitude of vibration on the measurement of damping coefficient.



Fig. 10 Anchorage system of the strand.

3.2 Experimental results

The temporal signal are represented on figures 11 et 12: The figure 11 represents the 5 impulsions applied to the cable. The figure 12 represents the cable vertical displacement given by the sensor located very close to the damper device at the half length of the cable. Obviously, the presence of the damper has a significant effect on the temporal signal.

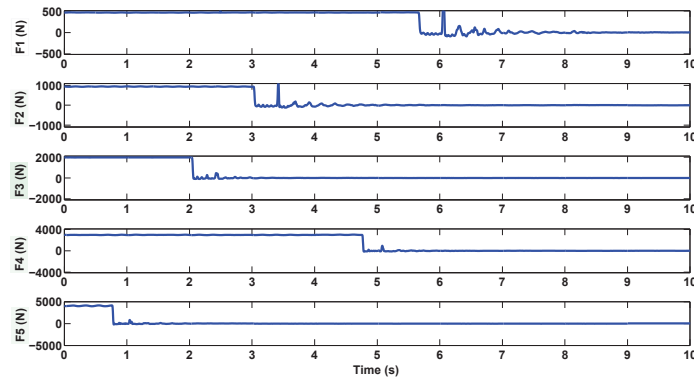


Fig. 11 Cable vertical loading forces

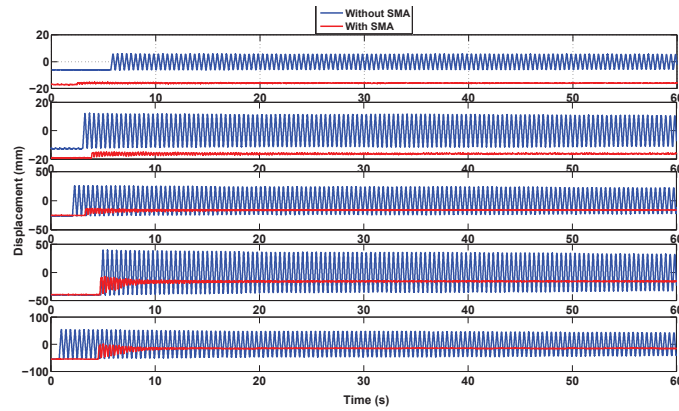


Fig. 12 cable vertical displacement

Figures 13 and 14 represent the cable frequency response function (FRF) for the first test ($F=0.5$ kN) and the last one (4 kN) respectively. The Blue curve (in dotted line) represents the power spectral density (PSD) of vertical cable acceleration not equipped with dampers and the red line curve for cable with two SMA wires damper. One notes that for the first modes the action of SMA reduces the maximal amplitude to at least 1/4 and increases the cable frequency, for instance, from 2.3 to 3.36 Hz for the first frequency. Results show also the SMA damper are more efficient for higher deflection amplitude ($F=4$ kN) due to their solid-solid phase transformation permits effective damping via the hysteresis cycle and the conversion of mechanical work in heat.

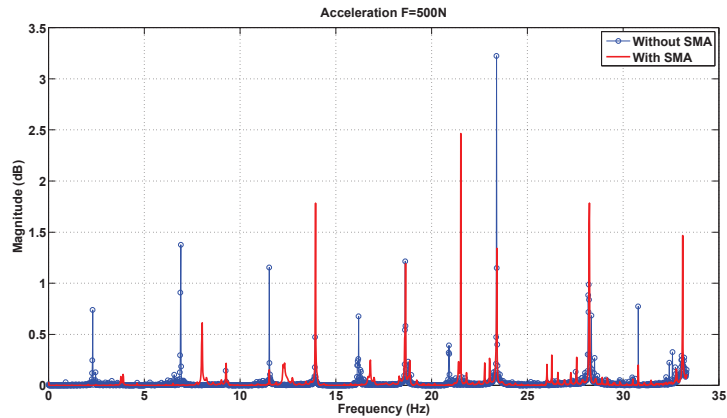


Fig. 13 Frequency Response Function - F = 0.5 KN

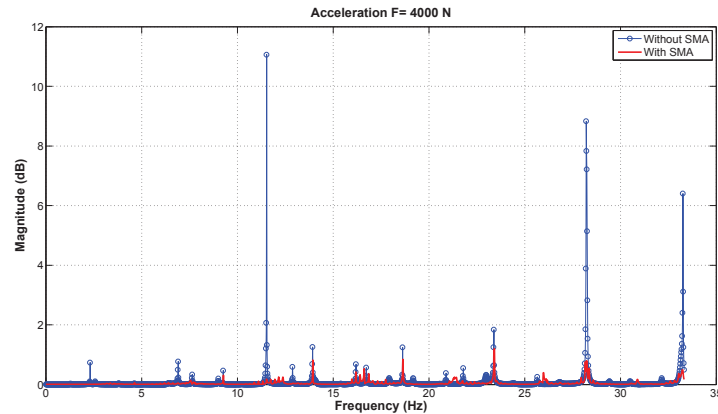


Fig. 14 Frequency Response Function - $F = 4 \text{ KN}$

4 Concluding and remarks

In this paper, the appropriate properties of Shape Memory Alloys for damping are outlined focused in application for civil engineering bridge i.e. damping of stayed cables for bridges. A brief description of SMA (NiTi) law behavior under tensile test is outlined using a super elastic model. Then the application of SMA as dampers, to mitigate the oscillations induced in realistic cables (50 m length) are presented. In tensile cycles, the samples increase their length spontaneously via a complex problem with two actions. One of them, via the accumulation de dislocations (plastic and permanent deformation) and, the other way relates some stabilized martensite. The experimental tests suggest that the SMA damper permits an effective reduction of the oscillation's amplitude to a quarter. The effectiveness SMA dampers depend on its position on the cable. Tests performed in this study favor the reduction of amplitudes of the first three modes. It would be necessary to perform tests to evaluate the influence of the position of the damper and optimize it. For a better effectiveness, for an in situ application, we must determine, first, the predominant vibration modes of the cable and find a best position of the dampers.

Acknowledgements Thanks to Daniel Bruhat, Richard Michel, Christophe Mingam and Grégoire Laurence for their participation in the experimental set-up and the measurements.

References

1. J. A. Shaw and S. Kyriakides, Thermomechanical Aspects Of Niti, *J. Mech. Phys. Solids*, Vol. 43, No. 8, pp. 1243-1281, 1995
2. V. Torra, A. Isalgue, F. Martorell, P. Terriault, F.C. Lovey, *Eng. Struct.* 29 1889(2007)
3. F.C. Lovey, V. Torra *Progr. Mater. Sci.* 44 (3) 189 (1999)
4. V. Torra, A. Isalgue, G. Carreras, F. C. Lovey, H. Soul, P. Terriault, L. Dieng, Experimental Study of Damping in Civil Engineering Structures Using Smart Materials (NiTi SMA). Application to Stayed Cables for Bridges, 1st International Conference on Mechanical Engineering (ICOME), VIRTUAL FORUM, June 7th-21st, 2010
5. Cable Stays : Recommendations of French interministerial commission on Prestressing. Issued by the SETRA - Centre des Techniques des Ouvrages d'Art, France (2002).
6. Falk, F. (1980) Model free energy, mechanics, and thermodynamics of shape memory alloys. *Acta Metall.* Vol. 28, pp. 1773-1780.
7. Muller, I. and Xu, H. (1991) On the pseudo-elastic hysteresis. *Acta Metall. Mater.* vol. 39, pp. 263-271.
8. Ericksen, J. L. (1991) Introduction to the Thermodynamics of Solids. Chapman and Hall, Londod.
9. Abeyaratne, R. and Knowles, J. K. (1993) A continuum model of a thermoelastic solid capable of undergoing phase transitions. *J. Mech. Phys. Solids* 41, 541-571.
10. Buehler, W. J., Gilfrich, J. V. and Wiley, R. C. (1963) Effect of low-temperature phase changes on the mechanical properties of alloys near composition TiNi. *J. Appl. Phys.* 34,1475-1477.
11. Wasilewski, R. J. (1971) The effects of applied stress on the martensitic transformation in NiTi. *Metallurg. Trans.* 2, 2973-298 1.
12. Jackson, C. M., Wagner, H. J. and Wasilewski R. J. (1972) 55-Nitinol-the alloy with memory :Its physical metallurgy, properties, and applications. NASA-SP5 110.

13. Ling, H. C. and Kaplow, R. (1980) Phase transitions and shape memory in NiTi. *Metallurg. Trans. A II*, 77-83.
14. Miyazaki, S., Otsuka, K. and Suzuki, Y. (1981) Transformation pseudoelasticity and deformation behavior in a Ti-50.6 at% Ni alloy. *Scripta Metall.* 15, 287-292.
15. L. Saint-Suplice, S.A. Chirani, S. Calloch, 3D super-elastic model for shape memory alloys taking into account progressive strain under cyclic loading, *Mechanics of materials* vol. 41 (2009) pp. 12-26
16. C. Bouvet, S. Calloch, C. LExcellent, Mechanical behavior of a Cu-Al-Be SMA under multiaxial proportional et non proportional loadings. *Eur. J. Mech. A Solids* Vol. 23 (2002), pp. 37-61.
17. School and Symposium on Smart Structural Systems Technologies, 6-9 April, 2010, a FEUP, Porto, Portugal (S3T-ESF Meeting). Published in S(3)T 2010, R. Barros, A. Preumont Eds., Faculdade de Engenharia da Universidade do Porto (2010), ISBN: 978-989-96697-0-3 1): Experimental study of damping in civil engineering structures using smart materials (Cu-Al-Be - NiTi SMA). Applications to steel portico and to stayed cables for bridges (The SMARTeR project), V. Torra, F.C. Lovey and P. Terriault, pp. 369-399.
18. SiDoLo, version 2.4495, notice d'utilisation, 2003.

Dynamic behavior of 'Palazzo Lombardia' helisurface, comparison between Operational and Experimental Modal Analysis

G. Busca¹, A. Cigada¹, E. Mola², F. Mola¹, M. Vanali¹
1 Politecnico di Milano, Via La Masa 1, Milano, Italy
2 ECSD S.r.l. Via Goldoni Milano, Italy

ABSTRACT

The 'Altra Sede' Tower, located in the heart of the city of Milan, has recently been completed. On January 22, 2010 an official ceremony marked the end of the construction phase and unveiled the new building to the citizens of Milano, a building which is currently the tallest in Italy, and one of the strongest features of the skyline of the city for years to come. Besides the main tower and the adjacent buildings an helicopter landing surface has been built. This paper deals with the dynamic testing of the surface, describing all the steps taken to identify the main vibration modes in the vertical and horizontal planes. Two different forcing systems have been employed and then the results coming from the forced response, experimental modal analysis results, have been compared to the ones obtained via operational modal analysis leaving the same sensors in place for a few days and continuously measuring the ambient vibrations. The obtained results describe the surface dynamic behavior in the range 0-10 Hz. All the resonant frequencies and associated mode shapes have been correctly identified. This modal parameter set is the reference to which future measurements should be compared in order to perform a structural health monitoring campaign on the surface.

INTRODUCTION

Structural health monitoring (SHM) has gained a lot of attention from the research community in last few decades. Among the several methods available, the integrity of civil infrastructures can be evaluated by extracting information from their dynamic response measurements. Modal parameters are some of the indicators mostly used in literature [1][2] to represent the structure behavior and therefore to assess the health status. For this reason, when a new building is constructed, it is common to execute not only static but also dynamic tests. In this way it is possible to validate the design, conformingly with anti seismic requirements, and to evaluate the dynamic parameters used as the reference in future structural health monitoring campaigns.

The dynamic behavior of a structure can be evaluated by two different approaches: applying a known excitation (by means of a hydraulic actuator, vibrodyne, etc.) or exploiting the unknown loading caused by environment load sources (such as traffic, wind, etc.). The former is called experimental modal analysis (EMA), whereas the latter is known as operational modal analysis (OMA) [3][1][7]. Usually both approaches are exploited when dealing with health monitoring campaigns.

EMA guarantees generally a total control on the test conditions: the excitation level may be fixed for every analysis and the results, obtained with different forcing amplitudes, can be compared each other. Moreover it is possible to keep a detailed record of all the external influencing parameters, such as temperature and humidity. Nevertheless EMA is expensive and time consuming, a proper actuator has to be placed on the structure and measurements cannot be taken continuously.

On the other hand, OMA does not keep the same control on the influencing parameters, as some of them are not even measurable. In this case the excitation input of the system is not known, only some assumption can be made and, sometimes, they are misleading [4] because it is due to sources such as traffic, wind, or people walking on the structure. However, this method is cheaper and easier to carry out. The only needs are a proper number of transducer placed on the structure and a continuous data acquisition system. By exploiting this set-up, a continuous monitoring of the modal parameters can be performed [3].

This paper deals with the comparison of the two above mentioned modal analysis methods applied to a real structure: the *Palazzo della Regione* helisurface, built in Milano. EMA and OMA techniques were applied to reconstruct the dynamic behavior in the range 0 – 10 Hz and the results will be compared in the following.

At first, a description of the structure is presented, then the chosen measurement setup is defined and justified. Finally, the obtained results are presented and discussed.

STRUCTURE

The considered helysurface with a circular layout is placed on the top of elevators and services group, called *core 4*, of the “*Altra Sede della Regione Lombardia*”. The structure is composed by a landing circular plane (34 m diameter), surrounded by a protection grid (2 m tall) along the perimeter. The access to the structure is possible by means of two metallic helicoidal stairs.



Figure 1 - Helysurface

The main structure is realized by sixteen double T beams (variable height from 130 cm to 40 cm) disposed in radial symmetry with a 22.5 degree angle among them. These beams are connected each other through secondary elements which realize concentric polygonal rings with wheelbase of about one meter.

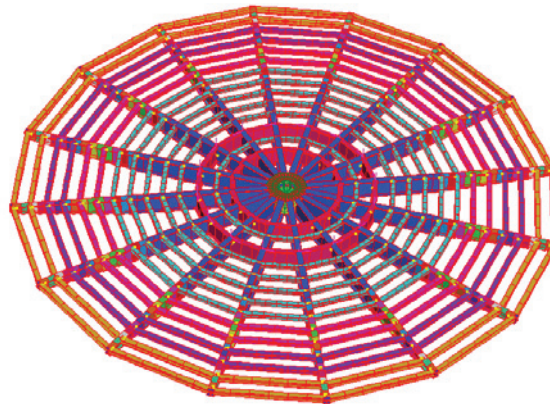


Figure 2 – beam structure of the helysurface

The deck is obtained with a 21 cm depth reinforced concrete slab. The radial beams are connected to the slab by mean of bolted joints. The structure supports are made of reinforced neoprene material, with a thickness of 47 mm. These support, thanks to their deformability, permit the thermal deformation of the structure minimizing the solicitations. Moreover, they represent a multidirectional joint for the horizontal solicitations. In the drawing of [Figure 2](#) the constraints are positioned in correspondence of the two inner violet circles. The seismic behavior of the helysurcafe is completely unrelated from the below building.

Due to the kind of adapted constraints both horizontal and vertical modes are considered of interest, and they have been analyzed. The experimental set-up is described in the next paragraph.

EXPERIMENTAL SETUP

This section describes the chosen measurements setup. The attention is focused on the transducer selection, based on their metrological performances, the data acquisition system and the instrumentation placement.

The sensors choice is a crucial task for a satisfying measurement campaign in terms of the quality of the acquired vibration signals. The sensors should be able to measure both low vibration levels, for example those due to environment excitation sources (wind, traffic, etc.), and higher levels, obtained by means of a forced excitation with a suitable actuator and in the case of a permanent monitoring by the operational loads on the structure (landing helicopter). This requirement

may be satisfied by transducers with a high sensitivity and consequently a low noise floor. Furthermore, the transducer bandwidth must guarantee the acquisition of the all frequencies of interest. The main natural frequencies of interest are limited to the range 0.5-10 Hz. Taking into account all the above statements, the piezo accelerometers PCB 393B12 were chosen, which are characterized by a 0.1 Hz – 500 Hz bandwidth, sensitivity 10 V/g and measurement range ± 0.5 g. All the sensors were conditioned and acquired by means of National Instruments device equipped with 24 bit acquisition modules with anti aliasing filter.

As explained in the introduction, the dynamic behavior was inspected both in horizontal and vertical directions. Moreover, the aim of this work is to compare the results obtained applying both experimental modal analysis (EMA) and operational modal analysis (OMA). The tests, consequently, were performed, both for horizontal and vertical direction, with environmental excitation sources and with a proper forced excitation source, as it will be explained in the following.

HORIZONTAL DIRECTION

Figure 3 shows the sensor placement, chosen for the horizontal direction. Assuming the helysurface as a planar circle, four measurement points were placed at half radius of the circumference (position from 1 to 4 in Figure 3). Every measurement point is composed by three accelerometers placed along the main directions: radial, tangential and vertical (red arrows in Figure 3). Although the forcing direction is in the horizontal plane, it is necessary to use vertical accelerometers, because the longitudinal excitation could generate rigid pitch motion of the structure around its support. This measurement set-up was chosen to detect the main vibration modes, conformingly with the results obtained from the computer simulation, and it is obviously the same for the EMA and OMA tests. The duration of OMA tests were about 48 hours to guarantee a sufficient amount of data and a robust estimation of the helysurface response spectral functions.

EMA tests have been carried out by forcing the structure with an inertial actuator. In this case, a linear permanent magnet motor was chosen. This was considered the best solution for exciting the structure as the long available stroke (1m) was enough to introduce a meaningful energy amount even at the lowest frequencies of interest (1 Hz). A stepped sine harmonic excitation, covering the band between 0.1 – 10 Hz, was used, imposing a frequency resolution of 0.05 Hz in correspondence of the resonances. Figure 3 shows the actuator placement at one-third of the radius of the helysurface (point 5 in Figure 3). In correspondence of the motor, three accelerometers were placed for measuring the vibrations introduced in the structure for the three main directions (radial, tangential and vertical). An accelerometer was also placed on the sliding mass in order to measure its acceleration and so the force transmitted to the structure.

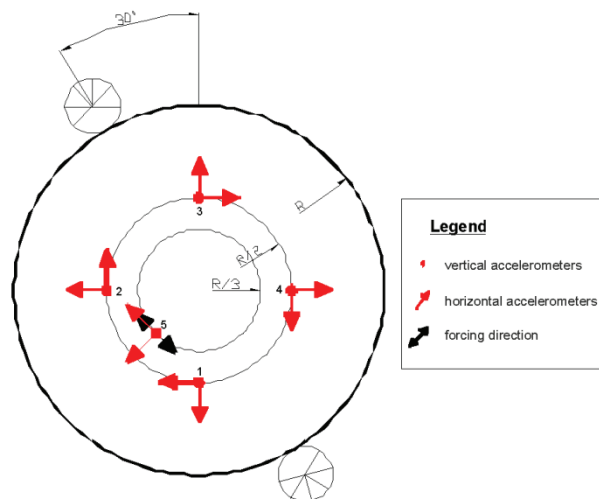


Figure 3 – Sensor placement for the horizontal direction

A sliding mass of 540 kg has been adopted during the tests, Figure 4 shows the actuator and the mass installed on the surface during the tests.



Figure 4 – Linear motor with slide and mass used as an actuator

The next section describes the set-up used for the vertical vibration measure the vertical vibrations.

VERTICAL DIRECTION

Figure 6 shows the sensor placement, chosen for the vertical direction. In this case, the number of the measurement point increases up to twelve. Every measurement point is composed only by one accelerometer placed along the vertical direction: seven accelerometers were located on the circumference (letter A in Figure 6), whereas five accelerometers were placed on one-third of the radius (letter B in Figure 6), inside the area of the constraints linking the platform to the main structure underneath. This measurement set-up was chosen to detect the main vibration modes, conformingly with the results obtained from the computer simulation, as in the case of horizontal tests. As for the horizontal direction, this measurement setup is the same for the EMA and OMA tests.



Figure 5 – hydraulic actuator and mass used

In this case an hydraulic actuator was placed in correspondence of point A3 and A6 of Figure 6 in order to perform EMA tests. The actuator moved an inertial mass of 120 Kg with a maximum oscillation amplitude of 50 mm. A stepped sine harmonic excitation, covering the band between 2 – 10 Hz, was used, imposing a frequency resolution of 0.05Hz in correspondence of the resonances. The need of two excitation points is given by the radial symmetry of the structure which requires more excitation positions to detect all the vibrations modes [9].

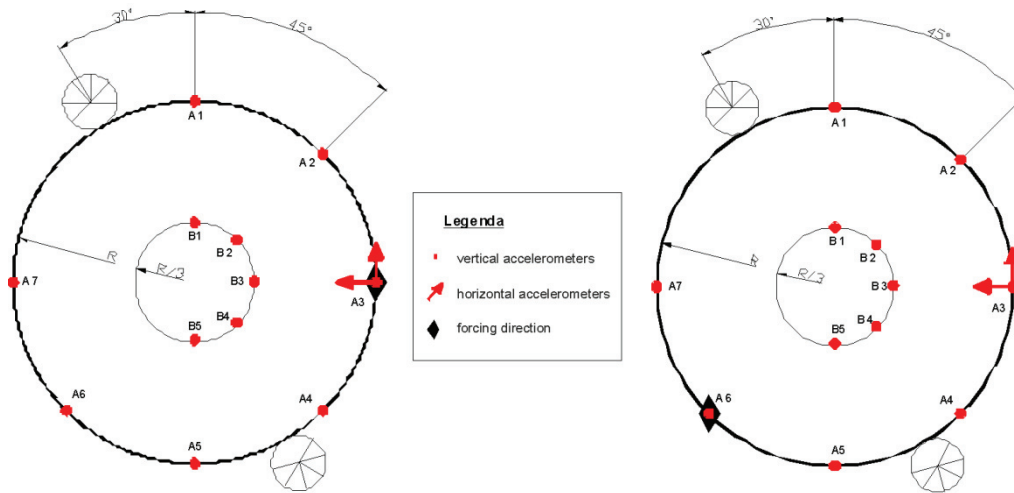


Figure 6 – Sensor placement for the vertical direction

In this case too 48h of ambient vibrations have been acquired and analyzed in order to perform modal identification applying OMA techniques.

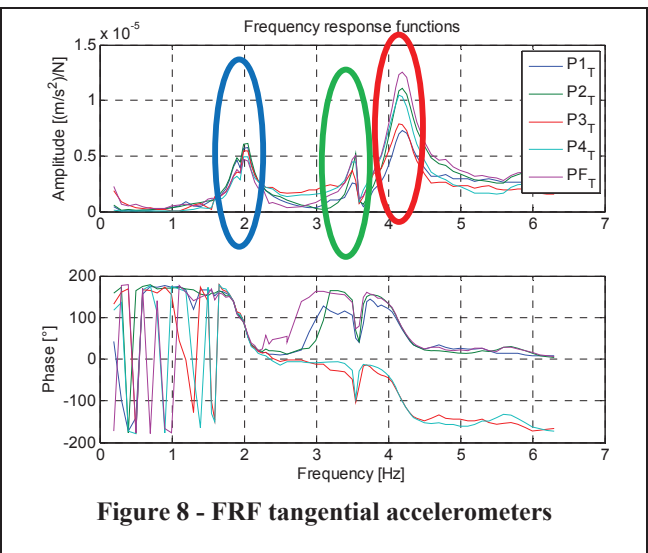
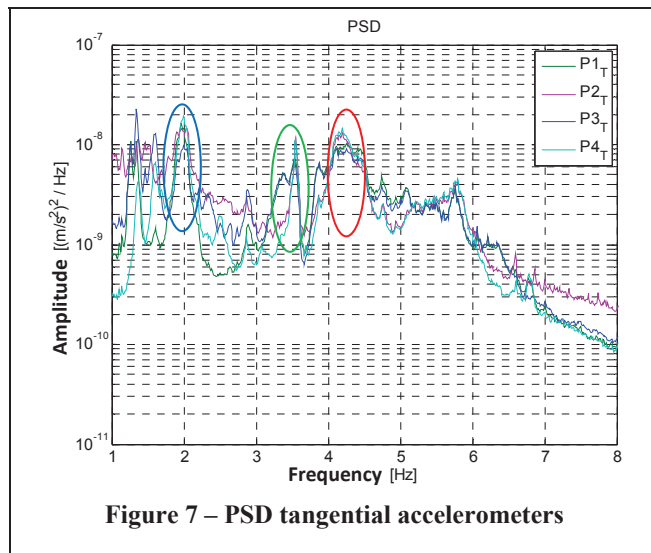
All the acquired data have been processed using the Polyreference least square frequency domain method suitable for both OMA and EMA approaches [7]. It must be noted that the input of this method is the frequency response function (FRF) of the system. In the case of OMA tests, the method cannot be applied in a strict way, because the loading is not measurable. Although, the same approach could be used if the loading is random and broad band enough. This algorithm is particularly suitable for highly damped structure, such as mixed concrete-steel ones. The obtained results are shown in the next section.

RESULTS

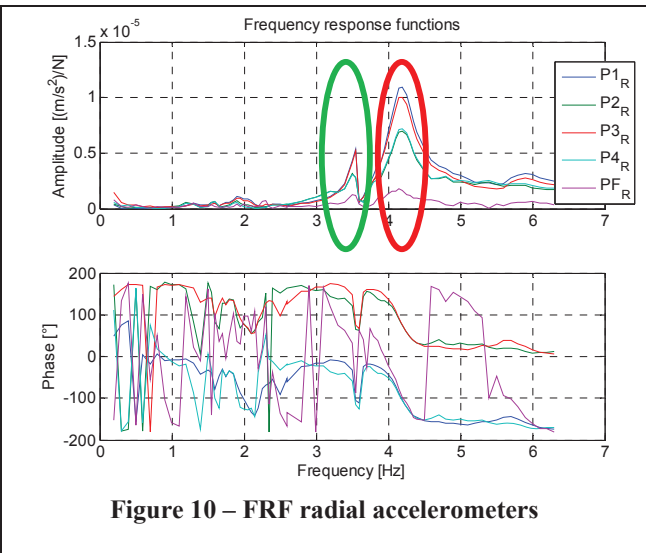
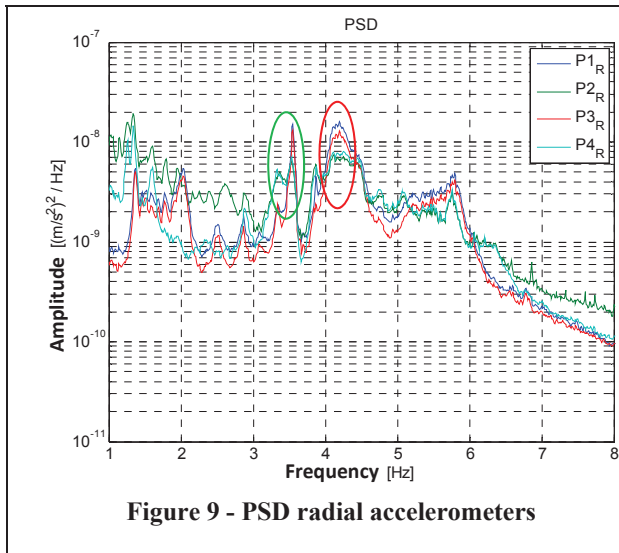
In this Section the results obtained from EMA and OMA are presented, both for horizontal and vertical directions. At first a visual comparison between the ambient vibration Power spectral density and the experimental transfer function is shown, then the identification results are compared. The first section describes the results coming from the horizontal measurement set-up.

HORIZONTAL DIRECTION

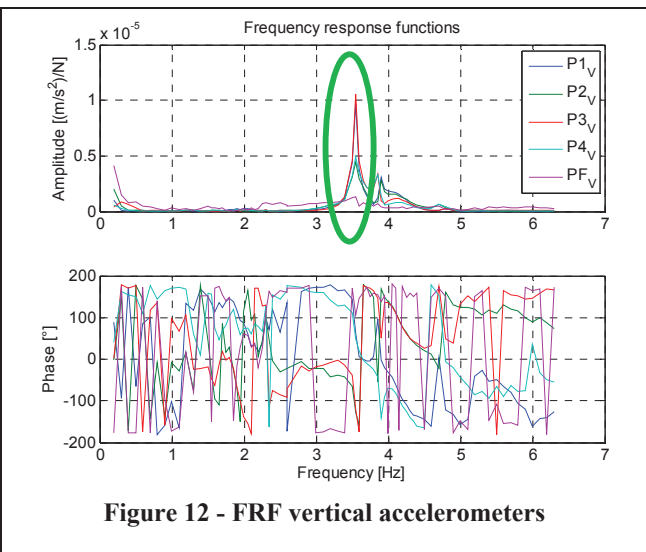
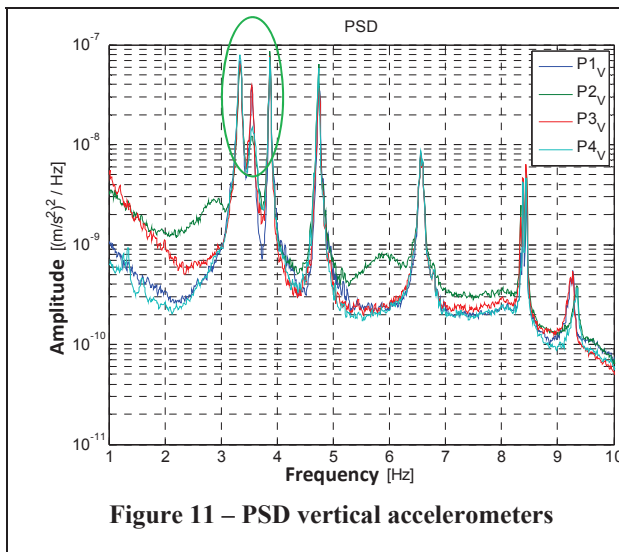
In this section the results coming from the horizontal measurement set-up are discussed. Figure 7 shows the estimated power spectral density (PSD) of the tangential accelerometers (refer to Figure 3 for the sensor position), three colored ellipses highlights the areas of main activity even if it is clear that no predominant peaks are present. Figure 8 shows the corresponding frequency response functions (FRF); three main peaks, circled with ellipses of the same colors used in Figure 7, are evidenced at frequencies that are compatible with the ones coming from operational data.



A similar situation is found looking at the Radial acceleration PSD's. The red and green ellipses in [Figure 9](#) highlight two areas of main activity, which are also found, as peaks, in the correspondent FRF's, see [Figure 10](#).



Things change if the vertical acceleration PSDs are considered. Looking at [Figure 11](#) it can be seen that many clear peaks are visible. Among those, the 3.5 Hz one is still present (green ellipse). The corresponding FRF practically shows only the peak around 3.5 Hz, see [Figure 12](#). This peak, as it will be better explained in the vertical results section, corresponds to a pitch motion along the forcing direction (mode with 1 nodal diameter).



Both data sets, Operational and Experimental, have been processed in order to estimate the modal parameters. [Table 1](#) shows a summary of the identified modes. A good agreement may be found in the frequency values, while damping values show higher discrepancies between operational and experimental analysis. The identified mode shapes are more or less the same, but it has to be noticed that the highest energy introduced during the EMA tests allow to obtain a better estimation of the modal residues. An example is mode 1, this is a rigid rotation of the disc around its axis, see [Figure 13](#). EMA results are clearer to interpret as the tangential measurement points are all with values around 1 and in phase; OMA results for the tangential directions are nearly the same but, if the other directions are observed, EMA gives a practically 0 value for all the residues, which is the correct value for this mode shape, while OMA has values higher than 0, probably due to the low vibration amplitudes. It has to be said that the residue values are normalized to the maximum of each eigenvector, and so, if the vibration amplitude is very low (nearly at the same level as measurement noise), there may be a little difference in the residue values between different points.

Mode	1 E	1 O	2 E	2 O	3 E	3 O
Freq. [Hz]	1.98	1.97	3.54	3.56	4.14	4.17
Damping [%rc]	5.26	4	0.7	1.2	3.81	3
	Modal residues					
P1_R	0.1	-0.5	0.6	0.55	-1.8	-1.1
P1_T	0.9	0.9	-0.3	0.45	1	1
P1_V	-0.1	0.2	-0.9	-1	-0.2	-0.5
P2_R	-0.1	0.6	-0.3	-0.45	1	0.8
P2_T	1	1	-0.5	-0.5	1.8	1
P2_V	0	-0.4	0.5	-0.75	0.2	0.6
P3_R	-0.1	0.5	-0.6	-0.5	1.6	1
P3_T	0.9	0.8	0.4	0.45	-1.2	-0.9
P3_V	0	-0.3	1	1	-0.2	0.5
P4_R	0.1	-0.3	0.3	0.45	-1.2	-0.9
P4_T	0.8	1	0.5	0.5	-1.6	-1
P4_V	0	0.2	-0.6	-0.8	0.2	-0.6
PF_R	0		-0.1		-0.4	
PF_T	0.7		-0.6		2	
PF_V	0		0.1		0	

Table 1 Identified frequencies, damping values and modal residues

The identified mode shapes for mode 1 and 3 are shown in [Figure 13](#) and [Figure 14](#). The first is the above mentioned rigid rotation around the central axis, while the second is a rigid translation of the disc in the excitation direction.

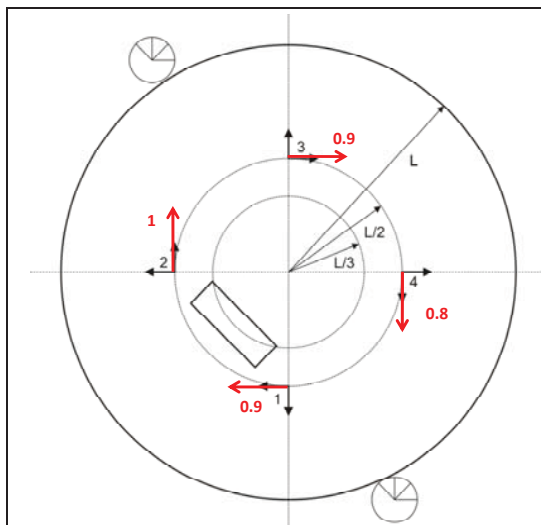


Figure 13 Mode shape for mode 1

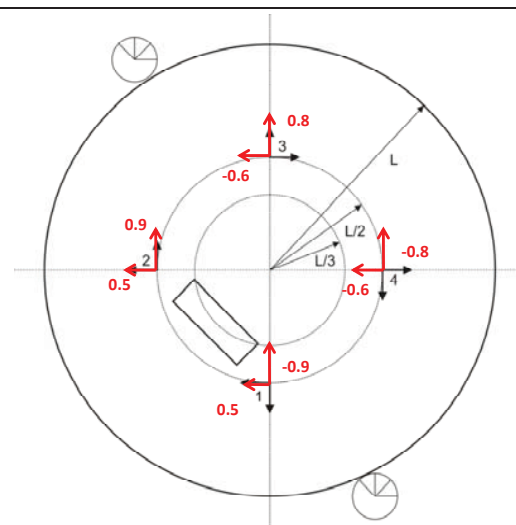


Figure 14 Mode shape for mode 3

Having analyzed the platform behavior in the horizontal direction, the next step is the vertical dynamics analysis.

VERTICAL DIRECTION

As previously stated, EMA tests in the vertical directions were repeated twice, changing the forcing point in order to identify all the “double” modes of this structure, which is practically axial symmetric. [Figure 15](#) and [Figure 16](#) show the PSD and FRF obtained for the vertical accelerations. At a first glance, it can be seen that the PSD obtained from the

vertical vibrations show a higher number of peaks in the same frequency range (red circles in Figure 15). These are probably due to harmonic excitation given by activities carried in the proximity of the helysurface that can be erroneously taken as vibration modes if only the operational data are considered[4].

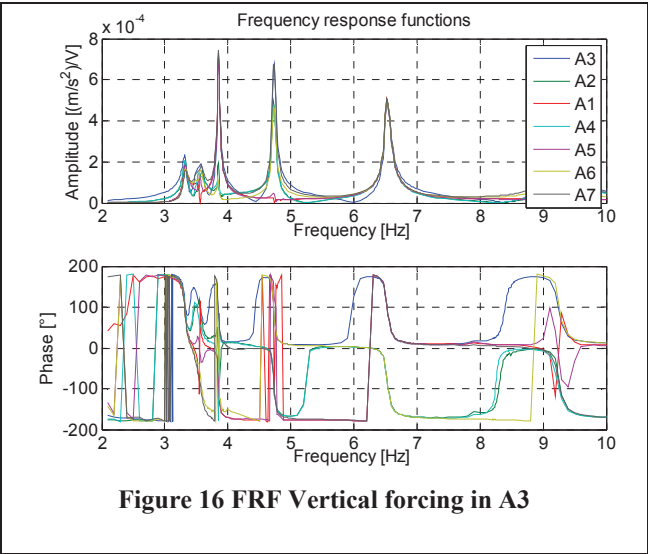
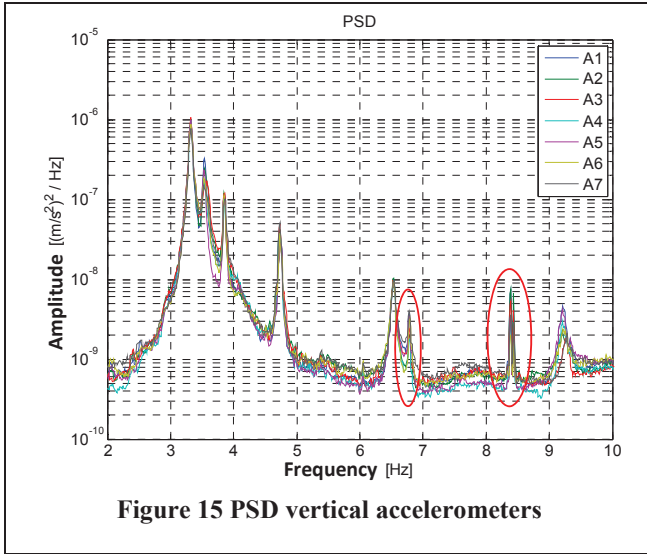
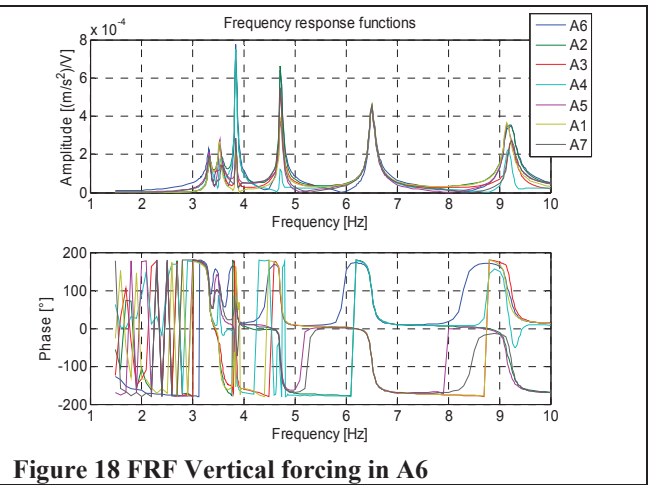
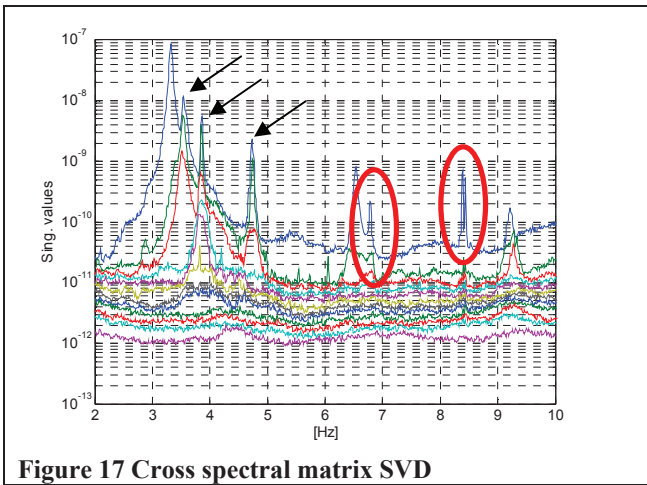


Figure 17 and Figure 18 show the singular value decomposition of the cross-spectral matrix, obtained from the ambient vibration data, and the frf response functions computed for the second forcing point. Looking at the singular values in Figure 17, it can be seen that the two peaks circled in red are still present, moreover a number of other peaks, indicated by a black arrow, are characterized by two singular values having a non neglectable amplitude. Even looking at these data, it is still easy to identify the spurious peaks (red circled) as structural modes [4]; the easiest way to discard these peaks is to look at the experimental data in which they totally disappear, see Figure 18. Nevertheless, the singular value decomposition applied to operational data clearly identifies the double modes in the structure. The same thing could be achieved in the forced tests, only by moving the excitation point as done in this case and then looking at the modal residues or applying the SVD to the forced response matrix [6] but this requires two different tests session and it is therefore time and money consuming.

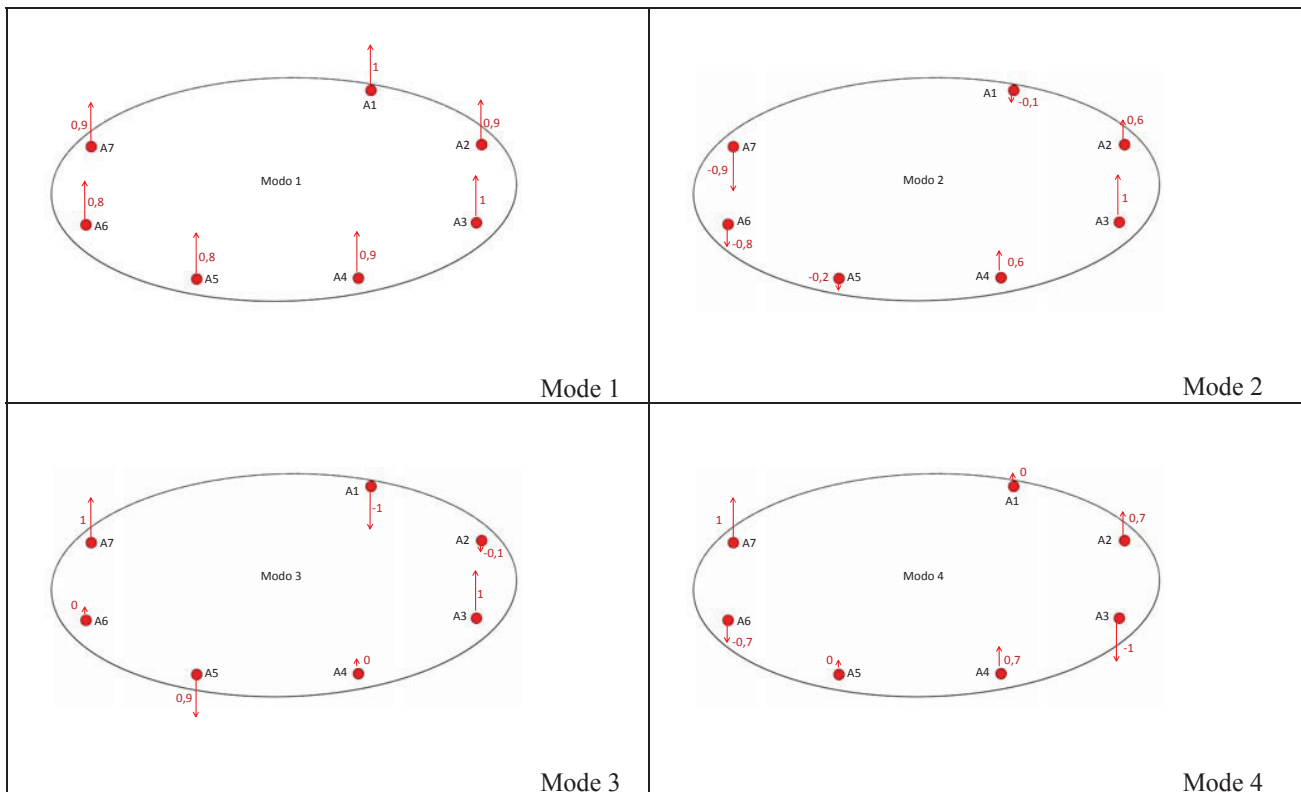


The Polyreference least square algorithm has been applied to the experimental data and a resume of the identified modes is given in Table 2 in terms of frequencies damping and modal residues.

Mode	1	2	3	4	5	6
Frequency [Hz]	3,32	3,56	3,85	4,73	6,53	9,25
Damping [r/rc] %	1,0	1,2	0,4	0,4	0,65	0,6
	Modal residues					
A1	1,0	-0,1	-1,0	0,0	-1,0	0,0
A2	0,9	0,6	-0,1	0,7	1,0	-0,7
A3	1,0	1,0	1,0	-1,0	-1,0	1,0
A4	0,9	0,6	0,0	0,7	1,0	-0,7
A5	0,8	-0,2	-0,9	0,0	-1,0	0,0
A6	0,8	-0,8	0,0	-0,7	1,0	0,7
A7	0,9	-0,9	1,0	1,0	-1,0	-1,0
B1	0,0	0,0	0,0	0,0	0,0	0,0
B2	0,0	0,0	0,0	0,0	0,0	0,0
B3	0,0	0,0	0,0	0,0	0,0	0,0
B4	0,0	0,0	0,0	0,0	0,0	0,0
B5	0,0	0,0	0,0	0,0	0,0	0,0
A3R	-0,1	-0,2	0,0	0,1	0,1	-0,1
A3T	0,0	0,0	0,0	0,0	0,0	0,0

Table 2 Modes identified in the vertical direction

The identified mode shapes are better understood, if their graphical representation is observed, see [Figure 19](#). In which the arrow represents the modal residue measured in each point and the number are the normalized residue amplitude (normalized to the maximum of each eigenvector).



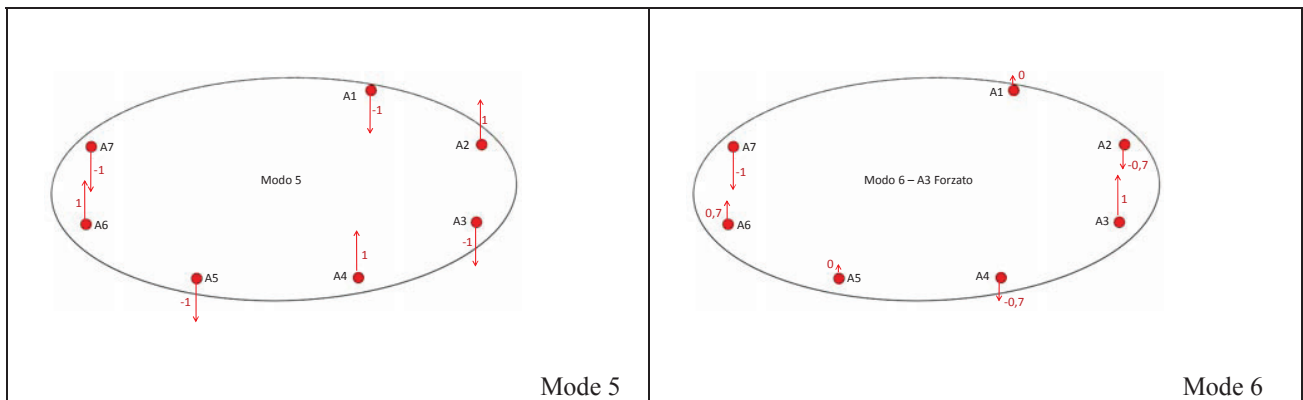


Figure 19 Identified mode shapes, forcing in A3

The same results, with the obvious phase shifts in the mode shapes, has been found for the second forcing point and similar results are obtained from operational data. In the latter case particular attention has to be paid to the double modes. In these cases a treating them as simple modes may lead to erroneous identification of the residue values. Table 3 shows the modal residues values identified for the first two modes for the three tests:

- EMA A3: Forced testing, forcing in A3
- EMA A6: Forced testing, forcing in A6
- OMA: ambient vibration testing

Looking at the results shown in Table 3 it can be seen that the agreement between the results is optimum for the first considered mode, a “single” mode; in this case frequency value are practically the same, damping is similar and the modal residue are the same, the MAC value is almost 100%. For mode 2 we have a little higher difference in the identified frequency and damping values; moreover the modal residues identified via EMA techniques, the ones identified by EMA A3 and EMA A6 in the table title line, refer to the same mode shapes (1 nodal diameter), shifted in space according to the forcing position. The modal residues identified via operational modal analysis, under the hypothesis that one mode is present, are misleading; values are similar in all points, while phases are sometimes 0 and sometimes 180°. In this case a deeper analysis has to be carried out taking into account the presence of two modes at approximately the same frequency.

Mode	1 EMA A3	1 EMA A6	1 OMA	2 EMA A3	2 EMA A6	2 OMA
Frequency [Hz]	3,32	3,33	3,32	3,56	3,53	3,54
Damping [r/rc] %	1,0	0,9	1	1,2	0,9	0,9
Modal residues						
A1	1,0	0,9	1	-0,1	0,9	1
A2	0,9	0,9	1	0,6	1,0	0,9
A3	1,0	0,9	1,1	1,0	0,6	0,8
A4	0,9	0,9	1	0,6	0,3	-0,7
A5	0,8	1,0	1	-0,2	-1,0	-0,8
A6	0,8	1,0	1	-0,8	-1,0	-0,8
A7	0,9	0,9	0,9	-0,9	-0,4	0,8

Table 3 Comparison between the first two identified modes, three different tests

Finally a little more can be said about the peaks appearing in the ambient vibrations and not corresponding to any evident structural mode. Figure 20 shows the time-frequency transform of a vertical acceleration during a 17h period. In the diagram on the x-axis is time, on the y-axis are the frequencies and the colors are proportional to acceleration amplitude.

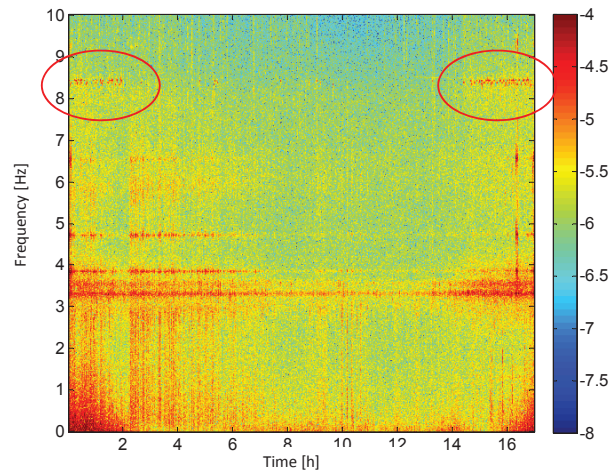


Figure 20 Time frequency diagram of a vertical acceleration during 17 h

The two circled area in [Figure 20](#) are in correspondence of the peaks around 8.2 Hz. As it can be seen, they are not continuously present in the diagram, appearing only at the beginning and at the end of it. On the other hand, in correspondence of the main structural resonances continuous line of high amplitudes are present through all the diagram. This diagram pushes toward the conclusion the frequencies around 8.2 Hz are not coming from any resonance, but they are produced from some kind of forcing, appearing or disappearing depending on the time of the day.

CONCLUSION

In this paper the problem of investigating the main vibration modes of the helicopter landing surface of the “Nuova sede Regione Lombardia” building has been faced. Two different kind of testing have been adopted, one exploiting experimental modal analysis techniques, and therefore applying a known loading to the structure; and the other exploiting natural ambient vibrations and Operational Modal Analysis techniques. Tests have been carried out in both horizontal and vertical directions. The main structural modes have been clearly identified and a comparison between experimental and Operational results has been shown. It has been highlighted that EMA results are sometimes useful to fully understand the Operational analysis one, while the latter techniques offer the possibility to perform a fast and reliable analysis without the need of an applied external load and it is therefore suitable for the long term monitoring of the structure.

REFERENCES

- [1] “Numerical modelling and experimental modal analysis of a concrete grand-stand structure to structural health monitoring purposes”, IMAC XXVI, Feb 4-7, 2008, Orlando, Florida.
- [2] “Long term monitoring of the G. meazza stadium in Milan, from the first measurements to the permanent monitoring system installation”, Eurodyn 2008, 7-9 Luglio, Southampton, UK.
- [3] “Vibration Testing at Meazza Stadium: Reliability of Operational Modal Analysis to Health Monitoring Purposes”, *J. Performance of Constructed Facilities*, 22, 228 (2008), ASCE: American Society of Civil Engineers - ISSN: 08873828
- [4] Mohanty, P., and Rixen, D. J. (2004). "Operational modal analysis in the presence of harmonic excitation" *J. of Sound and Vibration*, 270(1-2), 93-109.
- [5] Farrar, C. R. (1997). "System identification from ambient vibration measurements on a bridge" *J. of Sound and Vibration*, 205(1), 1-18, 1997
- [6] Modal Testing: Theory and Practice (Engineering Dynamics), Dj Ewins.
- [7] The PolyMAX frequency-domain method: a new standard for modal parameter estimation?, *Shock and Vibration*, Publisher IOS Press, ISSN 1070-9622 (Print) 1875-9203 (Online), Issue Volume 11, Numbers 3-4/2004
- [8] Cornwell, P. J., Farrar, C. R., Doebling, S. W., and Sohn, H. (1999). "Environmental Variability of Modal Properties" *Experimental Techniques*, Nov/dec, 45-48.
- [9] “Vibro-acoustic characterization of railway wheels”, *Applied Acoustics* ISSN: 0003682X, Volume: 69, Issue: 6, June, 2008, pp. 530-545

Human-Structure Interaction: Effects of Crowd Characteristics

Kelly A. Salyards¹, Robert J. Firman III²

¹Assistant Professor, Department of Civil and Environmental Engineering;

²Undergraduate Research Student, Department of Civil and Environmental Engineering

Bucknell University
Lewisburg, PA 17837

ABSTRACT

Design for vibration serviceability currently relies almost entirely on the estimation of dynamic properties of the empty structure to be utilized for estimating the dynamic response or, at minimum, to avoid resonance with the excitation. However, the use of the empty structure properties has been questioned due to a phenomenon referred to as human-structure interaction where the dynamic properties of the occupied structure can be significantly different from the properties of the empty structure. General trends include an increase in damping ratio and a decrease in natural frequency (although special cases of increasing frequency or new modes have been documented). These trends seem to be affected by the posture of the crowd occupying the structure, and potentially other crowd characteristics. This study aims to isolate several crowd characteristics including posture, distribution, and crowd size, to determine the relative effect that each has on the overall dynamic properties of the occupied test structure.

INTRODUCTION

Dynamic occupant-induced excitation in structures where large groups may gather, such as stadium structures, has become a notable serviceability design consideration for several reasons. Crowd activity is arguably livelier than in the past and it is more likely that synchronized crowd activity is encouraged by facility managers. The flexibility of these types of structures is increasing as more efficient design methods and higher strength materials are utilized to provide more unobstructed views. This increase in flexibility tends to decrease the natural frequency of the structure, potentially into the range where resonance or near resonance conditions with the crowd-induced excitation may occur. This type of serviceability issue is concerning because the potential for panic within the crowd exists and may impinge on the safety of the occupants.

In addition to the increased crowd activity and decreased natural frequency, monitoring of several occupied structures has suggested that another phenomenon, human-structure interaction, also impacts the behavior of the structure. It is hypothesized the human occupants of the structure act as a dynamic system that interacts with the dynamic system of the supporting structure. The result of this interaction is not fully understood but several studies suggest that the natural frequency of the combined system can be significantly different from that of the empty structure. Until this impact on natural frequency is fully understood and incorporated into design procedures, it is possible that a serviceability concern may arise in a structure that is designed considering only the natural frequency of the empty structure, as current guidance recommends.

BACKGROUND

Human-structure interaction in civil structures

To understand how the human dynamic system interacts with the structural system, it is valuable to understand how the human body is considered and modeled in other industries. A substantial amount of research has been conducted in the area of biomechanics for the aerospace and transportation industries considering large magnitude vibrations and a single individual. Although vibration serviceability in civil structures is concerned with small magnitude vibrations and a crowd of individuals, it is believed that some of the basic results may still be applicable. From these studies, various models of the human body have been proposed and the average natural frequency of the human body in the vertical direction has been determined to be between 4-6 Hz depending on the individual's age, gender, body type and posture [1]. This range contributes to the complexity of crowd dynamics and the human-structure interaction phenomenon.

Human-structure interaction occurs due to the contact between the occupants and the structure. This contact is not maintained when the crowd is active and jumping, so it is only the portion of the crowd that is passive or in contact with the structure that interacts with the structure. This study focuses on how the passive occupants of a crowd interact with the structure before exploring the more realistic combined components of an active and passive crowd.

The effects of human-structure interaction in civil engineering structures are believed to be most prevalent where crowds can occupy long, unsupported spans constructed with lightweight materials. These types of structures are likely to have natural frequencies within the range of 2-6 Hz [2], which corresponds to both the frequency over which occupants are able to excite a structure and to the frequency range over which humans are most sensitive to vibration.

Relevant dynamic studies

The first mention of human-structure interaction appeared in a research study conducted by Lenzen [3] in 1966 which compared the response of a structure when a simple mass is applied to the response of the structure when humans occupy the structure. The system damping increased for the human occupants generating the first acknowledgment of human-structure interaction.

In the 1990's, the monitoring of Twickenham Stadium revealed a decrease of 3 Hz in the natural frequency of the empty structure when it was occupied. In addition, another mode of vibration appeared with a natural frequency slightly higher than that of the empty structure [4]. This discovery prompted several laboratory experiments by Ellis and Ji [4], Brownjohn [5], Falati [6] and Hothan [7]. The laboratory tests investigated small-scale structures occupied by only one or two occupants. Equivalent mass tests were performed in each study confirming Lenzen's original observation. From these studies, it was observed that the effects of human-structure interaction are dependent on several factors including the natural frequency of the empty structure, the mass ratio of the occupants to the empty structure, and the occupant posture.

Existing guidance

Current guidance for incorporating dynamic excitation due to crowds into the structural design is generally limited to addressing the strength limit states and avoidance of a structural failure. For serviceability design in the United States, the most widely recognized source of guidance exists within Chapter 5 of AISC's Design Guide 11: Floor Vibrations Due to Human Activity [8]. A natural frequency-based design criterion, utilizing the natural frequency of the empty structure, is presented to limit the acceleration response of the structure to dynamic excitation. Human-structure interaction is not mentioned. Similar guidance exists in the United Kingdom through interim guidance titled "Dynamic Performance Requirements for Permanent Grandstands Subject to Crowd Action". A natural frequency-based limit is presented to establish when vibration serviceability should be considered in design and it is recommended that the natural frequency of the empty structure be utilized for this assessment. No mention of human-structure interaction is included. Several general recommendations have been made to consider the occupants as a single or multiple-degree-of-freedom systems attached to the structure [9]. Yet, despite research in the area, appropriate models are not available.

OVERVIEW OF STUDY

This study investigates human-structure interaction through an examination of the relationships between the dynamic properties of an occupied structure the dynamic properties of the empty structure with respect to varying crowd characteristics. The crowd characteristics under consideration in this study include the crowd distribution, the mass ratio of the occupants to the structure, and the stationary posture of the crowd.

The experimental investigation was performed on an open-web steel joist supported floor test structure that was specifically designed for studying vibration serviceability issues [10]. Experimental modal analysis techniques were utilized to estimate the dynamic properties of the empty structure and the dynamic properties of the structure when occupied by crowds of various sizes, prescribed densities, and postures. The results were examined for trends and relationships between the occupied natural frequencies and damping ratios for configurations involving the three variables listed above with respect to a single structural empty natural frequency.

EXPERIMENTAL METHODS

Test Structure, Equipment, and Study Participants

The test structure selected for this study is a non-composite concrete slab on open-web steel joists with overall dimensions of 27 feet by 11 feet as shown in [Figure 1](#). The structure is constructed with five equally spaced 14K4 joists spanning 26 feet. The joists are supported by W8x13 beams which span 10 feet between short pipe columns as shown in [Figure 1](#). A six inch overhang exists along the perimeter of the floor area. The steel joists support a 2.5 inch normal-weight concrete slab on 1 inch form deck. The natural frequency of the empty structure is estimated to be 6.82 Hz using AISC's Design Guide 11 methods.

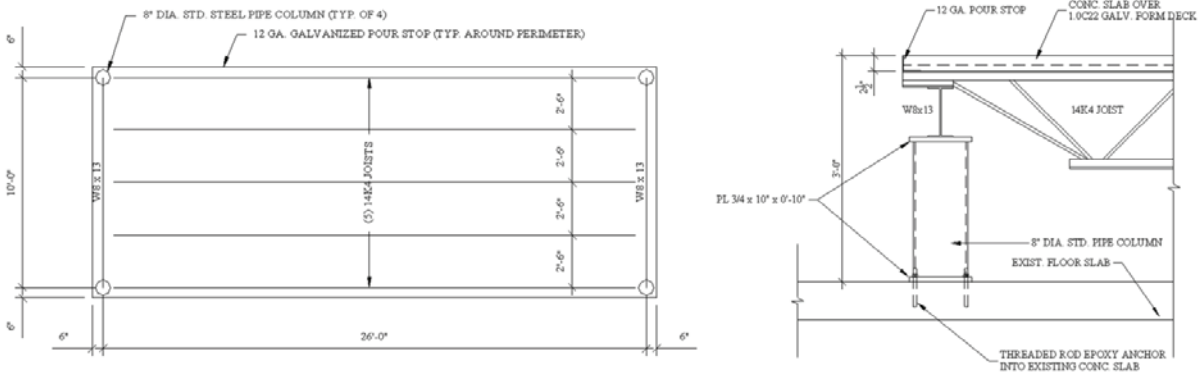


Figure 1: Plan and section view of test structure (from Raebel [10])

The experimental testing of both the empty and occupied structure in this study involved the controlled excitation and measurement of the acceleration response of the structure. The structure was excited by an electrodynamic shaker (APS Dynamics model 400) with a swept-sine forcing function and the applied load was measured by a custom force plate summing four shear beam load cells. The acceleration response of the structure was measured using seismic accelerometers (PCB model 383A03). The IOTech Wavebook 516/E with two eight-channel dynamic signal conditioning modules (WBK18) enabled the simultaneous collection of fifteen channels of acceleration and one channel of the applied loading function.

A real-time vibration analysis software package, eZ-Analyst, was utilized for generation of the swept-sine function and real-time frequency domain analysis of the structural response. The subsequent estimation of modal parameters, including natural frequencies, damping ratios, and mode shapes associated with each experimental test, was performed with Vibrant Technology's ME'scope VES software.

Previous laboratory studies investigating human-structure interaction involved small groups of occupants, typically only 1-4 people. This study utilizes a larger test structure which facilitates larger crowd sizes, up to 19 occupants, for each testing scenario. A total of 33 different participants volunteered for the experimental testing, five female and twenty-eight male subjects. The average age of all participants was twenty three. Each participant was presented with a brief overview of the research project and the overall testing procedure in accordance with the research protocol approved by the Institutional Review Board (IRB) for research involving human subjects.

Characteristics of the Crowd Considered

The three characteristics of the crowd that are considered in this study are the crowd distribution, the mass ratio of the occupants to the structure, and the stationary posture of the crowd. For the single test structure, the first crowd characteristic considered is the distribution of the crowd. For each crowd size, the crowd was positioned at two distributions, both centered on the middle of the floor. The first distribution is considered sparse and each occupant is located on a 28 inch grid with approximately 5.4 ft² of floor area per person. The second distribution is considered dense and each occupant is located on a 20 inch grid with approximately 2.8 ft² per person. With the first distribution, the live load is approximately 65 psf as compared to 33 psf for the second distribution. Both crowd distributions are less dense than the design load of 100 psf required for assembly structures such as stadium grandstands. A denser crowd distribution was not utilized to ensure safe loading of the test structure and to assure participant comfort.

The second crowd characteristic considered in this study was the mass ratio of the occupants to the structure. This was considered through the use of several crowd sizes. The desired mass ratios for this study were in the range of 0.25 to 0.75 to replicate typical mass ratios for stadium structures at full capacity [11]. Mass ratios from 0.02 to 0.43 were achieved with the structure occupied by 1, 4, 8, 16, and 19 people. Mass ratios greater than 0.43 were not feasible based on the maximum loading deemed safe for the floor structure. For each of the lowest three mass ratios, an equivalent mass was applied to the structure for comparison purposes.

The third crowd characteristic included in this study is the occupant's posture. Because human-structure interaction is only affected by the passive occupants of the crowd who are in contact with the structure, three postures were chosen to represent the range of postures possible. The three postures are illustrated in Figure 2. The first is a standing posture where the occupants are standing upright with their hands directly at the side of their body. The second is a standing posture with the occupants' knees bent which is intended to embody the effect that a bobbing crowd would have on the structure with respect to human-structure interaction. The third is a seated posture with the occupants knees forming a

90-degree angle and their feet planted flat on the ground and hands on their thighs. The seated posture utilizes wooden benches not permanently attached to the structure chosen for their portability and relatively lightweight nature.



Figure 2: Examples of postures used for experimental testing:
a. straight knees (posture a) b. bent knees (posture b) c. seated (posture c)

Experimental Procedure and Test Scenarios

Acceleration measurements were recorded at fourteen locations as shown in Figure 3 on a grid established by previous testing and modeling of the floor structure [10]. The shaker was located near the center of the floor but off the nodal lines expected for the three modes with lowest natural frequencies.

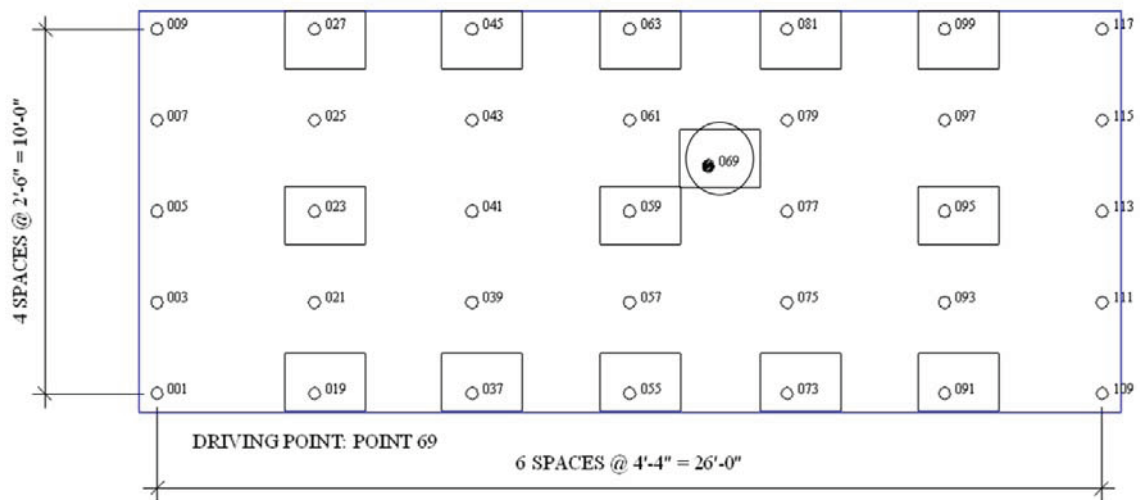


Figure 3: Test grid (accelerometer locations are boxed, shaker location is circled)

The experimental testing was carried out over four testing days to limit the time obligations of the volunteer participants. Initial tests of the empty structure were performed prior to testing on each day to establish a consistent baseline for comparison. For each crowd size and corresponding mass ratio, the participants were situated in both the sparse and dense distribution arrangements demonstrating each of the three postures. For each combination of crowd characteristics, the combined human-structure system was excited by an electrodynamic shaker and the acceleration response was measured.

Each test result is the average of 5 repeated measurements recorded over 8 seconds corresponding to the length of the swept-sine excitation signal for a frequency range of 0 to 50 Hz. The real-time frequency analysis capability of the eZ-Analyst software allowed for the examination of the coherence function between the five consecutive measurements and exclusion of flawed data. This is of particular importance when the structure is occupied because movement amongst the occupants will affect the quality of the resulting measurements.

RESULTS AND DISCUSSION

Empty Structure

The experimental testing of the empty structure generated the frequency response function (FRF) shown in Figure 4. The coherence function was greater than 0.95 for all frequencies above 5 Hz except at the frequency around 13 Hz corresponding to anti-resonance point. Utilizing the ME'scope software, the first mode identified at 6.7 Hz, is dominated by the first bending mode of the joists. The second mode identified at 8.2 Hz is a torsional mode and the third mode identified at 18.4 Hz is dominated by the second bending mode of the joists. This study focuses on the natural frequency associated with the first mode and how it is affected by the human-structure interaction. Effects of human-structure interaction on the second and higher modes were monitored but the effects were less pronounced and the uncertainty associated with the frequency estimation is greater, so these results are not presented herein.

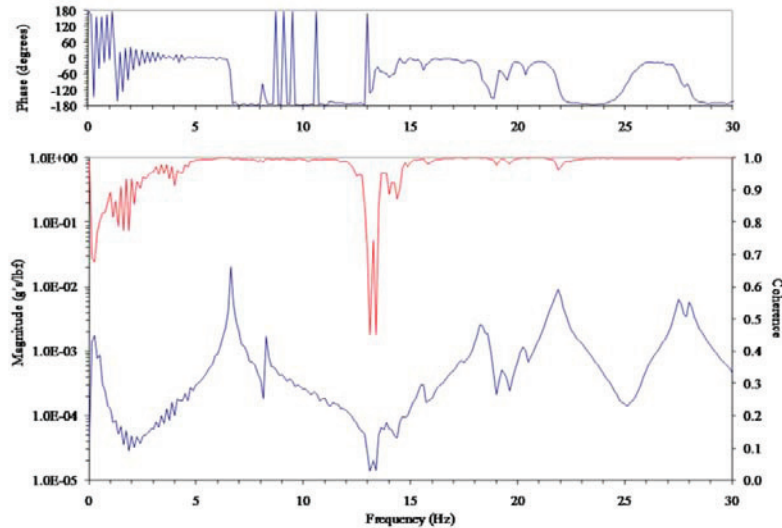


Figure 4: Driving point FRF for empty structure test

Equivalent Mass

For the smallest three crowd sizes of one, four, and eight people, corresponding to mass ratios of 0.02, 0.08, and 0.16, an equivalent mass was applied to the structure. The results, shown in Table 1, provide a baseline for the comparison of the effects due to human-structure interaction. These results were also confirmed with an analytical model of the floor system with a variety of applied masses.

Table 1: Frequency (Hz) of the first mode for dense configuration of varying crowd size and posture

Empty Structure	6.7 Hz				
	Crowd size (mass ratio)				
	1	4	8	20	24
	(0.02)	(0.08)	(0.16)	(0.33)	(0.43)
Equivalent mass	6.50	6.22	5.86	-	-
Standing (straight knees)	6.61	6.61	5.60	4.92	4.46
Standing (bent knees)	6.64	6.63	6.68	6.78	6.75
Seated	6.64	6.67	6.75	4.99	4.66

Varying Crowd Distribution

The natural frequency of the first mode of the occupied floor structure for both the sparse and dense crowd distribution was similar for the test scenarios involving the same crowd size and posture. The variation was minimal and was not consistent for a single posture or a single mass ratio, despite the fact that the dense distribution of occupants generated a distributed load approximately double that of the sparse distribution. The configuration of the occupants in both distributions was rectangular matching the aspect ratio of the floor and both were centered at the middle of the structure. It is possible that the effect of crowd density on human-structure interaction is not significant or that it is not apparent at these small crowd sizes. This variable will be excluded from the remaining discussions and the results relating to the dense configuration will be the focus.

Varying Mass Ratio

The crowd size and corresponding mass ratio will be considered with respect to each posture investigated. For the standing crowd with straight legs, the natural frequency of the system decreased from 6.7 Hz of the empty structure to 4.55 Hz when occupied by a crowd of 24 (mass ratio = 0.43). A decrease in natural frequency is expected as additional mass is added to the system; however, the magnitude of the decrease is not consistent with the equivalent mass model as shown in Figure 5. The effect of an equivalent mass applied to the structure on the natural frequency generated from an analytical model correlates well with the three experimental data points from the equivalent mass tests. This suggests that the effect of human-structure interaction on the natural frequency of the system is dependent on crowd size (or mass ratio). When the structure is occupied by the seated crowd, the change in natural frequency again does not follow the equivalent mass trend line, but the change in frequency is different from that generated by the standing crowd. This suggests that human-structure interaction is dependent on both crowd size and posture.

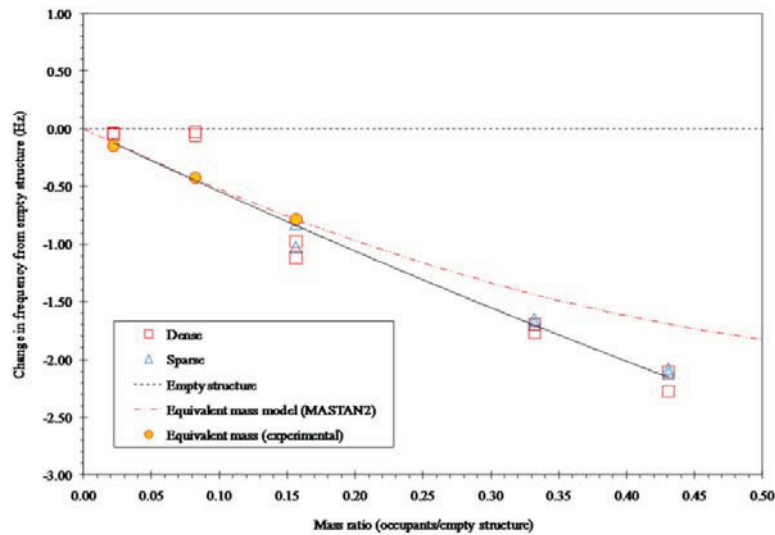


Figure 5: Experimental results for the change in frequency of the first mode when occupied by a crowd standing with knees straight

In addition to the change in frequency, human-structure interaction is also credited with an increase in damping. Because the damping ratio is difficult to accurately identify from experimental measurements, the trends will be the focus of this discussion. The damping ratio of the empty structure and the structure with the equivalent mass applied is approximately 0.5%. The damping ratio generally increases with any human occupants, but the magnitude of the increase is affected by both crowd size and posture as shown in Table 2. Within the scope of this study, it appears that once a critical mass of occupants or mass ratio is achieved, the damping ratio does not continue to increase significantly with increased crowd size. For such a lightly damped empty structure, the change in damping from the empty to occupied structure is noteworthy and would have a great impact on the response of a structure subjected to dynamic loading.

Table 2: Damping (% critical) of the first mode for dense configuration of varying crowd size and posture

Empty Structure	0.49% critical				
	Crowd size (mass ratio)				
	1	4	8	20	24
	(0.02)	(0.08)	(0.16)	(0.33)	(0.43)
Equivalent mass	0.51	0.40	0.24	-	-
Standing (straight knees)	2.59	11.35	12.60	11.20	13.15
Standing (bent knees)	0.74	2.44	4.04	5.59	2.18
Seated	2.19	7.76	12.95	16.40	9.33

Varying Crowd Posture

The third crowd characteristic investigated in this study is the occupant posture and it has a direct influence on the effects of human-structure interaction. The change in frequency due to a crowd standing with knees straight most closely emu-

lates the theoretical change in frequency due to an equivalent mass. However, the decrease in frequency for the human-structure system is more significant than the equivalent mass as the crowd size increases as shown in [Figure 5](#).

For the crowd standing with knees bent, the change in natural frequency was minimal. Unlike the other two postures, when the crowd stood with their knees bent, the natural frequency originally decreased with the first occupant but then increased slightly as the crowd size increased. The average natural frequency with this posture over the various group sizes was the same as the empty structure, 6.7 Hz. Small crowd sizes generated a small decrease in natural frequency and larger crowds generated a slight increase.

For the seated crowd, the change in natural frequency was not consistent. For one, four, and eight occupants, the frequency shifted only slightly. When twenty or twenty-four occupants were seated, the frequency decreased significantly – even greater than the decrease expected from an equivalent mass.

The effect of human-structure interaction on the damping of the system was also dependent on the posture. For occupants standing with knees straight, the increase in damping was fairly consistent for all crowd sizes to a level of around 12% damping. When the occupants' knees were bent, the increase in damping was considerably less – only increased to about 4%. When the occupants were seated, there was more variation in the increase in damping with the crowd size, but an average damping ratio was around 12%.

SUMMARY AND CONCLUSIONS

Previous studies in human-structure interaction have suggested that various crowd characteristics affect the interaction but this study isolates three of those characteristics to identify the effect that each has on the dynamic properties of the structural system. This study also provides experimental results that confirm the behavior of the structural system with an equivalent mass applied. Three different equivalent masses were applied to the structure and these three data points align well with the theoretical curve representing the expected change in natural frequency.

Previous studies involving in-service events have been valuable in that they have provided evidence from in-service events of human-structure interaction. However, these studies are often limited to single data points representing a single crowd size and unspecified postures. This study was able to control these aspects and provide experimental results across the range associated with each of these characteristics. It was determined that the two distributions included in this study, sparse and dense, did not impact the effect of human-structure interaction on the dynamic properties of the system. The results from the investigation of the other two variables in the study, crowd size and posture, indicated that each has an apparent impact on human-structure interaction.

An increasing crowd size and its corresponding mass ratio are linked to a decrease in the natural frequency of the structure and an increase in the system's damping ratio. The decrease in natural frequency exceeds the expected decrease in natural frequency of an equivalent mass system and the damping increases significantly. An increase in frequency, as was the case in a previous laboratory study [4], was not encountered in the scope of this study.

The effect of posture on human-structure interaction is revealed through an examination of standing with knees straight, standing with knees bent, and seated postures. The most significant change in natural frequency occurred with the standing with knees straight posture. The seated posture also induced a notable decrease in the natural frequency while the standing with knees bent posture had minimal impact on the natural frequency. The damping of the system was approximately 20 times greater for standing with knees straight and seated postures with a less significant increase in damping for the standing with knees bent posture.

These results provide experimental data points confirming the effects of human-structure interaction and emphasizing the need for continued investigation. The results reveal the potentially significant effects that human-structure interaction can have on the dynamic properties and consequently the dynamic response of a system. For these reasons, it is critical that these effects be acknowledged in future design guidance for vibration serviceability so that the dynamic response of a structure can be appropriately predicted.

ACKNOWLEDGEMENTS

The authors would like to thank Dr. Linda Hanagan of Penn State University for allowing the use of the test structure for this study. The authors are also grateful for the time and participation of the numerous volunteers involved in this study.

REFERENCES

1. Wasserman, D.E. and Wasserman, J.M. "The Nuts and Bolts of Human Exposure to Vibration." *Sound and Vibration* 36 (2002): 40-41.

2. Harrison, R.E., Yao, S., Wright, J.R., Pavic, A., and Reynolds, P. "Human Jumping and Bobbing Forces on Flexible Structures: Effect of Structural Properties." *Journal of Engineering Mechanics* (2008): 663-75.
3. Lenzen, K.H. "Vibration of Steel Joist-concrete Slab Floors." *American Institute of Steel Construction (AISC) Engineering Journal* 6th ser. 3.133 (1966).
4. Ellis, B.R., and T. Ji. *Human-structure Interaction in Vertical Vibrations*. Proc. of ICE: Structures and Buildings. Vol. 122, No.1. (1997): 1-9.
5. Brownjohn, J.M.W. *Energy Dissipation in One-way Slabs with Human Participation*. Proc. of Asia-Pacific Vibration Conference 1999, Nanyang Technological University, Singapore. Vol. 1. (1999).
6. Falati, S. "The Contribution of Non-structural Components to the Overall Dynamic Behavior of Concrete Floor Slabs." Thesis. University of Oxford, (1999).
7. Hothan, S. "Einfluß Der Verkehrslast - Mensch - Auf Das Eigen-schwingungsverhalten Von Fußgängerbrücken und Die Auslegung Linearer Tilger." Thesis. University of Hannover, (1999).
8. Murray, T.M., D.E. Allen, and E.E. Ungar. *Floor Vibrations Due to Human Activity*. American Institute of Steel Construction (AISC), Steel Design Guide Series, No.11 (1997).
9. Sachse, R., A. Pavic, and P. Reynolds. "Human-Structure Dynamic Interaction in Civil Engineering Dynamics." *The Shock and Vibration Digest* 35 (2003): 3-18.
10. Raebel, Christopher H. "Development of an Experimental Protocol for Floor Vibration Assessment." Thesis. The Pennsylvania State University, (2000).
11. Dougill, J.W. *Recommendations for Design of Grandstands Subject to Dynamic Crowd Excitation*. Proc. of 6th European Conf. on Structural Dynamics (EURODYN 2005). Munich, Germany: European Association for Structural Dynamics (EASD), (2005): 491-96.

Delamination Detection in Concrete Plates using Output-only Vibration Measurements

Shutao Xing

Department of Civil and Environmental Engineering, Utah State University, Logan, UT, 84322-4110

Marvin W. Halling

Department of Civil and Environmental Engineering, Utah State University, Logan, UT, 84322-4110

Paul J. Barr

Department of Civil and Environmental Engineering, Utah State University, Logan, UT, 84322-4110

Abstract

This paper addresses delamination detection of concrete slabs by analyzing vibration data from dynamic tests. Four concrete decks with different delamination sizes were constructed and experimental tests were conducted on these concrete slabs. Traditional peak-picking (PP), frequency domain decomposition (FDD) and stochastic subspace identification (SSI) methods were applied in the modal identification from real measurements of dynamic velocity responses. The modal parameters identified by these identification methods matched very well. The changes in modal frequencies, damping ratios, and mode shapes that were extracted from dynamic measurements were correlated to delamination size and can indicate presence and severity of delamination. Finite element (FE) models of reinforced concrete plates with different delamination sizes and locations were established. The modal parameters computed from FE models were compared to those obtained from real measurements and FE models were validated.

Introduction

Delamination in concrete bridge decks cause decoupling of concrete from its surrounding steel reinforcement and subsequent loss of serviceability of bridges. Delamination detection has been of great concern for bridges and routine inspection is necessary. Many methods have been developed to detect delamination, including conventional chain drag method, impact-echo, ultra-sonic tests, ground penetrating radar, imaging radar, infrared thermography. These inspection methods require deployment of professional people with devices to field sites and can be costly. With the development of structural health monitoring, more and more real-time monitoring systems are being placed on bridges and buildings. Taking advantage of instrumented sensors, delamination detection could be more effective with lower costs and vibration sensors are more flexibly deployed than the arrangements of other devices.

Many studies address delamination detection using vibration measurements for composites materials. Most of these studies are on beams, with only a few studies on plates. For civil engineering concrete structures, studies on delamination detection by vibration measurements are more rare.[1] investigated delamination detection by using vibration measurements for civil engineering concrete plates through numerical studies. This paper presents experimental studies of four reinforced concrete slabs with different delamination areas. Delamination was simulated by putting plexiglass inside reinforced concrete plates during concrete pouring. The dynamic tests were conducted four months after pouring concrete. The experiments were original and significant for the models were concrete plates with relatively big size and no such tests have been conducted before.

The primary purpose of this paper is to investigate the applicability of delamination detection of concrete plates by modal identification of real dynamic measurements. Random excitation, swept sine and impact excitation were generated separately. The results due to random excitations are presented to provide reference for output only systems (ambient vibration). Modal frequencies, modal damping ratios and mode shapes were extracted from the velocity responses. The differences in modal characteristics between different delaminated models were compared to determine the presence and severity of delaminations.

The modal identification methods used in this study includes peak-picking (PP), frequency domain decomposition (FDD) and a time-domain identification method, stochastic subspace identification (SSI) method. The results from the three methods are compared for verification, and are used as delamination indicators.

Finite element modeling of the undelaminated and delaminated concrete slabs were established using ANSYS software. The concrete, steel reinforcement, wood supports, delaminations and boundary conditions were modeled properly. The modal characteristics computed from the finite element models were compared with those from dynamic tests for validation. The finite element results can be used as reference for modal identification from dynamic response measurements.

Experimental setup and dynamic tests

The objective of the experiments is to investigate the feasibility of delamination detection of concrete structures by vibration measurements. Four reinforced concrete plates were built in the lab. Several delamination scenarios were introduced for these concrete plates. Each concrete plate has the same size 1.829m x 2.743m x 0.140m, same materials and same layout of #6 steel rebar. The concrete was placed into all the models from the same concrete batch in order to get same concrete strength. Thin plexiglass sheets (1.57mm thick) were placed in three of the plates to generate effects of delamination during concrete pouring and all were at the horizontal planes that were 0.089m from the bottom of the plates. The sizes of them are 0.914m x 1.219m (22.2% delamination), 1.219m x 2.134m (51.9% delamination) and 1.524m x 2.438m (74.1% delamination) respectively. One plate without plexiglass is included as the undelaminated model. Fig. 1 shows the plan and elevation views of the 22.2% delaminated model. The other models are similar. The two opposite longer edges of each concrete plate were placed on two wood supports, the other two opposite edges were free, therefore all the concrete slabs have the same boundary conditions. In finite element models, the wood supports are considered instead of modeling the boundary conditions as strictly simply supported.

The same dynamics tests were performed on the four models for convenience of comparison. Fig. 2 illustrates the layout of excitation sources and sensors. An APS shaker and an instrumented hammer were employed to generate excitations. Six vertical velocity transducers (V1~V6) were used to record the vertical velocity responses and one horizontal velocity transducer (V7) was used to record the horizontal responses. An accelerometer was attached on the shaker to record the real excitation input. In the dynamic tests, the APS shaker generated swept sine, random and impulse excitations on the models in sequence. Then the instrumented hammer applied impact excitations a few times on two locations. The velocity response and the acceleration input were recorded for further analyses. The recorded duration for each input of the shaker is 32 seconds. The sampling frequency is 1024 HZ.

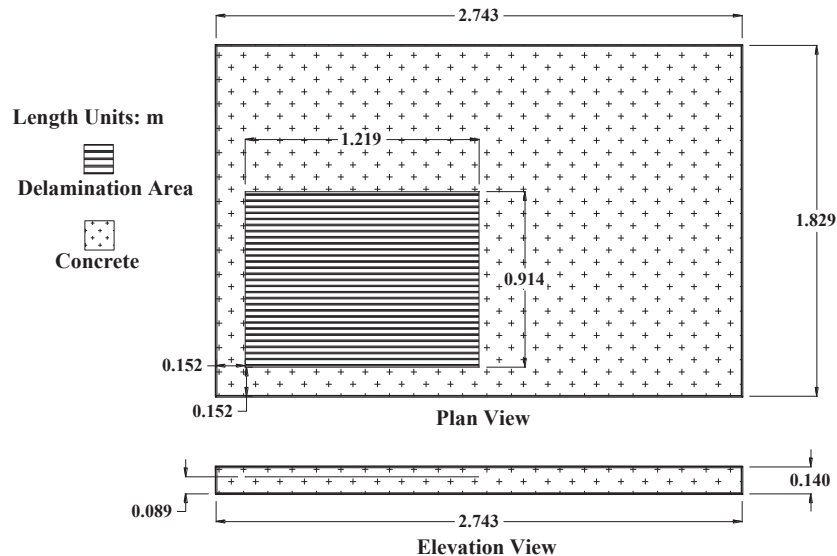
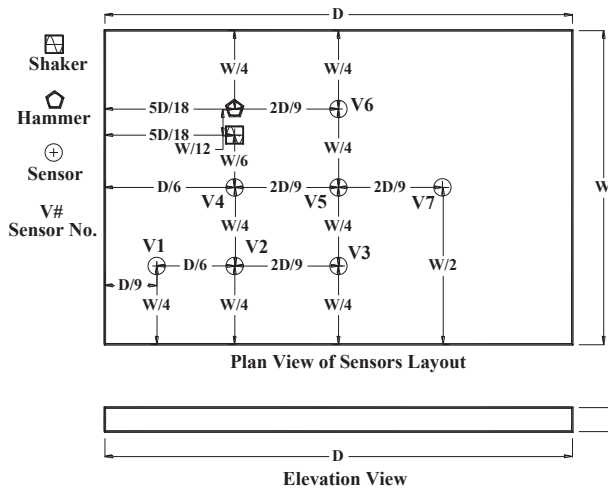


Fig. 1 The model with delamination size 0.914m x 1.219m (22.2% delamination)



(a) Layout of excitation sources and sensors



(b) One of the models for dynamic test

Fig. 2 Layout of excitation sources and sensors for dynamic tests

Modal identification methods for the output only systems

Classical peak-picking method (PP) was used. This simple signal processing technique computes the power spectra of time histories measurements by discrete Fourier transform and directly uses the peaks of the spectra to determine modal frequencies. Frequency domain decomposition (FDD) and stochastic subspace identification (SSI) methods were also adopted in this paper to extract modal characteristics from measurements of the dynamic tests. These identification methods were used to verify each other.

For the cases of lightly damped structures, a derived a relationship between response spectral density and modal parameters provides a basis for the FDD method [2]. In application of FDD identification algorithm, the power spectral density (PSD) of the output measurements $\hat{G}_{yy}(j\omega)$ are estimated and then decomposed at $\omega = \omega_i$ by taking the Singular Value Decomposition (SVD) of the PSD matrix.

$$\hat{G}_{yy}(j\omega_i) = U_i S_i U_i^H \quad (1)$$

where the unitary matrix $U_i = [u_{i1}, u_{i2}, \dots, u_{im}]$ holds the singular vectors u_{ij} and the diagonal matrix S_i holds the singular values s_{ij} . If only a k th mode is dominating at the selected frequency ω_i , there will be only one singular value in Eq. (1) and therefore the first singular vector u_{i1} would be an estimate of the k th mode shape, $\hat{\phi} = u_{i1}$. Damping can be obtained from the correlation function of the SDOF system [3].

Stochastic subspace identification method (SSI) is a time-domain identification method originally proposed in [4] and has been applied effectively in various types of civil and mechanical structures. This method can determine linear models from column and row spaces of the matrices computed from the input-output data [5]. This study used Data -driven SSI that doesn't need the computation of output covariance. The key idea of data-driven SSI is to project the row space of future outputs into the row space of the past outputs. An extension of the SSI called reference based SSI was developed in [6].

The discrete-time stochastic state-space model is defined as the normal model without input terms [7],

$$x_{k+1} = A x_k + w_k; \quad y_k = C x_k + v_k \quad (2)$$

where w and v are plant and observation noise vectors respectively, both of them are zero mean Gaussian white noise vectors. The SSI is used to identify A and C from the output-only measurements y_k . The identification steps in this study are concisely summarized in the following, for details refer to the literature.

(a) Construct Hankel matrix Y from the output measurements:

$$Y = \begin{bmatrix} Y_p \\ Y_f \end{bmatrix} \quad (3)$$

(b) Orthogonally project the row space of future outputs Y_f on the row space of past outputs Y_p :

$$T_i = Y_f Y_p^T (Y_p Y_p^T)^\dagger Y_p \quad (4)$$

where $^T, \dagger$ denote transpose and pseudo inverse respectively.

(c) Then apply SVD of the orthogonal projection:

$$T_i = USV^T = (U_1 \ U_2) \begin{pmatrix} S_1 & 0 \\ 0 & S_2 \end{pmatrix} \begin{pmatrix} V_1^T \\ V_2^T \end{pmatrix} \approx U_1 S_1 V_1^T \quad (5)$$

where U and V are orthonormal matrices, S is a diagonal matrix containing singular values in descending order, among which S_2 is a block containing small neglected values.

(d) Calculate the observability matrix from the reduced SVD from Eq. (5)

$$O_i = U_1 S_1^{1/2} \quad (6)$$

The definition of this observability matrix O_i is:

$$O_i = (C \ CA \ \dots \ CA^{i-1})^T \quad (7)$$

Then the discrete-time system matrices A and C can be calculated from Eq. (6) and (7),.

(e) Post-processing to obtain modal parameters.

$A = \psi \Lambda \psi^{-1}$, where $\Lambda = \text{diag}(\lambda_q)$ is a diagonal matrix containing the discrete time complex eigenvalues and columns of ψ are the corresponding eigenvectors. For continuous time system, the state matrices $A_C = \psi_C \Lambda_C \psi_C^{-1}$, after some derivations, it gives,

$$A = e^{A_C \Delta t}; \quad \psi_C = \psi; \quad \lambda_{C_q} = \frac{\ln(\lambda_q)}{\Delta t}; \quad \lambda_{C_q} \lambda_{C_q}^* = -\xi_q \omega_q \pm j \omega_q \sqrt{1 - \xi_q^2}; \quad \Phi = C \psi \quad (8)$$

where Δt is time step, ω_q is modal frequency, ξ_q is modal damping ratio, the columns of Φ are mode shapes.

Modal identification of the dynamic measurements

Classical peak-picking method (PP), frequency domain decomposition method (FDD) and stochastic subspace identification method (SSI) are used to obtain modal parameters from dynamic responses due to the random excitations. Typical time signals and FFT of them for PP method are shown in Fig. 3, and a typical singular value plot by FDD for undelaminated model is shown in Fig. 4. The system order n is 60 and the number of block rows d is 200 with the SSI used in this study, while it is needed to point out that even using n = 30, d = 150, most results are same or very close to those by using n = 60, d = 400. The modal frequencies extracted by using PP, FDD and SSI methods are shown in Table. 1 and the damping ratios by SSI method are shown in Table. 2. From Table. 1, the frequencies by the three methods agree well for most modes. The damping ratios in Table. 2 are reasonable values. In general, excellent agreements are obtained between modal frequencies and mode shapes by using FDD and SSI.

The effectiveness of using changes in modal frequencies and mode shapes as damage indicators of delamination can be examined in Table. 1-2. From Table. 1, the frequencies of delaminated models decreased compared with frequencies of undelaminated model, basically the larger delamination areas, the smaller frequencies for the corresponding modes. The 22.2% model was supposed to have higher frequencies than the corresponding ones of 51.9%, while they are slightly lower than expected, this is most probably because during concrete pouring, the 22.2% model was pouring slower than other models and even stopped for a while, which reduced the integral concrete strength. From Table. 2, it is observed that the larger delamination area, the higher damping ratios of the corresponding modes.

The analyses on responses due to impact and swept sine excitations are not included in this paper, the modal characteristics obtained from them agree very well with those presented here.

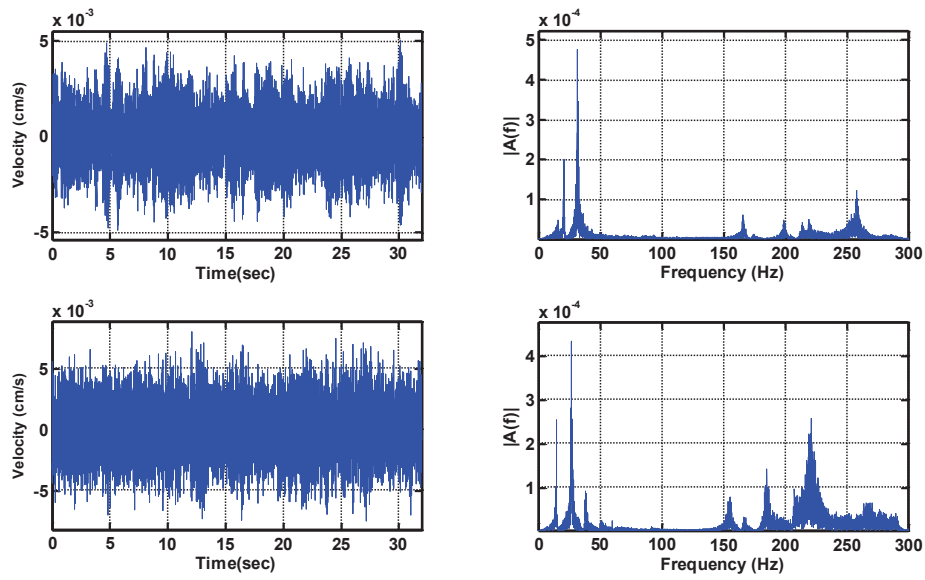


Fig. 3 Typical time signals of V4 and FFT of them for two models due to random excitations (left column is time signal, right column is FFT, upper row is for undelaminated model, lower row is for 22.2% delaminated model)

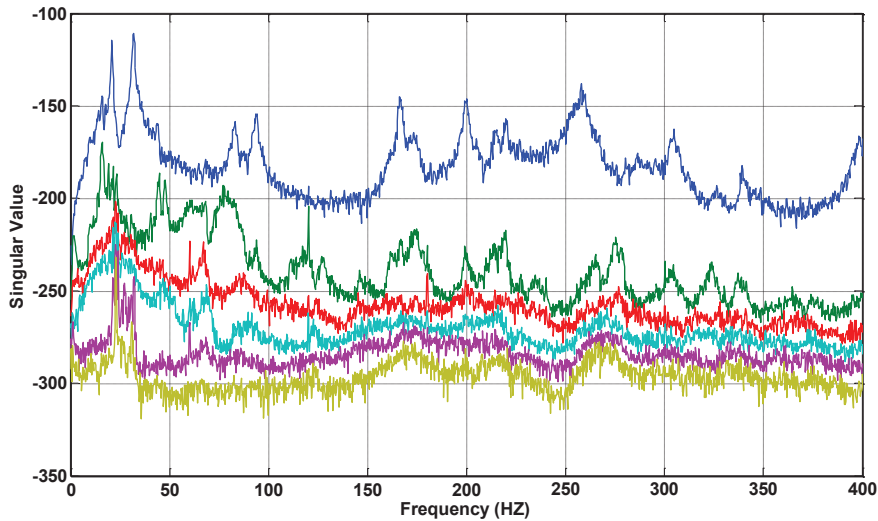


Fig. 4 Signal values of PSD of the responses due to random excitation for undelaminated model

Table .1 Modal frequencies obtained by PP, FDD and SSI (d=400, n=60) methods from responses due to random excitation

0% Delaminated	PP (HZ)	15.94	20.69	31.60	68.88	84.66	165.95
	FDD (HZ)	15.76	20.76	31.77	68.03	83.04	166.08
	SSI (HZ)	15.84	20.67	31.61	67.62(impact loc2)	82.60	166.37
22.2% Delaminated	PP (HZ)	14.72	-	26.69	51.00	-	-
	FDD (HZ)	14.76	-	27.01	50.77	-	-
	SSI (HZ)	14.57	-	26.83	50.67	-	-
51.9% Delaminated	PP (HZ)	14.66	-	27.60	-	-	-
	FDD (HZ)	14.01	17.51	27.51	49.47	-	-
	SSI (HZ)	13.99	-	27.56	-	-	-
74.1% Delaminated	PP (HZ)	9.09	-	24.41	44.69	-	84.38
	FDD (HZ)	9.00	-	24.01	44.77	-	84.54
	SSI (HZ)	8.93	-	24.31	44.37	-	84.63

Table . 2 The damping ratios by using SSI method

	Undelaminated	22.2% Delaminated	51.9% Delaminated	74.1% Delaminated
-	Freq = 31.61 HZ	Freq = 26.83 HZ	Freq = 27.56 HZ	Freq = 24.31 HZ
Damping ratios by SSI, ξ (%)	1.05	1.34	1.68	1.71

Finite element modeling

The finite element models of the reinforced concrete slabs were built using ANSYS software. Fig. 5 exhibits isometric view and front view of the entities, the origin of the coordinate system is at the left bottom point close to delamination as shown in Fig.1. The longitudinal steel rebar were put in the form work on the plane of $Y=0.051$ m. The transversal rebar were put immediately on the longitudinal rebar and they were wired together. The two opposite edges with $X = 0$ m and $X = 1.829$ m of concrete plates are supported on two timbers, the other two edges $Z = 0$ m and $Z = 2.743$ m are free. Elements solid65, link8 and solid45 were selected to represent concrete, steel rebar, and wood, respectively. The ground was modeled using solid65 elements with infinite strength. Dynamic characteristics are sensitive to the boundary conditions, so the wood support was modeled accurately instead of as idealized simple supports. Contact and target elements were used to simulate the contact between concrete and wood, and between wood and ground. The properties of contact elements were updated during modal analysis to match the results from real measurements. The delaminations were modeled by reducing the elastic modulus of the corresponding areas to very small numbers.

Based on 28 day compression tests, the concrete's elastic modulus is $E_c = 24,000$ MPa, ultimate uniaxial compressive strength $\sigma_c = 27.5$ MPa, ultimate uniaxial tensile strength $\sigma_t = 14.69$ MPa. The concrete density $\rho_c = 2300$ kg/m³. Poisson's ratio of concrete $\nu_c = 0.15$. The steel rebar's size is #6, its nominal diameter $d = 19.05$ mm, elastic modulus is $E_s = 200$ GPa, yield stress $f_y = 410$ MPa, Poisson's ratio $\nu_s = 0.3$, and the density $\rho_s = 7850$ kg/m³.

Modal analysis of all the reinforced concrete slabs were performed. The modal frequencies and mode shapes computed by the finite element modeling were compared with those from dynamic tests. Comparisons of frequencies are shown in Table 3 and one mode shape of undelaminated and 22.2% delaminated models are shown in Fig. 6. Table 3 demonstrates that some low order and even the higher order frequencies calculated by the ANSYS model and dynamic tests match well. From Fig. 6, it is discerned that the frequency of the delaminated model decreased and the mode shape changes in delaminated area. Fig. 7 compares the mode shapes for a same mode by FDD, SSI and ANSYS modeling, For easy comparison, the so called mode shapes in Fig.7 are plotted with respect to the transducer numbers in two dimension instead of the real locations of them in three dimensions. It is observed that the mode shape of ANSYS model is close to that obtained from real measurements. It is concluded that the finite element model can approximately model delaminated concrete slabs in the labs for modal analysis.

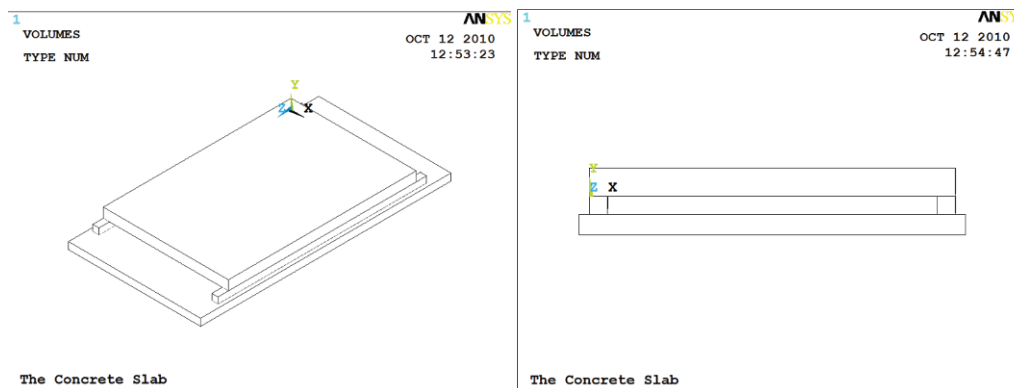
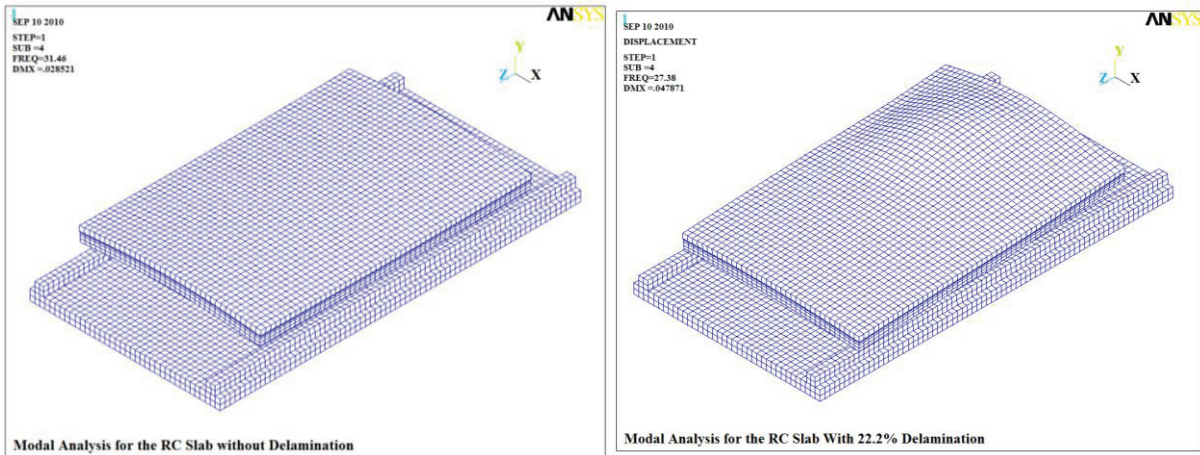
**Fig. 5** The coordinate system of the finite element model (left is isometric view, right is front view)

Table 3 . Comparison of modal frequencies by ANSYS modeling and FDD of the responses due to random excitation

-	-	Horizontal	Horizontal	Vertical Y+ bending along Z	Bending along X	Torsion in XY	Bending along X
0%	ANSYS (HZ)	15.52	20.90	31.46	69.13	81.68	165.80
Delaminated	FDD (HZ)	15.76	20.76	31.77	68.03	83.04	166.08
22.2%	ANSYS (HZ)	14.70	-	27.38	51.99	-	-
Delaminated	FDD (HZ)	14.76	-	27.01	50.77	-	-
51.9%	ANSYS (HZ)	14.73	16.26	26.98	50.81	-	-
Delaminated	FDD (HZ)	14.01	17.51	27.51	49.47	-	-
74.1%	ANSYS (HZ)	9.41	-	24.91	42.78	-	81.39
Delaminated	FDD (HZ)	9.00	-	24.01	44.77	-	84.54



(a) for undelaminated model, frequency is 31.46 HZ

(b) for 22.2% delaminated model, frequency is 27.38 HZ

Fig. 6 The mode shapes for the undelaminated model and the 22.2% delaminated model

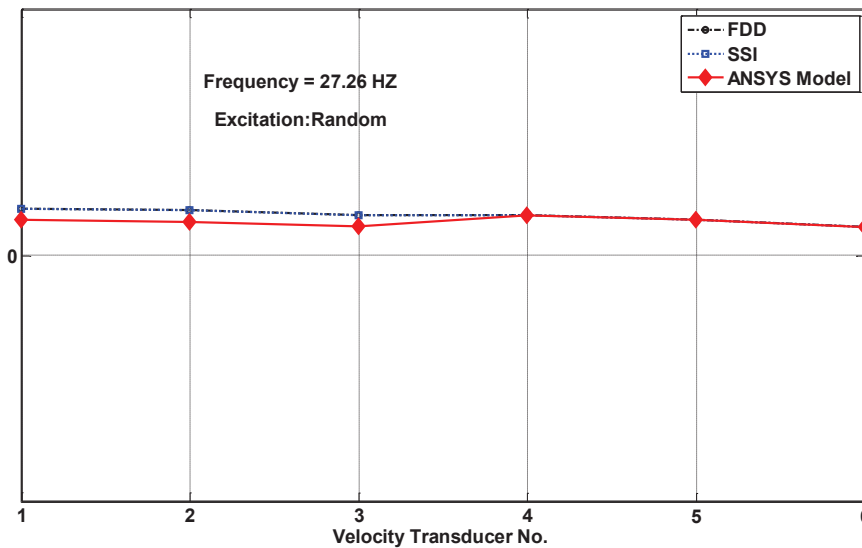


Fig. 7 Comparison of mode shapes by FDD, SSI and ANSYS model for 51.9% delaminated model at frequency of 27.26 HZ

Conclusions

This paper studies delamination detection of reinforced concrete slabs by modal identification of velocity responses. Four concrete plates with different sizes of plexiglasses inside to simulate delaminations were built and dynamic tests were conducted on them. In the analysis of real measurements, multiple identification methods are recommended to be applied in modal analysis to get more confidence. In this paper, peak-picking, frequency domain decomposition and stochastic subspace identification methods were used. The frequencies obtained by the three methods matched very well, and the mode shapes obtained by FDD and SSI agreed excellently. The damping ratios were also obtained by SSI.

Finite element (FE) models of concrete slabs were established by ANSYS software. Since the modal characteristics are sensitive to boundary conditions, the wood supports in this study must be modeled properly instead of using idealized simply supported conditions. The contact elements were used in modeling the real contacts between concrete and wood. The frequencies and mode shapes for most low order modes calculated by FE models agreed well with those identified from test data. It is concluded that the finite element models can approximately model delaminated concrete slabs for modal analysis.

Comparisons of modal frequencies and mode shapes for the concrete slabs with different delamination degrees showed that changes in frequencies and mode shapes indicate the occurrence and degree of delamination. The frequencies decrease with the increase of delamination sizes. From Table 2, the damping ratios increase with the increase of delamination sizes, this needs further research due to the complexity of damping. The mode shapes have abrupt changes in delamination areas, basically the response in those areas are bigger than the corresponding parts of undelaminated models.

More sensitive damage indicators of delamination are under study. Further work is necessary on more accurate and practical finite element modeling. Regarding the experiments, concrete decks with real delamination and more dense sensor arrays would be very beneficial for the future research.

References

1. Xing, S., Halling, M.J., Barr, P.W.: Delamination Detection and Location in Concrete Deck by Modal Identification. Paper presented at the Structures Congress 2010, Orlando, FL, USA,
2. Brincker, R., Zhang, L., Andersen, P.: Modal Identification from Ambient Responses using Frequency Domain Decomposition. In: Proceedings of IMAC 18, the International Modal Analysis Conference, San Antonio, TX, February 2000, pp. 625-630
3. Brincker, R., Ventura, C.E., Anderson, P.: Damping estimation by frequency domain decomposition. In: Proc., Int. Modal Analysis Conf., Kissimmee, Fla. 2001, pp. 698-703
4. Van Overschee, P., De Moor, B.: Subspace Algorithms for the Stochastic Identification Problem. *Automatica* **29**(3), 649-660 (1993).
5. Van Overschee, P., De Moor, B.: *Subspace Identification for Linear Systems: Theory, Implementation, Applications*. Kluwer Academic Publishers, (1996)
6. Peeters, B., De Roeck, G.: Reference-based stochastic subspace identification for output-only modal analysis. *Mechanical Systems and Signal Processing* **13**(6), 855-878 (1999).
7. Katayama, T.: *Subspace Methods for System Identification*. Springer, (2005)

Semi-Active Control of Staircase Vibration Under Human Excitation

R. Philp, P. Reynolds, D.S. Nyawako

Vibration Engineering Section

Department of Civil and Structural Engineering, The University of Sheffield

Sir Frederick Mappin Building, Mappin Street, Sheffield, S1 3JD, UK

ABSTRACT

Feature staircases in modern offices are often very slender and lightweight structures with minimal damping. This, combined with quite onerous human dynamic excitation, can result in large responses that cause discomfort and concern to occupants.

This paper presents the results of a study into the use of a semi-active tuned mass damper for mitigation of excessive vibrations in a staircase structure. A number of semi-active vibration control strategies are evaluated and other performance considerations, such as off-tuning and the effects of time delays, are investigated.

Semi-active control is demonstrated to be a feasible technique for mitigation of human-induced vibration in staircases.

1 INTRODUCTION

Modern materials have an increasing strength to weight ratio, allowing engineers to design more slender structures than their predecessors. These designs are widely accepted as being more aesthetically pleasing, while being structurally more efficient solutions. As a consequence of these developments, modern staircases tend to have low natural frequencies, coinciding with the lower harmonics of human pacing, due to a low stiffness to mass ratio [1]. This feature, coupled with low natural damping means they are struggling to meet their vibration serviceability criteria. Previous solutions to this have generally involved increasing the stiffness, often with the use of props under the half-landings. However, passive tuned mass dampers (TMDs) and semi-active tuned mass dampers (STMDs) are shown to be capable of significantly suppressing the human-induced vibration with a lesser impact on their architectural feature.

TMDs comprise of a secondary mass that is proportionally small in comparison to the mass of the primary structure and is connected to it through a spring-dashpot as shown in [Fig. 1\(a\)](#). They are often designed to target specific problematic modes of vibration in the structures for which they are designed and thus are not effective in suppressing other resonances. TMDs resonate close to the frequency of the problematic mode and thereby increase the damping of the primary structure around this mode [2]. Vertical TMDs are already used on footbridges such as the Abandoibarra Bridge in Spain and the Millennium Footbridge in London to reduce the effects of footfall induced vibration.

STMDs, also referred to as controllable passive devices, can be considered as a potential improvement to the passive TMDs. They comprise of alterations in the damping and stiffness features of the TMD in real-time, to improve performance as well as efficiency over a broader range of frequencies. For example, magnetorheological (MR) damping elements are used to replace the passive dashpot in a TMD, as shown in [Fig. 1\(b\)](#).

An MR fluid contains micron sized particles dispersed within a carrier fluid, usually oil, that when subjected to a magnetic field, align in the direction of the flux, altering the yield strength of the fluid in milliseconds. The yield stress can therefore be very accurately adjusted through changes in the strength of the magnetic field, which can be calculated using the Bingham model [3]. The time response of an MR damper is non-linear, with the exact time varying according to the change in current supplied. The greater the change in current the faster the response time [4].

A number of control algorithms have been developed in the past. For example, Pinkaew & Fujino [5] used an ideal condition of active damper and minimised the difference in performance. However, much of the recent research has focused on the use of groundhook logic [4, 6-9]. This takes its name from the idealised situation, given in **Fig. 1(c)**, of a damper connecting the main system to the ground [10]. This is achieved by varying the semi-active damping element between two fixed values: off-state damping and on-state damping.

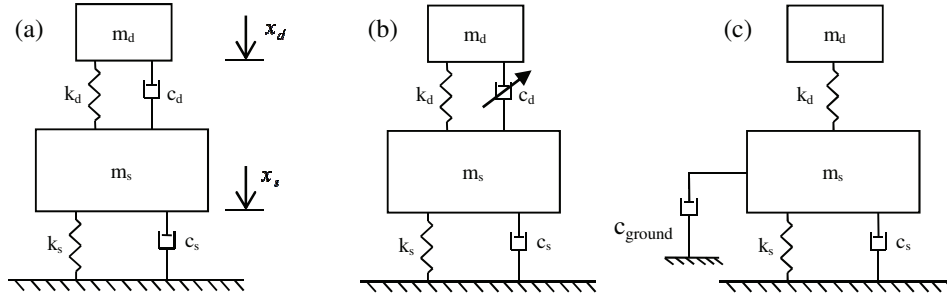


Fig. 1 2DOF system models of a structure with a (a) TMD (b) STMD, where (c) shows the ideal configuration of a groundhook STMD

This paper explores the use of some semi-active control strategies, developed by researchers in the past, for mitigation of human-induced excitation in a staircase structure. Modal properties of a case study staircase, used in the analytical studies, are derived from a Finite Element (FE) model. A passive TMD is designed based on these and various semi-active control studies are also undertaken.

Section 2 introduces some semi-active groundhook control strategies developed in the recent past. In section 3, the modal properties of the staircase structure are presented, as derived from the FE modelling, along with the nature of the forcing function used. Section 4 presents the vibration mitigation performances of passive and semi-active TMDs; while Section 5 explores the influence of the damper response time on the performance of the semi-active TMD and some conclusions are presented in section 6.

2 SEMI-ACTIVE GROUNDHOOK CONTROL TECHNOLOGIES

The semi-active groundhook control strategy is the approach used in this work. Amongst the semi-active groundhook control technologies, one of the simplest forms is the on-off velocity based groundhook TMD (VBG). For this, the damping is switched between a minimum and maximum level according to the following equations:

$$\dot{x}(\dot{x}_s - \dot{x}_d) \geq 0 \rightarrow c_d = c_{\max} \quad (1) \quad \dot{x}(\dot{x}_s - \dot{x}_d) < 0 \rightarrow c_d = c_{\min} \quad (2)$$

With another approach proposed by Setareh [9], the damping of the groundhook STMD is varied between a minimum and maximum level according to equations (3) and (4). G is a constant gain factor. Damping between the values of c_{\min} and c_{\max} is proportional to the modulus of the velocity of the primary mass, which is shown graphically in **Fig. 2(a)**. The gradient of the line between c_{\min} and c_{\max} is the value of G , which has an experimentally determined optimum.

$$\dot{x}_s(\dot{x}_s - \dot{x}_d) \geq 0 \rightarrow c_d = \min\{G|\dot{x}_s|, c_{\max}\} \quad (3) \quad \dot{x}(\dot{x}_s - \dot{x}_d) < 0 \rightarrow c_d = c_{\min} \quad (4)$$

Koo & Ahmadian [7] used the constraints defined in equations (3) and (4) to produce the following alternative continuous VBG equation, which has been adopted in subsequent research:

$$c_d = G \frac{\dot{x}_s}{\dot{x}_s - \dot{x}_d}, \quad c_{\min} \leq c_d \leq c_{\max} \quad (5)$$

where G again is a constant gain factor determining the gradient of the line shown in **Fig. 2(b)**. This provides a simpler model, bound by a single equation with limits, and is shown to provide a better performance as it accounts for the relative velocities when determining the intermediate damping values. Using equation (5), it can be seen that the diagonal line in **Fig. 2** would intercept the axis at the origin. Thus, a large value of gain places the line approximately vertically along the y-axis, effectively creating an on-off damper, shown in **Fig. 2(c)**; while a very low value would mean it never reaches c_{\min} , creating a passive TMD. A further extension of the groundhook control, the displacement based groundhook, was proposed by Koo et

al. [4, 6]. This follows the original logic but the relative velocity is, in this case, multiplied by the displacement of the primary mass, shown below for the on-off DBG:

$$x(\dot{x}_s - \dot{x}_d) \geq 0 \rightarrow c_d = c_{\max} \quad (6)$$

$$x(\dot{x}_s - \dot{x}_d) < 0 \rightarrow c_d = c_{\min} \quad (7)$$

and the continuous DBG:

$$c_d = G \frac{x_s}{\dot{x}_s - \dot{x}_d}, \quad c_{\min} \leq c_d \leq c_{\max} \quad (8)$$

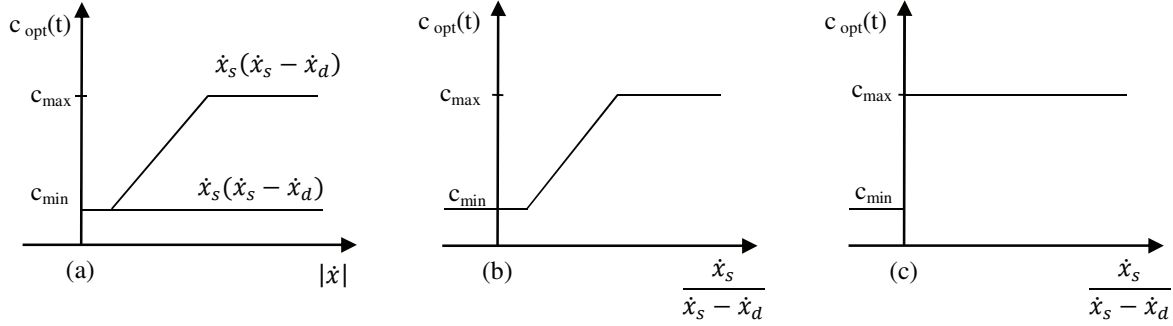


Fig. 2 Range of damping values according to (a) Setareh [equations (3) and (4)] and (b) Koo & Ahmadian [equation (5)], with (c) showing a high gain (G) resulting in an on-off damper

3 MODELLING AND FORCING FUNCTION

This section covers the FE model of the staircase and the forcing function. The FE model is used to calculate the dynamic properties of the staircase, while the forcing function is developed to impose a walking/transient force on the staircase subject to a group loading situation.

3.1 Finite Element Model

A finite element model of a staircase, with a known vibration serviceability problem, produces five natural frequencies below 30Hz, two of which are below 10Hz. ISO [11] and SCI [12] recommend fundamental frequencies of above 9 and 12Hz, respectively to avoid vibration serviceability problems, confirming the potential vulnerability of the staircase to human-induced vibration. The results show a fundamental frequency of 8.5Hz in the vertical plane, with the peak of the mode positioned approximately at midspan. It is therefore appropriate to model the effectiveness of a TMD and STMD attached to the staircase under the half landing. A modal mass of 4070kg is also calculated, while a modal damping ratio of 0.5% is assumed, as recommended in SCI Guide P354 [12].

3.2 Forcing Function

The loading modelled considers a group of 9 persons descending the staircase, with a footfall frequency of 4.25Hz, represented by equation 9.

$$P(t) = Wg \alpha_i G_r \cos(2\pi f_i t) \cdot \{\varphi\} \quad (9)$$

where W is the average mass of a person, taken as 72.5kg [13], α is the DLF at the i th harmonic, G_r is the group loading factor, f is the frequency of the i th harmonic and φ is the mode shape, accounting for the spatially varying nature of the load. The dynamic load factor is interpolated from the experimental data provided by Kerr & Bishop [14], while the group loading factor is interpolated from the experimental data provided by Bishop et al. [15]. This produces a peak amplitude of 332kN, with loading over a duration of 9.75s.

4 ANALYTICAL STUDIES

The staircase is modelled as uncontrolled, then with a TMD and STMD attached under the half landing. To appreciate the principles of semi-active control, the influence of varying the damping and stiffness properties of the TMD are carried out in this section. The various groundhook controls are then explored, varying their properties and detailing the effect on performance.

4.1 Passive TMD

The TMD's parameters are determined according to the following equations set out by Den Hartog [16]:

$$\mu = \frac{m_d}{m_s} \tag{10}$$

$$\xi_{d,opt} = \sqrt{\frac{3\mu}{8(1+\mu)^3}} \tag{11}$$

$$\kappa_{opt} = \left(\frac{\omega_d}{\omega_s}\right)_{opt} = \frac{1}{1+\mu} \tag{12}$$

$$\omega_d = \sqrt{\frac{k_d}{m_d}} \tag{13}$$

where μ is the mass ratio, ξ is the damping ratio and κ is the frequency ratio. A mass ratio of 0.04 is used to minimise the additional mass to the structure while still producing adequate performance. The response of a SDOF model of the staircase, subject to the excitation at resonance, is given in Fig. 3(a). The model is increased to a 2DOF system, with the addition of a TMD and the response, shown in Fig. 3(b), exhibits a reduction in peak RMS acceleration from 3.94m/s² to 0.43m/s².

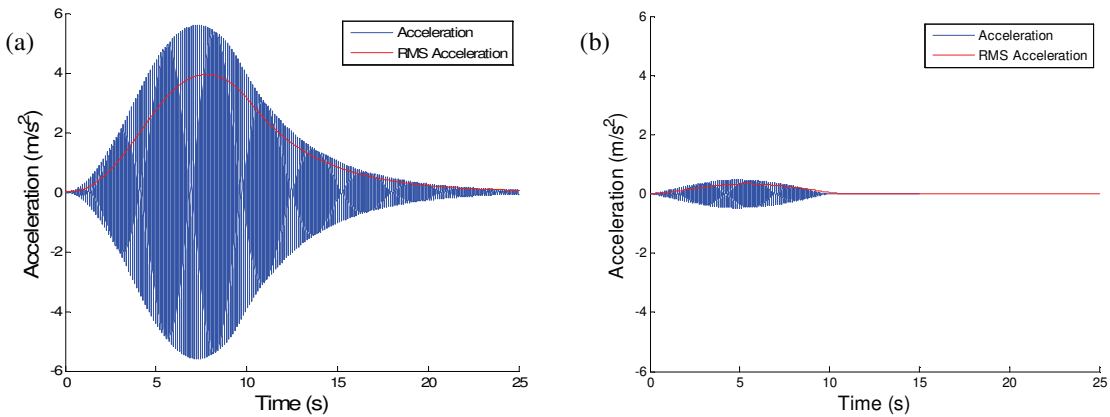


Fig. 3 The acceleration time histories of the staircase with (a) no damping device and (b) a passive TMD, subject to loading at 8.5Hz

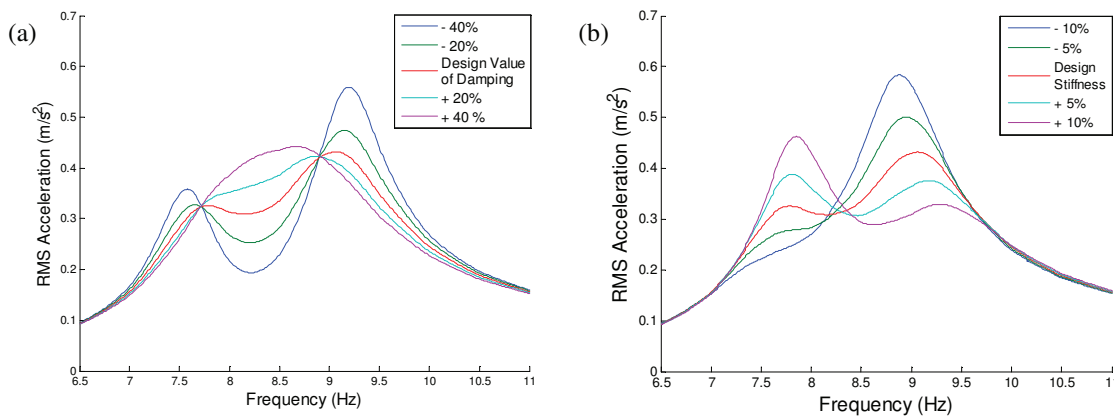


Fig. 4 The effect of the TMD (a) damping ratio and (b) stiffness on the amplitude of the structure over the given frequency range

Applying the forcing function at discrete intervals of 0.01Hz, over the frequency range of 6.5 to 11Hz, produces frequency response curves representing the peak RMS amplitude at each interval. This is shown in **Fig. 4(a)** and **Fig. 4(b)** in which parameters of damping and stiffness of the TMD are varied respectively. Increasing the damping ratio reduces the amplitude of the peaks at the expense of an increase in the valley. It is noticed that with an increase of 40% from the optimum, the response becomes a single peak; this is known as a saturation level, at which coupling of the TMD and structure occurs. Increasing the stiffness decreases the left peak, while increasing the right peak and vice versa. This continues in either direction until there is just a single visible peak and thus the stiffness is seen to have two saturation values, one above and one below the design value, for which coupling of the damper and structure occurs.

4.2 Semi-Active Tuned Mass Dampers

The damping ratio of the passive TMD is varied according to the on-off VBG and on-off DBG controls. The time delay of the MR damping element in this case is taken to be 15ms as specified in the current literature by LORD [17]. They are optimised by varying the values of on-state and off-state damping to minimise the peak RMS acceleration, with their performance shown in **Fig. 5**. The DBG control is found to optimise with the same values for on- and off-state damping, meaning the damper is in a passive state. The increase in performance noticed over the passive device is due to the nature of the tuning equations used for the passive device, which appear to optimise for displacement. However, the VBG exhibits a much greater level of performance, while also displaying a general leftward shift in the frequency response.

Introducing the gain feature to the on-off VBG creates a variable VBG, in which both Koo & Ahmadian's and Setareh's equations are modelled. Both of these gain values optimise at very high values, therefore producing an on-off damper. The frequency response of Koo & Ahmadian's tuning equation is shown in **Fig. 6**, with a similar response experienced using Setareh's equations. Due to the passive nature of the DBG it is not possible to test the effects of gain on the performance.

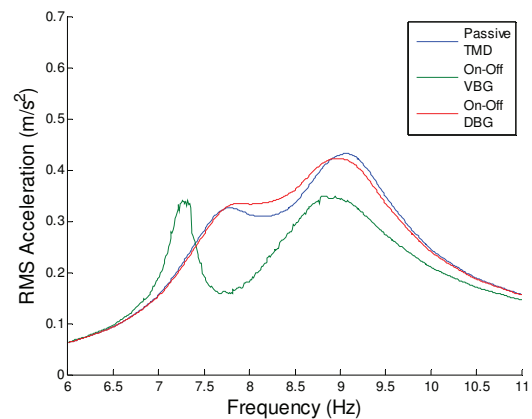


Fig. 5 The performance of each damper across the frequency range

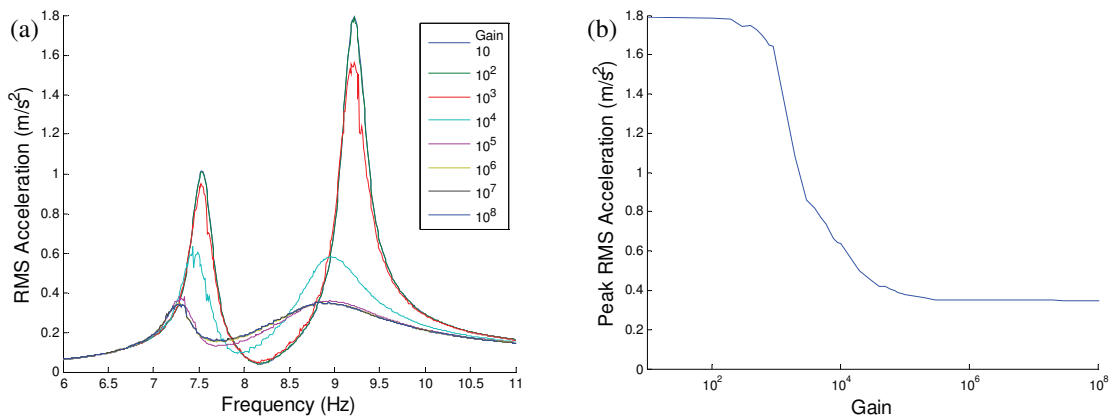


Fig. 6 The effect of varying the gain for a VBG (according to Koo & Ahmadian)

Fig. 7 and **Fig. 8** independently vary one of the damping parameters while maintaining all other variables as constants. **Fig. 7(a)** varies the value of on-state damping of the VBG around its optimum value. Increasing the damping reduces the left peak and increases the valley, while the right peak exhibits a minimum value. **Fig. 7(b)** varies the value of off-state damping of the VBG around its optimum value. The left peak reduces and the valley increases with an increase in off-state damping, while the right peak is seen to reduce. Unlike the on-state damping there is no optimum damping value exhibited in the right peak. The damping of the DBG is varied in **Fig. 8**, where (a) shows that an increase in the on-state damping increases the right peak, with a proportionally small change in the left peak; (b) shows that increasing the off-state damping reduces the right peak while increasing the valley.

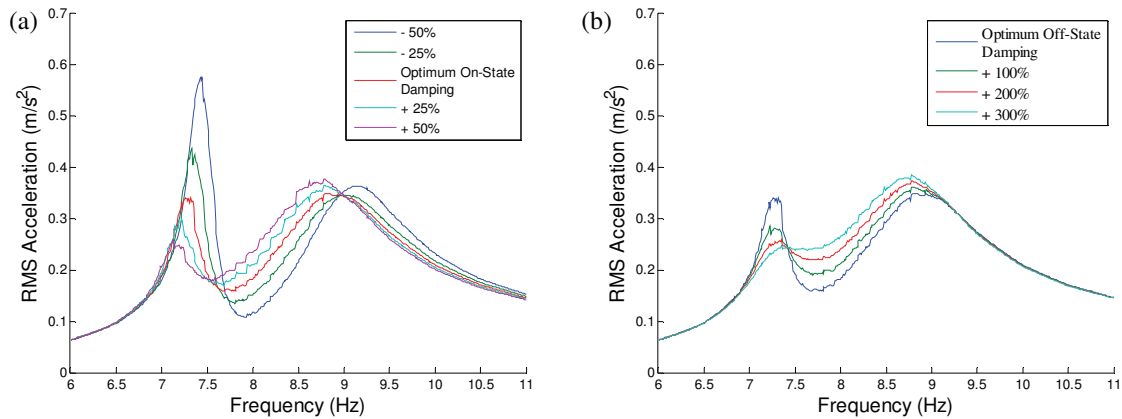


Fig. 7 Effect of varying the (a) on-state damping ratio and (b) off-state damping ratio on a VBG TMD

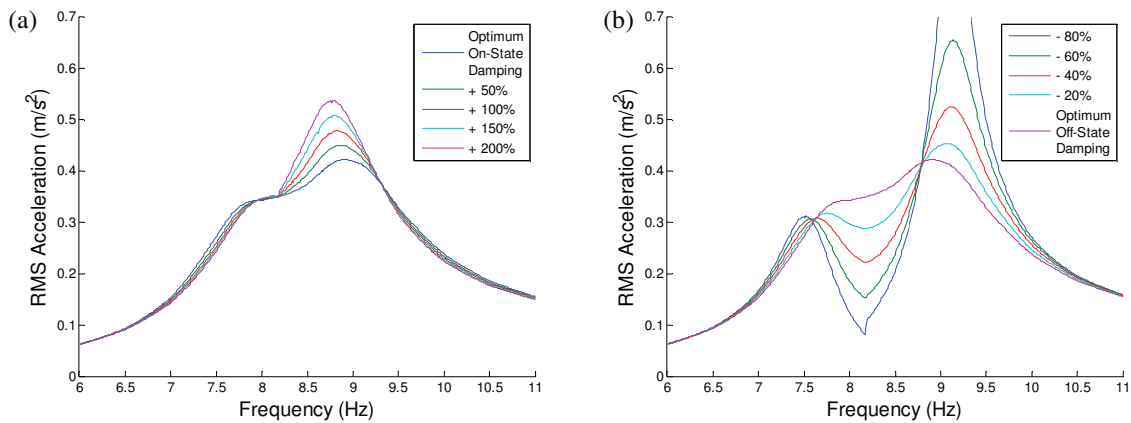


Fig. 8 Effect of varying the (a) on-state damping ratio and (b) off-state damping ratio on a DBG TMD

5 THE EFFECT OF DAMPER RESPONSE TIME

The effect of the time delay is assessed in two different ways. The first approach selects three different time delays and optimises the controls for each of the time delays. The second approach selects one time delay, of which the dampers are optimised to, and then the time delay is off-tuned and its effects on performance recorded.

5.1 Optimised to Varying MR Time Responses

The results of the previous section, with a time delay of 15ms, are combined with optimisations using 5ms and 10ms delays. 10ms is used in the studies conducted by Setareh [8, 9] providing what is currently a realistic damper response time, while techniques such as overdriving the damper [4] are likely to yield much lower response times in the future; thus 5ms is felt to be relevant. The optimised parameters, along with their peak response RMS accelerations, are provided in

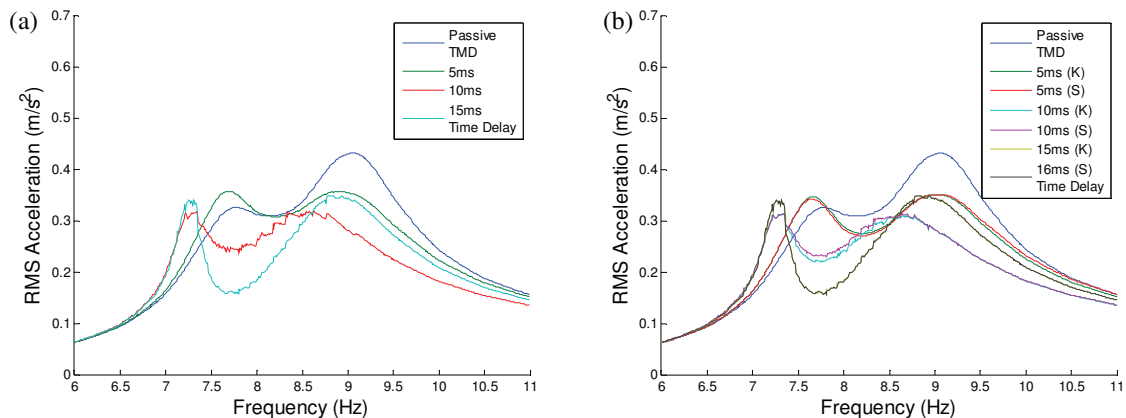
Table 1. The Damping values provided are presented as a ratio with passive device. **Fig. 9(a)** displays the response of the on-off VBG, where the 10ms response provides the greatest increase in performance, while all three provide large gains over the passive equivalent. **Fig. 9(b)** shows the frequency responses for both Koo & Ahmadian's and Setareh's equations of the VBG. It is noticed that there is little difference between the two but Koo & Ahmadian's equation does perform marginally better in each case. Both the 5ms and 10ms responses improve with an optimisation of the gain, while the 10ms response time once again provides the best performance. For the DBG, both the 10ms and 15ms responses optimise to a passive device, while the 5ms shows significant improvements, however, this is not improved further by making the device variable. The peak response of each device, with each time delay, is given in **Fig. 9(d)** as a percentage reduction in amplitude over the passive equivalent. From this it is clear that the variable VBG according to Koo & Ahmadian's equation is the best performing control with a 27% reduction over the passive TMD.

Table 1 The parameters of the optimised dampers with their respective peak accelerations (damping is provided as a ratio with the passive TMD)

Time Delay	Damping Control	Off-State Damping	On-State Damping	Gain	Peak Acceleration (m/s ²)
N/A	Passive	1.00	1.00	N/A	0.4320
5ms	On-Off VBG	0.72	1.63	N/A	0.3574
	Variable VBG (Koo)	0.72	1.63	4x10 ⁴	0.3512
	Variable VBG (Setareh)	0.72	1.63	1x10 ⁶	0.3515
	On-Off DBG	0.10	13.26	N/A	0.3371
	Variable DBG	0.10	13.26	> 4x10 ¹⁰	0.3371
10ms	On-Off VBG	0.21	9.95	N/A	0.3196
	Variable VBG (Koo)	0.21	9.95	1x10 ⁶	0.3140
	Variable VBG (Setareh)	0.21	9.95	6x10 ⁷	0.3147
	On-Off DBG	1.15	1.15	N/A	0.4218
	Variable DBG	1.15	1.15	N/A	0.4218
15ms	On-Off VBG	0.10	4.20	N/A	0.3485
	Variable VBG (Koo)	0.10	4.20	> 3x10 ⁸	0.3485
	Variable VBG (Setareh)	0.10	4.20	> 9x10 ⁸	0.3485
	On-Off DBG	1.15	1.15	N/A	0.4218
	Variable DBG	1.15	1.15	N/A	0.4218

5.2 Off-Tuning the MR Time Response

The dampers are optimised to a MR time response of 5ms as this offers the largest variety of controls to assess for off tuning. Each of the VBG controls, shown in **Fig. 10(a-c)**, exhibit a reduction in the left peak with an increase in the time delay. The right peaks either exhibit, or would exhibit, an optimum value if the range of off-tuning was increased. In comparison the left peak of the DBG contains an optimum value, with only small changes, shown in **Fig. 10(d)**, while the right peak produces proportionally large responses to the off-tuning. **Fig. 11** plots the peaks of these responses, clarifying the DBGs greater sensitivity to changes in the time response of the MR damping element. Underestimating the time delay in this case would predict a level of performance in excess of what would be achieved in reality.



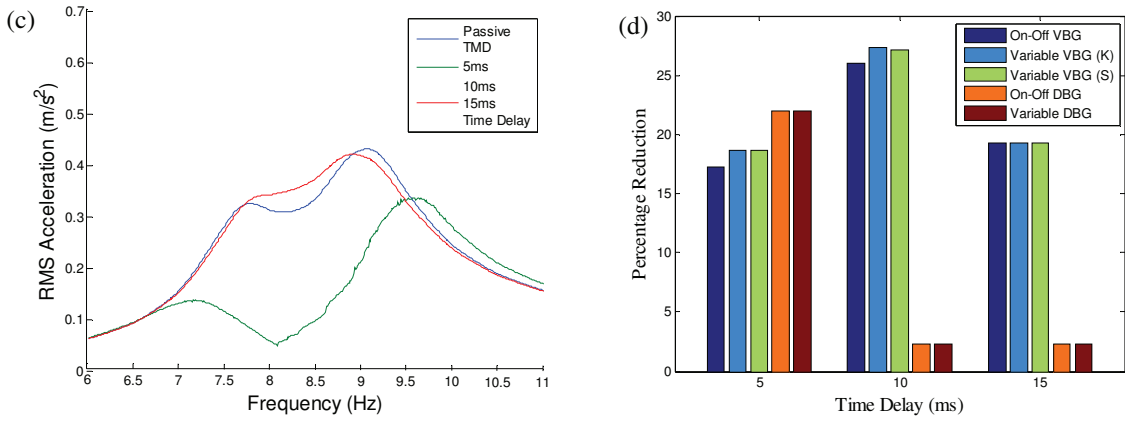


Fig. 9 Frequency profile for an (a) on-off VBG TMD, a (b) variable VBG TMD and a (c) on-off DBG TMD optimised to different time delays, where (d) is the percentage reduction in peak acceleration of each control from the peak acceleration of the passive TMD, with varying time delays [(K) and (S) represent Koo & Ahmadian's and Setareh's method of control respectively]

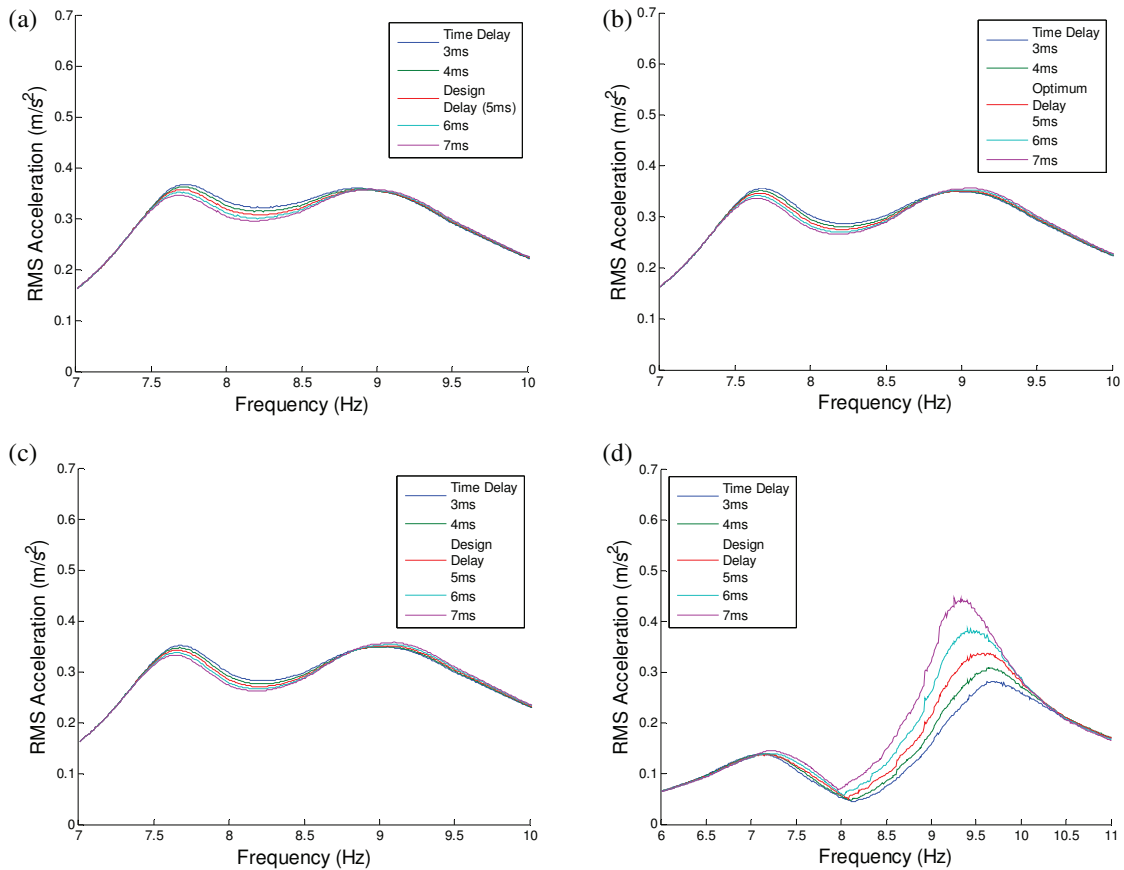


Fig. 10 Performance of the (a) on-off VBG TMD, (b) variable VBG TMD (K), (c) variable VBG (S) and (d) on-off DBG with off-tuned time delays

6 CONCLUSION

This paper presented a computational analysis of a passive tuned mass damper (TMD) and a semi-active tuned mass damper (STMD) in the reduction of the peak acceleration response of a staircase. The passive TMD was optimised using Den Hartog's equations, while the STMD was optimised by varying the off-state and on-state damping ratios and the gain. The parameters of the dampers were varied, with results that were in general agreement with previous studies. The STMD showed substantial gains in performance over the passive TMD in most instances.

When optimising the controls to varying time delays the variable VBG controls, with a 10ms delay, produced the best reduction in acceleration; with the DBG only optimising beyond a passive TMD with the 5ms time delay. Throughout each analysis the variable control technique proposed by Koo and Ahmadian was seen to perform marginally better than the control proposed by Setareh, while the variable DBG at no point offered any increase in performance over the on-off DBG. Further modelling of the time delays are required in which a more accurate time history representation of the response

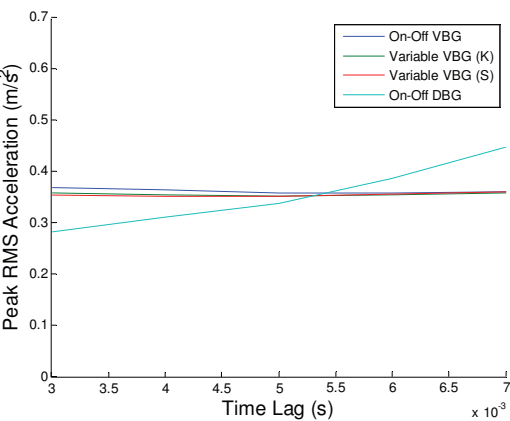


Fig. 11 Peak RMS acceleration with an off-tuned time delay, subject to different control algorithms

could be modelled, as opposed to the simplified on-off delay used here.

Off-tuning the time delay was found to have little effect on the performance of the VBG, but a much greater effect on the DBG, where its performance increased with a decreasing time delay. It would be interesting to extend the range of the off-tuning and also to assess this with other base time delays.

In future research it would be beneficial to calculate the reduction in mass that could be achieved by using a semi-active device over a passive device, while maintaining the same performance.

REFERENCES

- [1] Nyawako, D., Reynolds, P. Technologies for mitigation of human-induced vibrations in civil engineering structures. *Shock and Vibration Digest*. 39 (6). p 465-493. 2007.
- [2] Housner, G., Bergman, L.A., Caughey, T.K., Chassiakos, A.G., Claus, R.O., Masri, S.F., Skelton, R.E., Soong, T.T., Spencer, B.F., Yao, J.T.P. Structural control: Past, present and future. *Journal of Engineering Mechanics*. 123 (9). p 897-971. 1997.
- [3] Occhiuzzi, A., Spizzuoco, M., Serino, G. Experimental analysis of magnetorheological dampers for structural control. *Smart Materials and Structures*. 12 (5). p 703-711. 2003.
- [4] Koo, J.H., Ahmadian, M. Qualitative Analysis of Magneto-Rheological Tuned Vibration Absorbers: Experimental Approach. *Journal of Intelligent Material Systems and Structures*. 18 (12). p 1137-1142. 2007.
- [5] Pinkaew, T., Fujino, Y. Effectiveness of semi-active tuned mass dampers under harmonic excitation. *Engineering Structures*. 23 (7). p 850-856. 2001.
- [6] Koo, J.H., Ahmadian, M., Setareh, M., Murray, T.M. In Search of Suitable Control Methods for Semi-Active Tuned Vibration Absorbers. *Journal of Vibration and Control*. 10 (2). p 163-174. 2004.
- [7] Koo, J.H., Ahmadian, M. A qualitative analysis of groundhook tuned vibration absorbers for controlling structural vibrations. *Proceedings of the Institution of Mechanical Engineers, Part K: Journal of Multi-body Dynamics*. 216 (4). p 351-359. 2002.
- [8] Setareh, M. Floor vibration control using semi-active tuned mass dampers. *Canadian Journal of Civil Engineering*. 29 (1). p 76-84. 2002.
- [9] Setareh, M. Application of semi-active tuned mass dampers to base-excited systems. *Earthquake Engineering and Structural Dynamics*. 30 (3). p 449-462. 2001.
- [10] Ahmadian, M., Pare, C.A. A quarter-car experimental analysis of alternative semiactive control methods. *Journal of Intelligent Material Systems and Structures*. 11 (8). p 604-612. 2001.

- [11] ISO. ISO 10137: Bases for design of structures - Serviceability of buildings and walkways against vibrations. *International Standard Organisation (ISO)*. Switzerland, 2007.
- [12] Smith, A.L., Hicks, S.J., Devine, P.J. SCI Publication P358: Design of Floors for Vibration: A New Approach (Revised Edition, February 2009). *The Steel Construction Institute*. Ascot, UK, 2009.
- [13] Lyons, H. *EUreka: the European Union in Figures*. 2002.
http://www.statistics.gov.uk/downloads/horizons/Horizons23_Dec02.pdf [Accessed 24 February 2010]
- [14] Kerr, S.C., Bishop, N.W.M. Human induced loading on flexible staircases. *Engineering Structures*. 23 (1). p 37-45. 2001.
- [15] Bishop, N.W.M., Willford, M., Pumphrey, R. Human induced loading of flexible staircases. *Safety Science*. 18 (4). p 261-276. 1995.
- [16] Den Hartog, J.P. *Mechanical Vibrations*. *McGraw-Hill Inc*. New York, USA, 1947.
- [17] LORD *LORD Technical Data*. undated. <http://www.lordfulfillment.com/upload/DS7016.pdf> [Accessed 2 March 2010]

A System Identification Based Approach For Estimating Modal Frequencies of Bridges Under Environmental Influence

H. Nandan

Graduate student,

Department of Engineering Science and Mechanics,

Virginia Polytechnic Institute and State University Blacksburg, VA-24061, USA

hndanand@vt.edu

M. P. Singh

Program Director and Preston Wade Professor,

Hazard Mitigation and Structural Engineering,

National Science Foundation Arlington, VA-22230, USA

mpsingh@nsf.gov

Abstract

For health monitoring of bridge structures, vibration response-based methods offer several advantages due to the global nature of the approach. Vibration based structural health monitoring identify damage by detecting the abnormal changes in the dynamic characteristics such as the frequencies and mode-shapes extracted from the vibration response. However, the environmental fluctuations in temperature, radiation, convection, and humidity may change the dynamic characteristics of a bridge structure sometime more than those caused by structural damage and thus mask the damage effects. A method is being demonstrated to estimate the change in the dynamic characteristics directly from the body temperature measurements to separate them from those caused by the damage. In this paper, we use the stochastic subspace system identification technique to estimate the frequency, given the temperature records at specific locations within the bridge. The data used for development and validation of the presented approach has been generated using a finite element analysis capable of translating thermal environmental condition. In this paper, the finite element analysis setup and the identification approach used are presented. It is observed that the temperature and frequency records have prominent yearly and diurnal trends and the relation between temperature values and modal frequencies is nonlinear. A straightforward use of the stochastic identification approach does not provide acceptable frequency estimations, especially when tested on data for different environmental conditions. However, these observed seasonal and diurnal trends motivate us to use filters to improve the results of the identification model over an extended duration spanning the seasonal variations. The identified model is tested for both reproduction and generalization performances over seasonally varying thermal conditions and, in spite of nonlinear effects, the model is shown to provide very good estimates of the system frequencies in the simulation study even under the influence of large measurement noise.

Introduction

The need to safely operate and maintain civil infrastructure effectively and continuously requires cost effective and reliable automated algorithms to detect localizes and quantifies damage. The techniques that have been currently researched and developed can be broadly classified as local and global. Local techniques are much more accurate but are expensive and as the name suggest requires fair amount of knowledge of location of damage. The global techniques rely on global responses to detect, locate and quantify damage. Moreover, a combination of these two class of technique can be used to achieve a efficient and accurate structural health monitoring (SHM) strategy. Vibration based techniques belongs to class of global techniques. Vibration response-based techniques can be further divided in to model updating approaches and modal parameter-based approaches. In a model updating approach, one estimates the changes in system matrices from the measured response by using some optimization methods. In modal parameter-based approach, one first extracts modal properties such as frequencies and mode shapes for use in the damage identification. This study is concerned with the modal parameter-based approaches, as the accuracy of modal parameter based approach is highly dependent on the accuracy of the calculated modal parameter. It is well established by now that the modal frequencies and mode shapes serves as appropriate feature for damage detection, but this set of damage features are also affected by thermal environmental conditions.

Environmental and operational variations such as varying temperature, loading and boundary conditions can affect the dynamic response of the structure to an extent that it cannot be ignored. It is observed ([1]) that environmental factors can produce changes in modal frequencies which can often be big enough to mask the change in modal frequency due to actual damage in I-40 Bridge over Rio Grande in New Mexcico. Similar conclusion was reported by using the experimental data collected on Z-24 Bridge ([2]) in Switzerland. Field tests on a steel-concrete composite two-span bridge reported temperature induced variations in modal frequency of up to 2% in a given day ([3]). The problem of SHM is further complicated by interfering environmental and operational condition.

A linear adaptive filter to predict the frequency of Almosa Canyon Bridge (in New Mexico) given the recorded temperature on the bridge was proposed in [4]. The adaptive filter weights were obtained by a training process which included data from a summer day (one sample per hour for 24 hours) in 1996 and the filter was tested on data (one sample per hour for 12 hours) from approximately the same temperature regime around the same time in 1997. A further study in [5] employed a combination of AR (Auto Regressive) and ARX (Auto Regressive with eXogeneous inputs) modeling to extract damage sensitive features, auto-associative neural network to separate the damage and environmental effects, and hypothesis testing called sequential probability ratio test to infer about the damage state. Although motivated by bridge damage detection problem, the example problems of identification for a computer hard drive and a multi degree of freedom model are presented. Another study ([2]) used ARX model to determine the effect of temperature change on the frequency. The authors were able to identify damage by comparing the first four recorded modal frequencies to the modal frequencies and their respective bounds estimated by an identified ARX model. They observed a bilinear relationship between temperature and frequency with the transition around $0^{\circ}C$. In this analysis the low-temperature data were dropped to avoid the bilinear relation between temperature and frequency. The main focus of this study was damage detection in presence of environmental effects and localization and quantification of the damage were not addressed. Support vector machine are used to construct a nonlinear regression model ([6] and [7]) which relates modal frequencies to recorded temperature. Data recorded at Ting Kau Bridge in Hong Kong, which is a multi-span cable-stayed bridge carrying a dual three-lane carriage-way was used in [6]. The data used was 770 hours long that was collected at every hour. Alternate points (385 points) in the recorded data were used for regression parameter estimation and the left over points for testing the model. The results show sufficient degree of correspondence between the estimated and recorded frequency. Same data set is used in [7], but improved by applying PCA to reduce the size of measurement quantities needed for identification purposes.

Another set of techniques based upon principal component analysis (PCA) have been researched in [8], [9], [10], [11] with good potential for damage detection under varying environmental condition. The underlying assumption for applying PCA is that temperature induced variations in data are orthogonal to changes induced by damage. Use of PCA was demonstrated in [8] on the data recorded on a simulated three span bridge and a scaled down wooden bridge case. In the companion paper ([9]), use of local PCA was demonstrated for dealing with nonlinearities in the temperature-frequency dependence. The method involved a two-step procedure, namely, clustering of the data space into several regions and then the application of PCA in each local region. The authors also applied their method to Z-24 Bridge data. PCA was applied to the time series data of identified stiffness values of members for a 2 bay \times 2 bay, 4 story simulated model of a steel building (IASCM-ASCE benchmark problem) in [10]. Nonlinear PCA through the use of auto associative neural network was studied in [11] to detect abnormal variations in stiffness values. The

technique was demonstrated on a simply supported bridge model with nine line-elements including four elements representing concrete decks, three elements representing steel decks paved with asphalt, and two elastic springs. The author included temperature, humidity and varying boundary conditions in his simulations. Though the model, which has been used, is not a true representation of actual complexity of the bridge, the method demonstrates the potential to detect anomalous changes.

Most of the studies referred above are experimental studies and thus limits the testing of algorithm for robustness properties. The limitation is a practical constraint as most of the time it is not possible to damage a fully functional structure or and even in cases where it is possible there is not much freedom to repeatedly to do so without being affected by the previous state of the bridge. On the other extreme, researchers have used simplified beam models to represent concrete girder, which limits the spatial effect. Thus a numerical model is needed that can mimic the effect of environmental condition on modal characteristic which are often used for vibration-based SHM. Till recently the main aim of applying finite elements based thermal analysis to an actual bridge is to generate data for design purposes ([12], [13], [14]). A step further is needed to enhance these models for calculating the temperature dependent modal frequency variations. It is important to understand and take into account the effect of environmental variable when developing SHM techniques to be applied in real world scenario. In this study an effort has been made to study the mechanism by which environmental temperature variations effect the modal frequencies. As an example, we consider a typical medium span concrete box girder and T-beam systems subjected to the external thermal environment defined by actual recorded data at a site in Elizabeth City, North Carolina, USA ([15]).

Finite Element Analysis

The modal characteristics are known to be effected by various environmental factors such as thermal conditions, humidity, moisture, freezing, thawing etc. Though all factors have their own share of influences, in this study environmental thermal influences are considered. This section briefly explains the step involved in finite element analysis aimed at translating thermal environmental conditions to modal frequency variations. The analysis is applied to two kinds of concrete bridge decks and the results are presented. These results are used in subsequent data driven studies to develop a computationally inexpensive damage detection process.

Numerous techniques are available to extract modal frequencies from vibration response of a structure. Therefore this analysis have been setup assuming that modal frequency estimation can be performed using the existing techniques. The process of calculating modal frequencies begins with defining the geometric dimensions of the bridge deck, temperature dependent structural properties and thermal properties of materials corresponding to each component of the bridge deck. The next step is to define a mesh with density which can provide accurate enough modal frequencies while maintaining an acceptable computational load. While setting up the mesh the main aim of executing this analysis is to capture the trends in modal frequencies. In this simulation the modal frequency is calculated at every hour, thus the temperature distribution has to be calculated at end of every hour. To start the analysis, initial condition on each node is needed, which is calculated by applying the appropriate boundary condition using the environmental records at zero hours. The solar irradiance is applied on the top surface as heat flux, while the ambient temperature is used as the bulk temperature for convection boundary condition that is applied to all open surfaces. Once the initial condition is established a transient thermal analysis for one hour duration is conducted using a boundary condition applied in the above explained manner and linearly varying over the hour duration. The temperature obtained at the end of one hour is then used to calculate stiffness matrix using temperature dependent modulus of elasticity. This analysis is then followed by a thermo-elastic analysis, which computes the amount of stress generated due to given temperature field and physical boundary conditions. The stress analysis can be done independently of thermal analysis because the fastest dominant frequency in temperature are much smaller that the structural frequency. The stress matrix calculated is then used to calculate the geometric stiffness which is then combined with structural stiffness matrix and used by the modal analysis step. Once the modal analysis is complete the transient analysis is conducted over the next hour using thermal distribution at end of first hour and linearly varying boundary conditions between first and second hour. This is then followed by stress and modal analysis. The cycle is repeated till the desired time and at the end of each cycle temperature at some particular nodes and modal frequencies are recorded into a file.

The analysis is conducted on simply supported slab to validate the analysis procedure. The data used for validation has been taken from [16]. The dimension of the slab is shown in [figure 1](#), the environmental temperature and radiation records are shown in [figure 3](#). For this example the direct solar irradiance is used as the heat flux value on the top surface and the diffused solar irradiance is used as heat flux on side and bottom surfaces.

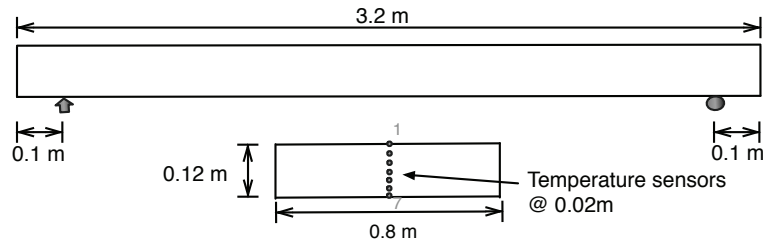


Figure 1: Dimension and support configuration of the slab.

Figure 3(a) and 3(b) shows the variation of modulus of elasticity of concrete ([17], [18]) and asphalt [19]. Though the asphalt layer has not been used in this example, but it has been used in box and T-beam girder whose results have been discussed later in this section. Other required parameter values are: Concrete mass density = 2316.6 Kg/m^3 , coefficient of thermal conductivity for concrete = $1.74 \text{ W/m}^\circ\text{C}$, specific heat value for concrete = $960 \text{ J/Kg}^\circ\text{C}$ and coefficient of thermal expansion = $13 \times 10^{-6} /^\circ\text{C}$. The dependence of the coefficient of convection on wind speed v is represented by equation 1 ([20], [21]). In absence of wind velocity records a constant wind velocity of 3m/s has been assumed.

$$\beta = \begin{cases} 5.6 + 4 \times v & v \leq 5\text{m/s} \\ 7.2 \times v^{0.78} & v > 5\text{m/s} \end{cases} \quad (1)$$

The recorded temperature and calculated temperature have been shown in figure 4 and they show good correspondence. The recorded and calculated first modal frequency have been compared in figure 5. Note that the calculated frequency is a deterministic quantity, while the recorded frequency is a estimated quantity and will have errors associated with estimation. These results show that the analysis has the capability of estimating modal frequency under thermal environmental condition.

Few of the commonly used bridge girders are studied using the above mentioned finite element analysis setup. The cross-section dimensions are shown in figure 6. The box girder has a length of 34 m and the T-beam girder has a length of 22.5 m, both the beams are simply supported. A 5 cm thick layer of asphalt is applied on both bridge girders whose temperature dependent modulus of elasticity property is shown in figure 3(b), the concrete modulus of elasticity variation is given in figure 3(a). Other required parameter values are: Concrete mass density = 2400 Kg/m^3 , asphalt mass density = 2200 Kg/m^3 , coefficient of thermal conductivity for concrete = $1.8 \text{ W/m}^\circ\text{C}$ and for asphalt = $1.45 \text{ W/m}^\circ\text{C}$, specific heat value for concrete = $808 \text{ J/Kg}^\circ\text{C}$ and for asphalt = $1024 \text{ J/Kg}^\circ\text{C}$. The dependence of the coefficient of convection on wind speed v is again given by equation 1. The thermal boundary conditions on the boundary elements have been defined using environmental records as shown in figure 7.

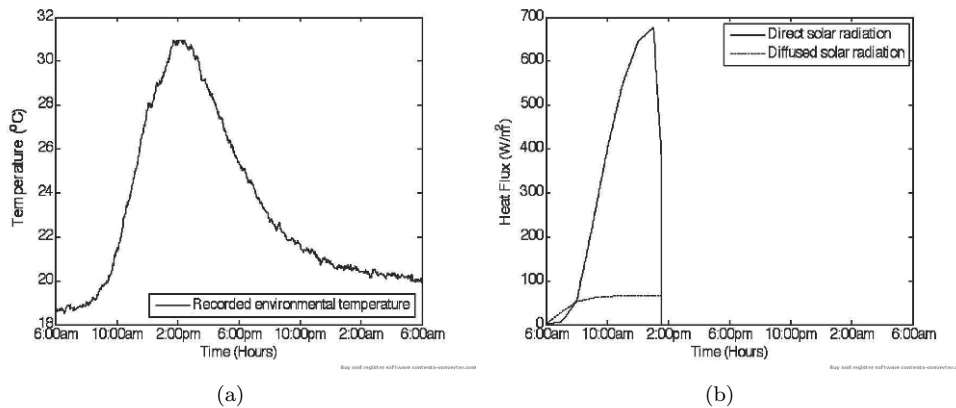


Figure 2: Site (a) temperature, (b) solar irradiance records.

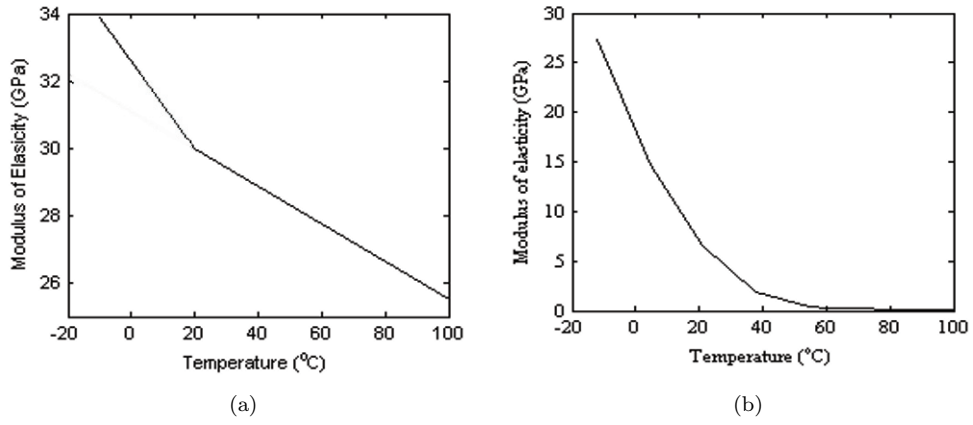


Figure 3: Modulus of elasticity (a) concrete, (b) asphalt.

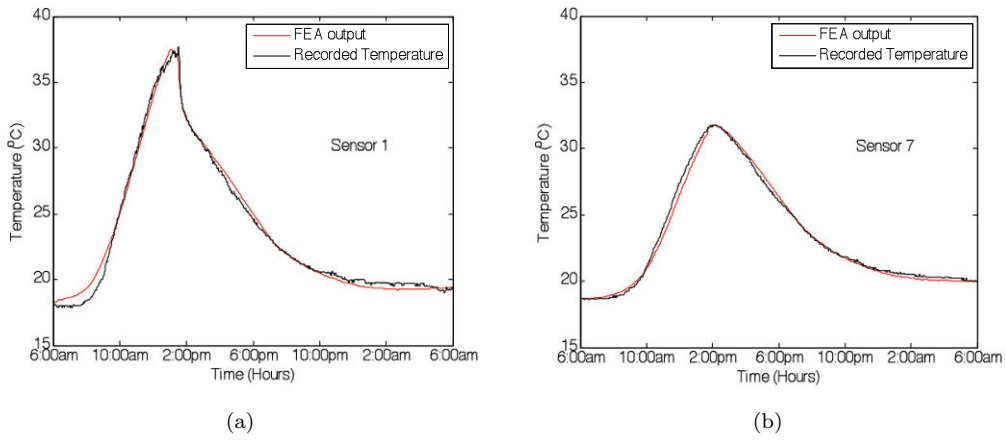


Figure 4: Recorded and estimated temperatures at top and bottom sensors attached to the slab.

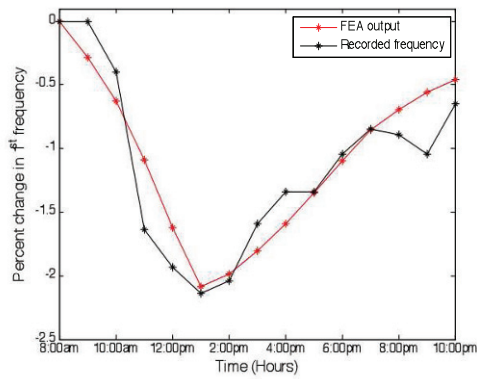


Figure 5: Percentage change in first modal frequency.

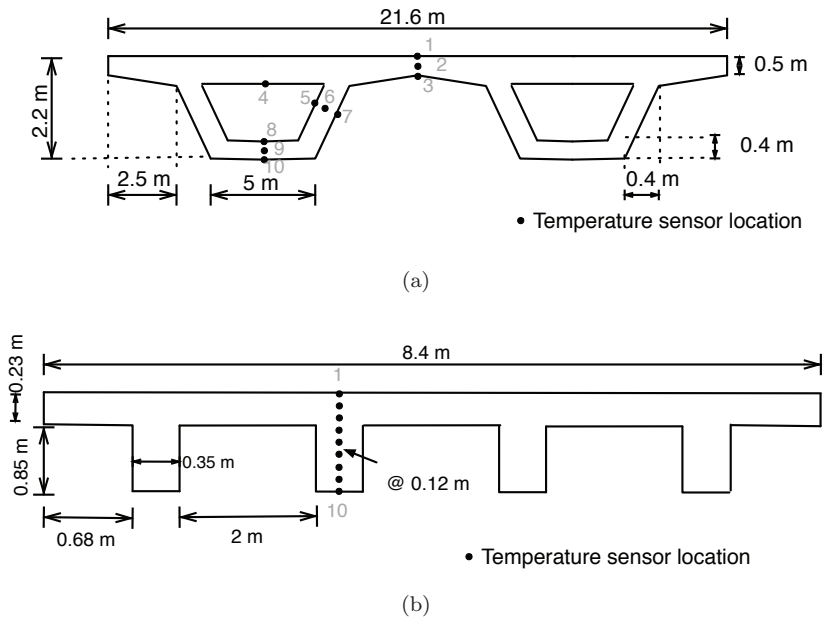


Figure 6: Dimension of bridge girder used in the study.

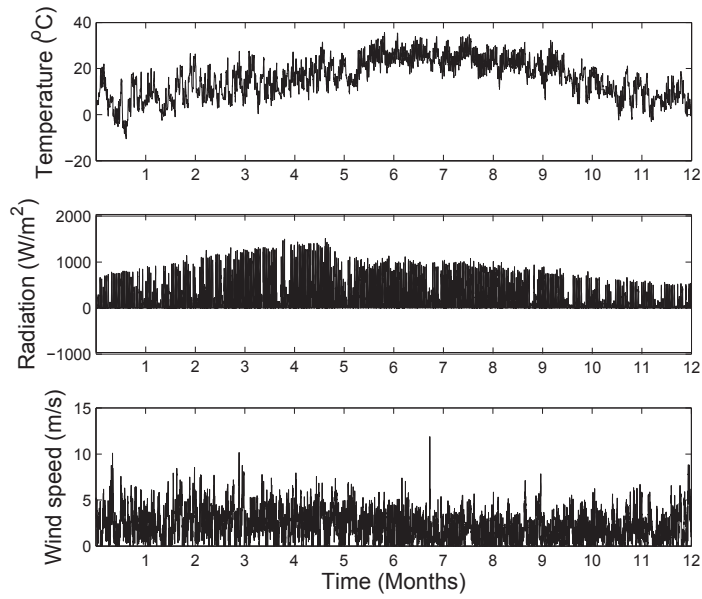


Figure 7: Environmental thermal conditions over a duration of one year in Elizabeth City, North Carolina, USA.

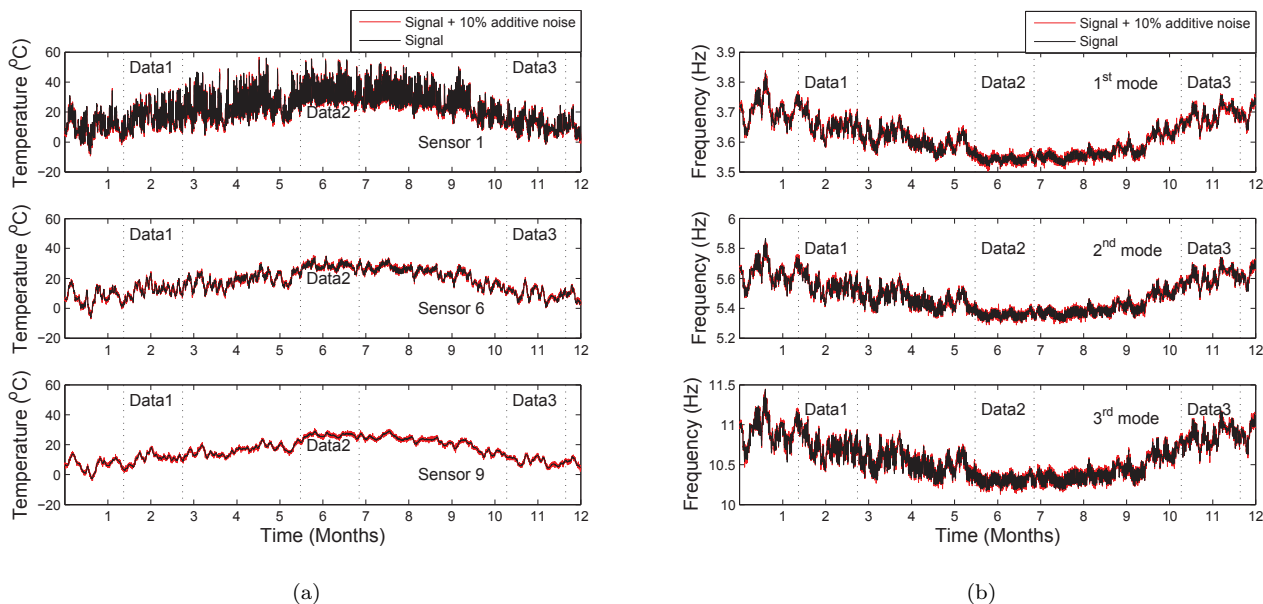


Figure 8: (a) Temperature values recorded within box girder at specified sensor locations, (b) Modal frequency of simply supported box girder sampled at a rate of one hour.

Although temperature at all the indicated sensor location have been recorded, but for the purpose of brevity only few records are plotted in figure 8(a), similarly in the case of modal frequencies first ten frequencies have been recorded but only three have been plotted in figure 8(b). Signals with additive white noise are also plotted in red and the full year data has been divided into three smaller data sets, these features in the plot has nothing concerning the finite element simulation, but will be utilized in the next section. Similar figures are plotted for the T-beam example in figure 9. It is seen through data analysis that both temperature and modal frequency records have annual and daily harmonics trends among few others when seen in frequency domain. To develop a more objective and computationally inexpensive technique for structural health monitoring we focus on system identification technique which can perform the tasks of SHM in the presence of environmental influences.

System Identification Based Approach

In this section a system identification based approach is adopted to create a numerical representation of the healthy structure. Damage detection can be performed by studying the deviations of the output quantity from the baseline model. In this section subspace identification is used and hence the identified model is in the state space form. The identified model is of the form:

$$\begin{aligned}
 \mathbf{x}_{k+1} &= A\mathbf{x}_k + B\mathbf{u}_k + \mathbf{w}_k \\
 \mathbf{y}_k &= C\mathbf{x}_k + D\mathbf{u}_k + \mathbf{v}_k \\
 \text{with: } \mathbf{x}_1 &= \tilde{\mathbf{x}}_o \quad k = 1, 2, 3, \dots
 \end{aligned} \tag{2}$$

where \mathbf{u} is $(p \times 1)$ input temperature vector, \mathbf{y} is $(q \times 1)$ output modal frequency vector, \mathbf{x} is $(n \times 1)$ the state vector, A is $(n \times n)$ system dynamics matrix, B is $(n \times p)$ input transform matrix, C is $(q \times n)$ output matrix and D is $(q \times p)$ direct feed-through matrix. Here p is the number of input temperature, q is the number of output frequencies and n is the number of states or order of the model. The term w_k is a $(n \times 1)$ vector which represents uncertainties in input-output relation and is called as process-noise. The term v_k is a $(q \times 1)$ vector which represents sensor noise and is known as measurement-noise. The state vector and matrices are abstract quantities in the model and in general may not have any physical meaning.

N4SID (Numerical Algorithms for State-Space Subspace Identification) algorithm has been used for subspace identification (it is noted that the identified state space model is linear and time-invariant). The mathematical

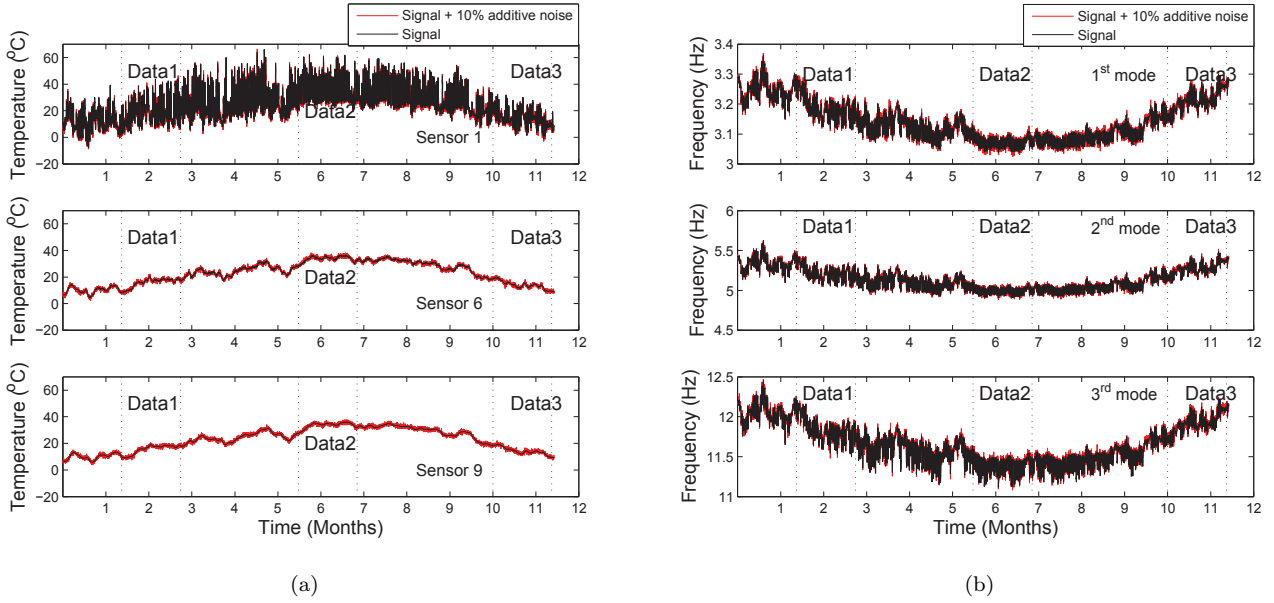


Figure 9: (a) Temperature values recorded within T-beam girder at specified sensor locations, (b) Modal frequency of simply supported T-beam girder sampled at a rate of one hour.

underpinnings of the algorithm are explained in references [22] and [23]. Herein the use of the model based on equation 2 implies that a linear model is used to represent the temperature-frequency relationship. However, it is observed that scaling the temperature by twice does not result in proportional scaling of frequency and hence the temperature-frequency relationship is not linear. It is difficult to quantitatively comment on suitability of using a linear model to represent a nonlinear relation but it is assumed that these nonlinear effects are small enough to be treated as process noise. The suitability of such application is justified by the results.

To define the structure of state-space model in equation 2 completely, number of inputs (p), number of outputs (q), model order (n) are to be specified and initial state vector ($\tilde{\mathbf{x}}_o$) is to be assumed or determined from the simulation data. The problem studied in this section has ten temperature reading, thus number of inputs is ten and four frequencies are considered, thus the number of outputs is four. Model order selection is done by comparing the performance of system in different region of operation is adopted. To achieve this task the measure of performance is chosen to be ‘goodness of fit’ value as given by equation 3. Here y is simulation output of the identified model and y_{target} is the measured output against which the simulation output has to be judged. The goodness of fit value provides a measure to explain the percentage of the output variation that is explained by the model and it can vary between a large negative value, to a value of 100%.

$$GOF = 100 \times \left(1 - \frac{\|y - y_{target}\|_2}{\|y_{target} - \text{mean}(y_{target})\|_2} \right) \%, \quad \|\cdot\|_2 = 2 \text{ norm} \quad (3)$$

To compute goodness of fit for a given model and input-output data set, the model needs to be simulated with the given input data (u) and some initial state vector ($\tilde{\mathbf{x}}_o$) to compute the output (y). The value of initial state vector is calculated such that it minimizes the one step prediction error norm between the model output and recorded output data for specified number of starting data points. The selection of initial state estimation length is also done parametrically by comparing the performance in both seen and unseen data. In addition to testing the capabilities of N4SID for finding temperature-frequency relation, the method is also tested for robustness by using input-output data with additive gaussian-white-noise whose standard deviation is 10% of the standard deviation of the signal. Figure 8 shows the input and output of the system. The figure shows three data regions namely ‘Data1’, ‘Data2’ and ‘Data3’, here ‘Data1’ and ‘Data3’ belongs to the colder duration of the year while ‘Data2’ belongs to the warmer duration of the year.

To elaborate on the discussion presented above results of box girder bridge with additive gaussian white noise has been presented in detail, while only final results are being presented for T-beam girder. Figure 10 presents the

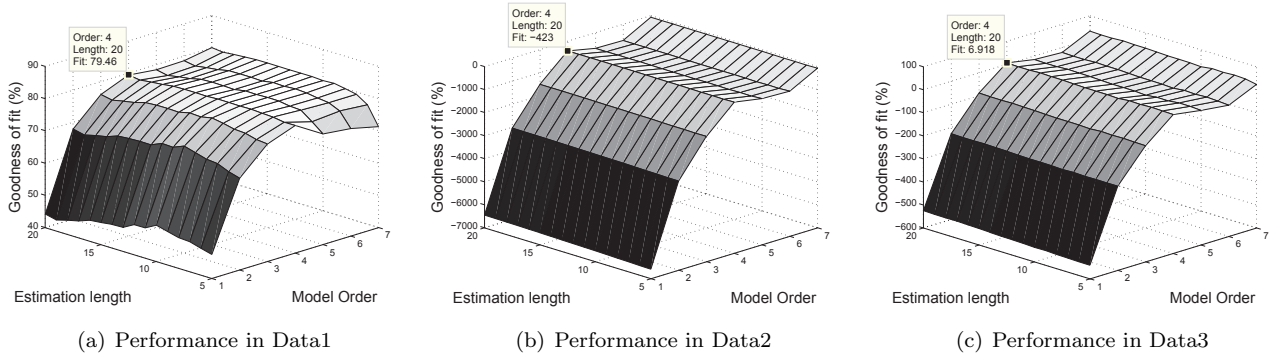


Figure 10: Reproduction and generalization performance of model identified using Data1 for first modal frequency.

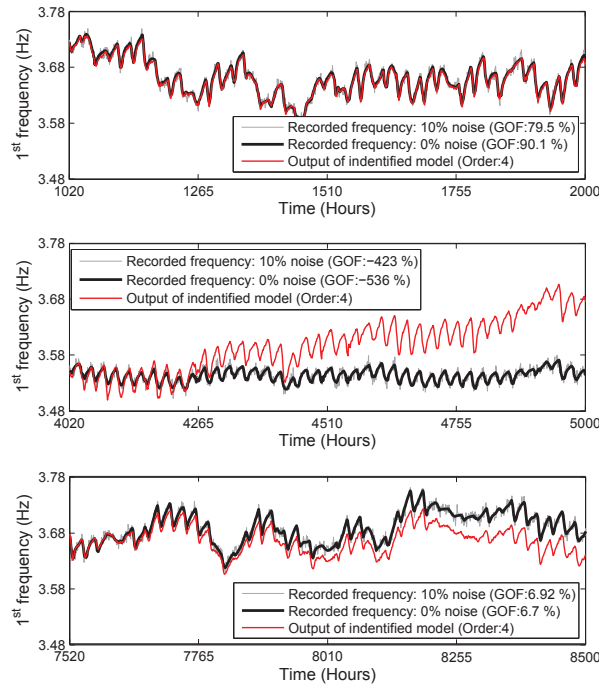


Figure 11: Comparison of recorded and estimated first modal frequency on different data regions with a model of order 4 identified using ‘Data1’.

performance of model identified using ‘Data1’ and then tested for reproduction and generalization performance. It is observed that the model order with best performance in reproduction is also the best for generalization. Also the model identified using the winter duration data (‘Data1’) does not perform well in summer duration data (‘Data2’). It is seen through time domain comparison that not only the generalization performance is poor, the estimated frequency starts to drift away from the recorded data in previously unseen data regions.

To improve the performance of the model identified through subspace identification process it is observed that there are seasonal trends in the data which are slow enough that do not need to be related using the dynamic model such as state space. Thus the slowly varying or low frequency components in both temperature and modal frequency records can be filtered out and only the remainder is used in the identification process. Similarly when simulating

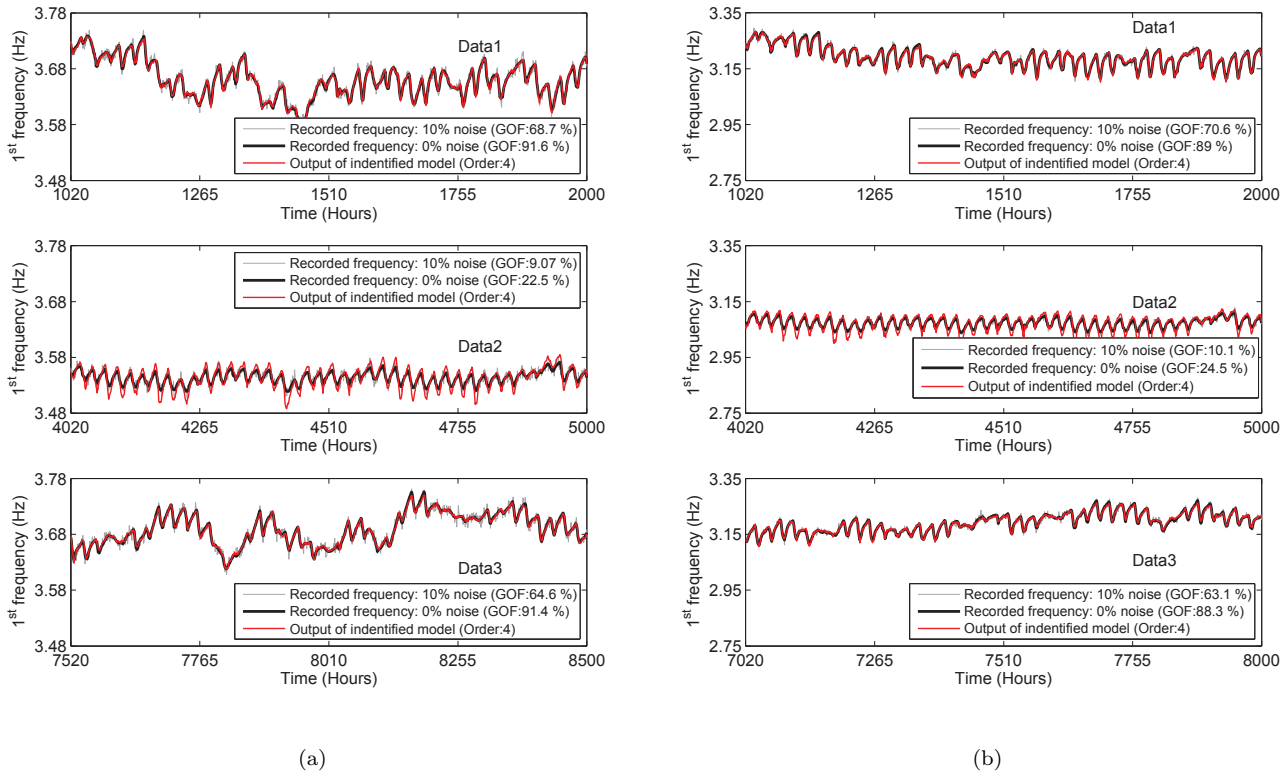


Figure 12: Comparison of recorded and estimated first modal frequency on different data regions with a model identified using ‘Data1’ (a) model order 4 used for box girder, (b) model order 5 used for T-beam girder.

with the identified model the the low frequency component should be striped off the input temperature record and the output should be compared to high frequency content of the modal frequency record. For the purpose of presenting the result the low frequency content of the modal frequency record has been added back to model output and plotted in figure 12. To filter out the low frequency component a FIR filter has been used with cutoff frequency of $1/8766$ (1/Hr) and $100/8766$ (1/Hr), the order of the FIR filter is 400 and hence it introduces a group lag of 200 hours which is approximately 8 days. Though damage detection has not been attempted using this estimation, but it is planned to be attempted using the model output data and comparing it with high frequency content in the modal frequency data.

Conclusion

This paper presents a computational framework for relating environmental thermal condition variations to the variations in modal frequencies. The finite element approach discussed in the first part of this paper can be used to relate environmental thermal variations to modal frequency changes through the use of temperature dependent modulus of elasticity property and geometric stiffness effects. As demonstrated in this paper and reported in various other experimental studies modal frequencies are susceptible to the outside thermal environment. Thus, it is imperative to include these effect in health monitoring schemes that rely on modal frequencies. Finite element based simulation is subjected to availability of exact mesh model, accurate material models and high-end computational hardware. In many cases one or more of above factors may not be available, thus we need a strategy which is objective and requires least human intervention. System identification is a promising answer for such an approach. As seen in the second half of this paper that linear system identification has significant potential in estimating the modal frequencies even in presence of model uncertainties and measurement noise. This research is on-going and various method are being tested to improve the performance of the discussed system identification technique, some of which have demonstrated

potential for improvement and will be presented in a subsequent paper.

Acknowledgement

This research is supported by National Science Foundation through grant number CMMI-0700558 with Dr. S. C. Liu and Dr. D. Foutch as the Program Directors. This support is gratefully acknowledged. Any opinion, findings, and conclusions or recommendations expressed in this study are those of the writers and do not necessarily reflect the views of the National Science Foundation. We also thank Dr. Yong Xia for making the details of his research available for use in this study.

References

- [1] C. Farrar, W. Baker, T. Bell, K. Cone, T. Darling, T. Duffey, A. Eklund, A. Migliori, Dynamic characterization and damage detection in the I-40 bridge over the Rio Grande, Tech. Rep. LA-12767-MS, Los Alamos National Laboratory (1994).
- [2] B. Peeters, G. D. Roeck, One-year monitoring of the Z24-bridge: environmental effects versus damage events, *Earthquake Engineering and Structural Dynamics* 30 (2001) 149 – 171.
- [3] A. Mosavi, E. Sumner, R. Seracino, S. Rizkalla, Effect of temperature on modal characteristics of steel-concrete composite bridge structures: Field testing, in: *Proceeding of the 4th International Conference on Structural Health Monitoring on Intelligent Structure*, Zurich, Zurich, Switzerland, 2009.
- [4] H. Sohn, M. Dzwonczyk, E. G. Straser, A. S. Kiremidjian, K. H. Law, T. Meng, An experimental study of temperature effect on modal parameters of the Alamosa Canyon Bridge, *Earthquake Engineering & Structural Dynamics* 28 (8) (1999) 879 – 897.
- [5] H. Sohn, K. Worden, C. R. Farrar, Statistical damage classification under changing environmental and operational conditions, *Journal of Intelligent Material Systems and Structures* 13 (2002) 561 – 574.
- [6] Y. Ni, X. Hua, K. Fan, J. Ko, Correlating modal properties with temperature using long-term monitoring data and support vector machine technique, *Engineering Structures* 27 (12) (2005) 1762–1773.
- [7] X. G. Hua, Y. Q. Ni, J. M. Ko, K. Y. Wong, Modeling of temperature-frequency correlation using combined principal component analysis and support vector regression technique, *Journal of Computing in Civil Engineering* 21 (7) (2007) 122 – 135.
- [8] A.-M. Yan, G. Kerschen, P. D. Boe, J.-C. Golinval, Structural damage diagnosis under varying environmental conditions—part I: A linear analysis, *Mechanical Systems and Signal Processing* 19 (4) (2005) 847 – 864.
- [9] A.-M. Yan, G. Kerschen, P. DeBoe, J.-C. Golinval, Structural damage diagnosis under varying environmental conditions—part II: local PCA for non-linear cases, *Mechanical Systems and Signal Processing* 19 (2005) 865–880.
- [10] D. F. Giraldo, S. J. Dyke, J. M. Caicedo, Damage Detection Accommodating Varying Environmental Conditions, *Structural Health Monitoring* 5 (2) (2006) 155–172.
- [11] T.-Y. Hsu, C.-H. Loh, Damage detection accommodating nonlinear environmental effects by nonlinear principal component analysis, *Structural Control and Health Monitoring* 17 (3) (2010) 338–354.
- [12] S. Moorthy, C. W. Roeder, Temperature-dependent bridge movements, *Journal of Structural Engineering* 118 (4) (1992) 1090–1105.
- [13] F. A. Branco, P. A. Mendes, Thermal actions for concrete bridge design, *Journal of Structural Engineering* 119 (8) (1993) 2313–2331.
- [14] P. J. Barr, J. F. Stanton, M. O. Eberhard, Effects of temperature variations on precast, prestressed concrete bridge girders, *Journal of Bridge Engineering* 10 (2) (2005) 186–194.

- [15] Renewable Resource Data Center. CONFRRM solar radiation data: Elizabeth city state university [online] (December 2009) [cited April 11, 2010].
- [16] Y. Xia, Z.-L. Wei, X.-Q. Chen, Y.-L. Xu, Temperature effect on structural vibration properties and damage detection, in: Proceedings of Fifth International Workshop on Advanced Smart Materials and Smart Structure Technology, 2009.
- [17] S. W. Kang, S.-G. Hong, Behavior of concrete members at elevated temperatures considering inelastic deformation, *Fire Technology* 39 (2003) 9–22.
- [18] G. C. Lee, T. S. Shih, K. C. Chang, Mechanical properties of concrete at low temperature, *Journal of Cold Regions Engineering* 2 (1) (1988) 13–24.
- [19] H. A. Ali, A. Lopez, Statistical analyses of temperature and moisture effects on pavement structural properties based on seasonal monitoring data, *Transportation Research Record* 1540 (1996) 48–55.
- [20] D. P. Bentz, A Computer Model to Predict Surface Temperature and Time-of-Wetness of Concrete Pavements and Bridge Decks, National Institute of Standards and Technology (August 2000).
- [21] E. Schlangen, User Manual of HEAT-MLS Version 8.5, FEMMASSE, The Netherlands (2000).
- [22] L. Ljung, System Identification: Theory for the User (2nd Edition), Prentice Hall PTR, 1998.
- [23] P. V. Overschee, B. D. Moor, N4SID: Subspace algorithms for the identification of combined deterministic-stochastic systems, *Automatica* 30 (1) (1994) 75 – 93.

FEATURE ASSIMILATION IN STRUCTURAL HEALTH MONITORING APPLICATIONS

Saurabh Prabhu¹, Jordan Supler² and Sez Atamturktur³

ABSTRACT

Next generation structural health monitoring (SHM) technology for early detection and mitigation of adverse structural effects holds the potential to aid in the proactive maintenance of various civil structures. SHM techniques eliminate the need for *a priori* knowledge of damage, and thus the need for access to the damaged portion of the structure. The underlying principle behind SHM is measuring changes in the system vibration response, which would ultimately indicate changes in the physical properties due to structural damage. A challenge to the successful application of SHM to civil structures is the selection of suitable vibration response features (damage indicators), that are highly sensitive to the presence and extent of damage, while having low sensitivity to ambient noise. Since it is not feasible (nor possible) to damage an in-service structure for research purposes, a scaled arch model made of PVC is utilized for laboratory testing in this study. The vibration response is measured both for the undamaged arch and then for the damaged arch once cracks are introduced to the system. The effect of noise on the vibration measurements is also studied.

Keywords: Vibration Testing, Data Fusion, Damage Sensitivity, Noise Sensitivity

1. INTRODUCTION

In current practice, structural inspection is completed either by visual observations or by localized techniques. Visual observations are highly dependent on the subjective opinion and experience level of the inspector. On the other hand, localized techniques invariably require both *a priori* knowledge of the vicinity of damage and direct access to the damaged portion of the structure. Also, localized methods typically exhibit high dependency to testing conditions. Both visual and localized techniques are labor intensive, time consuming and require experienced personnel. As evidenced by the deficiencies of current inspection techniques, development of global diagnostic methods is necessary to effectively maintain structures and to ensure the safety of their occupants.

Structural Health Monitoring (SHM) is a global monitoring technique developed to diagnose damage in a structural system prior to it reaching a critical stage. Although SHM is demonstrated to be a promising method for monitoring modern civil engineering systems of reinforced concrete or steel, the application of this new technology to other structural systems, such as unreinforced masonry, is still considered to be unresolved [1]. Unlike numerous studies that have focused on beam and plate-like systems, studies on curved structural elements commonly found in masonry construction, such as arches, domes, vaults, and buttresses, have been limited. Transforming SHM to a viable inspection solution for the assessment and inspection of masonry structures would only be possible by gaining a thorough understanding of the sensitivity of vibration response in curved structural systems. In this study, we investigate the vibration response of an idealized arch model, a very common structural form for masonry construction.

The underlying principle of SHM is straightforward. The onset of damage in a built system modifies the structural properties, such as mass, stiffness and damping, which in turn alters the vibration features of the system. Focusing on this indirect relationship between the structural damage and experimentally observed changes in the vibration response, SHM aims to detect the onset of damage as well as to determine damage characteristics.

¹ Graduate Student, Clemson University, Department of Civil Engineering, 110 Lowry Hall, Box 340911, Clemson, South Carolina 29634-0911, U.S.A. [Phone: 864-643-9135](tel:864-643-9135). [Fax: 864-656-2670](tel:864-656-2670). [E-mail: saurabp@clemson.edu](mailto:saurabp@clemson.edu).

² Graduate Student, Clemson University, Department of Civil Engineering, 110 Lowry Hall, Box 340911, Clemson, South Carolina 29634-0911, U.S.A. [Phone: 843-992-4879](tel:843-992-4879). [Fax: 864-656-2670](tel:864-656-2670). [E-mail: jsupler@clemson.edu](mailto:jsupler@clemson.edu).

³ Assistant Professor, [Mailing: Clemson University, Civil Engineering Department, 110 Lowry Hall, Box 340911, Clemson, South Carolina 29634-0911, U.S.A.](mailto:sez@clemson.edu) [Phone: 864-656-3000](tel:864-656-3000). [Fax: 864-656-2670](tel:864-656-2670). [E-mail: sez@clemson.edu](mailto:sez@clemson.edu).

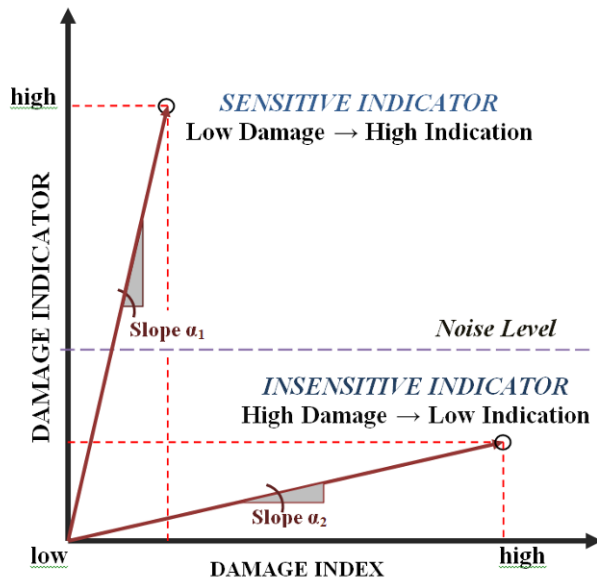


Figure 1: Sensitivity of damage indicators to varying levels of damage.

In an ideal situation, the experimentally observed changes in vibration response are directly correlated with the desired damage characteristics, which include existence, severity, type and location of damage. However, attempts to correlate raw time domain vibration measurements to damage characteristics are hindered by two factors: (1) the difficulty in monitoring the trends in the oversized measurement data and (2) the high sensitivity of the time domain measurements to extraneous factors caused by the natural variations in the operational and environmental conditions. As a result of these two difficulties, data processing of the raw time domain vibration response measurements becomes necessary to extract low dimensional vibration response features. Ideally, these vibration response features are sensitive to damage, but insensitive to extraneous factors. The measured change in selected vibration features as a result of damage is referred to as a *damage indicator*. While the most common damage indicators include changes in natural frequencies, mode shapes, and the basic properties of the time history response, such as peak acceleration, many other forms of global vibration features can be extracted from the raw time domain vibration measurements.

Since SHM relies on the global vibration features of the structure, the measurement locations need not coincide with the damage locations. However, this advantageous aspect is precisely what challenges diagnostic monitoring. Structural damage causes a local reduction in stiffness within the vicinity of the damage, which in turn causes a reduction in the global stiffness of the structure. For a successful detection of damage, the resulting changes in the global properties must be sufficiently high, so that they can be indicated by the selected vibration feature above the corresponding noise levels. There has been debate over the past two decades about whether vibration response features, from practical applications of SHM on civil structures, are significantly sensitive to damage, while remaining insensitive to noise [2,3]. For instance, while some studies [4,5,6,7] found vibration response to be insensitive to damage; other studies [8,9,10,11,12] observed vibration features to be reliable indicators of damage.

Figure 1 schematically illustrates the difference between a sensitive and insensitive damage indicator. A damage indicator represents the measured change in a vibration response feature associated with an increase in structural damage. A high damage indicator value corresponds to a large change in a vibration response feature, which would indicate a high sensitivity of that vibration feature to the corresponding damage index. The horizontal axis of Figure 1 contains the damage index, which quantitatively represents the extent of damage. The damage index ranges from a value of zero, representing an undamaged structure, to a value associated with the development of a collapse mechanism. The slope of the plot, denoted by α , defines the relationship between the damage indicator and the damage index. The steeper the slope of the plot, the more sensitive the feature is to the presence of damage. In the worst case, damage sensitivity can be zero denoting no sensitivity to damage and in the best case the damage sensitivity can be infinity denoting total sensitivity to damage.

However, the damage sensitivity must be considered in light of the typical noise levels of the feature. The schematic illustration in Figure 1 assumes a constant noise level in vibration response for all stages of damage. The presence of noise during vibration testing decreases the ability of vibration features to clearly indicate changes due to damage. As Figure 1 illustrates, insensitive damage indicators may remain below their noise level even for very high damage indexes. On the other hand, sensitive indicators are those that yield values significantly above noise levels at early stages of damage. Using FE model simulations of an arch, we first illustrate the proof-of-concept of feature sensitivity and assimilation. Section 2 introduces the FE model details of the prototype arch adapted for this proof-of-concept study. In Section 3, we investigate the sensitivities of common vibration features to cracks developing in the prototype arch.

Implicit in the definition of a damage indicating feature is the *reduction of the dimensionality* of raw time domain measurements. Dimensionality refers to the number of values used while comparing the response of a damaged and undamaged structure. When the dimensionality is too high, trends cannot be identified unambiguously. Also, direct comparison between the damaged and undamaged states of the system is hindered. Dimensionality reduction is essential to simplify the management and statistical analysis of the oversized raw time domain data. At the other extreme, one

must be careful not to reduce the dimensionality to the point where information regarding the damage is lost or having too few dimensions make it impossible for patterns in the data to be recognized. A remedial approach to severe dimensionality reduction is increasing the feature dimensionality by assimilating multiple low-dimensional features, as it will be described in Section 4. We contend that damage-sensitivity of a damage indicator can be improved by assimilating various vibration response features instead of focusing on a single feature. Focusing on the same proof-of-concept study, Section 4 demonstrates how assimilating multiple damage sensitive features can substantially increase the success of SHM in detecting the onset of damage.

Finally, in Section 5, the concepts introduced through a simulation based study are illustrated on an experimental campaign conducted on a scaled arch model. Although the features are limited to natural frequencies, this experimental study illustrates the importance of feature assimilation in SHM.

Aside from the dimensionality and damage-sensitivity, the noise-sensitivity of the selected vibration feature is also critical. Past research indicates that 5-10% variability in vibration measurements induced by environmental and operational conditions (i.e. noise) is inevitable for large scale masonry structures [15] (see the constant noise level indicated Figure 1). The damage-sensitivity of an ideal feature would be significantly higher than its corresponding noise-sensitivity. Although seeking after features, which are sufficiently sensitive damage indicators at sufficiently early stages of damage, is of vital value, in this paper a thorough discussion of noise sensitivity is left out of scope. However, in Section 6 provides a brief discussion on the relationship between noise levels and damage stage.

2. PROOF OF CONCEPT: ARCH PROTOTYPE

The case study structure is selected based on its characteristics common to most existing historic masonry systems, e.g. curvature and geometric dimensions. A semi-circular arch with a radius of 0.75 m on center, a width of 0.2 m, and a thickness of 0.05 m is modeled using ANSYS v.12, a commercially available FE package (Figure 2a). The arch is fully fixed against translation and rotation at both supports. A density of 1930 kg/m^3 , a Young's Modulus of 4 MPa, and a Poisson's ratio of 0.2 are used.

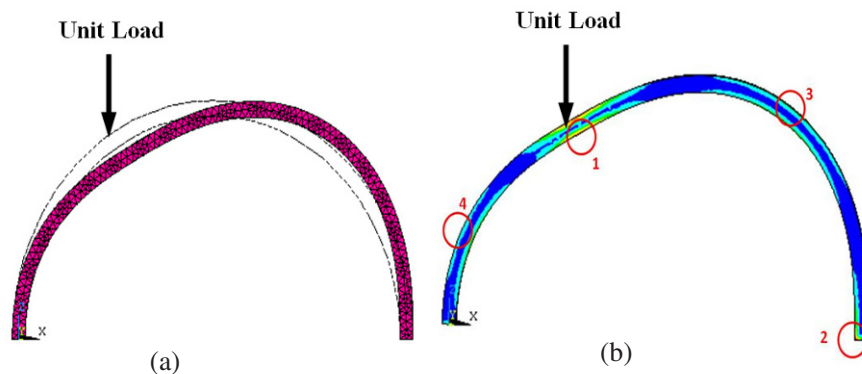


Figure 2: (a) Meshed arch with a static load at quarter span and the deflected shape, (b) Von Mises stress distribution under the unit load applied at quarter span.

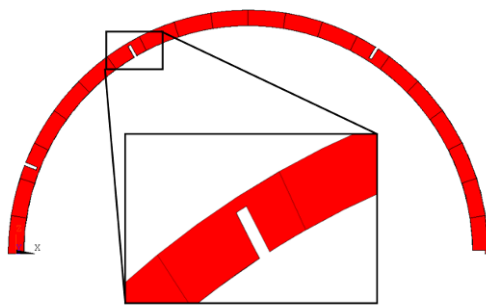


Figure 3: Arch experiencing maximum damage through artificial crack cut-outs.

In the FE model, the masonry mortar assembly is treated as a linear-elastic, isotropic and homogenous material. The structure initially exhibits a linear response before damage, and with linear-elastic material properties, it is assumed to continue to exhibit a linear response after damage. Therefore, the changes in the vibration response features can only be due to the changes in geometric properties, boundary conditions, and material properties caused by damage. Since the most common vibration response features used in SHM originate from linear dynamics, a linear-elastic FE model enables us to meaningfully simulate the commonly used damage indicators.

If a masonry arch is loaded beyond its capacity, cracks incrementally develop within the arch assembly. A crack propagating through the entire depth of the arch results in an internal hinge. According to

mechanism analysis, development of four hinges is needed for an arch with fixed supports to fail, where the location of these four hinges is dependent upon the loading condition. The locations of these four hinges are estimated for a static concentrated load applied vertically at the quarter span. The four distinct locations with high Von-Misses stress are accepted as approximate locations of cracks and hinges and artificial cracks are manually introduced at these locations (Figure 2b). Although they are approximate, the crack locations adapted herein are in close agreement with the previously published locations of cracks and hinges under this particular load condition [13].

To mimic the crack propagation, artificial cracks are incrementally introduced as cut outs from the initial geometry with increasing depths. The depths of these cut outs vary from as small as 1 cm to as large as 4 cm (Figure 3). The first crack develops at Point 1 shown in Figure 2b. The second crack is introduced after the first crack is fully developed to 4 cm. Consequently, after the second crack is fully developed, the third crack starts developing and so on. A total of 17 arches are generated with states of structural integrity varying from an undamaged arch to an arch with 4 cm cracks at all four damage locations. Within the capabilities of a linear FE model, this approach is an idealized and simplified representation of damage propagation in a masonry arch.

3. PROOF OF CONCEPT: VIBRATION FEATURE EXTRACTION

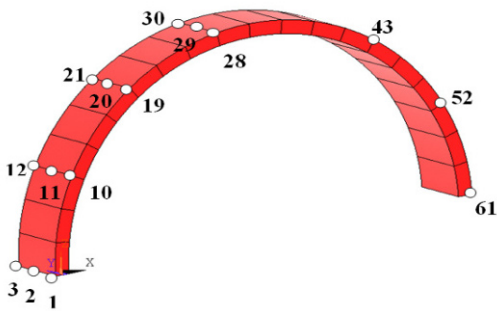


Figure 4: Virtual measurement points on the simulated arch.

We are interested in the transient response of a structure due to short duration loads, also known as impact loads. The goal of the simulations is to mimic and idealize an actual field experiment. The simulated experimental campaign involves a hammer impact at the crown of the arch while the response is recorded at the 63 virtual measurement points given in Figure 4.

The impact is simulated with a concentrated excitation force of 10 kN at the crown. The impact time is 0.0001 sec which will allow frequencies up to 10 kHz to be excited. The displacement response in the vertical direction is recorded for 1 sec. An artificial 10% proportional damping is applied to all the simulated data.

3.1 Natural Frequency Changes

Natural frequencies supply convenient, low-dimensional and physically meaningful vibration response features for SHM purposes. The success of earlier studies focusing on large scale historic masonry monuments in detecting damage based on modal parameters, makes changes in natural frequencies a viable damage indicator [13, 16]. Earlier studies have observed higher order natural frequencies to be more sensitive to localized changes in stiffness and thus to damage [for instance, see 17]. In contrast, our study indicates that the natural frequency of the first bending mode exhibits the greatest sensitivity to the propagation of cracks. Figure 5 represents the relationship between the reduction in natural frequencies (damage indicators) and the extent of damage (damage index). By k-means clustering, the data presented in Figure 5 can be clustered into three distinct damage level categories based on damage observability.

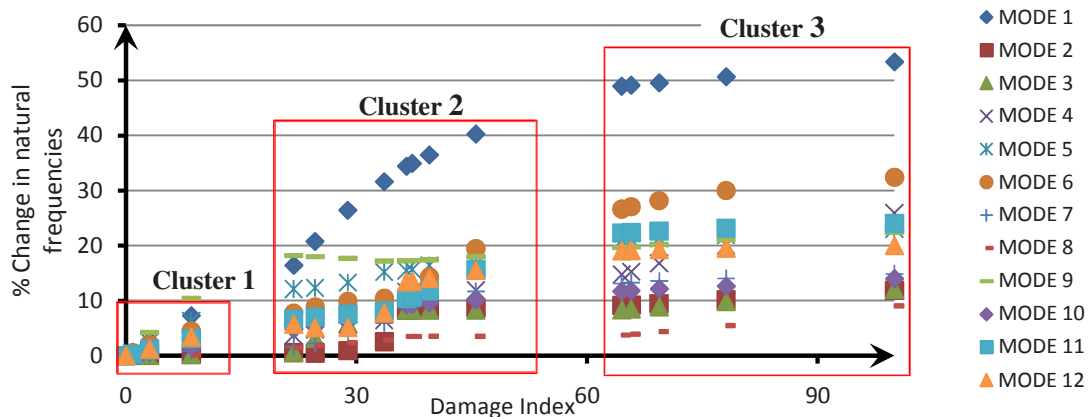


Figure 5: The percentage change in the natural frequencies for the first twelve modes.

3.2 Mode Shapes Distortions

The onset of system damage tends to distort mode shape vectors. Ewins and Ho review several different methods in which mode shape distortions can be used as damage indicators [18]. Figure 9 presents the comparison of the mode shape vectors of the undamaged arch with that of the 16 arches of varying damage levels. Also presented in Figure 9 is the percentage change in the sum of the absolute differences between the damaged arch and the undamaged arch mode shapes obtained for all 63 nodal points. The percentage change in mode shape difference is calculated as:

$$\frac{\sum_{i=1}^N |x_{di} - x_{ui}|}{\sum x_{ui}} * 100$$

where x_d is the modal displacement of damaged structure, x_u is the modal displacement of undamaged structure, and N is the number of measurement points.

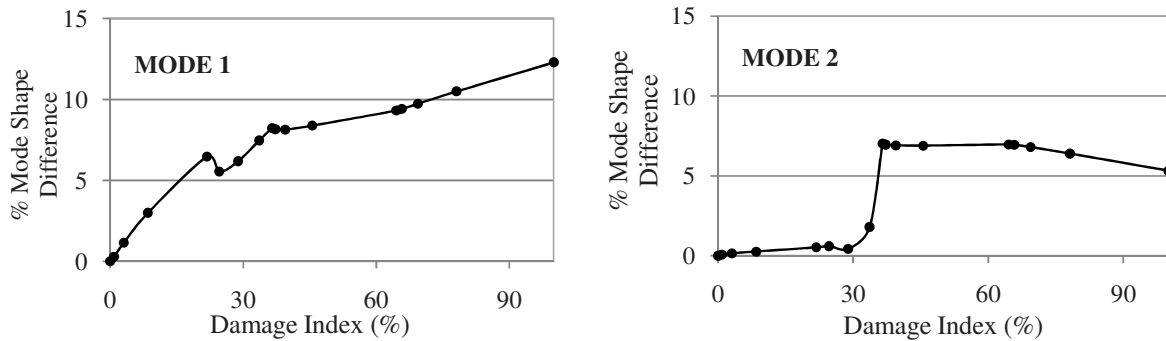


Figure 6: Plots displaying the cumulative percentage change in mode shape with progressive damage.

3.4 Mode Shape Curvature

Mode shape curvature is a localized vibration feature that is inversely related to the stiffness at the location it is calculated. Hence, the presence of a crack or separation decreases the stiffness in the vicinity of damage, which increases the mode shape curvature. In the present study, the lower modes are observed to clearly indicate the location of damage in the prototype arch. However, the higher modes are observed to disperse the damage over the whole structure making it difficult to isolate the peaks that indicate the location of damage. Figure 7 shows the total percentage change in the mode shape curvatures for the first 3 modes. Yet again the first mode shows a higher slope and a more consistent upward trend than other modes. The higher modes, although not shown herein, show a more erratic and low slope relation between damage level and change in curvature.

$MSC_i = \frac{\phi_{i+1} - 2\phi_i - \phi_{i-1}}{h^2}$, where ϕ_i is the modal displacement at degree of freedom i, and h is the distance between degree of freedom i+1 and i-1.

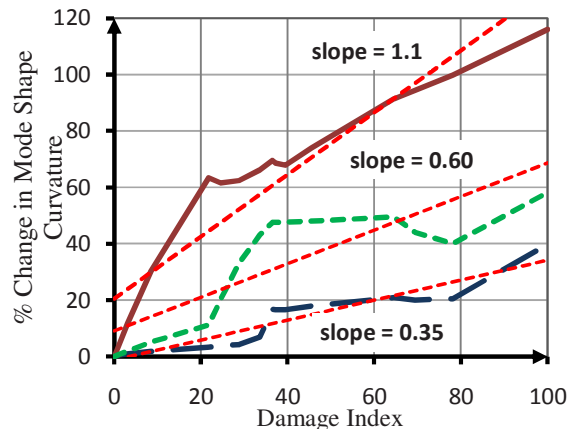


Figure 7: Percent change in mode shape curvature for first three modes.

3.5 Maximum Vibration Response

Since structural damage degrades the global stiffness of the structure, the maximum displacement is expected to increase for increasing levels of damage for a given load. *Absolute Maximum* = $\sum_{i=1}^n |Max(x_t)|$, where, n is the number of measurement points, and x_t is the displacement time-history at a measurement point.

Figure 8 presents both the maximum displacement and the absolute maximum displacement as a function of the damage index. Higher amplitude of vibration response signifies increase in flexibility and hence more energy flow in the system. In Figure 13, we plot the maximum displacements in the Z-direction with respect to the damage index. As seen, the increase in damage index leads to an increase in the maximum displacements.

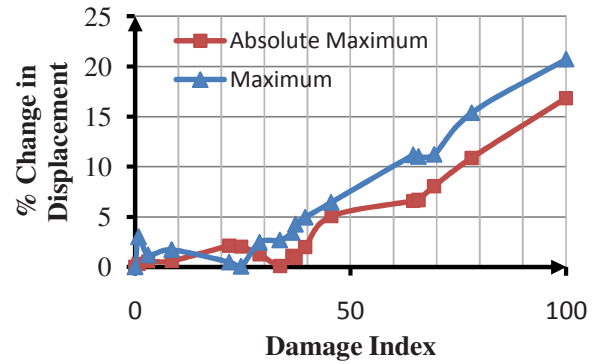


Figure 8: Summation of maximum and absolute maximum.

3.6 Root Mean Square

Root Mean Square (RMS) gives a good picture of the energy of a vibrating structure.

$RMS = \sqrt{\frac{\sum_{i=0}^N x_i^2}{N}}$, where, N is the number of time history data collected; and x is the displacement at time given by N. Figure 9 shows the summation of RMS values across all 63 points for each damage case. The sensitivity of RMS vibration response varies as the cracks incrementally propagate. While the first seven cases seem to follow the same linear relationship with the damage index, the full development of the second crack causes a sudden jump in the damage indicator. Following this jump, the trend follows a uniform trend. Figure 9 clearly illustrates how the sensitivity of a feature can change depending on the extent of damage in the system and emphasizes that the straight lines used to represent the damage sensitivity of indicators in Figure 1 must be improved to incorporate this dependency.

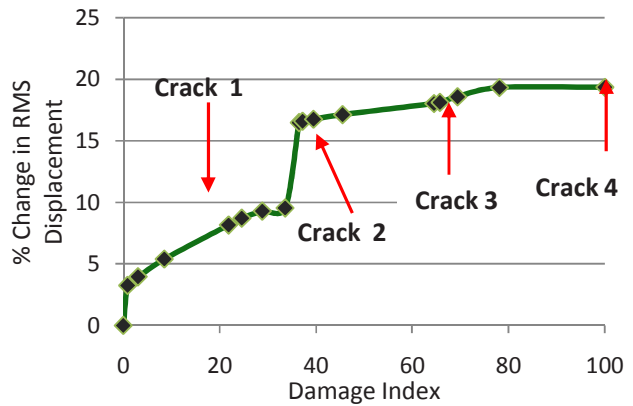


Figure 9: Summation of root mean square displacements.

3.7 Frequency Response Assurance Criteria

The frequency response function (FRF) provides an overview of the system’s response for a wide range of frequencies. As the damage level is increased, we observe the following: (1) the peaks of the FRFs shift as the damage level is increased and (2) modes are appearing and/or disappearing as the structural system is altered by the damage.

The Frequency Response Assurance Criterion (FRAC) is a statistical tool used to compare two FRFs with FRFs. Values of the FRAC range from zero to unity. FRAC values approaching zero correspond to a low correlation between analytical and experimental FRFs, whereas values approaching unity correspond to a high correlation. The following equation provides the mathematical formulation of the FRAC for comparing the analytical and experimental FRFs:

$$FRAC_{pq} = \frac{|\sum_{\omega=\omega_1}^{\omega_2} H_{pq}(\omega)H_{pq}^*(\omega)|^2}{\sum_{\omega=\omega_1}^{\omega_2} H_{pq}(\omega)H_{pq}^*(\omega) \sum_{\omega=\omega_1}^{\omega_2} H_{pq}(\omega)H_{pq}^*(\omega)},$$

where, H^{pq} =experimental FRF at node ω , and H^{pq} =analytical FRF at node ω .

Given a set of FRFs that have been generated from the experimental data and FE simulations, the equation above can be used to calculate the corresponding FRAC value associated with the set of FRFs. In Figure 10, we depict the relationship between the damage index and the percent change in FRAC.

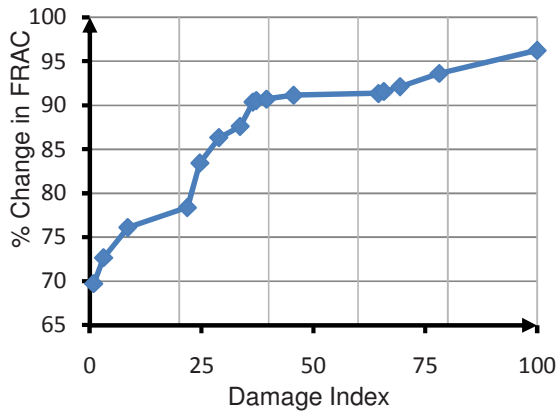


Figure 10: Percent change in FRAC with respect to damage index.

4. PROOF OF CONCEPT: VIBRATION FEATURE ASSIMILATION

The vibration features described in the previous section are advantageous, since they are low dimensional and thus make trends in the vibration response readily observable. The mathematical model-fitting process acts as a filter and to a certain extent, removes the extraneous effects of such noise factors from these low dimensional features. Therefore, these low dimensional features become preferable over the raw time history response. Figure 1 introduced the concept of determining the damage sensitivity of a vibration feature based on the slope between the damage indicator and damage index. Since a higher slope corresponds to a damage indicator with high damage sensitivity, it is desired to select damage indicators with the highest possible slopes. Figure 11 overlays several individual damage indicators in terms of percent change in the damage indicator with respect to the undamaged arch. The percent change in FRAC is not included in Figure 11 since there is no consensus in the pertinent literature whether the FRAC is a reliable option for assimilation. FRAC values can have high variation during real-time experiments due to a variety of causes other than the onset of structural damage itself.

The damage indicators in Figure 11 are normalized and are therefore dimensionless, which allows them to be compared directly with each other. Among the features plotted in Figure 11, the mode shape curvature for the first mode is the most damage-sensitive feature, with a slope of 1.10. This slope means for each percent change in the structure’s global stiffness, the damage indicator will undergo a 1.1% change. While the mode shape curvature for the first mode is the most sensitive feature, Figure 11 reveals that distortions in the first mode shape vector, as a result of damage, are an order of magnitude less sensitive with a slope of 0.11.

This approach can be extended to all possible combinations of vibration features, as long as the damage indicators derived from the changes in the vibration features are

For each of the 17 damage cases, the FRAC is calculated for the damaged and undamaged arch at each of the 63 measurement nodes on the arch. The percent change in FRAC between the damaged and undamaged arch is computed at each node and then the percent change in FRAC for all 63 individual nodes are summed for each damage case. Figure 16 is generated by plotting the total percent change in FRAC for all 63 nodes versus the corresponding damage index, or extent of structural damage in the arch. Figure 10 clearly shows that there is an increased change in FRAC values as the damage index increases. However, in order to confirm that percent change in the FRAC is a reliable damage indicator, there must be validation that the change in FRAC values is caused by the increased damage levels and not noise, or some other factor(s). This issue will be revisited in Section 6.

measurements since they tend to be less sensitive to extraneous factors. However, while operating with such low dimensional features, the danger becomes excessive reduction of the measurement data which may result in the lost of important information about damage. This section illustrates an approach to remedy this problem by assimilating multiple low dimensional vibration features.

treated as normalized percentages. Once all the damage indicators are normalized and made dimensionless, these damage indicators can be added together to increase the sensitivity to damage. Figure 11 also illustrates the assimilated damage indicator where several damage sensitive indicators are summed to obtain a more an indicator with higher sensitivity to damage. As seen in Figure 11, assimilation of various vibration features can greatly increase the success of SHM in detecting damage at early stages.

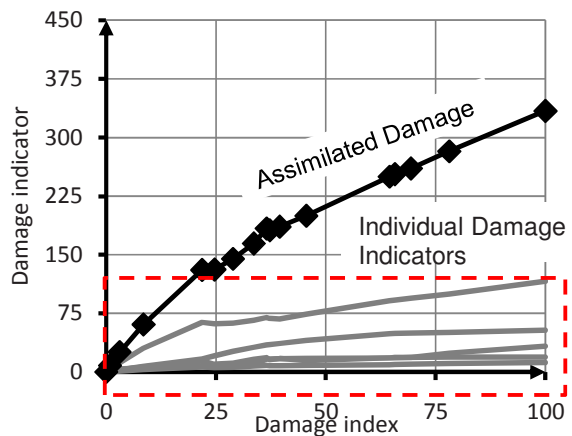


Figure 11: Damage sensitivity comparison of various damage indicators.

5. EXPERIMENTAL CAMPAIGN

In this section, we will overview the experimental campaign completed to illustrate the aforementioned concepts.

5.1 Experimental Setup

For experimental purposes, a PVC arch with a 12 inch radius, 2.5 inch depth and 1 inch thickness is used (Figure 12). The arch is damaged to four levels in succession, with a 4/5 inch crack at each of the most probable damage locations as shown in Figure 3. Hammer impact tests are performed for two drive points on the arch allowing the excitation of both bending and torsional modes. Piezoelectric IEPE Accelerometer, 500mV/g are used to measure the vibrations while Brüel & Kjær 8202 impact hammer is used to excite the structure. Commercially available software, PULSE Reflex of Brüel & Kjær is used for testing and analysis purposes. The tests are repeated in the presence of artificial random white noise to see the effect of damage levels on the noise sensitivity of FRFs. The results of the noise study will be discussed in Section 6.

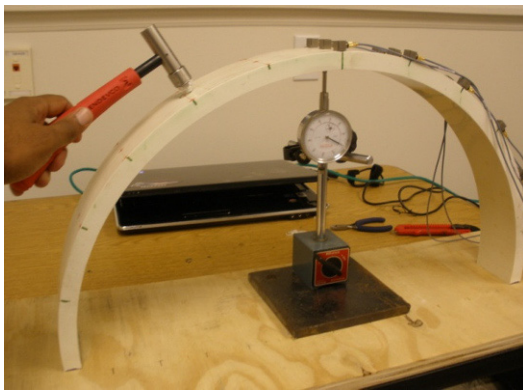


Figure12: Damage sensitivity comparison of various damage indicators.

5.2 Modal Analysis

Impact hammer tests with a frequency range of 0- 1.6 Hz are performed for the purpose of modal analysis. Anti-aliasing filters are used to prevent higher frequencies from contaminating the measurements. Averaged Frequency Response functions (FRF) are collected for each damage case and analyzed for natural frequency and mode shapes using the Rational Fraction Polynomial algorithm. The modes are selected from a combination of SUM and Multivariate Mode Indicator function (MMIF), which are popular mode indicator functions. The SUM function sums up the FRFs of all the measurement points to give a single FRF. The peaks of this FRF can be treated as possible modes. The MMIF is obtained by dividing the real part of an FRF by its magnitude. Combining these functions with engineering judgment, the first six modes of the model arch are selected. The natural frequencies decrease with increasing damage levels.

Figure 13 illustrates the percent change in natural frequency for each mode for each corresponding damage level. The percent change in natural frequency is calculated with respect to the natural frequencies of the undamaged arch. As illustrated in Figure 13, modes 1, 3, and 4 exhibit relatively high sensitivities to damage, with a maximum change of 18% for the most severe crack level. Whereas, modes 2 and 5 have a relatively lower sensitivities to damage with less than 10% maximum change for the most severe crack level.

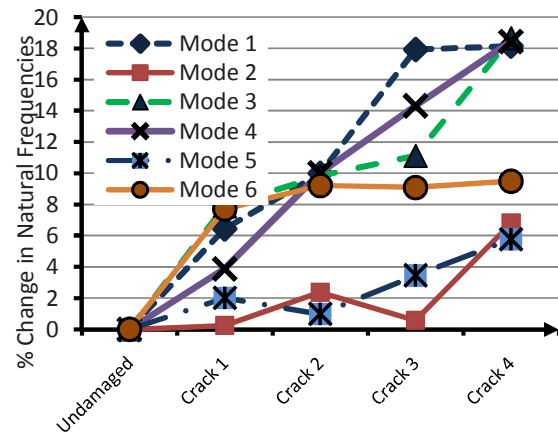


Figure 13: Percent change in natural frequency with respect to damage level.

5.2 Vibration Feature Assimilation

Figure 14 compares the performance of individual features in indicating damage to the assimilated damage indicator which fuses the information contained in all of the six natural frequencies. Evidently, damage indicator obtained by assimilating six natural frequencies is more sensitive to damage than any of the natural frequencies themselves.

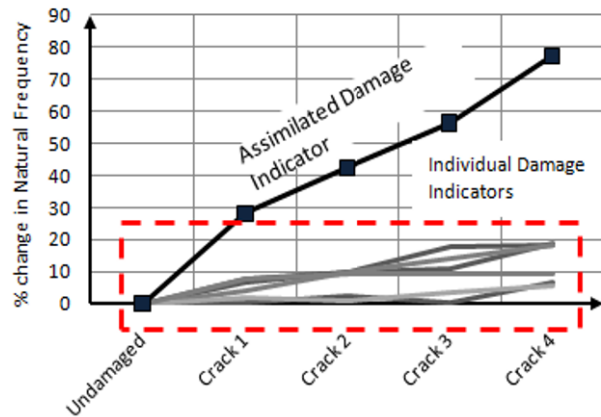


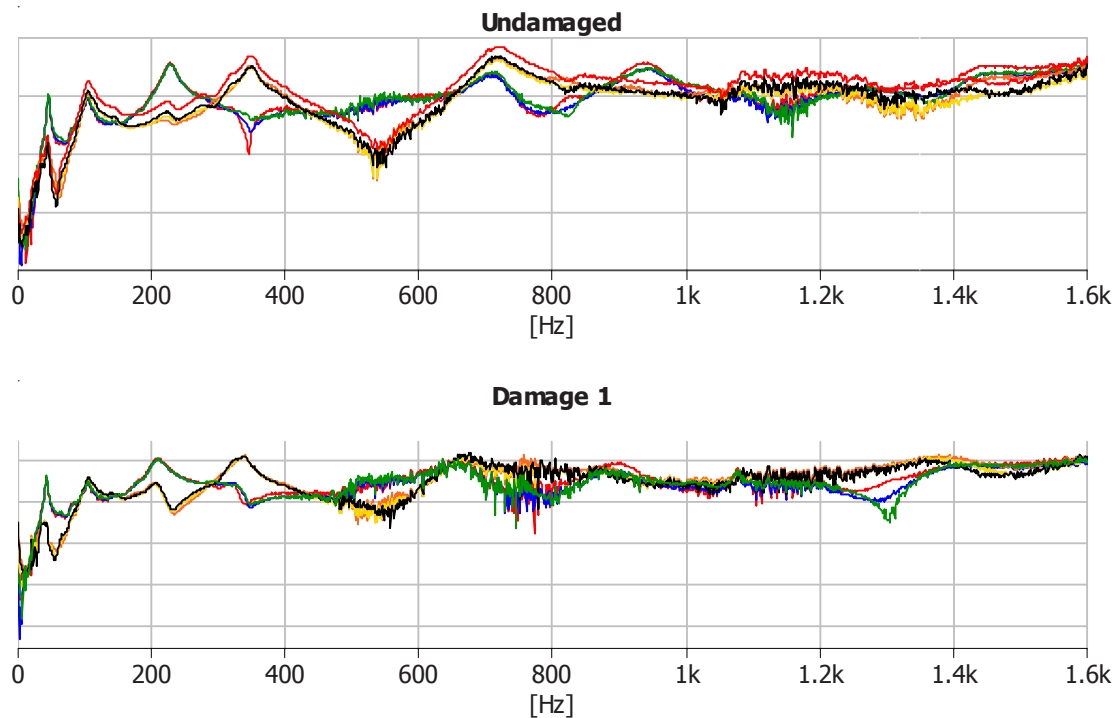
Figure 14: The improved sensitivity of assimilated damage indicator.

6 DISCUSSION AND CONCLUSIONS

SHM techniques based on global vibration measurements are particularly advantageous when structural problems occur internally, making visual identification of impending failure difficult. This is often the case for tensile problems in masonry systems. Through early diagnosis, the direct cost of repair can be reduced significantly. If ignored completely, the collapse of masonry structures can occur suddenly and without warning. Aside from the obvious economic and life-safety implications of a structural collapse, the cultural value of historic monuments also demands the development of well-defined SHM procedures for historic masonry structures.

Our contribution to the state-of-the-art is the concept of assimilating low dimensional vibration features to obtain a holistic indicator with increased damage-sensitivity. This study presumes the availability of measurements from the undamaged state of the structure of interest and this assumption, in real life applications, may reduce the practicality of the proposed method.

Determining the noise level inherent within these vibration response features is also an important aspect that warrants attention, but is not covered at any length within the scope of this paper. However, the depiction of noise as a constant threshold in Figure 1 warrants further discussion. We investigate the effects of ambient noise in the system identification of natural frequencies and mode shapes. A random white noise with amplitude of 0.25 Vrms and a frequency range of 0 to 1.6 KHz is applied to the scaled arch structure using shakers (LDS Vibrator V203,10/32UNF). It is seen that the increase in damage levels greatly affects the noise levels transferred in the structure. As can be seen from Figure 15, the noise-sensitivity of FRFs increases as the damage level increases. It becomes increasingly difficult to analyze the FRFs for modal analysis as damage progresses. The high noise sensitivity for increasing damage levels can be attributed to many factors including the loss of stiffness and increased flexibility which allows high energy vibrations due to noise within the structure. This observation emphasizes that assuming a constant noise level, as given in Figure 1, although a reasonable approximation and necessary first step, should be elaborated further in future studies and perhaps the schematic relationship given in Figure 1 should be represented in a three dimensional form illustrating both the damage and noise-sensitivity of a feature for varying stages of damage.



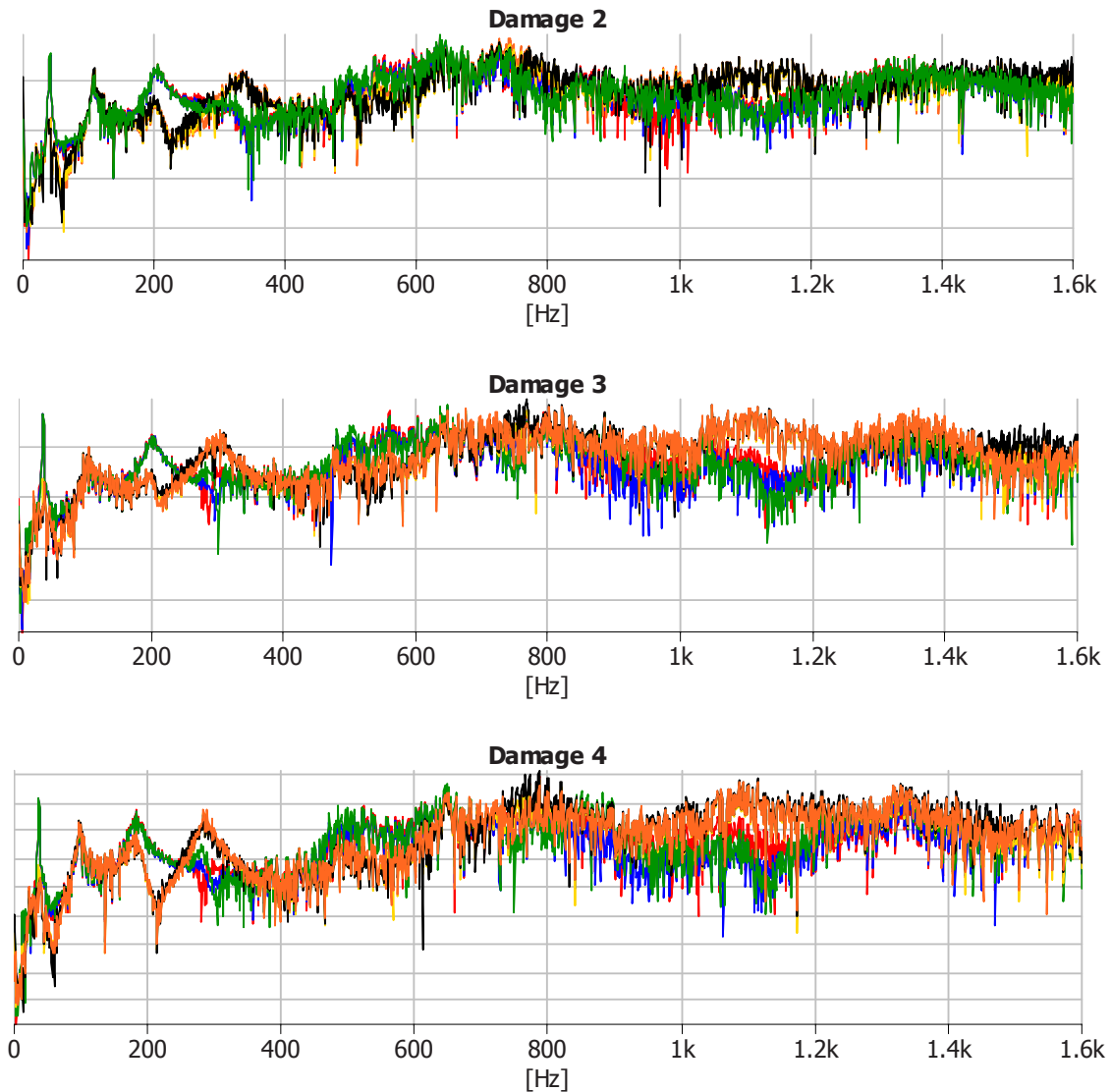


Figure 15: Comparison of FRFs as damage increases for a constant noise level.

7 ACKNOWLEDGEMENTS

This work is performed under the auspices of the PTT Grants program of National Center for Preservation Technology and Training (NCPTT) of Department of Interior: the Grant Agreement Number MT-2210-10-NC-01.

8 REFERENCES

- [1] Ceravolo R., De De Stefano A., and Ruocci G. "Modal identification of an experimental model of masonry arch bridge," *Key Engineering Materials*, 413-414, 707-714, 2009.
- [2] Maeck, J. *Damage Assessment of Civil Engineering Structures by Vibration Monitoring*, Ph.D Thesis, Katholieke University, Leuven, Belgium, 2003.
- [3] Garaygordóbil, J.C.A. *Dynamics Assessment of Structural Building Components*, Ph.D. Thesis, Universitat Politècnica de Catalunya, Barcelona, Spain, 2003.

- [4] Begg, R.D., Mackenzie, A.C., Dodds, C.J., and Loland, O. "Structural Integrity Monitoring Using Digital Processing of Vibration Signals," in Proceedings of 8th Annual Offshore Technology Conference, Houston, TX, 305-311, 1976.
- [5] Duggan, D.M., Wallace, E.R., and Caldwell, S.R. "Measured and Predicted Vibrational Behavior of Gulf of Mexico Platforms," in Proceedings of 12th Annual Offshore Technical Conference, 92-100, 1980.
- [6] Fox, C.H.J. "the Location of Defects in Structures: A Comparison of the use of Natural Frequency and Mode Shape Data," in Proceedings of the 10th International Modal Analysis Conference, 522-528, 1992.
- [7] Farrar, C.R., Baker, W.E., Bell, T.M., Cone, K.M., Darling, T.W., Duffey, T.A., Eklund, A., and Migliori, A. "Dynamic Characterization and Damage Detection in the I-40 Bridge Over the Rio Grande," Los Alamos National Laboratory report LA-12767-MS, 1994.
- [8] Ju, F. and Mimovich, M. "Modal Frequency Method in Diagnosis of Fracture Damage in Structures, In Proceedings of the 4th Internatinal Modal Analysis Conference, 1168-1174, 1986.
- [9] Rizos, P., Aspragathos, N. and Dimarogonas, A. "Identification of crack location and magnitude in a cantilever beam from the vibration modes," *Journal of Sound and Vibration*, 138(3), 381-388, 1990.
- [10] Dong, C., Zhang, P.Q., Feng, W.Q., and Huang, T.C. "The Sensitivity Study of the Modal Parameters of a Cracked Beam," in Proceedings of the 12th International Modal Analysis Conference, 98-104, 1994.
- [11] Meneghetti, U., Maggiore, A. "Crack Detection by Sensitivity Analysis," in Proceedings of the 12th International Modal Analysis Conference, 1292-1298, 1994.
- [12] Fritzen, C.P., Seibold, S., and Buchen, D. "Application of filter Techniques for Damage Identification in Linear and Nonlinear Mechanical Structures," in Proceedings of the 13th International Modal Analysis Conference, 1874-1881, 1995.
- [13] Ramos, L. F. 2007, "Damage Identification on Masonry Structures Based on Vibration Signatures," Ph.D. Thesis, University of Minho.
- [14] Chondros, T. G., Dimarogonas, A. D., and Yao J. "A Continuous Cracked Beam Vibration Theory," *Journal of Sound and Vibration*, 215(1), 17-34, 1998.
- [15] Atamturktur, S., Pavic, A., Reynolds, P., and Boothby, T. "FULL-SCALE MODAL TESTING OF VAULTED GOTHIC CHURCHES: LESSONS LEARNED." *Exp Tech*, 33(4), 65-74, 2009.
- [16] Gentile and Saisi. 2008.
- [17] Panday, A.K., Biswas, M. and Samman, M.M. "Damage detection from changes in curvature modes shapes," *Journal of Sound and Vibration*, 145(2), 221-332, 1991.
- [18] Ewins D. J. and Ho Y. K. "On the Structural Damage Identification with Mode Shapes," Proceedings of the Conference held in E.T.S.I. Aeronauticos, Madrid, June 2000, Universidad Politecnica de Madrid, Spain, 677-683, 2000.

Decentralized Modal Analysis and System Identification Using Embedded Markov Parameter Extraction within Distributed Wireless Sensor Networks

¹Junhee Kim, ²Jerome P. Lynch

¹PhD Candidate, Department of Civil and Environmental Engineering,
University of Michigan, Ann Arbor, MI 48105

²Associate Professor, Department of Civil and Environmental Engineering,
University of Michigan, Ann Arbor, MI 48105

ABSTRACT

As wireless monitoring systems continue to mature as a viable alternative to traditional wired data acquisition systems, scalable approaches to autonomously processing measurement data in-network are necessary. Embedded data processing has the benefit of improving system scalability, reducing the amount of wireless communications, and reducing overall power consumption. A system identification strategy based on Markov parameters is proposed for embedment within the decentralized computational framework of a wireless sensor network. Utilizing the computational resources of wireless sensors, individual sensor nodes perform local data processing to identify the Markov parameters of a structural system. Eventually, the global structural properties (*e.g.*, mode shapes) are assembled by the wireless sensor network base station via an eigensystem realization algorithm executed using the limited number of Markov parameters transmitted by the wireless sensor nodes. The proposed strategy is evaluated using input-output and output-only data recorded during dynamic testing of a balcony structure.

INTRODUCTION

System identification by modal analysis is as one of the most common data processing practices in the structural dynamics community. Identified dynamic properties represent the real structure's characteristics and can even serve as a valuable input to damage detection methods. Modal-based system identification (*i.e.*, modal analysis) is often conducted through two steps: 1) vibration data is conventionally collected using a centralized data acquisition (DAQ) system that employs wires to collect data from individual sensors; 2) data processing is then conducted manually off-line to extract modal parameters. While the conventional wired DAQ system is reliable for collecting measurement data, the extensive cabling required translates into high installation costs when installed in large civil structures. To overcome these limitations, wireless sensors have been proposed for structural monitoring [1]. In addition to being cost-effective, wireless sensors also offer on-board computational resources that can be used to locally process measurement data [2]. On-board computing reduces the amount of data to be transmitted; thus, the scalability of a wireless sensor network (WSN) is greatly enhanced. In addition, a reduction of wireless communication results in significant power savings because radio usage generally consumes more power than on-board computing.

Markov parameters (MPs) (*i.e.*, impulse responses functions) encapsulate the dynamic characteristics of the system. Markov parameter identification (MPID) is considered a time-domain system identification technique and is a counterpart to classical frequency-domain system identification (*e.g.* complex mode index function (CMIF) or its output-only version, frequency domain decomposition (FDD)). Two MPID techniques have been popularly used by the modal testing community to date: observer/Kalman filter identification (OKID) which is a deterministic MPID

method using input-output data [3] and natural excitation technique (NExT) which is a stochastic MPID method that uses output-only data [4]. More recently, a new deterministic MPID technique based on least squares was proposed by Van Pelt and Bernstein termed as μ -Markov parameter identification (μ MPID) [5]. In addition to having comparable accuracy to OKID [6], μ MPID does not require prior knowledge of the system order. This is in contrast to other system identification methods that require a skilled technician to determine (*e.g.*, using stability diagram) the system order. Since no user intervention is necessary, μ MPID can be autonomously executed in a WSN.

Subspace system identification has been under development since the work of Ho and Kalman [7] and has evolved more broadly into today's subspace-based state space system identification (4SID) family [8]. The 4SID methods are generally categorized into one of two groups: direct and indirect (realization-based) subspace 4SID. Direct 4SIDs [9] directly estimate a state-space model from input-output data or output-only data. Indirect 4SIDs, also introduced as eigensystem realization algorithm (ERA) [10], require estimation of MPs prior to realizing a state-space model. Thus, indirect 4SIDs are closely related to MPID. Furthermore, indirect 4SIDs are computationally less resource-intensive by decomposing the single-input multi-output (SIMO) system into parallel single-input single-output (SISO) systems. This type of decomposition is an attractive approach for WSNs, since smaller SISO analysis is properly scaled to the small computing and memory footprints present at each wireless sensor. By decomposing the problem into smaller computational parts, the global analysis can be more readily distributed to individual wireless sensors for execution. In this study, deterministic and stochastic MPID methods, specifically μ MPID and NExT, are embedded into a WSN to save energy and communication bandwidth by transmitting compressed data (*i.e.*, estimated MPs) rather than raw measured time histories. Then, the estimated MPs corresponding to individual SISO systems (as perceived by each wireless sensor) are aggregated at a single wireless server where a state-space model of the SIMO system is realized by ERA.

DETERMINISTIC MARKOV PARAMETER ESTIMATION USING INPUT-OUTPUT DATA

A linear time-invariant SISO system can be written with the n^{th} order auto-regressive moving average (ARMA) model as follows:

$$y(k) = - \sum_{j=1}^n a_j y(k-j) + \sum_{j=0}^n b_j u(k-j) \quad (1)$$

where k is the discrete time step, a_j are coefficients on the system output y , and b_j are coefficients on the system input u . If the at-rest system is excited by an arbitrary input from time 0, the output, $y(0)$, can be considered as an impulse response multiplied by the input, $u(0)$. By extracting the first MP at time step 0, $y(0)$, from the moving average part of the ARMA model, Eq. (1) can be rearranged as follows:

$$y(k) = - \sum_{j=1}^n a_j y(k-j) + h_0 u(0) + \sum_{j=1}^n b_j u(k-j) \quad (2)$$

This process can be repeated $\mu-1$ times to derive an ARMA model that displays μ values of the impulse response function ($h_0, h_1, \dots, h_{\mu-1}$):

$$y(k) = - \sum_{j=1}^n a_j^{(\mu-1)} y(k-j-\mu+1) + \sum_{j=0}^{\mu-1} h_j u(k-j) + \sum_{j=1}^n b_j^{(\mu-1)} u(k-j-\mu+1) \quad (3)$$

Here a_j' and b_j' are modified ARMA model coefficients. By applying Eq. (3) to the entire set of data spanning from $k=0, \dots, N-1$, a linear matrix equation can be formulated as:

$$\mathbf{y} = \Phi \boldsymbol{\theta} \quad (4)$$

where \mathbf{y} is the measured output vector, Φ is the measured input-output matrix, and θ is a vector of unknown parameters of Eq. (3). Here, Φ and θ are defined as:

$$\Phi = [\Phi_0^T \quad \Phi_1^T \quad \cdots \quad \Phi_{N-1}^T]^T \quad (5)$$

$$\Phi_k = \{-y(k-\mu) \quad \cdots \quad -y(k-n-\mu+1) \quad u(k) \quad \cdots \quad u(k-n-\mu+1)\} \quad (6)$$

$$\theta = [a_1^{(\mu-1)} \quad \cdots \quad a_n^{(\mu-1)} \quad h_0 \quad \cdots \quad h_{\mu-1} \quad b_1^{(\mu-1)} \quad \cdots \quad b_n^{(\mu-1)}]^T \quad (7)$$

The least squares solution of Eq. (4) can be calculated by a pseudo-inverse with the MPs ($h_0, \dots, h_{\mu-1}$) estimated.

STOCHASTIC MARKOV PARAMETER ESTIMATION USING OUTPUT-ONLY DATA

The ARMA model of the system defined in Eq. (1) is valid for a defined reference output, $y_{\text{ref}}(k)$, as:

$$y_{\text{ref}}(k) = -\sum_{j=1}^n a_j y_{\text{ref}}(k-j) + \sum_{j=0}^n b_j u(k-j) \quad (8)$$

Cross-correlation between an arbitrary output, $y_i(k)$, and the reference output, $y_{\text{ref}}(k)$, can be defined as:

$$R_{y_i, y_{\text{ref}}}(\tau) = E[y_i(k-\tau)y_{\text{ref}}(k)] \quad (9)$$

If Eq. (8) is multiplied by $y_i(k)$ and the expected value of all terms are written, the resulting equation would reveal that the original ARMA model also applied to the cross-correlation functions $R_{y_i, y_{\text{ref}}}$ and $R_{y_i, u}$:

$$R_{y_i, y_{\text{ref}}}(\tau) = -\sum_{j=1}^n a_j R_{y_i, y_{\text{ref}}}(\tau-j) + \sum_{j=0}^n b_j R_{y_i, u}(\tau-j) \quad (10)$$

If the input is a stationary Gaussian random process, then the autocorrelation function of the input is a Kronecker delta function, δ , scaled by an arbitrary constant, c_o' . This allows Eq. (10) to be rewritten as:

$$R_{y_i, y_{\text{ref}}}(\tau) = -\sum_{j=1}^n a_j R_{y_i, y_{\text{ref}}}(\tau-j) + c_o' h(0)\delta(\tau-j) \quad (11)$$

Eq. (11) implies a stochastic auto-regressive (AR) model with impulse at time step 0. Thus, it can be concluded that the cross-correlation sequences $R_{y_i, y_{\text{ref}}}(\tau)$ are essentially stochastic MPs.

EIGENSYSTEM REALIZATION ALGORITHM USING MARKOV PARAMETER

The block Hankel matrix can be assembled from the deterministic MPs as:

$$\mathcal{H} = \begin{bmatrix} \mathbf{h}(1) & \mathbf{h}(2) & \mathbf{h}(3) & \dots \\ \mathbf{h}(2) & \mathbf{h}(3) & \mathbf{h}(4) & \dots \\ \mathbf{h}(3) & \mathbf{h}(4) & \mathbf{h}(5) & \dots \\ \vdots & \vdots & \vdots & \ddots \end{bmatrix} \quad (12)$$

The state space model of the system provides a relationship between the impulse response of the system, $\mathbf{h}(k)$, and the system matrices \mathbf{A} , \mathbf{B} , \mathbf{C} : $\mathbf{h}(k) = \mathbf{C}\mathbf{A}^{k-1}\mathbf{B}$. Based on this relationship, the block Hankel matrix can then be factorized into an observability, \mathcal{O} , and controllability matrix, \mathcal{C} , as:

$$\mathcal{H} = \begin{bmatrix} \mathbf{C} \\ \mathbf{C}\mathbf{A} \\ \mathbf{C}\mathbf{A}^2 \\ \vdots \end{bmatrix} \begin{bmatrix} \mathbf{B} & \mathbf{A}\mathbf{B} & \mathbf{A}^2\mathbf{B} & \dots \end{bmatrix} = \mathcal{O}\mathcal{C} \quad (13)$$

From Eq. (13), the system matrices \mathbf{A} , \mathbf{B} , \mathbf{C} can be extracted by singular value decomposition. In the case of output-only data analysis, the system matrices \mathbf{A} and \mathbf{C} can be calculated directly from the definition of the stochastic MPs, namely, $\mathbf{h}(k) = \mathbf{C}\mathbf{A}^{k-1}\mathbf{C}$.

Modal parameters can be estimated from the system matrices derived during the input-output and output-only system identifications. For example, the estimated system matrix, $\hat{\mathbf{A}}$, can be decomposed by eigen-decomposition as:

$$\hat{\mathbf{A}} = \mathbf{\Psi}\mathbf{\Lambda}\mathbf{\Psi}^{-1} \quad (14)$$

where the diagonal matrix $\mathbf{\Lambda} = \text{diag}(\lambda_{di})$ consists of the discrete-time complex-valued eigenvalues. $\mathbf{\Psi}$ contains the eigenvectors in each column. The damping ratio and natural frequency of i -th mode can be calculated by converting the discrete-time eigenvalues to continuous-time eigenvalues. The mode shape vectors for i -th mode Φ_i , can be calculated as:

$$\mathbf{\Phi} = [\Phi_1 \quad \dots \quad \Phi_i \quad \dots \quad \Phi_n] = \hat{\mathbf{C}}\mathbf{\Psi} \quad (15)$$

Where $\hat{\mathbf{C}}$ is the estimate system matrix.

WIRELESS SENSORS AND IMPLEMENTATION

The *Narada* wireless sensor node (Fig. 1) is a low-cost wireless sensor designed explicitly for structural monitoring applications [11]. This study adopts *Narada* as the primary wireless sensing platform in which MP estimation is embedded. The *Narada* unit can accommodate up to 4 sensors interfaced at one time; interfaced sensor outputs are locally digitized using a 16-bit analog-digital converter (ADC) that can sample as fast as 100 kHz. Data collected is managed by an Atmel Atmega128 microcontroller. To accommodate sensor data storage, an additional 128 kB of random access memory (RAM) is included in the wireless sensor design. To enhance the capabilities of *Narada* when used to monitor large-scale civil structures, an extended-range 2.4 GHz CC2420 transceiver with a 700 m communication range is integrated with the *Narada* wireless sensor node [12].

The proposed system identification strategy by decentralized MP estimation consists of sensor-level computing and network-level computing. At the sensor level, MP estimation is conducted in parallel with MPs sent wirelessly to a control server. At the control server, network-level computing occurs by aggregating MPs and finding global system

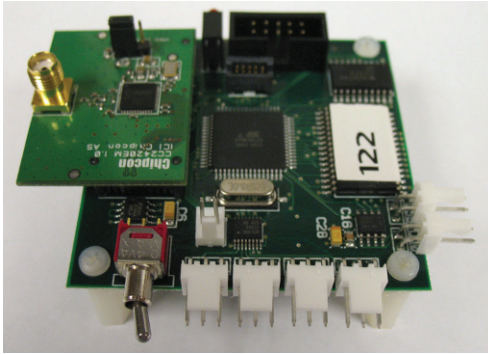


Fig. 1. The Narada wireless sensors

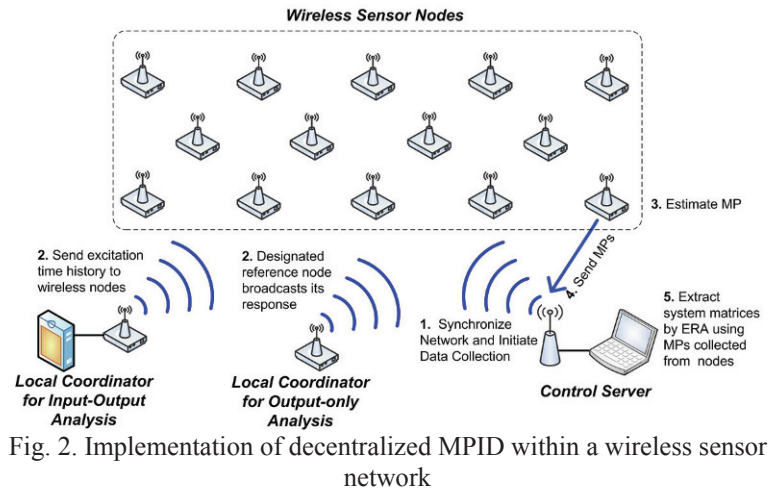


Fig. 2. Implementation of decentralized MPID within a wireless sensor network

properties by ERA. The detailed implementation of the decentralized MPID is depicted in Fig. 2. In short, the control server sends a beacon packet to the network to initiate data collection and execution of the embedded MPID algorithms. Upon receipt of the beacon packet, the local coordinator and wireless sensor nodes reset their internal clocks at the same time and begin to collect data for the prescribed time period. The local coordinator serves two roles depending on if MPID is input-output or output-only. In the case of input-output MPID, the local coordinator commends an exciter with a pre-defined forcing function. In the case of output-only MPID, the local coordinator works as a standard sensor whose measurements serve as a reference node for the analysis. Once the collection of data is over, the local coordinator broadcasts its raw time-history data (*i.e.*, excitation input during input-output MPID and the structure acceleration response during output-only MPID) to the wireless sensor nodes. Depending on the type of MPID, each wireless sensor node calculates its MPs by solving Eq. (4) by LU decomposition for input-output MPID or solving Eq. (9) for output-only MPID. Next, the control server receives the estimated MPs from each wireless sensor nodes and conducts ERA analysis.

VIBRATION TESTING OF BALCONY STRUCTURES

A total of 16 Narada wireless sensors with the proposed MPID algorithms embedded are installed in a 5 × 3 planar grid on the main balcony of the University of Michigan’s Hill Auditorium (Ann Arbor, MI) as seen in Fig. 3-(a). Two different types of microelectromechanical system (MEMS) accelerometers (*i.e.*, Crossbow CXL02 and PCB Piezotronics 3801D1FB3G) are adopted for integration with the 16 Narada wireless sensors in order to measure the vertical acceleration of the balcony during forced and ambient vibration testing. The sensitivity of the 3801D1FB3G accelerometer is 0.7 V/g, its acceleration range is ±3 g, and its noise floor level is 0.15 mg. For the CXL02 accelerometer, these three values are 1 V/g, ±2 g, and 0.5 mg, respectively. To improve the signal-to-noise ratio of the digitized acceleration signals, a signal conditioning board which is designed by Wang and Lynch [13] is interfaced

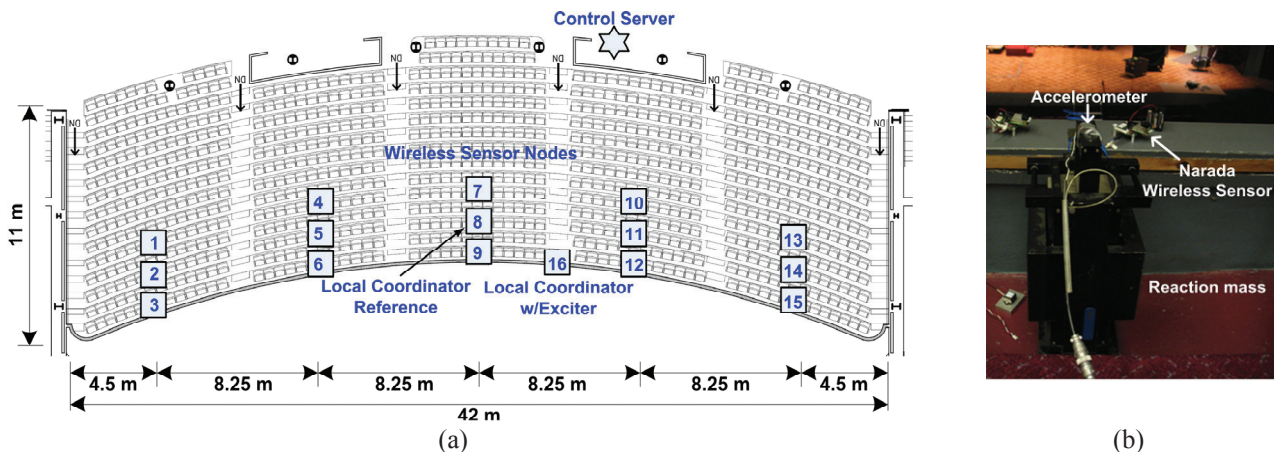


Fig. 3. Layout of the wireless monitoring system: (a) location of the control server, local coordinator, and wireless sensor nodes; (b) instrumented electro-dynamic shaker by sensor #16.

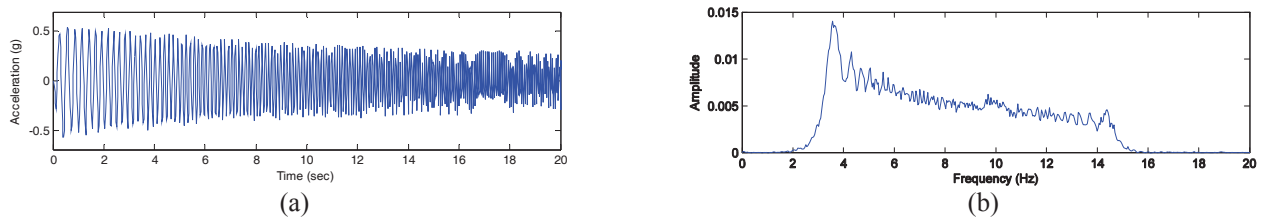


Fig. 4. Controlled excitation by electro-dynamic shaker: (a) measured acceleration of reaction mass; (b) corresponding frequency spectrum.

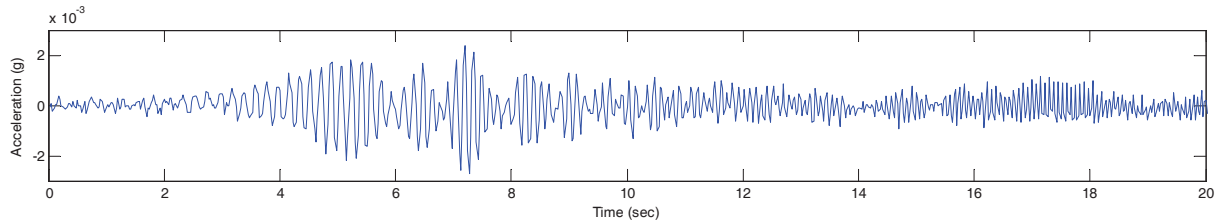


Fig. 5. Measured acceleration of wireless sensor #8 (Fig.3).

with each sensor. The signal conditioning board amplifies the accelerometer signal with a gain of 20 and provides a band-pass filter with a pass-band of 0.014 to 25 Hz.

For input-output MPID, the *Narada* node serving as the local coordinator commands an electro-dynamic shaker (APS Dynamics 400) to generate an input excitation to the balcony as shown in Fig.3-(b). The location of the input is determined to be at the front edge of the balcony above the third aisle; this location is selected to excite a maximum number of modes of the balcony. The shaker consists of a fixed body with permanent magnets (70.2 kg) and a moving armature with a reaction mass of 20.7 kg. The Model 400 Shaker is controlled by a *Narada* wireless unit with the assistance of a power amplifier. In this study, a saw-tooth chirp signal whose frequency range is 3 to 15 Hz is generated by the *Narada* unit. A total of five dynamic tests are conducted with varying durations of the chirp signal (*i.e.*, duration varying from 8 to 24 sec in 4 sec increments). In order to measure the acceleration of the shaker reaction mass, an accelerometer mounted on the top of the reaction mass is interfaced with a *Narada* unit. With the first five modes estimated to be below 10 Hz, a sampling rate of 40 Hz is selected. Each test is conducted for 30 sec resulting in 1200 points of data collected by the local coordinator and wireless sensor nodes. Decentralized deterministic MPID and stochastic MPID are conducted autonomously by the wireless monitoring system with each wireless sensor node programmed to estimate 105 MPs.

The communication of 105 MPs is more efficient than communicating raw time history data. If raw time history data is communicated by each wireless sensor, a total of 38.4 kbytes would be needed, since each data point is 2 bytes (*i.e.*, the ADC is 16 bits), 1200 points are collected, and a total of 16 wireless sensors are used (2 bytes \times 1200 points \times 16 units = 38.4 kbytes). In contrast, the proposed method of embedded MPID requires only 8.7 kbytes. This is based on 105 MPs being determined with each parameter a floating-point, 4 byte number. Also, one unit (*i.e.*, coordinator) transmits its time history data (1200 points \times 2 bytes) and the 15 remaining units send their 105 MPs (15 units \times 105 MPs \times 4 bytes). It can also be noted that greater transmission reduction can be achieved as the network size increases. For example, a wireless sensor network with 100 nodes results in an 81.7 % communication reduction. Again, the reduced communication in WSNs enhances scalability and reduces the overall power consumption of the wireless sensor nodes.

EXPERIMENTAL RESULTS

The acceleration of the reaction mass during the application of the 20 s chirp signal is displayed in Fig. 4-(a). Due to an electromagnetic field that impedes the electro-dynamic shaker during operation, the amplitude of the shaker mass acceleration decreases during the applied excitation. In addition, the dynamic coupling that occurs between the shaker and the balcony is evident in the time range from 16 to 20 sec. The Fourier spectrum of the reaction mass acceleration (Fig. 4-(b)) confirms the shaker is applying a controlled excitation in the 3 to 15 Hz frequency band. The acceleration response of the balcony center (*i.e.*, at wireless sensor #8) shows the resonance of the lower modes of the balcony

despite the low (3 mg) amplitude. To verify the precision of the decentralized MPID, offline subspace identification is conducted using the measured excitation and the response time history data collected by the wireless monitoring system. Excellent agreement is found between the deterministic MPs (Fig. 6-(a)) and stochastic MPs (Fig. 6-(b)) obtained.

Using the identified individual SISO systems estimated by each wireless sensor (*i.e.*, MPs), global MIMO system properties can be extracted by network-level ERA conducted at the control server. For example, the mode shapes are depicted in Fig. 7 along with those calculated from off-line subspace identification. Strong agreement is visually observed in the mode shapes as estimated by the three independent system identification methods (*i.e.*, input-output MPID, output-only MPID, and off-line subspace identification). To compare the modal characteristics estimated by the deterministic MPs and stochastic MPs in a more quantitative manner, Table 1 tabulates the modal frequencies and modal damping ratios extracted by the three system identification methods. As mentioned before, five tests are conducted depending on the duration of the chirp excitation. Every value in Table 1 is the average of the five tests. The balcony modal parameters obtained from the three system identification methods show excellent agreement except for mode 5. Since the damping ratio of mode 5 from the subspace identification method is very high (0.049) compared to those of the other modes, it is difficult to conclude that the modal parameters of mode 5 from the off-line subspace identification method are more accurate to those from the MPID-ERA method. Regardless, the proposed decentralized MPID proves accurate when compared to the centralized subspace identification method in both

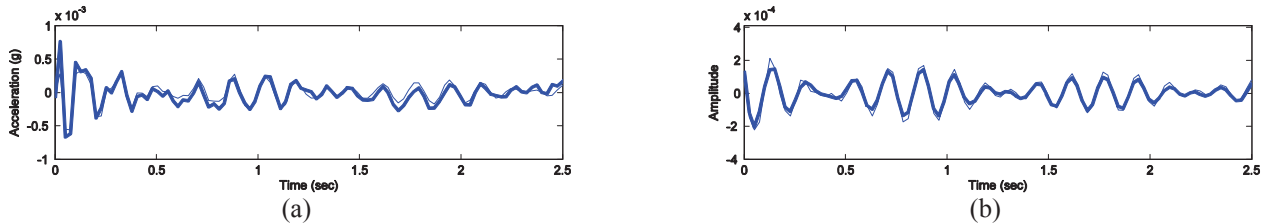


Fig. 6. Comparison of decentralized MPID (thick) and centralized MPID (thin) of wireless sensor #8 (Fig.3): (a) deterministic MPs; (b) stochastic MPs.

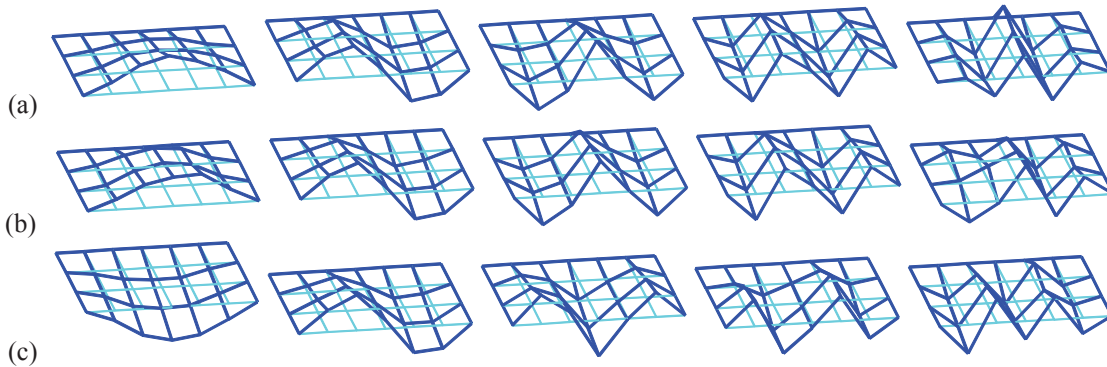


Fig. 7. Estimated five global mode shapes by: (a) network-level ERA from sensor-level deterministic MPID; (b) network-level ERA from sensor-level stochastic MPID; (c) off-line subspace method from input-output data.

Table 1. Summary of the identified modal parameters.

	Input-output Analysis					Output-only Analysis				
	Mode 1	Mode 2	Mode 3	Mode 4	Mode 5	Mode 1	Mode 2	Mode 3	Mode 4	Mode 5
Frequency (Hz)	5.617	6.048	6.718	7.611	8.619	5.619	6.047	6.722	7.618	9.160
Subspace Method	5.631	6.056	6.727	7.626	9.116					
Damping Ratio	0.013	0.011	0.008	0.008	0.009	0.013	0.010	0.008	0.007	0.013
Subspace Method	0.014	0.011	0.008	0.008	0.049					
MAC	0.998	0.982	0.995	0.933	0.548	0.973	0.993	0.990	0.968	0.479

deterministic and stochastic MPID analysis.

CONCLUSIONS

A global SIMO linear system can be equivalently treated as a set of parallel SISO systems. Parallel embedded data processing is a unique capability of wireless monitoring systems compared to traditionally tethered DAQs. By leveraging these two facts, a decentralized approach to system identification is proposed for embedment within a wireless structural monitoring system. Markov parameter identification for SISO systems using input-output and output-only data allows each node to convert its raw measurement data into a more compact representation prior to communication to a control server where ERA analysis is performed for identification of the global SIMO system properties. The scalable wireless sensing approach minimizes communication in the entire network yet proves accurate during vibration testing on a cantilevered balcony structure. The scalability and accuracy of the decentralized MPID system identification method is confirmed by extracting 105 MP from 1200 point response time history records at 15 wireless sensor nodes; this results in a compression of 77 %. While significant data compression is attained, system properties are identified with a high-degree of accuracy.

ACKNOWLEDGMENTS

The authors would like to gratefully acknowledge the generous support offered by the National Science Foundation under Grant CMMI-0726812 (Program Manager: Dr. S. C. Liu). Additional support was provided by the NIST Technology Innovation Program (Contract 70NANB9H9008). The authors would also like to thank Dr. Andrew Zimmerman, Mr. Kurt Thoma and Mr. Sean O'Connor (University of Michigan) for assistance during dynamic test at Hill Auditorium.

REFERENCE

1. Straser, E.G. and A.S. Kiremidjian, *A Modular, Wireless Damage Monitoring System for Structures*. 1998, John A. Blume Earthquake Engineering Center, Stanford University: Stanford, CA.
2. Lynch, J.P., Y. Wang, K.J. Loh, J.H. Yi, and C.B. Yun, Performance Monitoring of The Geumdang Bridge Using a Dense Network of High-resolution Wireless Sensors. *Smart Materials and Structures*, 2006. 15(6): p. 1561-1575.
3. Juang, J.N., M. Phan, and L.G.L. Horta, R.W., *Identification of Observer/Kalman Filter Markov Parameters: Theory and Experiment*. 1991, Langley Research Center: Hampton, Virginia.
4. James, J.H., T.G. Carne, and J.P. Lauffer, The Natural Excitation Technique (NExT) for Modal Parameter Extraction from Operating Structures. *The International Journal of Analytical and Experimental Modal Analysis*, 1996. 10(4): p. 260-277.
5. Van Pelt, T.H. and D.S. Bernstein. Least Squares Identification Using μ -Markov Parameterizations. in *37th IEEE Conference on Decision & Control*. 1998. Tampa, FL.
6. Holzel, M.S. and D.S. Bernstein. On the Accuracy of Least Squares Estimations of Markov Parameters Based on μ -Markov Models. in *15th International Federation of Automatic Control Symposium on System Identification (IFAC SYSID)*. 2009. Saint-Malo, France.
7. Ho, B.L. and R.E. Kalman, Effective Construction of Linear State-variable Models from Input-Output Functions. *Regelungstechnik*, 1965. 12: p. 545-548.
8. Viberg, M., Subspace-based Methods for the Identification of Linear Time-invariant Systems. *Automatica*, 1995. 31(12): p. 1835-1851.
9. Van Overschee, P. and B. De Moor, *Subspace Identification for Linear Systems*. 1996, Dordrecht, Netherlands: Kluwer Academic Publishers.
10. Juang, J.N. and R.S. Pappa, An Eigensystem Realization Algorithm for Modal Parameter Identification and Model Reduction. *Journal of Guidance*, 1984. 8(5): p. 620-627.
11. Swartz, R.A., D. Jung, J.P. Lynch, Y. Wang, D. Shi, and M.P. Flynn. Design of a Wireless Sensor for Scalable Distributed In-Network Computation in a Structural Health Monitoring System. in *5th International Workshop on Structural Health Monitoring*. 2005. Palo Alto, CA.
12. Kim, J., R.A. Swartz, J.P. Lynch, J.J. Lee, and C.G. Lee, Extended-range Narada wireless sensors for rapid reconfigurable vibration monitoring of highway bridges. *Smart Structures and Systems*, 2010. 6(5-6).
13. Wang, Y., J.P. Lynch, and K.H. Law, A Wireless Structural Health Monitoring System With Multithreaded Sensing Devices: Design and Validation. *Structural and Infrastructure Engineering*, 2007. 3(2): p. 103-120.

Comparison Study of Output-only Subspace and Frequency-Domain Methods for System Identification of Base Excited Civil Engineering Structures

¹Junhee Kim, ²Jerome P. Lynch

¹PhD Candidate, Department of Civil and Environmental Engineering,
University of Michigan, Ann Arbor, MI 48105

²Associate Professor, Department of Civil and Environmental Engineering,
University of Michigan, Ann Arbor, MI 48105

ABSTRACT

A number of practical issues must be considered when conducting system identification of civil engineering structures when using output-only data sets. In this study, system identification methods in the time- and frequency-domain are considered: stochastic subspace identification (SSI) and frequency domain decomposition (FDD), respectively. In order to evaluate these two output-only analyses, support-excited frame structures are selected as a common civil engineering structure of interest (*e.g.*, building structures exposed to seismic loads). Due to the absence of a direct means of mathematically evaluating the results of the output-only analyses, this study proposes an indirect method of comparison. Specifically, an input-output system identification study is first conducted by the subspace system identification method to estimate a full set of state-space model system matrices. Then, time-domain comparisons between the predicted and measured responses are conducted. Next, conversion of the input-output model to modal space is executed to allow a direct comparison between modal parameters extracted from the two output-only models can be made. Detailed experimental testing using a steel frame structure exposed to seismic ground motion is conducted to allow the accuracy of the two output-only analyses to be evaluated.

INTRODUCTION

Output-only system identification using the ambient vibrations of a structure have grown in popularity in the civil engineering community. Output-only system identification is popular because of the difficulties associated with obtaining input-output structural response data by introducing controlled, deterministic input forces to the structure. Based on ideal assumptions of white noise inputs, numerous output-only system identification methods have been proposed. Traditionally, the majority of time-domain methods focus on the estimation of the structural free decay response (*e.g.*, the Ibrahim time domain method [1]) or the correlation of the output (*e.g.*, NExT [2]). In the frequency domain, the complex mode identification function (CMIF) has been studied [3]. Similarly, frequency domain decomposition (FDD) has been formulated as a modified CMIF approach where the input power spectral density function is ignored [4]. For many of these time- and frequency-domain system identification methods, numerous limitations have arisen when conducting output-only system identification. Specifically, one of the most critical drawbacks associated with output-only system identification is the lack of mathematical methods of evaluation due to the lack of knowledge of the system input. In contrast, the accuracy of input-output system identification method can be evaluated by comparing the reproducibility of the system output from the estimated models [5].

Subspace system identification [6-8] was developed in the controls community to accurately formulate data-driven models without requiring physical formulation (*i.e.*, canonical parameterizations) and without any prior knowledge on the system properties. Recently, stochastic subspace identification (SSI), one type of subspace system identification, has been introduced to the civil engineering community as a powerful output-only identification [9]. SSI is well suited for output-only system identification because the method does not consider a deterministic input; rather, white process noise is assumed as the primary forcing function of the system. Currently, subspace system identification and its output-only versions have become common time-domain system identification methods in the civil engineering community due to MATLAB's numerical algorithms for subspace state-space system identification (*e.g.*, N4SID).

Despite the popularity of output-only system identification, a thorough comparison between each of the common methods has yet to be conducted by the civil engineering community. In this study, the accuracy of two of the most popular output-only system identification techniques is explored. First, the stochastic subspace identification (SSI) method implemented in the time-domain is considered. Second, the frequency-domain decomposition (FDD) method is also selected. Due to an absence of a mathematical methodology for directly comparing the accuracy of these output-only system identification methods, an indirect method is proposed. Towards this end, input-output system identification is first conducted to formulate accurate state space models of the system. The modal properties derived from the SSI and FDD output-only models are then compared to the input-output models. A steel frame structure excited at its base with ground motion is used for experimental validation.

NUMERICAL ALGORITHMS FOR SUBSPACE STATE-SPACE SYSTEM IDENTIFICATION

Due to the space limitations, N4SID algorithm is only briefly introduced for input-output system identification. The system input block Hankel matrix is constructed from past and future input data as follows:

$$\mathbf{U}_{0|2i-1} = \begin{bmatrix} \mathbf{u}_0 & \mathbf{u}_1 & \cdots & \mathbf{u}_{j-1} \\ \vdots & \vdots & \ddots & \vdots \\ \mathbf{u}_{i-1} & \mathbf{u}_i & \cdots & \mathbf{u}_{i+j-2} \\ \mathbf{u}_i & \mathbf{u}_{i+1} & \cdots & \mathbf{u}_{i+j-1} \\ \vdots & \vdots & \ddots & \vdots \\ \mathbf{u}_{2i-1} & \mathbf{u}_{2i} & \cdots & \mathbf{u}_{2i+j-2} \end{bmatrix} = \begin{bmatrix} \mathbf{U}_{0|i-1} \\ \mathbf{U}_{i|2i-1} \end{bmatrix} := \begin{bmatrix} \mathbf{U}_p \\ \mathbf{U}_f \end{bmatrix} \quad (1)$$

Similarly, the output block Hankel matrix, $\mathbf{Y}_{0|2i-1}$, is built from past and future output data. By defining the joint space of the past input and past output as $\mathbf{W}_p := [\mathbf{U}_p^T \quad \mathbf{Y}_p^T]^T$, an oblique projection of the row space of \mathbf{Y}_f onto the row space of \mathbf{W}_p along the row space of \mathbf{U}_f can be defined and denoted as $\mathbf{P}_i := \mathbf{Y}_f /_{\mathbf{U}_f} \mathbf{W}_p$. This oblique projection is equal to the production of the extended observability matrix and state sequence estimate as:

$$\mathbf{P}_i = \boldsymbol{\Theta}_i \hat{\mathbf{X}}_i = \begin{bmatrix} \mathbf{C}^T & (\mathbf{CA})^T & \cdots & (\mathbf{CA}^{i-1})^T \end{bmatrix}^T \begin{bmatrix} \hat{\mathbf{x}}_i & \hat{\mathbf{x}}_{i+1} & \cdots & \hat{\mathbf{x}}_{i+j-1} \end{bmatrix} \quad (2)$$

Singular value decomposition of the projection, \mathbf{P}_i , leads to:

$$\mathbf{P}_i = \mathbf{USV}^T \cong \begin{bmatrix} \mathbf{U}_1 & \mathbf{U}_2 \end{bmatrix} \begin{bmatrix} \mathbf{S}_1 & \mathbf{0} \\ \mathbf{0} & \mathbf{0} \end{bmatrix} \begin{bmatrix} \mathbf{V}_1^T \\ \mathbf{V}_2^T \end{bmatrix} = \mathbf{U}_1 \mathbf{S}_1 \mathbf{V}_1^T \quad (3)$$

By splitting the singular value matrix, the extended observability matrix and the state sequence estimate can be extracted from the decomposed projection matrix as:

$$\boldsymbol{\Theta}_i = \mathbf{U}_1 \mathbf{S}_1^{1/2}; \quad \hat{\mathbf{X}}_i = \mathbf{S}_1^{1/2} \mathbf{V}_1^T \quad (4)$$

Another oblique projection is defined as $\mathbf{P}_{i-1} := \mathbf{Y}_f^- / \mathbf{U}_f^- \mathbf{W}_p^+$ where $\mathbf{W}_p^+ := [(\mathbf{U}_p^+)^T \ (\mathbf{Y}_p^+)^T]^T$ is the joint space shifted forward by one time step. Similarly, the one-step shifted input and output block Hankel matrices are defined as:

$$\begin{bmatrix} \mathbf{U}_p^+ \\ \mathbf{Y}_f^- \end{bmatrix} := \begin{bmatrix} \mathbf{U}_{0|i} \\ \mathbf{U}_{i+1|2i-1} \end{bmatrix}; \quad \begin{bmatrix} \mathbf{Y}_p^+ \\ \mathbf{Y}_f^- \end{bmatrix} := \begin{bmatrix} \mathbf{Y}_{0|i} \\ \mathbf{Y}_{i+1|2i-1} \end{bmatrix} \quad (5)$$

Similar to Eq. (2), a new oblique projection, \mathbf{P}_{i-1} , is formulated equal to the extended observability matrix shifted one time step backwards and state sequence estimate shifted one time step forward: $\mathbf{P}_{i-1} = \mathbf{\Theta}_{i-1} \hat{\mathbf{X}}_{i+1}$. Thus, with the given projection \mathbf{P}_{i-1} and the observability matrix lacking the last block row, $\mathbf{\Theta}_{i-1}$, the one-step shifted state sequence estimate $\hat{\mathbf{X}}_{i+1}$ is calculated as:

$$\hat{\mathbf{X}}_{i+1} = (\mathbf{\Theta}_{i-1})^\dagger \mathbf{P}_{i-1} \quad (6)$$

The system equations can be written with previously calculated matrices as follows:

$$\begin{bmatrix} \hat{\mathbf{X}}_{i+1} \\ \mathbf{Y}_{i|i} \end{bmatrix} = \begin{bmatrix} \hat{\mathbf{A}} \\ \hat{\mathbf{C}} \end{bmatrix} \hat{\mathbf{X}}_i + \begin{bmatrix} \hat{\mathbf{B}} \\ \hat{\mathbf{D}} \end{bmatrix} \mathbf{U}_{i|i} + \begin{bmatrix} \boldsymbol{\rho}_w \\ \boldsymbol{\rho}_v \end{bmatrix} = \begin{bmatrix} \hat{\mathbf{A}} & \hat{\mathbf{B}} \\ \hat{\mathbf{C}} & \hat{\mathbf{D}} \end{bmatrix} \begin{bmatrix} \hat{\mathbf{X}}_i \\ \mathbf{U}_{i|i} \end{bmatrix} + \begin{bmatrix} \boldsymbol{\rho}_w \\ \boldsymbol{\rho}_v \end{bmatrix} \quad (7)$$

where $\boldsymbol{\rho}_w$ and $\boldsymbol{\rho}_v$ are residual matrices due to noise. Finally, a least squares estimate of the system matrices can be calculated by a pseudo-inverse:

$$\begin{bmatrix} \hat{\mathbf{A}} & \hat{\mathbf{B}} \\ \hat{\mathbf{C}} & \hat{\mathbf{D}} \end{bmatrix} = \begin{bmatrix} \hat{\mathbf{X}}_{i+1} \\ \mathbf{Y}_{i|i} \end{bmatrix} \begin{bmatrix} \hat{\mathbf{X}}_i \\ \mathbf{U}_{i|i} \end{bmatrix}^\dagger \quad (8)$$

Eq. (8) is termed the combined deterministic stochastic subspace identification (CDSI). Stochastic subspace identification (SSI) can also be formulated without considering the input $\mathbf{U}_{0|2i-1}$. In SSI, the system matrices are calculated as:

$$\begin{bmatrix} \hat{\mathbf{A}} \\ \hat{\mathbf{C}} \end{bmatrix} = \begin{bmatrix} \hat{\mathbf{X}}_{i+1} \\ \mathbf{Y}_{i|i} \end{bmatrix} \hat{\mathbf{X}}_i^\dagger \quad (9)$$

Modal parameters can be estimated from the estimated system matrices (*i.e.*, $\hat{\mathbf{A}}$ and $\hat{\mathbf{C}}$) by standard eigen-decomposition:

$$\hat{\mathbf{A}} = \boldsymbol{\Psi} \boldsymbol{\Lambda} \boldsymbol{\Psi}^{-1} \quad (10)$$

where the diagonal matrix $\boldsymbol{\Lambda} = \text{diag}(\lambda_{di})$ consists of the discrete-time complex-valued eigenvalues. $\boldsymbol{\Psi}$ contains the eigenvectors in each column. The damping ratio and natural frequency of i^{th} mode can be calculated by converting the discrete-time eigenvalues to the continuous-time domain. The mode shape vectors for i^{th} mode Φ_i , can be calculated as:

$$\boldsymbol{\Phi} := [\Phi_1 \ \dots \ \Phi_i \ \dots \ \Phi_n] = \hat{\mathbf{C}} \boldsymbol{\Psi} \quad (11)$$

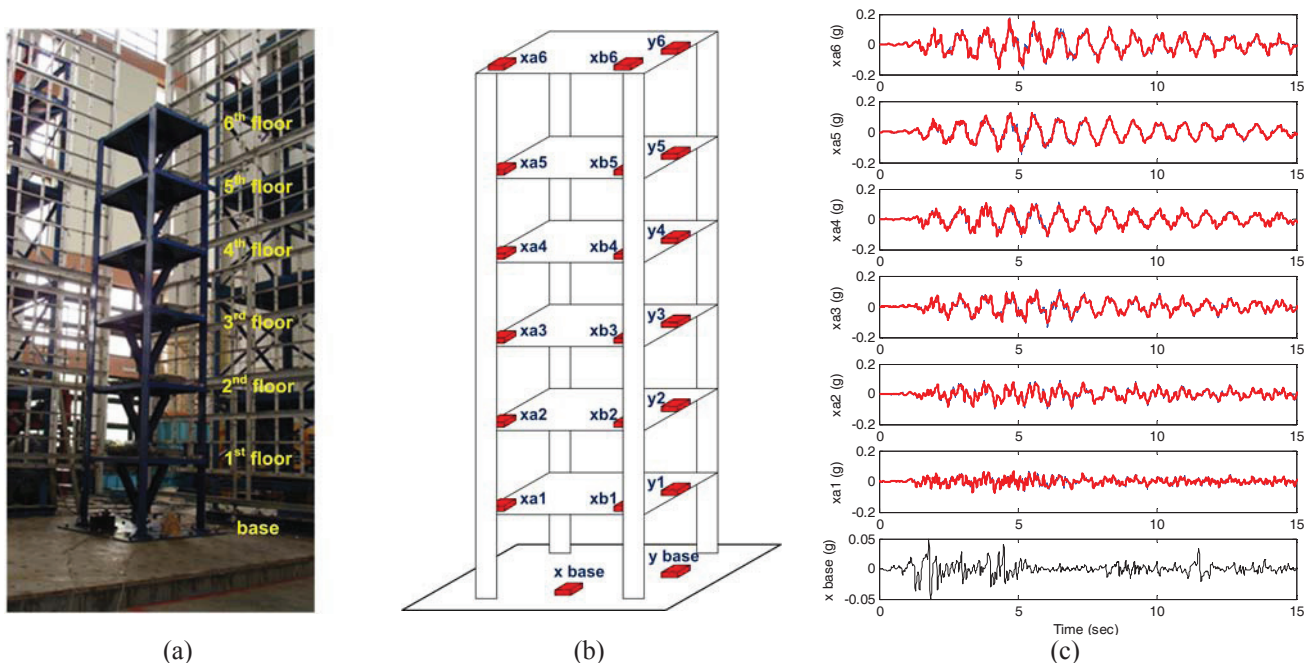


Fig. 1. Experimental set-up: (a) 6-story steel building structure pictured on the NCREE shaking table; (b) installation of 20 accelerometers in the structure; (c) measured signal (thin) vs. predicted (thick) response during the El Centro test.

FREQUENCY DOMAIN DECOMPOSITION METHOD

Frequency domain decomposition (FDD) is an output-only version of the conventional complex mode indicator function (CMIF) method [3, 10]. The relationship between the system input, \mathbf{u} , and the measured output, \mathbf{y} , can be expressed in the continuous-time frequency domain as follows:

$$\mathbf{G}_{\mathbf{y}\mathbf{y}}(j\omega) = \mathbf{H}(j\omega)\mathbf{G}_{\mathbf{u}\mathbf{u}}(j\omega)\mathbf{H}^H(j\omega) \quad (12)$$

Where $\mathbf{G}_{\mathbf{u}\mathbf{u}}$ is the power spectral density (PSD) matrix of the input, $\mathbf{G}_{\mathbf{y}\mathbf{y}}$ is the PSD matrix of the output, \mathbf{H} is frequency response function (FRF) matrix, and \mathbf{H}^H is its complex transpose conjugate. If the system input is known to be a Gaussian process (*i.e.*, ideal white noise), $\mathbf{G}_{\mathbf{u}\mathbf{u}}$ will simply be a constant matrix; hence, $\mathbf{G}_{\mathbf{y}\mathbf{y}}$ is directly proportional to the product of FRFs: $\mathbf{H}(j\omega)\mathbf{H}^H(j\omega)$. By applying SVD to Eq. (12), the output PSD matrix can be decomposed. At known modal frequencies, the singular vectors are correlated to the system mode shapes.

INPUT-OUTPUT SYSTEM IDENTIFICATION OF SUPPORT-EXCITED STRUCTURES

A steel frame structure (Fig. 1) is built on a shaking table at the National Center for Research in Earthquake Engineering (NCREE) at National Taiwan University (NTU) to serve as a test-bed structure for this study. The structure is a large-scale (6 m height) six-story single-bay steel building. Four rectangular steel columns support the floors with floor having an area of 1 m by 1.5 m. Each inter-story height is 1 m. Due to rectangular cross section of the columns, the structure has two orthogonal axes: the flexurally weak axis (termed the x-axis) and flexurally strong axis (termed the y-axis). To induce a dynamic response of the structure, two dimensional lateral excitations are applied to the structure by the laboratory shaking table. A total of 20 accelerometers were installed at each floor and shaking table as seen in Fig. 1-(b). Each floor was instrumented with three accelerometers: two are aligned to measure acceleration along the x-axis (denoted as x_a and x_b) and one aligned to measure the y-axis acceleration. Additionally, two accelerometers were placed orthogonally at the ground level to measure the two dimensional shaking table excitations. Two moderate excitation inputs were applied to both axes. A 40 s El Centro earthquake ground motion was applied along the two orthogonal axes (the recorded peak ground accelerations of the x- and y-axes were 0.053 g and 0.044 g, respectively). In addition, a 120 s white noise ground motion record with a variance of 0.061 g and 0.0745 g was applied to the x- and y-axes, respectively. During the tests, acceleration data was collected with a 100 Hz sampling rate.

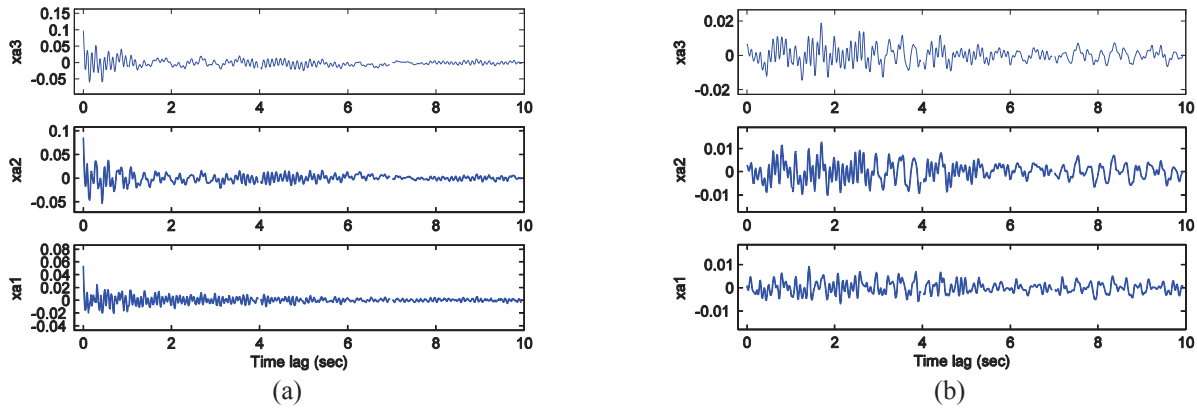


Fig. 2. Residual analysis for the El Centro test: (a) autocorrelations of the model residuals; (b) cross-correlations of the residuals and the original base excitation signal.

Subspace system identification (N4SID) was conducted off-line using 30 s of the input-output data sets corresponding to both sets of ground motion excitation. To validate the estimated model derived from input-output system identification, the model’s ability to reproduce the output signal from a given input signal is checked. This procedure is commonly termed as simulation or prediction [5]. Fig. 1-(c) depicts the measured and predicted output responses of the structure to the El Centro base motions. As seen, it is very difficult to discriminate between the two signals due to the excellent match. However, an extremely small discrepancy can be founded in the plot. The difference between the two signals seems to be arbitrary along the time axis and can be considered as a prediction-error or residual of the prediction. Thus, stochastic signal analysis was also conducted with the model residuals. Fig. 2 plots the autocorrelation of the residual time histories and the cross-correlation between the residual and input time histories. If the residual is considered as an innovation sequence, the residual represents a white noise sequence. As seen in Fig.2-(a), the autocorrelation of the residual closely resembles that of a Kronecker delta function which is the autocorrelation of a white noise process. However, small and arbitrary correlation between the model residual and the excitation input is found in Fig.2-(b) suggesting a strong independence of the estimated model from the deterministic input. Similar results are also confirmed for the estimated model derived from the white noise tests. Based on the results of the model’s ability to reproduce a deterministic input signal (Fig.1-(c)), the whiteness of the model residuals (Fig.2-(a)), and the model’s independence to the system input (Fig.2-(b)), it is concluded that an extremely accurate input-output system model exists. Hence, modal parameters calculated from the estimated model represent the real modal properties of the true system. A total of 12 mode shapes are identified up to 25 Hz for both models (*i.e.*, the model derived from the El Centro and white noise ground motions). Among the results, estimated mode shapes from

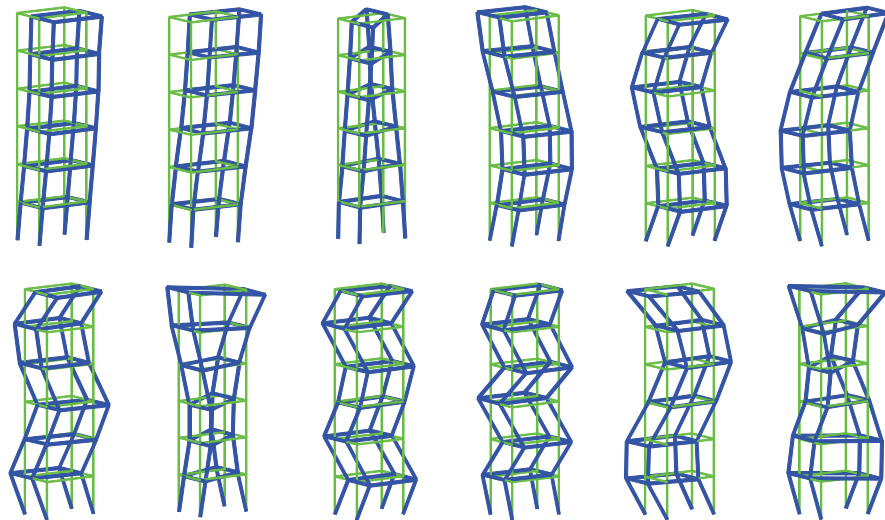


Fig. 3. The first 12 mode shapes estimated by input-output subspace system identification for the El Centro test.

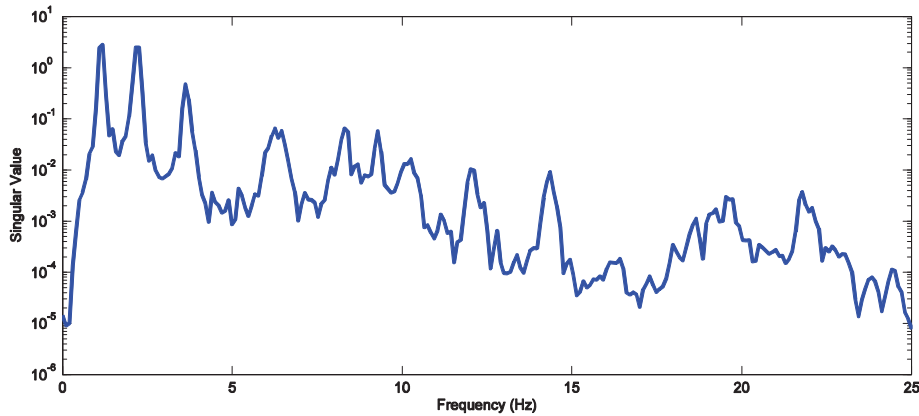


Fig. 4. Singular value spectra (0 to 25 Hz) for El Centro test.

the El Centro test are depicted in Fig. 3. The modes correspond to flexural modes in the x-direction (Mode 1, 4, 5, 7, 9, and 10), flexural modes in the y-direction (Mode 2, 6, and 11), and torsional modes (Mode 3, 8, and 12).

MODAL PARAMETER EVALUATION OF OUTPUT-ONLY SYSTEM IDENTIFICATION

Two output-only system identification methods are explored: time-domain SSI and frequency-domain FDD. Again, the collected output data from the aforementioned support-excited steel frame structure is used. In both output-only system identifications, the same 30s long segment of the output response used in the input-output system identification is used. First, FDD is conducted on the same data set. However, the quality of the FDD is based on the estimate of the PSD. There is a trade-off between a reduction of the noise and retention of the distinctive qualities of the modal peaks in output PSD estimation when averaging Fourier spectra to derive the PSD function [11]. The frequency resolution of the fast Fourier transform (FFT) is equal to the inverse of the sample time step multiplied by the number of points. Thus, given the limited number of data points used (3,000) and the sample time step (0.01 sec), there is also a trade-off between frequency resolution and distinctive peaks in the PSD estimation. The best frequency resolution is determined as 0.097 Hz ($=1/(1024 \times 0.01)$) which avoids any difficulty of finding distinctive peaks in the singular value spectra. Namely, estimation of the PSD is conducted by 3000 point output data by applying a 1024-point FFT using a Hanning window and with a 50% time-domain overlap between successive FFTs. By selecting very distinctive peaks in the singular value spectra (Fig. 4), the natural frequencies are determined and the mode shapes are automatically acquired from the corresponding first singular vector. In this study, damping estimation by FDD from the estimated PSD is skipped. Results of the estimated modal parameters for the El Centro test and white noise test are tabulated in Table 1 and Table 2, respectively.

Next, time-domain SSI is conducted first using the 30s long record (3,000 points) using Eq. (9). Using the estimate system matrices, the mode shapes are extracted. Modal damping ratio is one of the most challenging modal parameters to estimate, even for input-output system identification. Thus, analyzing the damping ratio error between input-output system identification and that derived from the SSI analysis can be difficult. In this study, a smaller error on the damping ratio is found during the white noise tests compared to the El Centro tests. Except for the modal damping ratio, it is assumed that the modal parameters of the input-output system identification represent those of the true system for comparison to the two output-only system identifications. Natural frequency estimation by SSI is much better than that of FDD, as seen in Table 1. The poor natural frequency estimation of FDD results from the low frequency resolution used in this study. Estimated mode shapes can be quantitatively evaluated by the modal assurance criterion (MAC). Based on MAC results, the mode shape estimated by FDD seem better than those offered by SSI. Since the mode shape of the second mode in the SSI analysis of El Centro data can be considered as an outlier of the system identification process, it is difficult to conclude that better mode shape estimation is attained by FDD.

In modal parameter estimation of the white noise test (Table 2), SSI estimates very precise natural frequencies. However, there is an outlier of mode shape estimation for the third mode. Due to the lower frequency resolution, there is about a 1 % natural frequency estimation error on the FDD results. Similar mode shape estimation accuracy is shown between SSI and FDD. The mode shape of the third mode can be considered as an outlier in both SSI and FDD.

Comparing the accuracy of both output-only system identifications, it can be concluded that: 1) similar accuracy of mode shape estimation is confirmed between the time-domain SSI and frequency-domain FDD methods; 2) in the case of output-only system identification with a limited number of data points, time-domain SSI is recommended rather than frequency-domain FDD due to the low resolution issues of FDD when estimating natural frequency.

Table 1. Comparisons of estimated modal parameters for El Centro test from input-output identification (Inp/Out) and two output-only identifications (SSI and FDD) with 30 sec long data.

Mode	Natural frequencies (Hz)					Damping ratio			MAC	
	Inp/Out	SSI	Error(%)	FDD	Error(%)	Inp/Out	SSI	Error(%)	SSI	FDD
Mode 1	1.115	1.125	0.880	1.172	5.099	0.013	0.006	57.477	0.999	0.998
Mode 2	2.206	2.192	0.643	2.246	1.801	0.019	0.008	57.384	0.037	0.980
Mode 3	3.056	3.198	4.650	3.320	8.656	0.062	0.051	16.855	0.927	0.407
Mode 4	3.626	3.630	0.123	3.613	0.339	0.010	0.010	0.558	0.990	0.991
Mode 5	6.324	6.310	0.227	6.250	1.172	0.009	0.017	85.510	0.998	0.998
Mode 6	8.454	8.333	1.432	8.691	2.802	0.015	0.026	70.177	0.996	0.951
Mode 7	9.225	9.254	0.323	9.277	0.572	0.009	0.011	19.914	0.989	0.987
Mode 8	10.270	10.240	0.286	10.254	0.153	0.011	0.015	30.130	0.997	0.965
Mode 9	12.122	12.055	0.556	12.402	2.310	0.004	0.009	152.256	0.861	0.968
Mode 10	14.329	14.337	0.052	14.355	0.184	0.004	0.004	3.457	0.963	0.997
Mode 11	19.544	19.583	0.202	19.531	0.063	0.010	0.023	121.802	0.832	0.996
Mode 12	21.870	21.812	0.262	21.777	0.422	0.016	0.016	3.332	0.971	0.983
Mean			0.803		1.964	0.015	0.016	51.571	0.880	0.935

Table 2. Comparisons of estimated modal parameters for white noise test from input-output identification (Inp/Out) and two output-only identifications (SSI and FDD) with 30 sec long data.

Mode	Natural frequencies (Hz)					Damping ratio			MAC	
	Inp/Out	SSI	Error(%)	FDD	Error(%)	Inp/Out	SSI	Error(%)	SSI	FDD
Mode 1	1.123	1.121	0.011	1.172	4.309	0.011	0.005	52.094	1.000	1.000
Mode 2	2.243	2.232	0.018	2.344	4.479	0.018	0.030	67.774	0.999	0.977
Mode 3	2.937	2.931	0.013	2.930	0.248	0.013	0.013	3.464	0.228	0.324
Mode 4	3.627	3.639	0.009	3.613	0.377	0.009	0.009	0.894	1.000	1.000
Mode 5	6.327	6.352	0.008	6.348	0.325	0.008	0.010	23.874	1.000	0.999
Mode 6	8.535	8.525	0.013	8.594	0.694	0.013	0.015	9.703	0.999	0.965
Mode 7	9.208	9.169	0.007	9.180	0.312	0.007	0.011	50.648	0.998	0.988
Mode 8	10.452	10.421	0.009	10.352	0.961	0.009	0.012	27.985	0.981	0.962
Mode 9	12.090	12.092	0.005	12.109	0.164	0.005	0.004	14.979	0.954	0.999
Mode 10	14.335	14.343	0.003	14.258	0.541	0.003	0.006	69.438	0.990	0.997
Mode 11	19.758	19.701	0.009	19.727	0.159	0.009	0.015	60.688	0.999	0.999
Mode 12	21.975	21.987	0.006	21.875	0.456	0.006	0.007	13.804	0.996	0.999
Mean			0.009		1.085	0.009	0.011	32.946	0.929	0.934

CONCLUSIONS

Experimental comparisons on the accuracy of two output-only system identification analyses is conducted. The time-domain stochastic subspace identification (SSI) and frequency-domain frequency domain decomposition (FDD) are explored in detail. Specifically, both system identification methods are presented for support-excited frame structures common in civil engineering applications. The modal properties extracted from both system identification methods are compared to those obtained from input-output SSI analysis. Overall, a similar performance was confirmed between the SSI and FDD methods. However, the results of the FDD analyses slightly suffered from low frequency resolution problems due to the limited number of data points. Even though SSI is free from this resolution problem,

SSI might generate more frequent outliers compared to FDD. Thus, statistical approaches entailing repeated experimentation of the same system maybe required when dealing with output-only modal analysis to avoid outliers.

ACKNOWLEDGMENTS

The authors would like to gratefully acknowledge the generous support offered by the National Science Foundation under Grant CMMI-0726812 (Program Manager: Dr. S. C. Liu). Additional support was provided by the NIST Technology Innovation Program (Contract 70NANB9H9008) and the Office of Naval Research (Grant N000141-01-0613). The authors would also like to thank Prof. C. H. Loh of National Taiwan University and NCREE staff for their generous support during the experimental testing at the NCREE shake table facility.

REFERENCE

1. Ibrahim, S.R. and S.R. Pappa, Large Modal Survey Testing Using the Ibrahim Time Domain Identification Technique. *Journal of Spacecraft and Rockets*, 1982. 19(5): p. 459-465.
2. James, J.H., T.G. Carne, and J.P. Lauffer, The Natural Excitation Technique (NExT) for Modal Parameter Extraction from Operating Structures. *The International Journal of Analytical and Experimental Modal Analysis*, 1996. 10(4): p. 260-277.
3. Shih, C.Y., Y.G. Tsuei, R.J. Allemang, and D.L. Brown, Complex Mode Indication Function and its Applications to Spatial domain Parameter Estimation. *Mechanical Systems and Signal Processing*, 1988. 2(4): p. 367-377.
4. Brinker, R., L. Zhang, and P. Andersen, Modal Identification of Output-only Systems Using Frequency Domain Decomposition. *Smart Materials and Structures*, 2001. 10(3): p. 441-445.
5. Ljung, L., *System identification: Theory for the User*. 1999, Upper Saddle River, NJ: Prentice Hall.
6. Larimore, W.E. Canonical Variate Analysis in Identification, Filtering, and Adaptive Control. in *29th Conference on Decision and Control*. 1990. Honolulu, HI.
7. Verhaegen, M., Identification of the Deterministic Part of MIMO State Space Models Given in Innovations form from Input-output Data. *Automatica*, 1994. 30(1): p. 61-74.
8. Van Overschee, P. and B. De Moor, N4SID: Subspace Algorithms for the Identification of Combined Deterministic-Stochastic Systems. *Automatica*, 1994. 30(1): p. 75-93.
9. Peeters, B. and G.D. Roeck, Reference-based Stochastic Subspace Identification for Output-only Modal Analysis. *Mechanical Systems and Signal Processing*, 1999. 13(6): p. 855-878.
10. Peeters, B. and C.E. Ventura, Comparative Study of Modal Analysis Techniques for Bridge Dynamic Characterizes. *Mechanical Systems and Signal Processing*, 2003. 17(5): p. 965-988.
11. Oppenheim, A.V. and R.W. Schaffer, *Discrete-time Signal Processing*. 1999, Upper Saddle River, NJ: Prentice-Hall Inc.

Footbridge Response Predictions and Their Sensitivity to Stochastic Load Assumptions

Lars Pedersen, Christian Frier

Aalborg University
Department of Civil Engineering
Sohngaardsholmsvej 57
DK-9000 Aalborg

ABSTRACT

Knowledge about footbridges response to actions of walking is important in assessments of vibration serviceability. In a number of design codes for footbridges, the vibration serviceability limit state is assessed using a walking load model in which the walking parameters (step frequency, pedestrian mass, dynamic load factor, etc.) are modelled deterministically. This is a simplification of matters, as the walking parameters are basically stochastic as they will be different from one pedestrian to the next. The present paper considers a stochastic approach to modelling the action of pedestrians for predicting footbridge response, which is meaningful, and a step forward. Modelling walking parameters stochastically, however, requires decisions to be made in terms of their statistical distribution and the parameters describing the statistical distribution. The paper investigates the sensitivity of results of computations of bridge response to some of the decisions to be made in this respect. This is a useful approach placing focus on which decisions (and which information) are important for sound estimation of bridge response. The studies involve estimating footbridge responses using Monte-Carlo simulations and focus is on estimating vertical structural response to single person loading.

NOMENCLATURE

f_0	Bridge frequency	f_s	Step frequency	f	Walking load
l_s	Stride length	m	Weight of pedestrian	p	Prob. density function
q	Modal load	L	Bridge length	M	Bridge modal mass
P	Prob. distribution function	a	Bridge acceleration	α	Dynamic load factor
ζ	Bridge damping ratio	μ	Mean value	σ	Standard deviation

1. INTRODUCTION

Vibrations in structures induced by walking are the subject of this paper. Focus is on vibrations in footbridges, but walking-induced vibration problems are also seen in flooring-systems. The London Millennium Bridge incident [1] certainly put walking-induced vibrations on the map, but still today there are unresolved issues when the agenda is serviceability evaluation of structures exposed to walking-induced vibrations.

Many codes of practise (such as [4,5]) rely on simplistic formula in which walking loads are modelled deterministically. By default the load amplitude of the harmonic excitation is fixed to a certain value even though research has shown that it depends on properties which are quite likely to vary between pedestrians. It would depend on the static weight of the

pedestrian, on the dynamic load factor of the pedestrian (which is not the same for all pedestrians [9]), and on the step frequency of walking (which neither is the same for all pedestrians [2,3]).

An alternative to the very simplified deterministic approach of walking load modelling is a recently developed probabilistic approach [3]. In this the parameters of the load model may be modelled as random variables. This approach is more difficult to operate. At least there are decisions to be made in terms of distribution types, standard deviations etc. It would be simpler if some of the parameters of the load model with reasoning, could be modelled deterministically.

A full probabilistic approach might not be necessary if the outcome of bridge response calculations (in this case a probability distribution function of bridge response) is insensitive to whether one or more parameters of the load model are treated deterministically or stochastically. Sensitivity studies reported in [10] have already suggested that for instance the pedestrian weight might not be necessary to model stochastically. This paper addresses the dynamic load factor, which along with pedestrian weight is a property that determines the load amplitude of walking.

The idea of the study (a sensitivity study) is to investigate whether very simplistic and deterministic approaches to modelling the dynamic load factor will do as fine as the reference case where the dynamic load factor is modelled as a random variable.

The parameters used for evaluating feasibility of the simplistic models for the dynamic load factor are selected characteristics of the probability distribution function for footbridge response, which is derived from numerical simulations. To facilitate the investigations, a footbridge model is required, and to this end a pin-supported footbridge (idealised as a single-degree-of-freedom system, SDOF-system) is employed. The response characteristic given focus is the midspan peak acceleration. Five different bridges with different fundamental frequencies are considered so as to widen the basis for evaluations.

Characteristics of bridges and walking loads are introduced in section 2. Section 3 outlines how load parameters (hereunder the dynamic load factor) are modelled, and section 4 describes how characteristics of probability distribution functions of bridge response are obtained. Section 5 presents the results, which are discussed.

2. CHARACTERISTICS OF BRIDGES AND WALKING LOADS

The dynamic characteristics of the bridges considered for the studies of this paper (A-F) are shown in Table 1, along with the assumed bridge length, L .

Table 1 Bridge dynamic characteristics

Bridge	f_0	M	ζ	L
A	1.60 Hz	$61.5 \cdot 10^3$ kg	0.5 %	54 m
B	1.75 Hz	$51.5 \cdot 10^3$ kg	0.5 %	49 m
C	1.90 Hz	$44.0 \cdot 10^3$ kg	0.5 %	45 m
D	2.05 Hz	$37.5 \cdot 10^3$ kg	0.5 %	42 m
F	2.20 Hz	$32.5 \cdot 10^3$ kg	0.5 %	39 m

Different bridge frequencies (f_0) are considered. They are all within the range of step frequencies of walking that are realistic, so resonant excitation is a possibility. Bridge C is the one that is expected to come into resonant vibrations most often, as its frequency is close to the mean value of step frequency assumed for the studies of this paper (1.87 Hz). Bridges A and F have frequencies which deviates the most from the mean value of step frequency.

The modal mass (M) is modelled such that it decreases with increases in bridge frequency, which is considered fairly realistic for a pin-supported bridge configuration. In the same way (and as modelled) it is considered realistic that the length of the bridge, L , increases with decreases in bridge frequency.

For all bridges a damping ratio, ζ , of 0.5 % of critical damping is assumed, which is a low value, but it could be even lower for some bridges. For the studies of this paper, it is not of great importance, which value is assumed for ζ as focus of the study is not on magnitudes of vibration. Focus is on how and whether the magnitudes of vibration change when simplified models for the dynamic load factor are introduced.

The dynamic load factor is a central parameter of the walking load model, which is introduced below. Focus is on walking loads in the vertical direction. The load time-history, $f(t)$, generated by a pedestrian may (in accordance with [6-8] and a number of other references), be computed from eq. 1 in which t is time.

$$f(t) = mg\alpha \cos(2\pi f_s t) \quad (1)$$

It is a harmonic excitation with a frequency, f_s , representing the step frequency of walking. The paper assumes that the value of f_s will change from one pedestrian to the next, hence f_s is treated as a random variable. When a pedestrian traverses the bridge, f_s will be modelled as a constant as normally done. How the dynamic load factor, α (non-dimensional), and the pedestrian weight, m (in kg), are modelled will be presented later. The parameter g represents acceleration of gravity (for simplicity $g = 10$ N/kg is assumed).

Super-harmonic load components (nf_s , $n = 2, 3, \dots$) would exist, but are not accounted for here, since for the SDOF bridges considered for the study, it would be the load harmonic shown in eq. 1 (with a load frequency in close vicinity of the bridge frequency) that excites the bridge system.

Making use of the modeshape function for the first vertical bending mode assumed to be:

$$\Phi(t) = \sin(\pi f_s l_s / L) \quad (2)$$

at the position of the pedestrian, it can be shown that the modal load on the bridge, $q(t)$, may be computed using eq. 3:

$$q(t) = mg\alpha \cos(2\pi f_s t) \sin(\pi f_s l_s / L) \quad (3)$$

This result assumes that the pedestrian traverses the bridge using a constant stride length, l_s , (or step length). This is assumed for the studies of this paper, but randomness in stride length is considered (that stride length may vary from one pedestrian to the next).

3. MODELS FOR PARAMETERS OF THE LOAD MODEL

Section 3.1 outlines assumptions for all parameters of the load model except for those assumed for the dynamic load factor. The different approaches to modelling the dynamic load factor are presented in section 3.2.

3.1 Models for some of the walking parameters

Step frequency (f_s), and stride length (l_s) are modelled as random variables as suggested in [3] and Gaussian distributions are assumed. The assumed mean values (μ) and standard deviations (σ) are shown in Table 2 along with the assumptions made for pedestrian weight (m).

Table 2 Mean values and standard deviations

Variable	Unit	μ	σ
f_s	Hz	1.87	0.186
l_s	m	0.71	0.071
m	kg	75	13.5

As it appears, the pedestrian weight is also modelled as a random variable and again a Gaussian distribution is assumed. In [3], the pedestrian weight was modelled deterministically, but for completeness a standard deviation is added in the present case. Studies reported in [10,11] investigated whether the deterministic approach used in [3] was meaningful. It was found that the bridge response characteristics in focus in this paper are not very sensitive to whether pedestrian weight is modelled deterministically or stochastically.

3.2 Models for the dynamic load factor

Kerr [9] studied the dynamic load factor and from experiments he found a relationship with step frequency, f_s (to be inserted in Hz in eq. 4):

$$\alpha = c_1 f_s^3 + c_2 f_s^2 + c_3 f_s + c_4 \quad (4)$$

where

$$c_1 = -0.2649 \quad c_2 = 1.306 \quad c_3 = -1.7597 \quad c_4 = 0.7613 \quad (5)$$

Eq. 4 is to be interpreted as the relationship between the mean value of the dynamic load factor (also denoted μ_α) for a given step frequency, f_s . The relationship is calibrated to measurement results in the frequency range of $1 \text{ Hz} < f_s < 2.7 \text{ Hz}$. Assuming a Gaussian distribution, Kerr also identified a standard deviation of the dynamic load factor (denoted σ_α), which was generally independent of f_s :

$$\sigma_\alpha = 0.16 \mu_\alpha \quad (6)$$

This approach of modelling the dynamic load factor (as a random variable) is quite refined compared with what can be found in current codes of practise. For instance [4,5] do not recognise that the dynamic load factor depends on step frequency. Simplifications will also be considered here, of which some will recognise that the dynamic load factor depends on frequency.

The studies of this paper will consider three different approaches to modelling the dynamic load factor, one of which directly employs the set of equations presented above (approach 1).

Table 3 Mean values and standard deviations for α

Approach	μ_α	σ_α
1	Eq. 4 for any value of f_s (random variable)	Eq. 6
2	Eq. 4 with $\alpha = \alpha(f_0)$	0
3	Eq. 4 with $\alpha = \alpha(\mu(f_s) = 1.87 \text{ Hz})$	0

Approach 1 is the most advanced approach. Here the value of the dynamic load factor will depend on both the step frequency of walking (which is modelled as a random variable), and on the non-zero standard deviation assumed for the dynamic load factor itself (also modelled as a random variable).

In approach 2 and 3, the dynamic load factor is modelled as a deterministic property only depending on frequency. Regardless of the fact that the step frequency is modelled as a random variable with different outcomes for each pedestrian, the dynamic load factor is modelled for a single frequency:

In approach 2, the dynamic load factor is picked from equation 4 with f_s set to the bridge frequency f_0 .

In approach 3, the dynamic load factor is also picked from equation 4, but with f_s set to the mean value of the step frequency $\mu(f_s) = 1.87 \text{ Hz}$.

A further simplification associated with approach 2 and 3 is that a non-zero standard deviation is not assumed for the dynamic load factor (in other words $\sigma_\alpha = 0$ is assumed).

The picking of values for the dynamic load factor for approach 2 and 3 is illustrated in Fig. 1 for bridge B (having a frequency f_0 of 1.75 Hz). For all 5 bridges considered in the study, the same value for the dynamic load factor will be picked using approach 3 (that at 1.87 Hz). Hence, approach 3 represents an approach in which α is modelled as a constant and in this way the approach has some resemblance with codified approaches.

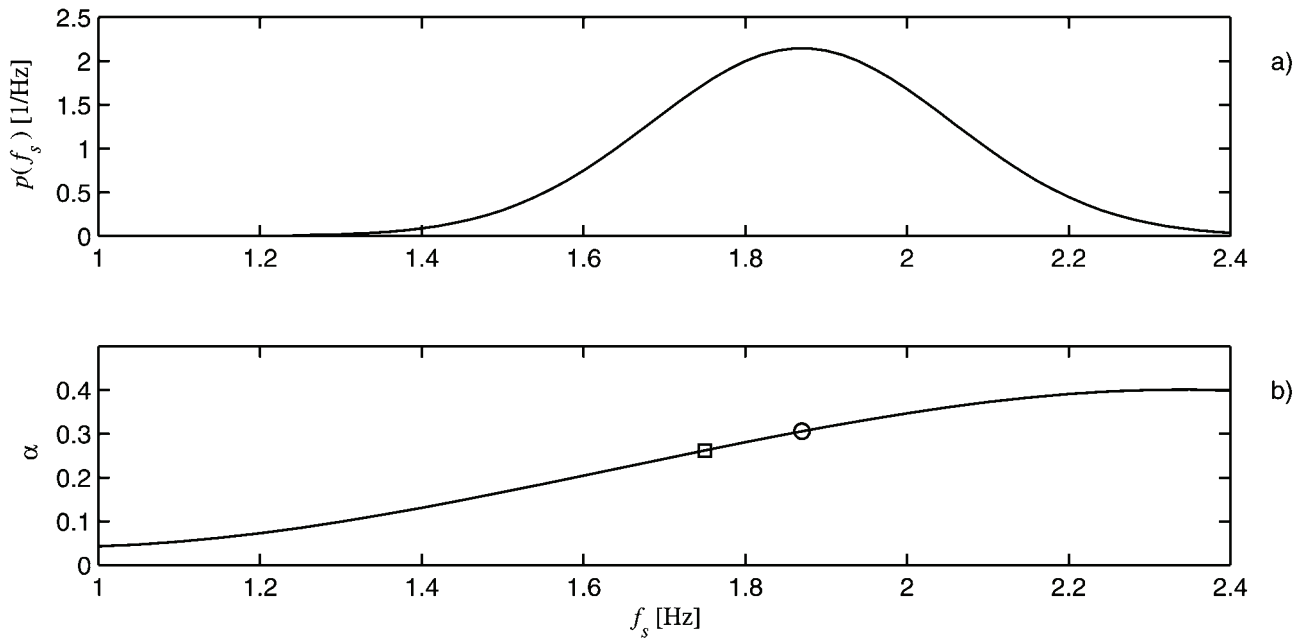


Fig. 1 a) Probability density function for f_s . b) Picking of values of the dynamic load factor from eq. 4.

Approach 2: \square , Approach 3: \circ

Naturally, the picking-approach from eq. 4 (illustrated in Fig. 1) is a simplification, as it does not recognise all mechanisms inherent in the findings of Kerr. However, the interesting part is whether probability distributions of bridge responses are sensitive to this simplification. If not, it would be a simpler strategy to implement approach 2 or 3 for calculations of probability distribution functions of bridge responses.

4. MONITORED CHARACTERISTICS DESCRIBING BRIDGE RESPONSE

Characteristics of the probability distribution function of bridge accelerations (quantiles) are used to evaluate the performance of different ways to modelling the dynamic load factor. It is the midspan peak accelerations that are considered and the probability distribution functions of bridge accelerations are computed using MonteCarlo- simulation methods accounting for the modelled randomness in the parameters of the load model. As many as 500,000 simulation runs (each emulating a pedestrian crossing the bridge) were made to provide confidence in the computed statistical distributions. For computing bridge response to the action of a single pedestrian, a Newmark time integration scheme was employed. High quantiles of the probability distribution function, such as a_{95} , are believed to be of primary interest. The acceleration level a_{95} is expected to be exceeded in 1 out of 20 bridge crossings. For completeness, some other quantiles were also monitored.

5. RESULTS

In terms of results, focus is first on the quantile a_{95} of bridge acceleration response, as this is the property most often in focus when considering a probabilistic approach to describing the bridge response.

For the different bridges (identified by their natural frequency f_0), the quantiles a_{95} ended up with the values shown in Fig. 2. The legend identifies the approach made for the analyses in terms of how the dynamic load factor was modelled.

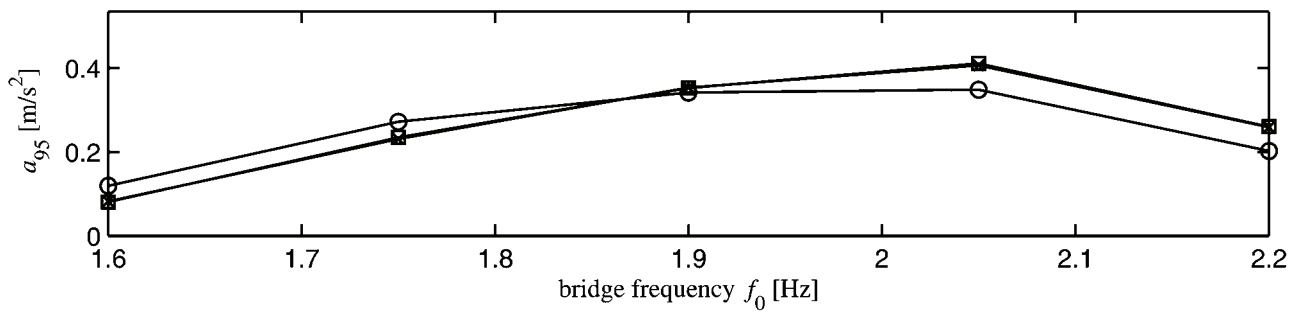


Fig. 2 Relationship between bridge frequency and a_{95} for approach 1 (x), 2 (□), and 3 (o)

It is recalled that approach 1 is the full stochastic approach. This is thus the reference. Approach 2 and 3 are the approaches being tested.

It can be seen that for bridge C both simplistic approaches (approach 2 and 3) give values of the quantile a_{95} , which are almost equal. This is by no means surprising, as for this bridge the mean value of step frequency (1.87 Hz) is almost identical to the bridge frequency itself (1.9 Hz).

Another item to notice is that for bridge C, there is a very good match between the values of a_{95} obtained using the three different approaches.

For the other bridges, it appears that approach 2 performs quite well in terms of predicting values of a_{95} that match those obtained employing approach 1. Generally, approach 3 does not perform as well as approach 2.

As previously mentioned not only a_{95} was monitored in calculations. Fig. 3 shows the calculated relationships between bridge frequency and the quantiles $a_{97.5}$ and a_{75} as computed using the three different approaches for modelling the dynamic load factor.

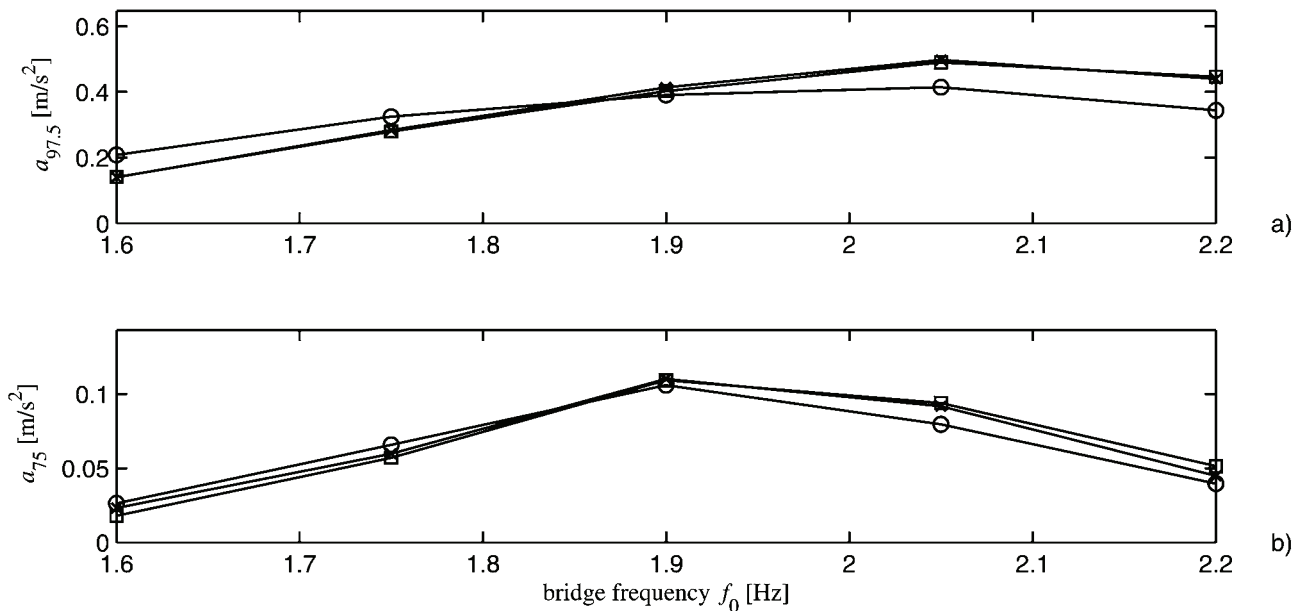


Fig. 3 Relationships between bridge frequency and $a_{97.5}$ (a) and a_{75} (b) for approach 1 (x), 2 (□), and 3 (o)

For the quantile $a_{97.5}$ again it is the tendency that approach 2 gives results that match those obtained using approach 1 quite well. For the quantile a_{75} , the performance of approach 2 is not as good as it was for the higher quantiles a_{95} and $a_{97.5}$. That a_{95} and $a_{97.5}$ are represented quite well by approach 2 is believed to have to do with the fact that the high responses are those caused by resonant action occurring when $f_s = f_0$. For somewhat lower characteristics of the probability distribution function (for instance a_{75}) probably also off-resonant action would contribute explaining that the value of α at f_0 is no longer the sole dominating value of α . The off-resonant action would most often occur in the vicinity of $f_s = \mu(f_s)$, which also explains why predictions of a_{75} calculated using approach 3 performs reasonably well (see Fig. 3), and better than predictions of a_{95} and $a_{97.5}$ using approach 3.

To illustrate these points, Fig. 4 shows the probability distribution function of bridge accelerations (a) calculated for bridge E ($f_0 = 2.20$ Hz) using the three different approaches for modelling the dynamic load factor.

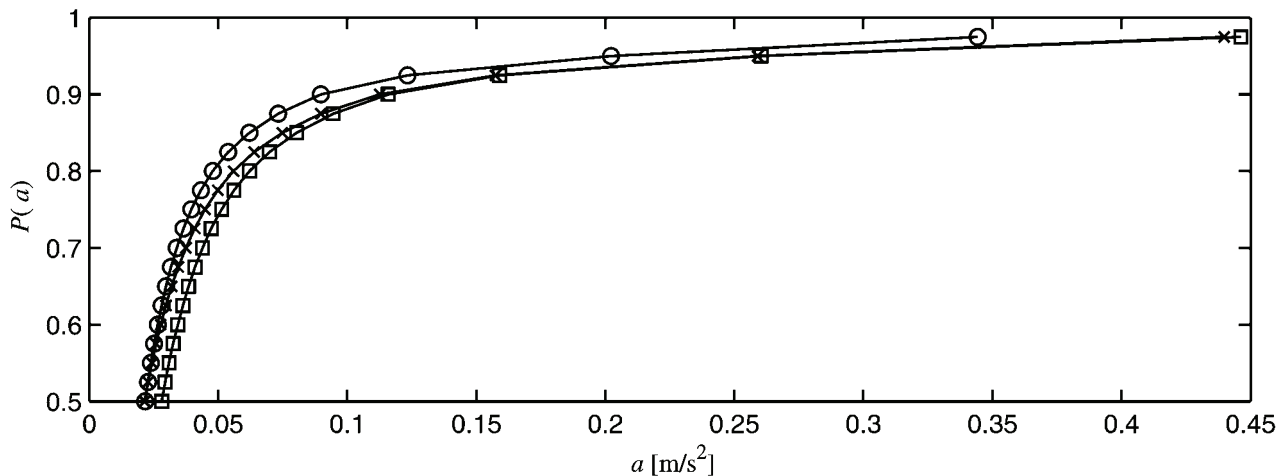


Fig. 4 Probability distribution functions of bridge acceleration. Approach 1 (x), 2 (□), and 3 (o)

In Fig. 4 it can be seen that for the higher bridge response characteristics (quantiles) there is a good match between results obtained using approach 1 and 2. The match between results obtained using approach 1 and 3 is not that good for the higher quantiles, but it improves for quantiles somewhat lower than these.

6. CONCLUSION AND DISCUSSION

For five different footbridges, the sensitivity of different characteristic parameters of the probability distribution function of footbridge response to various ways of modelling the dynamic load factor were examined.

The characteristics of the probability distribution function of footbridge response that are considered to be of primary interest are the higher quantiles (such as a_{95}). For such properties it is found that a quite simplistic approach to modelling the dynamic load factor (approach 2) performed almost as well as a full stochastic approach for modelling the dynamic load factor. In approach 2, the stochastic nature of the dynamic load factor is not considered and neither is it considered that different step frequencies (according to the relationship between step frequency and dynamic load factor reported by Kerr) should result in different values of the dynamic load factor. You simply pick the value of the dynamic factor from Kerr's results entering the bridge frequency instead of the step frequency and thus assume this value for all crossings and for all pedestrians.

This would immediately suggest that it might be unnecessary to model the dynamic load factor as a random variable. It should be recalled that this conclusion is derived studying only a few (SDOF) footbridges, and thus that it may not be valid for any footbridge. However, the paper may be considered as a baseline study which can be extended considering other bridges. It is however useful that findings suggest that central characteristics of the probability distribution function of footbridge response might be insensitive to a number of the choices to be made by the engineer (random or deterministic?, distribution type? etc.).

The results also suggest that there are limitations to the degree of simplification of matters that are sensible. An approach (approach 3) where the dynamic load factor was modelled as a constant (independent of bridge frequency) did not perform as well as approach 1 and 2 in terms of predicting higher quantiles of bridge response.

REFERENCES

- [1] Dallard, P., Fitzpatrick, A.J., Flint, A., Le Bourva, S., Low, A., Ridsdill-Smith, R.M., and Wilford, M., *The London Millennium Bridge*, *The Structural Engineer* Vol. 79, pp. 17-33, 2001.
- [2] Matsumoto, Y., Nishioka, T., Shiojiri, H., and Matsuzaki, K., *Dynamic design of footbridges*, *IABSE Proceedings*, No. P-17/78: pp. 1-15, 1978.
- [3] Živanovic, S., *Probability-based estimation of vibration for pedestrian structures due to walking*, PhD Thesis, Department of Civil and Structural Engineering, University of Sheffield, UK, 2006.
- [4] Ontario Highway Bridge Design Code, Highway Engineering Division; Ministry of Transportation and Communication, Ontario, Canada, 1983.
- [5] British Standard Institution, *Steel, concrete and composite bridges. Specification for loads*, BS 5400: Part 2, 1978.
- [6] Ellis, B.R., *On the response of long-span floors to walking loads generated by individuals and crowds*, *The Structural Engineer*, Vol. 78, pp. 1-25, 2000.
- [7] Bachmann, H., and Ammann, W., *Vibrations in Structures – Induced by Man and Machines*, IABSE Structural Engineering Documents 3e, Zürich, Switzerland, 1987.
- [8] Rainer, J.H., Pernica, G., and Allen, D.E., *Dynamic loading and response of footbridges*, *Canadian Journal of Civil Engineering*, Vol. 15., pp. 66-78, 1998.
- [9] Kerr, S.C., and Bishop N.W.M., *Human induced loading on flexible staircases*, *Engineering Structures*, Vol. 23, pp. 37-45, 2001.
- [10] Pedersen, L., and Frier, C., *Sensitivity of footbridge vibrations to stochastic walking parameters*, *Journal of Sound and Vibration* (2009), doi:10.1016/j.jsv.2009.12.022
- [11] Pedersen, L., and Frier, C., *Sensitivity Study of Stochastic Walking Load Models*, International Modal Analysis Conference (IMAC XXVIII), Jacksonville, Florida, USA, 2009

Modal parameter variations due to earthquakes of different intensities

Rodrigo P. Carreño¹, Rubén L. Boroschek²

¹ Structural Engineer. Department of Civil Engineering, University of Chile. rcarreno@ing.uchile.cl

² Associate Professor. Department of Civil Engineering, University of Chile. rborosch@ing.uchile.cl
Blanco Encalada 2002, Santiago. Chile.

1 Nomenclature

- ω_j : Modal angular frequency. Mode j.
 f_j : Modal frequency. Mode j.
 ξ_j : Modal damping ratio. Mode j.
 $ag_i(t)$: Recorded base acceleration. Direction i
 $L_{j,i}$: Modal participation ratio for base acceleration $ag_i(t)$. Mode j
 $\phi_{j,p}$: Modal shape vector at position p. Mode j.
 $y_j(t)$: Modal response. Mode j.
 $a_p(t)$: Estimated acceleration of MIMO algorithm at position p
 E : MIMO goodness of fit error.
 α_p : Weight coefficient at position p in MIMO goodness of fit error.
 $RMS_{\text{modal},j}$: Root Mean Square modal amplitude. Mode j
 $\bar{a}_{X^{\text{th}} \text{ floor}}(t)$: Measured acceleration, Xth floor.
 $\bar{\theta}_j$: Unit vector defined by the mode shape's principal direction. Mode j
 $[f_j - \Delta f_j, f_j + \Delta f_j]$: Modal frequency confidence interval. Mode j.
 $[X]_{[f_j - \Delta f_j, f_j + \Delta f_j]}$: Band-pass filtered signal, between $f_j - \Delta f_j$ and $f_j + \Delta f_j$.

2 ABSTRACT

This article presents the modal parameter variations during 55 low to high intensity earthquakes in a 22 story shear wall building located in Chile. Some of the earthquakes produced moderate damage in the structure. The building has been instrumented since 1997 with a network of 12 uniaxial accelerometers distributed on 4 different levels. Modal parameters are obtained through parametric Multiple Input - Multiple Output identification techniques. For the identified modal frequencies, decreasing values with respect to motion amplitudes are observed, in a range between 4% and 35% for the seismic records studied. For the modal damping ratios, increasing values with increasing motion amplitude are observed, with variation ranging from 50%, for the first translational modes, to over 120% for higher modes. For medium and low level earthquakes these variations disappear after the strong shaking has ended. This article also presents a preliminary analysis of the seismic records on the building during the Mw=8.8 earthquake occurred in Chile in 2010. Structural Damage was observed on the building and modal parameters changed significantly. During this seismic event, modal frequencies decreased up to 35% for the first translational modes. After the earthquake, modal frequencies had an 18% permanent decrease on average from initial values.

3 Introduction

Many studies on modal parameter variations of different buildings have been developed. For instance, Caltech's R.A. Millikan library has been monitored for this purpose, using accelerometers, since 1967. Studies like this have concluded that most of the variations observed in modal parameters, due to traffic, weather conditions (temperature, wind, rainfall, etc.), low to moderate intensity earthquakes, etc. do not necessarily implicate structural damage. In these cases, for example, modal periods have reported changes up to 3-4%, [1].

In particular, previous studies on the Chilean chamber of construction building, whose seismic records are analyzed in this research paper, have reported changes in the modal frequencies between 1% and 2% for ambient conditions, being temperature and rainfall the weather variables with the most environmental effect ([3]). As for the analysis of seismic records, a previous study on this building ([4]) found variations in modal frequencies up to 4 % during low to moderate intensity earthquakes, where none of which were reported to cause any structural damage.

4 Building properties

The Chilean Chamber of Construction Building, located in Santiago, Chile, is a 22 story, reinforced concrete, shear wall building. Since 1997, a continuous monitoring network has been recording both strong motion and ambient vibrations records of the building. The network consists of 12 uniaxial accelerometers located at four different levels of the structure, including its base, Fig.2.

As for its structural properties, the building is 85.5 meters high, and it is constituted of a wall-frame dual system, with most of the lateral loads resisted by walls. The walls are located mainly in the center, housing the stairs and elevator shafts. Small dimensions precast concrete wall panels are used on the perimeter. A common 1.50 m thick 305 square meter foundation slab supports the main structural walls and columns. Stories below ground level have a 300 mm thick perimeter wall, which resists both earth pressure and seismic loads. Wall area to plan area ratio is 6.3% for stories below ground and 4.0% for stories above ground. The floor slabs are 150 mm thick in all above ground stories and 170 mm thick below ground level. Soil foundation can be described as dense gravel, with a capacity of 1MPa for dynamic loads. Total floor area is 28,595 square meters, [7].

Since its installation, the structural health monitoring network has recorded several low and high intensity earthquakes. In this article, 55 of those seismic records, including the one corresponding to the recent M=8.8 earthquake occurred in Chile, are analyzed to determine modal parameter variations of the structure.



Fig.1 Chilean chamber of construction building. External views

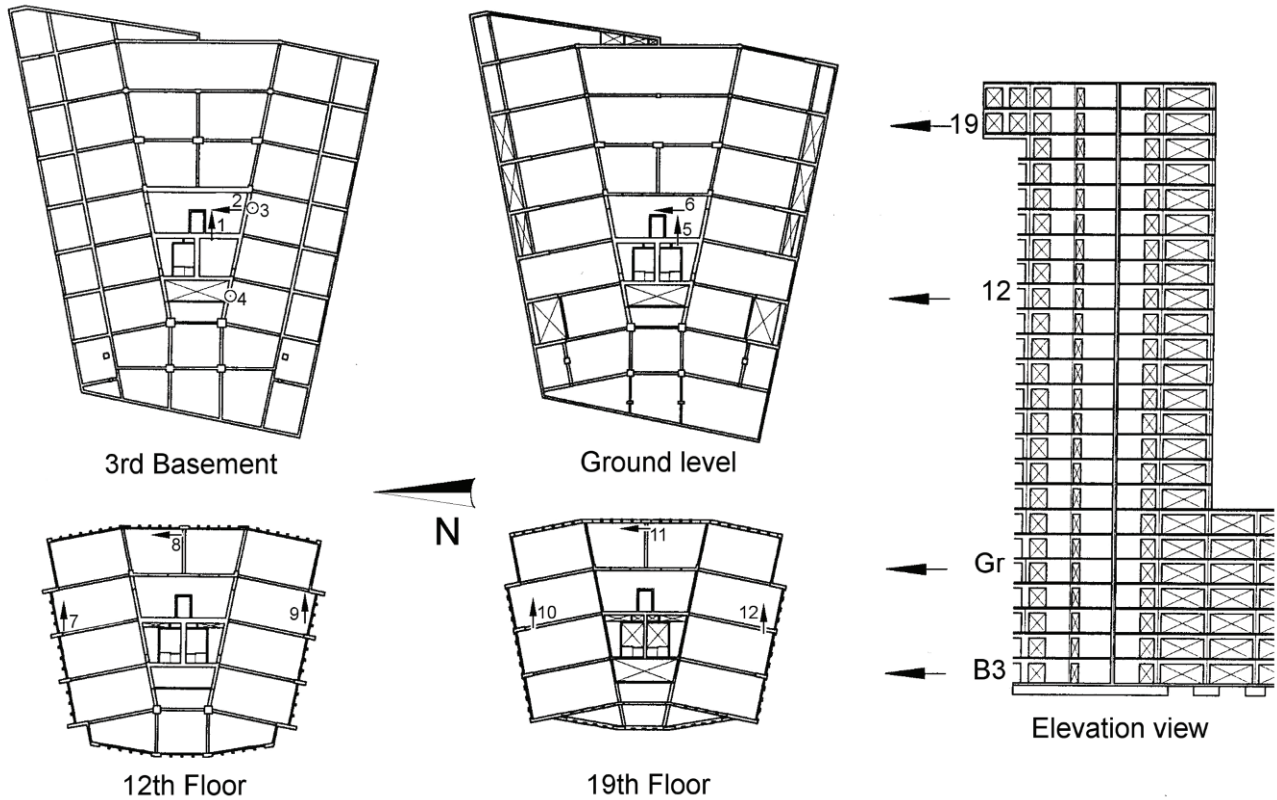


Fig.2 Sensor Location. Chilean chamber of construction building

5 System Identification Technique.

Modal parameters for the analyzed seismic records were obtained through a parametric Multiple Input – Multiple Output (MIMO. [2], [9] and [10]) identification algorithm developed during this study. Based mainly on the dynamic modal equilibrium equations ((1), (2)), this identification algorithm searches for the optimal combination of parameters that best fits the measured response of the structure. Because the number of variables and the complexity of the target function, (3), the identification algorithm requires of adequate initial and limit values for all modal parameters to identify (modal frequencies, damping ratios and mode shapes).

$$\ddot{y}_j(t) + 2 \cdot \omega_j \cdot \xi_j \cdot \dot{y}_j(t) + \omega_j^2 \cdot y_j(t) = \sum_{i=1}^k L_{j,i} \cdot ag_i(t) \quad (1)$$

$$a_p(t) = \sum_{j=1}^N \phi_{j,p} \cdot \ddot{y}_j(t) \quad (2)$$

The target function of the optimization problem, E , is a weighted least-square-error between $a_{0,p}(t)$ and $a_p(t)$. Weight coefficients α_p control the importance of each channel of the response record in the modal identification process. Thanks to the normalization component $\left(\sum_p \alpha_p \cdot \sum_t (a_{0,p}(t))^2 \right)$, E can be expressed in percentage units.

$$E = \sqrt{\frac{\sum_p \alpha_p \cdot \sum_t (a_{0,p}(t) - a_p(t))^2}{\sum_p \alpha_p \cdot \sum_t (a_{0,p}(t))^2}} \quad (3)$$

The Identification algorithm developed during this study reaches optimal modal parameters through an iterative process. First, building modes are classified according to their participation in the dynamic response during seismic events. Then, the iterative algorithm starts the identification process using only the modes with the highest response participation. At each iteration, a new group of modes is added to the process. Once all modes have been processed, only the ones with the most contribution to reduce the MIMO goodness of fit error (E) are kept. In a final step, the error E for each channel of the response record is calculated, if one of them shows an error higher than 30%, its corresponding weight coefficient α_p is increased accordingly and the process starts over. Fig.3 shows an explanatory flowchart of the Identification algorithm.

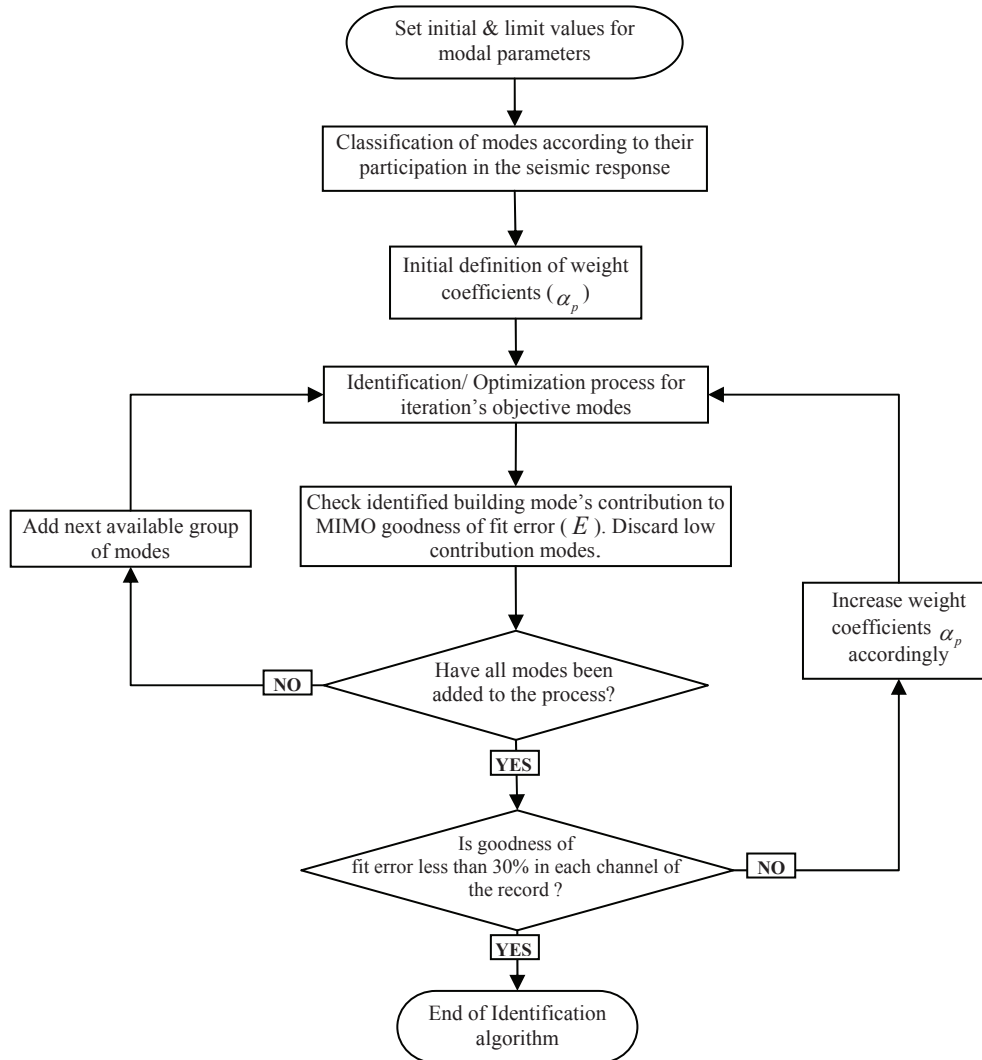


Fig.3 MIMO Identification Algorithm

5.1 Numerical Validation

A finite element model of the building was developed to verify the results of the previously described identification algorithm. The properties considered in the model are the following: Concrete modulus of elasticity of 38000 [MPa]; fix foundation; element stiffness calculated from gross sections; rigid diaphragms assigned on each floor; concrete density of 2500 [kg/m³]; dead loads equal to 1.5 times self-weight; Live Load of 250 [kg/m²] on above ground floors and 500 [kg/m²] on underground floors; seismic weight calculated as *100% of Dead load plus 25% the Live Load*.

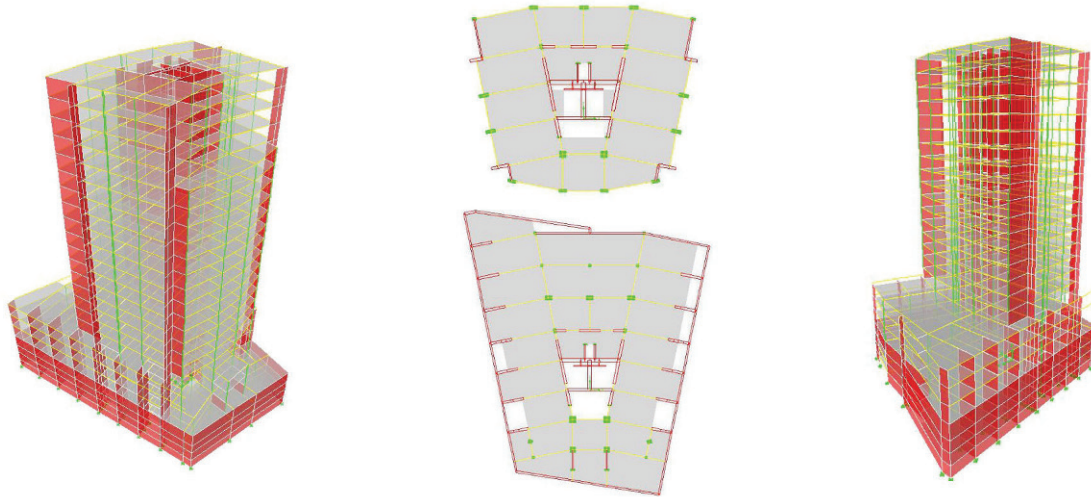


Fig.4 Finite element model of the building. 3D and plan views

From this computer model, several analyses were performed using acceleration time-series recorded at the base of the structure during seismic events. Such base motion records (Input) and the resulting response of the computer model (Output) were used to validate the MIMO Identification algorithm. For better resemblance to real conditions, the chosen output signals on the computer model match the sensor location on the real monitoring network. In addition, 10% of the record amplitude was added to the response records as random Gaussian noise before the identification process.

As an initial indicator of the good results of the identification process, the goodness of fit error (E) for these analyses ranged from 7% to 16%. [Fig.5](#) and [Fig.6](#) display an example of both the original contaminated time-series and the estimated fit. These figures show clearly how small the fit error is for the range of normalized error, E .

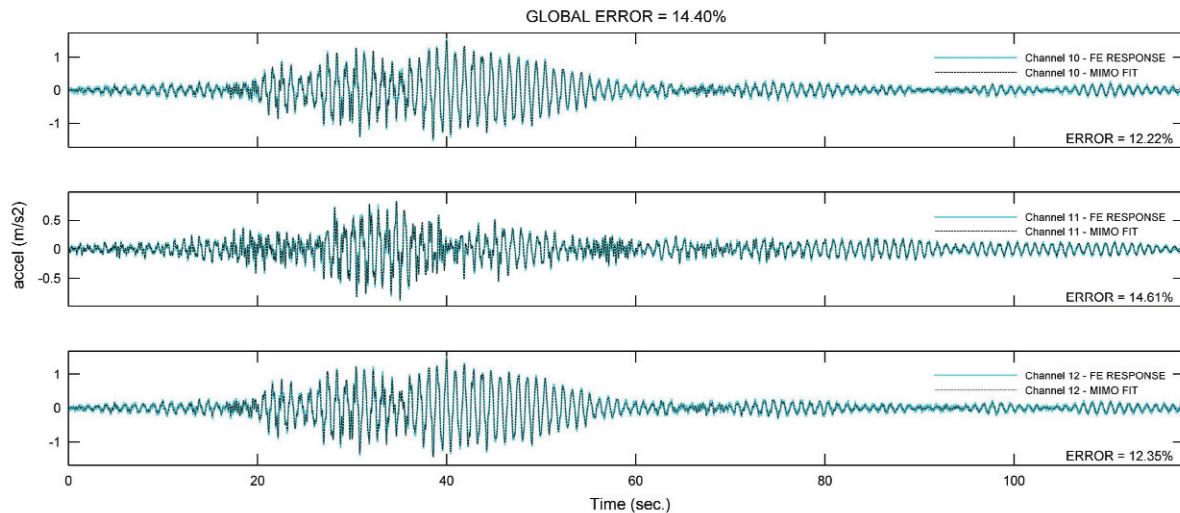


Fig.5 Validation of analytical procedure. Computer model's contaminated record vs. Estimation by identified modal parameters. 19th Floor

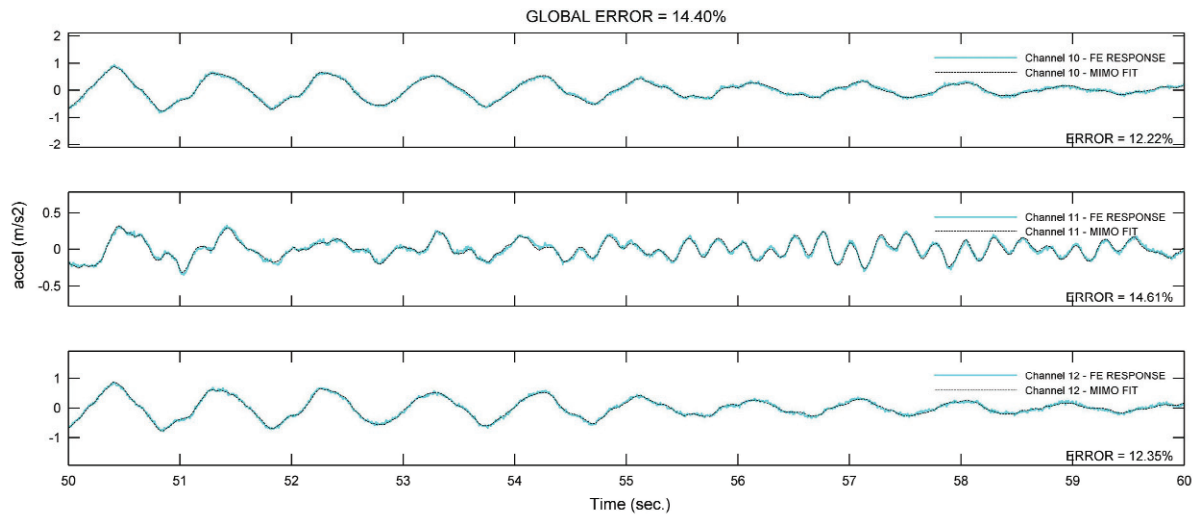


Fig.6 Validation of the analytical procedure. Computer model's contaminated record vs. Estimation by identified modal parameters. 19th Floor. Zoom

Modal identification over all analytical records with added 10% noise resulted in identified modal frequencies with less than 0.2% error. As for identified modal damping ratios, the error was less than 6%.

[Table 1](#) shows the results of the identification process for one time-history analysis; these results are compared to expected values from the FE computer model.

Table 1 Modal parameters: FE computer model vs. MIMO identification algorithm

FE computer model		Identified by MIMO		Relative Difference (%)	
Freq [Hz.]	ξ [%]	Freq [Hz.]	ξ [%]	Freq	ξ
1.05	1.00	1.05	1.00	0.01%	0.26%
1.09	1.30	1.09	1.28	0.01%	1.27%
1.46	0.50	1.46	0.52	0.01%	3.58%
3.94	3.00	3.94	2.87	0.01%	4.36%
4.05	2.40	4.05	2.47	0.18%	3.04%
4.18	0.80	4.18	0.83	0.02%	3.86%
6.85	1.00	6.84	0.96	0.06%	4.45%
8.10	3.00	8.10	2.94	0.05%	1.89%

6 Description of the seismic records

As mentioned before, this study involves the analysis of a total of 55 seismic records, obtained since 1997. The magnitude of the corresponding seismic events ranges between 4.2 and 8.8 (Mw). In addition, peak ground accelerations (PGA) at the base of the building ranged between 0.001g and 0.14g, meanwhile peak accelerations (PA) ranged between 0.002g and 0.31g. For all analyzed earthquakes, [Fig.7](#) shows epicenters location and histograms for Magnitude, peak ground acceleration and peak acceleration.

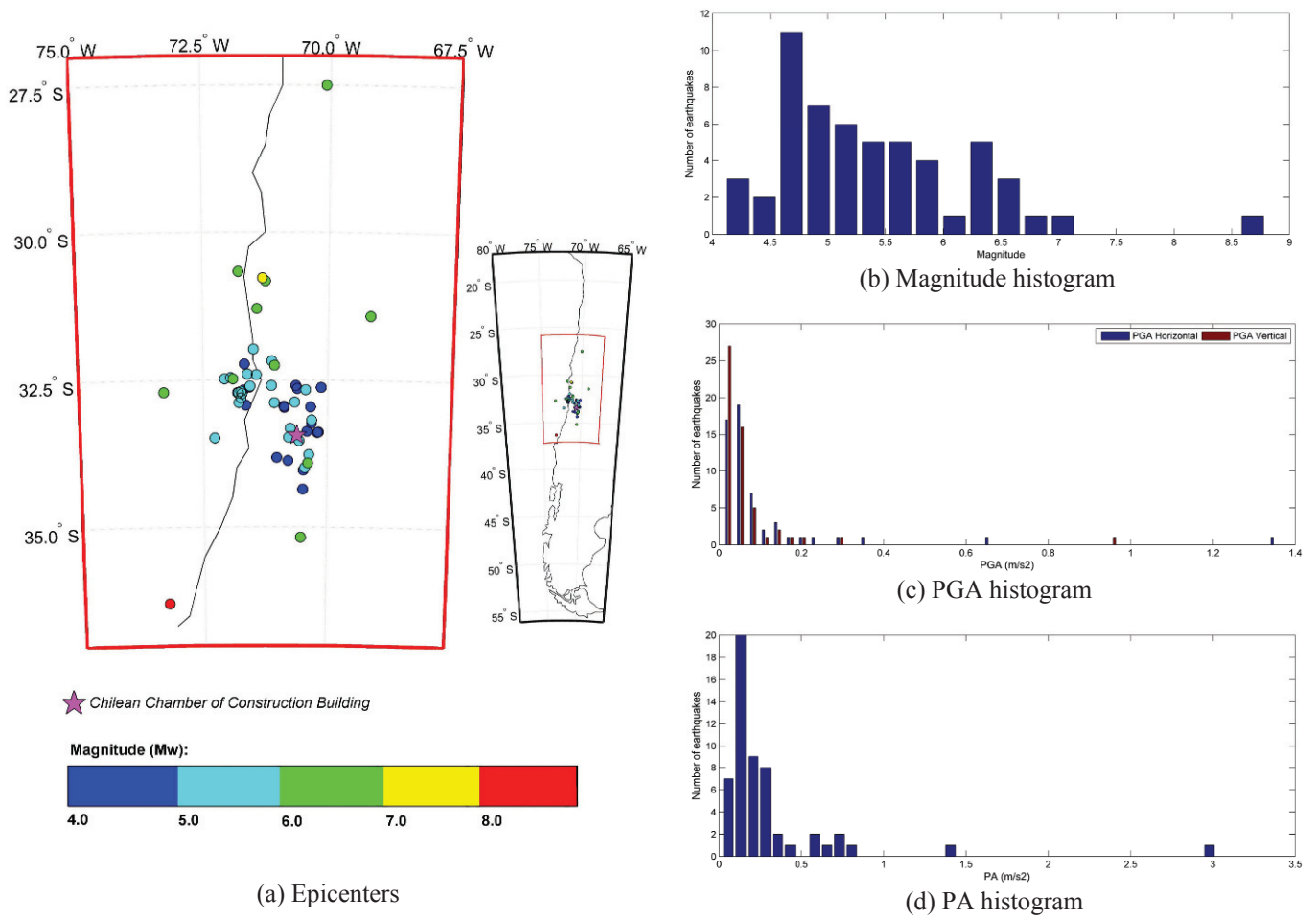


Fig.7 Properties of analyzed seismic events

7 The 2010 Chile Earthquake

From all the seismic events studied, only the $M_w=8.8$, 2010 Chile Earthquake caused visible damage on the building and permanent variations of its modal parameters. Despite this and the strong shaking of the building during the event (Maximum ground acceleration of 0.14g and structural acceleration of 0.31g), the structure only suffered minor and moderate damage, which was concentrated in non-structural elements (partition walls, ceilings, etc.), in addition to some visible shear cracks on the perimeter façade elements, Fig.8.



Fig.8 Observed damage after the 2010 Chile Earthquake

8 Results of the MIMO Analysis

Before presenting the results of MIMO identification analysis on the seismic records, Table 2 shows the average modal parameters of the building, determined from ambient vibration records and presented on previous studies of the building ([3], [4], [5] and [6]).

Table 2 Average modal parameters for ambient conditions. (Source: [5])

Mode	Frequency [Hz]	Damping Ratio (ξ) [%]	Modal shape orientation
1	1.04	1.1	Translational. East-West.
2	1.07	1.0	Translational. North-South.
3	1.63	0.6	Torsional.
4	3.60	1.5	Translational. East-West.
5	3.57	1.5	Translational. North-South.
6	4.8	1.2	Torsional.

For the processing of the seismic records with the MIMO Identification algorithm, some important considerations were taken into account: The input of the identification algorithm was considered as the records of the four sensors located at the base of the structure, including those oriented vertically. As for the output of the MIMO algorithm, only the records corresponding to sensors 7 to 12 were taken into account, since the presence of channels 5 and 6 (corresponding to sensors located at ground level) in the process usually led to less accurate results for the damping and frequency determination. Finally, the MIMO identification algorithm analyzed only the strong motion stage of each seismic event, defined for this purpose as the time between the arrivals of the S-wave until a few seconds (approximately 5 to 10 times the main period of the building) after base accelerations have returned to normal ambient amplitudes

From the initial processing of each seismic record, identification analyses led to MIMO goodness of fit error (E , Equation (3)) ranging between 13% and 40%, which fall within acceptable ranges according to previous studies on the MIMO identification techniques that use accelerations as a reference response parameter.

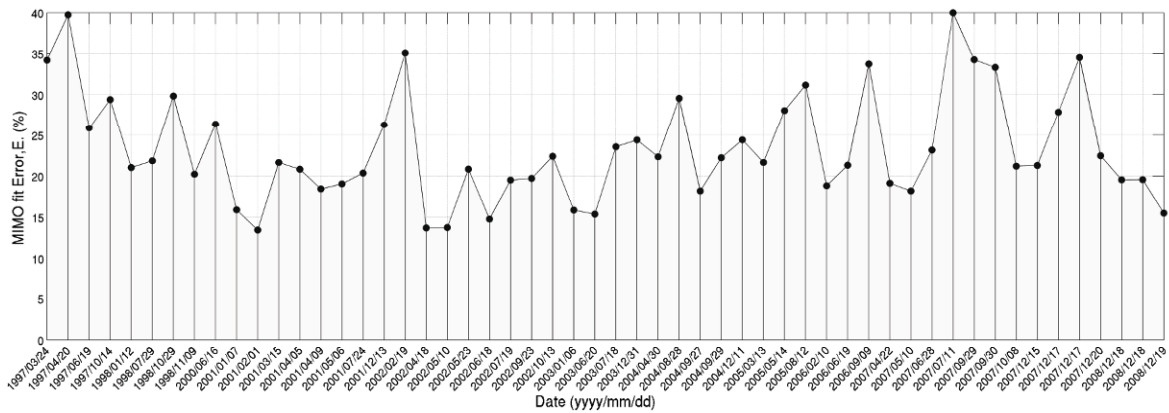


Fig.9 MIMO goodness of fit error for each seismic record

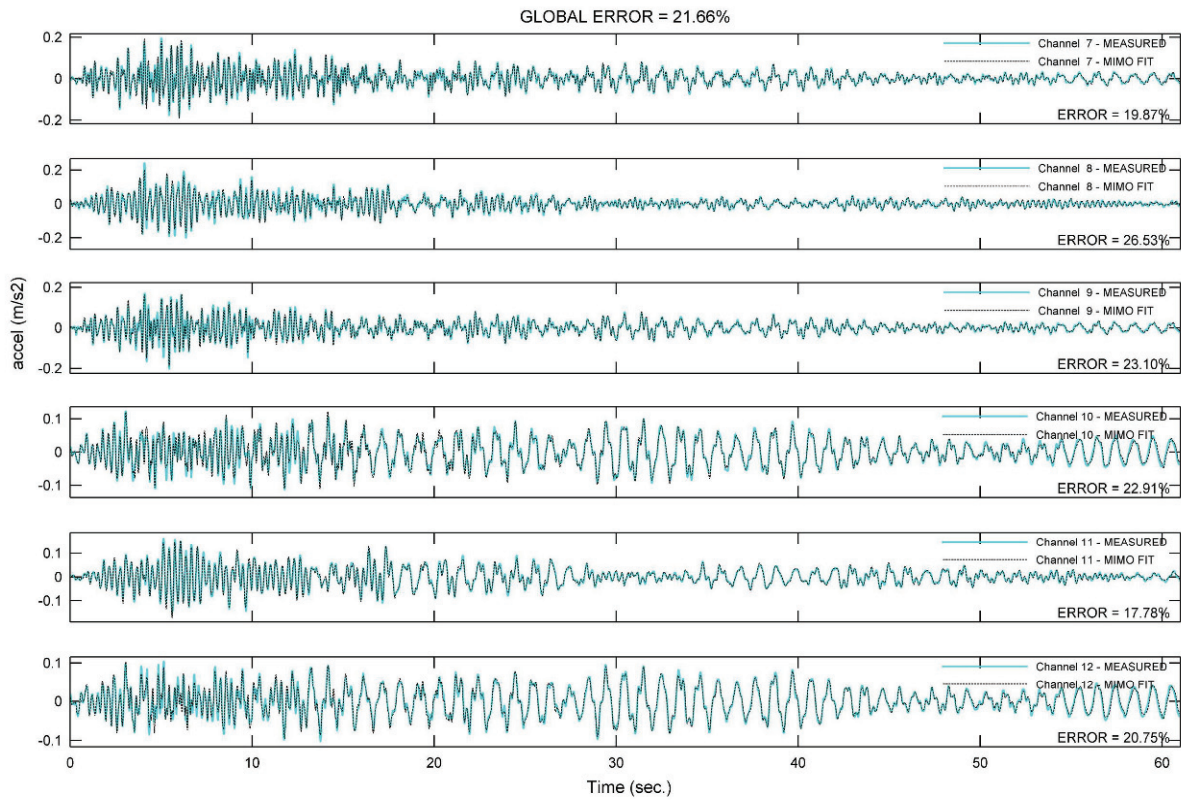


Fig.10 Seismic event 2001/03/15. Recorded response vs. corresponding estimation from MIMO identification process

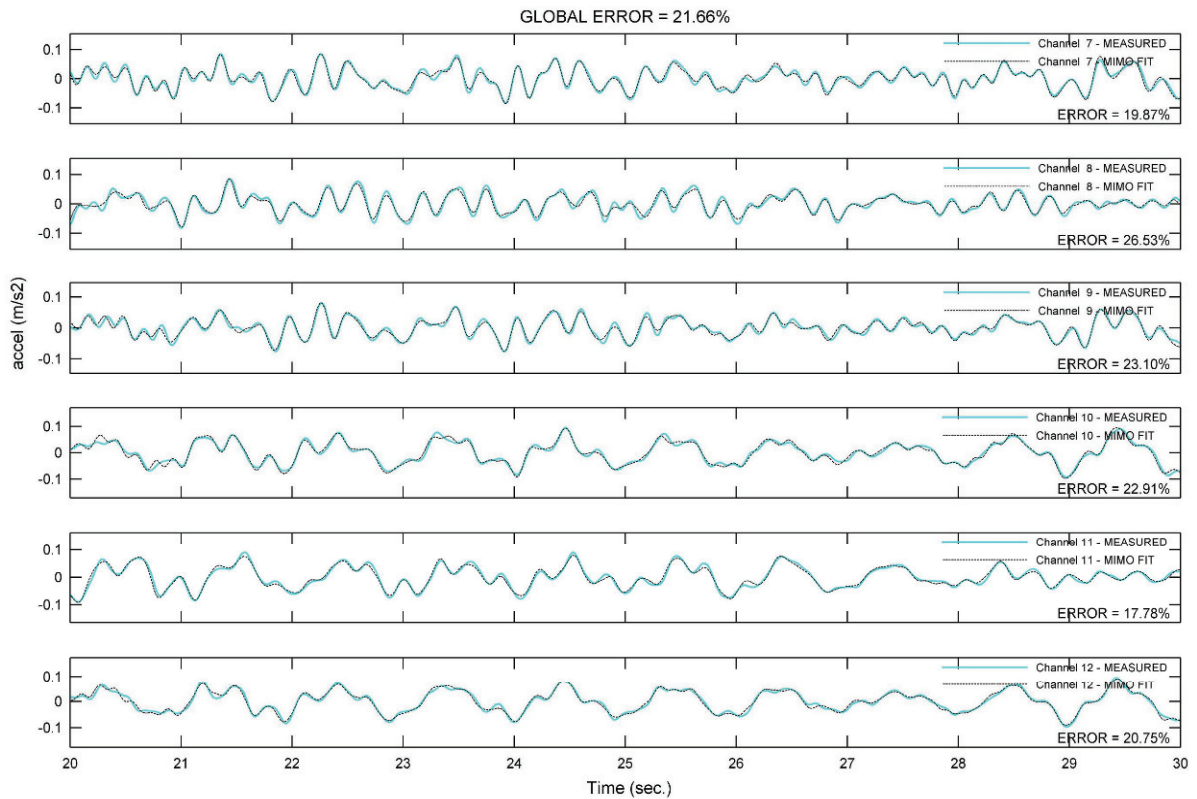


Fig.11 Seismic event 2001/03/15. Recorded response vs. corresponding estimation from MIMO identification process. Zoom

An important part of this study is the analysis of the correlation between identified modal parameters and the corresponding severity of shaking of the building. Since the latter doesn't have an unique definition, this had to be specified during the study. A number of criteria were tested to evaluate the severity of shaking, being the definition of "modal amplitude" the one that best correlated to the identified modal parameters (modal frequency and damping ratio). This criterion involves filtering the seismic records around the natural frequency that is being analyzed, and then calculating its root means square value.

$$RMS_{\text{modal},j} = \sqrt{\sum_t \left(\left[\bar{a}_{19\text{th floor}}(t) \cdot \bar{\theta}_j \right]_{[f_j - \Delta f_j, f_j + \Delta f_j]} \right)^2} \tag{4}$$

For all analyses, only modal parameters associated with the first 4 translational modes of the building (modes 1, 2, 4 and 5) were considered, since they are the ones with the highest participation on the structural response during seismic events. The torsional modes (3 and 6), had a small participation in all the analyses.

Fig.13 and Fig.14 show correlation graphs between the severity of shaking and the average modal parameters identified for each seismic record. A tendency line is included on each graph, resulting from a robust regression analysis of the data ([8]). As a general description, the robust regression analysis used in this study corresponds to a weighted least-square technique, where weight coefficients are assigned to each data point to minimize the influence of outliers. A comparative example between the results of a simple least-square analysis and a robust regression analysis is presented in Fig.12.

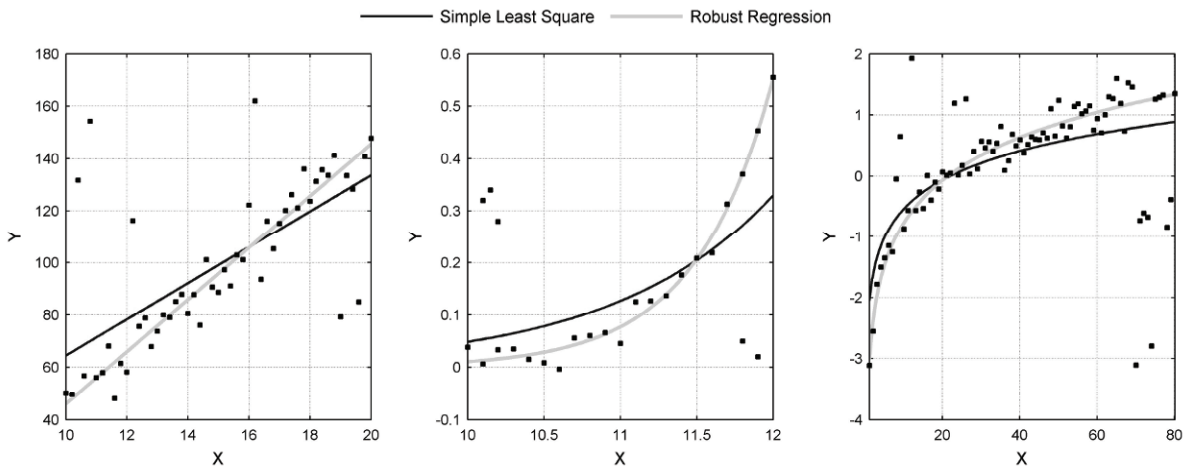
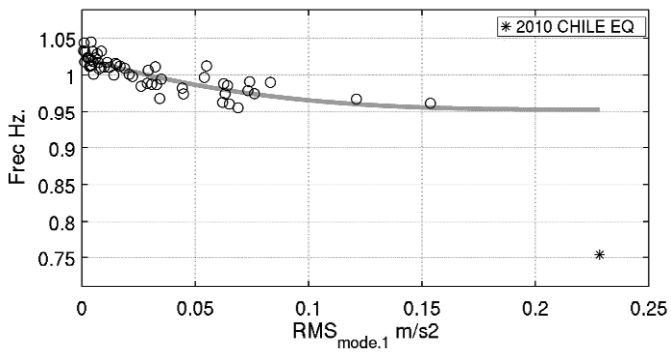
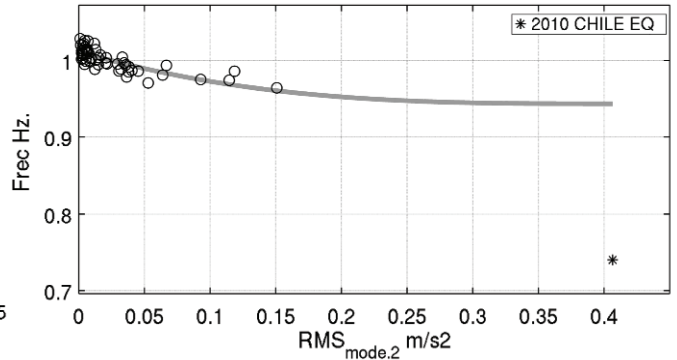


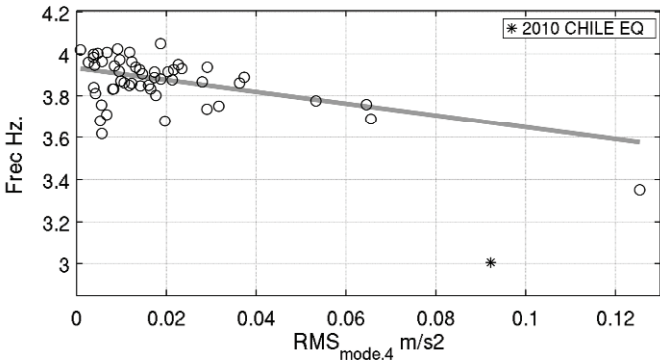
Fig.12 Comparative example. Simple Least Square Regression vs. Robust Regression.



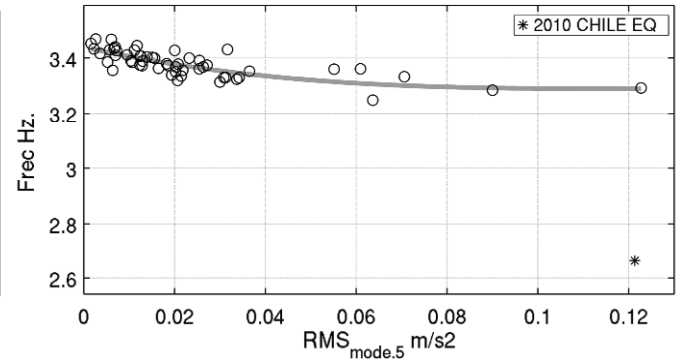
(a) Mode 1



(b) Mode 2

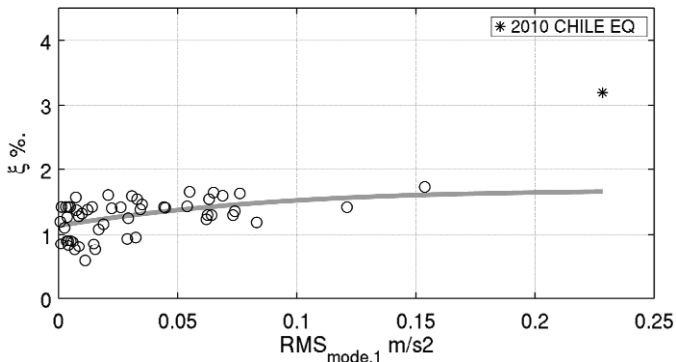


(c) Mode 4

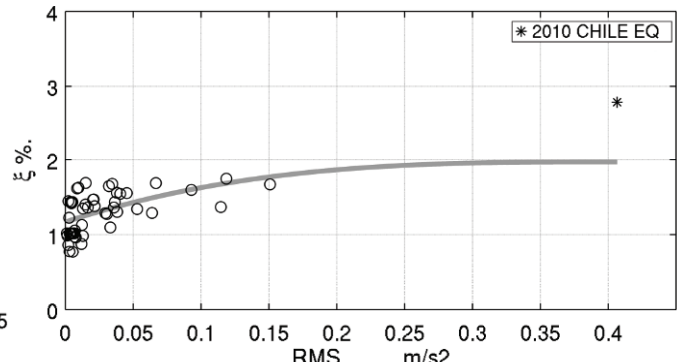


(d) Mode 5

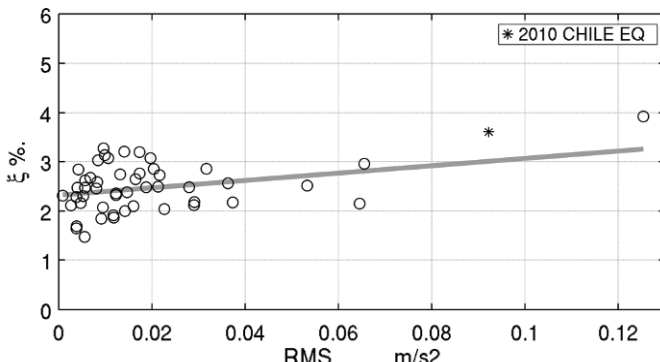
Fig.13 Identified modal frequencies vs. corresponding modal amplitude



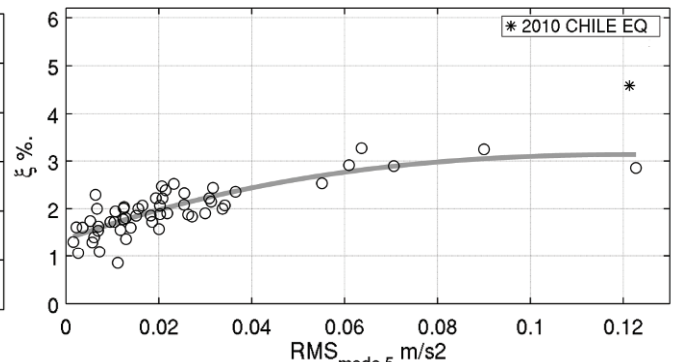
(a) Mode 1



(b) Mode 2



(c) Mode 4



(d) Mode 5

Fig.14 Identified modal damping ratios vs. corresponding modal amplitude

In Fig.13 and Fig.14, results for the Mw=8.8 Chile Earthquake are especially highlighted on each graph. The regression analyses considered these results as outliers so they are not considered in the determination of the tendency lines.

From the analysis of Fig.13 and Fig.14 the correlation between the “modal amplitude” of the building and the identified modal parameters becomes clear. On one hand, modal frequencies show decreasing values when the severity of shaking increases, reaching values up to 4% and 9% for low to medium intensity earthquakes and, on the other hand, modal damping ratios display the opposite behavior, with corresponding tendency lines showing maximum relative increases between 40% and 120%.

During the 2010 earthquake, the biggest temporary variation of the modal frequencies took place, decreasing up to 35% on average for translational modes. Table 3 shows modal frequencies at three different times during the seismic event, these results were obtained by dividing the seismic record into small windows and identifying the modal parameters, using the MIMO algorithm, for each one of them.

Table 3 Identified modal frequencies during 2010 Chile Earthquake

Mode	Start [Hz]	Minimum [Hz]	End [Hz]	Relative difference ³ [%]	
				Minimum	End
1	0.99	0.64	0.79	35.2	20.1
2	0.98	0.61	0.74	37.8	24.8
4	3.72	2.44	3.02	34.6	19.0
5	3.36	2.31	2.65	31.1	21.2
			Average	34.7	21.3

Furthermore, the modal frequencies of the building changed permanently after this event, decreasing on average an 18% for the first modes. This permanent change was verified using ambient vibration right after the earthquake event. Table 4 presents identified modal frequencies and damping ratios (obtained through Stochastic Subspace identification technique over ambient vibration records).

Table 4 Evolution of modal properties for ambient conditions. Before and after the earthquake

Mode	BEFORE EQ		AFTER EQ	
	Freq [Hz]	Damp (ξ) [%]	Freq [Hz]	Damp (ξ) [%]
1	1.01	0.6	0.84	0.6
2	1.03	0.7	0.86	0.6
3	1.54	0.6	1.22	0.8
4	3.45	1.1	2.91	1.1
5	3.44	1.2	2.86	1.1
7	4.62	1.1	3.67	1.1

For modal damping ratios, no distinguishable change can be appreciated between the two analyzed stages, because the observed differences fall within expected error for the employed identification technique (SSI, [12]).

9 Conclusions

In this study, a 22 story reinforced concrete shear wall building was analyzed to determine the correlation between its modal parameters and the severity of shaking during seismic events. The identification of the modal parameters was performed by a parametric Multiple Input- Multiple Output algorithm, which was developed and validated during this study.

From the testing of different criteria, a “modal amplitude” definition was chosen to quantify the severity of shaking, because it showed the best correlation to the identified modal parameters. For modal frequencies, decreasing values with the “modal amplitude” were observed, with corresponding tendency lines showing a maximum decrease between 4% and 9% for small to medium intensity earthquakes. As for the modal damping ratios, their values tend to increase with the severity of shaking, reaching a maximum relative increase, according to their tendency lines, between 40% and 120%

³ Relative to corresponding identified modal frequency at the start of the seismic event. For minimum:

$$\text{Rel_diff}_{\text{mode}, \text{min}} = \frac{(f_{j, \text{start}} - f_{j, \text{min}})}{f_{j, \text{start}}} \cdot 100$$

From all the seismic events analyzed during this study, the Mw=8.8, 2010 Chile earthquake was the only one that caused visible damage of the structure, and a permanent change of modal parameters. During the seismic event, modal frequencies decreased up to 35% from initial values. Shortly after the event, identified modal frequencies showed an 18% permanent decrease.

Results of this research paper are representative indicators of the behavior of modal parameters during and after seismic events for a wide range of intensities.

Acknowledgement

The Civil Engineering Department of the University of Chile and the Chilean Council for Research and Technology, CONICYT Fondecyt Project # 1070319 supported this research paper. The authors would also like to thank the Chilean Chamber of Construction and Civil Engineer Pedro Soto for their collaboration and support in the development of this study.

Reference

- [1] Bard PY, Celebi M, Dunand F, Gueguen P and Rodgers J “Comparison of the dynamic parameters extracted from weak, moderate and strong motion recorded in buildings”. First European Conference on Earthquake Engineering and Seismology, Geneva, Switzerland, 3-8 September 2006, Paper Number: 1021. 2006.
- [2] Beck. JL “Determining models of structures from Earthquake records”. Rep. EERL 78-01, Caltech, Pasadena, California. 1978.
- [3] Boroschek R, Lazcano P “Non-damage Modal Parameter Variations on a 22 Story Reinforced Concrete Building”. International Modal Analysis Conference, IMAC XXVI, Orlando 2008 Paper 255.
- [4] Boroschek R, Soto P “Changes in dynamic properties of an instrumented building during minor and moderated seismic events”. VIII Jornadas Chilenas de Sismología e Ingeniería Antisísmica (In Spanish), Valparaíso, Chile. 2002.
- [5] Boroschek R, Yañez F “Experimental verification of basic analytical assumptions used in the analysis of structural wall buildings”. Engineering Structures, (22) pp. 657-669. 2000.
- [6] Castillo A “Modal parameter identification for tall buildings using Stochastic Subspace Identification method”. Civil Engineering Thesis. Universidad de Chile. Santiago, Chile. 2005.
- [7] Lagos R “Structural Plans, Building of the Chilean Chamber of Construction”. 1987
- [8] Rosseeuw RJ, Leroy AM “Robust Regression and Outlier Detection”. New York, Wiley. 1987.
- [9] Mau ST, Li Y “A case study of MIMO system identification applied to building seismic records”. Earthquake engineering and structural dynamics, Vol 20, 1045-1064. 1991.
- [10] Mau ST, Li Y. “Learning from Recorded Earthquake motion of Buildings”. Journal of Structural Engineering, Vol. 123. Jan 1997. 1997.
- [11] Mau ST, Aruna V “Story-Drift, Shear, and OTM Estimation from Building Seismic Records”. Journal of Structural Engineering, Vol 20, No. 11, November, 1994.
- [12] Van Overschee P, De Moor B “Subspace Identification of Linear Systems: Theory, Implementation, Applications”. Kluwer Academic Publishers. 1996.

Operational Modal Analysis of a Historic Tower in Bari

Mariella Diaferio, Dora Foti, Michele Mongelli,
Technical University of Bari, Bari, Italy

Nicola Ivan Giannoccaro
University of Salento, Lecce, Italy

Palle Andersen
Structural Vibration Solutions A/S, Aalborg, Denmark

ABSTRACT

In this paper, the latest identification techniques both in the time and in the frequency domains, are applied to the data obtained from the dynamic monitoring of the reinforced concrete tower of the Provincial Administration Building of Bari (Italy). The tower, dating back to the thirties of the 20th century and about 60 m tall, is not only a typical example of the fascist architectural style, but it is an important symbol of the city itself.

The extraction of the modal parameters from ambient vibration data has been carried out by using the ARTeMIS Extractor Pro 2010 software. Three different Operational Modal Analysis (OMA) methods have been utilized: EFDD, SSI and Crystal Clear-SSI. The first two couples of bending mode shapes are also estimated and shown.

1. INTRODUCTION

The present study has been performed in order to identify the modal parameters of an important historical building, the tower of the Provincial Administration Building in Bari, Italy, with the final purpose to predict the performance of the tower to different combinations of static and dynamic loads, such as earthquakes or other induced vibrations.

In the last years, structural identification has received great attention due to its possibility of giving a complete description of the dynamic behavior of the structures, especially for monitoring existing structures. In this field, in fact, an important role is played by the identification techniques applied to ambient vibrations, in case of historical buildings for which the use of artificial dynamical excitation may not be possible. In particular, ambient vibration testing has become the main experimental method available for assessing the dynamic behavior of full-scale structures [1] because no excitation equipment is needed, involving a minimum interference with the normal use of the structure. The procedure is especially suitable for flexible systems, such as civic towers [2], bell-towers [3-6], masonries [7] and minarets [8].

One main problem in the Operational Modal Analysis (OMA) is the maintenance of the data acquisition system [9]. Field measurements, in fact, are often performed in very harsh environmental conditions, requiring high accuracy both in the control of the test set-up and in the analysis of the measured data. Moreover, measurements are usually noisy for the necessity of using very long cable transducers. Other relevant and common problems in the field of OMA are [10]: the difficulty to detect different mode shapes for very closely spaced modes; the subjectivity in the system order estimate; the need of a more efficient algorithm able to omit the spurious modes created by noise or redundant degrees of freedom of the model.

Ambient vibration tests have been carried out on the tower of the Provincial Administration Building in Bari, in a particularly windy day (24th July 2009), with the aim of determining its dynamic response and developing a procedure for modeling the tower. The Operational Modal Analysis has been performed both in the frequency domain and in the time domain to extract the dominant frequencies and mode shapes. The application of well-known identification techniques - the Enhanced Frequency Domain Decomposition (EFDD) [11], the Stochastic Subspace Identification (SSI) [12] and the Crystal Clear-SSI (CC-SSI) methods [13], the last recently implemented in a commercial software, yields to very similar results (in both frequencies and mode shapes) for all the identified modes, providing consistent information for the updating of the finite element model of the tower..

2.DESCRPTION OF THE BUILDING

The tower of the Provincial Administration Building in Bari, Italy (Fig.1), dating back to the thirties of the 20th century and about 60 m tall, is not only a typical example of the fascist architectural style, but it is an important symbol of the city itself.



Fig. 1. View of the Provincial Administration Building of Bari (a) and of the investigated tower (b)

Situated on the waterfront of the city, with the principal façade exposed to the North-West direction (that is the dominant wind direction), the tower has eleven floor, characterized by different heights, and a square plan with a side of about 9,0 m from the base to the 5th floor, a side of about 8,6 m from the 5th to the 9th floor, a side of about 7,6 m at the 10th floor, and a side of about 5,3 m at the 11th floor. It is made of massive concrete reinforced with a diffuse and superficial reinforcement and it stands on a foundation slab. The eleven levels of the tower consist of a basement, a mezzanine and nine floors. Up to the 5th floor, the tower is included in the main part of the building of the provincial administration, from which it emerges for six levels more (Figure 1), from 6th to 11th ones, with openings on the façades in the first floor up to the building of the provincial administration and in the upper two floors, the last of which (the bell chamber) has a smaller plan with respect to the others.

The tower was instrumented with thirteen SA-107LNC uniaxial servo-accelerometers placed at floors 5, 7, 9 and 10 and connected to a centralized data acquisition board by means of long transducer cables (Fig. 2). The accelerometers position along the height of the tower, referred to the xyz reference system is shown in Fig.3a while the quoted sections of the instrumented tower floors are showed in Fig.3b. The response obtained was registered by a HBM MGC Plus at a sample rate of 200 Hz. The signal conversion and the data acquisition were managed by a laptop in the framework of the CATMANv4 software package, which included an analogical filter with a cut-off frequency of 40 Hz.



Fig. 2. Accelerometers and acquisition board used for the tests.

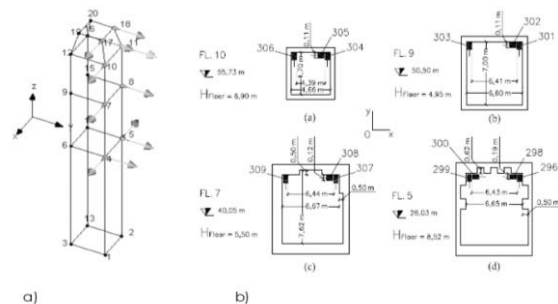


Fig. 3. Localization of the accelerometers on the tower.

During the data elaboration, it was found that accelerometers indicated with 301 and 307 in Figure 3b (floor 7 and 9) were out of order because their measurements were very noisy and no peak appears in their acceleration time-history plots when subjected to an impact force with a hammer.

In Fig. 4 the typical acceleration time-histories recorded by accelerometers 301 and 307 have been compared to the ones recorded by accelerometers 304 and 296. The inspection of Fig. 4 reveals a remarkable difference between the time histories, conceivably related to the different signal-to-noise (S/N) ratio of the four sensors.

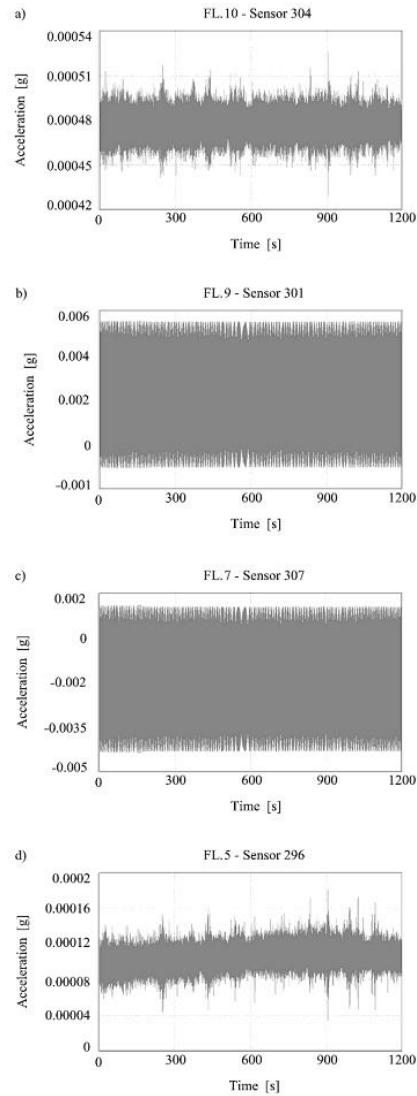


Fig. 4. Comparison between the acceleration time-histories recorded by sensors at different test point of the tower: (a) Floor 10; (b) Floor 9; (c) Floor 7; (d) Floor 5.

As a consequence, the data recorded from sensors 301 and 307 have been neglected from the analysis, i.e. these accelerometers are not be considered in the present work.

3.DATA PROCESSING AND OPERATIONAL MODAL ANALYSIS

The vibration data have been registered in a time interval of 220 minutes at a sample rate of 200 Hz. The signal conversion and the data acquisition were managed by the previously described laptop. The analysis of the recorded data was carried out dividing the time period of 220 minutes of continuous monitoring in eleven intervals of 20 minutes each; a statistical analysis was carried out [14] demonstrating the extreme repeatability of the identified frequencies in the different intervals. The extraction of the modal parameters from ambient vibration data was carried out by using the ARTeMIS Extractor Pro 2010

[13] and, in particular, EFDD, SSI and CC-SSI methods.

In this work the analysis was carried out with reference to one of the interval of length 20 minutes optimizing the characteristics of the used extractor software [13]. In particular, after a deep analysis of the Singular Value Decomposition diagrams (SVD only three channels were selected for the identification analysis. Fig. 5 shows the selected channels and their position on the building.

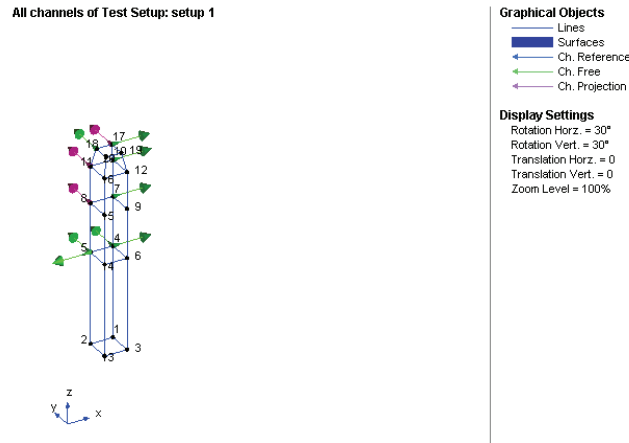


Fig. 5. Accelerometers position and selected channels for identification.

Fig. 6 shows the SVD values of the spectral density matrices carried out in the framework of the EFDD technique, while Figures 7 and 8 show the stabilization diagrams of the state space models obtained by SSI and CC-SSI techniques. It is worth noting that, while the SSI technique is based on an unconditionally linear least squares estimation of the model (through proper processing of the experimental data acquired from the ambient vibration tests), the Crystal Clear SSI technique [13] allows a conditional estimation: it is necessary to specify the maximum number of significant poles (eigenvalues) present in the measurements that should be estimated. This algorithm helps to get clear results leading to cleaner and more stable stabilization diagrams; the CC-SSI estimation feature allows a conditional estimation emphasizing a user defined number of physical modes and suppressing the remaining parts of the information in the data. The estimation algorithm [13] will then focus on the modes having these poles and any less significant noise poles are returned with a natural frequency estimate much higher than the Nyquist frequency, and a damping ratio of 100%, thus reducing their disturbing effects on the physical modes. It is possible to note that the CC-SSI technique (Fig.8) gives a stabilization diagram much more stable than SSI technique (Fig.7) also for high dimension of the estimation matrix (in this case the maximum dimension for SSI and CC_SSI was 150). Moreover, it is evident that SSI (Fig. 7) shows one false frequency around 1.8 Hz; analyzing the SVD diagram this frequency may be removed from the identified frequencies. On the contrary, CC-SSI (Fig.8) doesn't give this false information.

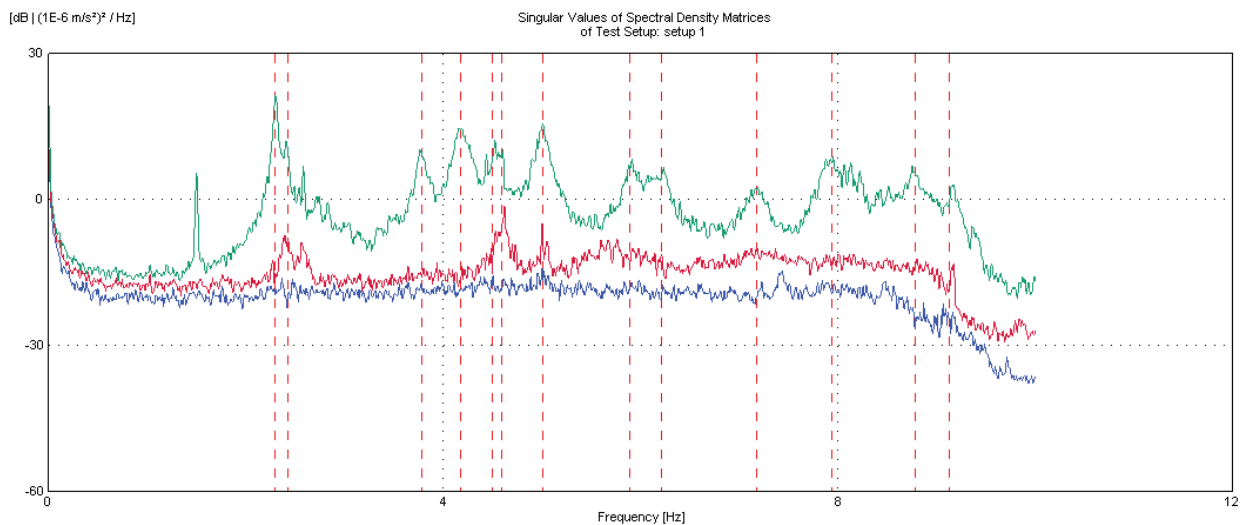


Fig. 6. Singular values of spectral density matrices by EFDD technique.

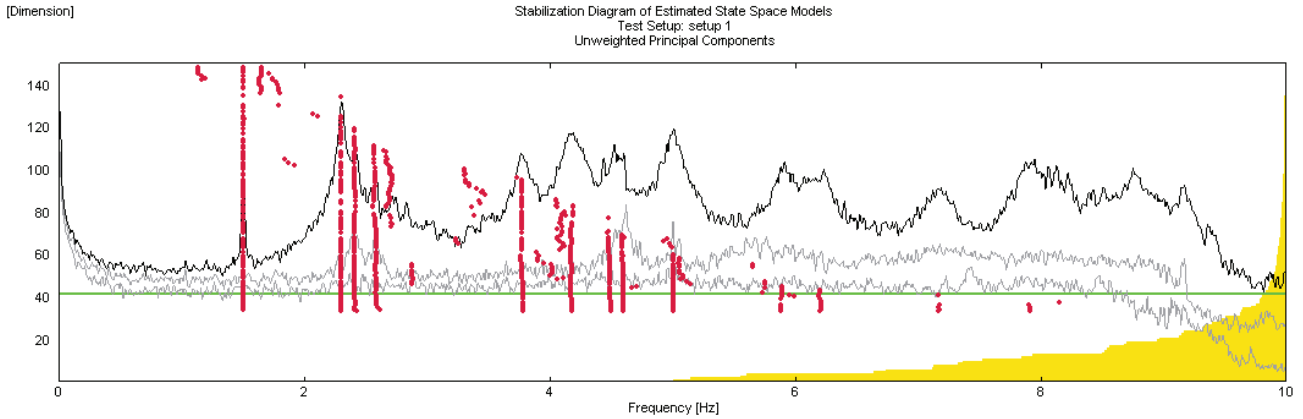


Fig. 7. Stabilization diagram of the state space model by SSI technique.

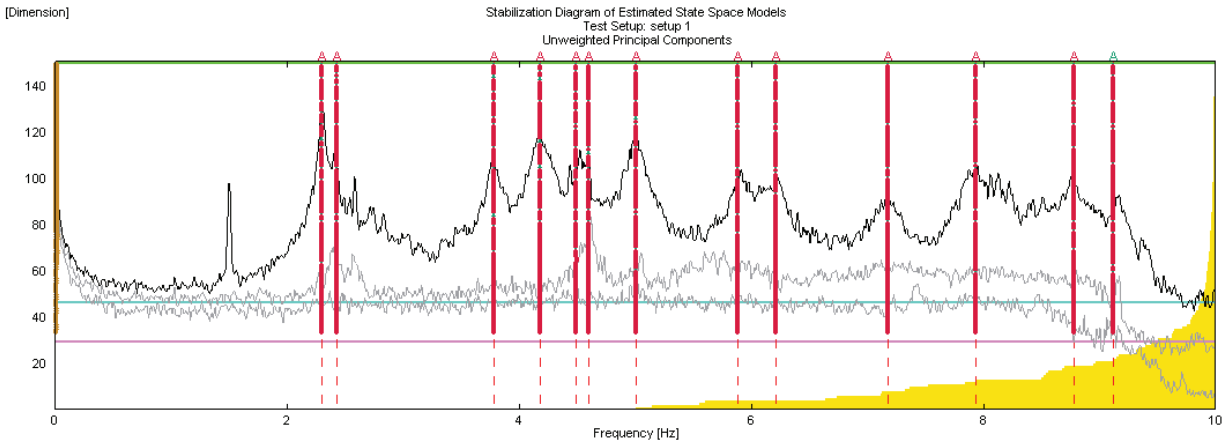


Fig.8. Stabilization diagram of the state space model by CC-SSI technique.

The first 6 frequencies identified for each method are shown in Table 1, demonstrating the consistency of the three methods; this results encourages to use them for a successive calibration of the theoretical model. It is possible to notice that the first two frequencies values are quite close, due to the symmetry of the tower section and, as demonstrated by the following modes identification, these frequencies are related to the first two principal bending modes of the building.

Table 1. First six natural frequencies identified from ambient vibration measurements

	EFDD [Hz]	SSI [Hz]	CC-SSI [Hz]	Mean [Hz]	Standard Deviation [%]
Mode 1	2.303	2.303	2.298	2.301	0.26
Mode 2	2.407	2.440	2.440	2.429	1.90
Mode 3	3.795	3.782	3.781	3.786	0.78
Mode 4	4.178	4.177	4.207	4.187	1.69
Mode 5	4.524	4.489	4.292	4.435	1.25
Mode 6	4.594	4.594	4.610	4.599	0.92

4. MODES IDENTIFICATION

The mode shapes identification has been carried out by introducing some relations between the measured and unmeasured degrees of freedom of the building. In the framework of the ARTeMIS Extractor Pro software [14], in fact, it is possible to define linear combinations of the measured signals (the so-called “Slave Nodes Equations”), which can be very helpful for defining rigid body motions and slave nodes relations. These equations can be used to evaluate the vibrations of the instrumented points, and, as a consequence, to obtain the mode shapes for the entire tower, even though the acquisitions are only available in a few nodes of the geometry. In particular, the data have been analyzed imposing that each floor of the tower is rigid in its plane. In this hypothesis, in fact, the movement of each floor plate can be described imposing mathematical equations between the nodes coordinates in the xy plane [13]. In particular, considering the nodes classification shown in Fig. 3a, equations were applied between the nodes groups (4,5,6,14), (7,8,9,15), (10,11,12,16), (17,18,19,20).

These equations can be used to make the complete geometry move, even though the acquisitions are only available in few nodes of the geometry.

All equations start in the same way as shown below:

$$\text{Node (“Node Number”, “Direction”) = ...} \quad (1)$$

This equation defines the motion of the node specified by “Node Number” in the direction specified by “Direction”. The “Direction” field is a number from 1 to 3: 1 corresponds to X direction, 2 corresponds to Y direction and 3 corresponds to Z direction. The data have been analyzed imposing that each floor of the tower was rigid in its plane. In this hypothesis, in fact, the movement of each floor plate can be described by two displacements and one angle. For the typical floor plate of the tower model the group (generic nodes of a plate depicted in Fig. 9) the plane equations are herein reported.

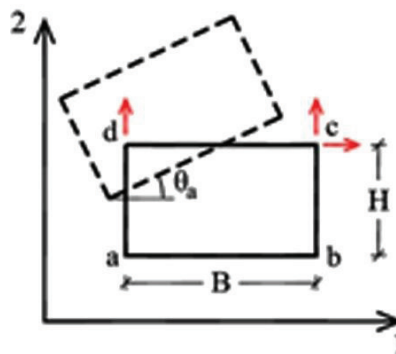


Fig.9. Slave nodes equations for the typical floor plane of the tower.

$$\left\{ \begin{array}{l} \text{node}(b,1) = \text{node}(a,1) \\ \text{node}(b,2) = \text{node}(c,2) \\ \text{node}(c,1) = \text{node}(d,1) \\ \text{node}(a,2) = \text{node}(d,2) \\ \text{node}(a,1) = \text{node}(c,1) + \theta_a \cdot H \end{array} \right. \quad (2)$$

The modes carried out by using the equations (2) are shown in Fig. 10. It is evident that from the identification procedure it is possible to classify mode 1 (y- direction), mode 2 (x- direction), mode 4 (y- direction) and mode 5 (y- direction) as bending modes, and modes 3 and 6 as torsional mode (following the nomenclature of Figure 10 where the number indicates the corresponding frequency). Modes 3 and 6, nevertheless it has been classified as a torsional mode, are not perfectly depicted, probably due to the sensors position on the floor; in fact this position is able to monitor the bending modes, but is surely inaccurate for the complete and correct reconstruction of the torsion modes. This choice, however, was obliged by the

impossibility of placing any accelerometer on the opposite side of the tower for the presence of an internal elevator vain and a stair-case.

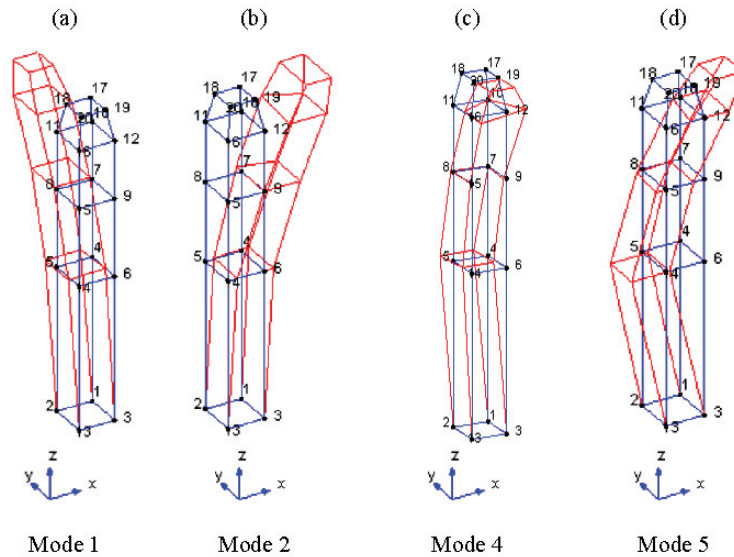


Fig. 10. Vibration modes identified from ambient vibration measurement.

5. CONCLUSIONS

The ambient-vibration based investigations carried out to assess the dynamical behavior of the tower of the Provincial Administration Building of Bari have been presented in this paper. Eleven consecutive ambient vibration tests have been performed for the accurate estimation of the dynamic characteristics, evaluating the statistical repeatability of the results. The response of each accelerometer to the impact of a hammer has been analyzed to check the correct functioning and polarity.

The following conclusions can be drawn from this study:

1. The fundamental mode of the tower, with a natural frequency of about 2.3 Hz, involves dominant bending in E/W direction (that is along the y- axis in the reference system introduced). The coupled motion (about 2.4 Hz) is referred to N/S direction (x- axis).
2. The second couple of bending modes are around 4 Hz and between these two couples of modes there is a torsion mode at a value lower than 4 Hz and immediately higher than the second couple of bending modes. Observing the experimental measurements the torsion mode is not really clear, probably due to the positioning of the accelerometers that, for the same instrumented floors, has been not sufficient to describe the torsional vibrations.
3. A very good agreement was found between the modal estimates obtained from the two classical OMA methods, EFDD and SSI, and the recently implemented CC-SSI method, for each of the consecutive acquisition time intervals; the CC-SSI methods helps to improve the results quality.

REFERENCES

- [1] Sepe V, Speranza E, Viskovic A. A method for large-scale vulnerability assessment of historic towers. *Structural Control & Health Monitoring* (2008);15(3):389-415.

- [2] Valluzzi MR, da Porto F, Modena C. Structural investigation and strengthening of the Civic Tower in Vicenza. Proc. of Structural Faults and Repairs ,Repairs, London UK: 2003
- [3] Ivorra S, Pallarés FJ. Dynamic investigations on a masonry bell tower. Engineering Structures 2006; 28(5):660-7.
- [4] Gentile C, Saisi A. Ambient vibration testing of historic masonry towers for structural identification and damage assessment. Construction & Building Materials 2007; 21(6):1311-21.
- [5] Julio ENBS, da Silva Rebelo CAS, Dias da Costa DASG. Structural assessment of the tower of the University of Coimbra by modal identification. Engineering Structures 2008; 30:3648-77.
- [6] Lepidi M, Gattulli V, Foti D. Swinging-bell resonances and their cancellation identified by dynamical testing in a modern bell tower. Engineering Structures, Elsevier 2009; 31 (7):1486-1500.
- [7] Ramos LF, Marques L, Lourenco PB, de Roeck G, Campo-Costa A, Roque J. Monitoring historical masonry structures with operational modal analysis: Two case studies. Mechanical Systems and Signal Processing 2010;24:1291-1305
- [8] Bayraktar A, Sevim B, Altunisik A C, Türker T. Earthquake analysis of reinforced concrete minarets using ambient vibration tests results. The Structural Design of Tall and Special Buildings 2008;19:257-73. DOI: 10.1002/tal.464.
- [9] Jacobsen NJ, Thorhauge O. Data acquisition systems for Operational Modal Analysis. Proc. of the 3rd IOMAC, 215-222, Porto Novo (Ancona) 2009.
- [10] Masjedian MH, Keshmiri M. A review on Operational Modal Analysis researches: classification of methods and applications. Proc. of the 3rd IOMAC, 707-718, Starrylink, Brescia 2009.
- [11] Brincker R, Zhang L, Andersen P. Modal identification of output-only systems using frequency domain decomposition. Smart Materials and Structures 2001;10:441-5.
- [12] Peeters B, De Roeck G. Stochastic System Identification for Operational Modal Analysis: A Review. Journal of Dynamic Systems Measurement & Control 2001;123(4):659-67.
- [13] ARTeMIS Extractor Pro software. Issued by Structural Vibration Solutions ApS. NOVI Science Park, Niels Jernes Vej 10, DK 9220 Aalborg East, Denmark; 2010.
- [14] Diaferio M, Foti D, Mongelli M, Giannoccaro NI. Dynamic behavior of a Historic Tower in Bari. Proc. of 14th European Conference on Earthquake engineering, 30 August-3 September 2010, Ohrid, Republic of Macedonia.

Monitoring of a Movable Bridge Mechanical Components for Damage Identification using Artificial Neural Networks

Taha Dumlupinar¹, F. Necati Catbas²

Department of Civil, Environmental and Construction Engineering
University of Central Florida, Orlando, 32816

¹ tahadlp@yahoo.com.tr
² catbas@mail.ucf.edu

ABSTRACT

This paper presents a review of the results of a structural health monitoring (SHM) study to track the performance of a gearbox and rack-pinion of an operating movable bridge. These mechanical components are critical parts of bascule type bridges and damage of these components need to be identified and diagnosed, since an early detection of faults may help to avoid major damage to the structure and also avoid unexpected bridge closures. The prediction of the gearbox and rack-pinion fault detection is carried out with artificial neural networks (ANN) using the time domain vibration signals. Several statistical parameters are selected as characteristic features of the time-domain vibration signals. Monitoring data is collected during regular opening and closing of the bridge, as well as during artificially induced damage conditions. The results indicate that the vibration monitoring data, with selected statistical parameters and particular network architecture, give good results to predict the undamaged and damaged condition of the bridge.

INTRODUCTION

Evaluation and assessment of machines is very critical in order to increase the reliability of machinery and to decrease the possible loss of production due to breakdowns. Such problems have been studied mainly for mechanical structures in industrial and manufacturing environments such as factories and plants. The operation, monitoring and assessment of heavy movable structures have not been fully studied and presented in the literature. The objective of this study is to detect frequently observed gearbox and rack-pinion problems of an existing movable bridge by analyzing Structural Health Monitoring (SHM) data with Artificial Neural Networks (ANN). Based on SHM data the inherent operational behavior of mechanical components is modeled using neural networks, resulting in an efficient and practical determination of the current state of system health. These components (gearbox and rack-pinion) which are critical for the opening and closings of movable bridges are monitored under healthy conditions for a sufficiently long period of time using accelerometers. While ANN methods have been used extensively for machinery for mechanical components or fixed structures, the implementation on a large scale heavy movable structure is quite unique.

BRIEF REVIEW OF ARTIFICIAL NEURAL NETWORKS (ANN)

Artificial Neural Networks (ANN) have been developed as computing methods for modeling complex relationships between inputs and outputs or to find patterns in data sets. Multi-layered feed-forward neural networks are one of the most commonly used neural networks in structural engineering applications and have demonstrated various

degree of success. ANN learns from the existing patterns capturing the subtle functional relationships among the patterns and then makes a prediction for the patterns which are not considered during learning.

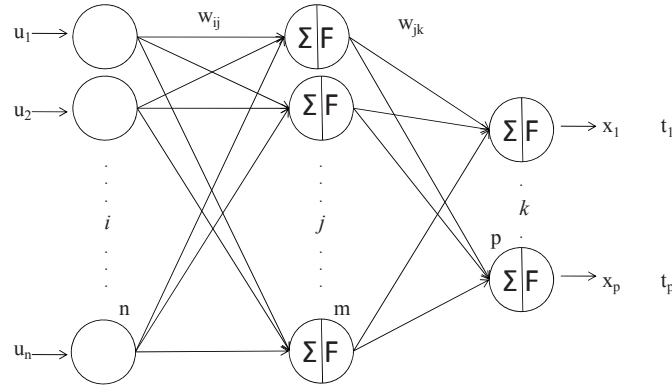


Figure 1 Single Hidden Layer Feed Forward Neural Networks

A multi-layered feed-forward neural network consists of multiple layers of computational units interconnected in a feed-forward way (Figure 1). The input vector distributes the inputs to the input layer. There is no processing in the input layer; rather it can be conceived as a sensory layer, where each neuron receives a sole component of the input vector “U”. The last layer is the output layer which outputs the processed data. The output of each neuron in this layer corresponds to a component of the output vector “X”. The layers between the input and output layers are referred to as hidden layers. Hidden layer(s) may have any number of neurons; however they should be chosen carefully to achieve some special effects in some cases [1].

STRUCTURAL HEALTH MONITORING (SHM) OF A MOVABLE BRIDGE

The authors investigated the most common issues associated with movable bridges and designed and implemented a comprehensive SHM plan on a movable bridge over Florida Inter Coastal water way (Sunrise Bridge, Figure 2). This bridge was constructed in 1989. It has double bascule leaves, each 73’10” (22.49m) long approximately, and 53’4” (26.15 m) wide, carrying three traffic lanes and opening about 15 times a day.

In this paper, the mechanical parts of the bridge are investigated by using the data from the accelerometers installed on these parts. The critical characteristics and distinct behavior change in dynamic response behavior were tracked over time with the SHM system. Two recurrent types of damage were identified for bridge components, namely, leakage from the gear box and inadequate lubrication of the open gear. The detection and diagnosis of damage in these parts are of great practical significance and paramount importance in the sense that an early detection of these faults may help to avoid performance degradation and major damage to the machinery itself. Therefore, these parts were monitored with accelerometer sensors. The Gearbox (Figure 2a) is instrumented with six accelerometers at different locations in both horizontal and vertical directions. The Rack-Pinion (Figure 2b) is instrumented with by one horizontal accelerometer to monitor the open gear. PCB accelerometers are used and are collecting at 250 Hz. A large number of data sets from the healthy condition of these parts were collected (Figure 2c and d).

The bridge owners provided a unique opportunity to artificially induce some of these possible issues as damage scenarios on the bridge. As a result, to see the effect of leakage from the gear box, 25% of oil from the gearbox was removed. In addition, to simulate inadequate lubrication of open gear, large portion of the grease on the open gear was removed. Under these damage conditions, the gearbox and the rack and pinion were monitored during the opening and closing of the leaves of the bridge (Figure 2e and f). Using healthy (baseline, undamaged) and unhealthy (altered, damaged) data sets, an artificial neural network-based framework was developed for detecting the mechanical alterations at the gearbox and the rack and pinion. Over a period of two months, more than 170 data sets were employed for the analysis of the data. Each data set corresponds to the opening-closing of the bridge for a duration varying from two to five minutes where the vibration signals were collected at 250 Hz as exemplified in Figure 2.

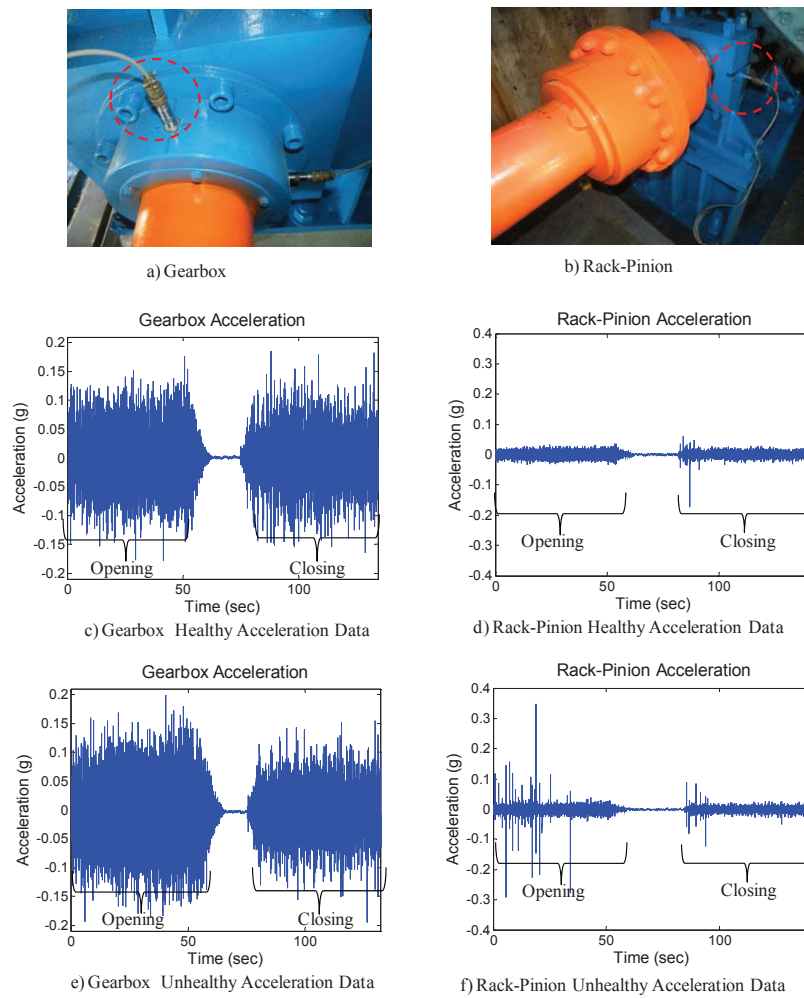


Figure 2 Sensors on gearbox and rack-pinion with corresponding sample acceleration data

FEATURE SELECTION

The vibration signal of mechanical components is composed of two parts, namely opening and closing (Figure 3). In this paper, only the opening part of the vibration signal is used since considered features are more sensitive to the damage and the opening part is sufficient for solving the problem without adding complexity. Statistical parameters were used and successful results were obtained for bearing and gear fault detection by Samanta and Al-Balushi [2], where root mean square, variance, skewness, kurtosis and normalized sixth central moment were used from the time-domain vibration signal as input to the network for fault diagnosis of rolling element bearings. In our study presented in this paper, several statistical parameters were tested initially for determining simple yet effective solutions. As a result, the characteristic features of the time-domain vibration signals were selected as maximum vibration (average of the ten largest to avoid extreme values) and minimum vibration (average of the ten smallest values) of the signals from the opening part of the data sets along with the standard deviation.

FRAMEWORK AND TRAINING OF ARTIFICIAL NEURAL NETWORK

As mentioned before, a large number of data sets from the healthy condition and several data sets from the unhealthy condition of monitored parts were collected. A thorough understanding of the damage-sensitive features from these measurements was needed in order to obtain accurate damage prediction. In this study,

statistical parameters were used to identify the certain features of the opening part of acceleration data. The statistical analysis of these features was used to determine the current state of system health. Statistical significance of the vibration signal changes in the extracted features was evaluated using neural networks. This statistical information was fed as inputs to the ANN.

One of the important considerations was to efficiently interpret the results from the ANN. As a result, no damage (healthy condition) was assigned “0” and damage was assigned “1” as output from the ANN. A total of 172 input-output patterns (pairs) were generated and were divided into three sets, namely, the training set, the cross-validation set and the test set.

In this study, the Levenberg-Marquardt algorithm was used for ANN learning rule, and the sigmoid function was used for activation function. The use of sigmoid function requires that the input and output data be scaled to the range of [0-1]. In the present study, the input and output data were scaled to a somewhat narrower range between 0.2 and 0.8, resulting in a considerable improvement in learning speed due to increased sensitivity of the sigmoid function within this range.

DIAGNOSTIC OF BRIDGE GEARBOX AND RACK-PINION DAMAGE

To make sure that the network training has been satisfactorily completed and the network is capable of generalization, a set of unseen patterns must be selected and the network should be tested using these patterns. For this purpose, a total of 7 testing patterns were used to observe the prediction performance of all the architectures considered in the study. As discussed before, out of 7 patterns, 1 pattern was used to identify the removal of 25% of oil from the gearbox, 3 patterns were used to identify the damage due to the inadequate lubrication of open gear, and the remaining 3 patterns were used to identify the no damage case. Table 1 shows the desired outputs and best network outputs for all testing patterns. It is clear that the prediction of the best networks for 7 unseen patterns is quite satisfactory. The best network yields maximum difference of 0.007% for the Gearbox and yields maximum differences of 0.005% for rack-pinion under the defined network parameters. This indicates that the networks trained successfully establish the relationship between the statistical parameters and damages and interpolate this relationship for other unseen data with a great accuracy. In addition, the coefficient of correlation between actual and predicted outputs is 0.999 for the gearbox and 1.000 for the rack-pinion. This indicates that the generalization performance of the network is very good and it is able to generalize within the range of the data used for training.

Table 1 Testing set with Actual Outputs and Best Network (6-(2-2)-2) Outputs

INPUTS						ACTUAL OUTPUTS		ANN OUTPUTS	
GB Max	GB Min	GB Stdev	RP Max	RP Min	RP Stdev	GB	RP	GB	RP
0.1650	-0.1682	0.0495	0.0276	-0.0321	0.0093	1	0	1.000054	0.000053
0.1332	-0.1398	0.0360	0.1585	-0.1442	0.0118	0	1	-0.000010	1.000018
0.1392	-0.1348	0.0358	0.1299	-0.1863	0.0125	0	1	0.000038	1.000020
0.1417	-0.1523	0.0364	0.1236	-0.1563	0.0114	0	1	0.000038	1.000020
0.1437	-0.1524	0.0416	0.0337	-0.0286	0.0094	0	0	-0.000025	0.000016
0.1481	-0.1484	0.0397	0.0313	-0.0295	0.0092	0	0	-0.000026	0.000016
0.1356	-0.1475	0.0404	0.0302	-0.0329	0.0092	0	0	-0.000025	0.000016

Once trained successfully, the network can confidently be used to predict accurate output values for new input data. The condition of the gearbox and rack-pinion using new input data can be obtained (e.g. “1” or “0”) from the trained neural network with a trivial computational time during the lifetime of the structure. In this section, the best ANN Model is used to evaluate the condition of the components for a certain period time.

CONCLUDING REMARKS

In this study, the data from structural health monitoring (SHM) of mechanical components of a movable bridge are briefly presented for predicting the condition using artificial neural network (ANN). The results indicate that artificial neural networks have the ability to identify the damage by using the correct network parameters with the right architectures. The statistical parameters obtained from the vibration signals of the gearbox and rack-pinion are employed as inputs. The best network is found to be one having 6-(2-2)-2 network geometry with Levenberg-Marquardt learning algorithms. It yields a maximum difference of 0.007% for the Gearbox (between actual and predictions) and yields a maximum differences of 0.005% for the Rack-Pinion under the defined network parameters for testing set, indicating accurate prediction of damage and undamaged conditions with the best networks. More details of the work presented in this research will be presented in more detail in another conference or journal paper once finalized by the researchers.

REFERENCES

1. Maier, H.R., Dandy, G.C., (2000), "Neural networks for the prediction and forecasting of water resources variables: a review of modeling issues and applications", *Environmental Modelling & Software*, Vol. 15, pp.101–124.
2. Samanta, B., Al-Balushi, K. R., (2003), "Artificial neural network Based Fault Diagnostics of rolling Element Bearings Using time-Domain Features", *Mechanical Systems and Signal Processing*, Vol. 17, No. 2, pp. 317–328
3. Rao, A.R., Kumar, B., (2007), "Predicting Re-aeration Rates Using Artificial Neural Networks in Surface Aerators", *International Journal of Applied Environmental Sciences*, Vol. 2, No. 1, pp. 155-166.
4. Hagan M. T., Menhaj M. B. (1994), "Training feed forward networks with the Marquardt algorithm. *IEEE Trans*". *Neural Networks*, Vol. 6, pp. 861–867.
5. El-Bakyr, M. Y. (2003) "Feed forward neural networks modeling for K–P interactions". *Chaos, Solutons & Fractals*. Vol. 18, No. 5, pp. 995–1000.
6. Cigizoglu, H. K. & Kişi, O. (2004) "Flow prediction by three back propagation techniques using k-fold partitioning of neural network training data". *Nordic Hydrol.*, Vol. 36, No.1.
7. Yetilmezsoy, K., Demirel, S., (2008), "Artificial neural network (ANN) approach for modeling of Pb(II) adsorption from aqueous solution by Antep pistachio (*Pistacia Vera L.*) Shells", *Journal of Hazardous Materials*, Vol. 153, pp. 1288–1300.

Ambient vibration based modal identification of a flexible retaining wall

C. Rainieri¹, A. Dey², C. Laurenza³, G. Fabbrocino⁴, F. Santucci de Magistris⁵

¹Ph.D., Research associate, Structural and Geotechnical Dynamics Laboratory *StreGa*, S.A.V.A. Dept., University of Molise, Via Duca degli Abruzzi – 86039 Termoli, Italy

²Ph.D., Research associate, Structural and Geotechnical Dynamics Laboratory *StreGa*, S.A.V.A. Dept., University of Molise, Via Duca degli Abruzzi – 86039 Termoli, Italy

³Ph.D. Student, Structural and Geotechnical Dynamics Laboratory *StreGa*, S.A.V.A. Dept., University of Molise, Via Duca degli Abruzzi – 86039 Termoli, Italy

⁴Associate Professor, Structural and Geotechnical Dynamics Laboratory *StreGa*, S.A.V.A. Dept., University of Molise, Via Duca degli Abruzzi – 86039 Termoli, Italy

⁵Assistant Professor, Structural and Geotechnical Dynamics Laboratory *StreGa*, S.A.V.A. Dept., University of Molise, Via Duca degli Abruzzi – 86039 Termoli, Italy

Abstract

Bridges and buildings are the commonly monitored structural typologies and hence, the dynamic behaviour of superstructures is extensively studied. Geotechnical aspects, instead, are less investigated; in particular, the dynamic and seismic behaviour of a flexible retaining wall is currently not fully understood. The Structural Health Monitoring system of the “Casa dello Studente” (Student House) at University of Molise has been designed and is currently under implementation in order to obtain a deeper knowledge about the dynamic behaviour of geotechnical structures and soil-structure interaction mechanisms. To fulfil this aim, a number of ambient vibration tests have been carried out and the results are used to refine the numerical model of the wall in operational conditions. In the present paper, the

main test results are reported and the numerical model of the soil-structure system is described. Due to the low level of ambient vibrations, an elastic model has been implemented and a number of simulations have been carried out in order to investigate the dynamic behaviour of the soil-structure system and the mechanisms of interaction, also through the comparison with the experimental results.

Introduction

Structural Health Monitoring (SHM) represents a promising answer to requirements of structural management and maintenance. Its increasing diffusion also in the field of civil engineering is related to the opportunity of a fast assessment of potential damage conditions, tracking their evolution and providing almost in real time information about the safety level of the structure itself. In particular, reduction of inspection costs, seismic protection, possibility to develop post-earthquake scenarios and support rescue operations are some of the main advantages related to implementation of effective SHM systems.

SHM is based on the integration of a number of different skills (electronic and civil engineering, computer science). SHM systems have been applied to different structural typologies [1]. However, a limited number of full-scale dynamic measurement systems are currently applied to geotechnical systems. In the present paper the opportunities of SHM and continuous dynamic measurements are explored through an application focused on a full scale flexible retaining wall. An integrated structural and geotechnical monitoring system for such a wall has been designed and it is currently under development at University of Molise.

The analysis of the dynamic response of the wall under operational and earthquake conditions plays a fundamental role for the enhancement of numerical models and the improvement of the current knowledge about the dynamic and seismic behaviour of flexible retaining walls. Moreover, dynamic measurements can be used to build an effective vibration-based SHM system which can be data-driven [1] or take advantage also of results of numerical analyses [2]. On the other hand, data recorded during seismic events may give a deeper insight in the soil-structure interaction, in particular during strong motion events. Collection of such data will be useful also to improve seismic design procedures.

Soil parameters obtained from in-situ geotechnical investigations have been therefore used for implementation of a Finite Element (FE) model of the wall. Results of dynamic monitoring are then used to assess the quality of the numerical model and improve it. This will bring, in a near future, in a better estimate of the values and the distributions of the stress states during earthquakes, thus improving the current design procedures.

Structural Health Monitoring

The monitored reinforced concrete (r.c.) flexible retaining wall is a part of the new Student House at University of Molise in Campobasso (Italy). It comprises of two rows of reinforced concrete (r.c.) piles of diameter 800mm and a length of about 18m, sustaining a free height of about 6m. The piles were constructed as drilled piles, with the usage of drilling buckets, and devoid of any sort of in-situ casing. No anchorages have been provided for the wall. A r.c. top-beam overlies the top of the retaining structure. The research activities have commenced subsequent to the structural design of the wall that was carried out by some consultants.

Table 1. Results of output-only dynamic tests

Mode	f_{exp} (Hz)	ξ_{exp} (%)
I	3.68	1.4
II	7.23	1.2

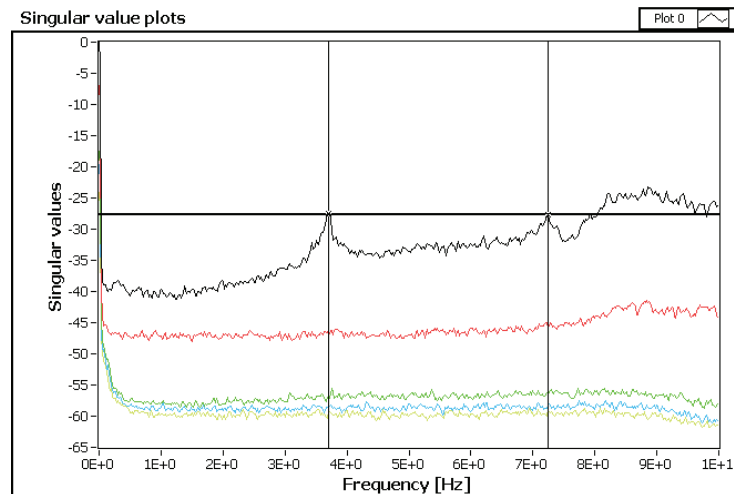


Fig. 1. FDD – Singular Value plots and identified natural frequencies

A detailed description of the SHM system is beyond the scope of this paper. Relevant to the present contribution, it is worth mentioning that two of the piles of the retaining wall have been instrumented with embedded piezoelectric accelerometers and some ABS plastic commercial inclinometer casings. The dynamic response of the wall is continuously monitored through a customized system developed in the framework of the activities of the research group. Further details of the above systems are provided in [3,4]. The dynamic response of the wall to ambient vibrations has been analyzed by different output-only modal identification procedures, such as the Frequency Domain Decomposition (FDD) [5], the Stochastic Subspace Identification [6,7] and the Second Order Blind Identification [8]. Re-

sults are summarized in Table 1, while the Singular Value plots provided by the FDD are shown in Figure 1, pointing out the location of the identified modes.

Geotechnical characterization and Finite Element modeling

Extensive investigations have been carried out to determine the geology of the region, as detailed in [9]. Prior to the construction of the retaining wall, two borehole investigations (total depth of 30 m from the ground level) were carried out for Stratigraphic Column extraction, Standard Penetration Test (SPT) and Down-hole Test (DH). Laboratory tests such as physical and chemical characterization, triaxial tests and direct shear tests were also conducted. A contour mapping of the area suggest that the boreholes have a level difference of about 8 m (Abs. ground level of Borehole S6 - ~676 m, Abs. ground level of Borehole S5 - ~668 m). The subsoil in the area is mainly constituted by varicoloured clay covered by man-made ground. Based on the results of in-situ investigations a simplified geotechnical profile with inclined stratigraphy and irregular bedrock is attempted and a Finite Element model of the soil+wall system (Figure 2) has been set in PLAXIS 2D v8.4 code [10]. In compliance with the non-availability of water in the geotechnical investigations, the water table has been considered to be deep enough to be away from the interaction with the geotechnical structures.

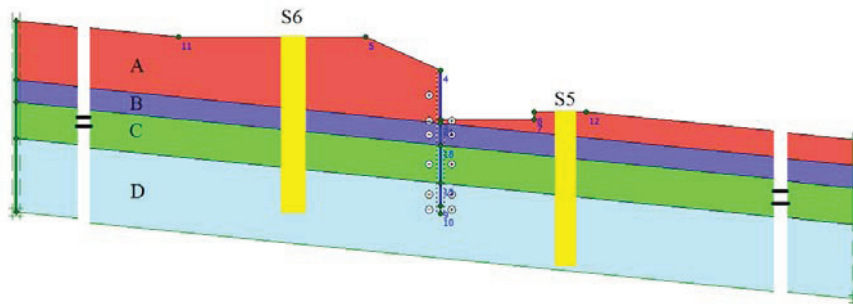


Fig. 2. Geometry and stratigraphy of the preliminary model

In order to investigate the dynamic behavior of the system in operational conditions, the soil has been modeled as Linear Elastic (LE) material in compliance with the low amplitude of ambient vibrations. Hence, the elastic modulus of the soil layers are chosen conforming to the shear wave velocity, as measured from the DH tests. Average values of the parameters obtained from the two boreholes have been adopted in the model. The embedded retaining wall has been modeled as a plate with rigid interface with adjacent soil layers. Table 2 shows the adopted soil parameters. The details about the contributory parameters affecting the numerical responses are mentioned in [4]. In order to simulate the propagation of

shear waves in the medium, a horizontal prescribed displacement of 1 unit in terms of displacement is used along the bedrock level, used as a multiplier to the Gaussian white noise input excitation.

The acceleration responses collected from PLAXIS are analyzed according to the above mentioned output-only modal analysis procedures in order to extract the dynamic properties of the model and compare them to the experimental results. The minimization of the scatter between numerical and experimental values of the dynamic properties has driven the model updating process.

Table 2. Material parameters adopted in the preliminary model

Soil Layer	Material Type	E_0 (10^5 kPa)	G_0 (10^5 kPa)	ν	γ (kN/m ³)	V_s (m/sec)	H_L (m) Left of wall	H_R (m) Right of Wall
A	LE	3.188	1.113	0.432	18.00	246.2	8	3
B	LE	4.086	1.433	0.426	19.03	271.6	3	3
C	LE	14.51	5.045	0.438	19.47	503.9	5	5
D	LE	26.49	9.243	0.433	19.98	673.3	10	10

Model refinement

The two above mentioned 30 m deep boreholes allow a reasonable identification of the soil layers but it is not possible to describe the location of the bedrock. From the SPT blow counts in Borehole S5, it is observed that the refusal of penetration has been recorded at 20 m and beyond, the SPT count being above 20; however, the borehole is further proceeded till 30 m, thus suggesting that at that depth still it cannot be adjudged as or a part of bedrock. For further clarification, the stratigraphical records of more boreholes in the near vicinity are studied and in most of the cases, the presence of the bedrock at a depth of 15 m from the ground level with an SPT blow-count >40 has been observed. Hence, it is possible that due to the spatial irregularity of the strata, S5 did not encounter rocky-like deposits; whereas, the same may be present along the longitudinal section of the retaining wall. Hence, in the refined model, the depth of the bottom-most layer is considered to be ~4m, so that the existence of the bedrock is nearly 15m from the ground level.

In contrary to the presence of several borehole investigations in the near vicinity on the excavated side of the wall, no other borehole studies were discovered on the uphill side that can justifiably verify the depth of the bedrock, or provide an indication about its irregularity in the transverse direction. Hence, two major uncertainties recognized in the numerical simulation are the depth of the bedrock and transverse profile of the bedrock.

Stiffness of the soil layers in the uphill side of the wall, as determined by the DH test in Borehole S6, also poses uncertainty. Hence, to clarify further, the effect of a change of the stiffness of the different layers in the ranges obtained from DH tests in S6 has been investigated.

The analysis of the model geometry reveals that the retaining wall represents a boundary between the two halves of the system. It separates the geological formation in two domains having significant level difference of 8m. The two halves of the system, when considered separately, are characterized by different frequencies of vibration. The retaining wall located at the boundary between the two halves will portray the responses of both of them in a kind of superposition representing the interaction of the two portions of soil in the model. This phenomenon was also observed in [11]. In order to study the nature of the interaction, a decoupled problem is framed wherein the two domains of soils are separated to form two four-layer inclined strata without the wall. When subjected to ambient motion, these models would provide the fundamental frequencies of vibration of each of the domain, which would further help to understand their combined behavior when the acceleration response of the soil+wall system is studied in frequency domain. The comparison of the natural frequencies of the uphill soil domain (4.6 Hz and 10.8 Hz), the right hand soil domain (6.8 Hz and 13.8 Hz) and the combined soil+wall system (roughly 4.7 Hz, 6.7 Hz, 10.7 Hz and so on) justifies the superposition of the frequency responses of the two halves and supports the proposed hypothesis.

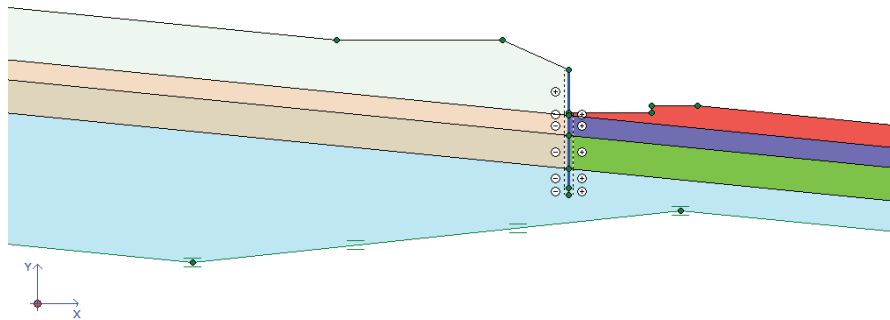


Fig. 3. Geometry and stratigraphy of the refined model (central section)

Moreover, it is also observed that the fundamental frequency of the spectra obtained from the response of the wall agrees with the fundamental frequency of the uphill soil domain, while the second higher frequency reasonably agrees with the fundamental frequency of the downhill soil domain. Similar results are observed with numerous other simulations. Hence, the response obtained from the wall can

be reasonable decoupled by controlling the soil parameters on both the sides of the wall. Hence, this insight provides a methodology by which an attempt has been made to refine the thickness of the lowermost stratum of soil on the uphill soil domain in order to achieve a reasonable agreement between the experimental and numerical results.

Based on the above studies, the modifications have been incorporated to frame a new geotechnical model. Numerous simulations have been carried out in order to arrive at the best possible solution, and the same is presented here. Table 3 provides the parameters of the newly developed model. Figure 3 depicts the geometry of the model. The analytical procedure carried out is identical as described for the preliminary model.

Table 3. Material parameters adopted in the refined model

Soil Layer	Material Type	E_{OL} (10^5 kPa)	E_{OR} (10^5 kPa)	ν	γ (kN/m ³)	H_L (m)	H_R (m)
A	LE	1.704	3.188	0.432	18.00	8	3
B	LE	2.930	4.086	0.426	19.03	3	3
C	LE	14.86	14.51	0.438	19.47	5	5
D	LE	26.49	26.49	0.433	19.98	20	4

The comparison of the experimental and numerical frequencies of vibration (Table 4) reveals a good agreement between the results, suggesting that keeping all the uncertainties in mind, the chosen model is one of the best representation of the stratigraphy in the nearby vicinity of the wall.

Table 4. Comparison between experimental and numerical results (refined model)

Mode	f_{exp} (Hz)	f_{FEM} (Hz)	Scatter (%)
I	3.68	3.60	-2.2
II	7.23	7.20	-0.4

Final remarks

The paper provides a detailed description of the numerical FE modeling of the flexible retaining wall built for the “Casa dello Studente” of the University of Molise, Campobasso, Italy. Borehole investigations have been used to identify the geotechnical profile of the site. A preliminary model has been thoroughly studied to identify the problems and uncertainties in different parameters associated with the numerical modeling. The problem of decoupling and superposition of responses from the two soil domains on the wall response has been successfully identified. It provided the insight and methodology to adjust and refine the model pa-

rameters in order to obtain a representative model of the behavior of the soil+wall system in operational conditions. However, further research and detailed investigation into the aspects related to the profile and depth of the bedrock are necessary and are carried out at present.

Acknowledgments

The present work is carried out within the activities of AT2 – LR 2 – Task 3 of the ReLuis-DPC Executive Project 2010-2013, rep. 823. Support of ReLuis Consortium is therefore gratefully acknowledged.

References

- [1] Doebling SW, Farrar CR, Prime MB, Shevitz DW (1996) Damage Identification and Health Monitoring of Structural and Mechanical Systems from Changes in their Vibration Characteristics: A Literature Review. Technical Report LA-13070-MS, UC-900, Los Alamos National Laboratory, New Mexico 87545, USA.
- [2] Link M, Weiland M (2009) Damage identification by multi-model updating in the modal and in the time domain. *Mechanical Systems and Signal Processing*, 23: 1734-1746, Special issue on Inverse problems in MSSP.
- [3] Fabbrocino G, Laorenza C, Rainieri C, Santucci de Magistris F (2009) Seismic monitoring of structural and geotechnical integrated systems. *Materials forum*, 33: 404-419.
- [4] Rainieri C, Dey A, Fabbrocino G, Santucci de Magistris F (2011) Sensor embedment, dynamic monitoring and model refinement for smart geotechnical structures. Proceedings of the First Middle East Conference on Smart Monitoring, Assessment and Rehabilitation of Civil Structures SMAR 2011, Dubai, UAE.
- [5] Brincker R, Zhang L, Andersen P (2000) Modal identification from ambient responses using frequency domain decomposition. Proceedings of the 18th SEM International Modal Analysis Conference, San Antonio, TX, USA.
- [6] Van Overschee P, De Moor B (1996) Subspace Identification for Linear Systems: Theory – Implementation – Applications. Kluwer Academic Publishers, Dordrecht, the Netherlands.
- [7] Peeters B (2000) System Identification and Damage Detection in Civil Engineering. Ph.D. Dissertation, Katholieke Universiteit Leuven, Leuven, Belgium.
- [8] Poncelet F, Kerschen G, Golinval JC, Verhelst D (2007) Output-only modal analysis using blind source separation techniques. *Mechanical Systems and Signal Processing*, 21: 2335-2358.
- [9] Dey A, Lanzano G, Rainieri C, Di Tullio M, Laorenza C, Santucci de Magistris F, Fabbrocino G (2011) A full scale instrumented retaining wall: interpretation of the measurements using numerical tools. Proceeding of the 5th International Conference on Earthquake Geotechnical Engineering, Santiago, Chile.
- [10] Brinkgreve RBJ (2002) Plaxis 2D version 8. A.A. Balkema Publisher, Lisse.
- [11] Visone C., Santucci de Magistris F. (2007). Some aspects of seismic design methods for flexible earth retaining structures. Workshop of ERTC12 - Evaluation Committee for the Application of EC8 Special Session XIV ECSMGE, Madrid, Patron Ed., Bologna.

Structural Health Monitoring of a Bridge Model Using ARX Models

Thomas Terrell¹, Mustafa Gul², F. Necati Catbas³

Department of Civil, Environmental and Construction Engineering
University of Central Florida, Orlando, Engineering II –211. Orlando, FL 32816

¹ tomkterrell@knights.ucf.edu

² mgul@mail.ucf.edu

³ catbas@mail.ucf.edu

NOMENCLATURE

$y(t)$: Output of the system	$B(q)$: Polynomials in the delay operator q^{-1}
$\eta(t)$: Noise-free input of the system	$C(q)$: Polynomials in the delay operator q^{-1}
$w(t)$: Disturbance term of the model	q^{-1} : Delay operator
$x(t)$: Output of the system	$y(t)$: Output of the ARMAX model
$f(t)$: Excitation force on the system	$u(t)$: Input to the ARMAX model
$A(q)$: Polynomials in the delay operator q^{-1}	$e(t)$: Error term in the ARMAX model

ABSTRACT

In this paper, studies for structural condition assessment of the movable bridge using the Structural Health Monitoring (SHM) data collected from a laboratory based 4-span bridge-type steel structure will be presented. For this purpose, the authors expand on a time series analysis method using ARX (Auto-Regressive with eXogeneous input) models for damage detection with free response vibration data. A series of ARX models were developed for reference locations using adjacent location acceleration values as inputs. After creating the baseline ARX models from the undamaged structure, they were used with the data from one of the simulated damage scenarios. The error term of these damaged models, expressed as a proportion of the fit ratios was used as the damage sensitivity feature. Use of a normalized distance factor for the damage features was also shown to be highly effective at visually presenting the results. This ARX based time series analysis method was shown to be effective for damage detection, locating, and assessment of the relative damage severity for this relatively complex laboratory structure.

INTRODUCTION

Every civil infrastructure project is designed and built with a specific design life. As the end of this design life is approached, or surpassed in some instances, evaluation and assessment of the structural condition becomes increasingly more important for safety and serviceability. Structural Health Monitoring (SHM), the research area focusing on condition assessment of different structures, offers a proactive approach to monitoring the state of our infrastructure. Damage detection is one of the most critical components of Structural Health Monitoring (SHM), and therefore, many different approaches have been developed to extract damage sensitive features (or damage features) from SHM data. Time series analysis methods using AR (Auto- Regressive), ARX (Auto-Regressive with eXogeneous input), and ARMA (Auto-Regressive Moving Average) models have been employed by various researchers and offer the distinct advantage of requiring only data from the undamaged structure during the training phase [1-4]. In a prior study, the authors proposed a time series methodology implementing ARX models. The proposed methodology developed a series of ARX models for reference locations using adjacent location acceleration values as inputs, to model the free response of different sensor clusters for damage detection [5]. In this paper, the methodology is examined on a more complex structure containing structural decking, where the systems' degrees of freedom are not as clearly defined.

OBJECTIVE AND SCOPE

The objective of this study is to examine the effectiveness of a previously developed time series analysis methodology at identifying and locating damage on a structure that is connected by decking, thus having different node-node connections than previously tested. This methodology can then be further expanded and applied on a comprehensive SHM system, implemented by the authors, on a movable bridge in Florida, the Sunrise Boulevard Bridge. The content of this paper will first examine the theoretical background of time series modeling and its relation to structural dynamics. Next, the experimental setup and ARX model development will be described. The experimental results from impact testing will then be presented in two different formats, demonstrating the effectiveness of the method at damage detection and localization.

THEORETICAL BACKGROUND

Generally, the methods which exist for damage detection using Structural Health Monitoring (SHM) data fall into two broad categories: 1) Parametric methods and 2) Non-parametric Methods. Parametric methods generally assume that a model representing the system is known; the *a priori* model. Non-parametric methods, unlike parametric methods, do not require knowledge of the underlying relations between damages and changes of structural parameters; in other words, a model of the system does not need to be known. In these methods, a combination of time series modeling and statistical pattern recognition is often used, requiring only data from the undamaged structure to train the model. In this manner, the model is constructed for a healthy/baseline condition and when data from the damaged structure is input into the model the outputs are likely classified as outliers. This can be described as a "black box" model approach, where the systems' input is related to the systems' output through a relationship that is unique to a specific condition of the structure. Time series modeling is a fundamental concept of this method and a brief discussion is presented below.

Time Series Modeling

Time series modeling is the statistical modeling of a sequence of data points that are measured at successive times spaced at uniform time intervals. Time series modeling makes it possible to model a system that cannot be easily modeled based on physical insights. A linear, time discrete, model of the system can be constructed which represents the relationship of the input, output and any error terms and is presented in Eqn. (1) (Ljung 1999) [6].

$$y(t) = \eta(t) + w(t) \quad (1)$$

where, $y(t)$ is the output of the model, $\eta(t)$ is the noise-free input of the model, and $w(t)$ is the disturbance term.

When this general form of the equation is further described through the use of a shift operator q , a model known as the Box-Jenkins model is derived. When the properties of the error/disturbance signals are not modeled, and upon further simplification, a model known as the ARMAX (Auto-Regressive Moving Average with eXogenous input) model is developed and described by Eqn. (2). $A(q)y(t)$ represents an AutoRegression, $C(q)e(t)$ a Moving average of noise, and $B(q)u(t)$ represents an external input

$$A(q)y(t) = B(q)u(t) + C(q)e(t) \quad (2)$$

Here, $y(t)$ is the output, $u(t)$ is the noise-free input, and $e(t)$ is the error term. The expanded form of this equation is given by Eqn. (3).

$$y(t) + a_1 y(t-1) + \dots + a_{n_a} y(t-n_a) = b_1 u(t-1) + \dots + b_{n_b} u(t-n_b) + e(t) + c_1 e(t-1) + \dots + c_{n_c} e(t-n_c) \quad (3)$$

Where, a_i , b_i , and d_i are the unknown model parameters, and the model orders are given by n_a , n_b , and n_d . By adjusting the model orders, different time series models are defined. The ARX model, which is used in this study, is obtained by setting n_c equal to zero. The ARX model structure is shown in Eqn. (4).

$$A(q)y(t) = B(q)u(t) + e(t) \quad (4)$$

Time Series Modeling for Structural Dynamics

The core premise of the methodology used in this study is that output of a degree of freedom (DOF) for a linear dynamic system is related to the outputs of the neighboring DOFs. In other words, the neighboring DOFs outputs can be used as inputs in the development of a time series model. This concept is explained by examining the equation of motion for an N DOF linear dynamic system in matrix form, as in Eqn. (5) (time, t is omitted).

$$\begin{bmatrix} m_{11} & \cdots & m_{1N} \\ \vdots & \ddots & \vdots \\ m_{N1} & \cdots & m_{NN} \end{bmatrix} \begin{Bmatrix} \ddot{x}_1 \\ \vdots \\ \ddot{x}_N \end{Bmatrix} + \begin{bmatrix} c_{11} & \cdots & c_{1N} \\ \vdots & \ddots & \vdots \\ c_{N1} & \cdots & c_{NN} \end{bmatrix} \begin{Bmatrix} \dot{x}_1 \\ \vdots \\ \dot{x}_N \end{Bmatrix} + \begin{bmatrix} k_{11} & \cdots & k_{1N} \\ \vdots & \ddots & \vdots \\ k_{N1} & \cdots & k_{NN} \end{bmatrix} \begin{Bmatrix} x_1 \\ \vdots \\ x_N \end{Bmatrix} = \begin{Bmatrix} f_1 \\ \vdots \\ f_N \end{Bmatrix} \quad (5)$$

Where $[M]$ is the mass matrix, $[c]$ is the damping matrix, and $[k]$ is the stiffness matrix. The vectors $\ddot{x}(t)$, $\dot{x}(t)$, $x(t)$, and $f(t)$ are acceleration, velocity, displacement, and the external forcing function respectively. If the first row of Eqn. (5) is expressed separately, the force term eliminated for free response case, and then rearranged, as in Equations. 6-7, it is shown that the acceleration output of the 1st DOF is expressed by the excitation force on the 1st DOF, physical parameters of the structure, and the outputs of the other DOFs.

$$[m_{11}\ddot{x}_1 \quad \cdots \quad m_{1N}\ddot{x}_N] + [c_{11}\dot{x}_1 \quad \cdots \quad c_{1N}\dot{x}_N] + [k_{11}x_1 \quad \cdots \quad k_{1N}x_N] = f_1 \quad (6)$$

$$\ddot{x}_1 = \frac{(m_{12}\ddot{x}_2 \quad \cdots \quad m_{1N}\ddot{x}_N) + (c_{11}\dot{x}_1 \quad \cdots \quad c_{1N}\dot{x}_N) + (k_{11}x_1 \quad \cdots \quad k_{1N}x_N)}{m_{11}} \quad (7)$$

Therefore, each row of Eqn. (5) can be thought of as a sensor cluster, composed of a reference DOF and its surrounding DOFs. Based on these concepts, if different ARX models are created for different clusters of sensors, then damage features can be selected from these models to detect damage. Therefore, in the ARX model expressed in Eqn. (2), the $y(t)$ term is the acceleration response of the reference channel of a sensor cluster, $u(t)$ is the acceleration responses of all the DOFs in the same cluster, and $e(t)$ is the error term.

Damage Feature (DF)

As discussed earlier, numerous approaches exist for extracting damage features from SHM data using a time series analysis. The damage feature(s) itself, however, also varies. In Gul (2009) [7] two different types of damage features (DFs) were extracted from the ARX models. The first approach was based on a direct comparison of the "B" term coefficients of the ARX model. While this method was demonstrated to be successful at giving exact information about the existence, location, and severity of the damage for simple models, this approach was not effective for complex models or with addition of data noise. The second approach used the difference in the ARX model fit ratios, Eqn. (8), as the DF (Gul and Catbas 2009) [5].

$$\text{Damage Feature (DF)} = \frac{\text{FR}_{\text{Healthy}} - \text{FR}_{\text{Damaged}}}{\text{FR}_{\text{Healthy}}} \times 100 \quad (8)$$

Where the fit ratio is expressed by Equation, 9.

$$\text{Fit Ratio (FR)} = \left(1 - \frac{\|\{y\} - \{\hat{y}\}\|}{\|\{y\} - \{\bar{y}\}\|} \right) \times 100 \quad (9)$$

$\{y\}$ is the measured output, $\{\hat{y}\}$ is the predicted output, $\{\bar{y}\}$ is the mean of $\{y\}$ and $\|\{y\} - \{\hat{y}\}\|$ is the norm of $\{y\} - \{\hat{y}\}$.

EXPERIMENTAL STUDIES

Test Set-Up

The laboratory setup used in this study was a four span bridge-type structure (Figure 1). Although not a scaled down bridge model, its responses are representative of typical values for medium-span bridges. It has two 120 cm approach end spans and two 304.8 cm main inner spans. Two HSS 25x25x3 girders separated 60.96 cm from each other support a 3.18 mm thick, 120 cm wide steel deck. The supports can easily be changed to roller, pin, or fixed boundary conditions, and the girder deck connection can be adjusted at different locations to modify the stiffness of the structure. The main spans are instrumented with various sensors, shown in Figure 2.



Figure 1. Experimental Setup

Instrumentation consisted of a total of sixteen PCB accelerometers, two dynamic tiltmeters, and 20 foil type strain gages. The data acquisition systems were controlled by a personal computer. The present study only utilizes the acceleration data, which was collected with a sampling frequency of 320 Hz using a VXI system from Agilent Technologies. These sensors provide a measurement range of ± 50 g and a broadband resolution of 350 μg .

Experimental Method

An impact hammer was used to excite the structure during a series of trials for each damage scenario. Two impact data sets were collected for all 16 data channels at four different locations, shown in Figure 2, totaling 8 data sets for each sensor.

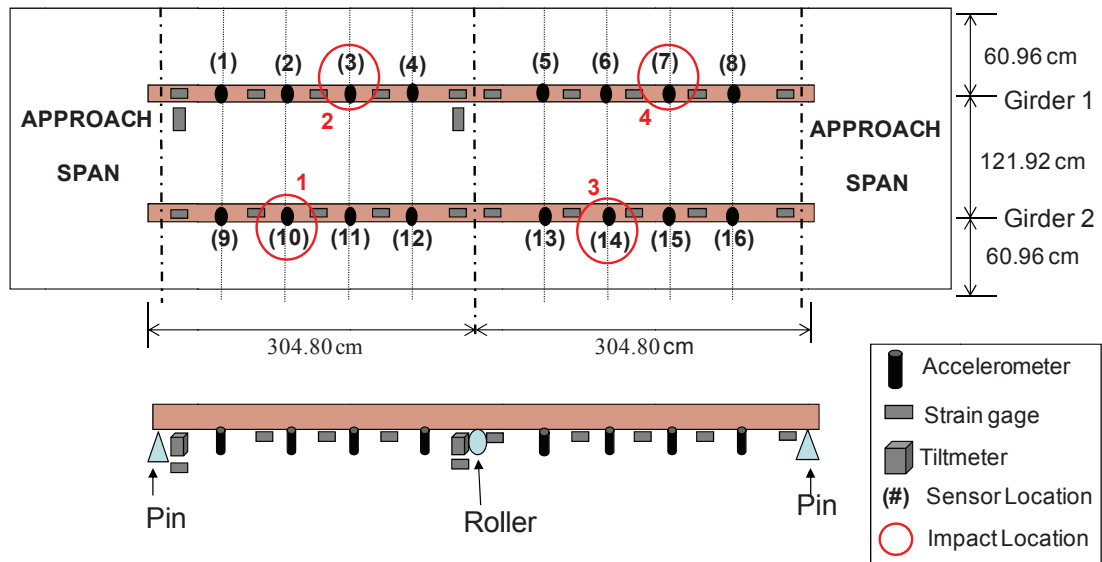


Figure 2. Experimental Setup with Sensor Locations

Damage Scenarios

Five separate damage cases were implemented on the laboratory setup and are shown in Figure 3. Based on feedback from Department of Transportation (DOT) engineers, these damage cases represent some of the most common damages affecting bridge performance. Cases 1,2,4, and 5 involve changes in the boundary conditions, and therefore can be considered global damage. Cases 1 and 2 modify the boundary conditions from pin and roller connections to fixed support. Case 4 switched the rollers at the middle support to elastomeric pads. Case 5 simulated support settlement by shortening the middle support by 1 inch. Case 3 simulate localized damage with loss of connectivity between composite sections. In case 3, a total of eight (8) bolts were loosened (4 each) at two girder-deck connections.

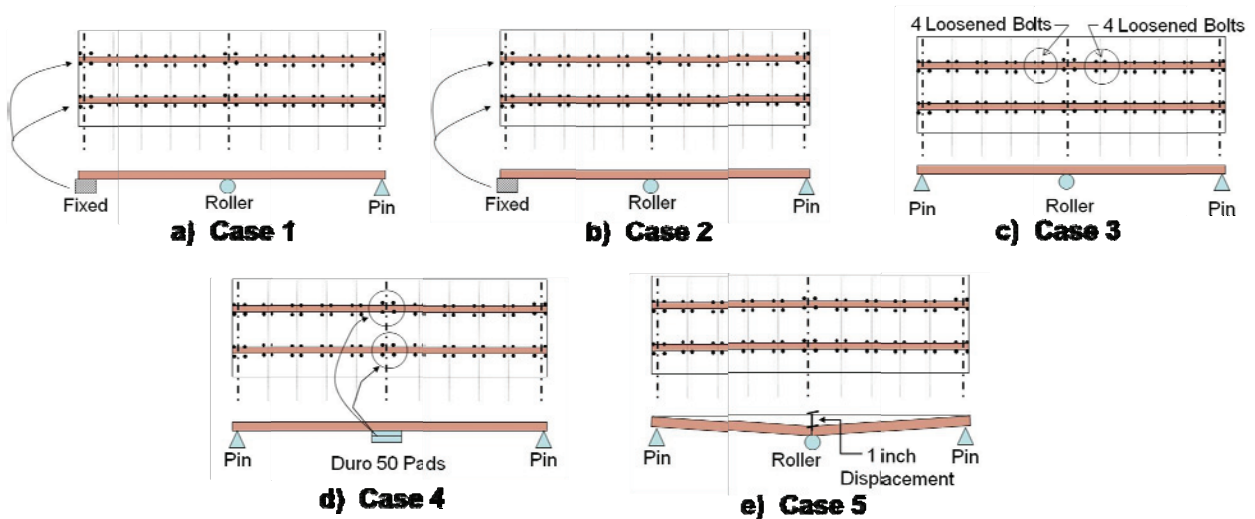


Figure 3. Damage Cases

DAMAGE DETECTION RESULT BASED ON ARX MODELS

Prior to generating the ARX models, each damage simulation was conducted and the DAQ collected the raw acceleration data from each impact trial. Two separate baseline cases with 8 trials each were executed for

comparison purposes. It is necessary that the ARX models be generated based on only the free response of the structure (not the impact event itself). For this reason, the data is windowed to model only the free response. A total of 16 different sensor clusters were created, one for each reference channel.

The model orders of the ARX models were selected as $n_a=1$ and $n_b=20$. These model orders were selected after examining the fit ratios for the baseline (undamaged) case and selecting model orders that generated fit ratios of approximately 95. The fit ratio reveals how good the model is at predicting the actual output. Or in other words, when the reference channel acceleration values are estimated from the adjacent channel accelerations, how close are they to the actual reference channel acceleration values.

ANALYSIS RESULTS

In this paper, only the impact results of the first damage scenario will be presented. Prior to damage identification with noisy data, however, a threshold for the DF must be established to distinguish changes in the DF due to damage from changes as a result of noise in the data. To determine the threshold level, the DFs of two sets of undamaged, baseline, data are found. The DFs resulting from the one baseline compared to another baseline represent the amount of noise in the system. The DFs for the second Baseline case are shown in .

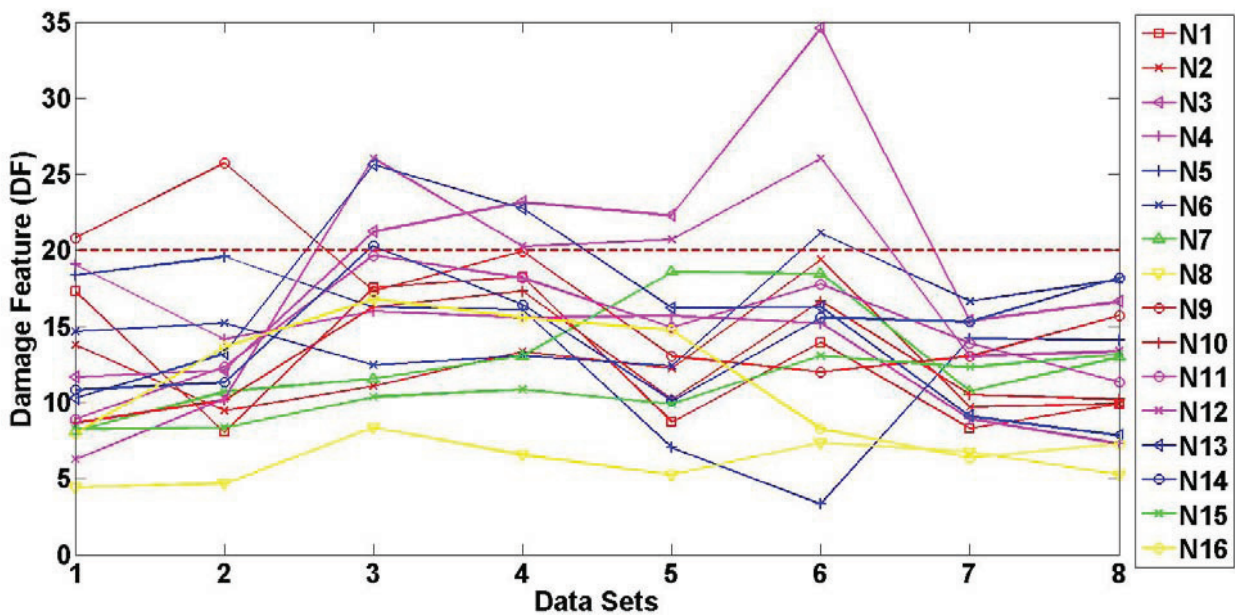


Figure 4. DFs for Baseline Case 2

From this plot and based on the performance of the ARX models a DF of 20 was selected as a threshold to identify damage. The damage features for Damage Case 1 were found using Eqn. (8) and can be plotted for each trial as shown in Figure 5 below.

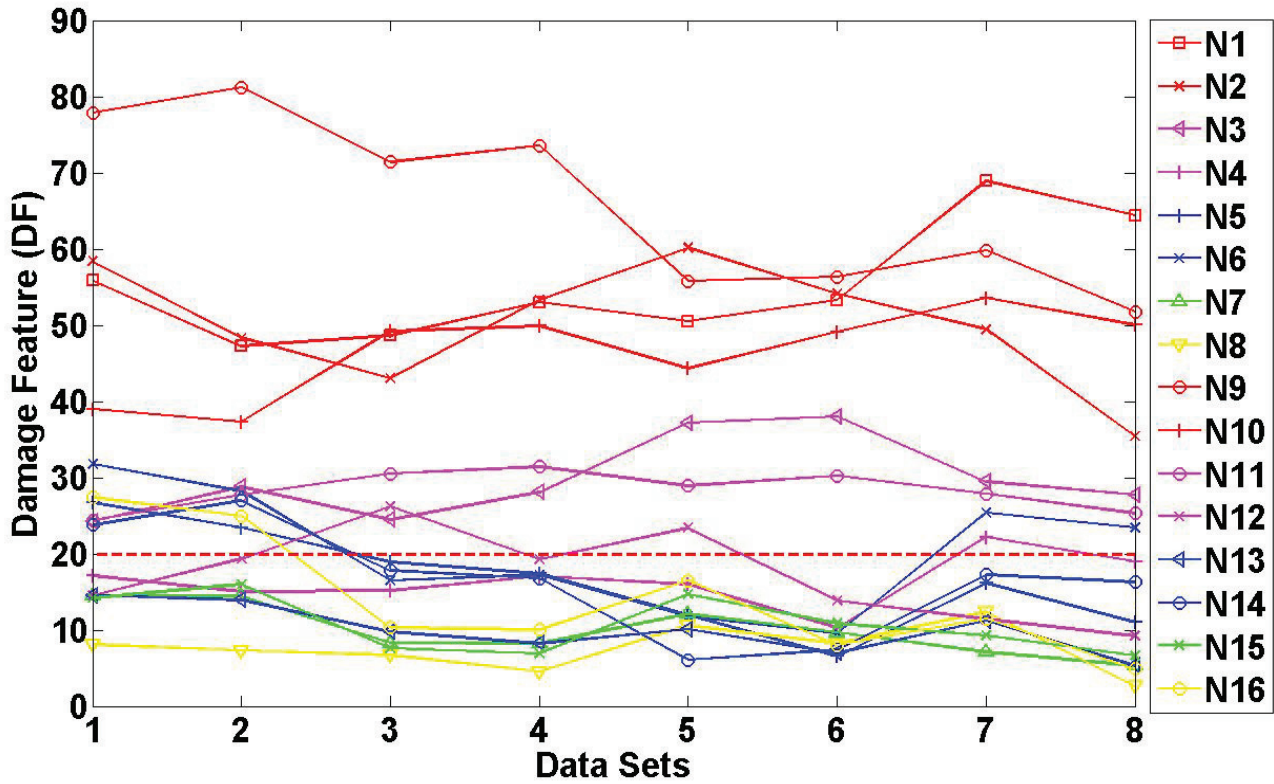


Figure 5. DFs for Damage Case 1 (Rusted Left Support)

In the plot, each node has been color ranked based on its proximity to the damage location, from closest to farthest (Red, Magenta, Blue, Green, Yellow). Based on this information, it can be seen from the figure that the DFs of N1,N2,N9,and N10 are noticeably higher than the other nodes. These 4 nodes were located closest to the fixed support, or damage location, and therefore were plotted in Red. As the node location moves further away from damage location the effects of damage would be expected to decrease. This is shown in the figure as the color ranking of each node corresponds well with the DF value.

To better visually locate damage, Zaurin (2009) [8] used a Normalized Distance expression. In this study, the normalized distance between DFs from a baseline case and DFs from an undamaged case will be used, as displayed in Eqn. (8).

$$\bar{N}_d = \frac{\left| \frac{\sum_{i=1}^{n_o} DF_{i(t=t_1)}}{n_o} - \frac{\sum_{i=1}^n DF_{i(t=t_0)}}{n} \right|}{\frac{\sum_{i=1}^n DF_{i(t=t_0)}}{n}} \left(\frac{n_o}{n} \right) \tag{10}$$

First, the mean of the DF values for the set corresponding to $t_0 < t < t_1$ and the mean of all outliers for the set $t_1 < t < t_2$ are calculated. If all of the calculated DFs from the set ($t_1 < t < t_2$) are outliers, the distance between their mean divided by the mean of the DF set for $t_0 < t < t_1$ can be considered as the normalized change, which can be denoted as N_d . Therefore, N_d is a normalized indicator between DFs obtained at two different times ($t_0 < t < t_1$ and $t_1 < t < t_2$) during the monitoring of the structure. Using this method the location of damage origination is more clearly seen then from simply examining the DF trend for each sensor. Figure 6 shows the normalized distance of the Damage Features for each sensor location in Damage Case 1: Rusted Rollers (First Support).

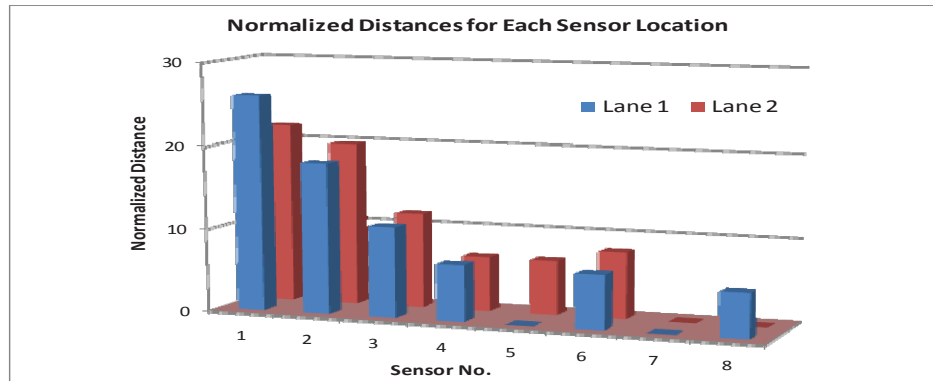


Figure 6. Damage Identification Damage Case 1: Rusted Left Support

Inspection of Figure 6 shows that the sensors nearest to the fixed support location have the largest normalized distances, indicating the damage location. This normalized distance method provides a very visual representation of the damage sensitive features. Therefore, it can be concluded that this methodology works adequately at detection and localization of damage in this experiment.

CONCLUDING REMARKS

In this study, a time series analysis methodology using ARX models for damage detection using free vibration data was expanded upon. Experimental data was collected for a four span bridge-type steel structure under simulated damage scenarios, which are representative of commonly found damage on movable bridges. The free vibration acceleration data for each sensor cluster was used to develop ARX models. A ratio describing the fit ratios, called the Damage Feature (DF), was used as the damage indicating feature. The results obtained from the impact tests for damage case 1 are presented. It was then demonstrated that damage could be identified and located using this approach, based on either the initial DF plot or another parameter called the normalized distance.

REFERENCES

1. Y.Lu,F.Gao, A novel time-domain auto-regressive model for structural damage diagnosis. *Journal of Sound and Vibration* 283 (2005)1031–1049.
2. Omenzetter, P. and Brownjohn, J. M. (2006). "Application of Time Series Analysis for Bridge Monitoring." *Smart Material and Structures*, Vol. 15), pp. 129-138.
3. H.Sohn, C.R.Farrar, N.F.Hunter, K.Worden, Structural health monitoring using statistical pattern recognition techniques, *Journal of Dynamic Systems, Measurement, and Control—Transactions of the ASME* 123 (2001)706–711.
4. K.K.Nair, A.S.Kiremidjian, Time series based structural damage detection algorithm using Gaussian mixtures modeling, *Journal of Dynamic Systems, Measurement, and Control—Transactions of the ASME* 129 (2007)285–293.
5. Gul, M., and Catbas, F. N. (2010). "Structural Health Monitoring and Damage Assessment using a Novel Time Series Analysis Methodology with Sensor Clustering." *Journal of Sound and Vibration*, (In Press).
6. Ljung, L. (1999). "System Identification: Theory for the User". Upper Saddle River, NJ, Prentice-Hall.
7. Gul, M., Investigation of Damage Detection Methodologies for Structural Health Monitoring, in *Civil, Construction and Environmental Engineering*. 2009,University of Central Florida: Orlando.
8. Zaurin, R. (2009). "Structural Health Monitoring with Emphasis on Computer Vision, Damage Indices and Statistical Analysis." Ph.D., University of Central Florida, Orlando, FL

Structural Health Monitoring and Evaluating Structural Performance of a Stadium

H. Ozerk Sazak¹, F. Necati Catbas^{1*}, Mustafa Gul^{1*}

¹Department of Civil, Environmental and Construction Engineering
University of Central Florida, Orlando, FL
[*catbas@mail.ucf.edu](mailto:catbas@mail.ucf.edu) (contact person)

ABSTRACT

Light and rapid constructions as well as considerations such as improved line of sight and increased capacity for modern stadium structures make them vulnerable for vibration serviceability problems. Especially when the individuals in a crowd are involved in some sort of a coordinated motion, this type of loading creates the highest potential for increased levels of vibration. In order to understand the causes of high vibration levels and serviceability and safety limits, detailed Finite Element Models (FEM) should be used in addition to the field studies. In this study, development of the FEM of a stadium is presented to investigate the structural performance of the stadium. After constructing the FEM, it is validated using the results of the modal analysis with human induced vibration data. In addition, laboratory studies are conducted to estimate the dynamic loading on the stadium

INTRODUCTION

Sport events are followed by many people all around the world and have become a major industry. Especially for popular games such as soccer, basketball and football, the number of fans is rising each day. Improvements for light and rapid constructions and considerations such as improving line of sight and increasing the capacity for modern stadium structures create possibility for vibration serviceability problems. Especially when the individuals in a crowd are involved in some sort of coordinated motion, this type of loading creates the most potential for high levels of vibration. As dynamic effect of people gain more importance, the incidence of problems with displacements and vibration serviceability started to increase. Structural Health Monitoring (SHM) techniques with methods of data evaluation can be implemented to understand the performance of a stadium structure during games such as football. In order to understand the causes of human induced vibration and vibration levels, occurring service and safety levels, SHM becomes important especially when repair or improvements on the structure are considered for the structure.

Pernica (1983) conducted one of the earliest stadium monitoring applications during a 3 hour rock concert to see how the audience response affects the dynamic behavior of a stand area having a fundamental frequency below 5 Hz. Reynolds and Pavic (2002) conducted modal testing of a sports stadium grandstand at a soccer stadium in the UK. Entire modal test and preliminary estimation of the modal properties of the structure were presented in the paper. Also results from the modal testing were compared with the results of a finite element analysis. At the end discrepancies between the FE model and the modal test results were highlighted. Reynolds and Pavic (2006) published another paper for modal testing and in-service monitoring of a large contemporary cantilever grandstand in the United Kingdom. Modal parameters during the stadium was empty were also investigated and in service monitoring results were described accordingly. Yao et al. (2006) described the direct measurement of human induced forces due to jumping on a moving force platform. A unique test rig was developed to permit a person to jump on an idealized single degree of freedom system with variable natural frequency and mass.

Analysis results from jumping in the region of half the natural frequency and of the natural frequency were presented. Also, the effect of contact ratio, which is the ratio of time in contact with the platform/period of jumping time was determined in the study. Salyards and Firman (2010) investigated the ability to estimate dynamic loading effect in more reasonable obtainable acceleration response of the structure during the events. They used experimental testing to investigate the accuracy and sensitivity of load estimation method for consideration when applying this method to large scale structures. During these experiments simple floor structure was subjected to dynamic forces generated by small groups and result were presented accordingly.

OBJECTIVE AND SCOPE

Previous studies about the effects of excessive vibration to human comfort and the dynamic characteristics of a football stadium have already been presented by the authors (Catbas et al., 2010). An investigation of a football stadium for human-structure interaction was conducted and results from crowd induced vibration monitoring for human comfort analysis and simulation of crowd dynamic excitation were discussed. The objective of this paper is to analyze the vibration effects by combining FE model studies with laboratory tests and to investigate the dynamic characteristics of a football stadium. In this study, FE model results by using the experimental analysis results are presented in the context of time and frequency domain. Laboratory studies are also performed on the basis of obtaining a better model for spectators jumping in the stadium where different experiments were conducted in the laboratory. Finally, simulations with dynamic loading and comparison of FEM dynamic loading results with field data results are discussed.

STADIUM AND INSTRUMENTATION

The stadium monitored in this research was completed in 2007 and the stadium was opened in the same year. The stadium is a steel frame structure sitting over 25 acres and has approximately 45,000 seating capacity. The sensors are installed at the student sections. The reason to choose student sections to monitor was the expectation of higher vibration levels than other sections of the stadium. Students mostly get more excited during the games and also the university band was located close to the monitored section, which created another reason for the students become more excited. Monitored section was one of the corners of the stadium; seating sections in that part are narrowing down frame sections. Rear ends of the monitored section have 60 ft opening and about 55 ft height while the front ends have about 15 ft opening and 7.5 ft height (Figure 1).

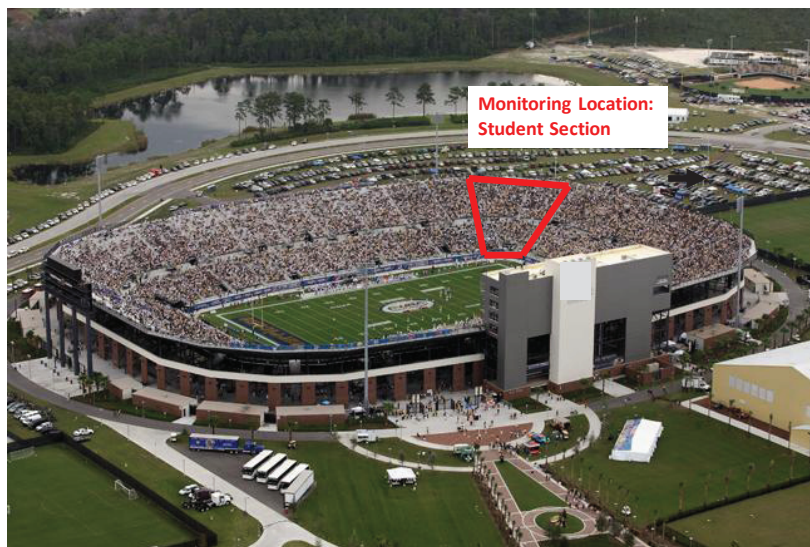


Figure 1: The section under investigation

The objective of choosing the locations of the accelerometers was to monitor different element types of the structure such as primary elements (main girders), secondary elements (floor girders) and tertiary elements (stringers). To identify the characteristic of these elements in investigated sections, twelve accelerometers were

placed in vertical, lateral, and longitudinal directions to measure the vibration levels in three different directions. Mid-points of the beams and stingers were chosen for the sake of maximum vibration. Eight of these accelerometers were in the upper section and the remaining four accelerometers were in the lower section.

Because of low frequency vibration of civil structures, high sensitivity PCB 393C accelerometers were considered appropriate to monitor the stadium. These accelerometers were designed to collect vibration measurements at low frequencies with a usable frequency range of 0.025 to 800 Hz, sensitivity of 1000 mV/g and range up to 2.5 g peak. The accelerometers were connected to the data acquisition system with insulated cables running over the frames. For data collection, digital data acquisition was performed using VXI-Agilent Technologies and PCB data conditioner, which had sixteen input channels in each system. Sampling rate was defined as 100 Hz because in stadium structures, frequency range of interest was mainly around 0-30 Hz. Data was collected before, during and after the game to obtain a general response of the stadium in each period. For the data collection durations, ten minute intervals were defined and approximately twenty five data sets were collected in each game.

FE MODEL DEVELOPMENT

The development of the finite element model of the stadium was performed to represent the real structure as close as possible that will help to simulate the dynamic effects due jumping of the spectators in the stadium. The first item that needed to be completed was to go over the blue prints and also pictures of the stadium. Next, CAD model was developed using lines to represent the different frame sections. The lines were then placed in different layers to represent the corresponding frame section. Once the CAD model was completed, it was imported into the FE analysis software.

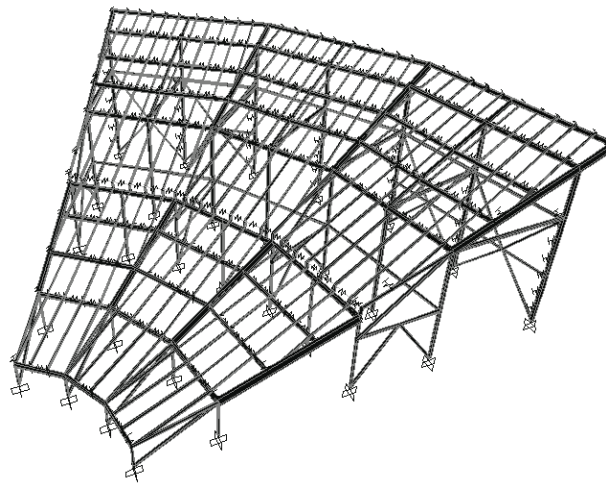


Figure 2: Developed FE model

A FE model having 365 frame elements, 609 nodes and 379 links was created. After properties were assigned to the frame members, a systematic approach was followed for the model check. First, the extruded views of the FE model elements were visually inspected for the orientation of the members and verified with field inspection. Next, displacements of the elements were checked if they were in a reasonable range. To accomplish this, one of the beams used in the model was taken out and another model was created with boundary conditions with pin and fixed connections at both ends and displacements were checked under live load. A live load of 100 psf was applied as defined in Florida Building Code (2004), after multiplied with the tributary area where the beam was taking the load from. Subsequently, the beam displacement from the model created for the investigated section of the stadium was also obtained and the results ([Table 1](#)) showed that the displacements were between the two boundary condition results.

Table 1: Displacement for different boundary conditions

Boundary Conditions	Beam Deformation Check Under 100 psf Live Load
Fix-Fix	0.45 in
Pin-Pin	2.34 in
Stadium FE Model	1.72 in

Final check was modal analysis check, where the FE model was compared with the results obtained from experimental modal analysis results. Experimental modal analysis was carried out by analyzing different data sets from different games and different years. Using output only data sets, a complex mode indicator function (CMIF) based system identification methodology was used in conjunction with the random decrement (RD) method to analyze experimental data sets for modal parameter identification. CMIF used the unscaled multiple-input multiple-output data sets generated using the RD method for parameter identification (Gul and Catbas, 2008). When experimental data sets were analyzed, it was seen that each data set showed similar dynamic characteristic and the first mode of the structure, which was a vertical mode, can be identified in most data sets. Three different data sets from three years were analyzed to obtain the distribution first mode of the structure. Due to spectator load, which means an extra mass for the structure, it was seen that the first mode varied between 2.1-3 Hz depending on the weight of spectators over the investigated section with a damping ratio of 4-5%. After the distribution was analyzed with probability density function and logarithmic curve fitting, it was more realistic to assume the stadium's first mode around 2.45 Hz (Figure 3).

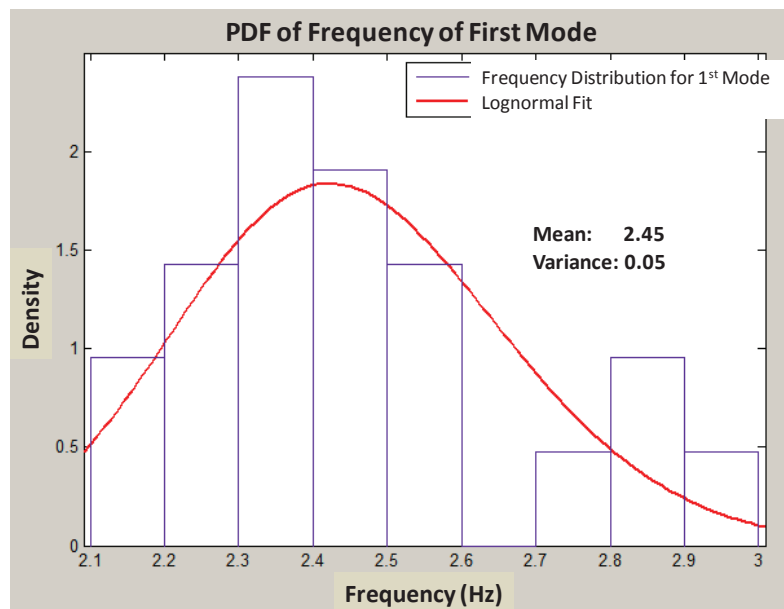


Figure 3: Frequency distribution for first mode

After experimental data sets were analyzed and modal frequencies were obtained, they were used for validation of the FE model. When frequencies from the FE and experimental data analysis were compared, it was seen that they were in an acceptable range. After last calibration steps due to boundary conditions were applied, for the sake of verification, modal assurance criterion (MAC) values were checked. MAC values had extra importance for modal assurance because the investigated section was not uniform or custom elevated structure and the FE model could not be fully calibrated. Results gave a high number of modes in 20 Hz range. For that reason, MAC values checked according to data analysis result of field data and 0.94 MAC value obtained for the first mode between first mode frequencies of experimental data and finite element model. Difference in first mode frequencies of experimental data and finite element model was 6%, which was an acceptable difference. Second

mode also had high MAC value and small differences in modal frequencies. When transversal and longitudinal motions took place more in movement of structure, MAC values started to decrease. It should also be mentioned that some of the MAC values between experiment and FE model are low. One reason for this may be the low spatial resolution of the sensor grid especially for lateral directions. As vertical motion got more dominant, as in sixth and seventh mode, MAC values started to increase again. Since the forcing function, which was spectator load, was vertical, the important modes of the structure were the vertical modes, the first two modes. When mode shapes were investigated in finite element model similar mode shapes were identified. The results for frequencies were not exactly same however; the difference was deemed acceptable (Table 2).

Table 2: Modal Analysis Results vs. FE Model Results

	Motion Type	Experimental Modal Analysis	Finite Element Model Freq.	% Difference	MAC
1st mode	Vert.	2.45 Hz	2.59 Hz	6	0.94
2nd mode	Vert.	4.89 Hz	4.12 Hz	15	0.98
3rd mode	Vert. & Trans.	7.49 Hz	8.06 Hz	7	0.56
4th mode	Trans.	12.73 Hz	10.85 Hz	14	0.48
5th mode	Vert. & Trans.	12.92 Hz	11.66 Hz	9	0.62
6th mode	Vert., Trans. & Long.	13.08 Hz	14.85 Hz	13	0.93
7th mode	Vert., Trans. & Long.	14.61 Hz	16.28 Hz	11	0.79

LABORATORY STUDIES

There have been several studies for reliable and practical descriptions of the loading coming from people jumping by measuring the interface forces between the floor and people's feet. Typical measured continuous force time-history functions in the vertical direction were assumed to simulate single peak pulses. There have been a number of investigators focusing on this subject. Bachmann and Ammann (1987) assumed that series of identical half-sine wave pulses may be represented by measured jumping force pulses. However, measured data could not fit the symmetric half-sine function. It was suggested that for dynamic analysis such a set of periodically appearing half-sine pulses can be presented more efficiently if expressed in terms of Fourier series with the fundamental harmonic, having a frequency identical to the jumping rate (Ji and Ellis, 1994; Bachmann et al., 1995). However even the sum of the six Fourier harmonics, which was the maximum number reported in the literature, could not match adequately enough the original half-sine forcing function for all contact times.

To obtain a better model for spectators jumping in the stadium, a small scale experiment was conducted in the laboratory. Researchers were made to jump on a beam in groups of one, two or three people while the popular song "Zombie Nation" was played at the same time. The aim of this study was to measure force difference between the persons' standing position and jumping with a song, which means with a specific frequency, and later to obtain a factor by dividing the effect of jumping to the normal body weight.

The beam used during jumping experiments was a 4 feet C-channel type beam (Figure 4). It was instrumented with four load cells and three accelerometers. Transducer Techniques load cells having a capacity of 5000 lbs each were placed under the corners of the C-type beam. However, flange thickness of the beam was so small that 4x4 square thin plates were welded to the corners of the beam to provide full contact between the beam and the load cells. For accelerometer selection, since the girder was expected to have higher frequency range, first, a simple frame model was created with SAP2000 and first mode frequency obtained from the software. Later, obtaining the first mode frequency around 80 Hz, PCB 603C01 type of accelerometer was chosen for the test. The accelerometer has a frequency range of 0.5 to 10k Hz, a sensitivity of 100 mV/g and a measurement range of 50 g. Three accelerometers were placed under the girder, one in the middle and the other two arbitrarily to get the maximum vibration and many modes of structure. Data acquisition was performed by using National Instruments: NI-SCXI 1001 chassis for signal conditioning, NI-SCXI1520 and NI-SCXI 1314 for strain gage input and NI-SCXI 1531 for accelerometer input. Sampling rate was defined as 100 Hz for load cells and 2048 Hz for

accelerometers. Data sets were collected for about 40-45 seconds each, where only about 25-30 seconds was jumping.

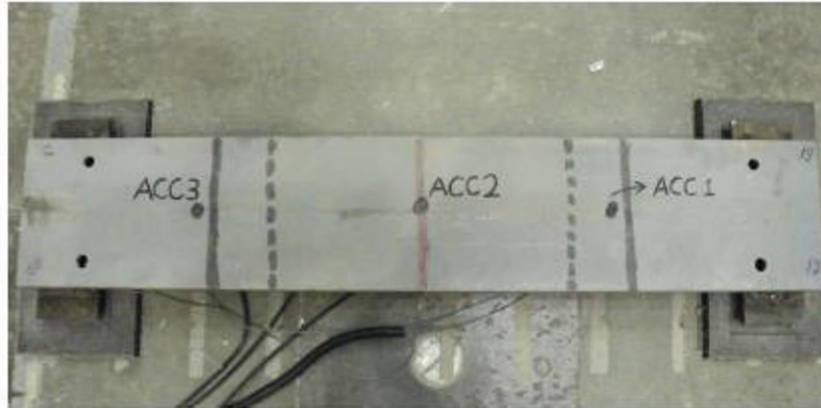


Figure 4: Beam used for lab studies and instrumentation

The experiment was conducted with three different persons in different combinations, and data sets were analyzed accordingly. Before obtaining the jumping load factor results, acceleration data sets and force data sets were checked in frequency domain analysis for resonance effect. The song played during the experiment “Zombie-Nation” had a frequency of 2.37 Hz, (Salyards and Firman, 2010) so it was expected the jumping frequency would have a close value. When frequencies of the forcing functions were analyzed, it was observed that frequency of the jumping varied in a range of 2.16 Hz to 2.41 Hz and the flexible range was due to the imperfection of the human response to the song. On the other hand, the frequency of the beam used during the experiments was around 80 Hz. That result showed that jumping frequency was away from the frequency of the beam and the results were not affected by resonance. Damping of the beam was also calculated. The stadium structure damping was defined as 4-5%, and to use the same jumping factors obtained in laboratory tests, beam and stadium structure should have close damping values.

The main objective of laboratory jumping tests was to create a jumping model that can simulate the jumping of the spectators during the games. To create the model, data from the load cells were normalized and applied to the FE model as a time-history function. In order to verify the validity of the time-history application, acceleration data collected from experiments were compared with the FE model acceleration results. Loading was applied in vertical direction as the people’s self weight obtained from experiments. However, data sets were collected with high sampling rates in both experiment and the FE analysis. On the other hand jumping of persons with the popular song had a frequency around 2.2-2.4 Hz and the beam used during experiments, 80 Hz. In order to get rid of high frequency sampling effects, a zero-phase 100 Hz low pass filter was applied to both experimental and the FE results. Also when the standard deviations of the absolute values of two functions, experimental and the FE model results, were analyzed, it was seen that standard deviation of the FE model results was 0.104 g and standard deviation of experimental results was 0.092 g, showing a 10% difference. Maximum value of experimental data was 0.123 g and FE model result was 0.127 g, and minimum value of experimental data was -0.104 g and FE model result was -0.086 g, which can be considered as an acceptable correlation between experiment and FE model results.

EVALUATION OF FEM UNDER DYNAMIC LOADING

As a preliminary study, one of the beams at the stadium structure was analyzed under dynamic loading. A W16x40 beam, which was used as secondary beam in the stadium structure, was chosen for the study. For the total loading force, the spectators above the beam were considered. A finite element model was generated for dynamic loading application. The tributary area that the beam took the load from was assumed as a rectangular area with the dimensions of 30 ft x 14.2 ft. Also, a 100 psf design load was used for stadium structures with bleachers according to the Florida Building Code (2004). Those dimensions and loading case brought a total load of 42.6 kip applied to the beam as point loads because of the connection of the beam with stringers. That load

was divided by the number of stringers over the beam and applied to the investigated beam as point loading with a time-history function. Time-history loading function was obtained from the laboratory studies during jumping load tests. When results are analyzed, it was seen that the vibration level for the middle point of the beam was around 1 g for the investigated part of jumping. This result was in acceptable range when field data results (max 0.6 g) were studied.

In order to see the spectators' jumping effect in the stadium FE model, the loading function obtained in section was applied to the structure in time-history analysis. Load was calculated as if the stadium capacity were full. In the existing stadium, seating places are connected to stringer directly and those stringers are connected to beams so the load is distributed to the stringers in gravity direction.

In the investigated stadium spectators were not jumping in a perfectly coordinated manner, which meant not everyone would jump up and fall down at the same time. Stadium loading forcing function was chosen according to that criterion. Figure 5 explained the realistic and non-realistic situations for jumping of the spectators obtained from laboratory studies. In order to apply a dynamic loading to the FE model, realistic part of the data set obtained during the jumping load test (Figure 5) was used as the forcing function of the spectators.

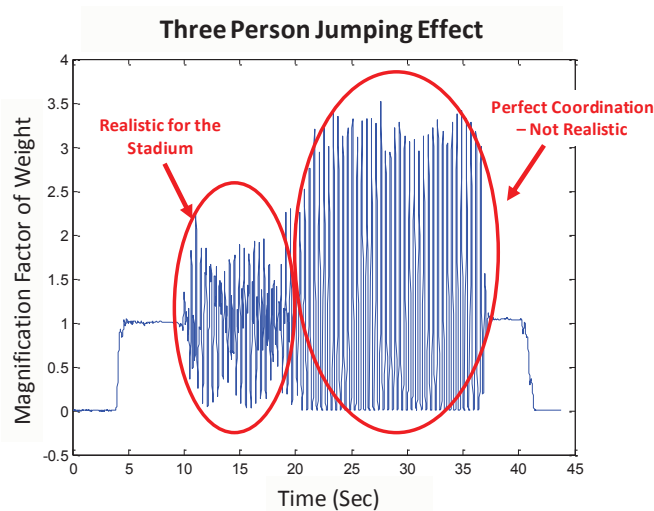


Figure 5: Jumping effect of a single person

When experimental data sets were collected during the games, vibration level of 0.6 g acceleration levels could be identified from the accelerometers positioned vertically in the lower seating section. When the results from FE model studies investigated, average 1-g vibration level was obtained from the node in closer location where field maximum value of vibrations obtained. Results are not expected to match exactly with the experimental data results because of the complexity of the structure, not having a fully updated FE model and especially the difficulty in accurately simulating the forcing function representing people jumping. Yet, the FE model results could be considered to be within an acceptable range for interpreting the reasons of vibration.

CONCLUSION

In this paper, investigation of dynamic characteristics of a football stadium by analyzing vibration effects is presented. First, a detailed FE model was developed and a systematic approach was followed to check the validity of the FE model. Once the FE model was improved, laboratory studies were conducted for dynamic loading simulations. Researchers jumped on a beam with the same popular song playing during the games to get the same effect as they were jumping in the stadium. Results obtained from experiments were compared with simplified beam FE model simulations. Verifying the match between experiment and simulations, same loading function was applied to detailed stadium FE model. When the FE model results were checked using the same spectator loading, it was seen that the vibration level was close to the vibration level obtained from field studies. Moreover, modal analysis results obtained from stadium FE model and field data showed that the stadium FE

model was simulating similar structural behavior with the investigated stadium section. For future work, the outcomes of this study will be used for different type loadings and performance evaluations under different type of loading cases to the stadium. It will be also used for evaluating the stadium structure for further structural changes such as retrofitting important sections or increasing the capacity of the structure with additional structural sections.

REFERENCES

- Allemang R.J., and Brown, D.L., (1982). "A correlation coefficient for modal vector analysis." Proc. 1st Int. Modal Analysis Conf. 1 pp. 110–116.
- Bachmann, H., and Ammann, W. (1987). "Vibration problems in structures induced by man and machines, structural engineering document no. 3e." International Association of Bridge and Structural Engineering, AIPC-IVBH, Zurich.
- Bachmann, H., Pretlove, A. J., and Rainer, H. (1995). "Dynamic forces from rhythmical human body motions." Vibration problems in structures: practical guidelines, appendix G, Birkhauser, Basel, Switzerland.
- Catbas, F. N., Gul, M., and Sazak H. O., (2010). "Dynamic Response Monitoring and Correlation to Crowd Movement at a Football Stadium." Proc., 27th Int. Modal Analysis Conference. Jacksonville, FL.
- Florida Building Code (2004). "Building-Structural Design."
- Gul, M. and F. N. Catbas (2008). "Ambient Vibration Data Analysis for Structural Identification and Global Condition Assessment." Journal of Engineering Mechanics 134(8): 650-662.
- Ji, T., and Ellis, B. R. (1994). "Floor vibration induced by dance type loads: theory." Struct. Eng., 72(3), pp 37–44.
- Pernica, G. (1983). "Dynamic live loads at a rock concert." Canadian Journal of Civil Engineering, 10(2), 185.
- Reynolds, et al. (2002). Modal testing of a sports stadium. Bellingham, WA, INTERNATIONAL, Society of Photo-Optical Instrumentation Engineers.
- Reynolds, et al. (2006). Vibration performance of a large cantilever grandstand during an international football match. Reston, VA, ETATS-UNIS, American Society of Civil Engineers.
- Salyards, K. A. and Firman, R.J. (2010). "Experimental Investigations of Dynamic Load Estiamtion Using Small-Scale Testing." Proceedings of the 28th International Modal Analysis Conference. Jacksonville, FL.
- Salyards, K. A. and Hanagan, L.M. (2007). "Analysis of Coordinated Crowd Vibration Levels in a Stadium Structure." Proceedings of the 25th International Modal Analysis Conference. Orlando, FL.
- Yao, S., J. R. Wright, et al. (2006). "Experimental study of human-induced dynamic forces due to jumping on a perceptibly moving structure." Journal of Sound and Vibration 296(1-2): 150-165.

Estimation of Damping for one of the New European Court Towers in Luxembourg

Rune Brincker,
Aarhus School of Engineering, Aarhus University,
Anders Brandt,
Department of Industrial and Civil Engineering, University of Southern Denmark,
Christos T. Georgakis and Joan Hee Roldsgaard
Department of Civil Engineering, Technical University of Denmark
Dietmar Schilz,
INCA Ingenieurs Conseils Associes

ABSTRACT

The two new high rise buildings for the European Court of Justice in Luxembourg have been tested by harmonic shakers and by Operational Modal Analysis. The background for the tests is to estimate the influence on the damping of one of the towers from an array of Tuned Liquid Dampers (TLDs) placed on top of the building. The TLDs have been designed to minimise the response of the buildings to wind loading, resulting in an increase in occupancy comfort. The harmonic excitation is performed to estimate the damping at a response level corresponding to moderate wind loading whereas the OMA has been performed under minimum wind loading. The paper presents the testing programme and the main results of which one is a clear non-linear behaviour of the introduced viscous damping system. To the authors' knowledge, no other structural excitation of this scale has been undertaken, before and after the application of tuned damping systems, in which the damping system is completely independent of the excitation system.

INTRODUCTION

The 4th extension of the Cour de Justice des Communautés Européennes in Luxembourg was in progress from 1996 to 2008 at the location: Kirchberg plateau, Grand Duché du Luxembourg, and in 2009 the buildings were in application, see [Figure 1](#). The architectural design was undertaken by Dominique Perrault Architecte and the structural design of the twin towers was done by INCA Ingenieurs Conseils Associes [1]. This paper describes the efforts to reduce vibrations in the east tower, see [Figure 1](#).

In order to investigate the effect of the wind forces on the occupancy comfort of the buildings several studies were carried out previous to the tests mentioned in this paper. These studies include

- in December 2002 wind tunnel studies investigating wind load on building and towers, time domain calculation of dynamic response of the towers and preliminary study of the effect of TLDs on the vibrations of the towers, [2]
- in July 2003 Preliminary study on the effect of installing TLDs on the roofs of the towers to reduce the vibration magnitude, [3]
- in April 2004 shaking table tests for testing the performance of the designed TLDs, [4] and FEM calculations of the reduced response in time domain after implementation of the TLDs on the Twin Towers, [5]
- in August 2004 some fine tunings of the TLD's in order to include some re-evaluations of the calculated dynamics together with initial measured estimates of the first natural frequencies, [6]
- in September 2009 some pilot OMA test providing estimates of the three fundamental frequencies based on ambient measurements recorded at the upper service level of the east tower
- in October 2009 fine tuning of the height of the liquid in the TLDs

The structural system of the two towers is indicated in [Figure 2](#). The four TLD arrays placed on the roof of the east tower is shown in [Figure 3](#). More information about both issues may be found in [7] and for the TLD array in [8]. The final tests planned to investigate the effect of the TLD's are the tests reported in this paper. These tests include



Figure 1. The new EU-court tower designed by Dominique Perrault Architecte and INCA Ingenieurs Conseils Associes. The considered tower is the east tower, to the right in the picture.

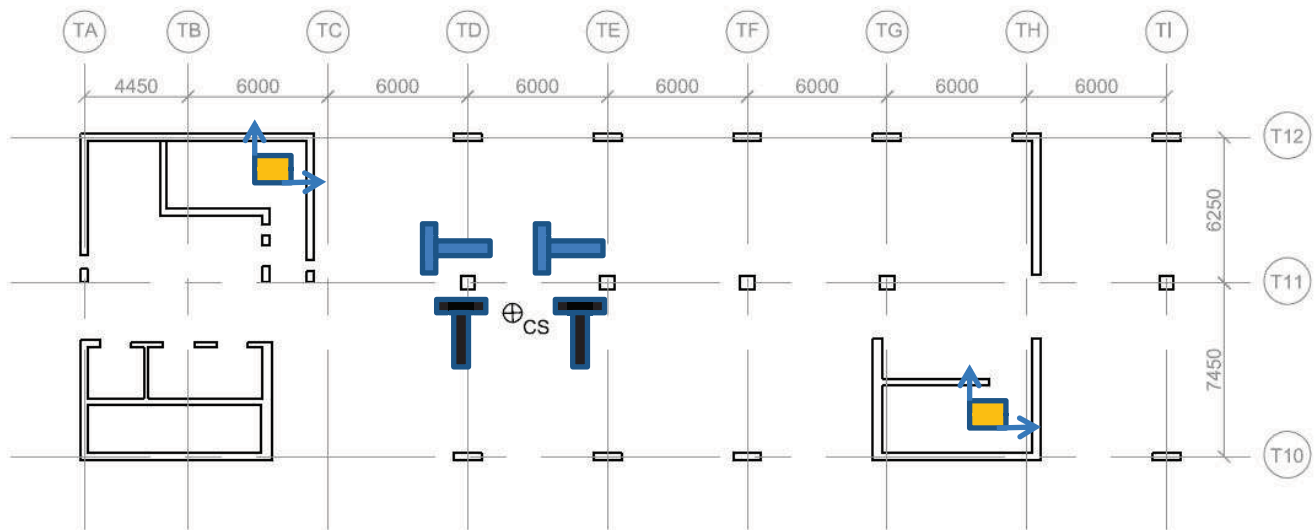


Figure 2. The two twin towers shown in [Figure 1](#) are nearly identical with regards to the structural system. The main structural system consists of concrete cores in both ends of the towers with a monolithic concrete floor spanning in between erected on columns. Positions of the OMA sensors in the two stair case structures are indicated together with positions of the shakers for mode 1 (blue) and 2 (black).

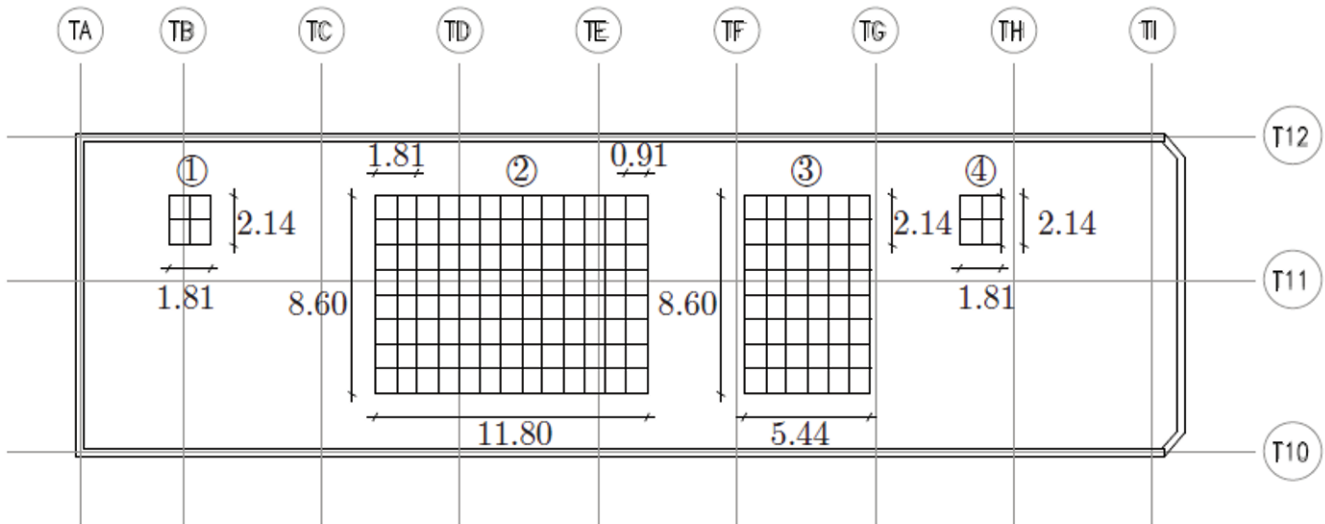


Figure 3. The four Tuned Liquid Dampers (TLDs) arrays placed on the roof of the east tower.

- Forced vibration testing with harmonic shakers in order to excite the structure to a response level close to that predicted for moderate wind loading
- Operational modal analysis based on ambient loads present during the testing sessions (practically no wind in all cases)

Both the forced vibration testing and OMA testing was performed before and after the TLD's were activated by filling the water tanks.

FORCED VIBRATION TESTING

Forced vibration tests were undertaken to determine the frequency response functions for each primary building mode, laterally, longitudinally and in torsion – with and without activation of the TLDs. By measuring the frequency at which the maximum normalized building response occurs in each direction, the natural frequency of the associated mode is determined. The damping is found through the logarithmic decrement of the free decays of the building response, at the end of each vibration test.

Centrifugal mass exciters (Fig. 4) were employed at level 25 of the buildings (99 m height) to produce sinusoidal forces in the three directions of interest. Each shaker is capable of producing a rotational frequency dependant load so that:

$$F = mr\omega^2$$

where m is the rotating mass, r is the radius from the center of rotation, and ω is the angular frequency of the exciter. A mass of approximately $m = 350$ kg was mounted on each shaker at a distance of $r = 0.4$ m from the centre of rotation. With 1 Hz rotation, it can be calculated that each exciter can produce a harmonic load with amplitude of approximately 5.5 kN. The shakers were positioned, as shown in Fig. 2, and were programmed to operate in-phase for each of the building's primary bending modes and out-of-phase for the primary torsional mode. The shakers were placed on rubber sheets directly on the concrete floor and covered in sandbags, in order to prevent them from sliding. Prior to the forced vibration tests, an estimation of the first three natural frequencies had been made, based on a long term ambient vibration measurement campaign. These were used as guide when choosing the excitation frequencies.

Accelerations were measured using a GeoSIG AC-63 accelerometer, with a 100 mg/V sensitivity. The tri-axial accelerometer was placed in the stairwell between TB and TC in Fig. 2. The measurements were verified with the OMA geophone sensors. The acceleration time-history for the excitation of the first lateral bending mode (0.442Hz) without TLD activation can be viewed in Fig. 5. Similarly, the acceleration time-history for the excitation of the first lateral bending mode (0.439Hz) with TLD activation can be viewed in Fig. 6. From these it can be seen that ambient vibration levels were relatively low, allowing for a good estimation of the damping.

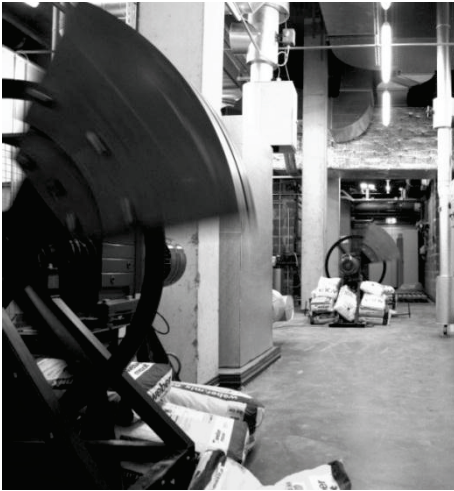


Figure 4. Centrifugal mass exciters (shakers) in motion; Picture taken at the technical floor (level 25)

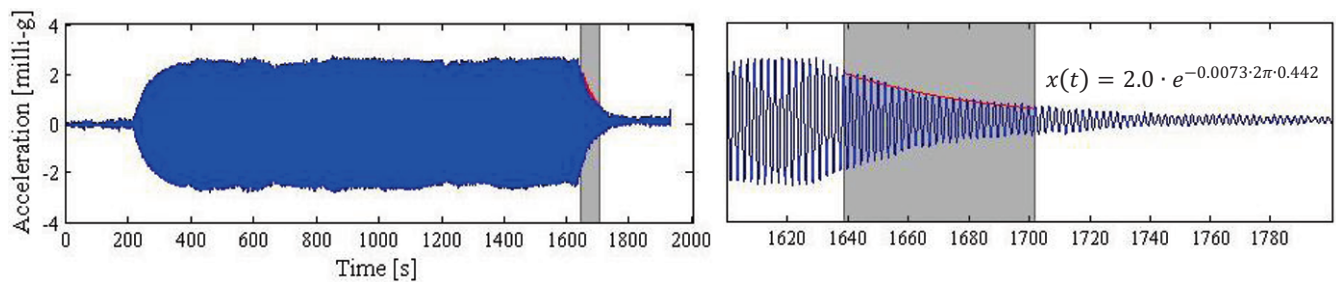


Figure 5. Building time-history response for the forced vibration tests at 0.44Hz - without TLD activation (left) and with fitted exponential decay function.

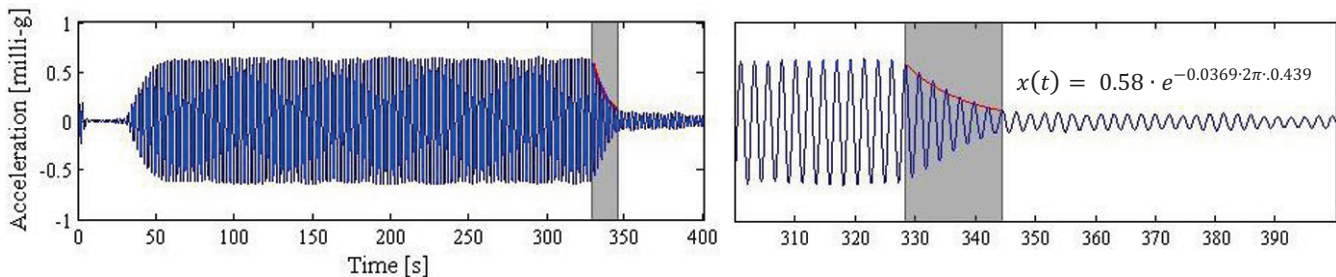


Figure 6. Building time-history response for the forced vibration tests at 0.44Hz - with TLD activation (left) and with fitted exponential decay function.

For the damping, the exponential decaying function for the time-histories is applied after the first 10% and before the last 20% of the free decay response – thus omitting any shaker shut-down noise and the remaining ambient vibration response. This approach is assumed to be valid for each mode, as the modes are well separated. The decaying functions for mode 1 without and with the TLDs activated can be seen in Figs. 5 and 6 (right), respectively.

The resulting resonant frequencies, damping and accelerations, obtained from the forced vibration measurements, for the primary modes of vibration – with and without the TLDs – can be viewed in Table 1, below. Note that mode 3 was not excited after the activation of the TLDs. It can be seen that the TLDs provide a significant increase in the damping for mode 1, whilst also proving a more moderate increase for mode 2.

OPERATIONAL MODAL ANALYSIS

The measurement system used for the OMA testing is a digital geophone based system consisting of a client/computer, a sensor base, and a measurement chain of sensor nodes, see Figure 7.a. Two such systems were used, one taking two horizontal measurement in a stationary point (the reference), and one taking three horizontal measurements in two sensor nodes.

Table 1. Measured modal frequencies, damping and accelerations during the forced vibration tests.

Mode	Frequency [Hz]	Damping ratio [%]	Max. acceleration [mg]
1	0.442	0.73	2.5
1 with TLDs	0.439	3.69	0.64
2	0.577	0.62	1.9
2 with TLDs	0.590	0.99	1.3
3	0.823	0.59	0.19

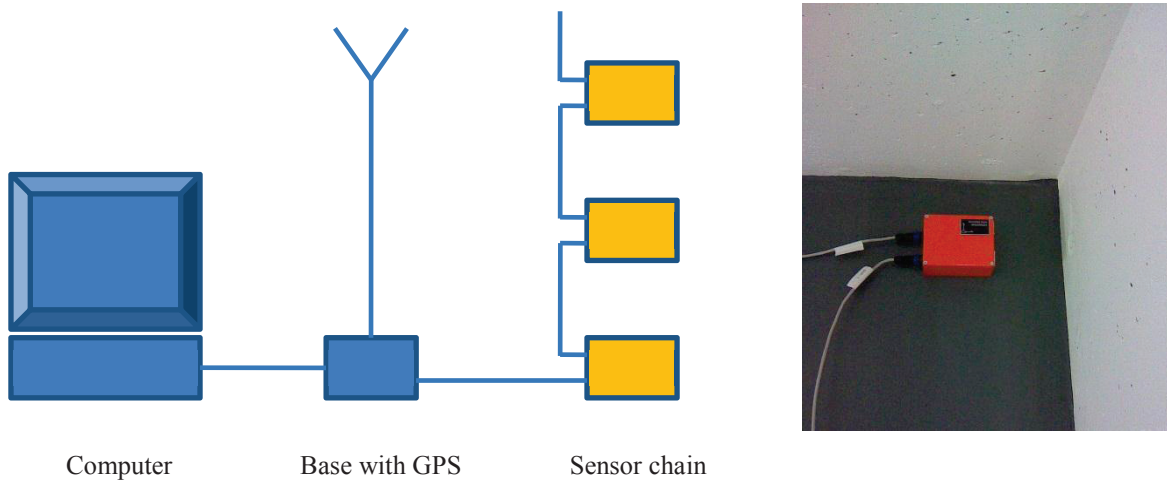


Figure 7. Left (a): The digital geophone based measurement system used for the OMA testing. Two systems were used, one for reference, and one roving for the different data sets. Right (b): One of the digital sensor nodes glued directly on top of the concrete floor in one of their cases of the building.

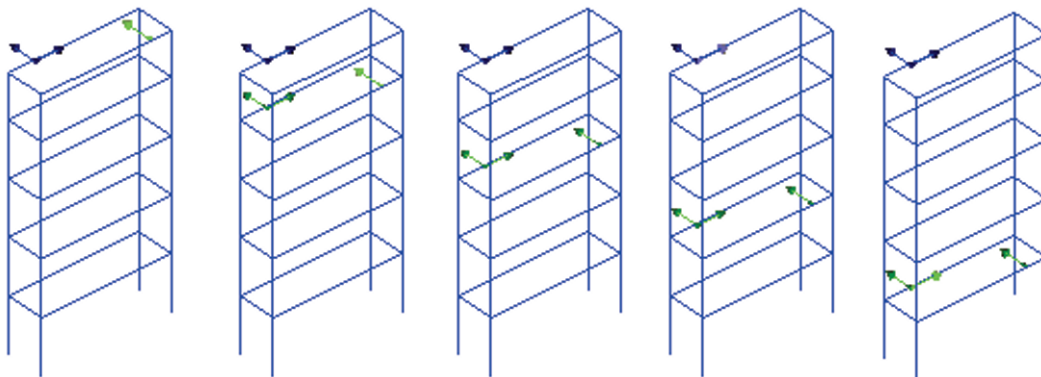


Figure 8. From the left data sets 1-5, first data set on the top office floor (no 24), second on the 20th floor, and then the 15th floor, the 10th floor and finally the last data set is on the 5th floor.

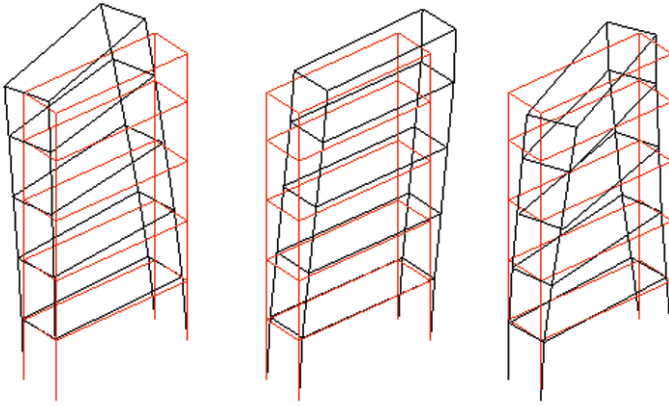


Figure 9. The first three mode shapes from OMA using EFDD, natural frequencies in Table 2 and 3.

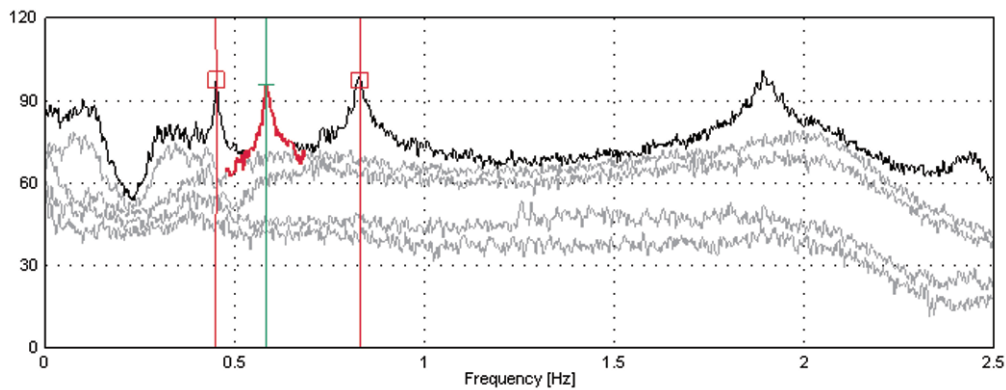


Figure 10. Singular values in dB of the spectral density matrix for test1, data set 1. All modes decomposed nicely and gave reliable damping estimates, a typical decay of a modal coordinates is shown in Figure 12.

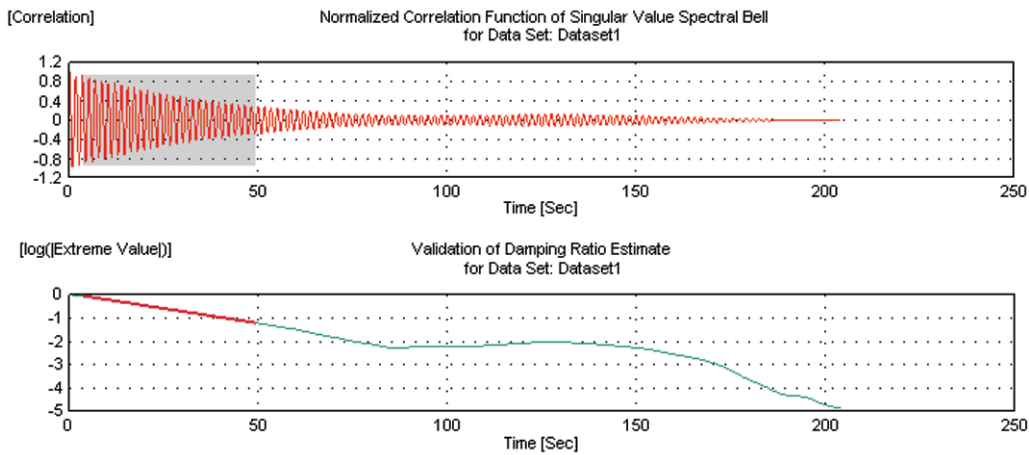


Figure 11. Top plot: The decay of the modal correlation function of mode 2 for test 1, data set 1. Bottom plot: Damping envelope showing linear decay in a logarithmic plot.

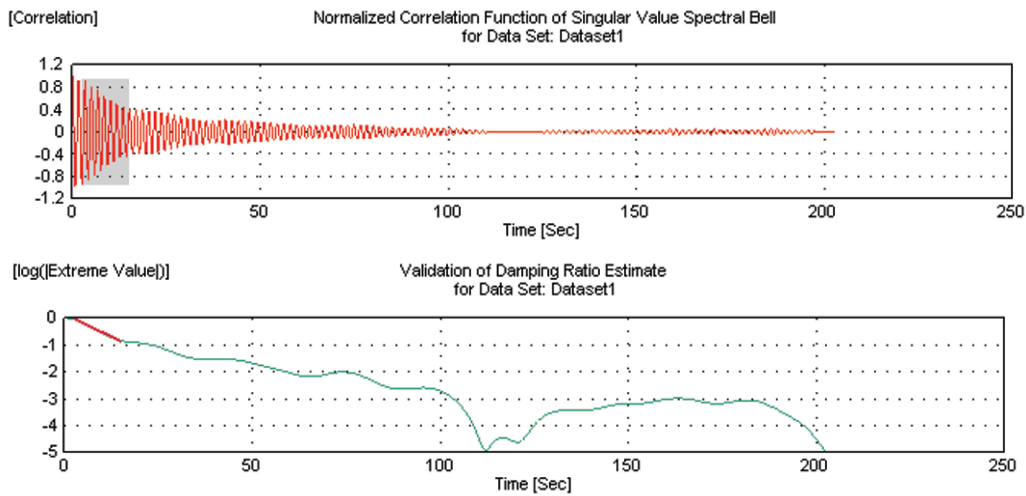


Figure 12. Top plot: The decay of the modal correlation function of mode 2 for test 2, data set 1. Bottom plot: Damping envelope showing increased damping and only linear decay in a logarithmic plot for the very first part.

The digital technology of the A/D converter is similar to the one described in Brincker et al [9]. The sensors have been produced by CAP2 ApS, Denmark, and further information can be found in web site cap2.dk.

The sensors were glued directly on top of the concrete in the two stair cases of the building, see Figures 2 and 7.b. Five data sets were recorded using a sampling frequency of 10 Hz and a duration of 30 minutes. Sensor positions for the five data sets are shown in Figure 8.

Only the first three modes have been considered in the OMA, but easily more modes could have been estimated. The SVD plot for the EFDD analysis is, [10], [11] shown in Figure 10. In Figure 10 is also indicated the isolation of the auto spectral density of one modal coordinate in the frequency domain. The corresponding auto correlation function and the linear decay in a logarithmic plot are shown in Figures 11 and 12. As it appears, for test2 a significantly higher damping is present, and further, only the very first part of the correlation function shows a clearly linear decay.

Using the Principal Component version of the SSI technique, [12], it was necessary to use a maximum model order of 160 eigenvalues and decimate the signal to a sampling rate of 5 Hz in order to obtain unbiased damping estimates. A typical stabilization diagram is shown in Figure 13. The final results of the EFDD and SSI OMA are shown in Tables 2 and 3.

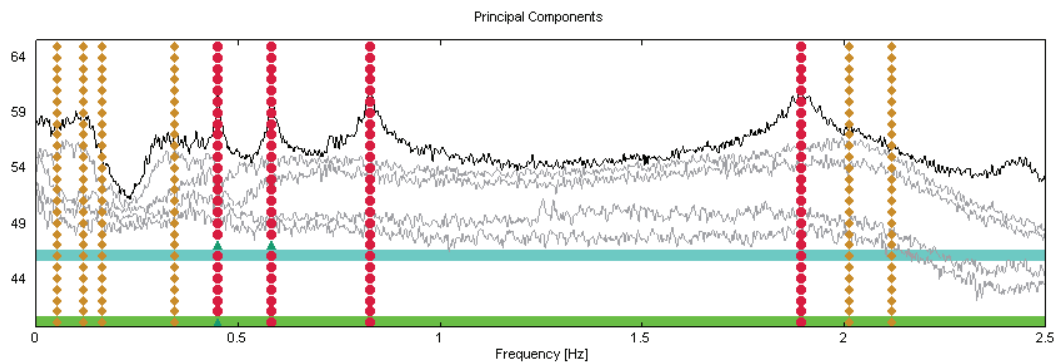


Figure 13. Stabilization diagram for data set 1, test1. Vertical axis shows the model order as the number of eigenvalues in the model. Selected model for further analysis is indicated by the blue bar.

CONCLUSIONS

Both the forced vibration testing results and the OMA results showed a significant increase of damping after filling water tanks of the Tuned Liquid Dampers (TLDs) placed on top of the building. The OMA showed less increase in the damping than the forced results from the forced vibration tests. This is consistent with the fact that liquid dampers have a non-linear behaviour where the damping increases with amplitude. Also from the auto correlation function of the modal coordinate a non-linear behaviour was indicated.

Table 2. The results of OMA for test 1.

Mode	Frequency [Hz]	Std. Frequency [Hz]	Damping Ratio [%]	Std. Damp. Ratio [%]
EFDD Mode 1	0.4486	0.00090	0.6598	0.289
EFDD Mode 2	0.5819	0.00093	0.5705	0.089
EFDD Mode 3	0.8272	0.00149	0.6349	0.212
SSI-PC Mode 1	0.4492	0.00052	0.6366	0.144
SSI-PC Mode 2	0.5819	0.00086	0.6113	0.071
SSI-PC Mode 3	0.8273	0.00043	0.6082	0.161

Table 3. The results of OMA for test 2.

Mode	Frequency [Hz]	Std. Frequency [Hz]	Damping Ratio [%]	Std. Damp. Ratio [%]
EFDD Mode 1	0.4399	0.00093	1.846	0.458
EFDD Mode 2	0.5895	0.00149	1.473	0.334
EFDD Mode 3	0.8263	0.00116	0.554	0.122
SSI-PC Mode 1	0.4420	0.00140	1.603	0.238
SSI-PC Mode 2	0.5886	0.00084	1.390	0.174
SSI-PC Mode 3	0.8260	0.00058	0.606	0.140

REFERENCES

- [1] INCA Ingenieurs Conseils Associes. www.inca-ing.lu. Technical report.
- [2] Danish Maritime Institutue: *Wind-tunnel tests with Salle de Concert a Luxembourg-Kirchberg*. Technical report, Danish Maritime Institute, Project Report, Ref. 2001208, April 2002.
- [3] Christos T. Georgakis: *Tuned Liquid Dampers for the Twin Towers of "Cour de Justice des Communautes Europeennes, Luxembourg Feasibility Study*. Technical report, Force Technology, 2003.
- [4] FORCE Technology: *Tuned Liquid Dampers for the Twin Towers of Cour de Justice des Commuautees Europeennes Luxembourg - Experimental Testing*. Technical report, FORCE Technology, April 2004.
- [5] FORCE Technology: *Tuned Liquid Dampers for the Twin Towers of Cour de Justice des Commuautees Europeennes Luxembourg - Detailed Analysis*. Technical report, FORCE Technology, Report, April 2004.
- [6] FORCE Technology: *Tuned Liquid Dampers for the Twin Towers of Cour de Justice des Commuautees Europeennes Luxembourg - TLD Re-Analysis*. Technical report, FORCE Technology, Report, August 2004.
- [7] Joan Hee Roldsgaard and Mads Christiansen: *Determination of the Dynamic Characteristics of Large Structures through Full-Scale Testing*, master thesis in the period September 1 to February 28 2010, Technical University of Denmark.
- [8] Georgakis, C.T., Koss, H.H., De Toffol, W.: *Tuned Liquid Dampers for the New European Court of Justice*, Luxembourg, Structural Engineering International, Vol.4, 2005, pp 228-231
- [9] Brincker, R., Bolton, B. and Brandt, A.: *Calibration and Processing of Geophone Signals for Structural Vibration Measurements*. In Proc of IMAC XXVII, A Conference on Structural Dynamics, Feb 1-4, 2010, Jacksonville, Floria, USA.

- [10] Brincker R, Zhang L, Andersen P.: *Modal Identification of Output-only Systems Using Frequency Domain Decomposition*. Smart Materials & Structures. 2001, 10(3):441-445.
- [11] Brincker R, Ventura CE, Andersen P.: *Damping Estimation by Frequency Domain Decomposition*. In: Proceedings of IMAC 19: A Conference on Structural Dynamics : februar 5-8, 2001, Hyatt Orlando, Kissimmee, Florida, 2001, Society for Experimental Mechanics. 2001, 698-703 pp.
- [12] Van Overschee, P. and De Moor, B. *Subspace identification for linear systems: Theory, implementation, applications*. Kluwer Academic Publishers 1996.

Use of Wireless Smart Sensors for Detecting Human Falls through Structural Vibrations

Benjamin T. Davis, Undergraduate Student, University of South Carolina,
300 Main St, Columbia, SC 29208

Juan M. Caicedo, Associate Professor, University of South Carolina,
300 Main St, Columbia, SC 29208

Scott Langevin, Ph.D. Candidate, University of South Carolina
315 Main St, Columbia, SC 29208

Victor Hirth, **Professor of Clinical Medicine, University of South Carolina, School of Medicine,
3010 Farrow Road, Suite 300A, Columbia, SC 29203**

Abstract

Falls are the leading cause of accidental deaths for people over the age of 65 because of the fall, fall related injury itself or related complications including hypothermia, dehydration, pressure sores and pneumonia. Several fall detection systems are commercially available including Life Alert, Life Link, and Alert One where the person wears a pendant that can be pressed in the case of an emergency or with newer models activates automatically when there is no motion. Pendant-based emergency systems become ineffective if the person is not wearing the pendant (refuses or forgets) or cannot press the pendant's button, for example when falling in a prone position on top of the device. In addition, the elderly are hesitant to use emergency systems for several reasons such as the concern of bothering others and personal pride. This paper proposes the use of structural vibrations to determine if a person has fallen. An Imote2 and an ITS400CA sensor board are used for the collection of structural vibrations induced by human activity, including falls. These sensors are discrete, and have shown potential for the data collection and diagnostic processing needed to detect human falls. The use of wireless smart sensors in the structure provides a non-intrusive method for human fall detection that does not require the use of any device by the person. A preliminary study of the classification of human induced vibration in a typical structure using traditional wired sensors is also discussed as well as a sensing framework used to study structural vibrations induced by human falls.

Introduction

As of April 2008 there were 1.4 million persons living in nursing homes in the US [1]. In addition, there may be three times as many persons living in assisted living facilities nationwide. One of the leading areas of nursing home litigation and accident related injuries are falls. Of older persons who die due to accidents, 50% of all injury-related deaths is due to a fall or the resulting complications [2]. The ability to detect falls in real time and to quickly respond would represent a huge improvement to the current mode of detecting falls (which is coincidental). Strides in the field of emergency response systems have been made in order to allow our elderly a more independent life. Companies such as Life Alert, Life Link, and Alert One provide the person a pendant to wear that can be pressed to signal help in the case of an emergency, like a fall. Unfortunately, these systems assume the person would be able to press the button and is wearing the pendant at the time of a fall. The ideal fall

detection system should be discrete, autonomous, low maintenance, low cost and not dependent on being worn. It should be part of the person's living environment that requires no actions from the person to function.

The use of accelerometers attached to the person to detect when a fall has occurred has also been proposed [4]. The authors concluded that it is possible to differentiate between a fall and normal activity while using a wireless sensor network with one dual-axis accelerometer affixed to the monitored person. However, this presents the challenge of whether or not the person is wearing the device and another of whether the device is charged, operational in the position on the body or whether the device would be functional in the bath or shower. Recent research has extended the use of accelerometers to deploy airbags as a means of protecting a person's hips [3]. Research using Asynchronous Temporal Contrast (ATC) Vision Sensors suggest that cameras can be used in a non-intrusive nor privacy violating application for fall detection [5]. The ATC Vision Sensors only detect pixel changes in the environment and record/display the pixel changes. This technique functions well under consistent lighting conditions, however, the absence of light or dynamic lighting changes, present a difficult challenge for the system. Alternatively, accelerometers and microphones can be deployed in a room to monitor floor vibrations and acoustic emissions for detecting human falls [6]. However, the challenge of cost and installation complexity arises. The system requires two software packages, a data acquisition card, and the accelerometers/microphones themselves. Lack of wireless capability creates installation issues due to the wiring and modules needed.

This paper presents a sensing framework to study human induced vibrations created by human falls. This sensing framework should support the two different phases needed to successfully develop algorithms for fall detection using structural vibrations: i) collecting of raw acceleration information from human induced vibrations (phase I) and ii) deployment of algorithms that will process part of the signals at the sensor level (phase II). During phase I raw acceleration data is captured to study how different human induced vibrations are expressed in the acceleration of floor and walls. During the second phase, pattern recognition algorithms will be developed based on the signal characteristics identified in phase I. These algorithms will be implemented on the sensing framework. The sensor modules used in this research contain a sensor stack consisting of an Imote2 processor/radio board, and an ITS400CA sensor board or an IIB2400 interface board for the base station. These wireless modules can be installed in discrete locations where each imote has computational and communication capabilities. The network configuration and performance of the system are described. In addition, results of a preliminary study performed to investigate whether or not signals from falls have different signal characteristics than those from other human activity are presented.

Proposed Sensing Framework

The system is composed of individual smart sensing units that are organized into a star network topology where each leaf node acts independently of one another but cooperate towards the same goal of identifying falls using structural vibrations (Fig. 1). In this star network a cluster of leaf nodes communicate with a central master node, which serves as the network's controller and gateway. Leaf nodes can be installed in unobtrusive places such as under beds or furniture or even under the floor itself if the subfloor is accessible such as in typical wood frame construction in the United States. The master node interfaces with a connected computer that can be placed in a closet or another area where communication with the leaf nodes is accessible via wireless signals. The computer

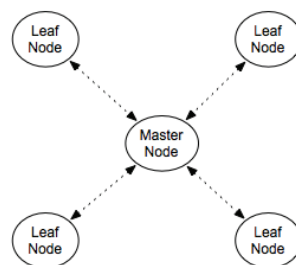


Fig. 1. Sensor network topology

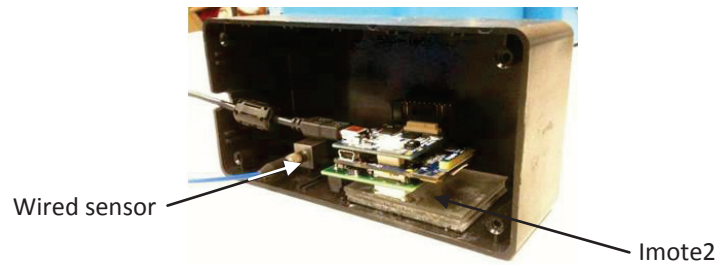


Fig. 2 Wired Accelerometer and Imote2 Stack

logs the activity of the network and communicates any fall detection via an internet or phone connection.

This system architecture was selected to facilitate a multiagent system design for fall detection in phase II of this research. Agents are abstract entities that can be described as autonomous hardware/software components having certain goals, internal beliefs and being able to communicate with other agents in order to accomplish these goals. As an example, consider a community of individuals containing two wheat farmers (leaf nodes) and a baker (master node). Each wheat farmer owns his own plot of land and grows wheat under completely different conditions but share the same goal of supplying the baker with wheat. Farmer 1 might be in desert and thus has to adapt to his environment by spending a lot time working the land in order to grow wheat to supply to the baker. Farmer 2 is in a lush valley with plenty of water and good soil where he can grow huge amounts of wheat, a more suitable environment requiring less work for large returns. Each individual farmer has adapted to his own circumstances and reacts to any change accordingly. Similarly, each sensor is presented with its own set of environmental circumstances and has to react accordingly. For example, depending on the location of the particular sensor each node will filter other human induced vibrations not related to a fall. Sensors installed close to the laundry room will have to adapt and filter the floor vibrations when the washer or drier are in use while sensors in bedrooms may not be similarly affected.

Wireless Node Characteristics

The Imote2 wireless sensor node was selected for the development of the fall detection network although the deployment could be performed using a variety of off the shelf sensors that are available in the market. The Imote2 (Fig. 2) utilizes a low-power 416 MHz Intel PXA271 X-Scale Processor with an Intel Wireless MMX DSP Coprocessor. It has 256 kB SRAM, 32 MB Flash memory, and 32 MB SDRAM. The board also includes an integrated 802.15.4 ChipCon 2420 radio with a 2.4 GHz Antenova Mica SMD onboard antenna. The ITS400CA board with a ST Micro LIS3LO2DQ tri-axial accelerometer with 12-bit resolution and a range of +/- 2g was selected to acquire acceleration signals. In addition, an IIB2400 board was used to connect the base node to the computer. The IIB2400 offers a Mini USB interface with a two serial ports at a speed of 110-921,600 Baud per port. It also has a standard 20-pin connector for JTAG port flashing and debugging.

Each Imote2 outfitted with an ITS400 sensing board has shown to have different sampling frequency due to the varying clock rates of the processor [7]. This can be problematic in some applications such as in structural health monitoring. However, in this application simultaneous sampling is not needed since the sensor nodes are expected to act independently in the data collection. The small differences in sampling rate can be taken into account at the time of data processing by re-sampling the data from all sensors to a common sampling rate.

Acceleration records of an Imote2 stack consisting of an IIB2400 Interface Board, ITS400CA Sensor Board, and an Imote2 Processor Board, was compared to a traditional wired system that served as the standard to determine the quality of the signal on the Imote2. The standard system consisted of a wired shear accelerometer from PCB Piezotronics, model 333B50, a National Instrument 8 channel input SCXI-1531 card connected to a DAQCard-6062E with 12-bit resolution. The Imote2 stack was secured to the box using a plexi-glass base and the wired accelerometer was attached beside the Imote2 stack (Fig. 2). The box was orientated so that the ITS400CA's z-axis

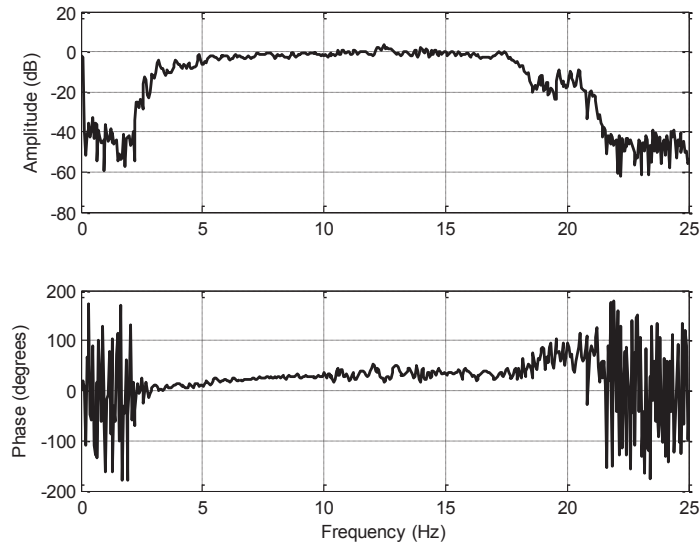


Fig. 3. Transfer function from 5 to 20 Hz

was pointed towards the floor. The sampling rate on the Imote2 was set for 200 Hz and the wired acquisition system was set to 1000 Hz. Both systems were later re-sampled to 200 Hz for comparison. A basketball was dropped once by a person and then allowed to bounce freely creating an induced vibration to compare the signals. All data was exported to MatLab for detrending and conversion to units of gravity (g). A time plot comparing the two signals can be seen in Fig. 3. Overall, the acceleration obtained from the Imote2 system is comparable to the acceleration acquired with the traditional wired accelerometer. The two accelerometers were also attached to a shake table with an effective frequency range from 5Hz to 20 Hz to compare the acceleration signals in the frequency domain. The transfer function between the signals is shown in Fig. 4, showing a good agreement between the two signals on the frequencies excited by the shake table (i.e. amplitude and phase are close to zero).

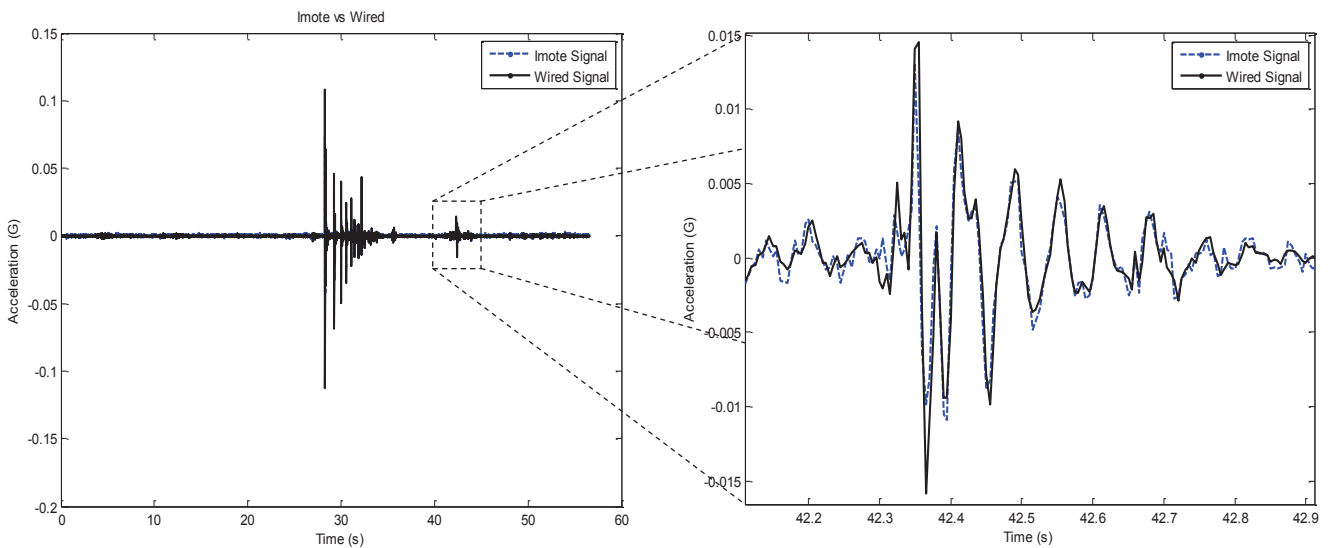


Fig. 4. Imote2 vs. Wired Acceleration-Time Graph

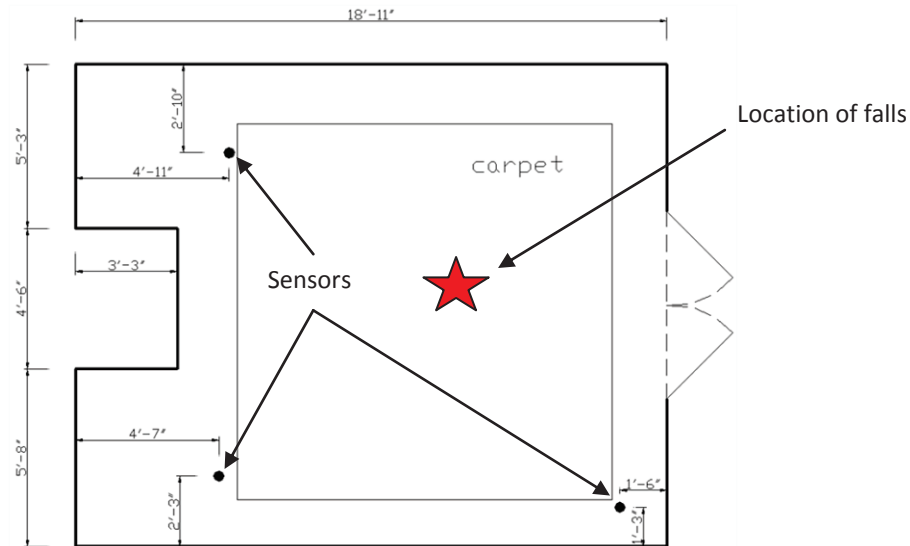


Fig. 5 Floor plan

Preliminary Study of Human Induced Vibrations

A preliminary study was performed to explore if structural vibrations from falls have different characteristics than other human induced vibrations. Geriatric specialists were consulted to determine several typical elderly fall profiles. Fall events were simulated by having people fall according to the identified elderly fall profiles. The tests were performed at a traditional two floor wood structure residential home, on the campus of Palmetto Health Richland. The events were simulated over a carpeted area over the wooden floor on the first floor. Out of the total of 38 tests (see [Table 1](#)), 18 simulated human falls and 20 represent other activity such as walking or room vacuuming.

Three accelerometers, usually used for vibration monitoring on civil structures, were used for the tests. Two accelerometers were capacitive PCB accelerometers Model 3701D1FA20G, each one with a PCB Model 478A01 signal conditioner. The other accelerometer was a Piezoelectric PCB accelerometer Model 393A11, with a PCB Model 480C02 signal conditioner. The two capacitive accelerometers have a sensitivity of 100 mV/g ($\pm 5\%$), a measurement range of ± 20 g, and a frequency range from 0 to 300 Hz ($\pm 5\%$). The piezoelectric accelerometer has a sensitivity of 10 V/g ($\pm 15\%$), a measurement range of ± 2.5 g, and a frequency range from 0.025 to 800 Hz ($\pm 5\%$). A National Instruments USB-6009 multifunctional data acquisition module was used to record the accelerations on a laptop computer. The USB module has an input resolution of 14 bits, a maximum sampling rate of 48 kHz and a variable input range from ± 1 to ± 20 Volts. [Fig. 5](#) shows the location of the sensors and the events

Number of tests	Description
1	No activity – baseline for noise
2	People walking
16	Ball of different sizes dropped at different heights
6	Two stage fall – Knee and trunk
3	Two stage fall – Back from chair
3	Two stage fall – Knee and side
4	Fall from chair
2	Fall over from chair
1	Vacuuming the room

Table 1. Human activities tested

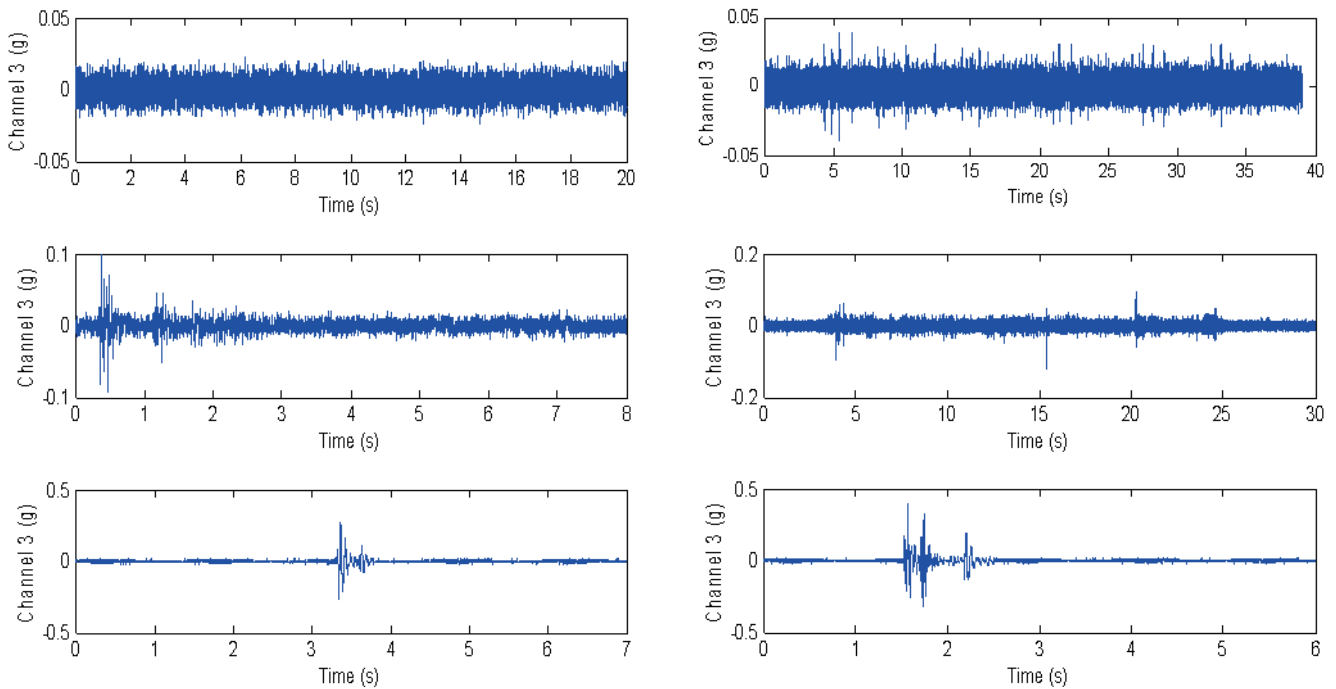


Fig. 6 (left to right) No Activity; One Person Walking; 6lb. Medicine Ball Drop; Vacuuming; Fall - Butt to Back; Fall - Knee to Torso on the floor plan of the room.

Fig. 6 shows typical acceleration records collected during testing. All plots correspond to Channel 3 which is the sensor located on the top on Fig. 5 and are very similar to the signals from other sensors. These results clearly show the differences between the different activities. The first clear difference is that the magnitude of the accelerations collected during human falls (bottom two plots) is significantly larger than those of other activities such as walking or even dropping a medicine ball (middle left). Dropping objects on the ground have periodic behavior corresponding to the rebounding of the object with each bounce reducing in amplitude. On the other hand, human falls tend to have a significantly different behavior. In cases such as the knee to torso fall (bottom right) three peaks of acceleration were detected and the time between the first and second peak is different than the time between the second and third peak. Falling back also produces a different acceleration signature with only two peaks (bottom left on Fig. 6). In a related paper, we plan to outline details of features extracted from the signals captured and the construction and evaluation of several pattern recognition systems used to classify acceleration signals as corresponding to a human fall event.

Conclusion

This paper presented the framework used to detect human falls based on structural vibrations. A star network topology where each leaf acts independently is proposed for the implementation of the framework. Each leaf sensor will act independently collecting acceleration data and determining if a human fall has occurred. The paper also describes a preliminary test performed by simulating human falls on a two story house. The signals collected by the simulated human falls are significantly different from those of other human activity such as walking or vacuuming, indicating the potential of using structural vibrations for human fall detection.

Acknowledgements

This work was supported by a grant from the Alzheimer's Association (ETAC-10-174499)

References

- [1] *Falls in Nursing Homes*. 2008; Available from: <http://www.cdc.gov/ncipc/factsheets/nursing.htm>.
- [2] *Falls and the Elderly*. 2010; Available from: <http://www.netwellness.org/healthtopics/aging/faq9.cfm>.
- [3] Shi, G.Y., et al., *Mobile Human Airbag System for Fall Protection Using MEMS Sensors and Embedded SVM Classifier*. *Ieee Sensors Journal*, 2009. **9**(5-6): p. 495-503.
- [4] Chen, J., et al., *Wearable Sensors for Reliable Fall Detection*, in *Engineering in Medicine and Biology 27th Annual Conference*. 2005, IEEE: Shanghai, China.
- [5] Fu, Z.M., et al., *An Address-Event Fall Detector for Assisted Living Applications*. *Ieee Transactions on Biomedical Circuits and Systems*, 2008. **2**(2): p. 88-96.
- [6] Zigel, Y., D. Litvak, and I. Gannot, *A Method for Automatic Fall Detection of Elderly People Using Floor Vibrations and Sound-Proof of Concept on Human Mimicking Doll Falls*. *Ieee Transactions on Biomedical Engineering*, 2009. **56**(12): p. 2858-2867.
- [7] Nagayama, T., *Structural Health Monitoring Using Smart Sensors*, in *Civil Engineering*. 2007, University of Illinois: Urbana-Champaign. p. 259.

Structural Health Indices for Steel Truss Bridges

Ryan Kent Giles, Doctoral Student,
Robin Kim, Doctoral Student,

Billie F. Spencer, Jr., Nathan M. and Anne M. Newmark Endowed Chair in Civil Engineering,
Department of Civil and Environmental Engineering, University of Illinois at Urbana-Champaign,
205 North Mathews Avenue, Urbana, IL 61801-2350

Lawrence A. Bergman, Professor

Department of Aerospace Engineering, University of Illinois at Urbana-Champaign, 104 S. Wright St.,
Urbana, IL 61801-2958

Carol K. Shield, Professor

Department of Civil Engineering, University of Minnesota, 500 Pillsbury Dr. SE, Minneapolis, MN
55455-0116

Steven C. Sweeney, Structural Engineer

Materials and Structures Branch, U.S. Army ERDC-CERL, P.O. Box 9005, Champaign, IL 61826-9005

ABSTRACT

Steel bridges represent a significant portion of the nation's aging bridge inventory. The United States Army's inventory has over two hundred steel bridges that are vital to the operation of nearly every Army Installation. The Army regularly inspects their bridges to ensure the continued functionality of the bridges. However, current inspection techniques and schedules may not be able to detect certain defects that could compromise bridge integrity. To supplement current inspection standards, the US Army Engineer Research and Development Center (ERDC), has contracted to install a structural health monitoring (SHM) system on the historic steel truss Government Bridge at the Rock Island Arsenal. ERDC envisions a system that measures strain, acceleration, tilt, and electrical resistance to determine the bridge's structural health. Research into the usefulness of the Damage Locating Vector (DLV) method, and the damage indices that the method calculates, in detecting corrosion damage has been conducted. Numerical studies on a finite element model of the Government Bridge have indicated that the DLV method has potential as a damage detection algorithm on such a large structure. Laboratory experiments using corroded members in a model truss have additionally shown that the DLV can be used to monitor corrosion induced damage.

INTRODUCTION

Metal bridges in the United States were a result of, and fuel for, the large scale industrialization that occurred in the late 1800s and early 1900s. The expansion of the country's railroads during this period led engineers to develop steel alloys with greater strength and ductility, and improvements in the manufacturing processes enabled mass production of standard shapes. The material and manufacturing advances made steel a cost-effective engineering solution for bridging the streams and rivers of the American hinterland. Governments, from the smallest municipal council ordering pre-fabricated bridges to span the local gully to state and federal legislatures hiring engineers to design custom spans over the great rivers and canyons, built a large stock of steel bridges across the country. The durable nature of steel and the engineers' often conservative designs have ensured that many of the bridges built over a century ago have remained intact and functional. However, these bridges require proper maintenance and inspection to remain a vital part of the national infrastructure.

The United States Army has over two hundred steel bridges, built over the last century, in current use in their inventory. Like many bridges in the inventories of departments of transportation across the nation, the Army's steel bridges have suffered from corrosion and material degradation. In fact, many of the bridges in the inventory of the Army and Department of Defense are considered fracture critical such that the failure of a single component could lead to collapse. Regular repair and

maintenance have extended the life of the bridges, but their load ratings, and therefore the allowable weight of vehicles crossing the bridge, have often been reduced as the corrosion degradation progresses. If the corrosion is allowed to continue unchecked, the bridge can be taken out of service altogether. In daily operations, taking a bridge out of service can perhaps be considered an inconvenience as traffic has to be rerouted. However, the reroute will cause economic losses due to the time lost and additional transportation costs. In an emergency or force protection situation, the reroute will reduce the ability of the Army to respond most efficiently and effectively.

To prevent collapse and identify needed repairs, steel bridges are regularly inspected visually and that inspection is sometimes supplemented with a variety of nondestructive methods such as dye penetrants, ultrasonic testing, and radiography. When used properly, current inspection regimens and nondestructive testing can detect most defects that are of concern to the bridge owners. However, they are not able to determine if the defects are actively growing or could lead to catastrophic structural failure. To help mitigate the risks, the US Army Engineer Research and Development Center (ERDC) are exploring continuous structural health monitoring (SHM) of the bridges. An array of sensors recording multiple metrics such as strain, acceleration, tilt, acoustic emissions, and electrical resistance (for corrosion monitoring) can provide a wealth of information about the bridge between regular inspections. With the knowledge derived from the SHM sensor array, bridge managers can make better informed decisions about the repair and maintenance of the bridge. Potentially, an SHM system can ensure public safety and reduce maintenance costs by making resource allocation more efficient. As a demonstration project, ERDC has selected the historic Government Bridge over the Mississippi River between Davenport, Iowa and Rock Island, Illinois.

GOVERNMENT BRIDGE

Built in 1896, Government Bridge at the Rock Island Arsenal (often referred to simply as the Arsenal Bridge) has an interesting history. The current bridge is the third built at or near the current location. Several hundred feet up stream from the Government Bridge, the Mississippi River is at its narrowest point for several hundred miles up or down stream. At this location, the first Arsenal Bridge, made of wooden trusses, was built in 1856, becoming the first bridge across the Mississippi River. Shortly after construction, a steamboat ran into one of the bridge's piers, exploded, and caused the bridge to burn down. The litigation that followed, initially with Abraham Lincoln as the defense attorney for the railroad company, created the legal precedent that bridges, if properly built, do not interfere with river traffic [1]. Though seemingly insignificant, this ruling allowed the creation of the intercontinental railroad with its first crossing of the Mississippi built at the location of the



Fig. 1 Government Bridge at the Rock Island Arsenal with Davenport, IA in the upper left (Spans are numbered from right to left)

present Government Bridge. The second Arsenal Bridge, built in 1872, was a metal seven Pratt truss structure that supported two decks with one truss that rotated to allow river traffic to continue unhindered. The lower deck was for pedestrian and carriage traffic while the upper deck carried the railroad. This arrangement was necessary so that the smoke and sparks of the steam engines would not upset the horses and oxen. Rail traffic grew in volume and weight so quickly that the second Arsenal Bridge soon became functionally deficient and



Fig. 2 Span II of the Government Bridge in its locked position to allow rail and vehicular traffic

the third and current Arsenal Bridge was built in 1896 on the piers of the 1872 bridge.

Like the second Arsenal Bridge, the Government Bridge is a multimodal transportation structure built to carry pedestrian, vehicular, and rail traffic, while allowing the free passage of river traffic below. The bridge consists of eight trusses: two Pratt trusses (one on each end), five Baltimore trusses, and a Camelback truss that can rotate around a center pivot over what is now Lock 15 of the Mississippi River lock system. These eight trusses support two decks. The upper deck spans all eight trusses and carries two sets of train tracks (though only the upriver set is used today). The lower deck now carries two lanes of traffic and two pedestrian walkways on the six middle trusses [2]. Fig. 1 shows the Government Bridge at the Rock Island Arsenal with the city of Davenport in the upper left hand side of the figure.

The ERDC has contracted the placement of strain gauges, accelerometers, acoustic emission sensors, and corrosion sensors on Span II, the swing span, of Government Bridge. Shown in Fig. 2, the swing span truss is 111.42 m (365'-7") long, 8.84 m (29') wide, and 18.90 m (62') tall at the center. The span can rotate 360° in either direction about a cylindrical chamber that supports the span at the center of the truss. The ability of the bridge to swing creates a unique opportunity for using structural health monitoring of the bridge span, because it has different boundary conditions during its two stages. When the bridge is locked in place to allow vehicular and rail traffic to pass over its lower and upper decks, respectively, the bridge span is simply supported by roller supports on the ends and resting on the cylinder at the middle of the span. During rotations, the ends of the bridge are unlocked from the roller supports and allowed to cantilever from the bridge's center.

FINITE ELEMENT MODEL

SHM requires more than just placing sensors on the bridge and storing the data produced. The data need to be processed using damage detection algorithms to locate and approximate the level of damage, if any has occurred. To investigate the effectiveness of an SHM system for the Government Bridge, a finite element (FE) model has been created to model the static and dynamic responses of the structure [2]. The Government Bridge was modeled as a three dimensional frame using MATLAB. The dimensions of the bridge members were determined using the original set of plans, in addition to sets of plans created during various repair and strengthening projects over the last century of the bridge's existence. These plans were provided by the US Army Corps of Engineers. Fig. 3 shows the FE model of the Government Bridge. In total there are 479 nodes and 1026 elements in the model.

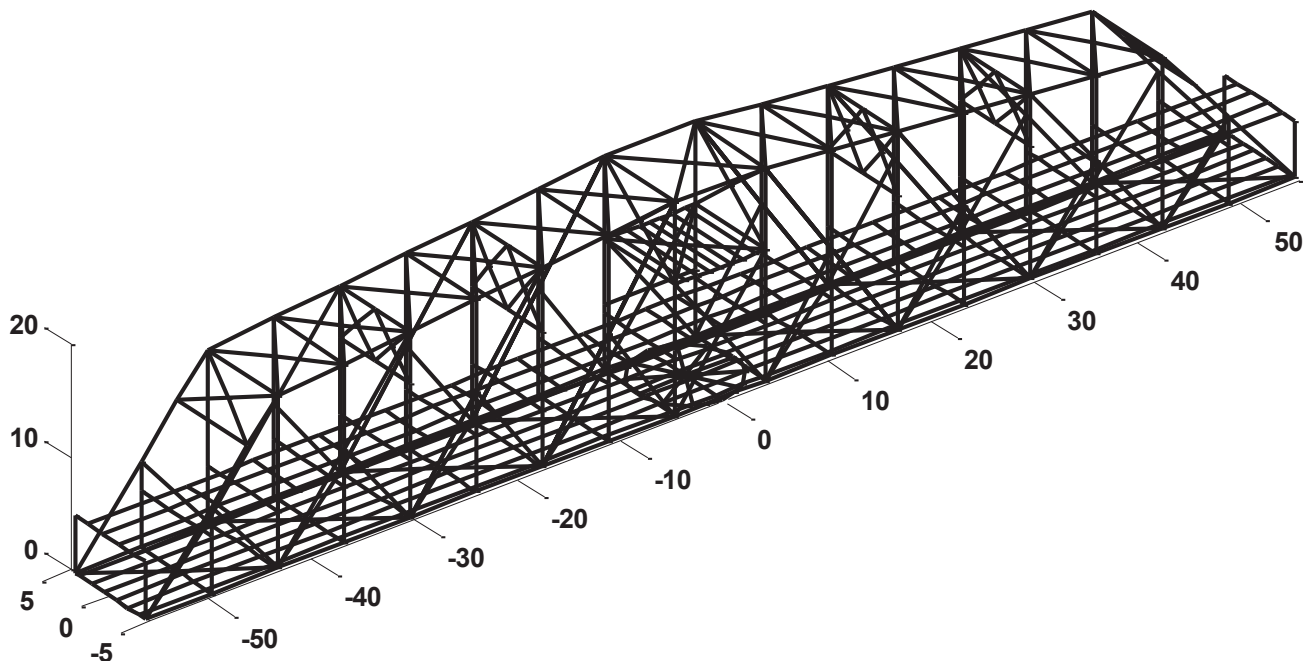


Fig. 3 MATLAB finite element model of Span II of the Government Bridge with units in meters

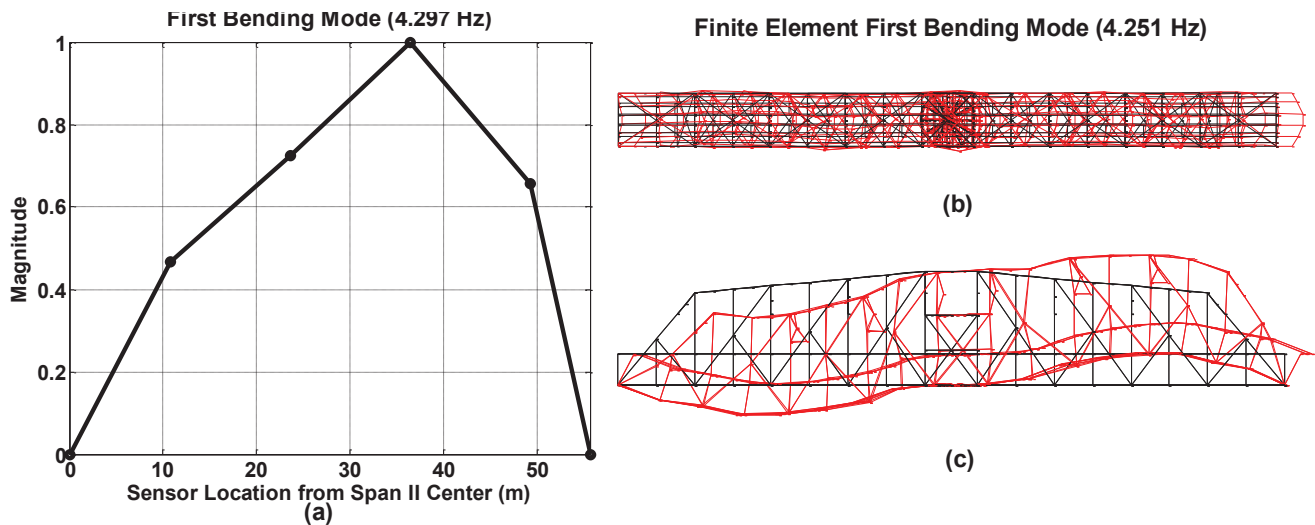


Fig. 4 (a) Experimentally determined first bending mode for right half of the bridge (b) Finite element model first bending mode overhead view (c) finite element model first bending mode planar view

To verify the model, wireless smart sensors using Intel’s Imote2 platform and software developed by the Illinois Structural Health Monitoring Project (ISHMP) [3], were temporarily installed on the bridge. The sensors measured the acceleration of the bridge at points along the bottom chord of the truss to calculate the natural frequencies of the physical structure and their respective mode shapes. The experimentally derived natural frequencies and mode shapes compared reasonably well to those calculated using the FE model. For example, the first vertical bending mode derived from the gathered data is shown in the Fig. 4(a). The experimental mode shape shown is the first vertical bending mode for only half of the bridge. Fig. 4(b) and Fig. 4(c) show the modes as calculated by the three dimensional frame MATLAB FE model.

DAMAGE LOCATING VECTOR (DLV) METHOD

Once the FE model of the Government Bridge was created, it was used to determine the effectiveness of the damage detection algorithm called the Damage Locating Vector (DLV) method. The DLV method was proposed by Bernal [4] and has been further expanded and investigated by him and many members of the Smart Structures and Technology Laboratory (SSTL) at the University of Illinois [5, 6, 7]. The essence of the DLV is that it looks for changes in the flexibility matrix between the undamaged and damaged bridge to locate members that are candidates for damage. The output of the algorithm is a number, called the damage index (DI), between 0 and 1 for every member. For an element to be a candidate damaged element, the elemental DI should be small.

For example, in the simple truss structure shown in Fig. 5(a), if element seven is damaged resulting in a loss of stiffness, the DIs plotted in Fig. 5(b) show that the DI for element seven is exactly zero. The other elemental DIs shown in Fig. 5(b) are not all exactly 1 due to the influence of the damaged element on the surrounding elements. As a rule of thumb with the DLV method, for the results to be meaningful, the element must be between two sensor nodes. In this example, sensors were simulated at all nodes so all elements produced meaningful results.

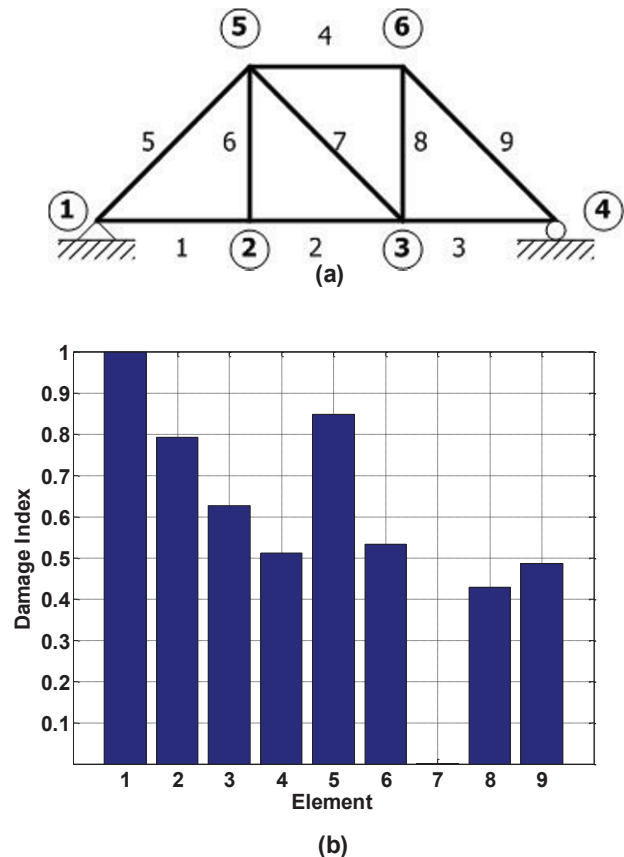


Fig. 5 (a) Simple 2D truss model with nodes and elements labeled (b) Graph of the damage indices computed using the DLV method for the truss shown where element 7 has been simulated as damaged

The previous example is a significantly less complex structure than the Government Bridge. To verify that the DLV method would still work on such a complicated structure, a damage simulation was run using the FE model of the Government Bridge. The large number of elements in the model makes graphs like those in Fig. 5(b) unwieldy. In the results of the DLV method for the Government Bridge model presented in Fig. 6, the DIs are represented as color gradients on the elements of the model. A red element is one that has a DI close to zero. The member shades change from red to purple to blue as the DI approaches one. Therefore, the redder the element, the more likely it is to be a damage candidate; and the bluer the element, the less likely the element has been damaged. Another change that has been implemented in the DLV for the Government Bridge model is that the algorithm does not use all the data available but focuses on groups of sensors [7]. Grouping sensors is important in wireless smart sensing networks to leverage the on-board computing capability of the sensors, making communication more efficient and consuming less power. Therefore, the elements that fall out of the sensor group have been grayed out because that sensor group does not provide meaningful information about those elements.

To simulate corrosion damage in the model, the stiffness of the element was reduced by a given amount. To test the effectiveness of the method, the number of members damaged and the location of the damaged members were varied. An ideal damage detection algorithm should be able to detect multiple damages in all critical members of the structure.

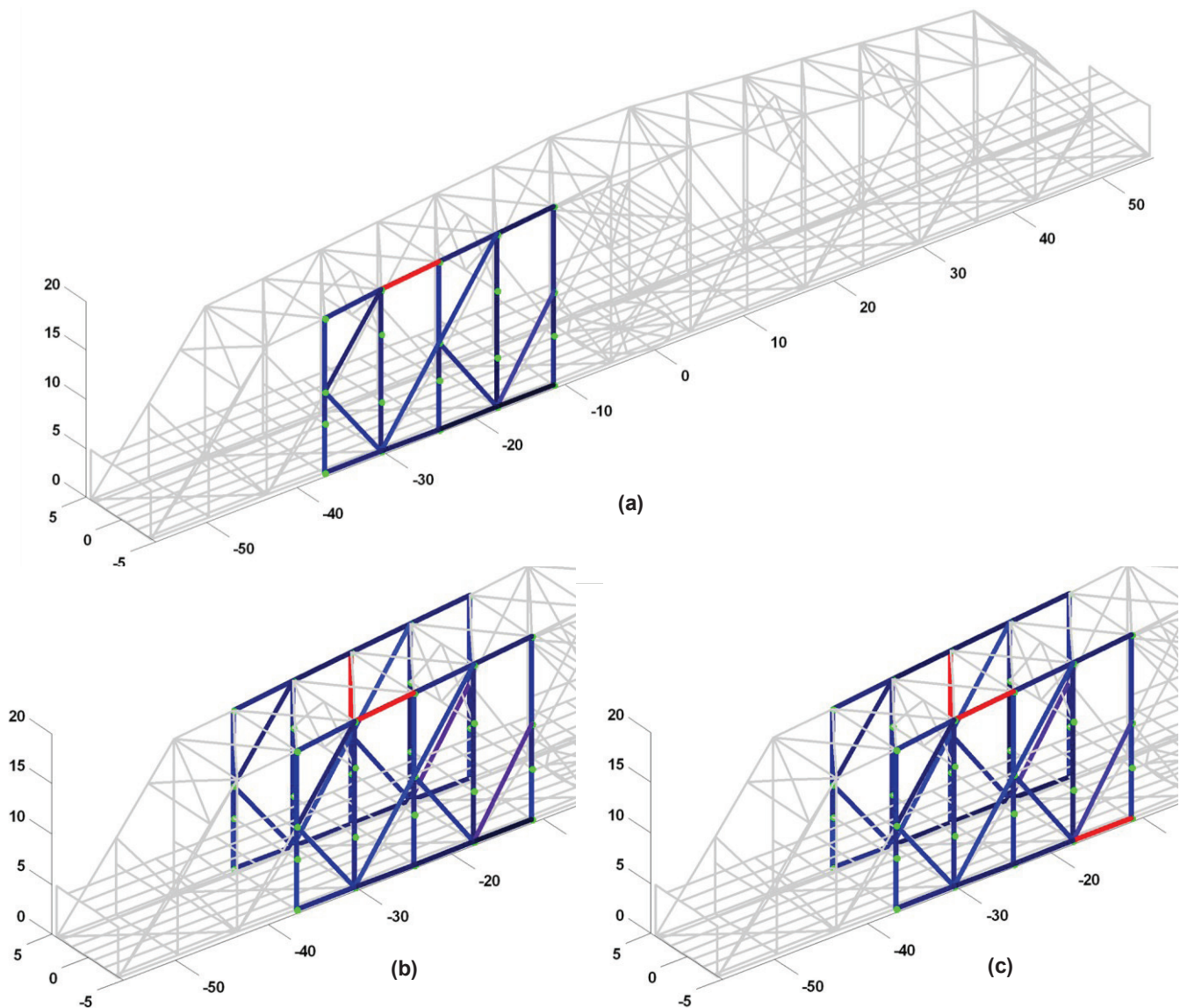


Fig. 6 Damage Index for elements included in measured group such that a red element are damaged elements, blue elements are undamaged elements, grey elements are unmeasured elements, and the green dots indicate the sensor locations for the following cases: (a) 10% reduction in one element and measured on one plane of the truss (b) 5% reduction in two elements on opposite planes of the truss and measured on both planes and (c) 5% reduction in three elements and measured on both planes of the truss

Fig. 6 shows a sampling of the results from the number of damage scenarios that were tested. Fig. 6(a) shows the results of a 10% reduction in the stiffness of a single member of the upper chord located using a simulated sensor group that is only on one side of the truss. The damaged element is clearly visible in red while the other members are various shades of blue. Fig. 6(b) shows the results of two damaged members with a 5% reduction in stiffness on opposite sides of the truss when the sensor group encompasses both sides of the truss. Once again, the damaged elements are shown in red and easily identified as the candidate damaged elements. Fig. 6(c) shows the results of the DLV method for three members with a 5% reduction in stiffness in different parts of both sides of the truss with the sensor group again including both sides of the truss. The three damaged elements in this example are harder to distinguish as they are not as pure red as in the previous figures. The decrease in the level of damage and the increase in the number of damaged elements have made them harder to detect and distinguish from the undamaged elements. However, overall the DLV method shows potential for use on the Government Bridge.

Experimental DLV Implementation

The implementation of the DLV for the tests of the FE model discussed in the previous section used the analytical flexibility matrix of the model structure. In an implementation of the DLV method on the Government Bridge, the exact flexibility matrix of the structure will not be known, but an approximation will need to be determined using system identification methods. To test the capability of the DLV method to detect corrosion in an existing structure, experimental tests were performed on a 14 bay three dimensional truss structure at the SSTL at the University of Illinois at Urbana-Champaign. This structure was designed for SHM testing and consists of members made of three lengths of bars, the different colored bars in Fig. 7, which can easily be removed from the structure and replaced with bars of varying cross-sectional or material properties. A Ling Dynamic System V408 actuator applying a band limited white noise is used to excite the structure.

In the experiment, the truss with bars that had equal cross-sectional and material properties was used. Damage was simulated in the truss by installing corroded bars in place of the normal truss members. The corroded bars were created by placing steel bars of the same size and properties of the normal colored bars into a salt fog tank at EDRC's Civil Engineering Research Laboratory (CERL). The salt fog tank is shown in Fig. 9(b). Every two weeks, the bars were removed from the tank, and the corrosion was removed with a wire brush so as to only remove the oxidized metal before replacing them back in the salt fog tank. Fig. 9(a) shows the bars after completing a two week cycle in the salt bath. Fig. 9(c) shows a close up of the truss elements after the oxidized material has been removed once the bars have reached approximately 18% weight loss. The pitting and texture caused by the corrosion process could not be duplicated through machining processes. The bars were weighed before the corrosion process began and after every cleaning. Typical percent weight loss for the members for every two week cycle was between 1% and 2% of the original weight. Multiple bars were corroded, and when the bars reached predetermined levels of corrosion, typically multiples of 5%, they were permanently removed from the salt fog tank and prepared for testing. Table 1 shows the progression of weight loss for a typical set of truss members. All the cycles in the table are two week periods except for the first two which are approximately eight and four weeks, respectively.

Table 1 - Cumulative Percent Weight Loss after Each Cycle in the Salt Bath

Cycle	Yellow Member	Blue Member	Red Member
1	6.31%	6.24%	5.95%
2	9.38%	8.45%	9.04%
3	10.77%	9.62%	9.47%
4	11.48%	10.35%	10.31%
5	13.38%	11.76%	12.05%
6	14.54%	12.96%	13.29%
7	17.61%	14.33%	14.74%
8	18.28%	16.17%	16.95%
9	19.44%	17.24%	18.04%
10	20.78%	18.58%	19.53%



Fig. 7 Experimental truss with removable members in the Smart Structures Technology Laboratory at the University of Illinois

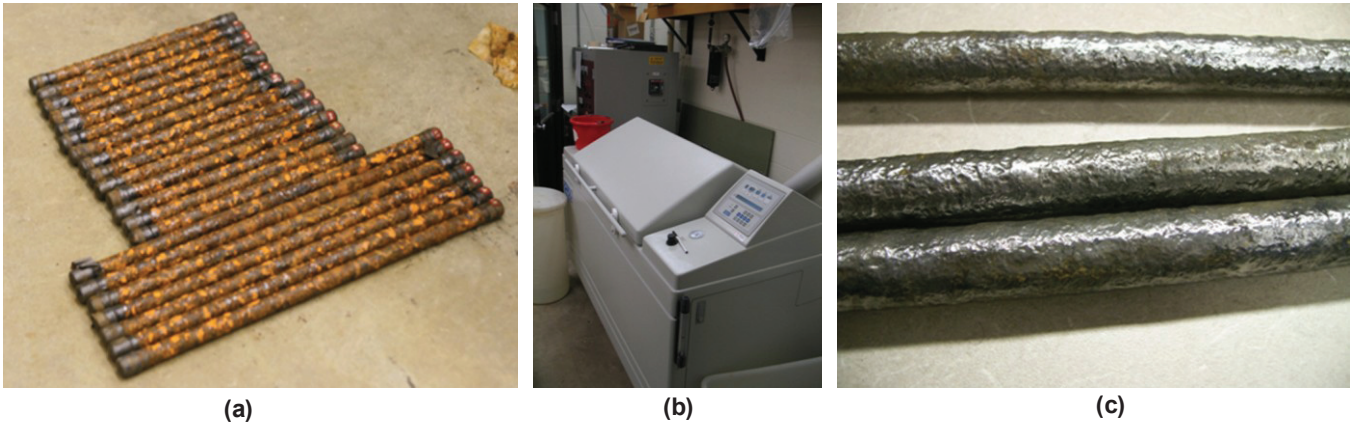


Fig. 9 (a) Experimental truss members after completing a corrosion cycle in the salt bath before being the corroded material is removed with a wire brush (b) CERL salt fog bath (c) close up of experimental truss members after having corroded material removed with a wire brush after the ninth corrosion cycle

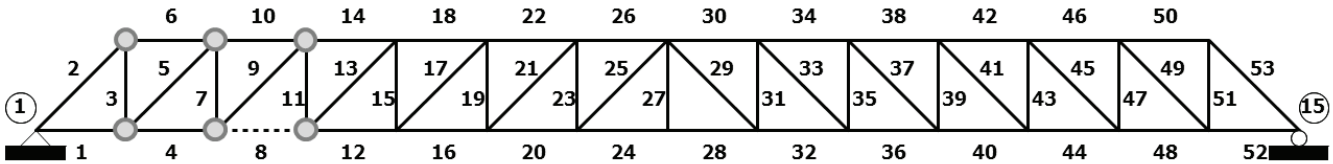


Fig. 8 Two dimensional representation of the SSTL experimental truss shown in Fig. 7 where the elements have been numbered and gray dots represent the sensor locations used in the experiment while the dotted line represents the truss element removed and replaced with a corroded element during testing

The experiments to determine the effectiveness of the DLV method to properly identify the damaged element were conducted with the amount of corrosion and the position of the corroded members as variables. Fig. 8 shows a typical experimental setup where just one member was damaged. Member 8, as noted by the dotted line, is the truss element that is replaced with a corroded element to form the damaged truss. The gray dots indicate the sensors used so the DLV will only give meaningful data for elements 3 through 11 as they have sensors on both ends. Acceleration data was recorded using PCB 353B33 piezoelectric high sensitivity accelerometers using a VibPilot vibration controller and dynamic signal analyzer. The data was then processed using system identification techniques to derive the experimental damaged and undamaged flexibility matrices. Then, the DIs for the members were calculated using the DLV method. All the calculations were performed using MATLAB.

For the setup shown in Fig. 8, where member 8 has been corroded such that the weight loss is 20%, the DLV method was still able to identify the corroded member as the most likely damaged element. Fig. 10 shows the graph of the DIs for the members that have sensors on both nodes. In the previous example shown in Fig. 6, the candidate damaged element had a DI of zero. In the experiment, the data noise and approximations used to compute the flexibility matrix of the truss cause the DI for element 8 to be nonzero. Similarly, having multiple damage sites and smaller amounts of corrosion made the damaged elements in the numerical full bridge example shown in Fig. 6(c) purple instead of red indicating

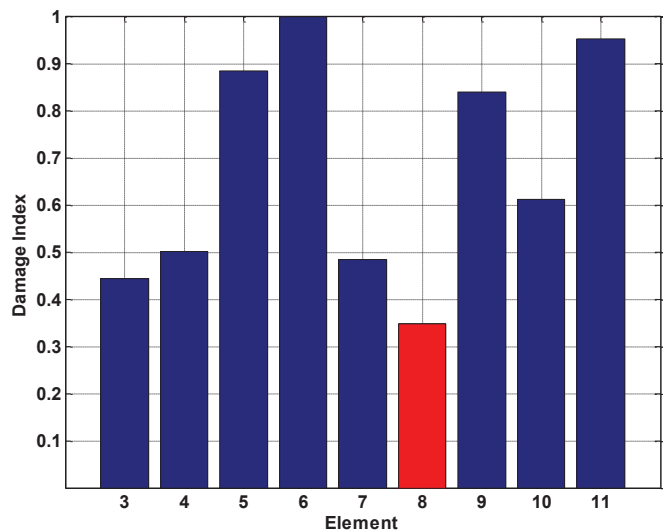


Fig. 10 Damage indexes computed using the DLV method when element 8 has been replaced with a member with 20% weight loss

the DIs of the damaged elements had also become nonzero. However, the DLV method is capable of identifying the most likely damaged element since the DI for element 8 in the experimental results is still the lowest of the DIs in Fig. 10.

Future experiments will continue to look at the effectiveness of the DLV, and its variants, in detecting damage due to corrosion in steel truss members. Once the understanding of how the levels and locations of corrosion damage are understood, the damage indices calculated using the DLV method will be correlated with the element rating system used by the American Association of State Highway and Transportation Officials (AASHTO) [8]. This will aid the bridge inspectors and owners in better understanding the structural health of the bridge and help them to make better decisions about the allowable loads and maintenance.

CONCLUSIONS

Continuing to use and maintain the nation's aging steel bridge inventory makes sense in terms of economics, sustainability, and history. Nevertheless, the safety of the public and the strategic benefits of the Army's steel bridges are paramount goals. A continuously monitored structural health monitoring system can help owners of steel bridges achieve their goals. Implementing a SHM system that takes multimetric data and processes it into useful conclusions using damage detection algorithms has the potential to extend the functional life of the structure and focus limited maintenance funds where they are most needed. This paper has shown that the implementation of a SHM system that uses the Damage Locating Vector method on a historic steel bridge over the Mississippi River is possible. The encouraging results of the numerical and experimental studies have shown the potential of the method. The limitations of this, and any other damage detection algorithm, must be understood, but compensating for the limitations using other techniques in concert with the DLV could help lessen the difference between the results obtained purely numerically and those obtained experimentally.

REFERENCES

- 1) Dirk, Brian. *Lincoln the Lawyer*. Urbana, IL: University of Illinois Press. 2007.
- 2) Hsiao, C.R., *Baseline Finite Element Modeling of Government Bridge* (Master's Thesis). University of Illinois at Urbana-Champaign, Urbana, IL (2009).
- 3) Rice, J. A. and Spencer Jr., B. F., "Flexible Smart Sensor Framework for Autonomous Full-scale Structural Health Monitoring," *NSEL Report*, No. 18, University of Illinois at Urbana-Champaign. 2009. <<http://hdl.handle.net/2142/13635>>.
- 4) Bernal, D., "Load Vectors for Damage Localization." *J. Engrg. Mech.* Volume 128, Issue 1, pp. 7-14 (January 2002)
- 5) Gao, Y. Spencer, B.F. Jr., and Bernal, D. "Experimental Verification of the Flexibility-Based Damage Locating Vector Method." *Journal of Engineering Mechanics*, Vol. 133, No. 10, October 2007, pp. 1043-1049
- 6) Jang, S.A., S.-H. Sim, and B.F. Spencer Jr. "Structural Damage Detection Using Static Strain Data," *Proc. of the World Forum on Smart Materials and Smart Structures Technology (SMSST'07)*. Leiden: Taylor & Francis. 2008.
- 7) Gao, Y. and Spencer Jr., B.F. "Structural Health Monitoring Strategies for Smart Sensor Networks," *NSEL Report*, No. 11, University of Illinois at Urbana-Champaign, 2008, <<http://hdl.handle.net/2142/8802>>.
- 8) Thompson, Paul D. & Richard W. Shepard. "AASHTO Commonly-Recognized Bridge Elements: Successful Applications and Lessons Learned". June 2000. <<http://www.pdth.com/images/coreelem.pdf>>